

International Symposium on
Wear Resistant Alloys
for the Mining and Processing Industry

International Symposium on Wear Resistant Alloys for the Mining and Processing Industry

Proceedings of the International Symposium on Wear Resistant Alloys for the Mining and Processing Industry. Held in Campinas, São Paulo, Brazil, 4 - 7 May 2015.

Editor-in-Chief

Hardy Mohrbacher, NiobelCon, Belgium

International Editorial Committee

Hardy Mohrbacher, NiobelCon, Belgium

Clovis Antonio de Faria Sousa, CBMM, Brazil

George Krauss, Colorado School of Mines, USA

Mathias Woydt, BAM Federal Institute for Materials Research and Testing, Germany

Mariana Perez de Oliveira, CBMM, Brazil

International Organizing Committee

Hardy Mohrbacher, NiobelCon, Belgium

Pascoal Bordignon, CBMM, Brazil

Mathias Woydt, BAM Federal Institute for Materials Research and Testing, Germany

Mariana Perez de Oliveira, CBMM, Brazil

Jef Vleugels, KU Leuven, Belgium



**Copyright © 2018 Companhia Brasileira de Metalurgia e Mineração
(CBMM)**

All rights reserved

Published by CBMM

Production work by The Minerals, Metals & Materials Society (TMS)

Editorial support provided by Beta Technology Ltd, UK

No part of this publication may be reproduced, stored in a retrieval system, or transmitted in any form or by any means - electronic, mechanical, photocopying, recording, scanning, or otherwise, except as permitted under Section 107 or 108 of the 1976 United States Copyright Act, without the prior written permission of CBMM.

Limit of Liability/Disclaimer of Warranty: While the publisher and author have used their best efforts in preparing this book, they make no representations or warranties with respect to the accuracy or completeness of the contents of this book and specifically disclaim any implied warranties of merchantability or fitness for a particular purpose. No warranty may be created or extended by sales representatives or written sales materials. The advice and strategies contained herein may not be suitable for your situation. You should consult with a professional where appropriate. Neither the publisher nor author shall be liable for any loss of profit or any other commercial damages, including but not limited to special, incidental, consequential, or other damages.

ISBN 978-0-692-05382-9

Printed in the United States of America.



TABLE OF CONTENTS

International Symposium on Wear Resistant Alloys for the Mining and Processing Industry

| | |
|---|-----|
| Preface | ix |
| Companhia Brasileira de Metalurgia e Mineração (CBMM) | xi |
| Opportunities for Ferrous Alloys Used in Copper Mining | 1 |
| <i>V. Pérez and D. Villaseca</i> | |
| From Monometallic to Composites and Ceramic Wear Resistant Materials: An Industrial Challenge | 19 |
| <i>H. François and M. Bonnevie</i> | |
| Development and Application of Advanced High-Strength Steels in Lightweight Cars for Heavy-Duty Mining Dump Trucks..... | 47 |
| <i>Linhao Gu, Zhenqiang Wang, Changwen Ma, Deguang Zhou, Yongqing Zhang and Aimin Guo</i> | |
| Collaboration to Reduce Wear and Corrosion Cost for the Mining Industry | 67 |
| <i>S. Hui</i> | |
| Increasing the Life Cycle of Buckets for Wheel Loaders Using High Strength and Abrasion Resistant Steels Microalloyed with Niobium | 75 |
| <i>H. Rosa, M.K. Ferreira Cardoso, É. França, J.L. Barreto, L.M. Silvestre and M.A. Stuart Nogueira</i> | |
| Fundamentals and Practical Approaches of Optimizing Martensitic Steels for Use under Severe Operating Conditions | 93 |
| <i>H. Mohrbacher, J.W. Morris and G. Krauss</i> | |
| High Performance Steels for Wear Applications | 159 |
| <i>A. Dietrich, A. Canpolat, A. Kern and H-J. Tschersich</i> | |
| The Role of Niobium for the Development of Wear Resistant Steels with Superior Toughness | 173 |
| <i>A.S. Schneider, J.L. Cayla, C. Just and V. Schwinn</i> | |
| High Performance Abrasion Resistant Steel Plates Using Microalloying Technology for Grain Refinement | 187 |
| <i>N. Takayama, A. Ohmori, Y. Murota and K. Araki</i> | |
| Wear- and Corrosion-Resistant Steels Containing Niobium Carbide | 197 |
| <i>M. Seifert, S. Huth, S. Siebert and W. Theisen</i> | |

| | |
|---|-----|
| Modern Pre-Hardened Tool Steels..... | 223 |
| <i>P. Hansson</i> | |
| Development of Nb-Bearing Heavy Steel Plates with Ultra High Strength and Excellent Toughness | 235 |
| <i>Zhao Sixin, Ding Jianhua, Yao Liandeng, Zhang Yongqing and Guo Aimin</i> | |
| Abrasion Resistant Metallic Alloys for the Mining Industry | 253 |
| <i>E. Albertin and A. Sinatora</i> | |
| Effects of Niobium Additions on the Properties and Life Cycle of Steels for Hot Working Tools | 277 |
| <i>F. Hippenstiel</i> | |
| The Challenge of Accurate Prediction of Industrial Wear Performance from Laboratory Tests | 289 |
| <i>J.D. Gates, P.J. Bennet, L.J. McInnes and B.R. Tunstall</i> | |
| Optimized Gear Performance by Alloy Modification of Carburizing Steels for Application in Large Gear Boxes | 351 |
| <i>Th. Tobie, F. Hippenstiel and H. Mohrbacher</i> | |
| Cutter Rings with Non-Uniform Niobium Carbide Distribution for Tunnel Boring | 385 |
| <i>B. Feistritzer</i> | |
| Influence of Niobium on the Microstructure and Properties of CrMo Cast Steel for Liner Plate | 393 |
| <i>Xiangru Chen, Ming You, Aimin Guo, Wei Zhang, Hiacheng Li, Yang Xu and Qijie Zhai</i> | |
| Development of FeNbC for Wear Resistant Applications | 407 |
| <i>E.B. Cruz and D.P. Fridman</i> | |
| The Tribological Property Profile of Hard Metals and Metal Matrix Composites Based on Niobium Carbide | 427 |
| <i>M. Woydt and H. Mohrbacher</i> | |
| Application of FeNbC as a Hardfacing Material Using Laser Cladding | 463 |
| <i>E.T. Galvani, S. Simões, C.H.N. Banov, H.L. Rosa and E.B. Cruz</i> | |
| Mechanical Characterization of Hard Phases by Means of Nanoindentation | 487 |
| <i>F. Pöhl, A. Weddeling and W. Theisen</i> | |

| | |
|---|-----|
| Formation of Niobium Carbide Coating on AISI L2 Steel Using Thermo-Reactive Diffusion (TRD) Technique | 505 |
| <i>M. Azizi and M. Soltanieh</i> | |
| NbC-Based Cermets: Influence of Secondary Carbide Addition and Metal Binder | 521 |
| <i>S.G. Huang, J. Vleugels, H. Mohrbacher and M. Woydt</i> | |
| Comparison of the Life-Span of NbC-Co and WC-Co Inserts during Different Machining Operations on 100Cr6 (SAE 52100) Bearing Steel | 535 |
| <i>G. Le Quilliec, R. Leroy, C. Richard, M. Woydt and A. Morandea</i> | |
| Wear and Mechanical Properties of Spark Plasma and Liquid Phase Sintered WC And NbC Based Cemented Carbide Inserts | 547 |
| <i>R.M. Genga, L.A. Cornish, M. Woydt, K. Sobiya and C. Polese</i> | |
| Common Acronyms and Abbreviations | 569 |
| Author Index | 581 |
| Subject Index | 583 |

A DVD containing the papers presented and videos summarizing the main technical conclusions, along with interviews with the hosts and selected speakers from the symposium, can be found at the back of this publication.

Preface

Wear is by no means the highest profile area of materials research and technological focus, but there can be no doubt that it ought to command our utmost attention. There have been continuous investments and studies on wear mechanisms, as the losses associated with its complex and varied damaging mechanisms have severe economic consequences through direct replacement costs, machine downtime and lost production. The challenges of wear are significant across a broad range of mechanical processing operations, some of which are carried out at elevated temperatures, and include crushing, drilling, conveying, mixing and separating. Although of immediate interest to the mining sector, other industries such as iron and steel production, cement manufacturing, power generation, recycling and environmental protection are also of significance in this context.

Over 40 years ago a major international symposium took place in Colorado, USA, that highlighted the importance of wear on materials and its impact on the industry. It is surprising to note that since then there have been few international events focused on this topic. Abrasive wear is the dominant issue and this is caused by the materials being handled, which include mineral species like silica sand, granite, metal ores and coal. Conveyors, ball mills, drills, chutes and dumper truck bodies are examples of equipment which can be exposed to abrasive wear when handling such materials. The classic engineer's rule of thumb states that "*the harder the material, the better the resistance against abrasive wear*". However, research has indicated that abrasive wear resistance not only correlates with hardness, but also with toughness. Consequently, substantial efforts have been made over recent decades to optimize steel and iron-based alloys to better withstand these harsh conditions and thus extend the life of equipment and components.

Since niobium is one of the key alloying elements that can be used to upgrade the functional profile of steels and irons against abrasive wear, Companhia Brasileira de Metalurgia e Mineração (CBMM), the world's premier supplier of niobium and niobium applications technology, believed it was timely to host a long overdue international symposium focusing on wear resistance. Accordingly, "Wear Resistant Alloys for the Mining and Processing Industry" was held during May 2015 in Campinas, São Paulo, Brazil.

Attended by over 170 delegates from around the world, expert speakers from the entire supply chain shared their experiences and this publication brings together a selection of papers presented at the symposium on topics such as abrasion-resistant high strength steels, forgings, castings, hard facing alternatives and intrinsically hard metals. In essence, the symposium provided a significant range of practical solutions and identified future opportunities for the efficient development of improved alloys for the mining and processing industry. These proceedings summarize the wealth of knowledge presented during the symposium and provide additional background information. The symposium stimulated a long overdue technical debate and showcased recent advances in the state of the art in wear resistant alloys. Let us hope the mining industry will not neglect this important subject for another 40 years!

The International Editorial Committee

Companhia Brasileira de Metalurgia e Mineração (CBMM)

CBMM is the world's leading supplier of niobium products and technology. The Brazilian company earned this market position through more than four strong decades of ongoing investment in processes and applications research across a wide spectrum of important end uses.

The company's goals are not only to satisfy the worldwide niobium demand in the form of ferroalloys, oxides and pure metal, but also to provide a framework of technological development with the objective of improving efficiency and performance, while adding value to products and supply chains.

CBMM is guided by a strategy of sustainable growth that is always conscious of energy savings, cost reductions and environmental protection. Even though the company's mineral resources are unrivaled in quantity and quality, CBMM constantly strives to improve the flexibility and efficiency of operations. The same approach is deployed to enhance the value that the effective, efficient use of the element can deliver to customers.

The company's niobium research and development program employs a strong technical group to develop niobium applications. This group works with industry, universities, research institutes and end users on diverse projects around the world, and pursues new partnerships to explore and optimize the use of niobium.

This symposium is another example of CBMM's commitment to continually improve materials, always striving for the best product.

Marcos Stuart
Director of Technology
CBMM

OPPORTUNITIES FOR FERROUS ALLOYS USED IN COPPER MINING

V. Pérez and D. Villaseca

Corporación Nacional del Cobre (CODELCO), Chile

Keywords: Copper Mining, Ferrous Alloys, Grinding Balls, Liners, SAG Mills, Molybdenum, Cost Saving, Wear Rates

Abstract

A study of ferrous alloys used in the Chilean mining industry was conducted in order to determine potential opportunities for the development and introduction of new ferrous alloys where benefits far outweigh cost increases. Two criteria were defined for determining the alloys of interest: demand for the alloy reaches at least 15,000 tonnes per year within the Chilean copper mining industry, and improving the alloy properties would have a positive economic impact and therefore be of interest to other mining companies.

The copper production chain was examined to identify at which points conditions caused impact and abrasion wear, and where chemically aggressive conditions existed that could cause corrosion. As a result of this analysis, it was concluded that grinding balls and SAG mill liners constitute interesting opportunities. In the case of grinding balls, it is the second greatest expense of a concentrator plant, after energy. The estimated consumption by the Chilean copper mining industry is 445,000 tonnes of steel per year. Given the large volume involved, there is a significant direct economic benefit to users if the consumption of grinding balls is reduced. Based on treatment of 50 million tonnes of ore per year, it is estimated that improved alloy properties, sufficient to reduce ball consumption in the copper mining industry by at least 10%, would, even with an increase in alloy cost of 4%, produce savings of approximately US\$1.56 million per year.

In the case of SAG mill liners, achieving an increase in liner service life is important, since downtimes of SAG mills have a direct impact on final production and thus on sales. It was estimated that, for plants treating 50 million tonnes of ore per year (estimated three SAG mills), the benefit stemming from a 5% increase in liner duration would be US\$2.62 million per year, per plant.

Introduction

In analyzing an appropriate context in which to introduce new or improved ferrous alloy products, the Chilean mining industry emerges as an attractive area within which to seek opportunities. Given its great size, the fact that it is a completely globalized industry and that it is a world leader in copper mining, all potential innovations should have an impact both locally and globally.

This study aims to determine the types of steel (ferrous alloys in general) in greatest demand within the Chilean mining industry, and to evaluate the potential opportunities to introduce improved steel and/or iron products.

Identification was made of those points in the copper production cycle (from extraction to finished product) where it was estimated there is a high tonnage use of ferrous alloys. This preliminary evaluation was based on the experience of the investigators, secondary data sources, rates of consumption, direct inquiry with suppliers, etc.

During visits to mines, the preliminary critical point assessments were compared to the on-site users' assessments of consumption volumes and the impact that an improvement in the performance of the iron and steel involved would have.

The analysis that yielded the definitive critical points in the process was carried out using the information gathered from visits, available secondary sources, contacts and visits to suppliers, ongoing professional contacts with mining professionals, consultations with mining experts, etc. These critical points were evaluated from the standpoint of annual consumption and impact on the client's business.

Identification and Analysis of Preliminary Critical Points

The largest consumption of steel in copper mining occurs at those points where high abrasion and/or impact and/or pressure stresses occur. These conditions exist, to a greater or lesser extent, for all equipment that comes into contact with mined material from the drilling stage onwards.

After identifying these points, the next step was to estimate annual ferrous alloy consumption at each critical point to determine whether it met the established baseline consumption criterion of 15,000 tonnes per year. Table I is a summary of the preliminary critical process points identified.

Drilling

During the drilling process, the drilling components that are subject to the greatest stresses, and thus have higher consumption rates, are tricones and drill bits, adapters and extension bars. The steels used in these components are structural and specialized tool steels (SAE 4340, 4140, 4130, etc.).

Based on information gathered from visits to the main suppliers in Chile, (Drillco, Atlas Copco and Sandvik), national consumption of these components does not exceed 6,000 tonnes/year. This consumption level was corroborated by information from the mining companies visited.

Table I. Preliminary Critical Process Points, their Characteristics and Estimate of Annual Consumption

| Critical points (process) | Component | Equipment | Alloy | Microstructure | Estimated steel consumption (tonne/year) |
|---------------------------------|---------------------------|------------------------------------|--|----------------|--|
| Drilling | Tricone/drill bit | Drill | Low-alloy steel (4340-4140-4130-3310-3315) | Various | <6,000 |
| | Adapter | | | | |
| | Bar | | | | |
| Loading | Wear protections | Rope shovel | Low-alloy steel | Martensitic | 9,080 |
| | | Bulldozer | | | |
| | | Wheeldozer | | | |
| | | Front-end loader | | | |
| | Crawler shoes | Rope shovel | Low-alloy steel | Austenitic | 530 |
| | | | Mn steel | | 3,000 |
| Transport and Haulage | Anti-wear plates | Truck-hopper, chutes, etc. | Low-alloy steel | Martensitic | NA |
| Primary crushing | Concaves and mantles | Primary crusher | Mn steel | Austenitic | 2,360 |
| | | | Cr-Mo steel (concaves) | Martensitic | 650 |
| Secondary and Tertiary crushing | Mantle and concave | Cone crusher | Mn steel | Austenitic | 6,800 |
| SAG grinding | Liners | SAG mill | Cr-Mo steel | Pearlitic | 20,500 |
| | Balls | | Low-alloy Cr steel | Martensitic | 167,000 |
| Ball grinding | Liners | Ball grinder mill | High Cr white iron | Martensitic | 7,520 |
| | | | Cr-Mo steel | Pearlitic | 3,500 |
| | | | Low-alloy Cr steel (forged) | Martensitic | 278,000 |
| | Low-alloy Cr steel (cast) | | | | |
| Pumping | Volutes | Slurry pump | High Cr white iron | Martensitic | 2,600 |
| | Feeding plates | | | | |
| | Impellers | | | | |
| Transport | Anti-wear plates | Conveyor belt, chute, feeder, etc. | Low-alloy steel | Martensitic | NA |
| Electrowinning | Cathode | Electrowinning cell | 316L | Austenitic | 1,600 |

NA – Not Available

Loading

In the loading category, the anti-wear elements utilized in shovels, bulldozers, wheel loaders, front loaders, etc. are, for the most part, associated with low-alloy cast steel parts used to protect buckets and dozers attached to the equipment. The parts are mainly teeth, tooth adapters, lateral shields, blades, rippers, etc.

It is estimated that 20% of these components are forged (mainly tips and adapters) or fabricated from plates of 500 HB hardness (mainly blades and rippers). These types of parts have a wear-consumption rate of 3.2 grams of steel for each tonne of material moved. Assuming a total of 810,592,000 tonnes per year of ore processed and a sterile-ore ratio of 2.5:1, the total tonnage moved in the open pit copper mines would be 2,837,072,000 tonnes per year. This figure, multiplied by the material loss rate of 3.2 grams per tonne, yields an approximate consumption of 9,080 tonnes per year for these types of alloys.

This consumption figure was confirmed by comparison with information gathered from field visits.

Primary Crushing

This process point mainly focuses on rotary crusher concaves and mantles which are the types primarily used in large-scale copper mining. Manganese steel consumption is low at around 2,300 tonnes per year.

SAG (Semi-Autogenous Grinding)

SAG mills generate significant consumption of grinding balls and liners which is proportional to the tonnage treated in the mills. Table II shows the tonnage of ore treated per plant in the large-scale Chilean copper mining industry. This point will be discussed in detail in later sections.

Ball Grinding

In ball grinding, as well as SAG grinding, significant consumption of the relevant balls occurs and this point will be analyzed further in the subsequent stages of this study.

In the case of high-chrome white iron liners, consumption amounts to 7,520 tonnes annually. This was calculated based on the total tonnage passed through ball-grinder mills at concentrator plants in the mining sector, 522,133,000 tonnes per year, multiplied by the wear rate of 12 g/tonne and adding 20% to cover vertical mills, medium and small mining mills and mainly, gold and iron treatment mills. This tonnage, combined with the 3,000 tonnes/year estimated as the consumption of slurry pump replacement parts, does not reach the minimum value of 15,000 tonnes per year set as the required minimum for further consideration.

Table II. Ore Treated per Plant in Large-Scale Chilean Copper Mining

| Plant | | Ore treated | | | |
|-------------------------|-------------------------|----------------------|--------------------------------|-----------------------|------------------------------|
| | | Total (tonne/day) | Per SAG mill (tonne/day) | Total (tonne/year) | Per SAG mill (tonne/year) |
| Concentrated Ore Plants | Minera Escondida | 225,000 | 225,000 | 82,125,000 | 82,125,000 |
| | Los Pelambres | 180,000 | 180,000 | 65,700,000 | 65,700,000 |
| | Codelco Norte | 171,000 | 60,000 | 62,415,000 | 21,900,000 |
| | Collahuasi | 140,000 | 140,000 | 51,100,000 | 51,100,000 |
| | El Teniente | 123,000 | 85,000 | 44,895,000 | 31,025,000 |
| | Caserones | 100,000 | 100,000 | 36,500,000 | 36,500,000 |
| | Esperanza | 98,000 | 98,000 | 35,770,000 | 35,770,000 |
| | Andina | 95,000 | 36,000 | 34,675,000 | 13,140,000 |
| | Candelaria | 75,000 | 75,000 | 27,375,000 | 27,375,000 |
| | Los Bronces | 56,000 | 56,000 | 20,440,000 | 20,440,000 |
| | Carmen de Andacollo | 55,000 | 55,000 | 20,075,000 | 20,075,000 |
| | División Ministro Hales | 50,000 | 50,000 | 18,250,000 | 18,250,000 |
| | El Salvador | 33,500 | | 12,227,500 | |
| | El Soldado | 18,000 | 18,000 | 6,570,000 | 6,570,000 |
| Mantos Blancos | 11,000 | | 4,015,000 | | |
| Oxidized Ore Plants | Radomiro Tomic | 160,000 | | 58,400,000 | |
| | Gabriela Mistral | 130,000 | | 47,450,000 | |
| | El Abra | 114,000 | | 41,610,000 | |
| | Spence | 55,000 | | 20,075,000 | |
| | Zaldivar | 55,000 | | 20,075,000 | |
| | Minera Escondida | 55,000 | | 20,075,000 | |
| | Cerro Colorado | 48,000 | | 17,520,000 | |
| | Lomas Bayas | 36,000 | | 13,140,000 | |
| | El Tesoro | 26,000 | | 9,490,000 | |
| | Manto Verde | 25,000 | | 9,125,000 | |
| | Quebrada Blanca | 21,000 | | 7,665,000 | |
| | Codelco Norte Mina Sur | 19,000 | | 6,935,000 | |
| | Doña Inés de Collahuasi | 17,300 | | 6,314,500 | |
| | Minera Michilla | 16,000 | | 5,840,000 | |
| Mantos Blancos | 13,000 | | 4,745,000 | | |

Slurry Pumping

Large-sized slurry pumps use high-chromium white iron replacement parts, alloys similar to those used in ball-grinder mill liners. Based on contact with personnel from Weir Minerals Chile, the leading national provider of slurry pumps, the consumption of high-chromium white iron pump replacement parts was estimated at 2,600 tonnes/year.

The estimate takes into account the existence of 50 large-sized slurry pumps, with an impeller (the main wearing part) lifespan of 3 months on average. This means an annual consumption of 200 impellers for these pumps, with an approximate weight of 7 tonnes/impeller. These large-sized pumps would thus generate a consumption of 1,400 tonnes/year. To this is added 400 tonnes for consumption of volutes. It is considered that this amount represents 70% of the total national consumption of slurry pump parts, so the overall total is estimated at approximately 2,600 tonnes/year.

Secondary and Tertiary Crushing

During the steps of secondary and tertiary crushing, manganese steel is consumed as the main alloy used to manufacture crusher mantles and concaves. Additionally, manganese steel is also consumed in the primary crushing stage and the loading stage, as the alloy is used in the manufacture of shovel crawler shoes. Accounting for these applications, the total sum for manganese steel consumption reaches 12,160 tonnes per year, which is insufficient to be considered for further analysis.

Electrowinning (EW)

In the electrowinning process, permanent cathodes of stainless steel grade AISI 316L are used. Based on information from available technical literature [1] and corroborated by contacts in the mining industry, it was established that in Chile there are 350,000 operating cathodes, each with an average lifespan of six years. This would generate a replacement consumption of approximately 58,000 cathodes per year. The weight of each cathode is 28 kg, generating an annual consumption of approximately 1,600 tonnes, which is far below that required for further analysis in the current study.

Transport

Ore transport is required at all stages of copper mining extraction and comminution, and each phase, to a greater or lesser extent, has associated abrasion and impact stresses. Plates with a hardness of approximately 500 HB are widely used for structural protection for equipment involved in ore transportation.

Critical Analysis and Identification of Opportunities

The preliminary analysis of the critical process points led to the selection of SAG Grinding and Ball Grinding as worthy of further analysis. Since the general aim of the study is “to determine potential opportunities for the development and introduction of new ferrous alloys where benefits significantly exceed cost,” the analysis of the opportunities was made based on alloy type. Therefore, the opportunities to be analyzed are:

- Low-alloy Cr steel used in grinding balls;
- Cr-Mo steel used in SAG mill liners.

The remaining points were discarded as final critical process points since ferrous alloy consumption for each was below the 15,000 tonnes/year criterion. Additionally, insufficient interest was shown by mining companies' operational managers who were visited during the execution of this project.

Table III shows the final critical process points and the annual consumption of different types of parts and alloys in each, along with their estimated 2014 tonnage totals.

Table III. Final Critical Points and Estimated Consumption of Alloys that Exceed the 15,000 tonne/year Threshold. Estimates are for 2014

| Opportunity | Annual consumption by critical points – tonnes | | | |
|---|--|--------------|---------------|---------|
| | Primary crushing | SAG grinding | Ball grinding | Total |
| Cast and forged grinding balls Low-alloy Cr steels | - | 166,600 | 277,900 | 444,500 |
| Cast liners Cr-Mo steels | 650 | 20,500 | 3,500 | 24,650 |

Low-Alloy Steel Used in Grinding Balls

Description of Use

Balls are grinding bodies whose function is to reduce, or help to reduce, the size of the ore that passes through the mills. They are used in both SAG mills and Ball mills:

SAG MILLS: Large mills, ranging between 28 and 40 ft in diameter, which mainly use forged balls with diameters between 5.0 and 6.0 in, whose function is to use impact and abrasion to reduce the size of the ore. As the mill turns, some of the balls and ore are lifted and dropped on the rest of the load, which generates high impact and abrasion stresses.

BALL MILLS: These mills are of smaller diameter, although they are now reaching sizes of up to 26 ft. They employ mostly 3.0 in diameter (1.0 in for regrind mills) forged or cast balls. Their primary function is to reduce the ore size by abrasion, and therefore the primary ball stresses are those caused by abrasion.

Characterization of Balls

Typical chemical composition ranges of grinding balls are shown in Table IV. This information was taken from the suppliers' websites. The molybdenum content in the 5.5 in diameter forged balls was less than 0.08% according to chemical analyses done on locally manufactured and imported balls in 2013. Niobium was not found in any of the ball compositions.

Table IV. Typical Chemical Composition Ranges of Both Types of Grinding Balls

| Ball type | Mill type | Chemical composition (wt.%) | | | | |
|--------------|--------------------|-----------------------------|-------------|-------------|-------------|-------------|
| | | C | Mn | Cr | Si | Mo |
| Forged balls | SAG and Ball mills | 0.55 - 0.90 | 0.70 - 1.25 | 0.37 - 1.20 | 0.18 - 0.70 | 0.00 - 0.20 |
| Cast balls | Ball mills | 0.75 - 0.95 | 0.40 - 1.10 | 0.20 - 1.10 | 0.30 - 0.60 | residual |

Table V shows the property characteristics normally offered by suppliers, as product specifications, to their clients, which are available on their websites.

Table V. Available Grinding Ball Characteristics

| Ball type | Mill type | Features | | | |
|-------------|-----------|---|--------------|---------------|--|
| | | Microstructure | Hardness HRC | Diameter (in) | Mechanical requirements |
| Forged ball | SAG mill | Tempered martensite with retained austenite | 55 - 63 | 5 - 6 | High impact, moderate abrasion resistances |
| Forged ball | Ball mill | | 55 - 65 | 2 - 3 | High abrasion, moderate impact resistances |
| Cast ball | Ball mill | | 60 - 66 | 1 - 3 | High abrasion, moderate impact resistances |

In general, the forged ball has a tempered martensite microstructure with retained austenite present throughout the entire section thickness. The hardness profile is fairly even with no more than a 4 point HRC (Rockwell Hardness) variation between the ball's center and surface. They have practically no internal discontinuity defects since they are manufactured from laminated bars that are cut and hot forged.

The cast grinding ball has a similar microstructure, but with all of the characteristics of a cast section; chemical segregation and presence of discontinuities (pores, shrink holes, etc.). This results in the cast grinding ball having inferior mechanical properties, making it unsuitable for use in SAG mills where, due to high impact stresses, failure by fracturing would occur.

Reason for Ball Replacement

In the case of SAG mills, the replacement balls are added at the same rate they leave the mill, ie. when they reach an internally specified size. Normally this size is between 2 and 3.5 in. In Ball Grinding, the grinding media leave the mill when of a size capable of being carried off by the slurry. In this case, there is no classification and the slurry runs off through a spillway.

Ball consumption is mainly due to wear in ball grinder mills and also due to fracturing in SAG mills (approximately 10%) [2]. In large size, 38 to 40 ft diameter SAG mills, ball fracturing can account for a higher percentage of consumption due to increased impact energies. In these cases the quality of the ball becomes more important.

Ball Consumption

It is commonly accepted practice in concentrator plants to measure the consumption of grinding media in grams per tonne treated (g/tonne); that is to say, the weight of the balls, in grams, that is consumed to treat one tonne of ore at the plant. Also it is known in mining circles that the average value for SAG mills is around 390 g/tonne, and for ball grinder mills around 535 g/tonne. These figures were corroborated by site visits to plants and through consultation with national experts [3]. The figures shown in Table VI are based on these rates and the tonnage treated annually at the concentrator plants.

Table VI. Estimated Ball Consumption in Large-scale Chilean Copper Mining, 2014

| Process | Ore treated | Ball consumption | |
|------------------------|---------------------|-------------------------|---------------------|
| | (tonne/year) | (g/tonne) | (tonne/year) |
| SAG grinding | 429,970,000 | 390 | 167,688 |
| Ball grinding | 522,132,500 | 535 | 279,340 |
| Total ball consumption | | | 447,028 |

Considering that Chile is responsible for one-third of the global copper mining production [4], the total market for balls could reach figures of close to 1.35 million tonnes annually, in this industry alone.

Economic Impact for Abrasion and Impact Resistant Grinding Balls

The economic impact on companies can be estimated in terms of direct and indirect benefits. The direct benefits are related to lower annual costs, from the reduced need to renew grinding balls in this case. The indirect benefits are those generated as a result of using a new, higher-performance product, for example, increased plant availability, lower operating costs, increased safety, reduced environmental impact, etc.

In order to obtain a direct benefit (savings due to reduced ball consumption), the potential price increase due to higher alloy content or change in manufacturing route must be offset by reduced consumption from the improved performance of the new alloy balls.

In consultations, concentrator plant managers and superintendents agreed that a 5% cost decrease in grinding media would be of interest to them, especially considering that grinding balls are the second highest cost item in a concentrator plant, after energy. This equates to an overall cost saving of 5% over and above any additional costs incurred due to a change in alloy composition and/or change in process route to manufacture the grinding balls. As an example, for a SAG plant treating 50 million tonnes of ore per year and assuming a ball wear rate of 390g/tonne this indicates a ball consumption of 19,500 tonnes per year. Typically, ball cost is currently US\$1250/tonne which equates to an annual ball consumption cost of US\$24.38 million. If the ball parameters changed such that cost increased to US\$1300 per tonne but the ball consumption reduced by 10% (due to improved wear and impact performance) then the annual direct costs due to ball consumption would be US\$22.82 million. This represents a potential saving of 1.56US\$ million/year which is greater than a 6% saving on ball consumption costs. The above

simple cost analysis serves to illustrate that the potential savings from improved ball wear and impact resistance are significant and that improving ball properties is a goal worthy of further research.

Indirect benefits, as listed below, are difficult to quantify and their magnitude depends on individual companies:

- Better resource usage owing to longer ball service life (less loss of material due to wear);
- Decreased materials handling cost owing to reduced consumption;
- Decreased occupational risk from materials handling;
- Environmental and sustainability benefits through reduced transportation, reduced energy consumption generally, smaller carbon footprint, etc.

Key Business Players

The Chilean grinding ball market is dominated by Moly-Cop, a national manufacturer of forged balls, which holds approximately 39% of the market. Table VII shows the participants in this market, comprising 100% of the supply.

Ball manufacturers are significant players because they manufacture the final product, have extensive market knowledge and have a commercial relationship with the client. The key players in the Chilean market are Moly-Cop and Elecmetal (Changshu Longteng).

Table VII. Major Suppliers of Mill Grinding Balls

| Suppliers | Company | Ball type | Diameter (in) | Domestic market share (%) |
|------------------|-------------------|------------------|----------------------|----------------------------------|
| National | Moly-Cop | Forged | 1 - 6 | 39 |
| | Sabo Chile | Forged | 1.25 - 6 | 10 |
| | Proacer | Forged | 2 - 4 | 18 |
| Foreign | Changshu Longteng | Forged | 1 - 6 | 30 |
| | Others | | | 3 |

Bar manufacturers are important in this market as well because the performance of the forged ball depends to a large degree on the quality of the bar and because any study related to changes in chemical composition of the ball will affect the bar production process. In Chile, the only bar supplier is the Huachipato Steel Company (Compañía Siderúrgica Huachipato).

Cr-Mo Steel Used in SAG Mill Liners

Of the total amount of Cr-Mo cast steel used in mining, 81% is used in SAG mill liners, 16% in large ball grinder mill liners and 3% as primary rotating crusher concaves. Given this distribution, the analysis will focus on SAG mill liners.

SAG mills play a key strategic role in those mining sites that use this type of equipment, because between 50% and 100% of processed ore flows through these mills depending on plant configuration and existing operating lines. This means that most or all the plants' production depends on their smooth functioning, as any stoppage of the mill leads to a total or partial shutdown of the mine.

Description of Use

Liners are used in a mill's interior to protect the structure and to shape the motion of the load. They can be classified as cylinder liners and cover liners:

CYLINDER LINERS: consist of a lifter and plates. The lifter is responsible for lifting the load in order to generate the impact energy necessary to reduce the ore size. The cylinder lifters are the heaviest parts, weighing as much as 4.5 tonnes;

COVER LINERS: also made up of a lifter and plates. In this case, the lifter is intended to provide wear protection more than to lift the load. Grates are used in the discharge cover to classify the ore's output size.

The main function of a SAG mill is ore size reduction, achieved through the impact produced by the grinding balls and from the large-dimension rocks that feed the mill and fall on the internal load. This is the reason for the large diameters seen in this equipment, which currently stand at 40 ft in the largest mills. The liners are subject to high impacts, produced mainly by grinding balls of up to 6 inches in diameter and they must be sufficiently tough not to fracture under normal operating conditions.

Additionally, abrasion stresses produced inside the mill load are significant; therefore, wear resistance is also a required property of these alloys.

Characterization of Cr-Mo Steel

The chemical composition of the Cr-Mo steel used in liners does not adhere to any particular standard. However, the large majority of the suppliers manufacture their products in a composition range as shown in Table VIII. When requested, this information is delivered to customers. In some cases it is also available on the supplier's website.

It is important to note that there has been virtually no change in these types of alloys in the last 20 years, which suggests that there is little applied research on the topic.

Table VIII. Typical Chemical Composition Ranges of Cr-Mo Steel Liners

| Application | Chemical composition (wt.%) | | | | |
|-------------------------|-----------------------------|-------------|-------------|-------------|-------------|
| | C | Mn | Cr | Si | Mo |
| SAG and Ball mill liner | 0.50 – 0.75 | 0.75 – 1.00 | 2.00 – 2.50 | 0.40 – 0.60 | 0.30 – 0.45 |

Table IX shows the information about characteristics and mechanical properties which is normally delivered by the suppliers to their end-use customers (when requested). Only some of it is published on their websites. In general, this is information that suppliers provide only selectively.

Table IX. Typical Microstructural, Mechanical and Stress Characteristics of the Cr-Mo Steel Used in Mill Liners

| SAG mill liner features | | | | | |
|--------------------------------|--------------------|--|--|--|--|
| Microstructure | Hardness HB | Tensile strength (kgf/mm²) | Yield strength (kgf/mm²) | Resilience (lbf/ft²) | Mechanical requirement |
| Pearlitic | 300 - 400 | 110 - 135 | 85 - 115 | 35 - 100 | High impact, high abrasion resistances |

In general, these castings seek to obtain a fine pearlite microstructure since this offers a better toughness vs. hardness balance for this application. In the case of very thick parts, such as cylinder lifters for example (over 14 in), the microstructure varies greatly across the thickness of the part. On the surface, martensite, bainite and fine pearlite can be found. Then fine pearlite becomes predominant and finally at the center of the part coarse pearlite is found. The hardness gradient is high in these parts, with differences of up to 50 HB between core and surface. Thinner parts, such as plates for example (6 to 8 in) are more microstructurally homogeneous and the hardness gradients are lower.

Grates, being mechanically less resistant to impacts, are manufactured in lower hardness ranges (290 to 340 HB) in order to increase toughness and prevent fracturing during operation. Naturally, decreased hardness means higher wear rates.

Reasons for Liner Replacement

Replacement is carried out owing to wear and/or fractures in liners. Replacement owing to wear is carried out during planned stoppages, whereas liner fracturing causes unforeseen stoppages, accounting for about 10% of the replacements required. Although in both cases production stops, the annual plan only considers scheduled maintenance, which means that unplanned stoppages have the additional effect of jeopardizing the achievement of company goals. Because high percentages of plant production pass through the SAG mill, any stoppage leads to significant revenue loss for mining companies. Therefore, SAG mill liners are considered to be strategic items.

For purposes of scheduling liner changes, an empirical determination is made as to what the minimum liner thickness can be without affecting production, without risk of breakage or structural damage. From this point of view, liners are designed to cause the fewest stoppages and to take the least possible time to replace. This is due to the fact that an increase in mill availability means increased plant availability and thus increased production.

Improving liner performance would require: increasing abrasion resistance while maintaining toughness, increasing toughness while maintaining abrasion resistance, or improving both properties at the same time. The effect of improving liner alloys is highly valuable to company revenues, primarily as a function of increased equipment availability, as this is where the majority of production comes from.

SAG Mill Liner Consumption

Total consumption was calculated based on wear-rate parameters in grams of steel per processed tonne (g/tonne). The value used, 40 g/tonne, is an average estimate for the domestic mining industry. This parameter is known for each mine and was corroborated during visits and consultations with experts carried out during this study. The value of the tonnage processed by all SAG plants operating in copper mining in Chile was determined based on the tonnages processed by each establishment that operates with SAG mills, Table II. The estimated total Cr-Mo steel consumed in SAG mill liners is shown in Table X.

The value of “Consumption due to other factors” is related to unplanned changes, for SAG mill consumption in gold mining and in small plants, for obsolete designs, etc. This value was estimated at 20% of wear consumption.

Table X. SAG Mill Liner Consumption Estimated Based on Average Wear Rate

| Annual tonnage processed by SAG plants in Chilean Copper Mining (tonne/year) | Average wear rate for SAG mill liner (g/tonne) | Estimated total consumption for wear (tonne/year) | Consumption due to other factors (tonne/year) | Estimated total consumption (tonne/year) |
|---|---|--|--|---|
| 429,970,000 | 40 | 17,199 | 3,470 | 20,669 |

Economic Impact on Mining Companies

To obtain a direct benefit, the increased price of any new alloy developed (due to higher alloy content or change in process route) must be offset by the lowered costs from reduced liner consumption and a longer service life.

To make a direct-benefit analysis, a hypothetical mill that consumes mill linings at a rate equivalent to the average SAG mill rate will be considered. The estimates are:

- Total annual mill lining consumption in Chile: 20,669 tonnes/year, Table X;
- Total mills considered: 24 [5];
- Average annual SAG mill lining consumption: 860 tonnes/year;
- Current average spending per SAG mill: US\$2,580,000 At an average liner price of US\$3,000/tonne.

As an example of a cost analysis and using the figures above for liner consumption and cost, if the liner cost increased by 5% and the liner life increased by 10% (due to improved wear resistance) then the annual liner consumption cost would be US\$2.438 million which represents a saving of US\$142,000. This represents a small saving and much less than that associated with the savings possible from improved ball performance.

The principal indirect benefit from an increase in liner service life is from increased mill availability, as there is always a potential bottleneck at this point in the process, and time spent on liner changes is the main variable controlling the number of SAG mill downtime hours. In other words, if liner durability is improved, mill availability increases, thereby raising plant productivity.

A hypothetical SAG mill operating under average market conditions (same assumption as made to estimate direct benefits) will be used in estimating indirect benefits. The assumed conditions are:

- Daily SAG mill treatment average is 49,086 tonne/day;
- Average hourly treatment of 2,045 tonne/hour;
- 0.86% Cu average ore grade [6];
- Copper price of US\$2.57/pound, US\$5.65/kg [7];
- Average SAG production income of 99,556 US\$/hour;
- A six month liner service life (assuming a constant tonnes per day figure);
- Average downtime due to complete liner change is 92 hours;
- Average total weight for all parts is approximately 410 tonnes;
- A complete liner kit has an average cost of US\$1,230,000;
- The alloy price increases proportionally to the increase in service life duration.

Under these assumed conditions, Table XI shows the benefit estimates from increased availability under different increments of liner durability.

Table XI. Indirect Annual Benefits from Plant Availability as a Function of Increased Service Life and Price Increases for a SAG Mill that Meets the Conditions Specified Above

| Estimated annual benefits of increasing availability | | | |
|---|---------|-----------|-----------|
| Increase in new alloy liner lifespan (%) | 5 | 10 | 15 |
| Duration for base alloy liner (months) | 6 | 6 | 6 |
| Duration for new alloy liner (months) | 6.30 | 6.60 | 6.90 |
| Time for saving one change (months) | 126 | 66 | 46 |
| Time for saving one change (years) | 10.5 | 5.5 | 3.8 |
| Time for change (h) | 92 | 92 | 92 |
| Additional time available for production, per year (h) | 8.76 | 16.73 | 24.00 |
| Additional income from additional hours (US\$/year) | 872,111 | 1,665,572 | 2,389,344 |

As can be seen, the benefits are significant. In the case where there is a 5% service life increase, (where the direct financial benefit is zero), the indirect benefit is US\$872,111 per year.

In the case of a plant that treats 50 million tonnes per year (three SAG mills estimated), the indirect benefit stemming from increased availability from a 5% increase in liner life would be US\$2,616,333 per year, per plant. This is the same order of magnitude as the possible direct benefits estimated for the grinding balls. Thus, the indirect benefit that comes from increased plant availability is valuable to the mining industry and possible developments in this area should strongly arouse their interest. In fact, plant availability is an important benefit indicator for mills.

These benefits are not sensitive to the price of the alloy. The benefit estimates assume percent price increases for the alloys commensurate with their service life increases. Thus, alloy price increases of the order of 10% to 15% will not significantly affect the overall benefit to the customer.

Other indirect benefits stemming from increased abrasion and/or impact resistance are safety associated with less downtime and operational versatility, and better reliability.

Liner changes pose potential risks to worker safety, given the weight of the parts involved, working conditions, etc. A reduction in the number of hours spent on liner changes due to longer liner service life, and/or avoiding having to change liners due to fracturing, reduces exposure to risk, which is always valued by mining companies.

As an alternative to increased availability, increased abrasion resistance from the alloys could be used to manufacture thinner liners while maintaining service life duration. Operationally, this decreased weight would allow for an increased percentage of grinding balls which raises production capacity. Moreover, an increase in liner toughness could lead to an improvement in impact resistance, which could be exploited operationally by using greater mill spin velocity without fear of direct load impact causing liner fracturing. This could mean an increase in production without an increase of the downtime due to liner breakage.

Key Players for Mill Liner Supply

The manufacturers of mill liners are ferrous foundries which specialize in these types of mining parts. In Chile there are two manufacturing companies, Elecmetal and Aceros Chile. Elecmetal has the larger market share (around 60%) and is a Chilean-owned international company with plants in the USA. They are a major player nationally and internationally. Other participants in the domestic market are shown in Table XII.

All the foundries achieve the desired steel composition by the use of classified scrap steel as the raw material and then make adjustments to the composition using ferro- and virgin alloys. Therefore, manufacturing a new alloy depends exclusively on them and not on third parties as is the case with grinding balls.

Table XII. Major Mill Liner Suppliers

| Country | Company | Estimated market share |
|-----------|--------------|------------------------|
| Chile | Elecmetal | 60% |
| | Aceros Chile | 20% |
| Indonesia | PT Growth | 20% |
| Canada | Norcast | |

Conclusions

Faced with the overall objective of finding opportunities for the introduction of new or improved ferrous alloy products in mining operations, the study concluded that:

1. Two types of alloy could provide an opportunity for new products: low-alloy steel for use in grinding balls and Cr-Mo steel used as SAG mill liners.
2. Material consumption for balls, 445,000 tonnes/year in the Chilean copper mining industry, is an order of magnitude greater than for any other alloy used in mining operations.
3. For a SAG mill plant that processes 50 million tonnes of ore annually, the benefit of a 10% extension of grinding ball life, given a 4% increase in cost due to extra alloy content and/or change in process route, is estimated as US\$1.56 million per year.
4. SAG mill liners do not represent such a large volume of steel usage as grinding balls. However, alloy development leading to an increase in liner life, and thus reduced downtime for liner changes, would have a significant beneficial economic impact which justifies the alloy development investment. It was estimated that, for plants treating 50 million tonnes of ore per year (estimated 3 SAG mills), the benefit stemming from a 5% increase in liner duration would be US\$2.62 million per year, per plant.
5. New product development should result in a strong competitive differentiation for any new player in the market since alloys for balls and liners have shown little evolution over the last 20 years.

References

1. Portal Minero, Guía de Ingeniería en Operaciones Mineras. 2005/2006.
2. J.E. Sepúlveda, “Criteria for the Selection, Application and Evaluation of Grinding Mill Media” (Paper presented at the First International Ore Processing Meeting, Antofagasta, Chile, 26 – 28 July, 2006), 20.
3. Luis Magne, private communication with authors, Universidad de Santiago, August 2014.

4. Comisión Chilena del Cobre, Yearbook: Copper and Other Mineral Statistics, 1993 – 2012, 2013, 137.
5. Editec, Catastro de Equipamiento Minero 2013-14, Febrero 2015.
6. Consejo Minero, Gran Minería en Chile: Desafíos de Productividad, Agosto 2013, 16.
7. Comisión Chilena del Cobre, Informe Semanal del Mercado Internacional del Cobre, Semana del 16 al 20 de Marzo de 2015.

FROM MONOMETALLIC TO COMPOSITES AND CERAMIC WEAR RESISTANT MATERIALS: AN INDUSTRIAL CHALLENGE

H. François and M. Bonnevie

Magotteaux SA, Rue A. Dumont, 4051 Vaux-sous-Chèvremont, Belgium

Keywords: Chromium Iron, Metal Matrix Composite, Abrasive Wear, Impact Wear, Mining, Cement and Aggregates

Abstract

The methodology adopted by Magotteaux for the development of wear resistant materials is described based on the wear mechanisms observed. This approach consists of six steps from identification of wear mechanisms and mechanical constraints to continuous improvement of the industrial supply chain.

This method is currently used for monometallic balls and liners for grinding mills and allows the optimal selection of steel or iron composition and heat treatment. Based on a large database of marked ball and liner tests, application-specific products and wear models have been established for tube mills.

The same basic approach is also used for the mining industry based on slurry chemistry, recovery, grinding efficiency and wear reduction.

The development of composite and ceramic materials is reviewed. The metal matrix composite (MMC) parts are based on two families, namely oxides and carbides. Manufacturing challenges to produce these new wear resistant materials are described regarding the required properties and size of the castings.

Some examples and wear results for vertical roller mills and crushers are also presented. Finally, ceramic beads are discussed for ultrafine grinding applications.

Introduction

Magotteaux International, a Sigdo Koppers Group company, started in Belgium in 1918 as a small foundry producing grinding media for the cement industry. Shortly after it was established, an 'in-house' R&D laboratory and a pilot foundry were created to study and test wear resistant materials. After a few years, Magotteaux started to develop castings for cement mills' internal components, and then also to develop products for the mining industry, with balls and liners for grinding tube mills using high chromium steels and irons. Magotteaux then pursued development in other grinding and crushing equipment, as well as in other markets (aggregates, dredging and power stations, etc.). Magotteaux now supplies a wide range of optimized solutions to industries involved in comminution, including high carbon forged balls for tube mills and Semi Autogenous Grinding (SAG) mills, ceramic beads for ultrafine grinding and Metal Matrix Composites (MMC) for wear parts.

This paper describes the development of wear resistant products in the Magotteaux Group. General wear mechanisms literature is also reviewed and listed in references [1-11].

Background on Wear Mechanisms

Wear is a complex synergistic mechanism that removes pieces of an equipment part and affects its efficiency [4,5]. One cannot construe wear as an intrinsic characteristic of a material, mainly because wear also depends upon the environment. According to Zum Gahr [1], four different wear mechanisms can be identified, namely: adhesion, abrasion, tribochemical reaction and surface fatigue, Figure 1.

In crushing and grinding activities, we disregard adhesion as irrelevant to the comminution process.

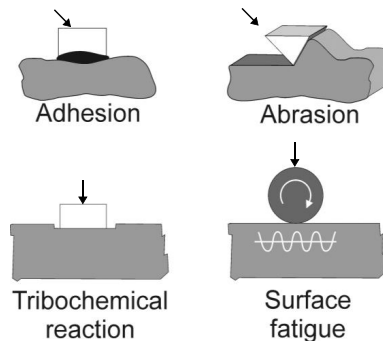


Figure 1. The four wear mechanisms [1]. Arrow refers to applied load.

Abrasion

Abrasion is defined as 'displacement of material caused by the presence of hard particles, between or embedded in one or both of the surfaces in relative motion, or by the presence of hard protuberances on one or both relatively moving surfaces'. Abrasion includes four mechanisms: microploughing, microcutting, microfatigue and microcracking [1], Figure 2.

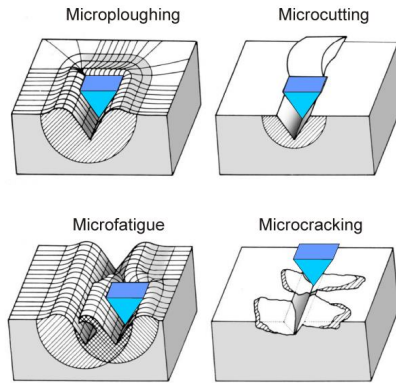


Figure 2. The four abrasion mechanisms [1].

As an example, SEM views of microcutting on a wear part of a crusher are shown in Figures 3 and 4.

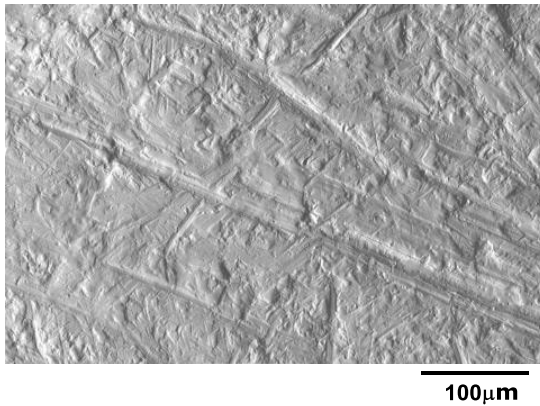


Figure 3. SEM image of microcutting surface (BEI).

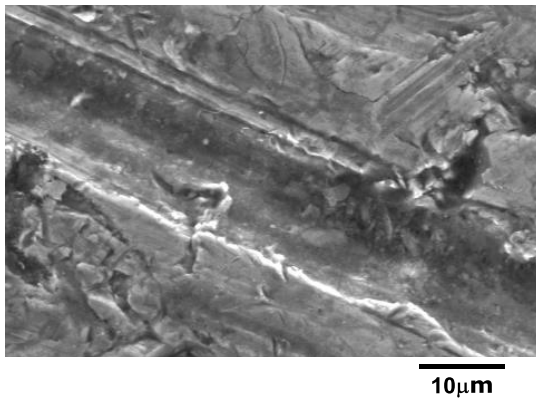


Figure 4. SEM image of microcutting surface (SEI).

Surface Fatigue

This mechanism is defined by ‘crack formation and flaking of material caused by repeated alternating loading of solid surfaces’ [1]. As an example, SEM views of microfatigue on a first chamber cement grinding ball are shown in Figures 5 and 6.

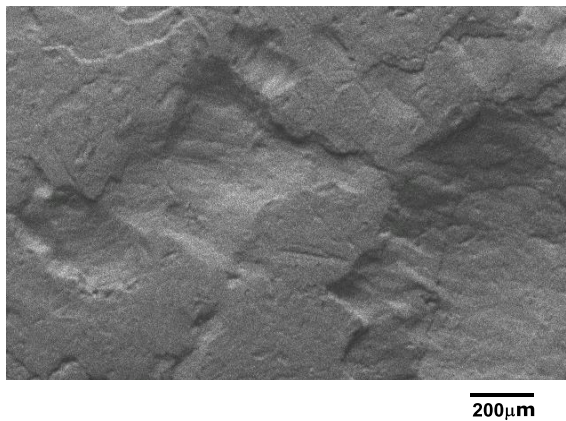


Figure 5. SEM image of microfatigue (BEI).

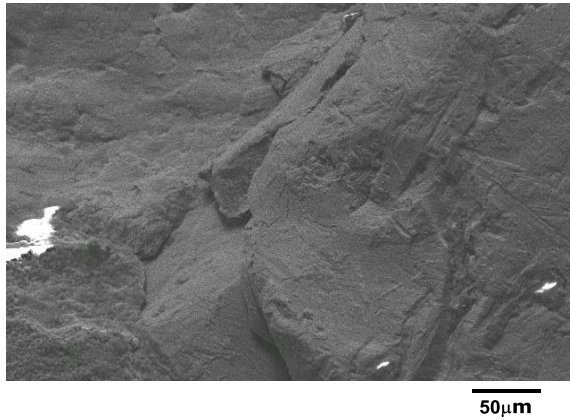


Figure 6. SEM image of microfatigue, detail (BEI).

Tribochemical Reaction

The tribochemical reaction (tribocorrosion) is defined by the same author [1] as the ‘rubbing contact between two solid surfaces that react with the environment’. The corrosive environment can be gaseous or liquid. The wear process proceeds by continual removal and new formation of reaction layers on the contacting surfaces [1]. As an example, SEM views of tribocorrosion on an iron ore secondary mill grinding ball are shown in Figures 7 and 8.

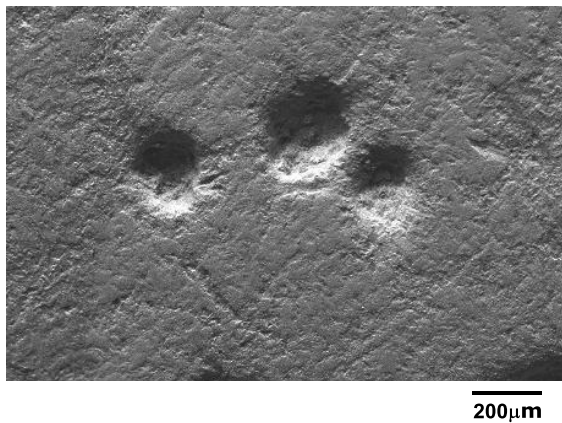


Figure 7. SEM image of tribocorrosion (BEI).

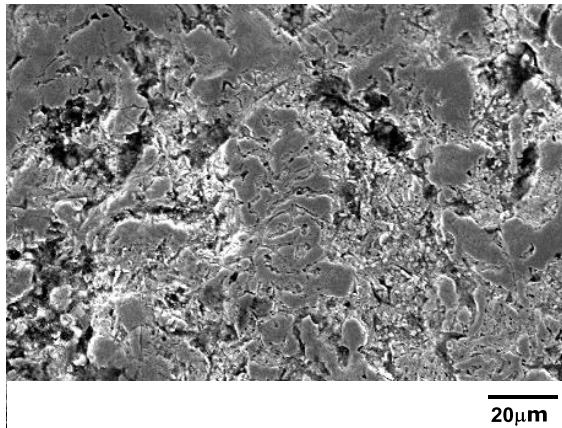


Figure 8. SEM image of tribocorrosion, detail (BEI).

In practice, it is generally difficult to identify just one acting wear mechanism in industrial processes.

Methodology for Material Selection

We employ a very similar scheme for any wear part under development:

- Identify and understand the wear mechanism and mechanical constraints on existing parts;
- Select some potential solutions;
- Test the solutions in the laboratory;
- On site testing;
- Validation and agreement;
- Continuous improvement.

We can easily and directly test some potential solutions in the field for equipment, such as grinding balls or vertical shaft crusher parts which have short lifetimes. For long-lasting parts, modelling and simulation have to be used.

Selection of material with optimal mechanical characteristics will be described here. As parts can be fixed to the equipment, we have to reconcile mechanical (machinability, formability) and wear aspects. Due to the large expansion of the possible range of materials available and thanks to the development of new simulation tools, as well as of new measuring equipment, it is now important to apply a rigorous methodology such as the one described by Ashby [6] to select and design the optimum material based on the customer application. Empiricism is no longer sufficient and we need a methodology to reduce time to market of new products.

The first step consists of the characterization of our current materials.

The second step is to measure or calculate the level of micro-stresses induced in the material during service. These stresses will then be simulated using laboratory equipment. From the analysis of the failure modes it should be possible to make a link between the observed wear mechanism and the material properties and microstructure.

White Irons and Steels

Through the years, many 'in-house' compositions for chromium irons and steels have been developed and patented by Magotteaux for balls and internals in tube mills. We revealed that the advantage of these alloys lies in the ability to fine tune the final properties by various heat treatments. The microstructure of the irons usually consists of a natural composite with a variable amount of chromium carbides surrounded by a complex matrix comprising martensite, some residual austenite and secondary chromium carbides, Figures 9 and 10.

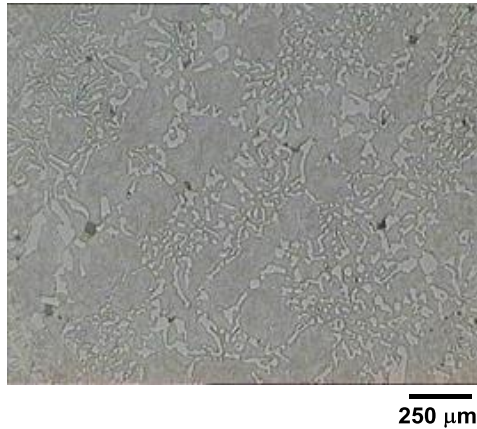


Figure 9. White iron optical micrograph.

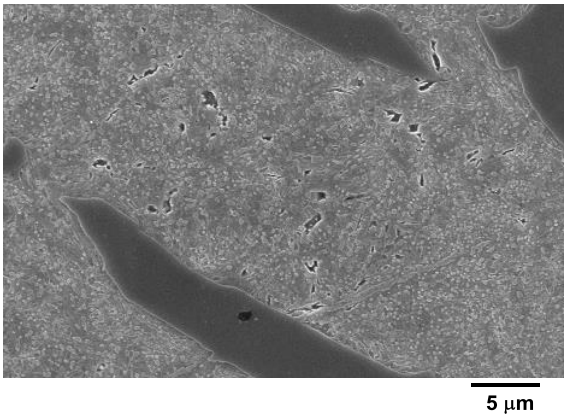


Figure 10. White iron SEM image (SEI).

The microstructure of wear resistant steels usually consists of martensite, some bainite and some residual austenite, Figures 11 and 12.

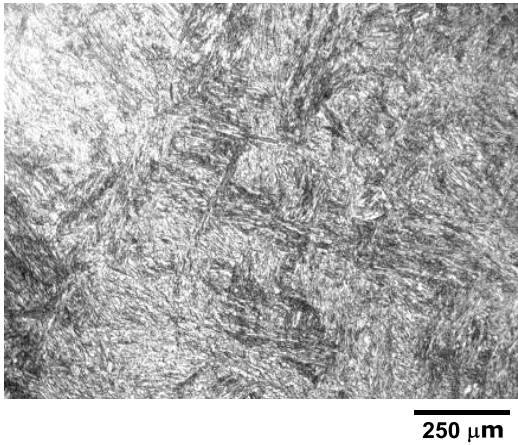


Figure 11. Wear resistant steel showing martensite.

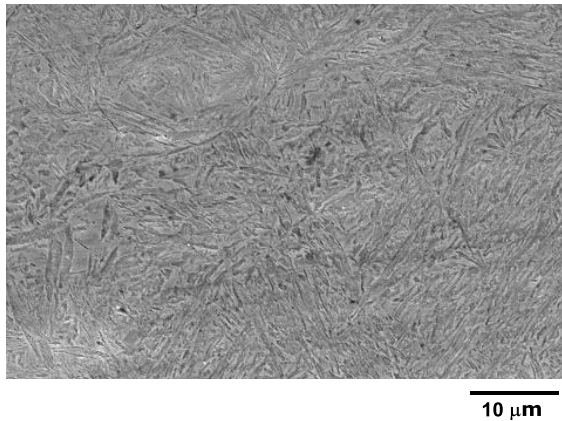


Figure 12. Wear resistant steel showing martensite, SEM image.

Grinding Media Development

The grinding medium is the historical product of Magotteaux's development for which many alloy compositions and heat treatments were investigated.

Wear mechanism studies are undertaken on used balls. In wet and dry grinding, wear is a result of abrasion; surface fatigue and corrosion being the major players as explained above [2]. It is important to note that the total wear is not a simple summation of each mechanism.

Wet grinding is the most common practice in the mining industry; corrosion is therefore active. The corrosion layer can be protective and does not represent the bulk metal characteristics. The abrasion destroys the existing protecting layer and creates a new corrosion-active surface. The same effect can occur for impact and deformation. Hence, the parameters work in synergy and the total resulting wear can be much higher than that expected from simply combining the individual wear mechanisms.

In comparison, for dry conditions like cement, corrosion is much lower and comes only from the moisture within the raw materials.

Our expertise is based on very long experience and on a very large number of tests made in all grinding environments, from dry cement to any wet ore application. When developing a new application in grinding, the following procedure is used:

- Study of the feed ore and discharge slurry for each mill;
- Discharge-slurry corrosion evaluation;
- Impact level evaluation;
- Marked ball test for fine tuning the properties;

- An industrial test to confirm results on a large time-base.

Feed Ore and Discharge Slurry Characterization. All minerals present are identified and their hardness measured, especially those with a high hardness, Figure 13.

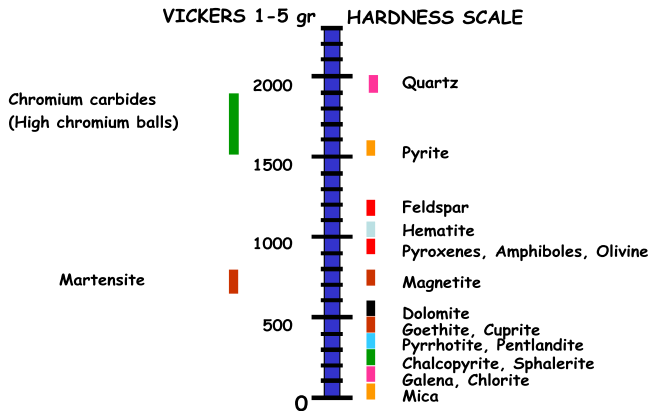


Figure 13. Hardness scale of minerals versus metallic grinding media.

This figure was established by Magotteaux using the Vickers hardness procedure. Those minerals with higher hardness levels will significantly affect the wear rate. Quartz, garnets and feldspar are considered as the most abrasive minerals. Hematite, chromite and pyrite are considered as medium hard minerals.

This study also includes a size and shape evaluation of the abrasive minerals and ore liberation from the gangue.

Discharge Slurry Corrosion Evaluation. Magotteaux has developed a battery of tests to evaluate the corrosiveness of the discharge slurry. It includes a chemical analysis for pH, temperature and ion measurements.

In the case of chromium white irons, Magotteaux are particularly interested in halogens, such as chlorides and fluorides that destroy the corrosive protective layer by pitting.

A comparison of the potentiodynamic response to pitting of the different alloys is performed as in Figure 14, which presents an example for the Duromax grades R, K and G.

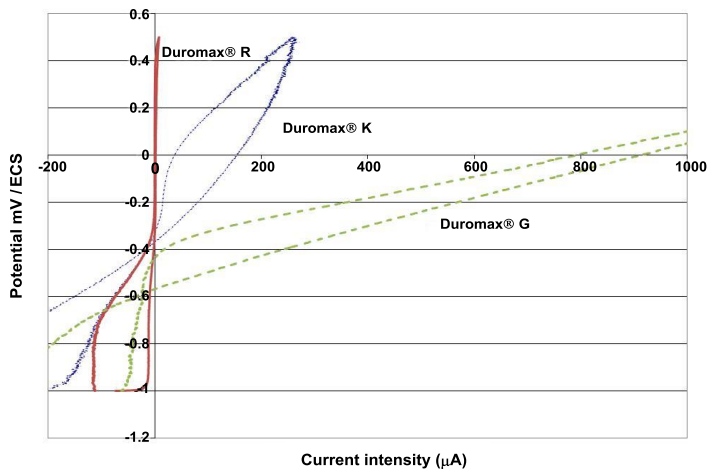


Figure 14. Example potentiodynamic curve comparison of corrosion susceptibility.

In the present example, three different chromium level alloys are compared in the same slurry.

One can see that Duromax®G shows immediate pitting, Duromax®K shows some unstable passivation and Duromax®R shows perfect passivation behavior. This comparison helps evaluation of the ‘safety’ of the proposed solutions. Other ‘in-house’ tests are run to confirm the alloy choice.

Impact Level Evaluation. Impact level assessment is also performed. The parameters controlling this evaluation are geometrical and mechanical rather than chemical. A complete questionnaire is completed, including information on rotation speed, inside diameter, liner and feed end shape. The charge movement is directly fixed by the chosen design. The slurry density is another factor affecting the media motion inside the mill and which Magotteaux controls. Finally, a survey and complete examination of the existing grinding media status completes the picture.

Marked Ball Test Procedure. Magotteaux has decided from the beginning to apply the ‘Norman’ or Marked Ball Test (MBT) procedure to compare the wear of different steels and irons. [7,8,11]. The MBT wear evaluation procedure is a consequence of the difficulty of finding a reliable laboratory test that includes all the parameters existing in a tube mill. Based on ball weights, the millimeters lost on diameter per hundred hours’ wear are calculated for each quality. Absolute comparison between alloys and heat treatment is then possible. Any new result is added to the database and helps to consolidate know-how.

Industrial Test at Medium to Large Scale. On the basis of the MBT results, the optimized alloy and heat treatment can be proposed. Generally, the new alloy is added at regular intervals on to the existing grinding media and not as a complete new charge; therefore, the reduction of wear will not be seen immediately but as a progressive improvement. An 'in house' computer model allows simulation of the wear evolution. Accompanying the supply of new media, regular visits to the mill help assessment of the wear evolution.

Magotteaux's production capabilities enable the supply of forged and cast balls used in mills from fine grinding mills to SAG mills. Ball sizes can vary from 10 mm to 160 mm.

In addition to wear studies, Magotteaux has also developed a multifold approach called Chemillurgy®, including grinding efficiency and slurry chemistry. Nevertheless, this optimization affecting recovery, grade and reagent consumption during ore processing will not be described here [2].

Tube Mill Internal Development

As the mill internals are linked to the grinding media, the same approach is used, ie.:

- Collection of all the geometrical parameters of the different mills (size, speed, type of discharge, etc.);
- Study of the feed ore and discharge slurry from each mill;
- Comparison to our database.

In addition to the alloy and heat treatment, the design must also be considered. A bad design can increase sliding or ball impacts on the lining and reduce lifetime. Special care has to be taken regarding the maintenance time and the concerns of the customer. As the liner will transmit the energy to the tumbling media charge, a specific approach has to be adopted for obtaining and maintaining the optimum energetic efficiency during the life of the liner. Based on these geometrical parameters, a simulation study is performed to design new internals.

Field tests have been run comparing liner alloys and heat treatment, as has been done for balls, but these are difficult to run.

A large database of confirmed results is used as a help for the designers. Figure 15 shows an example of tube mill internals.



Figure 15. 3D view of tube mill internals. Colors refer to different castings.

Metal Matrix Composites

During the nineties, Magotteaux started to produce Metal Matrix Composite (MMC) wear parts in the pilot foundry. These parts were tested in some chosen industrial plant. Successful results in some low impact applications encouraged the development of those composites. Two metal matrix composite families have been developed and patented. A similar approach, as already described above, was undertaken for the cast parts of each type of equipment.

The MMC approach allows one to keep the functionality of the casting by reinforcing only those areas which would be subject to wear.

Oxide Based MMC

Xwin®, neoX® and Recyx® are Metal Matrix Composites based on millimeter-sized oxide particles forming a ceramic core. Different challenges have to be considered to manufacture a successful composite casting.

The Choice of the Ceramic Material. Among all the different tested oxides, the alumina-zirconia system gave the best results. Depending on the zirconia content, the alumina-zirconia system allows one to get a good compromise between toughness and hardness.

Typical mechanical properties of the metal matrix and oxide ceramic grains are given in Table I below.

Table I. Mechanical Properties

| Material | HV | K_{1c} (MPa√m) |
|---------------------|-----------|-------------------------------|
| White iron (26%Cr) | 800-850 | 25-30 |
| High alumina | 1650 | 4-6 |
| Low alumina | 1350 | 8-14 |

Hardness is measured using Vickers indentations.

Toughness is measured using VIF (Vickers Indentation Fracture), Figures 16 and 17.

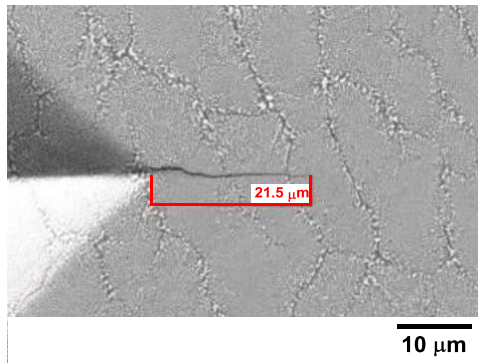


Figure 16. Vickers indentation on MMC with high alumina/zirconia ratio showing a crack from the corner of the indent.

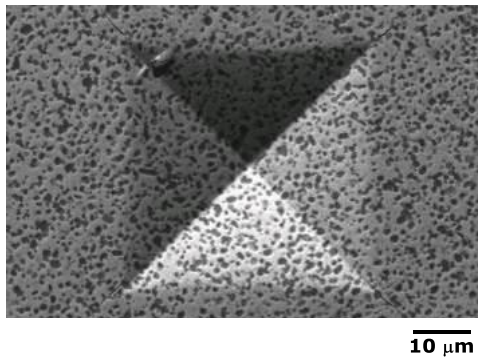


Figure 17. Vickers indentation on MMC with low alumina/zirconia ratio showing no cracking from the corners of the indent.

Values in the table are obtained using the LAWN formula [12]:

$$K_{Ic} = 0.028 \cdot (E/HV)^{0.5} \cdot HV \cdot a^{0.5} \cdot (a/c)^{3/2} \quad (1)$$

K_{Ic} : fracture toughness ($\text{MPa} \cdot \text{m}^{1/2}$)

HV: Vickers hardness (GPa)

E: elasticity modulus (GPa)

a: half average length of the diagonal of the Vickers marks (microns)

c: average length of the cracks measured from the center of the Vickers marks (microns)

The Size of the Ceramic Grains. A ceramic grain size between 1 to 3 mm is used as a compromise between the manufacturing capability for the casting and wear behavior. Figure 18 shows a 3D view of a worn surface of a composite roller.

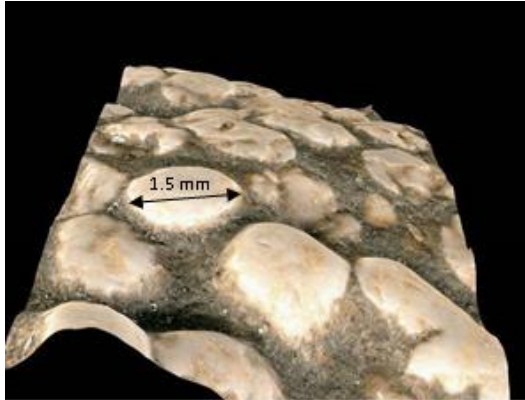


Figure 18. MMC roller detail.

Choice of the Matrix Alloy. As Magotteaux is a steel and iron foundry and manufactures wear resistant castings, the starting point for the matrix chemistry is naturally based on ferrous alloys. White iron or steel is chosen depending on the operating conditions.

Ceramic Core Design. Two main factors drive the design of the porous ceramic core. One is related to manufacturing considerations and the other to wear resistance efficiency.

- Manufacturing considerations.

A good penetration of the ceramic core by the liquid metal, as well as an acceptable stress level in the casting are required. For example, a honeycomb structure is shown in Figure 19.

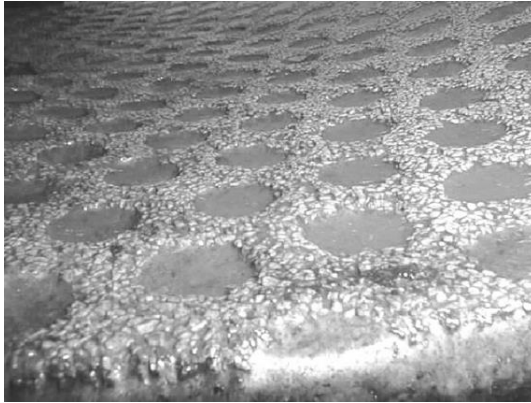


Figure 19. MMC with honeycomb structure.

- Wear resistance efficiency.

The ceramic core is designed based on the observed wear profile of a classical monometallic wear part.

The intrinsic heterogeneity of the composite material properties allows one to get some specific effects on the wear profile and on the customer's process efficiency, if needed. The wear profile during the component's lifetime can be tailored by adjusting the ceramic core design.

Manufacturing Parameters. Different challenges need to be overcome to be able to manufacture castings weighing from a few kilograms to twenty tons. Due to the density difference between metal and ceramic, the concept of the mold has been revised. Even though alumina-zirconia ceramics with a high content of zirconia have a closer thermal expansion coefficient to steel than do the other oxides, there is still a significant difference. In addition to that, both alumina-zirconia and the metallic matrix undergo martensitic transformations with different shrinkage and expansion stages at different temperatures and times. Heat treatments of the castings have been optimized to accommodate these expansion mismatches.

Field Operating Conditions. The wear resistance improvement of the ceramic metal composites can vary over a large range depending on the operating conditions in the different applications (abrasion, impacts). Thus, MMC is not a universal solution but it covers a wide range of applications.

To extend the range of possible application with these materials, Magotteaux has now built its own manufacturing plant to produce ceramic grains. It is now possible to control the final microstructure and properties of the ceramic grains to get the desired composite materials. This composite material based on ceramic oxides is now widely used in crushers for the aggregate and recycling businesses, as well as in vertical roller mills used in power station (coal mills) and cement plants.

A good example can be presented for vertical roller mill wear reduction. Figure 20 shows an industrial vertical mill used in raw milling in the cement industry and coal milling in power stations.



Figure 20. Vertical roller mill.

For the rollers two options are used:

- One option called Duocast® consists of a roller body made in ductile iron to achieve good mechanical properties with white iron inserts, themselves incorporating a ceramic core. The wear resistant inserts are located at the surface of the roller, Figure 21.

Figure 22 shows the wear pattern (1), the white iron insert (2) and ceramic core (3).



Figure 21. Duocast® roller.

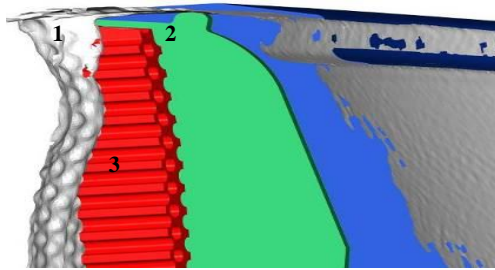


Figure 22. Duocast® roller sketch and wear profile.

- In the second option, the roller is made in white iron with ceramic cores located at the wearing surface. Figure 23 shows MMC rollers and table.

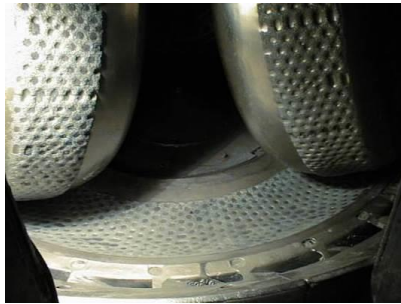


Figure 23. MMC rollers and table.

The wear reduction usually observed in those applications ranges from 1.5 to 5 times the lifetime of white iron rollers.

Crushing Mill Wear Reduction

A vertical shaft impact crusher (VSI) is depicted in Figure 24. Composite impellers and anvils are shown in Figures 25 and 26.

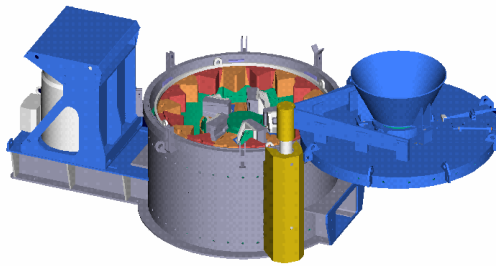


Figure 24. 3D view of VSI crusher.



Figure 25. MMC impeller of VSI crusher.



Figure 26. MMC anvil of VSI crusher.

Another widely used crusher is the horizontal shaft type used in aggregate and recycling applications, Figures 27 and 28.

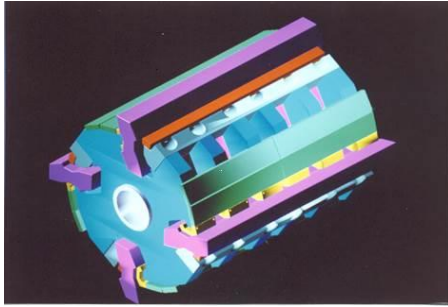


Figure 27. 3D view of a horizontal shaft impact crusher.



Figure 28. MMC blowbar of a horizontal shaft impact crusher.

The total amount of ceramic phase is about 3 to 5% by weight for a total lifetime improvement of about 100%.

Carbide Based MMC

Xcc® is another metal matrix composite based on carbide reinforcement. In the oxide based MMC, the reinforcement particles have a size of a few millimeters. In this case, the carbide reinforcement has a rounded shape, with a size of a few microns. One interesting carbide is TiC which has a very high hardness (3000 HV). The carbide reinforcement is surrounded by a ferrous metal matrix, Figure 29.

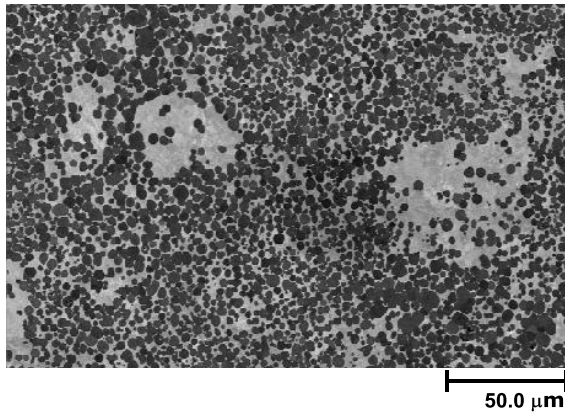


Figure 29. Microstructure of TiC surrounded by the ferrous metal matrix, SEM image.

As for the oxide based MMC, only the wear zone of the casting is reinforced, to maintain the reliability of the casting. The reinforcement could be monolithic, or with a hierarchical structure. In the former case, the wear zone is reinforced with a solid insert, containing about 50% of rounded micron-sized carbides, the remainder being the ferrous metal matrix. In the latter case, the wear zone is reinforced with grains of a few millimeters containing about 50% of rounded micron-sized carbides. The ferrous metal matrix is located between the both the millimeter grains and the micrometric carbides, Figure 30.

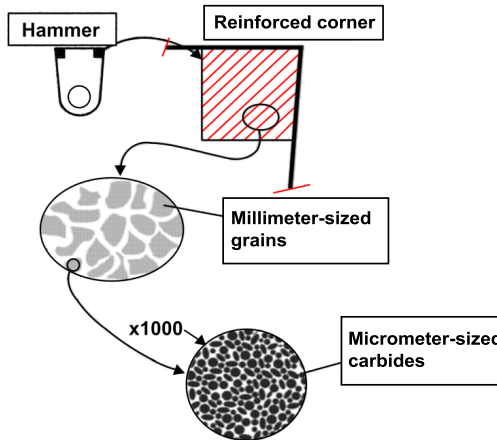


Figure 30. Hierarchical structure of MMC carbide reinforced hammer.

This hierarchical structure combines the wear resistance obtained by the reinforced grains containing around 50% of carbides, and the toughness (due to the ferrous metal which surrounds the grains and the carbides). According to this technique, the volume percentage of carbide reinforcement can vary from around 25% up to 70%.

One of the products developed by Magotteaux using this technology is based on titanium carbide (TiC) reinforcement. The metal matrix could be a martensitic steel or white iron. Typical properties are given in Table II.

Table II. Typical Mechanical Properties of the Metal Matrix and Carbides Grains

| Material | HV | K_{Ic} (MPa.m^{1/2}) |
|----------------------------|-----------|---|
| White iron matrix (25% Cr) | 800-850 | 20-30 |
| Martensitic steel (9Cr) | 600-700 | 250-300* |
| TiC | 3000 | 3.8** |
| Composite steel/TiC | 900-1400 | 50-60 |
| Composite white iron/TiC | 1000-1600 | |

*Reference [9]

**Reference [10]

The same challenges exist as for the oxide based composites:

- Choice of the type of carbide reinforcement;
- Monolithic or hierarchical reinforcement, regarding manufacturing and wear;
- Choice of the metallic matrix alloy;
- Ceramic core design;
- Manufacturing parameters;
- Type of application.

Although the challenges are the same for both composites, the ranges used and limits differ.

Some examples of castings using this technology are shown in Figures 31 to 34.



Figure 31. New Xcc® cement hammer.



Figure 32. Xcc® clinker hammer.



Figure 33. Xcc® primary crusher hammer.



Figure 34. Xcc® dredging teeth compared to mono metal.

An increase of the lifetime by a factor of two to four is usually observed in the case of hammers and dredging teeth compared to the classical steel solution.

Ceramic

About ten years ago Magotteaux started to manufacture Keramax® beads for ultrafine grinding applications, Figure 35. The size of these ceramic beads ranges from about 1 to 5 mm. Fine grinding using stirred mills and ceramic beads is quite new in the mining industry. Such a capability is provided by the IsaMill™, Figure 36.



Figure 35. Ceramic beads used in ultrafine grinding.

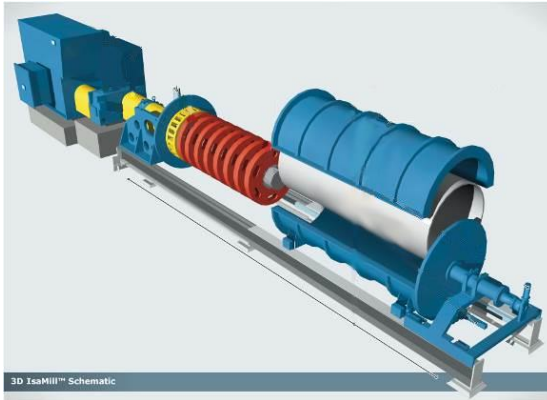


Figure 36. Schematic of an IsaMill™ copyright Xstrata.

Media selection has a major influence on mill parameters such as energy efficiency, internal wear and operating costs.

The wear mechanism of grinding beads is mainly due to a combination of microcutting and surface fatigue processes.

Magotteaux's laboratory is equipped with two IsaMill™ test rigs: LM4 & LM20, Figure 37.



Figure 37. Magotteaux LM20 pilot plant.

These items of equipment are used to evaluate wear and grinding efficiency during fine grinding in conditions close to the industrial ones.

Conclusions

Based on a large database of marked ball and liner tests, application-specific products were established for tube mills in the cement and mining industries. Chemical composition and heat treatment were selected based on the wear mechanisms involved.

Exploring new markets like aggregate processing, power stations and dredging, for which wear is also an issue, classical materials have proven to be useful but with variable success.

Based on those new challenges Magotteaux R&D developed new materials comprising Metal Matrix Composites (MMCs) and ceramics, which turned out to be a promising response to the new market needs.

An ever increasing and deeper knowledge of the wear mechanisms is now required to develop new materials. This is why Magotteaux now invests in simulation tools, and collaborates with international organizations to make best use of their combined skills.

Whatever are the particular challenges of our customers, these all come down to ensuring maximum cash generation. Our role consists of providing process optimization solutions. Starting with a detailed knowledge of their complete value-chain, we combine expert advice, service, resources, products and equipment, and use all relevant levers to help them make technical specifications meet financial requirements.

References

1. K-H Zum Gahr, *Microstructure and Wear of Matrils* (Elsevier, 1987).
2. C. Greet and A. Van den Bosch, "The Use of High Chromium Content Grinding Media in the Mining Industry," *Centromin*, (2014).
3. F.W. Zok and A. Miserez, "Property Maps for Abrasion Resistance of Materials," *Acta Materialia*, (Elsevier, 2007), 6365-6371.
4. D.A. Rigney and W.A. Glaeser, *Source Book on Wear Control Technology* (ASM, 1978).
5. M.B. Peterson and W.O. Winner, *Wear Control Handbook* (ASME, 1980).
6. M.F. Ashby, *Materials Selection in Mechanical Design*, Third edition (Elsevier, 2005).
7. L. Vermeulen and D. Howat, "Abrasive and Impactive Wear of Grinding Balls in Rotary Mills," *Journal of South African Institute of Mining and Metallurgy*, (April 86), 113-124.
8. L. Vermeulen, "Contribution to 'Ball Wear and Ball Size Distribution in Tumbling Ball Mills'," *Powder Technology*, 46 (2-3) (1986), 281-285.

9. P. Konopik and H. Viehrig, "Fracture Toughness Characterization of the Martensitic Chromium Steel," *Proceedings of the 2nd International Conference on Recent Trends in Structural Materials*, November 21st - 22nd, 2012, Parkhotel Plzen, Czech Republic, EU, 91.
10. The National Institute of Standards and Technology (NIST).
11. T. Norman and C. Loeb, "Wear Tests on Grinding Balls," *Metals Technology*, (April 1948), *Mining Technology* (May 1948), 339-352.
12. E. Rocha-Rangel, "Nanocomposites with Unique Properties and Applications in Medicine and Industry," *Fracture Toughness Determinations by Means of Indentation Fracture*, ed. Dr. J. Cuppoletti (InTech, 2011), 21-38.

DEVELOPMENT AND APPLICATION OF ADVANCED HIGH-STRENGTH STEELS IN LIGHTWEIGHT CARS FOR HEAVY-DUTY MINING DUMP TRUCKS

Linhao Gu¹, Zhenqiang Wang¹, Changwen Ma¹, Deguang Zhou², Yongqing Zhang³
and Aimin Guo³

¹Shougang Research Institute of Technology, No.69, Yangzhuang Street, Shijingshan District, Beijing, China

²Qinhuangdao Shouqin Metal Materials Co., Ltd., Duzhuang Town, Qinhuangdao City, Hebei Province, China

³CITIC Metal Co., Ltd., Room 1901, Capital Mansion 6, Xinyuan Nanlu, Chaoyang District, Beijing, China

Keywords: Heavy-duty Mining Dump Truck, AHSS, Niobium, Lightweight, Toughness, Weldability, Wear Resistance

Abstract

With the rapid development of the automobile industry in China, energy consumption and environmental pollution problems have become increasingly serious issues, and therefore, lightweight vehicles have received more and more attention. Shougang Group has developed advanced high strength steels (AHSS) of NM450 and Q690CF (crack-free) grades by using a Nb-Mo-B microalloyed design and two-stage rolling with quenching and tempering processing. Whilst maintaining the high strength, the toughness and weldability of the AHSS were improved by reducing the carbon equivalent. For the high strength wear-resistant NM450 grade, the yield strength is higher than 1100 MPa, the tensile strength is higher than 1350 MPa, the elongation is greater than 15%, and the low temperature (-40 °C) Charpy impact energy value is not less than 60 J. The abrasion resistance of NM450 is five times that of the typical Q235 grade. For the high-strength structural steel (Q690CF), the yield strength is greater than 750 MPa, the tensile strength is above 800 MPa, the elongation is higher than 20%, and the low temperature (-40 °C) Charpy impact energy value is more than 200 J. These AHSS grades are successfully applied in Shougang's SGE150[®] heavy dump body tub, resulting in a reduction of body weight, an improvement of the lifespan of the mine car and a reduction of the transportation costs.

Introduction

With the rapid development of the Chinese economy, China's automobile production and sales have ranked number one in the world for many years, leading to an increase in energy consumption and increasingly serious environmental pollution. Currently, reducing energy consumption and environmental pollution and saving resources are very important and urgent issues in China. The lightweight design of the vehicle car body is a key solution in improving the vehicle fuel efficiency, thus reducing the energy consumption, and reducing the environmental pollution [1-3]. According to the European Aluminum Association, reducing the vehicle weight by 10% can decrease the fuel consumption by 6-8% [4]. Since body mass accounts for about 40% of the total mass of the car, lightweight vehicle bodies play an important role.

Heavy dump trucks are widely used to transport soil, rocks, ore and other materials in mining and various other industries. In recent years, with the improvement of mechanization in the Chinese mining industry, the carrying capacity is gradually increasing, creating a high demand for heavy-duty mining dump trucks. In order to improve the transport efficiency and reduce costs, many large mines tend to use big tonnage mining dump trucks, which promote development of larger vehicles to meet the needs of the mining user. The statistics for the Chinese market for mine dump trucks show that there was a demand for nearly 7000 vehicles during the period 2010-2015. It is predicted that the needs will become even bigger in the next few years [5]. In developed countries, the S355 steel and/or higher strength structural steel grades are commonly used to manufacture heavy dump mine car bodies. However, in China the main material is still the conventional structural steel Q235, together with a small amount of low-alloy structural steel Q345 being used for special parts. There are obvious opportunities for the use of other steels to manufacture heavy-duty dump trucks in China compared with international practice.

This paper describes the development and application of AHSS in a heavy dump tub lightweight car body. It is of practical significance for the light-weighting process of Chinese heavy-duty mining dump trucks.

Lightweight Car Design of the Heavy-duty Mining Dump Truck

Figure 1 shows the heavy-duty mining dump truck of type SGE150[®] produced by the Shougang Heavy Duty Truck Manufacturing Company. The mine car with a weight of 105 t has a rated loading capacity of 136 t, and is mainly used for mining transportation. Shougang Heavy Duty Truck Manufacturing Company and CBMM (Companhia Brasileira de Metalurgia e Mineração) have made a lightweight car design together, see Figure 2. Instead of the original Q235 grade, the NM450 and Q690CF AHSS are used to reduce the weight of the car and hence energy consumption, increase the transportation load and the lifespan of the mine car, and decrease the maintenance costs.



Figure 1. Heavy-duty mining dump truck SGE150[®].

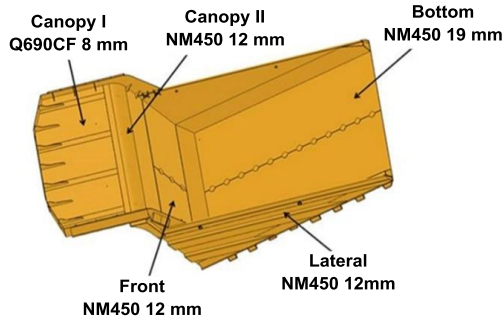


Figure 2. Lightweight car design.

Q235 plate is the main constituent material of the dump truck compartment. The yield strength of this material is about 250 MPa. The basic principle of the new lightweight design is that Q235 is replaced by the AHSS without changing the original structural strength and structural integrity. In the lightweight design process, the following formula is commonly used [6]:

$$\frac{t_2}{t_1} = \sqrt{\frac{R_{eL1}}{R_{eL2}}} \quad (1)$$

where:

- t_2 - thickness of high strength steel
- t_1 - thickness of low strength steel
- R_{eL1} - yield strength of low strength steel
- R_{eL2} - yield strength of high strength steel

Based on the above formula and considering the stress under different conditions, the lightweight design procedure is conducted for the various parts of the body.

Table I. Changes in the Thickness from Original Materials to New Materials

| | | Original Material (Q235) | New Material (NM450) | New Material (Q690CF) |
|---------------------|----------------|-----------------------------|-------------------------|--------------------------|
| Yield Strength, MPa | | 250 | 1100 | 700 |
| Canopy I | Thickness (mm) | 10 | | 8 |
| Canopy II | | 16 | 12 | |
| Front Plate | | 16 | 12 | |
| Lateral Plate | | 16 | 12 | |
| Bottom Plate | | 25 | 19 | |
| Stiffener | | 10 | | 8 |

Table I shows the changes in the thickness from the original material to the new materials. The new canopy I was made of Q690CF steel with a thickness reduction from 10 mm (Q235) to 8 mm (Q690CF). Both the canopy II and the front plate are now made of NM450 with a thickness reduction from 16 mm (Q235) to 12 mm (NM450). The lateral plates are made of NM450 with a thickness reduction from 16 mm (Q235) to 12 mm (NM450). The bottom plates are made of NM450 with a thickness reduction from 25 mm (Q235) to 19 mm (NM450). Also, all the stiffener plates are made of Q690CF with a thickness reduction from 10 mm (Q235) to 8 mm (Q690CF). Due to the lightweight design, the total weight of the car can be reduced from 23.5 t down to 19.7 t (a reduction of 3800 kg (16%)).

After the lightweight car design, a force analysis by computer aided engineering (CAE) was carried out under different conditions, such as full-load motionless, full-load moving on uneven road, or braking and cornering. The stress state of the whole car changed little, and the maximum stress was 570 MPa, which is much lower than the yield strength of the new materials. The new materials, therefore, meet the production requirements of the new mine car.

Production Design of the AHSS

According to the requirements of lightweight car design, the AHSS (NM450 and Q690CF) with good mechanical properties were developed using Nb-Mo-B microalloying, two-stage rolling and quench and tempering processing. Under the condition that sufficient strength was obtained, the formability and weldability of the AHSS were improved by adding Nb, while reducing C and certain other alloying element contents.

B is a very powerful hardenability element that is added to steel in small amounts, usually less than 50 ppm. Since B is a strong nitride former, Ti is usually added at around the stoichiometric ratio for TiN precipitates ($\text{wt.\%Ti} = 3.4 \times \text{wt.\%N}$) to protect B, and thus maximize its effectiveness. Moreover, the combined addition of Mo and Nb can improve the effectiveness of B [7-9].

Nb is often added to structural steels as a typical microalloying element, usually less than 0.05%. Nb plays an important role in the microstructure evolution at all stages during hot working and hence in determining the final mechanical properties. Beneficial effects of Nb are used in many kinds of heat treatment. During the off-line heat treatment (RQ-T), the combination of Nb with Mo and B can improve the hardenability, refine the microstructure and improve the toughness of the high-strength steel. Nb precipitates form Nb(C,N) in austenite and the amount of precipitate depends on the temperature and the contents of C and N. When the steel is heated above Ac₃, the fine Nb(C,N) particles precipitate in the matrix. With the increase of the heating temperature, the precipitates first form and then gradually dissolve into γ . The complete dissolution temperature depends on the contents of Nb, C and N. Figure 3 shows the solubility of Nb(C,N) in austenite. It can be seen that a large amount of Nb will precipitate to form Nb(C,N) from austenite in the 900-950 °C temperature range. Due to the relatively low temperature, the particle size of these Nb(C,N) precipitates is very small, which is beneficial for the control of the austenite grain size during the reheating process.

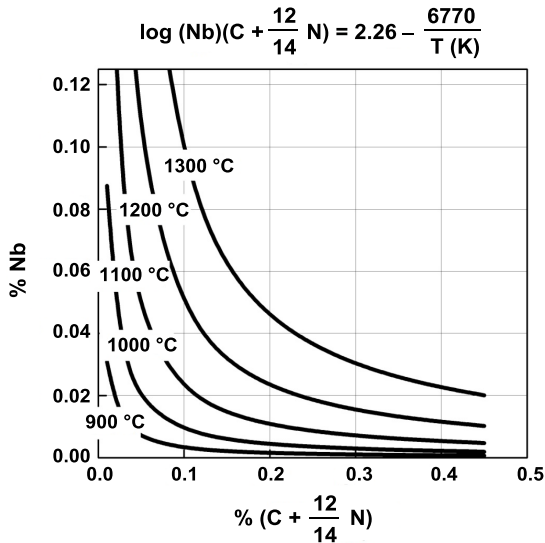


Figure 3. Solubility of Nb carbonitride.

Laboratory Investigation

In order to obtain the optimum addition of Nb, NM450 and Q690CF plates with different additions of Nb were evaluated in the laboratory. The appropriate production processing conditions were obtained through studying the effects of different routes. Theoretical studies showed that to achieve the best results, the addition of Nb in the quenched and tempered steel should not be more than 0.05%. This level of Nb addition could be fully dissolved during slab reheating. Niobium additions of 0%, 0.03% and 0.05% were compared in the experiments, Table II.

Table II. Chemical Composition of the Trial Steel (wt.%)

| Steel | C | Si | Mn | P | S | Alt | Nb | Other | Mo | B | CET* |
|--------|------|------|------|-------|-------|-------|-------------|--------|------|--------|------|
| NM450 | 0.18 | 0.30 | 1.20 | 0.008 | 0.003 | 0.025 | 0/0.03/0.05 | Ti, Cr | 0.25 | 0.0020 | 0.33 |
| Q690CF | 0.09 | 0.20 | 1.40 | 0.010 | 0.003 | 0.025 | 0/0.03/0.05 | Ti, Cr | 0.20 | 0.0020 | 0.27 |

*CET=C+(Mn+Mo)/10+(Cr+Cu)/20+Ni/40

Mechanical Properties

Wear-resistant steel is widely used in the production of machines and equipment which require wear resistance in industry, agriculture and construction. Typical fields of application are machines to excavate or transport raw materials, such as coal, ores, and stone. These steels contain characteristic alloying elements, Mn, Cr, Mo, Ni, B and are based on a C content up to 0.40%. Consequently, they attain high hardness values of 400 to 600 HB by quenching the steel to a martensitic microstructure [10]. The wear-resistant steel, NM450, with a chemical composition of 0.18%C-0.25%Mo-20 ppm B and Brinell hardness of 425-475 HB is produced by the Shouqin company. A significant increase of the toughness could be achieved by the addition of Nb, whilst still guaranteeing the strength and hardness, as shown in Figure 4. Enough strength and hardness could be obtained by C, Mn, Mo, Cr and B interactions and the martensite transformation during the water-quenching heat treatment. Refinement of the martensitic microstructure by the addition of Nb leads to the observed increase in toughness.

High-strength structural steel, with good toughness and weldability, is mainly used in the structural parts of engineering machinery. The AHSS grade Q690CF with the chemical composition of 0.09%C-0.20%Mo-20 ppm B, with a yield strength of 690 MPa and low welding crack susceptibility is produced by the Shouqin Company. The results in Figure 5 demonstrate that the strength was obviously increased by the addition of Nb, but this effect saturated when the content of Nb reached 0.03%.

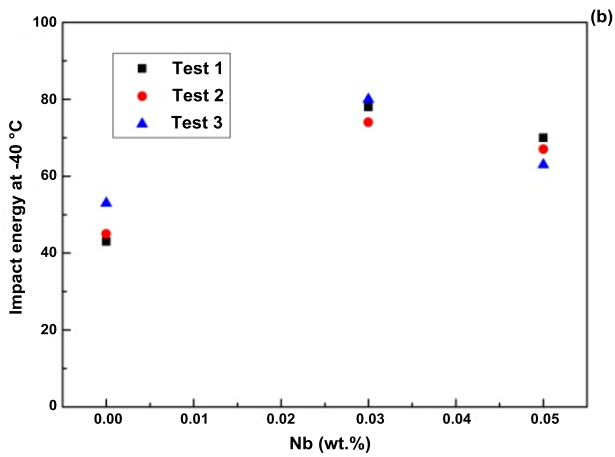
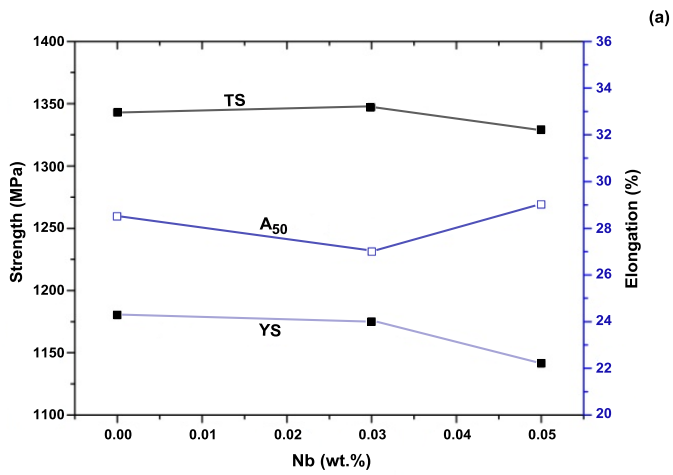


Figure 4. Variation of mechanical properties of NM450 wear resistant steel with Nb content; (a) tensile properties and (b) Charpy impact energy at -40 °C.

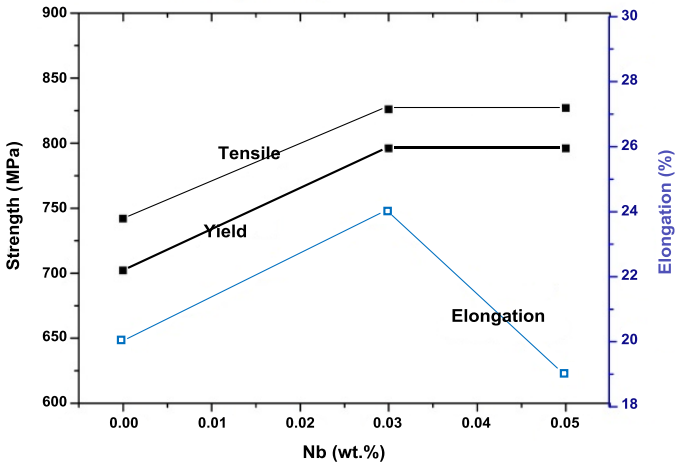


Figure 5. Variation of tensile properties of Q690CF high strength steel with Nb content.

Microstructure

Figure 6 shows the effect of Nb on the prior austenite grain size of the NM450 steel. The average prior austenite grain size (PAGS) of the steel without Nb is 17.9 μm , while the average PAGS of the steel with 0.03%Nb is only 12.3 μm . The major role played by Nb in steel is the austenite grain refinement via the delay of austenite recrystallization during hot rolling. Nb(C,N) first dissolves in austenite during the slab reheating process, and then precipitates during finish rolling. These fine Nb(C,N) precipitates can effectively pin the austenite grain boundaries or dislocation substructure, which is beneficial for the refinement of the as-rolled phase-transformed product. Moreover, the remaining Nb can continue to precipitate during the reheating process, which favors the refinement of the austenite grain size before quenching. Figures 7 and 8 show the refinement effects of Nb additions in NM450 and Q690CF, respectively. Obvious refinement was observed by comparing the steels with and without Nb addition.

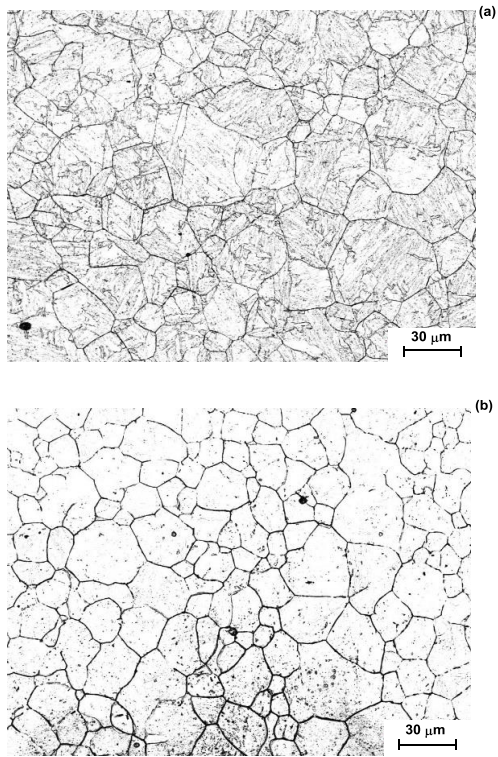


Figure 6. Light optical micrographs of prior austenite grain size; (a) without Nb in steel and (b) with 0.3%Nb steel.

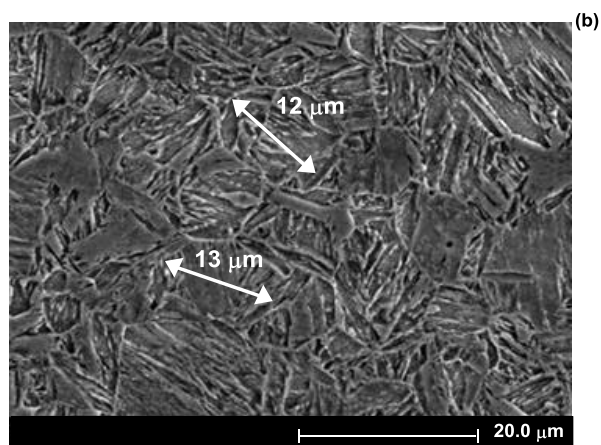
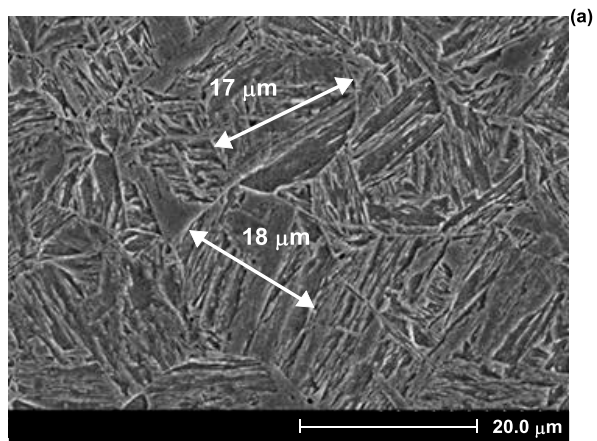


Figure 7. SEM micrograph of the microstructure of quenched and tempered NM450 steel; (a) without Nb and (b) with 0.03%Nb.

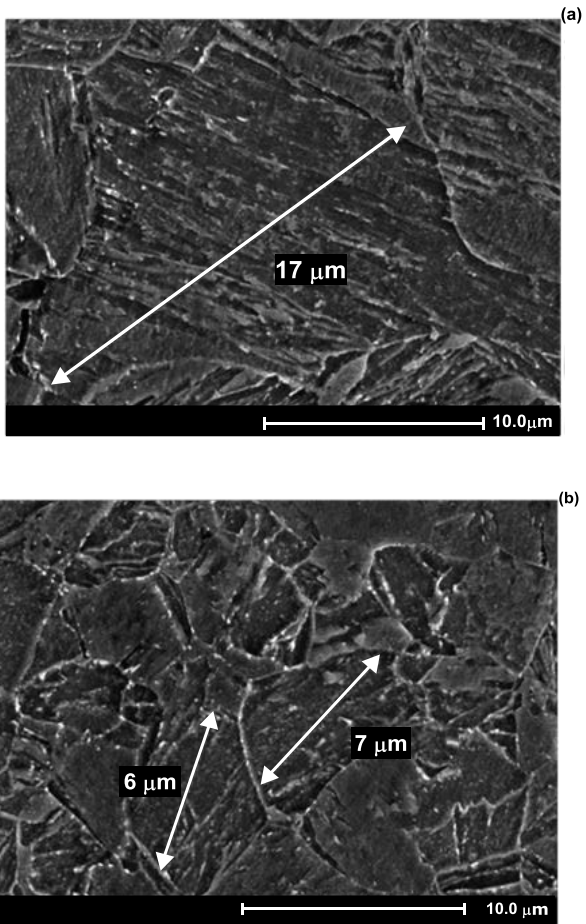


Figure 8. SEM micrograph of the microstructure of quenched and tempered Q690CF steel; (a) without Nb and (b) with 0.03%Nb.

Both the finer microstructure and the finely dispersed precipitation of carbo-nitrides are obtained by Nb-Mo-B microalloying. The toughness of the steel is improved through refining the microstructure. Precipitates with the size ranging from 10-40 nm in the NM450 steel with 0.03%Nb are shown in Figure 9. The precipitates are dispersed and identified as Nb(C,N) by EDS analysis.

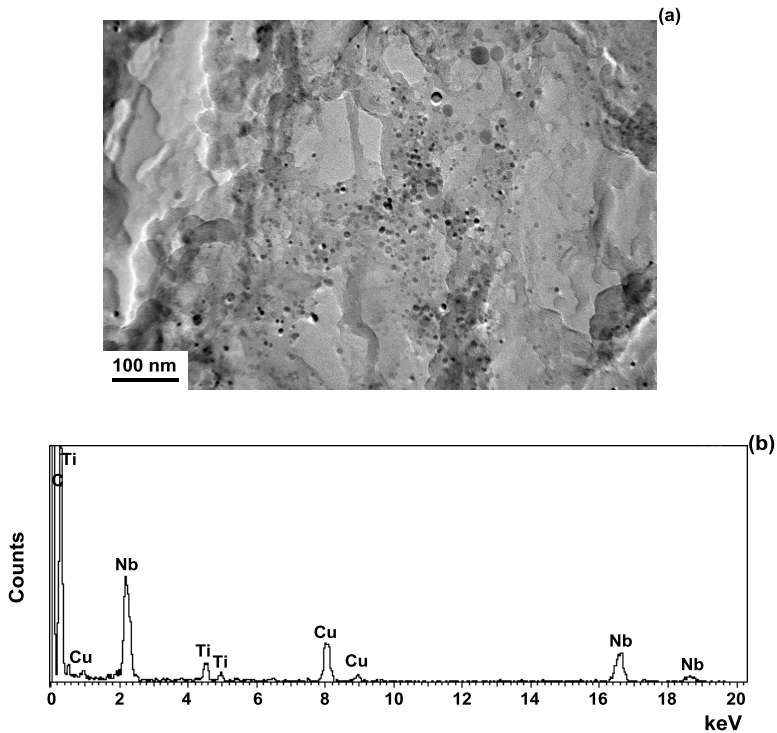


Figure 9. (a) TEM micrographs of the precipitate in quenched and tempered NM450 steel with 0.03%Nb. Dispersed carbide size ranges from 10–40 nm, (b) energy dispersive spectroscopy (EDS) analysis of Nb(C,N) precipitate. (The peaks of Cu are from the Cu-grid which supports the carbon replica.)

Toughness

Toughness is an important property for the applications of wear resistant steel. Tempering of the quenched plate is a commonly used process; higher tempering temperature leads to the reduction of strength and hardness. For wear-resistant steel, NM450, the tempering temperature ranged from 200-250 °C. In this case, the toughness has not been improved compared with the as-quenched steel, but the internal residual stress can be reduced and consequently cracking susceptibility is reduced to an extent. By the addition of microalloying elements such as Nb, Mo and B, with a lower C content, the strength and hardness of the steel can be maintained, and meanwhile the toughness of the steel can be improved. In particular, a significant improvement of toughness was obtained through adding the element Nb. Figure 10 shows the beneficial effect on toughness in the NM450 steel of Nb microalloying. Over the entire range of testing temperatures, the impact energy is significantly improved with a Nb addition.

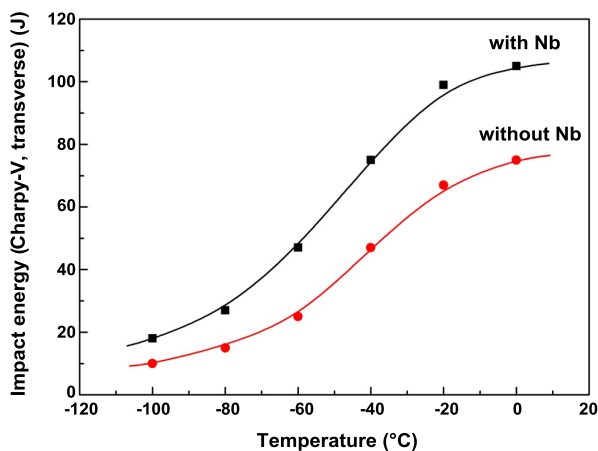


Figure 10. Charpy-V impact energy variation with temperature for NM450 without and with Nb microalloying.

Abrasion Resistance

Abrasion resistance is an important indicator of the potential performance of wear-resistant steel. The internationally recognized method for relative abrasion resistance measurement is a pin on disc abrasion technique. The wear resistance tests on the NM450 trial plate were carried out using a two-body abrasive wear test, on the ML-10 abrasive wear tester. Details of the pin on disc testing used for the relative abrasion resistance comparison are as follows:

- Sample size - 6.0 mm diameter × 25 mm length;
- Disc rotation - 60 rpm, Load – 42 N;
- Abrasive Paper - 80 Grit, SiC wet sand paper;
- Sample radial feed rate - 4 mm/revolution;
- Starting radius - 13 mm;
- Termination radius - 103 mm;
- Wear tip - 8.2 mm.

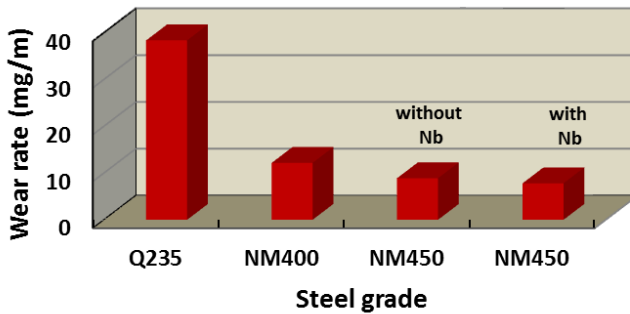


Figure 11. Increase of wear resistance in NM450 through addition of Nb.

The characteristic wear type is ploughing leading to abrasion. Thereby, the plate surface gets scratched when exposed to an abrasive and hard material, such as sand or typical minerals, and is then removed. A high hardness of the material is, therefore, one important factor for promoting good wear resistance. Furthermore, higher material toughness improves the wear resistance and thus reduces the material loss, because it changes the wear mechanism from micro-ploughing into micro-machining [10,11]. Figure 11 shows the results from this study on the wear properties of the various steels. The service life of NM450 with 0.03 %Nb is five times that of Q235, 1.56 times that of NM400, and is increased by around 14% compared with that of NM450 without Nb. As a result of the addition of Nb, the martensitic microstructure is refined and the toughness is improved. Nb microalloying not only improves the wear resistance of NM450, but also can reduce the probability of the appearance of cracks in a low temperature environment, thus increasing the material's service life [12]. Figure 12 shows the scratch morphology of NM450 without Nb and with Nb after wear testing. The NM450 with a Nb addition exhibits more uniformly distributed and shallow furrows on the worn surface, compared with NM450 without the Nb addition, indicating that the former has better wear resistance.

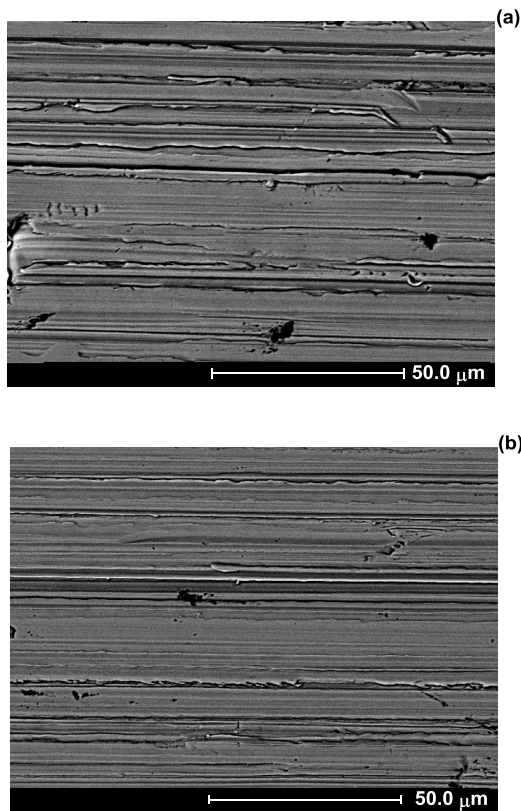


Figure 12. Scratch morphology for NM450; (a) without Nb and (b) with Nb after wear testing.

Industrial Production

The industrial production of AHSS was conducted on the 4300 mm rolling line of Shouqin.

The smelting process was as follows: blast furnace molten iron - hot metal desulfurization - converter smelting - LF+RH refining - slab continuous casting. The contents of P, S, O and N were reduced as much as possible, and the contents of microalloying elements were required to be accurately controlled during smelting.

In order to fully utilize the grain refinement role of Nb, thermomechanical controlled processing (TMCP) was employed. The number of rolling passes, rolling temperatures and cooling schedule need to be strictly controlled. Two-stand rolling was conducted on the 4300 mm rolling line. A

relatively large force was applied to ensure that there was enough rolling reduction during roughing. The finish rolling temperature was controlled and the accelerated cooling (ACC) system was used to cool the plate.

The mechanical properties of as-produced AHSS plates are given in Table III. The NM450 and Q690CF plates have superior mechanical properties to the previous grades. The yield (YS) and tensile (TS) strength of NM450 are more than 1100 MPa and 1350 MPa respectively. The elongation (A_{50}) is greater than 15% and the average Charpy impact energy at $-40\text{ }^{\circ}\text{C}$ exceeds 60 J. The Brinell hardness (HB) is not lower than 430 HB. For Q690CF plate, the YS is greater than 750 MPa, the TS is larger than 800 MPa, the A_{50} is greater than 20%, and all the Charpy impact values at $-40\text{ }^{\circ}\text{C}$ are not less than 200 J.

Table III. Mechanical Properties of As-produced AHSS Plates

| Steel Grade | Plate Thickness mm | YS MPa | TS MPa | A_{50} % | Charpy Impact Value $-40\text{ }^{\circ}\text{C}$ J | | | AVE | Hardness HB | | | AVE |
|-------------|--------------------|--------|--------|------------|---|-----|-----|-----|-------------|-----|-----|-----|
| | | | | | 70 | 92 | 91 | | 84 | 438 | 435 | |
| NM450 | 12 | 1186 | 1383 | 18 | 70 | 92 | 91 | 84 | 438 | 435 | 432 | 435 |
| NM450 | 19 | 1124 | 1375 | 21.5 | 57 | 59 | 78 | 65 | 436 | 431 | 434 | 434 |
| Q690CF | 8 | 829 | 847 | 24 | 224 | 236 | 230 | 230 | | | | |
| Q690CF | 10 | 799 | 828 | 24.5 | 253 | 216 | 237 | 236 | | | | |
| Q690CF | 30 | 786 | 818 | 32 | 253 | 241 | 246 | 247 | | | | |

Cold Bending

A series of cold bending tests with various radii and a constant angle of 180° were carried out. When the plate thickness was not more than 20 mm, the thickness of the cold-formed sample was the same as the plate thickness, and the width of that was 40 mm. When the plate thickness was greater than 20 mm, the thickness of the cold-formed sample was thinned to 20 mm, and the width of that was again 40 mm.

Table IV. Results from Cold Bending Tests

| Steel Grade | Plate Thickness (mm) | Bending Sample Size (mm) | | Bending Radius (t =plate thickness) | | | | |
|-------------|----------------------|--------------------------|-----------|--|-------|-------|-------|-------|
| | | Width | Thickness | 5.0 t | 4.0 t | 3.0 t | 2.0 t | 1.5 t |
| NM450 | 12 | 40 | 12 | ○ | ○ | △ | × | × |
| Q690CF | 10 | 40 | 10 | ○ | ○ | ○ | △ | × |
| Q690CF | 30 | 40 | 20 | ○ | ○ | ○ | ○ | ○ |

Note: ○ - no crack, △ - tiny crack, × - crack

Table IV gives the results of a series of cold bending tests. It can be seen that when the radius is only 1.5 or 2.0 times the thickness, big cracks appear on the surface of NM450 after cold bending. When the radius equals 3.0 times thickness only micro-cracks appear. In the case of a bending radius of 4 t, no cracks on the surface of NM450 were observed. For Q690CF, when the radius is not less than 3.0 t, no cracks appear on the surface. These results indicate that the cold bending properties of NM450 and Q690CF plates are good enough to meet the requirements of high-grade engineering machine production.

Welding

The weldability of the AHSS grades, NM450 and Q690CF, was evaluated against the criteria used in the production of dump trucks. The butt joint welding test between NM450 plates and lap joint welding CTS test were carried out.

The butt joint, rigid restraint welding cold crack test refers to GB/T13817-1992. The dimensions of the NM450 test piece were 19 x 450 x 220 mm. The rigid base plate was Q345B steel with the dimensions of 50 x 600 x 440 mm. Before welding, the oxide skin, oil and rust on the touching surfaces of the two plates and around the weld joint were cleared. The processing parameters of welding are given in Table V.

Table V. Processing Parameters for Welding

| Method | Type of welding wires | Size of welding material (mm) | Current (A) | Arc voltage (V) | Welding rate (mm ^s ⁻¹) | Interpass temperature (°C) | Post-welding heat treatment |
|-----------------------------|-----------------------|-------------------------------|-------------|-----------------|---|----------------------------|-----------------------------|
| manual electric-arc welding | ER50-6 | Φ1.6 | 160-280 | 28-30 | 6-7 | ≤250 | No |

The specimen is fixed on the rigid base plate by spot welding, and then the restrained joint is welded. The height of the weld joint is the same as the thickness of plate. Three experiments were performed. For the first experiment, only one joint was welded with no preheating. For the second and third experiments, again only one welding joint was welded, but with preheating. After cooling and 48 h holding, the specimens were cut equally into six parts along the length direction. The presence of cracks was checked by the naked eye or a magnifying glass after grinding and polishing.

The lap joint welding CTS test refers to GB/T4675.2-1984. The base plate was NM450 with the dimensions of 19 × 175 × 100 mm. The tested Q690CF steel had the dimensions of 8 × 100 × 75 mm. Before welding, the oxide skin, oil and rust on the touching surfaces of the two plates and 50 mm around the weld joint were cleared. The welding processing parameters are given in Table VI. The Q690CF specimen was fixed on the base plate by screw bolts. The restrained joints were welded, and two-side passes were performed. After the specimen was fully cooled down to room temperature, the other joint was welded. This operation was repeated two times. After 48 h holding, every welding joint was cut into three parts. The specimens were examined on a macroscopic scale and checked for the presence of cracking.

The butt joint, rigid restraint welding cold crack test and lap joint welding CTS test results show that during the production of the tested steel, the low carbon and Nb-Mo-B microalloying were correctly designed, the elements that influence the C equivalent were appropriately controlled and the contents of P, S and gases (eg. N, O, H) were also properly controlled. This resulted in a low sensitivity to weld cracking in the tested steel. Optical observation showed that a good joint was obtained between the welding materials and parent materials. No cracks were observed in the welded joint and heat affected zone (HAZ). The microstructure of the welded joint was

homogeneous. The parent materials mainly consisted of tempered martensite (M). The HAZ was composed of granular bainite (GB) and a small amount of M. The results of hardness testing showed that the HAZ had no softened zone. The occurrence of GB in the HAZ indicates that the HAZ of wear resistant steel has a low hardenability and a low sensitivity to cracking.

Conclusions and Prospects

The Shougang Heavy Duty Truck Manufacturing Company and CBMM (Companhia Brasileira de Metalurgia e Mineração) have collaborated to design, produce, and put into service an improved dump truck car tub of 136 t load capacity. Instead of the original Q235 grade, the NM450 and Q690CF AHSS grades were developed and used to reduce the weight of the car and hence energy consumption, increase the transportation load and the lifespan of the mine car, and decrease the maintenance costs. The developed steels employed Nb-Mo-B alloying methodology to achieve the required higher strength to allow thinner, lighter sections to be employed in the car construction whilst maintaining or exceeding all the other requirements such as weldability, toughness and wear resistance.

The NM450 Charpy impact energy is significantly improved and the service life under abrasive wear is increased by around 14% compared to the standard grade, and the Q690CF strength is obviously improved, and the weldability and cold bending of the AHSS comfortably meet requirements. The development of the AHSS fully met the requirements for the new dump truck tub.

The AHSS of NM450 and Q690CF were applied in the SGE150 heavy dump body tub, reducing the weight of the truck by 3800 kg, decreasing the energy consumption by 10-13%, and reducing the transportation costs by over 3%. The development of these AHSS, therefore, provides further opportunities for lightweight materials for the development of other cars and components in the mining dump truck industry.

References

1. M. Ma and H. Yi, "Application of High Strength Steel to Manufacturing Auto," *Heat Treatment*, 26 (6) (2011), 9-19.
2. D. Cornette and A. Galtier, "Influence of the Forming Processing on Crashing and Fatigue Performance of High Strength Steels for Automotive Components," (Paper presented at the Society of Automotive Engineers, World Congress, Detroit, USA, 2002), 1-6.
3. F. Junfeng and C. Ming, "Ordinary Discussion on the Way Toward the Lightweighting of Chinese Automobile," *Foundry*, 10 (55) (2006), 995-998.
4. J.C. Benedyk, "Light Metals in Automotive Applications," *Light Metal Age*, 10 (1) (2000), 34-35.

5. T. Xu and Z. Cheng, "Research and Analysis of Forecasting 'The 12th Five Years Plan' Market Mix of the Mining Dump Truck," *Mining and Metallurgical Engineering*, 32 (2012), 468-472.
6. S. Fan et al., "Shell-thickness Calculation of SPV's Structures in Strength Design by Using the High Strength Steel," *Special Purpose Vehicle*, 1 (2009), 36-37.
7. H. Mohrbacher, "Mo and Nb Alloying in Plate Steels for High-performance Applications" (Paper presented at the 2011 International Symposium on the Recent Development in Plate Steels, Winter Park, Colorado, 19-22 June 2011), 169-178.
8. K. Hulka, A. Kern and U. Schriever, "Application of Niobium in Quenched and Tempered High-strength Steels," *Materials Science Forum*, (500-501) (2005), 519-526.
9. A. Courtney et al., "Effect of Austenitizing Conditions on Hardenability of Boron-added Microalloyed Steel" (Paper presented at the 2011 International Symposium on the Recent Development in Plate Steels, Winter Park, Colorado, 19-22 June 2011), 273-282
10. A. Kern, P. Feinle and U. Schriever, "Heavy Plate Made of Wear Resistant Special Structural Steels – Manufacture, Processing, Application" (Paper presented at the Proceedings of EUROMAT '01: European Conference on Advanced Materials and Processes, Rimini, Italy, 10-14 June 2001), 765.
11. K.H. Zum Gahr, *Microstructure and Wear of Materials* (Oberursel, Germany: DGM-Informationsgesellschaft, 1987), 21.
12. J. Bian et al., "Application Potential of High Performance Steels for Weight Reduction and Efficiency Increase in Commercial Vehicles," *Advances in Manufacturing*, 3 (2015), 27-36.

COLLABORATION TO REDUCE WEAR AND CORROSION COST FOR THE MINING INDUSTRY

S. Hui

Energy, Mining and Environment, National Research Council Canada,
4250 Wesbrook Mall, Vancouver, BC, Canada, V6T 1W5

Keywords: Wear Evaluations, Wear Resistant Materials, Abrasion, Slurry Erosion, Erosion-corrosion, Oil-sands, Hard Rock Mining, Cost Reduction, Collaboration, Consortium

Abstract

It is a common objective for all the mining industries to reduce the cost of maintenance and reliability due to wear and corrosion issues. Larger gains and faster progress could be achieved by a more concerted collaboration. With this vision, the National Research Council (NRC)/Industry Mining Materials Wear and Corrosion Consortium was founded in 1996. The consortium has expanded to 14 members, including mining companies, equipment manufacturers and materials suppliers. During the last 19 years, through the collaborative wear materials research program within the consortium, the expertise, the unique capabilities, and the materials database, NRC have helped the consortium members to reduce the severe wear and corrosion damage that translates to high costs and production losses incurred during mining and mineral processing. Some very significant improvements in the battle to control wear/corrosion and improve performance are presented.

Introduction

Wear and corrosion issues can be found for almost all the equipment employed in mineral processing within the mining industry. While the grinding process is responsible for the major cost of the wear and corrosion in the hard rock mining sector, components in the slurry transportation process have been the key challenge for the oil sands industry [1]. A typical nickel mine in 2014 could spend more than C\$20 million on the grinding media. The grinding of lower grade ores and the harder iron ores could cost much more. The same expense is likely for a hydro-transport line of 70 km for the oil sands operator in 2014. Some of the key components, such as slurry pumps and pipeline u-bends for oil sands, only have a lifetime of less than three months. In 2013, wear was estimated to cost over C\$15 billion for maintenance, repair and operations (MRO) for the Canadian mining/mineral processing industry. A major portion of the cost has been attributed to equipment wear and corrosion loss, including materials, labor, and productivity loss. The cost has been increasing significantly with the scale up of production and a decrease of ore grade quality. The MRO budget at a major oil sands producer has increased from C\$450 million in 2003 to C\$1.5 billion in 2012.

Wear is usually considered as a materials issue, but is actually a system characteristic in terms of properties of abrasion, properties of wear materials, and contact conditions between the abrasion media and wear resistant materials. Many factors can contribute to the wear loss of materials as summarized in Table I [2]. Any parameter listed in the table could influence the materials performance dramatically, such as the impact angle [3]. Materials evaluations carried out on a laboratory scale have to combine different characterization mechanisms and apply conditions close to the field applications in order to make meaningful conclusions. There are no perfect materials existing to resist wear and corrosion, but wear-resistant materials and operation conditions could be optimized to reduce the wear and corrosion loss. However, the situation for controlling wear issues is complex in the mining processes; it has been a significant challenge for mining operators to select the right materials for further improvement of the operation performance [4-6].

Table I. Factors that Influence Wear Behavior [2]

| Abrasive Properties | Wear Material Properties | Contact Conditions |
|----------------------------|---------------------------------|---------------------------|
| Particle size | Hardness | Force/impact level |
| Particle shape | Yield strength | Velocity |
| Hardness | Elastic modulus | Impact/impingement angle |
| Yield strength | Ductility | Sliding/rolling |
| Fracture properties | Toughness | Temperature |
| Concentration | Work-hardening characteristics | Wet/dry |
| | Fracture toughness | pH |
| | Microstructure | |
| | Corrosion resistance | |

NRC/Industry Mining Materials Wear and Corrosion Consortium

The Energy, Mining and Environment (EME) portfolio at the National Research Council (NRC) Canada delivers advanced technology solutions to improve the productivity and competitiveness of Canada’s natural resource and utility sectors. We apply our multidisciplinary capabilities to strategic R&D programs that target stakeholder-endorsed challenges to strengthen Canadian supply chains and help companies develop and maintain competitive positions in target markets at home and abroad. Co-investment from clients and stakeholders ensures our program activities remain aligned to market needs and deliver public and private return on investment, enhancing economic, social and environmental well-being. The industry sectors addressed by EME comprise the value chains of mining, oil and gas extraction and processing, primary and fabricated metal products, and electricity and natural gas utilities.

NRC has built comprehensive testing and characterization facilities for evaluation of wear and corrosion-resistant materials and coatings. These facilities include not only commercially available equipment such as low stress abrasion (dry sand rubber wheel/ASTM G65), air jet erosion (ASTM G76), slurry abrasion (ASTM G75/G105) and gouging abrasion (ASTM G81), but also specialized unique testing equipment designed and built by researchers at NRC, such as a scouring erosion system, slurry jet erosion, slurry erosion-corrosion pot and high load scratch test. These facilities cover broad properties for ceramic, metallic, and polymeric materials. These facilities enable the prediction of materials’ relative performance under different wear and

corrosion attack mechanisms. They provide tools for comparing materials, developing and assessing new materials for particular applications, obtaining information on specific process influences, and quality assurance and specification purposes. NRC also provides materials modeling and simulation packages for optimization and industrial coatings development by thermal spray and cold spray technologies.

As a common objective for all the mining industries is to reduce the cost of maintenance and reliability due to wear and corrosion issues, larger gains and faster progress could be achieved by a more concerted collaboration. With this vision, the NRC/Industry Mining Materials Wear and Corrosion Consortium was founded in 1996, which includes mining operators, equipment manufacturers, and materials suppliers. All the members can access the mining material data from the evaluations at NRC and share the results obtained by the members. In addition, NRC provides technical solutions to clients through collaboration projects by either co-investment or fee-for-service projects for exclusive delivery.

Along with the critical influences of process conditions and equipment design on the extent of wear attack, the selection and development of optimized/improved wear resistant materials is of extremely high importance to control and mitigate damage and losses. This dictated the agreed consortium collaboration strategy which has been formulated as:

- Identify and focus performance improvement efforts on the most important problem areas;
- Confirm attack mechanisms and correlate worn surfaces from service to those obtained in testing;
- Increase wear evaluation and characterization capabilities to meet critical needs;
- Determine and compare the properties and structures of the entire spectrum of mining wear materials under a variety of relevant abrasion and erosion conditions that simulate industrial service, correlate properties and material systems with conditions, and establish fundamental influences;
- Produce a comprehensive Wear Materials Properties database that is updated regularly and is accessible to qualified industrial sponsors;
- Use the database as an in-house reference and provide controlled external access and consulting resources to assist in materials selection, for Quality Assurance and specifications/standards compilation, in wear parts failure analysis, and to facilitate development of more wear resistant products.

NRC has compiled a database from materials evaluation programs performed since 1996. To date the properties of these materials include air jet erosion, ASTM G65, high stress abrasion, impact abrasion, and slurry jet erosion. The database also includes wear and hardness test results and associated conditions/compositions and SEM images of the materials' microstructures. The materials are from multiple forms and manufacturing processes such as bulk materials and surface modification systems, including weld overlays, claddings, coatings, and diffusion layers. Figure 1 shows an illustration of online access to the NRC wear materials properties database. The database has been widely used for design, materials specification and construction. Along with the consortium operation, the members have found the following benefits:



Figure 1. Illustration of online access for the NRC wear material properties database.

- Access to the world class research facilities, including specialized equipment developed at NRC;
- Utilization of a comprehensive database of wear-related properties for industrial material selection;
- Participation in a valuable biannual forum to connect with companies, along the value chain, at review meetings;
- Gaining of knowledge on wear and corrosion resistant materials that would have been hard to find otherwise;
- Finding solutions for wear issues through shared success stories;
- Understanding of the needs of end users to optimize or develop products;
- Understanding of the progress of materials suppliers and potential applications for operators;
- Networking for new business opportunities.

Success Stories from the Consortium

During the last 19 years, through the collaborative wear-materials research effort in the consortium, the expertise, the unique capabilities, and the materials database at NRC, consortium members have been able to reduce severe wear of equipment and corrosion damage related to high costs and production losses in mining and mineral processing. Wear is not avoidable, but equipment lifespan can be improved with fresh approaches for the wear and corrosion challenges as shown in Figure 2. NRC has saved the mining industry millions of dollars annually in operating costs by providing materials selection solutions, components design and materials

processing improvement. Some selected cases in the battle to control wear and corrosion and improve performance are summarized in Table II.

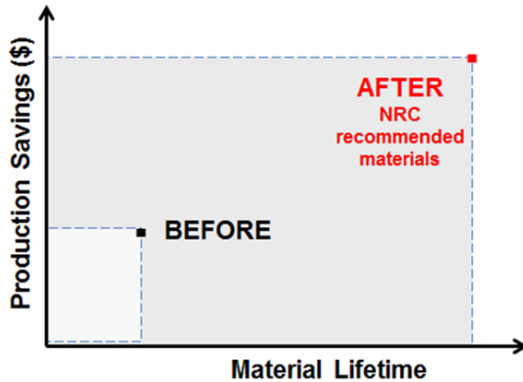


Figure 2. Illustration of NRC impact to the production savings of clients.

Table II. Selected Success Cases to Reduce Wear and Corrosion Loss

| Case | Challenge | Solution | Results |
|-------------------------|--|---|---|
| Primary Separation Cell | Significant wear loss on a pipe bend in the primary separation cell (PSC) at an oil sands producer | Upgrading PSC line from chromium-carbide overlay (CCO) to a more impact-resistant material identified from the consortium database | Service life increased from 5 weeks to >1 year (Jan. 2015); saved C\$112 M/ year from production loss, materials cost, and labor cost |
| Breaker Plates | Initial medium carbon steel screens required 10 days maintenance per 20 days operation at the field of an oil sands operator; CrC bulk weld and Plasma Transferred Arc Welding (PTAW) WC/Ni-based overlay tried as most successful materials | Laminated CrMo white iron (very high gouging and good sliding abrasion resistance in jaw crusher tests) | Lifespan now >12 months, double the PTAW WC/Ni overlay; increased uptime and production; reduced maintenance charges with comparable plate costs; saving about C\$1 million per breaker per year and there are seven breakers in operations |
| Slurry Mixing Cyclones | Significant wear-loss of slurry mixing cyclones at major oil sands producer | Changed cyclone materials from neoprene-lined carbon steel (CS) to more abrasion-resistant materials found in NRC Database; validated through further testing | Life increased from 300-400 hours to >24,000 hours (March 2015) |

| Case | Challenge | Solution | Results |
|---|--|--|--|
| Tailings Solvent Recovery Units (TSRU) | Severe wear in downstream TSRU vessels for diluent recovery from heated tailings for hydroheater steam mixing system and feed nozzles in Albian Sands production; service life <1 wk for Stellite overlays on stainless steel hydroheater components, CrC weld overlay, and surface modification coatings on spray nozzles | Sintered tungsten carbide designs for both applications based on NRC Database | Lifetime extended by several months in certain situations |
| Rotary Coupling for HD Blast Hole Drill | Cracked shock absorber coupling at a hard rock mine; in-house and supplier repairs and modifications unsuccessful | Found failure related to high load/torque system; Designed larger wall section with higher strength weldable steel; Modified welding procedure with finite element analysis; Revised construction material | Superior performance compared to both standard rig and to new advanced OEM option |
| Shovel Track Link Pads | Numerous (29) failures after very limited service life in cast steel lugs (austenitic Mn); High replacement costs, downtime and production losses | Examined fracture face and microstructure features causing failure; Revealed very poor foundry practice/ inferior workmanship | Facilitated warranty settlement; contributed to future manufacturing and quality assurance improvement |

The highest quality ore grades available for mining are declining, hence mining will have to process lower grade ores in the future. A finer grind size is needed for low-grade ores, which will lead to an increase of wear and thus greater costs in the future [7]. In Canada, on average, every ton of copper extracted produces more than 99 tons of waste material. The amount of gold extracted per ton of material excavated is even less. For example, the ores have to be milled down to ~20 µm in order to concentrate to 23% of copper (Cu) and 18g/ton of gold (Au) from the ores which originally contain 0.62% Cu and 0.95g/ton Au at the NewGold Afton Mine. The NRC mining materials wear and corrosion consortium is continuously providing unique service and knowledge to the mining industry to address the challenges. In addition to the laboratory-scale materials evaluation and analysis, the consortium is also repositioning roles to have a greater impact on the NRC's High Efficiency Mining (HEM) program by expanding research capabilities, using the consortium as a platform to bring more business opportunities, and collaborating with other international associations.

Conclusions

Material loss due to wear and corrosion is a well-known issue for the mining industries and the estimated cost was around C\$15 billion in Canada in 2013. The NRC/Industry Mining Materials Wear and Corrosion Consortium, founded in 1996, has demonstrated a successful approach in achieving larger gains and faster progress by a more concerted collaboration. The expertise, the unique capabilities, and the materials database at NRC have helped the consortium members to reduce severe wear and corrosion damage, yielding cost reduction and profit growth of over C\$100 million a year. The NRC Mining Materials Wear and Corrosion Consortium is continuously providing a unique service and is expanding capabilities to benefit more members in the future.

Acknowledgements

The authors would like to acknowledge the support from the consortium members, the team at NRC and Rees Llewellyn at RJL Materials Technology Inc.

References

1. T. Norman, *The Wear Control Handbook* (New York, NY: The American Society of Mechanical Engineers United Engineering Center, 1980), 1009-1052.
2. P.J. Mutton et al., eds., *Abrasion Resistant Materials for the Australian Minerals Industry*, vol. 1 (Melbourne: Australian Minerals Industries Research Association Limited, 1988), 60.
3. B. Bhushan, ed., *Modern Tribology Handbook*, vol. 1 (Boca Raton, FL: CRC Press, 2001), 1331-3170.
4. R. Llewellyn, "Materials for Controlling Wear in Surface Mining," *CIM Bulletin*, 89 (1002) (1996), 76-82.
5. R. Llewellyn, "Resisting Wear Attack in Oil Sands Mining and Processing," *CIM Bulletin*, 90 (No.1012) (1997), 75-82.
6. R. Llewellyn, W. Leith and E. Magel, "Wear Materials Guide for the Mining and Mineral Processing Industry" (Vancouver: The Mining Association of British Columbia, 1996).
7. CRC ORE http://www.grida.no/graphicslib/detail/average-ore-grades-over-time_f07c.

INCREASING THE LIFE CYCLE OF BUCKETS FOR WHEEL LOADERS USING HIGH STRENGTH AND ABRASION RESISTANT STEELS MICROALLOYED WITH NIOBIUM

H. Rosa¹, M.K. Ferreira Cardoso¹, É. França², J.L. Barreto³, L.M. Silvestre²
and M.A. Stuart Nogueira²

¹Maintenance Department, CBMM - Companhia Brasileira de Metalurgia e Mineração, Araxá, MG, Brazil

²Technology Department, CBMM – Companhia Brasileira de Metalurgia e Mineração, São Paulo, SP, Brazil

³Mining Department, COMIPA – Companhia Mineradora do Pirocloro de Araxá, Araxá, MG, Brazil

Keywords: Wheel Loaders, Buckets, Steel, Wear, Niobium

Abstract

CBMM applied niobium microalloyed steels in two types of buckets for wheel loaders operating at its facility in Araxá, Brazil. The objective was to evaluate the benefits of these steels relating to cost reduction, productivity and component life cycle. One of the analyzed loaders collects hot pieces of ferroniobium after ingot stripping and loads them into crusher silos. The use of wear resistant and tool steels solved the problems of deformation, wear and cracks during service, increasing bucket life by about 190%. The other machine was a wheel loader operating at the niobium ore mine. The new design with wear resistant and high strength steels reduced bucket weight by 14%, with a corresponding increase in load capacity. The extra capacity made loading the 42-tonne mine trucks more efficient. With the new materials, the cracks that previously occurred in the wheel loaders' buckets were eliminated, while the same wear resistance of the original chromium carbide clad steel was retained. Furthermore, investment costs were reduced by over 7%.

Introduction

CBMM strives to provide niobium technology to develop applications where this element can help to overcome the key challenges faced around the world: to achieve economic growth wisely and sustainably. In order to accomplish this, CBMM employs a technical group that works with steelmakers, research universities, institutes and end users. This technology program sponsors the development of materials that minimize raw material consumption by increasing component life cycles and optimizing process efficiencies to save energy and raw materials. A component of the program includes testing concepts developed on equipment operating at CBMM facilities in Araxá, Brazil.

Higher strength and more wear resistant steels are critical to create structures that have longer service lives, and to use less material in components that must withstand harsh working conditions. The loaders for different operations at CBMM facilities in Araxá face many challenges since they

work in abrasive conditions, suffer oxidation and, in some cases, are subjected to high temperatures.

The lightweight design concept has been very well developed for different applications [1-5]. Niobium is particularly effective in simultaneously increasing the strength and toughness of steel, and now there are many papers reporting niobium's effect on wear resistance as well [6-7]. By increasing steel strength, it is possible to use thinner components, with corresponding reductions in weight. Since toughness is also increased, structural integrity is improved. As bucket weights decrease, loading capacities increase, leading to gains in operational efficiency.

The principal driver for this development was to improve the service life of the buckets and their loading efficiency, by applying high strength and wear resistant steels in the form of niobium microalloyed steels. This paper provides two examples of bucket loaders using these steels and the resulting benefits.

Description of the Two Case Study Wheel Loader Buckets Operating at CBMM Facilities

Stripped FeNb Ingot Loading Bucket

After being processed in electric arc furnaces, liquid ferroniobium (FeNb) is cooled in molds. Following solidification, the FeNb is stripped from the molds and collected by a loader for crusher feeding, Figure 1. During this transport operation, the FeNb can be at temperatures of up to 350 °C.



Figure 1. Loader collecting FeNb after ingot stripping.

FeNb remains in the bucket for no longer than ten minutes, but because the material is hot, the buckets suffer temperature-related deformation, Figure 2, and cracks, Figure 3.



Figure 2. Bucket deformation after 200 hours in service.



Figure 3. Bucket cracking after 200 hours in service.

The average service life of this kind of bucket had been 320 hours, with the best performance reaching 570 hours. The new bucket was developed to increase service life, and eliminate the cracking and deformation that makes it very difficult to collect FeNb from the floor.

Niobium Ore Loader Bucket

The second bucket developed was for wheel loaders transporting niobium ore at CBMM's mine, Figure 4. The main problem with the original bucket was the appearance of structural cracks, Figure 5. Service life for these components is reduced by such cracks since they start to appear at 1,600 to 2,000 hours. The goal is to achieve total service life over 11,000 hours. The wheel loaders' buckets experience very little wear, this only being important for the ground engaging tools (GET). GET wear will not be addressed in the current paper.



Figure 4. Wheel loader bucket at niobium ore mine.

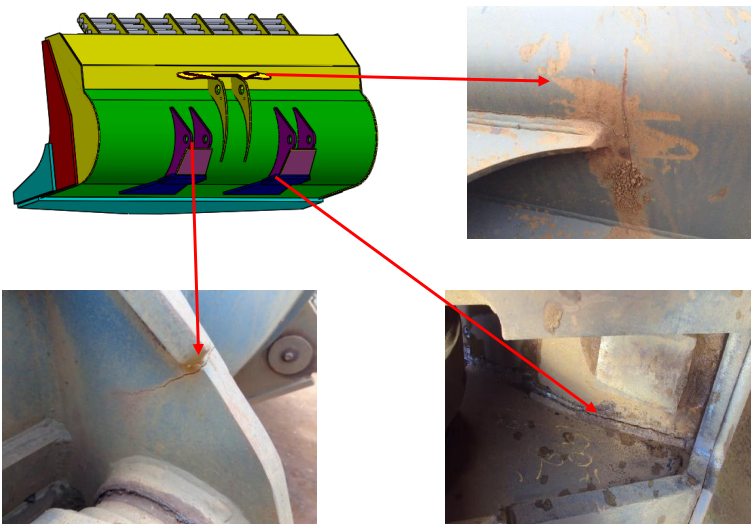


Figure 5. Structural cracks in the ore loader bucket after 2,000-3,000 hours of work time.

Materials and Description of the Developed Components

Stripped FeNb Ingot Loading Bucket

Figure 6 shows the bucket design, including selected dimensions. The bucket weighs about 364 kg and has a load volume of 0.24 m³. The original model was made with carbon steel grades, Figure 7. Because microalloyed steels were used in the new bucket, the purchase cost was 42% higher than the original model. This investment must achieve payback through increased service life and lower maintenance.

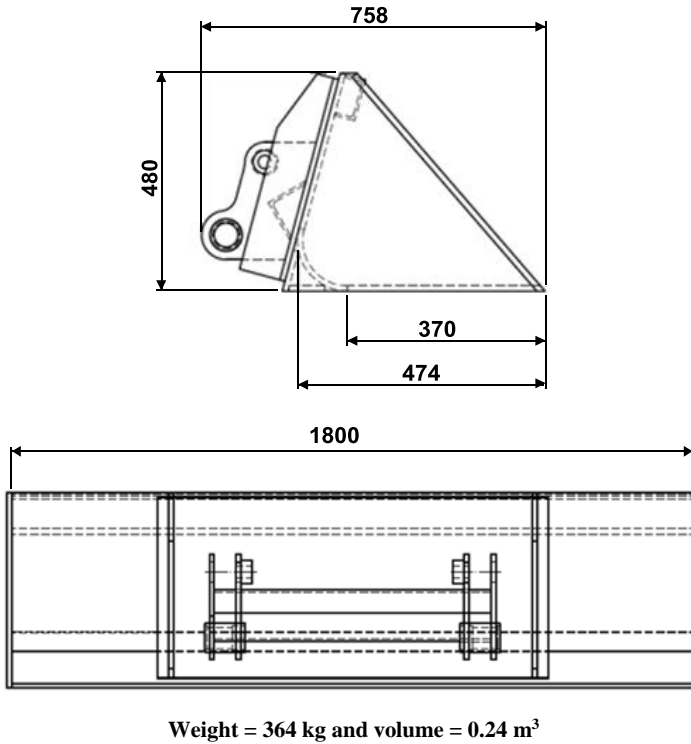


Figure 6. Main dimensions (mm) of the stripped FeNb ingot loading bucket.

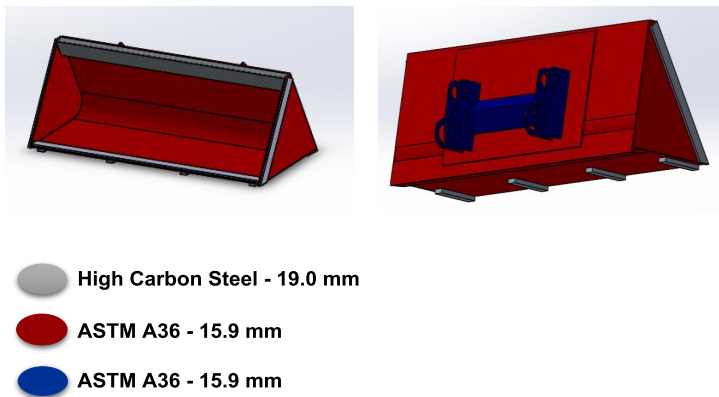
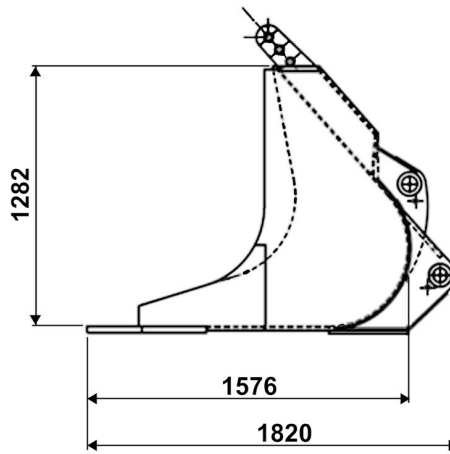
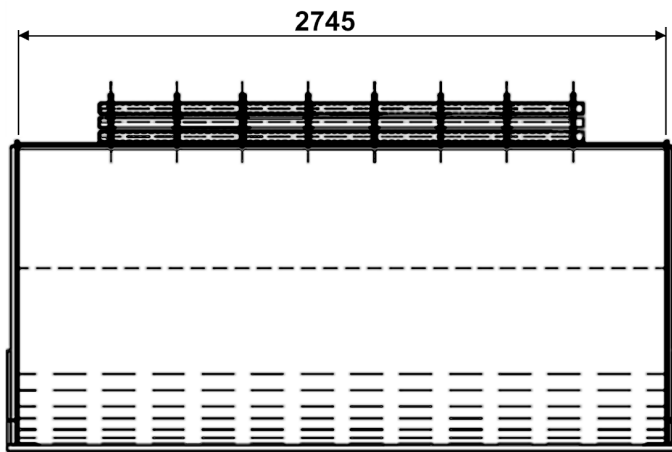


Figure 7. Steels used in the original stripped FeNb ingot loading bucket.

Niobium Ore Loader Bucket

Figure 8 shows the design and selected dimensions of the bucket used for the ore. The bucket weighs about 3,508 kg and has a load volume of 4 m³. This bucket was originally made with carbon steel grades and the internal face was plated with chromium carbide, Figure 9. The trucks have a 42-tonne capacity to haul niobium ore from the mine to the ore conveyor belt that links to the homogenization yard. The original buckets had a 10,370 kg capacity per manufacturer specifications. Since it is impossible to achieve the maximum allowed load in real working conditions, more than four bucket loads were necessary to fill the truck. Therefore, an increase in bucket capacity to achieve loading the truck with four buckets would be highly beneficial.

The investment cost of the original bucket was US\$20,606 per unit.



Weight = 3,508 kg and volume = 4 m³

Figure 8. Main dimensions (mm) of niobium ore loader bucket.

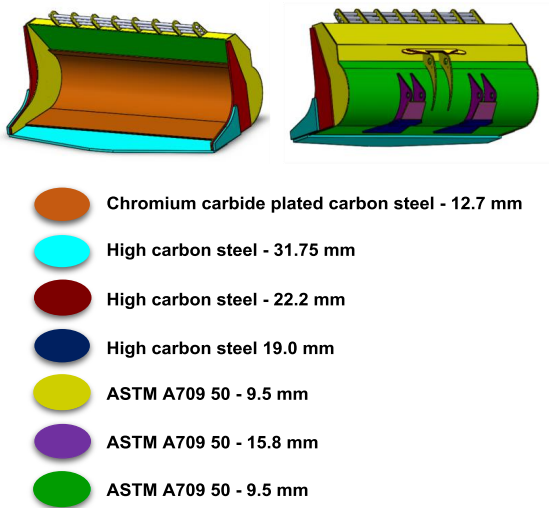


Figure 9. Steels used in the niobium ore loader bucket.

Steels

Table I presents the chemical compositions of the steels used in the old and new bucket designs. Table II shows the typical mechanical properties of the steels [8].

Table I. Steels Used in Bucket Structures

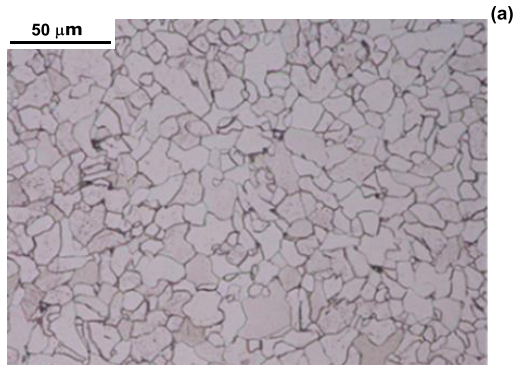
| Steel | C | Si | Mn | P | S | Cr | Ni | Mo | Other | Nb |
|--|-------|-------|------|-------|-------|------|------|------|-------------------------------|-------|
| ASTM A36 | 0.25 | 0.50 | 1.70 | 0.035 | 0.035 | - | - | - | - | - |
| High carbon steel | 0.32 | 0.40 | 1.50 | 0.03 | 0.015 | 0.80 | | 0.40 | B - 50 ppm Cu - 0.20 | - |
| ASTM A709 50 | 0.23 | 0.40 | 1.35 | 0.04 | 0.05 | - | - | - | V - 0.14 Cu - 0.20 | - |
| Tool steel for plastic mold | 0.26 | 1.08 | 0.80 | 0.008 | 0.004 | 1.35 | 0.66 | 0.80 | V - 0.14 | 0.015 |
| Structural steel YS >700 MPa | 0.063 | 0.062 | 1.79 | 0.017 | 0.003 | - | - | - | V - 0.010 | 0.060 |
| Wear resistant steel | 0.16 | 0.21 | 1.37 | 0.011 | 0.003 | 0.15 | 0.10 | - | B - 0.001 | 0.012 |
| High strength structural steel with good welding properties | 0.15 | 0.30 | 1.20 | 0.012 | 0.003 | 0.30 | 0.10 | 0.15 | - | 0.011 |

Table II. Typical Mechanical Properties of Applied Steels [8] (ASTM and NBR Standards)

| Steel | YS (MPa) | TS (MPa) | Hardness (HRC and HB) |
|--|----------|----------|-----------------------|
| ASTM A36 | 270 | 550 | - |
| High carbon steel | 450 | 550 | 360 – 400 HB |
| ASTM A709 50 | 345 | 450 | - |
| Tool steel for plastic mold | 1,300 | 1,450 | 45 HRC |
| Structural steel with YS >700 MPa | 765 | 810 | - |
| Wear resistant steel | 1,270 | 1,450 | 450 ~ 500 HB |
| High strength structural steel with good welding properties | 650 | 930 | - |

The microstructures of the steels are shown in Figures 10-12. The high strength structural steel has a ferritic microstructure with some pearlite, but with a very fine grain size that guarantees higher mechanical strength compared to the carbon steel grades, Figure 10. The tool steel and the wear resistant steel have tempered martensite microstructures with fine carbides, which ensures their wear resistance capacity, Figure 11. The high strength structural steel chosen for its good weldability has a similar microstructure of tempered martensite.

The tool steel and the wear resistant steel have much higher yield and tensile strengths compared to the other materials, having a specified hardness to guarantee wear resistance, Table II.



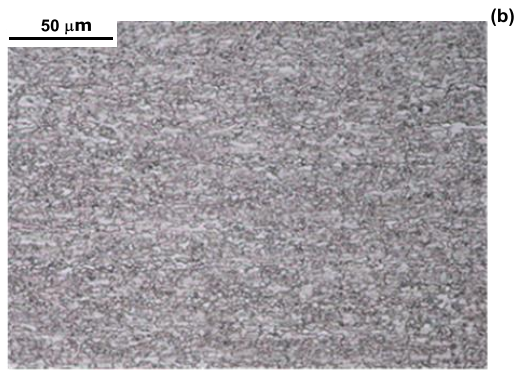
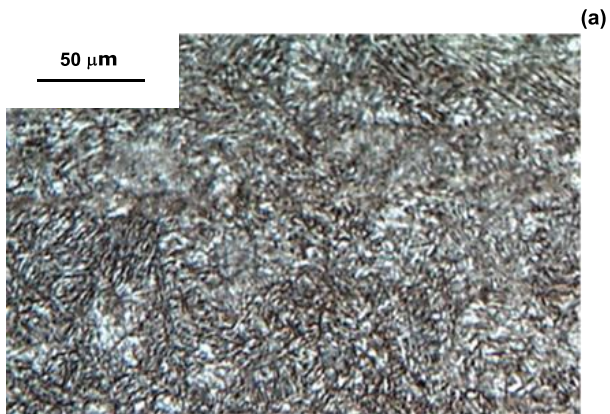


Figure 10. Carbon steel (a) and high strength structural steel with $YS > 700$ MPa (b). Ferrite with small regions of pearlite. For the carbon steel, the mean grain size was $9 \mu\text{m}$ and for the high strength structural steel the mean grain size was $3 \mu\text{m}$.



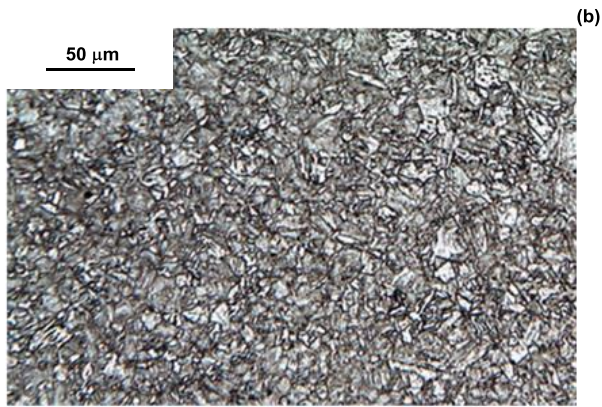


Figure 11. Microstructures of the tool steel (a) and wear resistant steel (b). Tempered martensite with fine carbides.

Chromium carbide plating is a technique used when very high wear resistance is required. Figure 12 shows chromium carbide plating over a carbon steel base. The as-cast chromium carbides were deposited on the carbon steel and solidified growing from the base metal, Figure 12. These carbides guarantee the high wear resistance of the material. This chromium-plated material was substituted with a standard wear resistant steel in order to reduce the cost of this component, motivated by the fact that excessive wear was not a factor that limited the bucket service life.

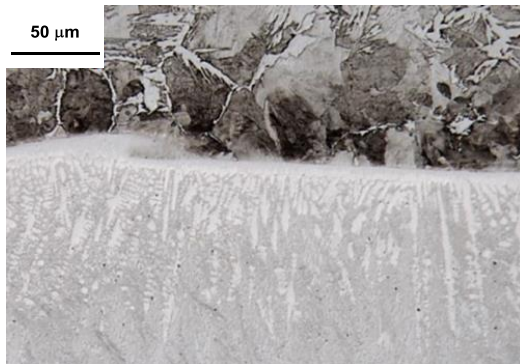


Figure 12. Microstructure of chromium carbide plated material. Upper section is the carbon steel with pearlite and ferrite at the grain boundaries. Bottom section is the chromium carbide plate, as-cast microstructure.

Results

Stripped FeNb Ingot Loader Bucket

The new bucket design is presented in Figures 13 and 14. The 15.9 mm strip of carbon steel was substituted with a 9.5 mm tool steel. This was the modification that was mainly responsible for reducing the weight by 25%, from 364 kg in the original model to 274 kg in the new design. Bucket load volume increased by 21%, from 0.24 m³ to 0.29 m³.

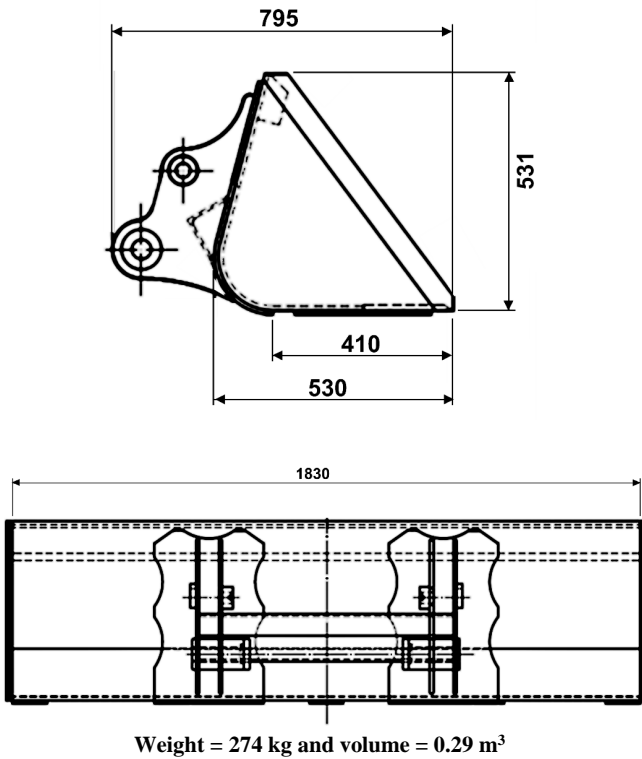
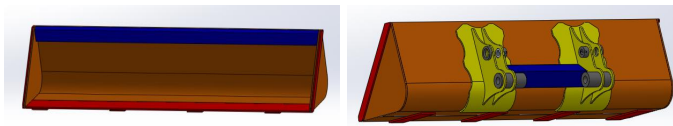


Figure 13. Main dimensions (mm) of the new bucket design.



-  Tool steel for plastic mold (YS = 1300 MPa) - 9.5 mm
-  Wear resistant steel (YS = 1200 MPa) - 12.7 mm
-  High strength structural steel for welding (YS = 700 MPa) - 6.35 mm
-  High strength structural steel for welding (YS = 700 MPa) - 9.5 mm

Figure 14. Steels used in the stripped FeNb ingot loader bucket.

To date, the new bucket has been working for 1,650 hours problem-free, which represents a 190% increase in service life over the best ever result for the original model, and a 415% increase over the original average life, Figure 15. The carbon steel parts that were susceptible to cracking in the original design were substituted with the tool steel and the cracks that normally appeared after 200 hours are absent in the new bucket. The tool steel worked well at the high temperatures involved when collecting hot FeNb and no deformation occurred in service, Figure 15. Figures 16 and 17 show the wear surface of the bottom strip at the front of the bucket, the part that has direct contact with FeNb on the floor. Scratches and adhesions of FeNb are visible, and there is some corrosion, but the resulting wear does not limit the bucket life cycle.

The initial higher investment for the new bucket containing high strength steel achieved payback after 800 working hours. The cost per working hour is as follows:

- Carbon steel based design – US\$4.70/working hour
- High strength/wear resistant design – US\$2.30/working hour



Figure 15. New bucket design after 1,650 hours of work time. No cracks and no deformation.

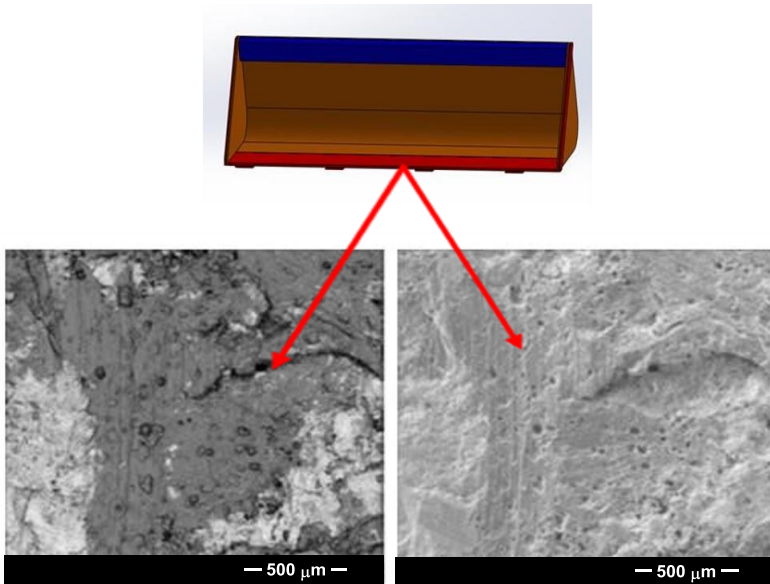


Figure 16. Wear surface of wear resistant steel with FeNb adhesion, scratches and corrosion.

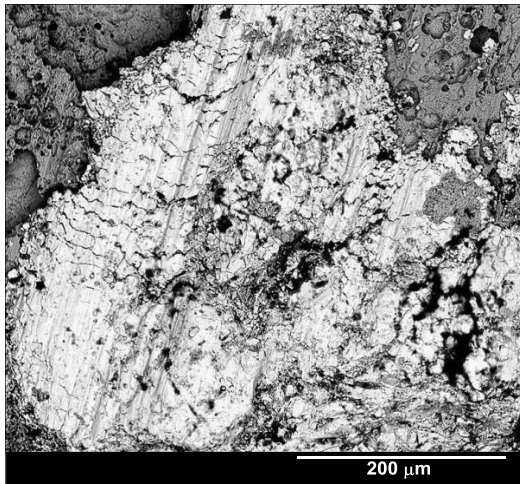


Figure 17. Surface of wear resistant steel.

Niobium Ore Loader Bucket

The new bucket has the same dimensions as the original, Figure 8. There was a 14% reduction in weight, from 3,508 kg to 3,013 kg due to reductions in thicknesses of the materials, Figure 18.

The 12.7 mm strip of chromium carbide plate was replaced by a 9.5 mm wear resistant steel, which was primarily responsible for the weight reduction. There were no cracks and no wear in the bucket after 11,000 service hours, showing that the higher strength steels have better fatigue resistance and that the chromium carbide plate was not necessary for the type of ore transported by the loader.

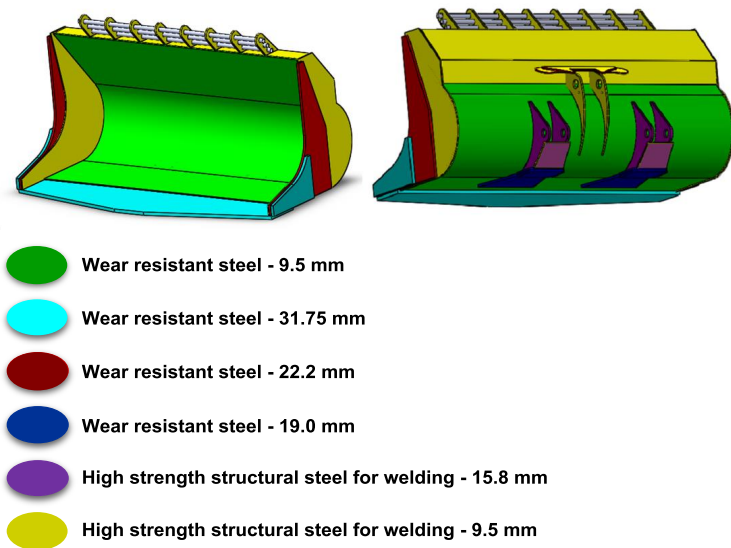


Figure 18. High strength and wear resistant steel used in the new niobium ore loader bucket.

The payload capacity increased by 4.7% while maintaining the maximum load allowed by the manufacturer specifications. With the 495 kg reduction in the bucket weight, it was possible to increase payload from 10,370 kg to 10,865 kg. Given the impossibility of working at the maximum allowed limit, this increase in payload made it possible to fill a 42-tonne capacity mine truck with four wheel loader buckets to 97% nominal capacity. The original design bucket required more than four buckets to fill the truck.

The cost of the original bucket was US\$20,606. For the new design, since the plates treated with chromium carbide were replaced with a single wear resistant steel, the cost was reduced by 7.4% to US\$19,090.

Conclusions

The application of high strength steels and a temperature resistant tool steel for the stripped FeNb ingot loader buckets made it possible to:

- Reduce bucket weight by 25%;
- Increase bucket load volume by 21%;
- Eliminate deformation caused by high temperatures;
- Eliminate structural cracks in the bucket, increasing service life by about 190% to date over the best recorded result for the existing design, and by over 415% compared to the average life;
- Reduce the cost of investment per working hour from US\$4.70/h with the carbon steel design to US\$2.30/h for the high strength steel design.

The following were achieved by redesign of the niobium ore loader bucket:

- Reduced bucket weight by 14%;
- Eliminated cracks even after 11,000 work hours, demonstrating that the higher strength steels have better fatigue resistance. There was no significant wear, indicating that the chromium carbide plate was not necessary for the type of ore being transported by the loader bucket;
- Increased payload capacity by 4.7% while maintaining the maximum allowable load as per the manufacturer's specifications. With this, four bucket loads were sufficient to fill the 42-tonne mine truck, allowing this process to be more productive;
- Reduced investment cost by over 7%.

References

1. A. Streisselberger, V. Schwinn and R. Hubo, "Microalloyed Structural Plate Rolling Heat Treatment and Applications," *Proceedings of the International Conference Niobium 2001*, Orlando, USA, 2001.
2. B. Donnay and H. Grober, "Niobium in High Strength Weldable Beams and Other Structures," *Proceedings of the International Conference Niobium 2001*, Orlando, USA, 2001.
3. L.M. Silvestre et. al., "High Strength Steel as a Solution for the Lean Design of Industrial Buildings," *Proceedings of the Value-Added Niobium Microalloyed Construction Steel Symposium*, Singapore, 2012.
4. K. Olsson et al., "Niobium Microalloyed Sheet Steels for Automotive Applications," *Microalloyed High Strength Steels for Reduced Weight and Improved Crash Performance in Automotive Applications* (TMS - The Minerals, Metals & Materials Society), 2006.

5. H.L. Rosa et al., "Increasing Transportation Efficiency by Using High Strength Niobium Microalloyed Steel for Truck Dumpers" (Paper presented at the International Seminar of Application of High Strength Steels in the Lightweight Design of Commercial Vehicles, São Paulo, 2013.)

6. K. Hulka, A. Kern and U. Schriever, "Application of Niobium in Quenched and Tempered High-Strength Steels," *Materials Science Forum*, 500-501 (2005), 519-526.

7. N. Ishikawa et al., "High-Performance Abrasion-Resistant Steel Plates with Excellent Low-Temperature Toughness," *Proceedings of the 2011 International Symposium on the Recent Developments in Plate Steels*, Winter Park Mountain Lodge, Winter Park, Colorado, 19-22 June, 2011, 81-92.

8. SSAB Brochure:

http://www.ssab.com/Global/Plate/Brochures/en/041_SSAB_plate_general_product_information_UK.pdf

FUNDAMENTALS AND PRACTICAL APPROACHES OF OPTIMIZING MARTENSITIC STEELS FOR USE UNDER SEVERE OPERATING CONDITIONS

H. Mohrbacher¹, J.W. Morris² and G. Krauss³

¹NiobelCon bvba, 2970 Schilde, Belgium

²University Emeritus Professor, University of California, Berkeley, CA 94720, USA

³University Emeritus Professor, Colorado School of Mines, Golden, CO 80401, USA

Keywords: Martensite, Effective Grain Size, Fracture Modes, Embrittlement, Tempering, Reheat Quenching, Direct Quenching, Case Carburizing, Precipitates, Niobium, Molybdenum

Abstract

Martensitic steel is a well-established material for the equipment and tooling used in mining and processing. Martensitic steel was originally chosen for its high strength and hardness. However, the overall performance of industrial machinery requires that a number of other properties be considered, including toughness, ductile-to-brittle transition temperature, fatigue strength, resistance to temper and hydrogen embrittlement, corrosion, creep, abrasion resistance, bendability (cold forming), and machinability. Often, a number of these properties should be optimized simultaneously. This optimization is achieved by adjusting alloy composition or thermomechanical processing, or ideally, by a well balanced combination of both. A clear understanding of the microstructure of martensitic steel and how it governs properties must precede any optimization exercise. Accordingly, we begin by outlining some fundamental considerations concerning the microstructure of martensite and its influence on strength, toughness and failure mechanisms. Next, we discuss the role of the various alloying elements and typical impurities on the microstructure and, hence the relevant properties. Typical alloying elements such as carbon, molybdenum, niobium, chromium, manganese and boron not only have primary effects, but also have cross-effects and synergies when added in combination. Thirdly, we describe the variety of thermomechanical processes that make it possible to tailor properties to a particular performance profile. These span the range from traditional quench-and-temper (Q&T) treatments to more recent processes, such as direct quenching, quench-and-partition and intercritical heat treatments. Each step of each treatment must be analyzed for its influence on the final microstructure and thus, the ultimate combination of properties. Finally, we present specific examples of technologically successful martensitic steels. We describe their composition and processing, particularly focusing on the effects and benefits of niobium and molybdenum as alloying elements.

Introduction

As-quenched martensite is the hardest and strongest microstructure of carbon steel. After tempering it produces many excellent combinations of properties making it suitable for a wide variety of demanding applications. Particularly for applications in the mining and processing industry, hardness and strength are fundamental assets providing good functionality and sufficiently long life of components under severe service conditions. Thereby, hardness is associated with resistance against wear in general and abrasion in particular. High strength allows sustaining high loads and forces without having to design components of excessively heavy gage, thus reducing their weight and dimensions. Beyond that fundamental aspect, a wide range of severe operating conditions exist requiring additional properties and characteristics that have to be implemented into martensitic steels. In many applications components are subjected to high impact loads. Accordingly, toughness and ductile-to-brittle transition behavior have to be considered, the latter being particularly important when operations are taking place in cold climate conditions. In many applications the steel is in contact with aggressive media, such as acids, bases or seawater. Thus, corrosion resistance of the material is an important aspect. Since corrosion reactions typically also serve as a source of generating free hydrogen, resistance against hydrogen embrittlement and delayed cracking needs to be considered as well. Other applications take place in hot environments requiring resistance against tempering and creep, heat conduction, as well as resistance against thermal fatigue and oxidation. It is quite obvious that there is no ideal material fulfilling all these requirements in an optimum way. Besides, such a widely performing material would be too expensive for most of the simpler application profiles. Therefore, the steel has to be tailor-made to the application concerning design of its microstructure, as well as alloy concept.

The microstructure is adjusted by modification of the alloy concept and processing route. Consequently, the present paper initially analyzes how features of the martensitic microstructure relate to properties. Subsequently, the effects of various alloying elements relevant to martensitic steels will be considered. Inherently, these alloy effects have also to be seen in the light of the processing route chosen to produce the steel. Thus, customary processes such as reheat quenching, direct quenching and case carburizing are addressed. On that basis of understanding, practical approaches of optimizing martensitic steel will be discussed, thereby particularly focusing on the effects and benefits of niobium and molybdenum as alloying elements.

Microstructure and Properties

General Considerations

Martensite, being the hardest microstructural variant of steel, is formed from austenite when the cooling speed is fast enough to prevent diffusion-controlled transformation. The hardness (and thus strength) of fully quenched martensite increases nearly linearly with the carbon content over the range of 0 to 0.5%C, Figure 1 [1]. Simultaneously, the start temperature of martensite transformation decreases with increasing carbon content from around 550 °C for very low carbon content to below 350 °C when approaching 0.5% carbon. Therefore, the lower the carbon content, the more prominent self-tempering effects become under industrial quenching conditions. In as-quenched martensite, carbon atoms, either trapped in octahedral interstitial sites

of the body-centered-tetragonal lattice, or segregated to dislocations or interfaces, dominate the strengthening mechanism.

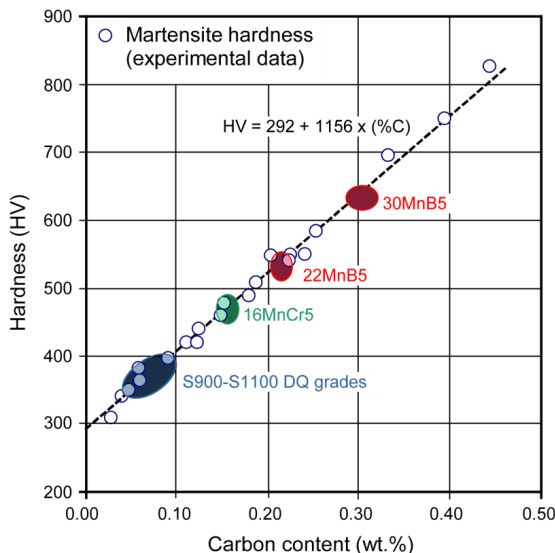


Figure 1. Correlation between carbon content and as-quenched martensite hardness (indication of commercialized grades).

Steels are often divided into three categories based on their carbon content. Low-carbon steels have carbon contents remaining below 0.2%. Medium-carbon steels have carbon contents between 0.2 and 0.5% and high-carbon steels have carbon contents above 0.5%. Although this classification may appear arbitrary at first sight, there are sound metallurgical arguments justifying it. At carbon concentrations below 0.2%, about 90% of the solute carbon atoms segregate to dislocations during the quenching process, Figure 2. Above 0.20% these defect sites become almost saturated and carbon atoms remain in octahedral interstitial sites [2]. Unless the rate of cooling during quenching is increased greatly, 0.2%C is also the point at which the martensite crystal becomes measurably tetragonal. The boundary between medium- and high-carbon steels is considered to be at 0.50%C because above this level steels become susceptible to intergranular fracture in the as-quenched and quenched-and-low-temperature-tempered conditions [3]. Furthermore, quenched steel containing carbon higher than 0.5% forms more complicated microstructures, as lath martensite is gradually replaced by plate martensite and the fraction of retained austenite increases.

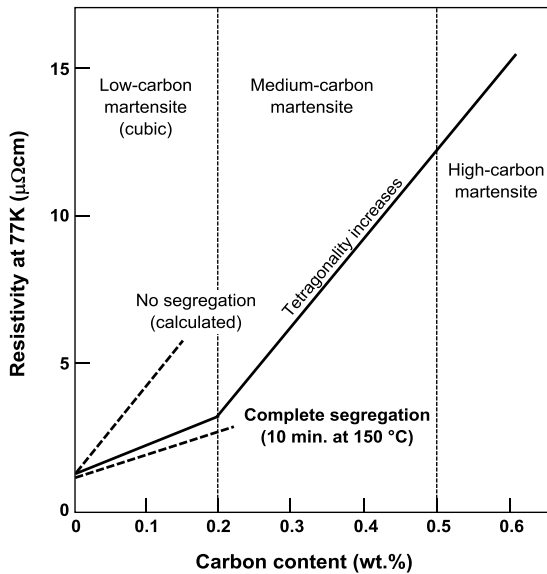


Figure 2. Carbon segregation during quenching of iron-carbon martensites measured by electrical resistivity (adapted from G.R. Speich [2]).

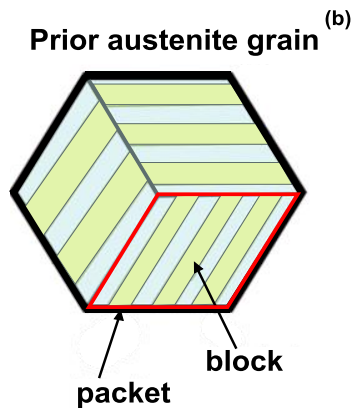
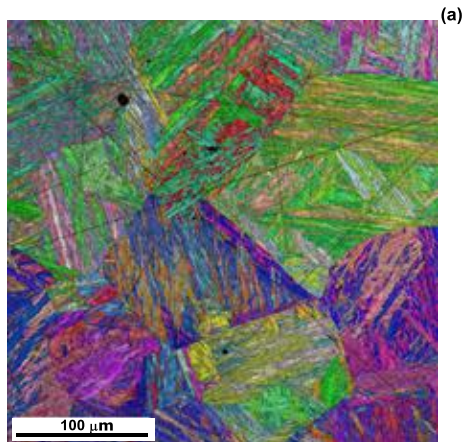
Low- and medium-carbon steels are the types most commonly used in the mining and processing industry. Low-carbon steels are often used in the as-quenched (optionally tempered) condition for structural applications requiring strength in the range 900 to 1400 MPa. Medium-carbon steels are widely used in the quench and tempered condition. These serve, for instance, in abrasive resistant applications, tools and dies for material processing, power transmission units, seamless pipes and ballistic plates. Since these are all lath martensitic steels, the microstructural features of lath martensites, their relationship to properties, and the effect of various tempering treatments will be discussed in some detail in the following section.

Microstructural Characteristics of Lath Martensite

In low- and medium-carbon steels the martensite microstructure consists of laths that are grouped into blocks and subsequently, into packets, Figure 3. The laths are highly dislocated. The crystal structure of low-carbon lath martensite is body centred cubic (bcc), but at carbon contents in excess of 0.20% the structure becomes slightly tetragonal.

To understand the basic microstructure of low-carbon lath martensitic steel, it is important to recognize two basic crystallographic relations between the parent face centred cubic (fcc) austenite and the product bcc ferrite [4,5]. Firstly, the two crystal structures are connected by the “Bain strain”, the bcc unit cell is derived from fcc by compressing the fcc cell along one of the

$\langle 100 \rangle_\gamma$ cube axes, while expanding it homogeneously in the perpendicular plane. There are hence three “Bain variants” of the transformation, corresponding to the three possible choices of the compression axis. Secondly, after transformation, the crystal axes of the martensite laths are oriented in (or very close to) the Kurdjumov-Sachs (KS) orientation relations, with the close-packed planes and close-packed directions of the bcc product parallel to those of the fcc parent: $\{110\}_\alpha \parallel \{111\}_\gamma$, $\langle 111 \rangle_\alpha \parallel \langle 110 \rangle_\gamma$.



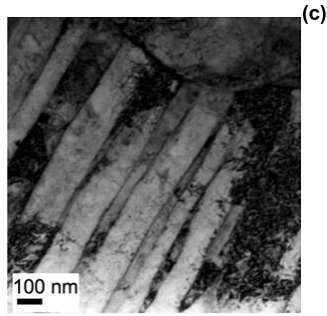


Figure 3. Martensitic substructure within a prior austenite grain of low-carbon steel; (a) EBSD map of prior austenite grains [5], (b) Schematic drawing showing packets and blocks, (c) TEM micrograph showing laths within a block. (TEM micrograph courtesy of J.R. Yang, National Taiwan University).

There are four independent choices for the $\{111\}_\gamma$ plane and for each choice of $\{111\}_\gamma$, there are six independent ways to choose the bcc close-packed plane and direction to satisfy the KS relations. These are illustrated in Figure 4. It follows that there are 24 “KS variants” of the transformation. Eight of these, two per choice of $\{111\}_\gamma$, are examples of each of the three Bain variants of the transformation.

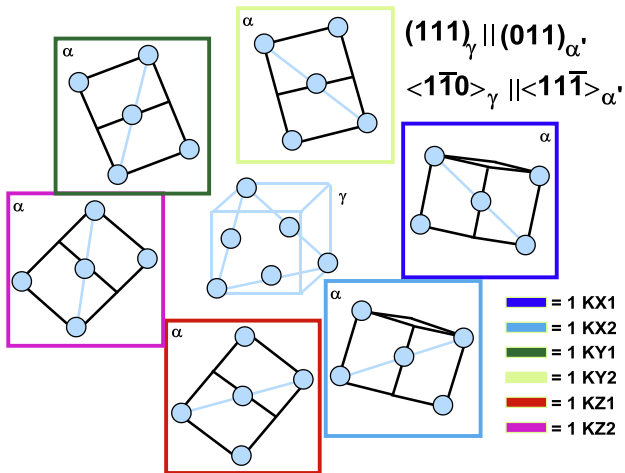


Figure 4. The six crystallographic variants of bcc that satisfy the KS relation on $(111)_\gamma$. Variants of the same color (red, blue, green) have the same Bain axis. Variants that share the same close-packed direction are twinned with respect to one another. Variants colored dark (light) are rotated 120° from one another in the plane.

In the basic microstructure of lath martensitic steel [5-8] each prior austenite grain is subdivided into packets, Figure 3. There are four crystallographically distinct packets, each based on one of the four choices of $\{111\}_\gamma$ plane. Each packet is a composite of laths that have one of the six KS relations that share the $\{111\}_\gamma$ plane of the packet. The packet is then subdivided into “blocks” which are plates with $\{110\}_\alpha$ habit planes that are stacked to fill the packet. Each block is a composite of two “sub-blocks,” each of which is built up of laths from one of the two KS variants that belong to the packet and have the same Bain axis, Figure 4. The final structure is shown in Figure 3(a) and, schematically, in Figure 3(b).

While this highly organized structure may seem complex, it actually has a fairly simple interpretation [9,10]. Given the large strain involved in the fcc-bcc transformation, there must be an efficient way to accommodate this strain for the transformation to happen at all and there must be an efficient way to relax the overall strain to prevent “quench cracking” as the transformation proceeds. It can be shown [10] that, with a suitable choice of slip systems, a composite plate (block) made up of two KS variants from the same packet with the same Bain axis has an invariant plane with the fcc parent that parallels the common $\{110\}_\alpha$ plane ($=\{111\}_\gamma$ plane) of the packet. It follows that the six KS variants within a given packet can be gathered into parallel plates (blocks) of three distinct types, and these can simply be stacked to fill space. If the volume fractions of the three blocks are the same, the only residual shear strain is due to a linear expansion perpendicular to the plates. If all four distinct blocks appear with similar volume fractions in a prior austenite grain, the four linear expansions balance, and the net strain of the whole grain is a simple dilatation; the transformation shear is fully relaxed. Given this microstructural pattern, a polygranular austenite can transform martensitically to a polygranular product with little or no residual shear strain.

This microstructural pattern has several important consequences, including: (1) while the individual blocks are composites of two KS variants, the boundary between them is a low-angle boundary. Since the boundaries between the individual laths in the block are even smaller, the blocks behave essentially as single crystals, as has long been observed [9]. (2) The boundaries between blocks that have different Bain variants are high-angle boundaries, but the angles have one of a few discrete values, as observed [6,8]. (3) Given the need to minimize elastic energy, the same microstructural pattern is favored for all prior austenite grains of reasonable size. It follows that the block and packet sizes tend to scale linearly with the prior austenite grain size (PAGS) until the grain size becomes so small that surface effects become dominant, as observed [7].

The dislocated lath microstructure described here is found generally in low-carbon martensites, excepting the very finest prior austenite grain sizes, where boundary effects become important. The microstructural pattern becomes less regular at higher carbon contents, due to a combination of carbon-induced tetragonality and carbon redistribution during the transformation. In high-strength, medium carbon steels such as AISI 4140 there is a significant population of single-variant blocks with lath and block boundaries sheathed in retained austenite or precipitated carbide.

The Effective Grain Size

Many important properties of polycrystalline materials are related to the grain size. Smaller grain size in ferritic steels increases strength and toughness and simultaneously it lowers the ductile-to-brittle transition temperature, according to Hall-Petch type relationships. In polygonal ferritic steels, the grain size can easily be determined by light optical microscopy. In martensite, however, determination of the grain size is not trivial and requires more sophisticated microstructural analysis tools, such as EBSD and TEM. Yet, the initial question that needs to be answered is: “*which is the relevant definition of grain size in martensitic steel?*” Morris and co-workers [9] have approached this question by defining an “effective grain” size in martensite that may be different for the various properties. Strength, cleavage resistance, and ductile–brittle transition temperature are related to the effective grain size (d_{eff}) as follows:

The yield strength (σ_y) is given by the classic Hall–Petch relationship:

$$\sigma_y = \sigma_0 + K_y d_{eff}^{-1/2} \quad (1)$$

where K_y is the Hall–Petch coefficient for strength. σ_0 is a material constant for the starting stress for dislocation movement.

The cleavage fracture stress (σ_f) obeys a relationship of the form:

$$\sigma_f = K_f d_{eff}^{-1/2} \quad (2)$$

where K_f is the Hall–Petch coefficient for cleavage.

The ductile–brittle transition temperature often obeys a constitutive equation of the form:

$$T_B = T_0 - K_B d_{eff}^{-1/2} \quad (3)$$

where K_B is the appropriate Hall–Petch coefficient. T_0 is the temperature at which yield strength becomes equal to the cleavage stress.

It is important to recognize that “grain size” has a different meaning for each of the properties of interest.

Maki et al. [7] analyzed correlations of substructure size and parent austenite size in some detail. As expected, the packet size decreases as the prior austenite grain size decreases. Larger austenite grains transform into a substructure consisting of several packets. For a prior austenite grain size finer than 10 μm , the packet size approaches that of the austenite grain size. By further refinement, it is possible that some prior austenite grains consist of a single packet (or even a single block). However, the effect of prior austenite grain size on the lath width is small.

Effective Grain Size for Strength

Early work by Cohen [11,12] found the yield strength of carbon-free martensite to be inversely proportional to the square root of the parent austenite grain size. The constant of proportionality in this Hall-Petch type relationship is such that a decrease in prior austenite grain size from 1 mm to 10 μm would raise the yield stress of the corresponding martensite by approximately 420 MPa. By extrapolating this relationship to $d^{-1/2} = 0$, a value for the yield strength of a hypothetical single crystal of martensite is obtained; this value is roughly 350 MPa. For an austenite grain size in the region of 50 μm , a yield strength of approximately 690 MPa is obtained. The total contribution due to grain size is therefore 340 MPa. If it is now assumed that the addition of carbon to martensite alters the σ_0 term, but not the constant K_y in Equation 1 (an assumption that is valid in the case of ferrites), it becomes apparent that the grain size contribution to the strength of high yield stress martensite is relatively small.

Later work on Fe-0.20C-Ni-Cr-Mo steel considered the packet size as the effective grain size for lath martensite [13]. This correlation was well supported by Wang et al. [14] on similar steel. When the prior austenite grain size in 17CrNiMo6 steel was refined from 199 μm to 6 μm , the yield strength increased by 235 MPa (representing a 25% increase), indicating that grain refinement is not very effective in increasing the strength. The work also demonstrated an almost equally good correlation between yield strength and the inverse square root of either packet size or prior austenite grain size, respectively (which is expected if the two microstructural measures scale together).

Recent work by Morito and Obha [15] showed that the replacement of packet size by block size in the Hall-Petch relationship for Fe-0.2%C and Fe-0.2%C-2%Mn steels produced a more consistent value of the Hall-Petch coefficient, and in fact, a value that is reasonably close to that found in ferritic Fe-Mn and in pure Fe, where the grain size is more easily defined. Lath size may be expected to have little effect on strength as there is little crystallographic distinction between adjacent laths, indeed *in situ* indentation studies [16] have demonstrated that the lath boundary presents almost no barrier to dislocations in the absence of boundary films.

In a review article, Morris [17] also argued that the block size is the effective grain size for strength. While it may seem obvious that the block size should be the effective grain size for strength, since it provides the smallest significant crystallographic discontinuity, a closer examination shows that the role of the block boundary involves some subtlety, particularly when the blocks are used to subdivide a prior austenite grain that is much larger in size. The first issue is topological. Crystallographically distinct blocks are different Bain variants of the parent austenite. Since there are only three of these, it is geometrically impossible to design a microstructure in which each block is surrounded by dissimilar neighbors. The effective grain size of lath martensitic steel is always some multiple of the block size.

The second issue is physical, and concerns whether a block boundary is an effective barrier to the transmission of plastic deformation [16,18,19]. The problem is that the Bain variants share common slip planes and hence, may not effectively inhibit slip. The experimental evidence on this issue is ambiguous and puzzling. For example, intercritical heat treatments used to refine the effective block size in lath martensitic steels show very little effect on the yield strength. On the

other hand, others [15] have found a strong Hall-Petch strengthening from block boundaries, comparable to that associated with high-angle boundaries generated by powder processing or incoherent transformations. A plausible explanation for this inconsistent behavior is found in the recent work of Ohmura and Tsuzaki [19] who combined nano- and micro-indentation to compare the intragranular and polygranular hardnesses of martensitic steels. Their data appears to show that strengthening by block or packet boundaries (ie. by Bain variant boundaries) is largely due to boundary decoration by carbon or carbide films. Their results may provide the key to understanding the influence of block size on strength. Decorated block boundaries strengthen much as incoherent boundaries do, while the relatively clean boundaries in low-carbon, gettered or tempered martensites have a much smaller effect on the strength.

Effective Grain Size for Toughness

Two fracture modes, quasi-cleavage and ductile fracture, were observed by Irani [20] in an early study on the fracture behavior of martensitic steel. In an impact test, the former is expected to absorb a lesser amount of energy than the latter. This correlation has been confirmed, as the absorbed impact energy increases with the amount of ductile fracture. Quasi-cleavage proceeds by the nucleation and growth of submerged cracks ahead of the advancing fracture front. The crack front advances in a stepwise manner as the cracks in front of the fracture tip grow until coalescence takes place, Figure 5. The advance of a quasi-cleavage fracture crack through a martensitic structure is transgranular with respect to the prior austenite grains. The quasi-cleavage fracture surface shows fractures characteristic of both true cleavage and plastic rupture. Firstly, extensive flat facets are seen on the fracture surfaces indicating true crystalline cleavage. This also holds for the formation of steps (S) during the growth of the facet. Secondly, tear ridges (T) are observed on fractographs. These are formed during the linking up of micro-cracks with the advancing fracture front. In this respect, quasi-cleavage resembles plastic rupture.

Naylor et al. [21,22] pointed out that micro-cracks formed within laths are too small to start cleavage due to the limited lath width. Micro-cracks in adjacent laths must join together to create a crack of critical length to propagate as cleavage. This crack experiences small deflections when crossing lath or sub-block boundaries and larger deflections when passing block boundaries, where they are often arrested. The blocks are thought to coincide with the facets seen in fractography.

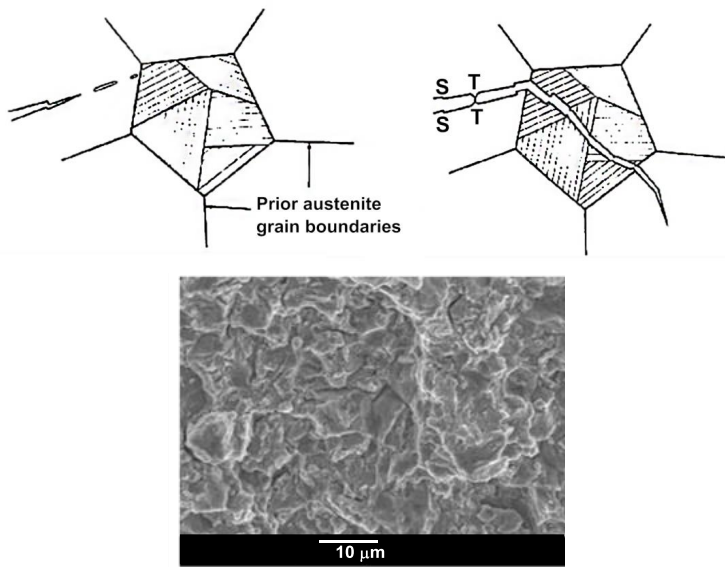


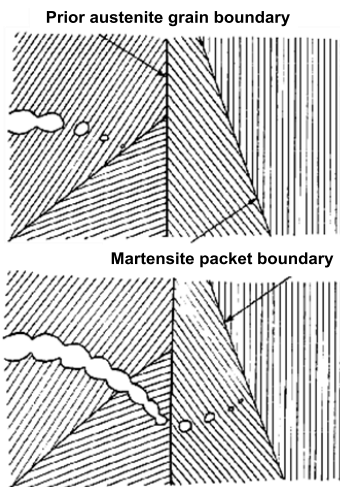
Figure 5. Schematic crack propagation with formation of steps (S) and tear ridges (T) and appearance of quasi cleavage fracture.

The microstructural mechanism of cleavage in ferritic steels is well known; ferritic steels cleave along $\{100\}$ planes. It follows that, in the case of lath martensitic steels, the effective grain size is the coherence length on $\{100\}$ planes, which determines the cleavage crack length. The $\{100\}$ coherence length is fixed by the “block” size, which is the basic crystallographic unit. Refining the block size of martensitic steel is hence an effective means of increasing its resistance to transgranular cleavage fracture, since Bain variant boundaries are crystallographic discontinuities in the $\{100\}$ cleavage planes. Consequently, block refinement is a very successful approach to lower the ductile-brittle transition temperature (DBTT) of steel whose transition is governed by transgranular cleavage. Morris et al. [23] used profile fractography and EBSD to show the specific role of block boundaries in arresting cleavage cracks in 9%Ni steel.

In similar work, results reported by Wang et al., [14] on 17CrNiMo6 steel demonstrated a marked increase of toughness at 77 K when the packet size becomes smaller than $10\ \mu\text{m}$. It is worth noting that the packet size effect on toughness was much larger than that on yield strength. The same authors [24] used EBSD techniques to show the boundary-induced decrease in cleavage crack length with block refinement in lath martensitic steel. Hanamura et al., [25] obtained similar results, but with less definitive microstructure characterization. Ishikawa et al., [26] analyzed the fracture behavior of 0.15%C abrasive resistant steel treated to 420 HV hardness. Charpy tests conducted at $-196\ ^\circ\text{C}$ revealed a relatively straight crack path for a conventional Q&T steel, while that of an ausformed steel (niobium microalloying + TMCP)

showed a much more corrugated crack path. This was due to many deflections at packet boundaries leading to higher energy consumption (the fracture mode still being brittle in both materials). Charpy tests performed at $-40\text{ }^{\circ}\text{C}$ indicated a marked increase in energy consumption when the prior austenite grain size was reduced to below $30\text{ }\mu\text{m}$. The fracture appearance was becoming increasingly ductile at smaller prior austenite grain sizes.

The dimpled topography of ductile fracture is due to the concave depressions formed by the growth and coalescence of spherical micro-voids with the advancing crack front, Figure 6. These micro-voids may be nucleated at any heterogeneity, hence, the size and distribution of heterogeneities have an important influence on the formation, growth and coalescence of voids. The size to which a micro-void can grow depends partly on the work hardened state of the matrix, and thus the number of voids required for the propagation of a fracture front will increase with an increase in the work hardened condition of the matrix. Improving the cleanness of steel is an important means of increasing energy absorption in ductile fracture mode. In very clean steels voids can be generated at grain corners, setting the limit to this means of improvement.



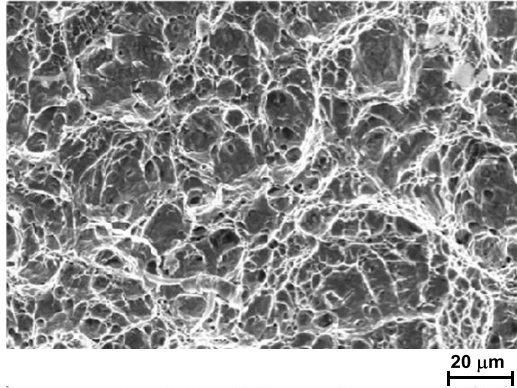


Figure 6. Schematic crack propagation and appearance of ductile fracture.

Lowering the Ductile-to-Brittle Transition Temperature

In ferritic steel the ductile-to-brittle transition temperature, T_B , can be efficiently lowered by reducing the carbon content and refining the grain size. Grain refinement compensates the loss of strength originating from the carbon reduction. This principle has found its culmination in modern TMCP steels.

In martensitic steel the transition temperature from a ductile dimple-type fracture to brittle cleavage-type fracture depends on the block size and the hardness (strength). Reducing carbon is not always an option as carbon is needed for strength and the trade-off with Hall-Petch strengthening from grain refinement may be insufficient. The linear correlation between the inverse square root of the packet size (hence, by inference, block size) and T_B according to Equation 3 was demonstrated for different alloys [27]. The Hall-Petch coefficient K_B was found to be larger in magnitude when the steel has a higher carbon content.

The connection between DBTT and the cleavage fracture stress can be understood on the basis of a model that was originally suggested by the Russian physicist, Yoffee, in the early 20th century [28]. The Yoffee diagram suggests two generic ways to suppress the ductile-brittle transition: raising the brittle fracture stress (σ_F) or lowering the effective yield strength (σ_y). Since high yield strength is a desirable feature of a structural steel, most of the relevant research has concentrated on raising the brittle fracture stress. The peak tensile stress in the process zone of a crack tip in an elastic-plastic material, σ_T , scales with the yield strength, σ_y , and is of the order of (3–5) σ_y . It follows that this stress increases as the temperature drops. Assuming that the brittle fracture mode is cleavage, then so long as σ_T is below σ_F , the crack tip material yields before cleavage and the fracture is ductile. But in typical ferritic or martensitic steel the thermal increment in σ_y has the consequence that decreasing temperature eventually raises σ_T above σ_F .

When this happens, the material becomes liable to brittle fracture. The ductile–brittle transition occurs at a temperature close to the crossover point.

As illustrated in Figure 7, the most direct way to decrease DBTT is to raise the brittle fracture stress. Grain refinement is an effective way to do this. There are three generic ways to refine the effective grain (block) size of lath martensitic steel:

1. Refine the prior austenite grain size;
2. Break up the block by inserting a second Bain variant;
3. Break up the block by inserting a second phase (usually austenite) along the lath boundaries.

Either thermal or thermomechanical methods allow accomplishing each of these.

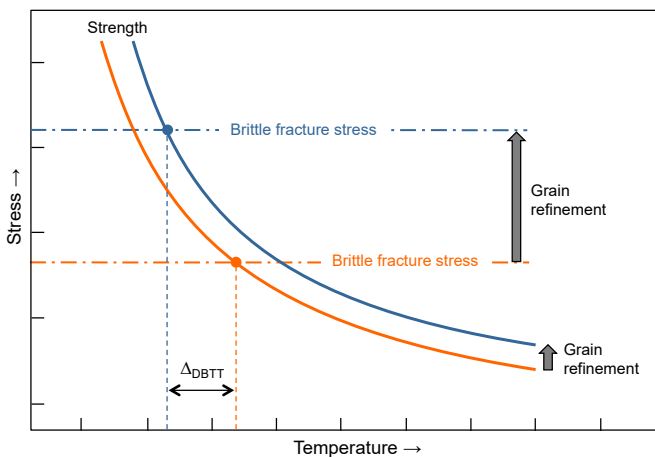


Figure 7. The Yoffee model indicates that ductile–brittle transition occurs when the crack-tip stress exceeds the brittle fracture stress. Refining the grain size raises both stresses, but the effect on fracture stress is generally larger, with the result that DBTT decreases.

Effective Grain Size Against Boundary Embrittlement

Thus far, brittle fracture was associated with transgranular (quasi-) cleavage fracture. However, under certain circumstances, intergranular brittle fracture can be observed. Prior austenite grains usually constitute the facets of that fracture type. The condition for intergranular fracture to occur is the grain boundary cohesion being weaker than the yield strength and cleavage stress.

There are three principal origins for weakening of austenite grain boundaries:

1. Segregation of solutes and impurities to the austenite grain boundary;
2. Precipitation of particles (carbides, nitrides) at the grain boundary;

3. Hydrogen embrittlement.

Refinement of the prior austenite grain size results in an enlarged total grain boundary area. Solute atoms and impurities tend to segregate to the austenite grain boundary. This effect can take place in the austenite phase, ie. before quenching but also after transformation, eg. during a tempering treatment. The increased concentration of interstitials such as carbon, nitrogen, boron in the grain boundary area also leads to a preferred precipitation of metal carbides, nitrides or intermetallic compounds due to the locally increased solubility product. On first sight it may seem that an increased total grain boundary area should lead to a “geometrical dilution” of segregated elements. However, Asahi and Ueno [29] pointed out, based on calculations, that the change in concentration of segregated elements in the grain boundary due to grain refinement is expected to be negligibly small. Therefore they also did not observe a change in distribution and size of precipitates upon tempering.

Hydrogen embrittlement appears to be a boundary phenomenon in ferritic or martensitic steels. Ordinarily, the hydrogen-induced fracture separates prior austenite grain boundaries [30-35] occurring by intergranular decohesion at rather low stress intensities. Increasing yield strength enhances the sensitivity for hydrogen embrittlement, because it increases the local hydrogen concentration at the tip of a stressed crack or notch, and also allows the local cohesive stress to be reached. (Higher yield strength allows higher stress without plastic deformation and as a consequence the lattice dilation caused by the larger stress attracts more hydrogen). Transgranular cracking due to hydrogen embrittlement has also been observed. This fracture mode occurs at higher stress intensities than intergranular decohesion and appears to propagate along planes of maximum shear stress [36]. The fracture appearance resembles that of quasi-cleavage.

Both fracture modes have recently been observed in steel grade 22MnB5 (10B22) in the as-quenched state [37]. The standard 22MnB5 steel comprising an average PAGS of 17 μm had a yield strength of around 1050 MPa and a tensile strength of around 1750 MPa. Charging that steel with hydrogen under a constant applied load led to failure by intergranular fracture at stresses in the range of 400 to 600 MPa, Figure 8. The same steel was then additionally microalloyed with niobium (0.05%), reducing the average PAGS to 6 μm . The strength was marginally increased (+50 MPa) due to this grain refinement. After hydrogen charging, the grain-refined steel showed transgranular cracking with a quasi-cleavage appearance in the fracture initiation area, Figure 9. The fracture stress for this steel was in the range of 1150 to 1250 MPa, ie. above the as-quenched yield strength. Large parts of the fracture surface even showed a ductile dimple-type appearance.

Krauss and co-workers [38] did similar hydrogen embrittlement tests on 10B22 steel and found almost exactly the same drop in fracture stress down to 400 MPa after hydrogen charging, with the appearance of intergranular cracking. Instead of grain refinement, they performed tempering treatments. By low-temperature tempering (150 °C) the same effects in terms of fracture stress and appearance were obtained as in grain-refined 22MnB5.

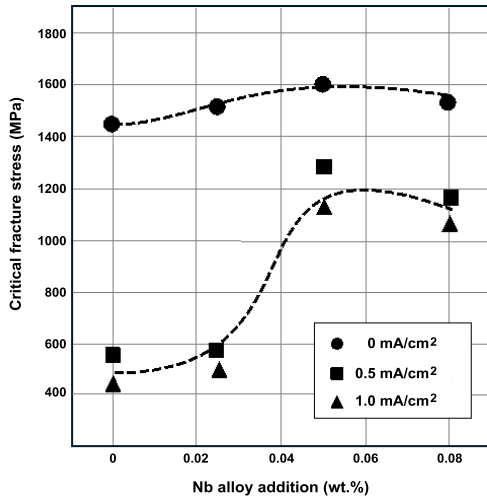


Figure 8. Effect of niobium microalloying on the fracture stress of as-quenched steel 22MnB5 subjected to various conditions of hydrogen charging.

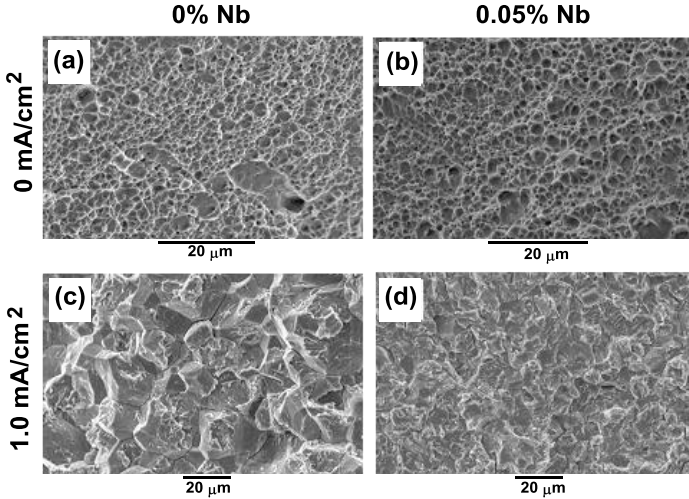


Figure 9. Appearance of fracture surfaces; (a), (b) dimple-type ductile fracture, (c) intergranular brittle fracture, (d) transgranular quasi-cleavage fracture.

In clean or gettered lath martensitic steels, the hydrogen resistance is relatively good and the fracture mode is transgranular [32]. A closer examination shows, however, that even in this case the fracture is primarily interfacial, propagating along martensite lath boundaries. If the fracture is along grain or lath boundaries, then the effective grain size is the length of the semi-planar boundary segments. In lath martensitic steels the boundaries extend across the packet, so the effective grain size is the packet size. To overcome hydrogen embrittlement, it is necessary to refine the packet size to the optimal degree. Rapid reversion treatment ($\alpha' \rightarrow \gamma \rightarrow \alpha'$) produces a coherent product with a submicron packet size, which can make the steel virtually immune to hydrogen embrittlement [28,31].

Effects of Low-temperature Tempering (LTT)

Low-temperature tempering (LTT) improves toughness of as-quenched martensite, but maintains hardness and strength at high levels. In as-quenched martensite the strength originates from carbon atoms trapped in octahedral lattice sites or segregated to dislocations and interfaces of the martensitic structure [1].

When as-quenched martensite is tempered in the temperature range of 150 to 200 °C, transition carbides precipitate in the martensite crystals and retained austenite is stable, Figure 10. Tempering at temperatures above the LTT range causes the transformation of retained austenite and the replacement of the transition carbides by coarser particles of cementite, leading to lower strengths and tempered martensite embrittlement. Krauss [39] explained that the key strengthening mechanism of the LTT structures across the entire spectrum of carbon contents is the strain hardening associated with dynamic interactions of dislocations with the fine transition carbide/dislocation substructure of the tempered martensite [40]. With increasing carbon content, the intensity of these interactions increases as the density of the sub-structural features increases and the spacing of the obstacles to dislocation motion decreases. Secondary factors influencing strain hardening are martensite morphology, prior austenitic grain size (through its effect on martensite packet size), and retained austenite content and distribution.

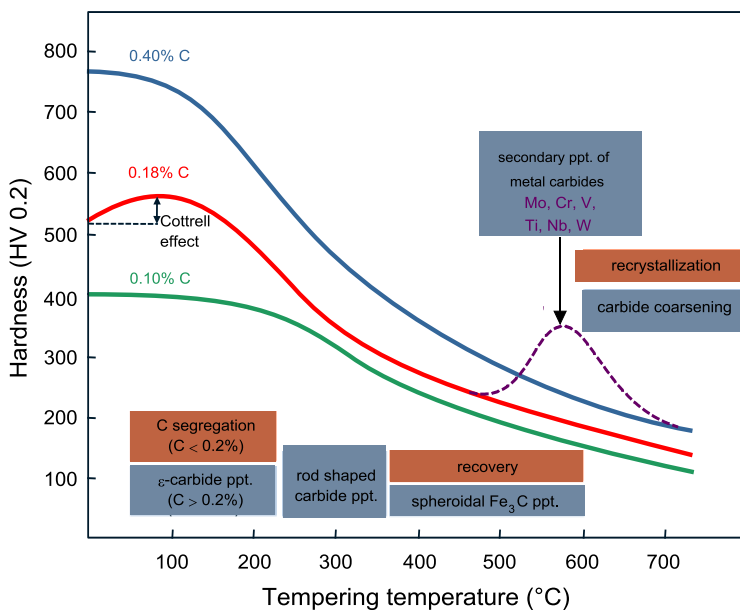


Figure 10. Metallurgical effects occurring during tempering.

Low-carbon martensitic steels are most often produced as plate or sheet and processed into components by cold forming. Therefore, good ductility (in the sense of elongation) is required. As-quenched martensite has high strength but very low total elongation, usually below 10%. LTT brings a small improvement of total elongation at the expense of a moderate loss in tensile strength [41]. The “roundhouse” shape of the stress-strain curve is retained.

Medium-carbon steels are usually hot formed, (eg. by forging, press hardening) so that room temperature elongation is not so important. Such steels require, however, toughness and fracture resistance at ambient and sub-ambient temperatures. Martensitic medium-carbon steels tempered at around 150 °C show significant ability to plastically deform and fail by ductile fracture mechanisms [40]. Engineering stress-strain curves for the low-alloy medium-carbon steels 4130, 4140, and 4150 quenched and tempered at 150 °C show systematic changes in strength and ductility with increasing carbon content. Yield and ultimate tensile strengths of the LTT microstructures increase with carbon content and all measures of ductility, except uniform elongation, decrease with increasing carbon content.

The fracture of all of the LTT martensitic medium-carbon steels occurs by ductile fracture mechanisms, ie. by microvoid nucleation, growth and coalescence, and the macroscopic fracture appearance of the tensile specimens is that of cup-and-cone fracture [40]. Only two components of the LTT martensitic microstructures in medium-carbon steels vary systematically with carbon

content - amount of retained austenite and the density of the transition carbides, which precipitate in the laths of martensite. The more important of these two by far is the transition carbide density. Dislocation movement through the transition carbide/dislocation substructure of the tempered martensitic matrix accomplishes most of the plastic deformation. The higher the transition carbide density, the shorter the dislocation segments which can glide, and the higher the stresses required for dislocation motion and plastic flow. Continuing dynamic interactions between glide dislocations and the transition carbide/dislocation substructure of the tempered martensite during straining, lead to high flow stresses and high rates of strain hardening.

Effects of High-temperature Tempering (HTT)

As-quenched martensitic microstructures are highly unstable during high-temperature tempering [42,43]. The supersaturation of carbon and other elements present in the steel is relieved by precipitation, resulting in dispersions of iron carbides and alloy carbides within the matrix microstructure of the martensite, Figure 10. Retained austenite transforms and produces new distributions of cementite and ferrite.

High-temperature tempering produces remarkable changes in martensitic microstructures. The many types of boundaries change in shape and quantity, changing the shape and size of the crystals, which they enclose. The high density of dislocations produced by the martensitic transformation introduces strain energy into the martensite crystals and drives recovery mechanisms or even recrystallization of tempered martensitic crystal microstructures. In the extreme, microstructures of spheroidized cementite particles and equiaxed ferrite crystals with very low strengths and very high ductilities are produced. However, preceding the formation of such spheroidized microstructures, there are tempering conditions that produce microstructures with excellent combinations of high strength and high fracture resistance. Although the strengths are much reduced from that of as-quenched or low-temperature tempered martensite, the strengths, combined with high toughness, are higher than produced by other processing approaches. Despite the fact that HTT relieves the supersaturation of as-quenched microstructures and produces combinations of ferrite and dispersed carbide particles, high-temperature tempered microstructures still merit the term tempered martensite because martensite is the origin of the structure and traces of the parallel crystal, packet, and block morphology of lath martensite are retained.

The changes produced by high-temperature tempering are continuous as a function of increasing time and temperature of heating and dependent on alloying. Changes that affect performance are the degree to which the dislocation substructure is retained and modified, the elimination, growth, and stabilization of as-quenched martensite crystals (the effective grain size), and the formation of carbide particle dispersions.

Figure 11 shows a light optical micrograph of highly tempered lath martensite in Fe-0.2%C steel [44]. The martensitic microstructure has undergone considerable coarsening, but some parallel boundary alignment of lath martensite is retained. Coarsening of the structure has occurred by the elimination of many of the very fine martensite crystals produced by the martensitic transformation. It appears that the only residual feature of the as-quenched martensite is a block structure in which there are no individual crystals within the blocks. Consistent with current

understanding of lath martensite microstructures in low-carbon steels, the elimination of low angle boundaries probably occurred in blocks of the as-quenched martensite. In addition to the ferritic matrix, dispersed carbide particles (appearing as small dark features) are also part of the HTT microstructure.

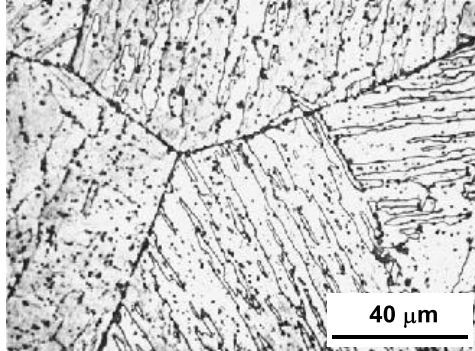


Figure 11. Microstructure of lath martensite in Fe-0.2%C steel after tempering at 700 °C for two hours (light optical micrograph, Nital etch) [44].

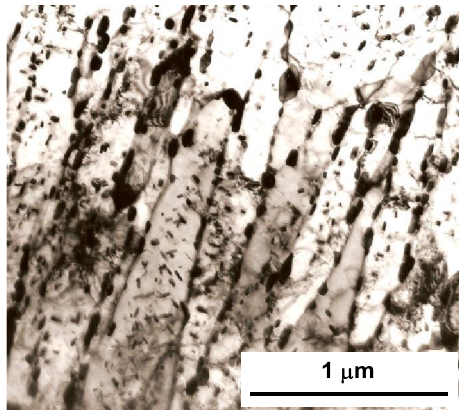


Figure 12. Tempered martensite in 4130 steel heated at 650 °C for one hour (TEM micrograph. Courtesy of F. Woldow while at the Colorado School of Mines).

Not only does the martensite crystal morphology alter during HTT, but the substructure within the martensitic crystals also changes, and as noted relative to Figure 11, carbide particles nucleate and grow. Figure 12 shows a high-magnification TEM micrograph of the microstructure of martensite in a 4130 steel tempered at 650 °C for one hour. Elongated sections of martensite crystals are still parallel. Dispersed carbide particles have formed within martensite crystals and on martensite crystal boundaries and the high dislocation density present within as-quenched martensite has been substantially reduced.

Strengthening would, therefore, come from the very fine grain size, ie. the surviving martensite crystals and perhaps some dispersion strengthening from the carbide particles. The combination of high strength and high toughness of many HTT steels is consistent with the fundamental principle established for ferritic microstructures: grain size refinement is the only strengthening mechanism that increases both strength and toughness [45]. Thus, despite the fact that there is a degree of coarsening of the as-quenched size of the martensite crystals during HTT, the residual very fine crystals or grains account for a major strengthening mechanism in highly tempered martensite. The mechanism and degree of crystal growth, especially in alloy steels, need further research.

Practical applications requiring moderate strength and high toughness are often manufactured from HTT steel. The ductile-to-brittle transition occurs at much lower temperatures than that of microalloyed medium-carbon steels with precipitation-strengthened ferrite/pearlite microstructures treated to comparable hardness. Steels that require good resistance to hydrogen embrittlement are also highly tempered to lower hardness, a property related to the reduction of dislocation density in HTT martensitic steels [29,46-48]. The precipitation of nano-sized alloy carbides in the temperature range of 500 to 650 °C induces a secondary hardening effect. The magnitude of that effect depends on the actual size distribution, as well as type of carbides and can at least compensate in part for the microstructural softening.

Temper Embrittlement

The optimization of strength and toughness by tempering is impeded by the phenomenon of temper embrittlement appearing in the temperature range of 250 to 400 °C and featuring predominantly intergranular cracking along the prior austenite grain boundaries [1]. The embrittlement is concurrent with the replacement of ϵ -carbide by interlath cementite during tempering and the mechanical instability of interlath films of austenite (as a consequence of carbide precipitation) during subsequent loading, but only occurs in the presence of impurities [49]. Addition of a sufficient amount of silicon to the steel can inhibit the formation of cementite in the critical temperature range. The combination of cementite precipitates and residual impurity elements on prior austenite grain boundaries leads to fracture by intergranular cracking in the embrittlement range.

In the current context, the question arises whether grain refinement would have an effect on temper embrittlement. It has been established that the susceptibility to reverse temper embrittlement (RTE) of tempered martensitic microstructures increases with increasing grain size [50]. This effect can be explained in terms of the ease of brittle crack propagation. In clean, (ie. impurity-free) alloyed steel, the DBTT appears to be insensitive to grain size, in contrast to

plain carbon steels. Substructural features, rather than prior austenite grain size, determine the stress required for brittle cleavage crack propagation in the quenched and tempered alloy steel. When impurities, (eg. Sn, P) are present in the steel, a significant shift of the DBTT towards higher temperatures can be observed, Figure 13. This is accompanied by a change in brittle fracture mode to intergranular, Figure 14. When the grain boundary cohesion is reduced to below the cleavage stress as a consequence of segregated impurities, it equals the yield strength at higher temperature. As expected, intergranular crack propagation is promoted as grain size increases, although segregation occurs at all high-angle grain boundaries. Countermeasures to this effect are to get solute impurity atoms preventing them from segregating to the grain boundaries. On the other hand, segregation of transition metal atoms can increase the boundary cohesion and counteract intergranular fracture. This effect will be explained in more detail in a later section.

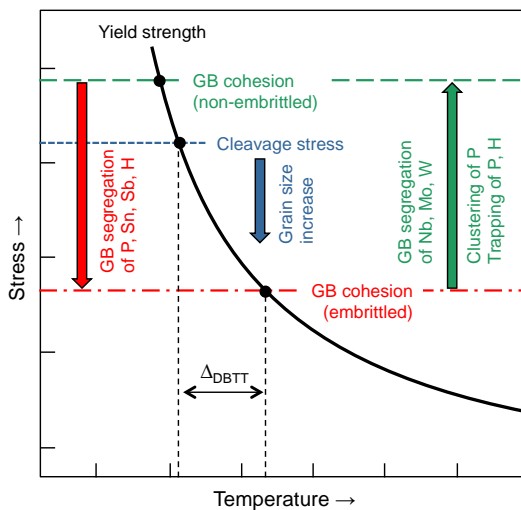


Figure 13. Effect of temperature on the appearance of brittle fracture, influence of boundary embrittlement and metallurgical remedies.

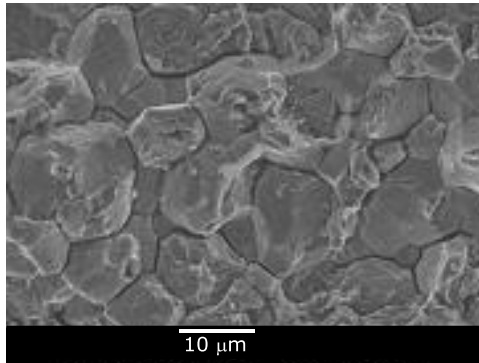


Figure 14. Appearance of intergranular fracture of an embrittled martensitic steel.

As outlined before, the grain size effect on segregated impurity concentration on the boundary is negligible. On the other hand, diffusion distances to boundaries are a direct function of grain size and thus an effect on segregation kinetics should be expected.

Alloy Design and Related Effects

General Considerations

Conventional martensitic steels are usually quenched carbon-manganese grades, often microalloyed with a small amount of boron. In such steel, hardness is determined directly by the carbon content [51]. However, with increasing hardness the toughness of the quench hardened steel decreases to very low values. Alloyed steel types are applied where toughness matters and where through-hardening at heavier gages is required. Guaranteed minimum toughness, (eg. 21 J or 27 J) can be adjusted at low temperature, (eg. 0 °C or -40 °C) by controlling the carbon content and the alloying concept, in combination with appropriate heat treatment. Such grades produce an enhanced service lifetime in applications where impact loads prevail, especially in cold climates.

Alloy Design for Hardenability

A fundamental aspect in designing the alloy for a martensitic steel is hardenability. The alloy design, in combination with the quenching method, must achieve sufficient hardness (strength) over the entire specified depth or thickness of the component. In conventional carbon-manganese steel, the hardening depth is limited to a few millimeters. However, for specific applications, much heavier gages of hardened material are required. Thus, a precisely tuned amount of alloying elements, in combination with high cooling rates, is needed to achieve a high hardness value in the core of thicker plates or components and to obtain a homogeneous microstructure. Even though surface hardness is easily achieved by a quenching or carburizing treatment, hardness tends to decline towards the core of a heavy gage component, with the cooling rate decreasing with distance from the quenched surface. Therefore, hardenability needs to be

enhanced by other alloying elements, such as molybdenum, chromium, copper and nickel. In estimating hardenability by Grange's technique [52] it is assumed that the hardenable diameter for iron is zero. The influence of single alloying elements on the change of the hardenable diameter can be estimated from Figure 15. Besides carbon, molybdenum has the strongest effect before manganese and chromium. Accordingly, adding 0.25%Mo to a Fe-0.2%C base alloy would increase the hardenable cylinder diameter with 90% martensite at the center, by approximately 4 mm.

For a first judgment of the achievable hardening depth, the classic Grossman relationship is often applied [53]. Accordingly, the hardenability of an alloyed steel characterized by the critical diameter DI can be calculated based on the critical diameter of the iron-carbon base composition (D_{IC}) and multiplying factors (MF) for each alloyed element. As mentioned before, a smaller austenite grain size reduces the base hardenability.

$$D_I = D_{IC} \times MF_{Si} \times MF_{Mn} \times MF_{Cr} \times MF_{Mo} \times MF_{Ni} \times MF_V \times MF_{Cu} \times MF_B \times 25.4 \text{ (mm)} \quad (4)$$

$$D_{IC} = (C/10)^{1/2} \times (1.70 - 0.09n) \quad (\text{in}) \quad (5)$$

C: carbon content in weight percent and n : austenite ASTM grain size number.

The use of this method is described in ASTM standard A255-02.

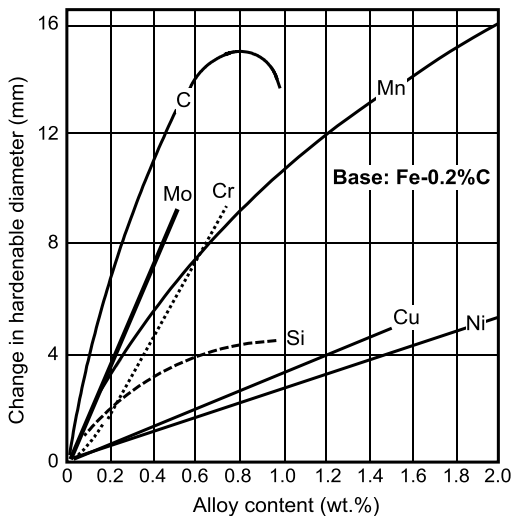


Figure 15. Influence of single alloying elements on the change of the hardenable diameter using Grange's technique.

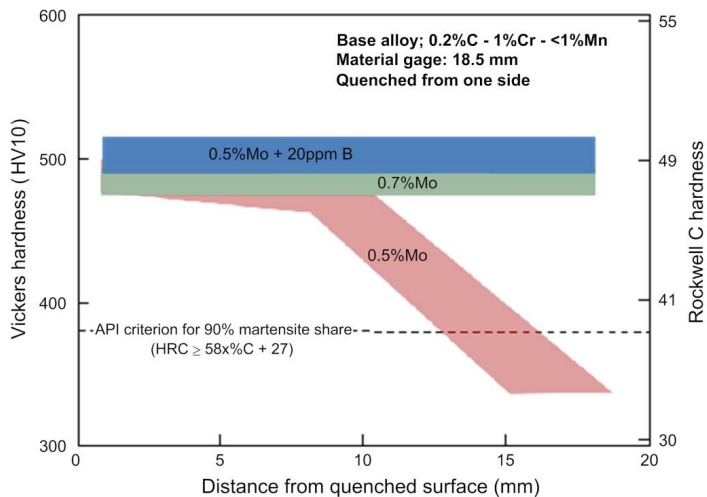


Figure 16. Through-hardening as a function of Mo and Mo-B dual alloying.

The addition of boron is an efficient method of increasing through-hardening [54], Figure 16. The specific hardening effect of boron is to obstruct ferrite nucleation at the austenite grain boundaries. This effect is different from that of manganese, chromium or molybdenum, which lowers the activity of carbon in austenite. To have its effect, solute boron needs to segregate to the austenite grain boundaries before quenching. To keep boron in solid solution, boron nitride formation in austenite needs to be suppressed. This is achieved by adding titanium, which is a much stronger nitride former than boron. Inevitably, TiN particles are formed which have a negative effect on toughness. The grain boundary segregation tendency of boron increases with lowering the austenite temperature. Since carbon also segregates to the austenite grain boundaries, a high carbon-boron solubility product is reached locally. Simultaneously, the solubility limit decreases with the austenite temperature. Consequently, precipitation of intermetallic $Fe_{23}(C,B)_6$ particles on the grain boundary at lower austenite temperatures is likely [55]. The hardening effect of boron is then lost. Furthermore, these grain boundary precipitates are brittle and deteriorate toughness and DBTT. When the quenching temperature of austenite is too high, insufficient grain boundary segregation of boron occurs and the hardening effect is hence insufficient. Some processing routes, for instance press hardening or direct quenching, involve a deformation immediately before quenching. Such deformation introduces dislocations on slip planes and develops deformed boundaries at extremely high strain rates [56]. The deformed boundaries are insufficiently covered with boron and the hardening effect is lost.

Manganese offers a high hardenability effect. However, the element has a pronounced tendency to segregate during casting. These segregation bands are not removed by reheating. Carbon co-segregates with manganese so that the segregation bands have a much higher hardenability than the neighboring areas. Furthermore, the enhanced carbon and manganese content in the segregation band results in a significantly lower martensite start temperature. The consequence is, firstly, an inhomogeneous hardness distribution in the quenched steel and, secondly, the presence of high residual stresses due to the difference in martensite start temperature. Both effects are detrimental to toughness, Figure 17. Moreover, macroscopic residual stresses lead to distortion, negatively affect fatigue resistance and in the presence of hydrogen, promote delayed cracking.

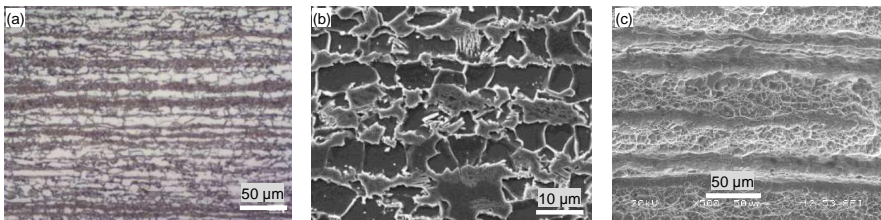


Figure 17. Banded ferritic-pearlitic microstructure of hot rolled 22MnB5 (1.8% Mn) prior to hardening; (a) LOM and (b) SEM. (c) Tensile test at room temperature showing brittle fracture in Mn segregation bands, ductile fracture in softer Mn-depleted areas.

As mentioned before, molybdenum is particularly efficient in providing good hardenability. It does not show the segregation tendency of manganese and its effect on lowering the martensite start temperature is weaker. Molybdenum's hardenability effect is demonstrated in Figure 18 for a steel with a base composition of 0.5%Mn and 0.3%Si at carbon levels ranging from 0.1 to 1.1%. The Grossmann relationship is based on the assumption that there are no interactions between carbon and the alloying elements or between the various alloying elements. However, from Figure 18 it becomes evident that molybdenum's multiplying factor varies with the carbon content [53].

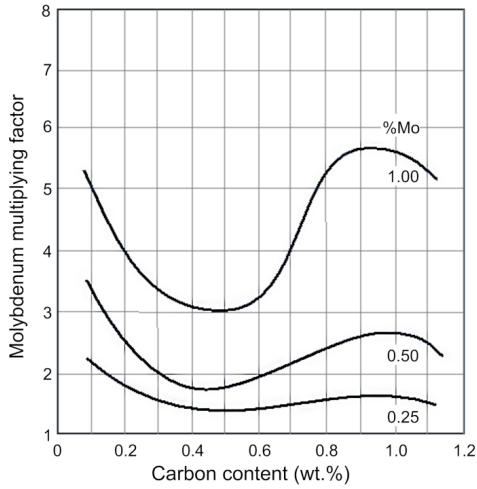


Figure 18. Effect of molybdenum and carbon on the molybdenum multiplying factor of steels containing 0.5% Mn and 0.3% Si.

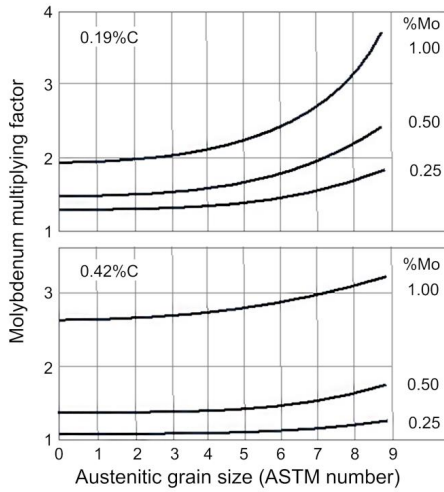


Figure 19. Effect of austenite grain size on the molybdenum multiplying factor of steels containing 0.5% Mn and 0.3% Si.

Especially in the range of low- and medium-carbon steels, the multiplying factor decreases with increasing carbon content reaching a minimum at around 0.45%C. This means that molybdenum is particularly effective in raising the hardenability of such steels with reduced carbon equivalent (CE). The amount of molybdenum needed naturally depends on the hardened gage to be produced. Thicker gages require a larger Mo addition.

Especially at lower carbon levels, the multiplying factor for molybdenum also strongly depends on the PAGS [57]. When the austenite grain size decreases, the multiplying factor increases progressively, Figure 19. Thus, molybdenum alloying can effectively counteract the loss of hardenability caused by grain refinement. This effect is very important since grain refinement of the austenite structure is to be aimed at according to the reasons outlined before.

With regard to further increasing hardenability, the combination of molybdenum with chromium appears to have a strong synergy. The combined effect of these two elements is much stronger than that of manganese and chromium, Figure 20. Accordingly, the production of heavy gaged steel typically relies on combined alloying of molybdenum and chromium. The further addition of nickel is particularly interesting when good low-temperature toughness is desired.

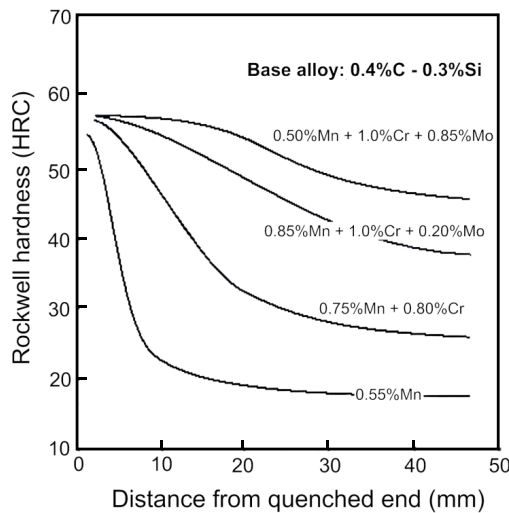


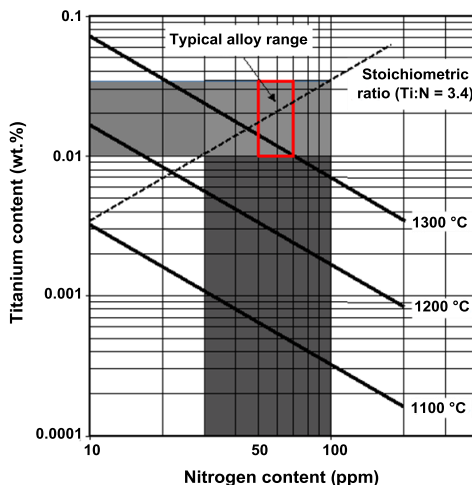
Figure 20. Effect of alloying elements on the Jominy hardenability curves of steels containing 0.4% C and 0.3% Si.

Alloy Design for Grain Refinement

Based on the fundamentals detailed at the start of this paper, it is very evident that grain refinement is the major target in optimizing mechanical properties of martensitic steel. Considering the various processing routes for producing martensitic steel, the following steps have an influence on the PAGS:

- Soaking treatment (>1100 °C) – austenite grain growth;
- Roughing hot deformation – austenite grain homogenization and moderate refinement;
- Finish hot deformation – austenite grain refinement depending on rolling schedule;
- Annealing after cold deformation – recrystallization and ferrite grain growth;
- Reheating before quenching – austenite grain coarsening;
- Case carburizing treatment – austenite grain coarsening.

Any grain refining action starts from the grain size distribution present in the hot steel at the end of the soaking treatment. Depending on temperature and duration of soaking, the austenite grains can become rather large in size. A successful way of limiting the austenite grain growth during soaking is the dispersion of fine TiN particles. TiN has very high-temperature stability, Figure 21, and can thus pin austenite grain boundaries. In order to have this pinning effect maximized, it is advisable to adjust the titanium addition to a near-stoichiometric ratio with the residual nitrogen in the steel (nitrogen is in the range of 30 to 100 ppm depending on the steelmaking process). Considering the stoichiometric ratio of 3.4, the optimum titanium addition is in the range of 100 to 350 ppm. Over-stoichiometric addition of titanium leads to precipitation of coarse TiN particles in the liquid steel, Figure 21. The presence of such particles is harmful to toughness. This guideline should also be observed when adding titanium for protecting boron against nitrogen.



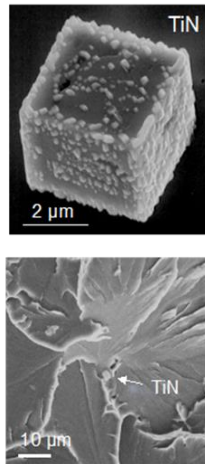


Figure 21. Solubility isotherms for titanium nitride and morphology of coarse TiN particle initiating fracture in a Charpy impact test.

Roughing hot deformation should be done at temperatures above the recrystallization limit temperature (RLT) to allow a thorough homogenization of the microstructure. Multiple deformation passes with subsequent recrystallization can achieve moderate grain refinement. The addition of recrystallization delaying elements, such as niobium and molybdenum has to be matched to the temperature window available for roughing.

Finishing hot deformation below the recrystallization-stop temperature ($FRT < RST$) allows achievement of the largest grain size reduction. It is well established that niobium is most effective in retarding the static recrystallization (SRX) of austenite at high temperatures, Figure 22. This effect of niobium strongly increases up to an addition of 0.06% and then levels off [58]. Molybdenum, as a single alloying element, does not remarkably retard SRX. However, the combination of Mo and niobium leads to a synergetic increase in retardation of SRX. Earlier experiments performed by Akben et al., [59], revealed the effect of molybdenum additions on the dynamic recrystallization (DRX) of microalloyed steels. When microalloyed steels are deformed above the solution temperature of their respective carbonitrides, the addition of molybdenum leads to a distinct retardation in the initiation of dynamic recrystallization. The solute retarding effect of molybdenum alone is intermediate between that of niobium, which has the greatest and that of vanadium, which has the least effect, on an equal atom fraction basis. The addition of boron alone can slightly retard SRX. However, when boron is combined with niobium, the effect is larger than the sum of the separate effects. According to He et al., [60], this has been attributed to the formation of Nb-B complexes exerting a strong dragging force on the grain boundaries and hence reducing their mobility. Increasing the recrystallization stop temperature (RST) to values of 900 °C or above results in a particularly large processing window for finish rolling. The increased recrystallization limit temperature (RLT) observed for co-addition of boron can be a

concern, as full recrystallization is desired during roughing. Especially for plate mills, the operating window is narrowed due to the relatively low slab discharge temperature.

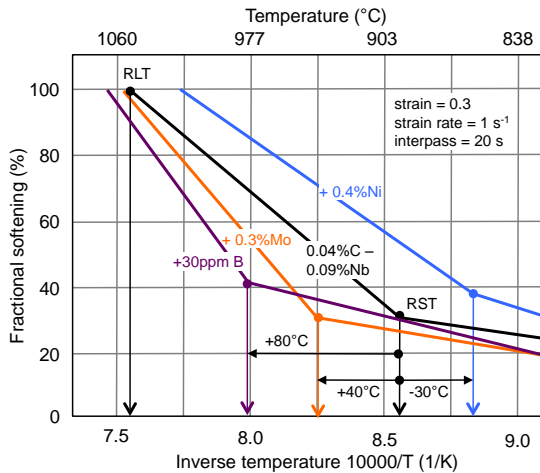


Figure 22. Effect of boron, molybdenum and nickel on the recrystallization behavior in low-carbon, high-niobium steels.

When niobium microalloyed steel is ausformed below the solution temperature of its carbide or carbonitride, in-situ precipitation of small particles results in a further component of retarding recrystallization. In this case, the addition of molybdenum involves two opposing effects. One is an increased retardation of recrystallization due to its effect as a solute. The other is a decrease in the amount of precipitation due to reduced activity of carbon and nitrogen. It was observed that the onset of precipitation of niobium in a 0.05%C-0.04%Nb steel takes twice as long when 0.3%Mo is added [59]. More recent results by Cao [61] confirmed this effect and indicated that the precipitation start in a 0.02%C-0.08%Nb steel is delayed by one order of magnitude after adding 0.15%Mo. It is evident that an increased portion of niobium can be retained in solid solution. Niobium prevailing in solid solution after finish rolling has a significant capability of reducing the transformation temperature. Solute molybdenum and niobium both strongly reduce the diffusivity of carbon in austenite [62]. This effect is stronger for niobium than for molybdenum. However, niobium's solubility is limited and decreases with temperature, whereas molybdenum remains fully soluble. Since molybdenum retards the niobium precipitation as explained above, their individual effects on reducing the carbon activity are additive in dual alloyed steel. Hara et al. [63] have explained the effect of reduced carbon activity by Nb-C or Mo-C cluster formation. Microalloying elements available in solid solution after finish rolling have two important effects. Firstly, they delay the transformation from austenite to ferrite to a lower temperature. This effect increases with the cooling speed. Secondly, solute microalloying elements have the potential to precipitate during or after the phase transformation to a much finer particle size than that of precipitates formed in austenite. Upon direct quenching these precipitates can provide effective secondary hardening during a subsequent tempering treatment.

Alloy Design for Tempering Resistance

In steels alloyed with strong carbide-forming elements, such as chromium and molybdenum, high-temperature tempering permits the diffusion of the alloying elements into the cementite which precipitates and grows in HTT microstructures. It has long been known that those elements significantly reduce the rate at which hardness decreases during high-temperature tempering [51]. Recently, atom probe tomography has made it possible to determine the distribution of elements on an atomic scale. Accordingly, the carbide forming elements are shown to be beginning to diffuse into the cementite of 4340 steel tempered at 575 °C [64]. The study also showed that at a lower tempering temperature of 325 °C cementite forms without any substitutional alloying elements. Thus at the higher temperatures at which substitutional atoms can noticeably diffuse, their partial but still sluggish diffusion restricts cementite particle growth.

Molybdenum mitigates the strength loss during high-temperature tempering in two further ways: through solid solution strengthening, as well as secondary precipitation of complex carbides, together with other elements, such as chromium and niobium. Through its capability of forming such carbides, molybdenum is very efficient in delaying the loss of strength during tempering while improving fracture toughness. Figure 23 demonstrates this effect of molybdenum in combination with chromium and niobium for various Holloman-Parameters (HP) defined as:

$$HP = T x (20 + \log t) x 10^{-3} \quad (6)$$

where T is the tempering temperature in Kelvin and t the tempering duration in hours. Increasing molybdenum content clearly improves the tempering resistance of the Mn-Cr steel, however, superior tempering resistance is obtained by a combination of molybdenum and niobium, Figure 23. For a selected HP value, one can either temper at lower temperature for longer time or at higher temperature for a shorter duration. Tempering at high temperatures in the region below the A_{c1} -transformation point brings about the most desirable microstructure in terms of SSC (sulfide stress cracking) resistance. A well-recovered matrix with uniformly dispersed spheroidized carbide particles are the main characteristic of this microstructure.

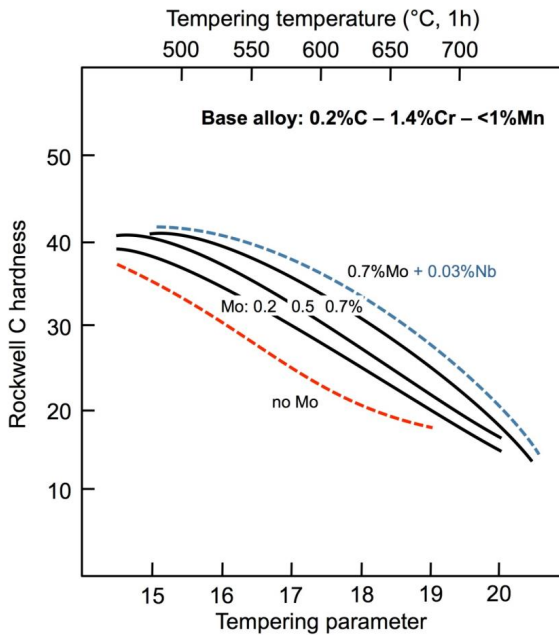


Figure 23. Tempering behavior of quenched steel for various molybdenum additions and niobium microalloying.

As testimony of molybdenum-alloyed steel's good tempering resistance, the martensite in a 0.12%C-steel alloyed with 1.40%Mn and 0.29%Mo was found to contain a reduced but still high dislocation density upon tempering at 675 °C [65]. Figure 24 shows the beginning of recrystallization in this HTT steel, a mechanism that converts the tempered martensite into an equiaxed ferrite/spheroidized microstructure with substantially lower hardness and strength than the tempered martensite it replaces.

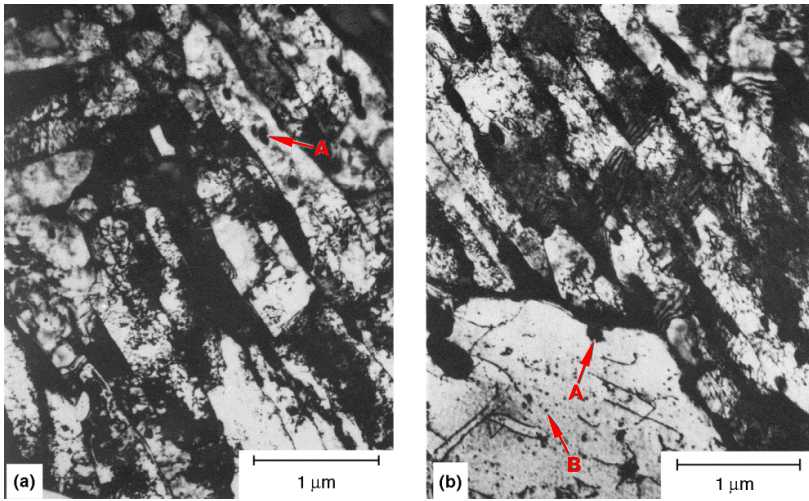


Figure 24. TEM micrographs showing the onset of recrystallization in a 0.12% C steel alloyed with 1.40% Mn and 0.29% Mo; tempered at 675 °C for; (a) one hour and (b) two hours [65].

A and B show larger and smaller spheroidized cementite and carbide particles within recrystallized ferrite grains

Boron microalloyed Cr-Mo steel has a higher tempering resistance than boron-free steel, especially at elevated tempering temperatures. However, boron-treated steel, tempered at higher temperature, has clearly inferior room temperature toughness as compared to the boron-free steel. Particularly when tempering at 600 °C, boron-treated steel tends to have low toughness due to formation of continuous cementite films on the lath boundaries. After tempering above 700 °C, boron-free steels show extensive recovery with the onset of recrystallization resulting in good toughness, whereas in boron-treated steel, recrystallization is retarded so that its toughness is still inferior. A significant problem is the formation of $\text{Fe}_{23}(\text{C},\text{B})_6$ precipitates on the prior austenite grain boundaries. This intermetallic phase is brittle and significantly impairs the DBTT. Maitrepierre et al., [66], discussed this phenomenon in detail showing that over-alloying with boron is particularly harmful. The best compromise between hardenability and toughness, after high-temperature tempering, is found for boron additions between 10 and 30 ppm. However, in practice it is a challenge for the melt shop of a steel mill to meet this narrow window.

The carbide reactions in molybdenum steels are extremely slow, and therefore, hard to complete by heat treatment at 700 °C [67]. As a result of this, it is often observed that carbides present in a steel transformed isothermally at 700 °C, differ from those in steel tempered at the same temperature. M_{23}C_6 is found in tempered structures of molybdenum-alloyed steels containing chromium as an additional alloying element. In this carbide type, molybdenum substitutes a fraction of the chromium atoms.

Long-time annealing of molybdenum-only alloyed carbon steel results in the formation of needle-shaped Mo_2C precipitates in the grain interior [68], Figure 25. Depending on the C/Mo ratio they can be nearly pure Mo_2C [69]. This is particularly the case when the atomic C/Mo ratio is around stoichiometry. The needles have a preferred orientation and grow along the $\langle 100 \rangle$ direction in the ferrite lattice, Figure 25. The average length of Mo_2C needles increases with the annealing duration. These Mo_2C needle shaped precipitates should be avoided, as they are particularly harmful when hydrogen is present in the steel. Lower molybdenum content ($\leq 0.3\%$) does not cause this problem, Figure 26. For higher molybdenum contents, the addition of stronger carbide formers (microalloys) is advisable.

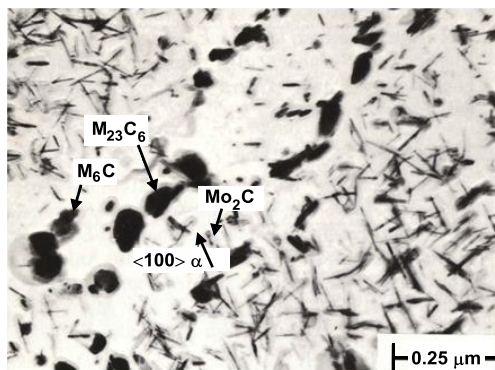
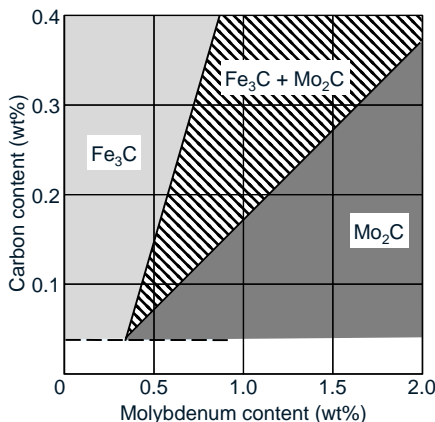


Figure 25. Types of molybdenum-containing precipitates in a 0.2% C-0.5% Mo steel after tempering for 16 h at 700 °C [67].



Several other alloying elements have an influence on strength during high-temperature tempering. The effects of the most typical alloying elements in Q&T steels have been determined by a range of experiments and subsequent multiple regression analysis. The strength correlations for a given quench and temper condition are shown in Table I [70].

According to the formulae in Table I, manganese alloying leads to a yield strength reduction, whereas molybdenum raises yield and tensile strength. Thus, molybdenum not only provides a better hardenability than manganese but also boosts secondary hardening during tempering.

Table I. Effect of Alloying Elements in wt.% on Strength after Q&T Treatment
(930 °C/30 min. → oil-quench → 600 °C/60 min. → air-cool)

| | |
|-----------------------------|--|
| Yield strength = (MPa) | $715 + 1880 [C]^2 - 1663 [C]^3 + 67 [Si] - 774 [Mn] + 920 [Mn]^2 - 330 [Mn]^3 + 74 [Cr] - 16 [Cr]^3 - 3.5 [Ni]^2 + 453 [Mo] - 181 [Mo]^2 + 124 [W]^2 + 1820 [V] - 5226 [V]^2 + 4957 [V]^3 + 425 [Nb] + 22114 [Al]^2 + 12550 [N] - 972 \times 10^4 [N]^3$ |
| Tensile strength = (MPa) | $534 + 865 [C] + 162 [Si] - 62 [Si]^2 + 3 [Ni]^2 + 579 [Mo] - 252 [Mo]^2 + 291 [W] - 368 [W]^2 + 1389 [V] - 2305 [V]^2 - 252 [Ti] + 10635 [N] - 783 \times 10^4 [N]^3$ |

Alloy Design Against Temper Embrittlement

Impurity elements such as phosphorus, antimony and tin are notorious for their embrittling effect. Therefore, the content of these elements must be limited as much as possible during steelmaking. Phosphorous is one of the most frequent impurities in steels. It can affect material properties strongly, even at small bulk concentrations of 100 ppm if it is segregated at the grain boundaries. In simple carbon steels the tendency for grain boundary segregation of phosphorus is reduced due to site competition at the grain boundary [71]. In alloy steel, however, a significant portion of carbon becomes tied up as metal carbide during high-temperature tempering and phosphorus grain boundary segregation can occur. The problem also appears in high strength interstitial-free (IF) steels for automotive applications. These steels, which are phosphorus alloyed and where carbon is completely tied up, are vulnerable to secondary work embrittlement. The traditional remedy against embrittlement is the addition of 5-10 ppm boron, Figure 27. Site competition by solute boron can successfully avoid grain boundary segregation of phosphorus during annealing treatments [72,73]. Later it was demonstrated by Urabe et al., [74], that boron-free high strength IF steel with an over-stoichiometric niobium addition produces a similar resistance against embrittlement. Two different metallurgical reasons can explain the anti-embrittlement effect of niobium. In carbon-free steel (such as IF steel) niobium has been shown to form NbP clusters or even precipitates [75]. This effect disappears when solute carbon is present leading to NbC precipitation. Likewise, titanium forms TiP clusters in carbon-free steel, reducing embrittlement. When solute niobium and titanium are segregated to the grain boundary they appear to increase boundary cohesion. Starting from first-principles quantum mechanical calculations on the strengthening and embrittling effects of alloying metals on the grain boundary cohesion, it was found that many transition metals of the groups IVa to VIIa have the potency of increasing cohesion, Figure 28 [76]. Of those technically relevant in steelmaking, tungsten, niobium and molybdenum have the largest effects in descending order. Titanium and vanadium have a clearly smaller cohesion enhancing effect, whereas manganese has a cohesion reducing effect, thus supporting embrittlement.

Both molybdenum and tungsten have rather good solubility in medium carbon steel [77], contrary to niobium and accordingly these are most suitable to deploy the cohesion enhancing effect, especially in medium-carbon and high-carbon steels. Again it appears that higher manganese additions should be avoided.

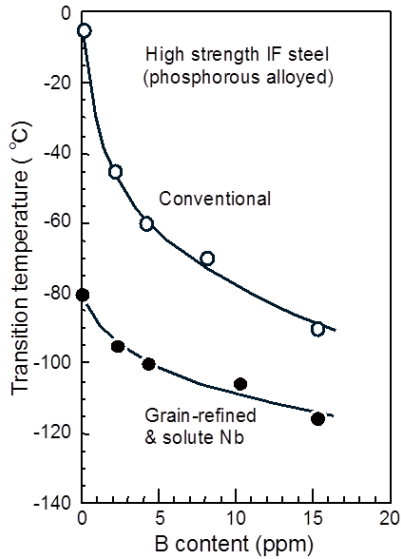


Figure 27. Avoidance of phosphorus grain boundary embrittlement by boron and solute niobium [74].

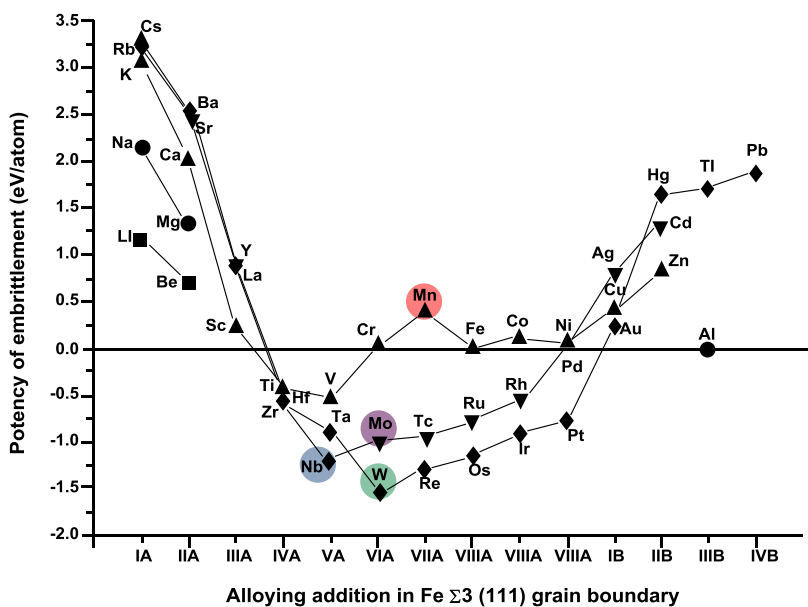


Figure 28. Embrittlement potency of substitutional additions in Fe $\Sigma 3(111)$ grain boundary [76].

Alloy Design Against Hydrogen Embrittlement

Hydrogen embrittlement is a severe concern in practically all ultra-high strength steels. The principal effect of hydrogen embrittlement has been already discussed in this paper where grain refinement was identified as a feasible means of reducing this detrimental effect. Another means of reducing hydrogen embrittlement is that of hydrogen trapping.

The concept of hydrogen trapping, Figure 29, has significant potential with regard to reducing the sensitivity of steel to hydrogen induced delayed cracking. Various traps are characterized by their binding energy of hydrogen, Table II [78-81]. Flat traps with binding energies of <20 kJ/mol can be discerned from deep traps with binding energies of >50 kJ/mol [79]. Grain boundaries, coherent precipitates, and dislocations form a class of reversible traps, which can only weakly bind hydrogen at temperatures of interest. Incoherent precipitates, voids, etc. are much stronger irreversible traps. It is the latter type of trap that appears most effective in modifying susceptibility to delayed cracking in the presence of hydrogen. Both improvement and degradation are possible depending on the shape, location and specific properties of irreversible traps. However, reversible (weak) traps can also play an important role since they may strongly affect the kinetics of hydrogen transport. In particular, their presence can often reduce susceptibility by increasing the time necessary to reach some critical local hydrogen concentration [78]. Important exceptions are mobile dislocations, which transport hydrogen in

their core or as Cottrell-type atmospheres. These mobile traps can transport hydrogen at a much faster rate than by lattice diffusion and with a specificity of location that provides an efficient means of rapidly localizing the hydrogen concentration at strong microstructural traps [82]. If these are local failure centers, embrittlement can be enhanced. There is evidence for the occurrence of this scenario in a number of alloy systems [83-87].

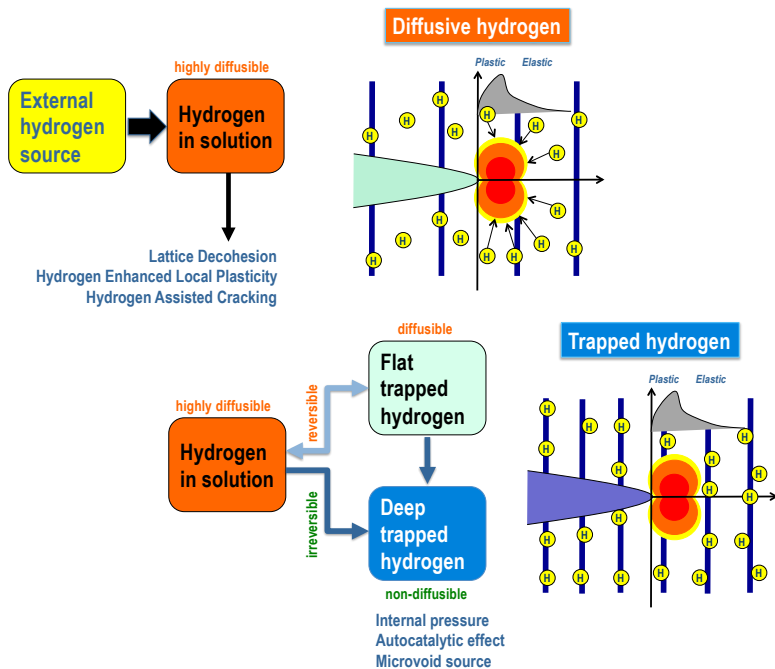


Figure 29. Effects of diffusible hydrogen and concept of hydrogen trapping.

Table II. Hydrogen Trapping Energy of Various Nitrides and Carbides in an Iron Matrix [79]

| Alloy system | Fe-Zr-N | Fe-Ti-N | Fe-Nb-N | Fe-V-N | Fe-Mo-N |
|-----------------------|---------|---------|---------|--------|---------|
| Flat traps (kJ/mol H) | -20.4 | -20.7 | -18.2 | -18.9 | -19.3 |
| Deep traps (kJ/mol H) | -56.1 | -60.5 | -54.9 | -56.0 | -56.0 |
| Alloy system | Fe-Zr-C | Fe-Ti-C | Fe-Nb-C | Fe-V-C | Fe-Mo-C |
| Flat traps (kJ/mol H) | -19.9 | -20.6 | -18.3 | -17.2 | -13.9 |
| Deep traps (kJ/mol H) | -58.5 | -58.5 | -56.0 | -57.0 | -56.5 |

Numerous studies have confirmed the hydrogen trapping performance of microalloy precipitates. Asahi et al., [88], identified vanadium carbide as a hydrogen trap site in a steel with a tempered martensite structure. The activation energy for de-trapping is in the order of 30 kJ/mol. The de-trapping of hydrogen is very slow while the trapping presumably proceeds rapidly. Similar experiments by Yokota and Shiraga [89] showed that the tempering condition is very important to optimize the trapping effect of vanadium carbide. Wei et al., [90], demonstrated the trapping capability of TiC in a quenched and tempered steel of 0.42%C. TiC is present in a bimodal size distribution. Fine TiC particles were found to be more effective in trapping hydrogen than coarse particles with the same volume fraction.

In high strength seamless tubes, the distribution of spheroid shaped carbide precipitates was shown to allow a significantly higher critical stress level under hydrogen loaded conditions [91,92]. In such medium carbon (0.25-0.45%) steels, niobium has been microalloyed up to 0.08%, providing a fine-grained microstructure and a homogeneous distribution of precipitates. Additions of vanadium in combination with a suitable tempering treatment further increase the performance under hydrogen-loaded conditions by creating additional trapping sites.

In spring steels, vanadium and titanium precipitates were shown to trap hydrogen and thus to improve corrosion fatigue properties. It appeared that titanium precipitates had a bigger effect than those of vanadium [93]. A suspension spring steel designed for 1200 MPa shear stress by Daido Steel [94] makes use of boron and niobium microalloying to increase the delayed fracture strength. Simultaneously, the corrosion-fatigue resistance is also significantly improved. Perrard et al., [95], identified a microalloying combination of niobium and titanium as the most effective solution, particularly with respect to corrosion-fatigue endurance, when developing ultra-high spring steel.

When designing the alloy concept for hydrogen trapping by precipitates, the intended processing route needs to be considered with respect to the precipitation behavior of the various transition metal carbides. When producing as-quenched or low-temperature tempered martensite, vanadium or molybdenum carbides have very little chance to form. This is due to their high solubility in austenite. Accordingly, at the quenching temperature, be it in a direct quenching process or in a reheat-quenching process, both elements are in solution and have no chance to precipitate during the transformation due to kinetics. Low-temperature tempering does not provide conditions for precipitation of these elements (Mo, V) either. On the contrary, niobium and titanium under these processing conditions can exist as precipitates. In a direct quenching process, these microalloys will at least partially precipitate during ausforming. The size of such strain-induced precipitates is typically in the range of 20 to 100 nm. In a classic reheat-quenching process, no or little ausforming is done and in this case niobium remains, for the most part, in solid solution and will precipitate only during transformation to ferrite. In this case the precipitates will be in the lower nanometer range. When reheating to austenite before quenching, remnants of solute niobium will precipitate as well but practically no precipitated niobium will re-dissolve at temperatures below 1000 °C. Thus in both processes one can expect a mix of coherent and incoherent niobium precipitates in the martensitic matrix.

Other Alloy Design Considerations

Applications of mining and tooling materials often occur in the presence of aggressive media. Chromium additions of up to 1.5% have proven to be very effective against wear in weakly acid media, enhancing the wear life by more than 35% [96]. In corrosion-resistant plastic mold steels, chromium contents are raised to 12-15% (grade 1.2083) and additionally increased molybdenum alloying (grade 1.2316) is applicable.

In other tooling applications, such as aluminum die casting, the steel may require improved heat conductivity. This demands a generally low level of solid solution elements and particularly reduced nickel additions [97].

For applications in LNG or LPG environments, the steel needs to remain ductile and crack resistant at such ultra-low temperatures. The base concept for such steels is a low carbon content (<0.10%) and nickel alloying in the range of 5-9%. Phosphorous and sulfur residuals are kept at very low levels. During production, the steel undergoes a quench and temper treatment and for higher demands, a double-quench and temper treatment. The second quench is then executed from the two-phase (α - γ) temperature region. Addition of molybdenum was found to give a further increase in strength and toughness [98]. Niobium microalloying proved to be especially useful for improved heat affected zone toughness after welding [99].

The surface of plastic molds is often etched to obtain a certain surface texture on the final plastic part. Thus, the plastic mold steel must have good etching capability and should not produce flaws or other irregularities. Therefore, the steel must be very clean, free of macro-segregation, and fine-grained and it should have a low content of carbides. The fine grain structure can be effectively achieved by niobium microalloying. The manganese content is kept at a low level, avoiding macro segregation. Carbide forming alloys are also put at a reduced level. An increased silicon level helps avoid carbide precipitation during operating temperatures in the range of 200 to 440 °C.

Steel to be subjected to extensive machining should offer increased cutting efficiency and suffer little shape distortion after machining. Concerning the latter demand, a low level of residual stress is required. Reduced content of hard carbides being dispersed in the steel matrix is beneficial to machining speed and tool life. Furthermore, Hoseiny et al., [100], demonstrated that an increase in the martensite packet size led to higher cutting force and shorter tool life. Simultaneously, tool life appears to be extended, which is due to the generally lower cutting force and smaller variation of cutting force. Niobium microalloying should be beneficial in this respect for providing a small packet size and a narrow packet size scatter. The fine and homogeneous grain size distribution will inherently reduce residual stresses since the martensite start temperature depends on austenite grain size [101]. For the same reason, manganese segregation should be limited, as was explained above.

Creep resistance is a key property in steels that are exposed to high temperature and stress for extended periods. Molybdenum is an established alloying element in such materials as it improves resistance to creep and high-temperature corrosion. Niobium has been applied more recently and is contained in nearly all the latest high strength steels belonging to the group of

9-12%Cr steels [102]. Increasing the chromium content to above 7% leads to a group of CrMo steels which have a martensitic microstructure as a common feature. The addition of the microalloying elements niobium, vanadium and boron as well as tungsten, further improves the creep strength and provides an improved resistance against hot hydrogen attack.

Examples of Optimization Strategies for Various Martensite Processing Routes

Conventional Reheat-quenching

The conventional process of reheating and subsequent quenching in water or oil is commonly applied for plate products, forgings and castings. In many cases, the hot deformation stage is performed at rather high temperatures so that ausforming is not performed or only to a weak degree. After hot deformation the material usually cools down slowly, typically into a ferritic-pearlitic equiaxed microstructure. This microstructure, depending on the cooling rate, is not especially fine-grained. Reheating to a temperature of around 950 °C leads to re-austenitization. The austenite grains grow in size during the holding stage at the austenitization temperature. Subsequent quenching develops the martensite substructure within these austenite grains.

Two possible approaches for martensite microstructural refinement can be defined. A conservative approach is the addition of niobium in combination with hot deformation at a high finishing temperature. Under these conditions, little or no austenite conditioning occurs. Yet, niobium carbide particles precipitate during down cooling to the intermediate ferrite-pearlite microstructure. These particles can limit austenite grain growth during the subsequent re-austenitizing phase, Figure 30. A more progressive approach is lowering the finish deformation temperature in combination with niobium microalloying. This leads to austenite pancaking and subsequent transformation into a fine-grained intermediate ferrite-pearlite microstructure. Upon reheating, existing NbC precipitates further act by pinning the austenite grain boundaries as in the more conservative approach. The conservative approach has been practiced for decades in specific applications. Often it was applied when an increased resistance against hydrogen or sulfide stress cracking was required [47,91,103]. In abrasive resistant steel it was utilized to increase toughness and to lower DBTT [26,104].

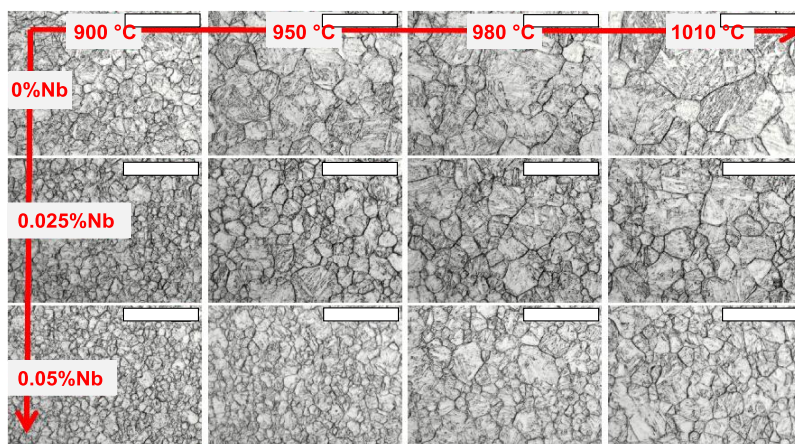


Figure 30. Grain coarsening behavior of austenite in steel 22MnB5 during reheating (one hour) depending on austenitizing temperature and niobium addition (scale marker = 20 μm).

The simple C-Mn-B grade 22MnB5 was originally developed as a low-cost hardenable steel for production of agricultural equipment. Since the year 2000, this steel has increasingly been used for ultra-high strength components in car bodies. Therefore, this steel, in the form of thin sheet, is heated up to around 950 $^{\circ}\text{C}$, completely austenitized and subsequently hot formed in a stamping die. The austenitic microstructure is soft and well formable. When the die is in full contact with the deformed sheet, quick heat transfer quenches the hot austenite into martensite. The formed component is then assembled into the car body structure, which will, after completion, be painted and baked for about 20 minutes at 180 $^{\circ}\text{C}$. Accordingly, the thermomechanical history of such a component consists of the following steps:

hot rolling (usually no TMCP) \rightarrow coil cooling into ferrite-pearlite \rightarrow cold rolling \rightarrow recrystallization annealing (batch or continuous annealing) \rightarrow re-heating to austenite \rightarrow quenching into martensite \rightarrow low-temperature tempering (paint baking).

The obtained mechanical properties are a minimum of 1500 MPa tensile strength, around 1200 MPa yield strength and between 5 and 7% total elongation. Additionally, toughness is a property that also matters since such components are typically used in areas where impact is expected in the case of a vehicle collision. This property is, however, not specified by carmakers and would be difficult to measure in thin sheet. Carmakers instead apply a quasi-static bending test in a three-point configuration with a sharp bending radius, Figure 31, VDA 238-100 [105]. On this basis, a minimum critical bending angle is specified, typically in the range of 55 to 65 degrees. The higher the critical bending angle, the more resistant is the component against collapse as a consequence of bend-cracking and the larger is the energy consumption of the component. High-temperature tempering treatment can improve the bendability and thus energy absorption but at the expense of strength, Figure 31.

In an extensive program of optimizing the critical bending angle in as-quenched Mn-B steel, most of the principles discussed previously in this paper have been verified [106]. It became evident that refinement of the PAGS is an important step in increasing the critical bending angle. In most of the trials done so far, grain refinement was achieved using conservative hot rolling and adding niobium in the range of 0.03 to 0.08%, resulting in a PAGS of ASTM 8-10. In the non-optimized standard steel the PAGS is usually ASTM 5-7. By combining a conservative grain refining approach with, at the same time, relatively low manganese content, critical bending angles of up to 100 degrees can be obtained, Figure 32. The avoidance of pronounced segregation bands by lowering the manganese content is beneficial to the bendability. Adding a small amount (0.10-0.15%) of molybdenum also proved successful and increased the critical bending angle. This could be due to the effect of solute molybdenum enhancing grain boundary cohesion. Trials using Nb-Mo dual alloying in combination with TMCP rolling resulted in further PAGS refinement to ASTM 12-14.

It has already been discussed above that PAGS refinement of 22MnB5 provides increased resistance against hydrogen embrittlement. Detailed analysis indicated that the improved hydrogen resistance is not only related to PAGS refinement. Figure 33 shows the hydrogen diffusivity as a function of the niobium content in 22MnB5. A pronounced minimum value of hydrogen diffusivity for a niobium addition of around 0.05% is evident, Figure 33. The origin of this variation of hydrogen diffusivity is related to the size distribution of NbC precipitates in the steel. Detailed analysis by transmission electron microscopy [107] revealed the presence of a precipitate population in the size range from 50 to 250 nm, irrespective of the niobium content. A second precipitate population was found having sizes smaller than 30 nm. Those steels with a high fracture stress after hydrogen charging and showing reduced hydrogen diffusivity revealed a particularly high share of precipitates with sizes smaller than 10 nm, Figure 34. It must be concluded that hydrogen trapping by these very fine precipitates is responsible for the observed phenomena.

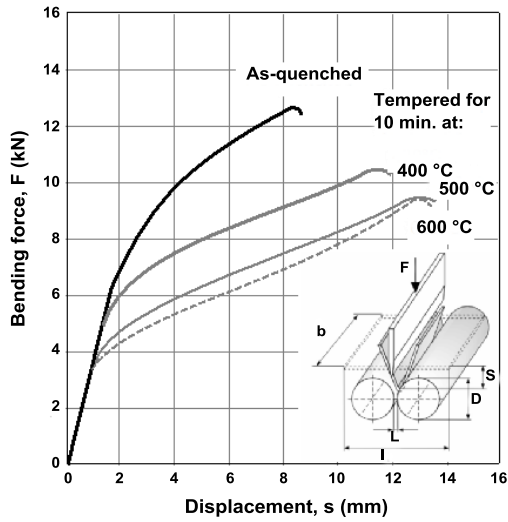


Figure 31. Bending test according to VDA238-100 on steel 22MnB5 in as-quenched and tempered condition.

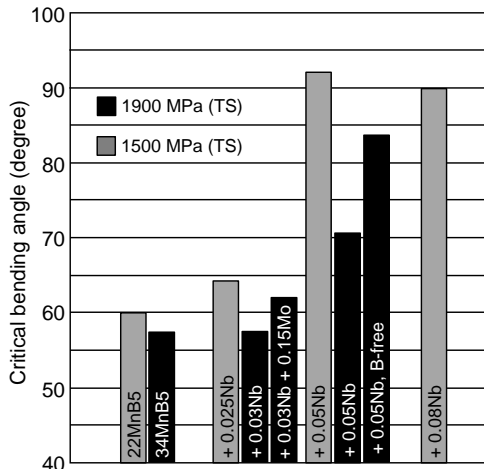


Figure 32. Improvement of critical bending angle (VDA238-100) by microalloy concepts in as-quenched steels 22MnB5 and 34MnB5.

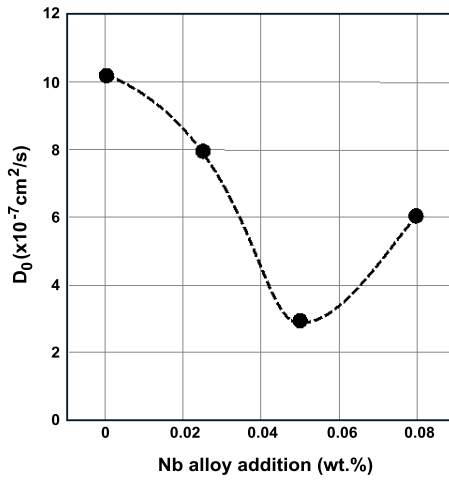


Figure 33. Dependence of hydrogen diffusivity on niobium addition in press hardened (martensitic) steel 22MnB5.

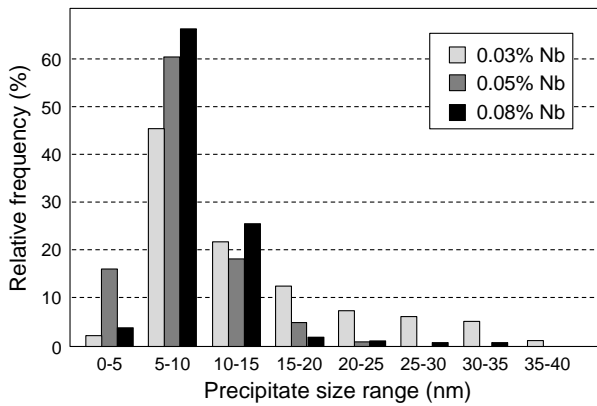
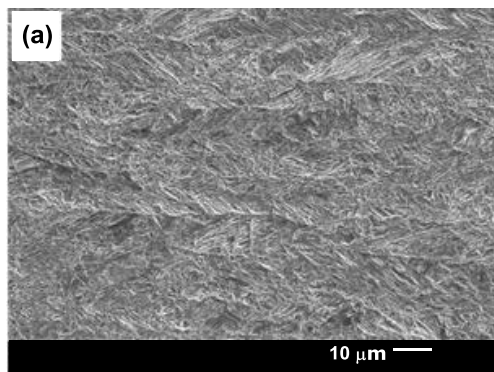


Figure 34. NbC precipitate size distribution in steel 22MnB5 after press hardening treatment.

Direct Quenching

Direct quenching (DQ) after hot deformation has gained considerable interest for the production of ultra-high strength steel. The austenitic material is subjected to high cooling rate and a low cooling stop temperature, immediately after hot deformation. Self-tempering (LTT) or furnace tempering (HTT) are additional processing options. Products such as plate, strip and forgings can be produced in this way. Direct quenching avoids the second reheating operation, thus offering a cost-optimized processing route. From a metallurgical point of view, there are several important differences as compared to the traditional reheat-quenching process. Depending on the ausforming conditions before quenching, the austenite microstructure is not or only partially recrystallized and the grain shape is not globular. This is in contrast to a reheat-quenching process where the steel passes twice through a phase transformation providing a normalized microstructure with an equiaxed austenite grain morphology. The consequence of an elongated austenite grain shape before quenching is an anisotropy of the martensitic microstructure, Figure 35 and hence of particular material properties. Secondly, the state of solute carbide formers is far more out of equilibrium in a direct quench process. During ausforming under industrial processing conditions, niobium only partially precipitates due to relatively slow precipitation kinetics. Any solute niobium present after the finish of deformation remains in solution under direct quenching, whereas in the reheat-quenching process, most of the solute niobium will precipitate during the γ - α phase transformation or during the reheating to austenite. Solute niobium, present in as-quenched martensite, reduces the diffusivity of carbon at lower tempering temperatures and finally precipitates as fine particles during high-temperature tempering, thus providing tempering resistance and pronounced secondary hardening.

A product that is being increasingly produced by direct quenching is hot-rolled strip having yield strength in the range of 900 – 1000 MPa. Applications of these steels are found in truck frames, crane booms and machinery structures, with the aim of reducing component weight. Regarding manufacturing of such components, flatness of the sheet steel, as well as cold bendability are the most important criteria while fatigue resistance and toughness are the decisive properties during component service life.



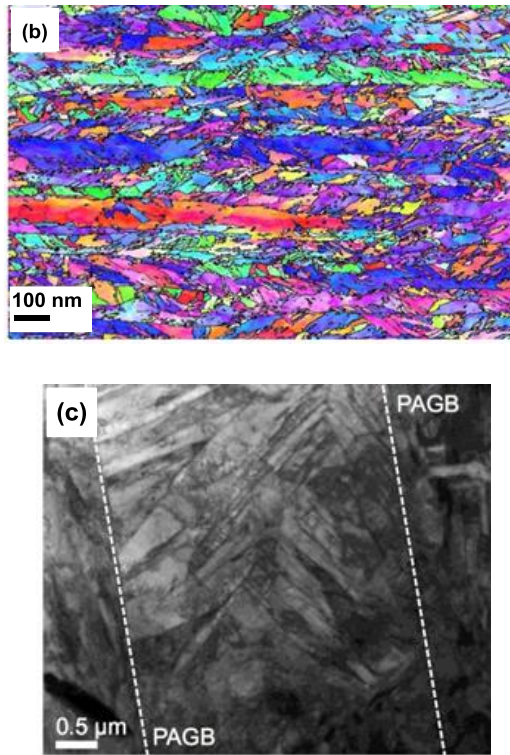


Figure 35. Martensitic microstructure obtained by direct quenching of pancaked austenite; (a) SEM, (b) EBSD, (c) TEM (micrographs courtesy of J.R. Yang – National Taiwan University).

Typical alloy design concepts are based on a carbon content in the range of 0.07 to 0.10%. Such hypo-peritectic alloy design helps avoid segregation and the formation of surface cracks during continuous casting. Increased additions of manganese and chromium are usually chosen to provide sufficient hardenability. Often molybdenum alloying and/or boron microalloying are utilized to further boost hardenability. For applications requiring high toughness at very low temperatures, nickel alloying has been long established.

Niobium microalloying in such steel has the effect of obstructing austenite recrystallization during finish rolling and thus providing a larger degree of austenite pancaking. Already a small addition of niobium (~0.02%) in combination with a low finish rolling temperature (<850 °C) results in a remarkable reduction of the austenite grain thickness in the through-thickness direction.

For higher finishing temperature (>900 °C) this pancaking effect is much less pronounced even at larger niobium additions. A strong synergy between niobium and boron further increases the obstruction of recrystallization so that significant pancaking occurs even at high finish rolling temperatures [108]. At lower finish temperatures, however, niobium as such dominates the austenite pancaking effect. The reduction of austenite grain dimension in the sheet normal direction translates into an equivalent refinement of the effective grain size, which in turn leads to an increase of yield strength, Figure 36. It appears that the gain in yield strength obtained by severe pancaking is of the order of 120 MPa. This strength gain by microstructural refinement offers the possibility of reducing the carbon content by around 0.03%, thus providing better toughness and lower DBTT for a specified strength level. On the other hand, it also extends the maximum strength level that can be achieved with a hypo-peritectic alloy design. The avoidance of segregation, as well as a homogeneous cooling pattern are prerequisites for a low level of residual stress in the final product and thus the prevention of shape distortion upon further manufacturing processes.

It has been reported that the pronounced microstructural anisotropy in martensite produced from pancaked austenite provokes a marked difference in the cold bending behavior when bending along the rolling direction as compared to the transverse direction. The poor bendability along the transverse direction has been attributed to the localization of strain in narrow shear bands and the presence of upper bainitic microstructures, containing martensite-austenite (MA) islands, oriented parallel to the rolling direction [109]. Reducing the severity of austenite pancaking, i.e. by raising the finish rolling temperature or reducing the total reduction could improve the transverse bendability. This approach would, however, sacrifice strength. Another possibility is to provoke dynamic recrystallization of heavily pancaked austenite, resulting in globular-shaped ultrafine austenite grains prior to quenching [110]. Besides, multiple and thorough recrystallization during roughing rolling leading to a homogeneous and fine grained globular austenite microstructure at the entry of finish rolling is recommended. Optimizing the reduction schedule and matching the alloy concept to the roughing temperature can achieve this.

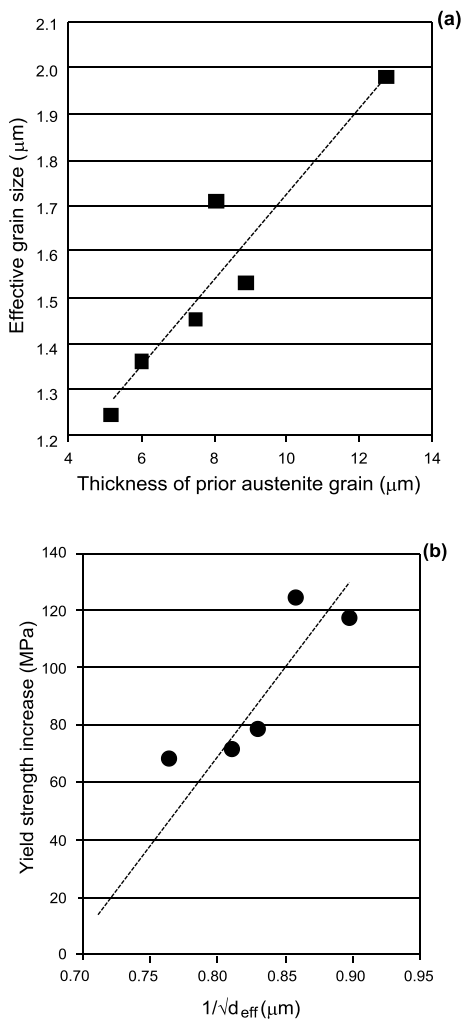


Figure 36. Influence of austenite conditioning (pancaking); (a) on the effective grain size and (b) yield strength in a low-carbon steel subjected to direct quenching.

Case Carburizing

Case carburizing is a thermochemical treatment by which carbon diffuses into the surface of typically medium carbon steel. Therefore, the steel is heated to a temperature in the austenite range for an extended period of time. The carbon enriched case layer transforms upon quenching into martensite of increased hardness as compared to the underlying base material. The case depth, d_{case} , is determined by the carbon diffusion coefficient, D , and the carburizing time, t , as:

$$d_{case} \sim \sqrt{D \cdot t} \quad (7)$$

where $D = D_0 \exp(-Q/R \cdot T)$. (8)

with D_0 being the maximum diffusion coefficient, Q being the activation energy for diffusion, R being the gas constant and T being the absolute temperature. The required minimum case depth can accordingly be achieved by a given carburizing time at a given temperature. Raising the carburizing temperature markedly shortens the treatment time. The maximum allowable carburizing temperature is determined by the onset of severe austenite grain coarsening. Specifications require that 90% of the grains are smaller than ASTM 5 and grains coarser than ASTM 3 are not allowed at all. Furthermore, it is recommended that the grain size scatter within the material be in a narrow range. Mixed grain size causes residual stresses as larger austenite grains transform into martensite at higher temperatures than smaller grains. The resulting residual stresses cause part distortion after quenching [111] and negatively influence the fatigue behavior [112].

Austenite grain size control in carburizing steel has been traditionally achieved by aluminum nitride (AlN) precipitates that have the capability of pinning the austenite grain boundaries [113]. This pinning effect requires the size of the precipitates to be of the order of 50 nm. Under unfavorable treatment conditions, AlN particles either coarsen or dissolve and the pinning effect is lost. Furthermore, the pre-treatment temperature prior to carburizing has an important influence on the pinning capability of AlN, as shown in Figure 37, since it determines the size of existing AlN particles.

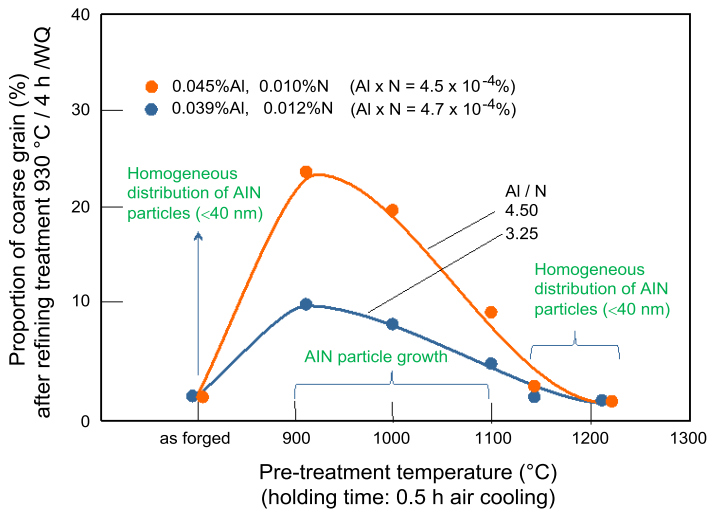


Figure 37. Influence of pre-treatment temperature and Al:N ratio on the grain coarsening behavior of steel 16MnCr5.

Particle size and stability are controlled by the stoichiometric ratio, rather than by the solubility product. The effect of AlN particles is best when the Al:N ratio is close to stoichiometry (Al:N = 2:1). Excessive addition of aluminum causes cleanliness problems and increased scale forming, while too high a nitrogen content leads to nil-ductility issues during hot deformation. Therefore, the optimization of grain coarsening resistance, based on AlN particles, with the aim of higher temperature carburizing is difficult to achieve.

TiN particles are very stable even at the highest austenite temperatures. Therefore, titanium microalloying is expected to allow treatments at higher temperatures without excessive grain coarsening [113,114]. Ideally the titanium addition is set to around three times the nitrogen content in weight percent. Over-stoichiometric titanium addition leads to the formation of coarse primary TiN particles, which have no pinning capability and a detrimental effect on toughness. Yet, co-alloying of niobium to an under-stoichiometric Ti:N ratio significantly increases the temperature of initial grain coarsening, Figure 38 and also reduces the tendency for forming a mixed grain size distribution, Figure 39.

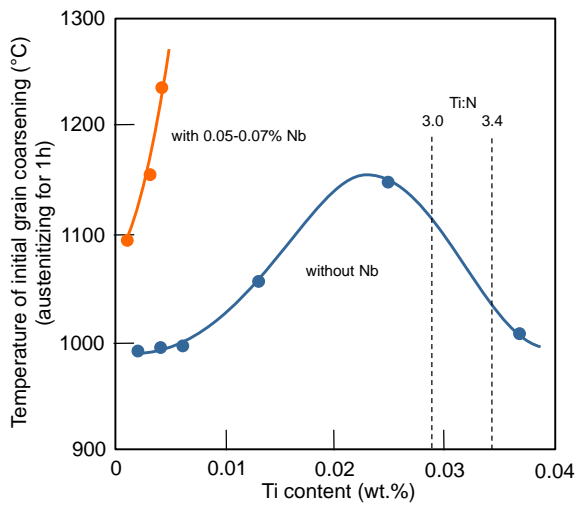


Figure 38. Effect of titanium and niobium microalloying on the grain coarsening resistance in steel 16MnCr5.

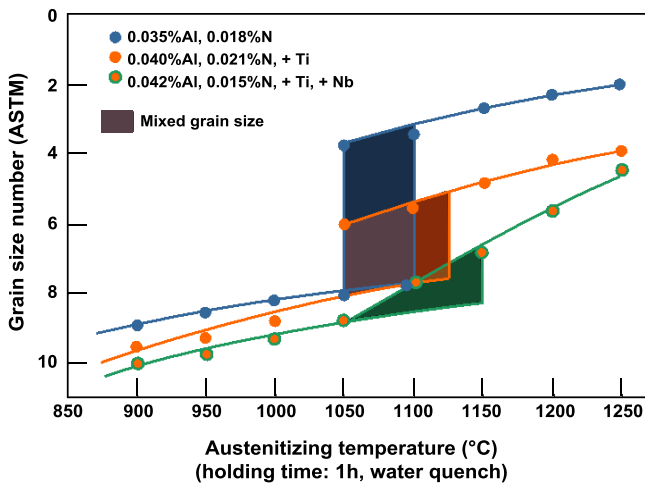


Figure 39. Influence of austenitizing temperature on grain size in steel 16MnCr5 with different microalloy modifications.

The higher grain size controlling efficiency of the Nb-Ti dual microalloyed steel lies in a fine dispersion of particles in the size range of 20 to 50 nm. This particle size range has a high capability for grain boundary pinning [113,115]. More detailed analysis revealed that the particles typically have a mixed chemistry appearing as titanium-niobium carbonitride, Figure 40. Based on solubility considerations, it is feasible that TiN particles precipitate first, serving as nucleation sites for Nb(C,N). The effectiveness of the dual microalloy concept has been verified in steel 16MnCr5, Figure 41. The base alloy, as well as microalloyed variants, have been subjected to solution annealing at 1150 °C for 40 minutes. Subsequently, the steel samples were carburized at 1050 °C for nearly three hours, followed by oil quenching. The base alloy with only nitrogen and aluminum addition shows impermissible grain coarsening. An optimized Nb-Ti microalloy concept, however, provides a much finer average grain size, thereby completely avoiding grain sizes of ASTM 5 or smaller.

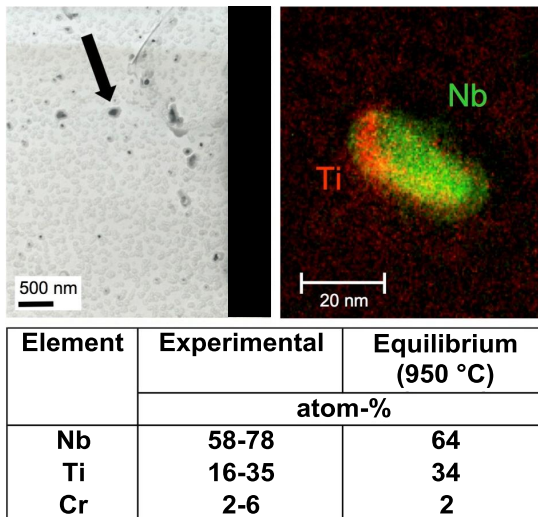


Figure 40. Morphology and chemical composition of precipitates in Nb-Ti microalloyed steel 16MnCr5.

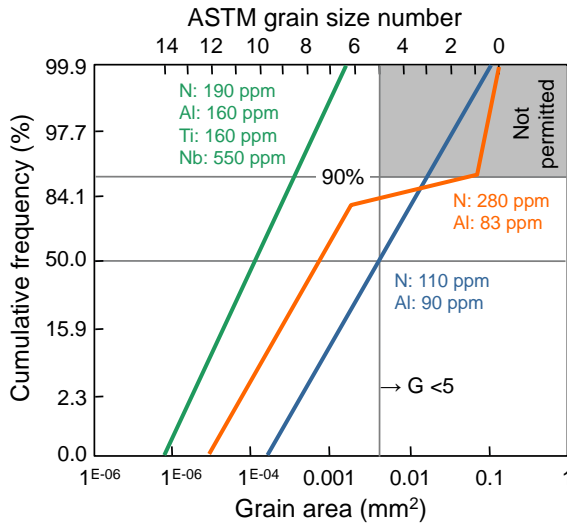


Figure 41. Grain size distribution in steel 16MnCr5 after solution annealing at 1150 °C for 40 minutes followed by case carburizing at 1050 °C for three hours/oil quenching.

Meanwhile, the dual microalloy concept has been successfully applied to various other case carburizing grades for automotive, as well as industrial applications [116,117]. Steel grade 18CrNiMo7-6 is often used for large size industrial gears requiring case hardening depths of several millimeters and thus long carburizing times. By applying the Nb-Ti dual microalloying concept, the steel can withstand high carburizing temperatures with only minor grain coarsening, thus, allowing a substantial shortening of the carburizing time, Figure 42 [117]. For instance, a typical case depth specified for a heavy machinery gear requiring a diffusion time of 20 hours at 950 °C can be shortened to nine hours at 1050 °C according to Equations 7 and 8.

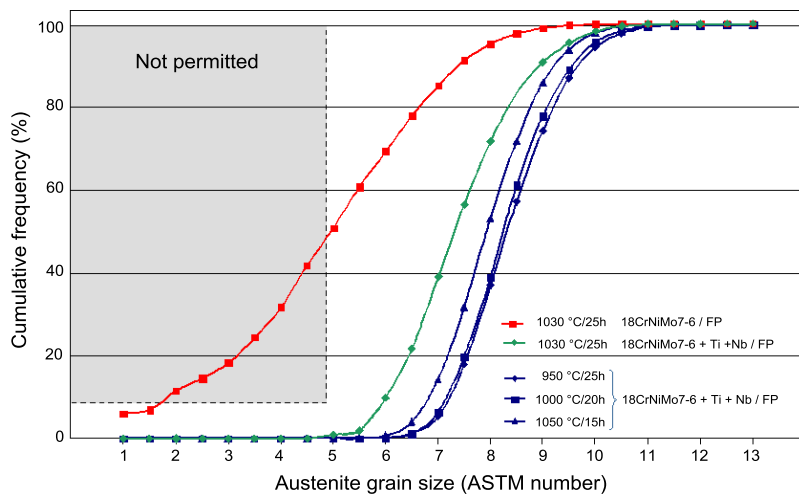


Figure 42. Prior austenite grain size distribution of steel 18CrNiMo7-6 and Nb-Ti microalloyed modifications after various case carburizing conditions.

Conclusions

This review has clearly demonstrated that microstructural refinement in martensite is predicted, based on theoretical considerations, to have considerable benefits with regard to relevant application properties. Experimental results and practical experience have confirmed this prediction in various aspects. Strength, fracture stress, as well as ductile-to-brittle transition temperature, can be improved by refining the microstructure. Furthermore, bendability, fatigue resistance and shape stability also benefit from a finer and more homogeneous microstructure. It was pointed out that these properties are not necessarily all related to the same microstructural feature, hence “effective” grain sizes have been defined. From a practical point of view, it is thought most relevant to refine the prior austenite grain size, which is essentially the limiting size for any substructural feature.

Various practical examples over a wide range of products have shown that niobium microalloying is the most powerful and versatile means of controlling the prior austenite grain size. Niobium can exert its grain refining effect in a passive and active way depending on the processing conditions. Synergies with other alloying elements, most notably molybdenum, boron and titanium, enhance the microstructure controlling effect of niobium.

Due to the very high yield strength of martensite, hydrogen embrittlement is a severe problem and it can lead to unexpected catastrophic failure. Microstructural refinement and hydrogen trapping were proven useful remedies to alleviate this problem. In this respect, niobium is beneficial due to its refining effect on precipitation producing nano-sized trapping particles. As hydrogen embrittlement is a boundary phenomenon, reinforcement of boundary cohesion is

another helpful tool. Solute molybdenum and also niobium have this beneficial effect. The same effect also combats embrittlement by impurity segregation to the grain boundaries.

Tempering of as-quenched martensite is an established method of balancing the requirements of ductility and strength. Molybdenum and niobium are amongst the most powerful alloying elements for promoting tempering resistance.

Molybdenum is not only one of the most powerful hardenability alloys but it also provides a high tempering resistance. Competing hardenability elements, such as manganese or boron can produce negative effects on other properties such as toughness. Furthermore, the use of these alternative hardenability alloys requires tighter process control in order to avoid enhanced property scatter.

Therefore, it may be concluded that alloying with niobium and molybdenum in martensitic steels offers great optimization potential, allowing safe and reliable performance of components subjected to the severe operating conditions in the mining and processing industry.

References

1. W. Leslie, *The Physical Metallurgy of Steels* (McGraw Hill, 1981), 216.
2. G.R. Speich, "Tempering of Low Carbon Martensite," *Trans. TMS-AIME*, 245 (1969), 2553-2564.
3. G. Krauss, *Steels Processing, Structure, and Performance*, Second Edition, (ASM International, 2015).
4. Z. Guo, C.S. Lee and J.W. Morris Jr, "On Coherent Transformations in Steel," *Acta Materialia*, 52 (19) (2004), 5511-5518.
5. C.C. Kinney et al., "The Microstructure of Lath Martensite in Quenched 9Ni Steel," *Acta Materialia*, 69 (2014), 372-385.
6. S. Morito et al., "The Morphology and Crystallography of Lath Martensite in Fe-C Alloys," *Acta Materialia*, 51 (6) (2003), 1789-1799.
7. T. Maki, K. Tsuzaki and I. Tamura, "The Morphology of the Strengthening of Lath Martensite in Steels," *Transactions of the Iron and Steel Institute of Japan*, 20 (1980), 207-215.
8. S. Morito et al., "Effect of Austenite Grain Size on the Morphology and Crystallography of Lath Martensite in Low Carbon Steels," *The Iron and Steel Institute of Japan International*, 45 (1) (2005), 91-94.
9. J.W. Morris Jr., C.S. Lee and Z. Guo, "The Nature and Consequences of Coherent Transformations in Steel," *The Iron and Steel Institute of Japan International*, 43 (3) (2003), 410-419.

10. L. Qi, A.G. Khachaturyan and J.W. Morris Jr., "The Microstructure of Dislocated Martensitic Steel: Theory," *Acta Materialia*, 76 (2014), 23-39.
11. M. Cohen, "The Strengthening of Steel," *Trans TMS-AIME*, 224 (1962), 638- 656.
12. M. Cohen, "On the Development of High Strength in Steel," *Journal of the Iron and Steel Institute*, 201 (10) (1963), 833-841.
13. Y. Tomita and K. Okabayashi, "Effect of Microstructure on Strength and Toughness of Heat-treated Low Alloy Structural Steels," *Metallurgical Transactions A*, 17 (7) (1986), 1203-1209.
14. C. Wang et al., "Effect of Microstructure Refinement on the Strength and Toughness of Low Alloy Martensitic Steel," *Journal of Materials Science and Technology*, 23 (5) (2007), 659.
15. S. Morito and T. Ohba, "Fundamentals of Martensite and Bainite toward Future Steels with High Performance," ed. by T. Furuhashi and K. Tsuzaki, *The Iron and Steel Institute of Japan International*, Tokyo, (2007), 57.
16. T. Ohmura et al., "Dislocation-grain Boundary Interactions in Martensitic Steel Observed Through in Situ Nanoindentation in a Transmission Electron Microscope," *Journal of Materials Research*, 19 (12) (2004), 3626-3632.
17. J.W. Morris, "On the Ductile-Brittle Transition in Lath Martensitic Steel," *The Iron and Steel Institute of Japan International*, 51 (10) (2011), 1569-1575.
18. Z. Guo, C.S. Lee and J.W. Morris Jr., "Grain Refinement for Exceptional Properties in High Strength Steel by Thermal Mechanisms and Martensitic Transformation," *Proceedings of the Workshop on New Generation Steel, Chinese Society for Metals*, Beijing, (2001), 48-54.
19. T. Ohmura and K. Tsuzaki, "Fundamentals of Martensite and Bainite toward Future Steels with High Performance," ed. by T. Furuhashi and K. Tsuzaki, *The Iron and Steel Institute of Japan International*, Tokyo, (2007), 35.
20. J.J. Irani, "Fracture of Martensite with Particular Reference to Ausformed Martensite," *Proceedings of Physical Properties of Martensite and Bainite*, Special Report 93, (The Iron and Steel Institute, 10-12th May 1965, Scarborough), 193.
21. J.P. Naylor and B. Blondeau, "The Respective Roles of the Packet Size and the Lath Width on Toughness," *Metallurgical Transactions A*, 7 (5) (1976), 891-894.
22. J.P. Naylor and P.R. Krabe, "Cleavage Planes in Lath Type Bainite and Martensite," *Metallurgical Transactions A*, 6 (3) (1975), 594-598.
23. J.W. Morris Jr. et al., "Microstructure and Cleavage in Lath Martensitic Steels," *Science and Technology of Advanced Materials*, 14 (1) (2013), 041208

24. C. Wang et al., "Effect of Microstructural Refinement on the Toughness of Low Carbon Martensitic Steel," *Scripta Materialia*, 58 (6) (2008), 492-495.
25. T. Hanamura, F. Yin and K. Nagai, "Ductile-Brittle Transition Temperature of Ultrafine Ferrite/Cementite Microstructure in a Low Carbon Steel Controlled by Effective Grain Size," *The Iron and Steel Institute of Japan International*, 44 (3) (2004), 610-617.
26. N. Ishikawa et al., "High-Performance Abrasion-Resistant Steel Plates with Excellent Low-Temperature Toughness," *Proceedings of the International Symposium on the Recent Developments in Plate Steels*, AIST (2011), 82-91.
27. S. Matsuda et al., "Toughness and Effective Grain Size in Heat-Treated Low-Alloy High-Strength Steels," *Proceedings of the International Symposium toward Improved Ductility and Toughness*, Climax Molybdenum Company, Kyoto, Japan, (1971), 45.
28. J.W. Morris Jr. et al., "The Limits of Strength and Toughness in Steel," *The Iron and Steel Institute of Japan International*, 41 (6) (2001), 599-611.
29. H. Asahi and M. Ueno, "Effect of Austenite Grain Size on Sulfide Stress Cracking Resistance of Low Alloy Martensitic Steels," *The Iron and Steel Institute of Japan International*, 32 (9) (1992), 1021-1026.
30. C.J. McMahon, "Effects of H on Plastic Flow and Fracture in Fe and Steel," *Hydrogen Effects in Metals*, ed. by I.M. Bernstein and A.W. Thompson, (Warrendale, PA: TMS, 1981), 219-234.
31. Y.H. Kim, "A Study of Hydrogen Embrittlement in Lath Martensitic Steels" (Ph.D. thesis, Department of Materials Science and Engineering, University of California, Berkeley, 1985).
32. Y.H. Kim and J.W. Morris Jr., "The Nature of Quasicleavage Fracture in Tempered 5.5Ni Steel After Hydrogen Charging," *Metallurgical Transactions A*, 14 (9) (1983), 1883-1888.
33. Y.H. Kim, H.J. Kim and J.W. Morris Jr., "The Influence of Precipitated Austenite on Hydrogen Embrittlement in 5.5Ni Steel," *Metallurgical Transactions A*, 17 (7) (1986), 1157-1164.
34. S. Yusa, T. Hara and K. Tsuzaki, "Grain Boundary Carbide Structure in Tempered Martensitic Steel with Serrated Prior Austenite Grain Boundaries," *Journal of the Japan Institute of Metals and Materials*, 64 (12) (2000), 1230-1238.
35. Y. Weng, W. Hui and H. Dong, "Workshop on the New Generation Steel-NG Steel '2001," The Chinese Society for Metals, Beijing, (2001), 62.
36. Y. Takeda and C.J. McMahon Jr., "Strain Controlled vs Stress Controlled Hydrogen Induced Fracture in a Quenched and Tempered Steel," *Metallurgical Transactions A*, 12 (7) (1981), 1255-1266.

37. S. Zhang et al., "Effect of Nb on Hydrogen-induced Delayed Fracture in High Strength Hot Stamping Steels," *Materials Science & Engineering A*, 626 (2015), 136-143.
38. S-J. Lee et al., "Hydrogen Embrittlement of Hardened Low-carbon Sheet Steel," *The Iron and Steel Institute of Japan International*, 50 (2) (2010), 294-301.
39. G. Krauss, "Heat Treated Martensitic Steels: Microstructural Systems for Advanced Manufacture," *The Iron and Steel Institute of Japan International*, 35 (4) (1995), No. 4, 349-359.
40. G. Krauss, "Verformung und Bruch Martensitischer Stähle," *Hart. Tech. Mitt.*, 46 (1991), 7.
41. S. Okamoto, D.K. Matlock and G. Krauss, "The Transition from Serrated to Non-serrated Flow in Low-carbon Martensite at 150 °C," *Scripta Metallurgica et Materialia*, 25 (1) (1991), 39-44.
42. A.R. Marder and G. Krauss, "The Formation of Low-Carbon Martensite in Fe-C Alloys," *Transactions of the American Society of Metals*, 62 (1969), 957.
43. G. Krauss, "High-Temperature Tempering: Defining Structure and Properties of Martensitic Derivative Microstructures," *Proceedings of the International Conference on Advances in Metallurgy of Long and Forged Products*, AIST (2015), 127-136.
44. R.N. Caron and G. Krauss, "The Tempering of Fe-C Lath Martensite," *Metallurgical Transactions*, 3 (9) (1972), 2381-2389.
45. F.B. Pickering, *High Strength, Low-Alloy Steels - A Decade of Progress, in Microalloying* 75, (New York, NY: Union Carbide Corporation, 1977), 9-30.
46. J.A. Straatmann and P.J. Grobner, *Molybdenum Containing Steels for Gas and Oil Industry Applications*, (Climax Molybdenum Company, 1978), 64.
47. F. Nakasato et al., "Development of Delayed Fracture Resistant High Strength Steel ADS-2," *The Sumitomo Search*, 37 (1988), 1.
48. R. Garber, "Higher Hardenability Low Alloy Steels for H₂S-Resistant Oil Country Tubulars," *Corrosion - NACE*, 39, (3) (1983), 83-91.
49. R.M. Horn and R.O. Ritchie, "Mechanisms of Tempered Martensite Embrittlement in Low Alloy Steels," *Metallurgical Transactions A*, 9 (8) (1978), 1039-1053.
50. J.M. Capus, "Austenite Grain Size and Temper Brittleness," *Journal of the Iron and Steel Institute*, 200 (1962), 922-927.
51. R.A. Grange, C.R. Hibral and L.F. Porter, "Hardness of Tempered Martensite in Carbon and Low-alloy Steels," *Metallurgical Transactions A*, 8 (11) (1977), 1775-1785.

52. R.A. Grange, "Estimating the Hardenability of Carbon Steels," *Metallurgical Transactions*, 4 (10) (1973), 2231-2244.
53. M.A. Grossman, "Hardenability Calculated From Chemical Composition," *Transactions of the American Institute of Mining, Metallurgical, and Petroleum Engineers*, 150 (1942), 227-259.
54. R.A. Grange and J.B. Mitchell, "On the Hardenability Effect of Boron in Steel," *Transactions of the ASM*, 53 (1961), 157-185.
55. M. Ueno and T. Inoue, "Distribution of Boron at Austenite Grain Boundaries and Bainitic Transformation in Low Carbon Steels," *Transactions of the Iron and Steel Institute of Japan International*, 13 (1973), 210-217.
56. S. Watanabe, H. Ohtani and T. Kunitake, "The Influence of Hot Rolling and Heat Treatments on the Distribution of Boron in Steel," *Transactions of the Iron and Steel Institute of Japan International*, 23 (1) (1983), 31-37.
57. R.V. Fostini and F.J. Schoen, "Effects of Carbon and Austenitic Grain Size on the Hardenability of Molybdenum Steels," *Symposium on Transformation and Hardenability in Steels*, (Climax Molybdenum Company, 1967), 195-209.
58. L. Cuddy and J. Raley, "Austenite Grain Coarsening in Microalloyed Steels," *Metallurgical Transactions A*, 14 (10) (1983), 1989-1995.
59. M.G. Akben, I. Weiss and J. Jonas, "Dynamic Precipitation and Solute Hardening in A V Microalloyed Steel and Two Nb Steels Containing High Levels of Mn," *Acta Metallurgica*, 29 (1) (1981), 111-121.
60. X. Wang and X. He, "Effect of Boron Addition on Structure and Properties of Low Carbon Bainitic Steels," *The Iron and Steel Institute of Japan International*, 42 (Suppl) (2002), S38-S46.
61. J. Cao, "Study on the Precipitation of Carbonitride in Nb-Mo-bearing Steel" (Dissertation, Kunming University of Science and Technology, 2006).
62. T. Tanaka and T. Enami, "Metallurgical Variables Involved in Controlled Rolling of High Tensile Steels and Its Application to Hot Strip," *Tetsu-to-Hagané*, 58 (13) (1972), 1775.
63. T. Hara et al., "Role of Combined Addition of Niobium and Boron and of Molybdenum and Boron on Hardenability in Low Carbon Steels," *The Iron and Steel Institute of Japan International*, 44 (8) (2004), 1431-1440.
64. A.J. Clarke et al., "Atomic and Nanoscale Chemical and Structural Changes in Quenched and Tempered 4340 Steel," *Acta Materialia*, 77 (2014), 17-24.

65. S.J. Tua et al., "Structural Changes Induced by High-Temperature Tempering of Martensitic Plate Steels and a Mechanism for the Recrystallization of Martensite," in *Fundamentals of Aging and Tempering in Bainitic and Martensitic Steel Products*, eds. G. Krauss and P.E. Repas, (Warrendale, PA: ISS, 1992), 53-66.
66. Ph. Maitrepierre et al., *Heat Treatment '76* (London, UK: The Metals Society, 1976), 177.
67. B. Aronsson, *Proceedings of Symposium on Steel-Strengthening Methods* (Zürich, Climax Molybdenum Company, 1969), 77-87.
68. S. Yamasaki and H.K.D.H. Bhadeshia, "Modelling and Characterisation of Mo₂C Precipitation and Cementite Dissolution During Tempering of Fe-C-Mo Martensitic Steel," *Materials Science and Technology*, 19 (6) (June 2003), 723-731.
69. T. Sato, T. Nishizawa and K. Tamaki, "Carbides in Molybdenum Steels," *Transactions of the Japan Institute of Metals*, 3 (4) (1962), 196-202.
70. W. Bentz, H. Kneider and H. Pircher, Vergütungs-sonderstähle hoher Festigkeitsstufe, Thyssen Technische Berichte, Heft 1/87 (1987), 57-66.
71. H. Erhart and H.J. Grabke, "Equilibrium Segregation of Phosphorus at Grain Boundaries of Fe-P, Fe-C-P, Fe-Cr-P, and Fe-Cr-C-P alloys," *Metal Science*, 15 (9) (1981), 401-408.
72. M.P. Sidey and J. Neutjens, "Cold Work Embrittlement of IF Steel" (European Commission Report EUR 18642 EN, 1998).
73. C.M. Liu et al., "Effect of Boron on the Grain Boundary Segregation of Phosphorus and Intergranular Fracture in High-purity Fe-0.2 Pct P-B Alloys," *Metallurgical Transactions A*, 23 (1) (1992), 263-269.
74. T. Urabe et al., "State-of-Art Nb-Bearing Cold-Rolled Steel Sheet for Automotive Application," *Proceedings of the International Symposium on Niobium Microalloyed Sheet Steel for Automotive Applications*, TMS, (2006), 409-425.
75. H.J. Grabke et al., "Effects of the Alloying Elements Ti, Nb, Mo and V on the Grain Boundary Segregation of P in Iron and Steels," *Surface and Interface Analysis*, 10 (4) (1987), 202-209.
76. W.T. Geng, A.J. Freeman and G.B. Olson, "Influence of Alloying Additions on Grain Boundary Cohesion of Transition Metals: First-principles Determination and Its Phenomenological Extension," *Physical Review B*, 63 (16) (2001), 165415.
77. E.J. Pavlina, J.G. Speer and C.J. Van Tyne, "Equilibrium Solubility Products of Molybdenum Carbide and Tungsten Carbide in Iron," *Scripta Materialia*, 66 (5) (2012), 243-246.

78. G.M. Pressouyre and I.M. Bernstein, "An Example of the Effect of Hydrogen Trapping on Hydrogen Embrittlement," *Metallurgical Transactions A*, 12 (5) (1981), 835-844.
79. H.J. Grabke, F. Gehrman and E. Riecke, "Hydrogen in Microalloyed Steel," *Steel Research*, 72 (5+6) (2001), 225-235.
80. A.J. Kumnick and H.H. Johnson, "Deep Trapping States for Hydrogen in Deformed Iron," *Acta Metallurgica*, 28 (1) (1980), 33-39.
81. W.M. Robertson and A.W. Thompson, "Permeation Measurements of Hydrogen Trapping in 1045 Steel," *Metallurgical Transactions A*, 11 (4) (1980), 553-557.
82. J.K. Tien et al., "Hydrogen Transport by Dislocations," *Metallurgical Transactions A*, 7 (6) (1976), 821-829.
83. M. Kurkela and R.M. Latanision, "The Effect of Plastic Deformation on the Transport of Hydrogen in Nickel," *Scripta Metallurgica*, 13 (10) (1979), 927-932.
84. J. Albrecht, I.M. Bernstein and A.W. Thompson, "Evidence for Dislocation Transport of Hydrogen in Aluminum," *Metallurgical Transactions A*, 13 (5) (1982), 811-820.
85. G.M. Pressouyre, "Trap Theory of Hydrogen Embrittlement," *Acta Metallurgica*, 28 (7) (1980), 895-911.
86. T. Asaoka et al., "Observation of Hydrogen Trapping in Fe-0.15 Wt% Ti Alloy by High Resolution Autoradiography," *Corrosion*, 34 (2) (1978), 39-47.
87. G.M. Pressouyre, "A Classification of Hydrogen Traps in Steel," *Metallurgical Transactions A*, 10 (10) (1979), 1571-1573.
88. H. Asahi, D. Hirakami and S. Yamasaki, "Hydrogen Trapping Behavior in Vanadium-added Steel," *The Iron and Steel Institute of Japan International*, 43 (4) (2003), 527-533.
89. T. Yokota and T. Shiraga, "Evaluation of Hydrogen Content Trapped by Vanadium Precipitates in a Steel," *The Iron and Steel Institute of Japan International*, 43 (4) (2003), 534-538.
90. F. Wei et al., "Hydrogen Trapping in Quenched and Tempered 0.42C-0.30Ti Steel Containing Bimodally Dispersed TiC Particles," *The Iron and Steel Institute of Japan International*, 43 (4) (2003), 539-547.
91. A. Ikeda, Y. Morita and N. Matsuki, "Recent Progress in Tubular Products for Oil and Gas Production," *The Sumitomo Search*, 37 (Nov 1988), 43-64.
92. K. Kobayashi et al., "Development of High Strength C110 Grade Steel and 13% Cr Stainless Steel for OCTG in Corrosive Wells" (Kawasaki Steel Technical Report, No. 19, 1988), 3.

93. N. Yoshihara et al., "Effects of Titanium and Vanadium on the Spring Corrosion Fatigue," *Transactions of Japan Society of Spring Engineers*, 2006, no. 51:1-7.
94. Y. Kurebayashi and A. Yoneguchi, "High Strength Spring Steel, 'ND120S'," *Denki Seiko*, 71 (1) (2000), 95-102.
95. F. Perrard et al., *Proceedings of Steels in Cars and Trucks 2008*, Verlag Stahleisen Düsseldorf (2008), 106.
96. ThyssenKrupp Steel Europe, XAR-Steels for Reliable Use and Long Service Life in Crushing and Screening Plants, Market Focus Crushers, (2005), Company Brochure.
97. S. Naimi and S.M. Hosseini, "Tool Steels in Die-Casting Utilization and Increased Mold Life," *Advances in Mechanical Engineering* (2014), Article ID 286071.
98. K. Hickmann et al., "Production and Properties of High-strength Nickel-alloy Steel Plate for Low Temperature Applications," *Proceedings of the 1st International Conference on Super-High Strength Steels*, Rome (2005), paper 95.
99. T. Kubo, A. Ohmori and O. Tanigawa, "Properties of High Toughness 9% Ni Heavy Section Steel Plate and its Applicability to 200000 kl LNG Storage Tanks" (Kawasaki Steel Technical Report, No. 40, 1999), 34-38.
100. H. Hoseiny et al., "The Effect of the Martensitic Packet Size on the Machinability of Modified AISI P20 Prehardened Mold Steel," *Journal of Materials Science*, 47 (8) (2012), 3613-3620.
101. H-S. Yang and H.K.D.H. Bhadeshia, "Austenite Grain Size and the Martensite-start Temperature," *Scripta Materialia*, 60 (7) (2009), 493-495.
102. I. Von Hagen and W. Bendick, "Creep Resistant Ferritic Steels for Power Plants," *Proceedings of the International Symposium Niobium 2001*, TMS (2001), 753.
103. C.P. Linne, F. Blanchard and F. Puissochet, *Proceedings of Corrosion '98*, NACE (1998), paper 117.
104. A. Kern and U. Schriever, "Niobium in Quenched and Tempered HSLA-Steels," *Proceedings of the Symposium - Recent Advances of Niobium Containing Materials in Europe*, 20th May, 2005, Dusseldorf, 30 Year Anniversary Event of Niobium Products Company.
105. VDA 238-100 (Test Specification), Editor: Verband der Automobilindustrie e.V. (VDA), www.vda.de (December 2010).
106. J. Bian et al., "Development of Niobium Alloyed Press Hardening Steel with Improved Properties for Crash Performance," *Advanced Materials Research*, 1063 (2014), 7-20.

107. B-M. Huang and J.R. Yang, private communication, February 2015.
108. H. Mohrbacher, *Proceedings of the International Symposium on the Recent Developments in Plate Steels*, AIST (2011), 169-179.
109. A.J. Kajjalainen et al., "Effect of Austenite Pancaking on the Microstructure, Texture, and Bendability of an Ultrahigh-Strength Strip Steel," *Metallurgical and Materials Transactions A*, 45 (3) (2014), 1273-1283.
110. G. Zhu and S.V. Subramanian, "Recrystallization Behavior Design for Controlling Grain Size in Strip Rolling Process," *Journal of Iron and Steel Research International*, 15 (1) (2008), 39-44.
111. A. Randak and R. Eberbach, "Einfluß der Austenitkorngröße auf einige Eigenschaften des Stahles 16MnCr5," *HTM Härterei-Technische Mitteilungen*, 24 (3) (1969), 201.
112. S. Hock et al., "Einfluß von Umform- und Wärmebehandlungsfolgen auf Korngröße und Schwingfestigkeit von einsatzgehärteten Bauteilen," *Härterei-Technische Mitteilungen* 54 (1) (1999), 45-54.
113. B. Huchtemann and V. Schüler, "Beitrag zur Beeinflussung der Austenitkorngröße von Edelbaustählen," *Thyssen Technische Berichte, Heft 1/93* (1993), 97-106.
114. T. Tanaka et al., "Austenite Grain Stability of Titanium-Modified Carburizing Steel," *Solid State Phenomena*, 118 (2006), 3-8.
115. K.A. Alogab et al., "The Influence of Niobium Microalloying on Austenite Grain Coarsening Behavior of Ti-modified SAE 8620 Steel," *The Iron and Steel Institute of Japan International*, 47 (2) (2007), 307-316.
116. K. Klenke et al., "Improved Performance by High Temperature Carburizing Shown by the Example of VW4521+Nb," *Proceedings of Steels in Cars and Truck 2008*, Verlag Stahleisen Düsseldorf, (2008), 173.
117. F. Hippenstiel, "Tailored Solutions in Microalloyed Engineering Steels for the Power Transmission Industry," *Materials Science Forum*, 539-543 (2007), 4131.

HIGH PERFORMANCE STEELS FOR WEAR APPLICATIONS

A. Dietrich, A. Canpolat, A. Kern and H-J. Tschersich

ThyssenKrupp Steel Europe AG, Heavy Plate Unit, Duisburg, Germany

Keywords: Wear Resistant, Niobium, Molybdenum, Wear-simulation

Abstract

One of the main problems across many industries is damage to, and possible failure of, components and products due to wear. The resulting financial losses even have a measurable impact on a country's economy. Looking at the mining and related industries, wear causes expensive downtimes and production losses. To minimize the effect of wear it is vitally important to choose the correct material for component manufacture and steel, as a very versatile material, plays the most significant role. New high performance steels for wear applications have been developed and improved over the years and are available with different hardness levels. The steels generally feature high hardness combined with satisfactory toughness and show good surface quality and homogeneity.

This paper presents an overview of the metallurgy behind the application of microalloying elements, especially Nb and Mo, in quenched or quenched and tempered wear resistant steels. The important role of Nb in controlling the austenite microstructure during rolling and heat treatment is discussed. Additionally, the remarkable improvements in toughness and brittle fracture resistance, due to a very fine microstructure and finely dispersed Nb-carbonitrides in a martensitic microstructure, are highlighted. The improvement in strength and toughness properties is demonstrated by comparison of Nb microalloyed steels with Nb-free steels.

The influence of Mo on the martensite start temperature and the start of transformation times, as well as the effect of forming high hardness, $(\text{Fe},\text{Mo})_3\text{C}$ is also discussed, in terms of both the hardness and through-hardening behaviour of the steel, as well as the wear behaviour. Results of mechanical testing and the newest developments are presented.

Modelling is often used to predict all the microstructural effects of microalloying elements, but modern steel development also uses modelling tools to predict the final steel properties. Other modelling tools are also available to support steel selection and to determine a suitable steel grade as a function of the wear stress. One of these tools is presented in this paper.

Introduction

One of the main problems in engineering is damage to, and possible failure of, components and products due to wear. The resulting financial losses even have a measurable impact on a country's economy. Notably in the mining and raw material handling industries, excessive wear causes high downtimes due to short maintenance cycles which hinder operation in an economically viable and sustainable manner.

Large-scale wear problems, for example, in dump truck bodies, shovels, buckets and crusher units, are caused by abrasive particles, gravel or even rocks which interact with the steel through different types of motion such as sliding, rolling and impact. As a result, the failure of the components can be mainly attributed to a combination of abrasive wear and surface fatigue. Due to this fact, one of the primary requirements of these industries is to improve abrasion resistance and thus enhance the durability of the components.

The right choice of material has a large impact in defining the best solution for increasing wear resistance. Steel is the most significant material in the field of wear resistance, however, cost effectiveness, processing properties, as well as wear characteristics, have to be taken into account when defining best solutions. Driven by the need for better products with enhanced durability, new high performance steels for wear applications have been developed and improved over the last few decades and are available over a large hardness range. These steel grades feature high hardness combined with good toughness and show a good surface quality, as well as a high level of homogeneity through the thickness of the product.

This paper presents an overview of the various ways in which microalloying additions, especially Nb and Mo, can be utilised in wear resistant steels.

Real experiments are still an essential element when it comes to predicting the effects of microalloying elements. However, modern steel development is increasingly supported by modelling tools to predict the steel properties. Further modelling tools are applied to determine a suitable steel grade as a function of the wear stress and assist in choosing the appropriate steel grade. One of these tools will be presented in this paper.

Production of Wear Resistant Steels

In order to fully satisfy the increasingly stringent demands of the market for wear resistant steels, it was essential that progress was made, not only in metallurgy, but also in rolling and heat treatment techniques. In the steel works of ThyssenKrupp Steel Europe (TKSE), steel is produced according to the Thyssen blowing-metallurgy (TBM) process. The liquid steel is stirred in this procedure by blowing gas through the converter bottom; thereby a better mixing of metal and slag is achieved. The TBM process produces lower contents of phosphorus and sulphur as well as a higher degree of purity, Figure 1(a). The ladle metallurgy, Figure 1(b), is similarly important as it reduces the demands on the converter process and allows very precise control of the targeted chemical composition, specifically in controlling the sulphur content to extremely low values. This low sulphur level produces a steel with a high level of purity; which is beneficial to toughness and reduces the risk of brittle fractures, and also produces a steel with a very low level of anisotropy in terms of toughness and deformation properties.

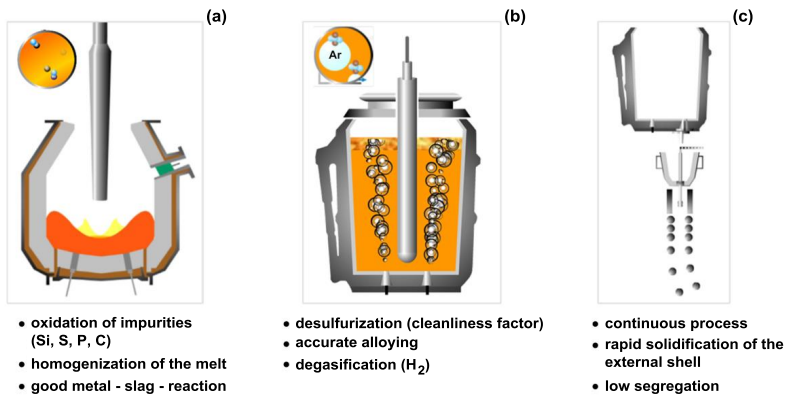


Figure 1. Steelmaking process; (a) steelmaking, (b) secondary metallurgy, (c) continuous casting.

The steels exhibit hardness values in the range 300 to 600 HB with adequate toughness properties. The steels are produced mainly by water-quenching and tempering. The steel plate is usually rolled and then re-austenitized and rapidly quenched in water in order to ensure transformation to a martensitic or bainitic microstructure. The plate can also be directly quenched after rolling (direct quenching).

The carbon content of the steel is important during rolling as this has a crucial influence on the hardness after quenching. In further studies, it was evident that the advantages of microalloying with Nb and B could be used for this group of steels. Nb has several positive effects on metallurgical mechanisms, which determine the properties of quenched and tempered steels, such as grain refinement, the retardation of transformation and precipitation hardening. A schematic assessment of the effects of Nb in comparison to other commonly used microalloying elements is given in Table I.

Table I. Schematic Assessment of the Positive and Negative Effects of Microalloying Elements

| Microalloy | Affinity to C, N | Fine precipitates | Retardation of transformation | Grain refinement |
|------------|------------------|-------------------|-------------------------------|------------------|
| Nb | ++ | + | +++ | +++ |
| V | + | ++ | o | o |
| Ti | +++ | +/- ¹⁾ | + | + |

+ positive effect
 - negative effect
 o no significant effect

¹⁾ depending on Ti-content

The addition of B, together with an adequate fixing of N, shifts the transformation of ferrite to longer times and thus increases the hardenability. The combined addition of Nb and Ti leads to an effective fixing of N which leaves the B free to have a maximum effect on hardenability.

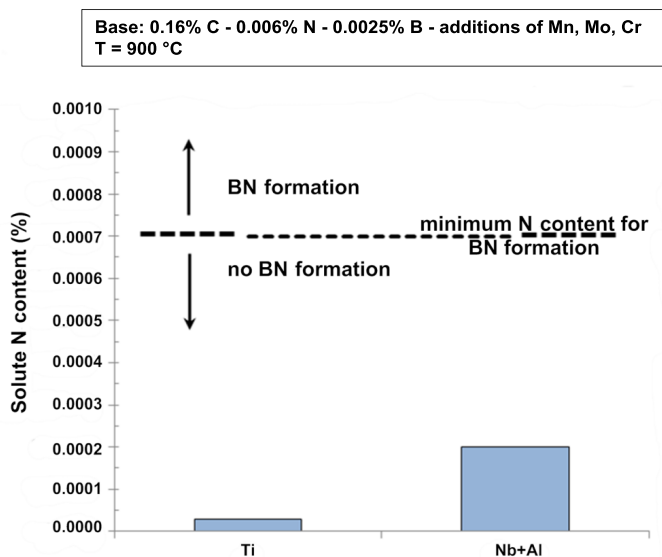


Figure 2. Solute N content depending on the used microalloying concept.

Figure 2 demonstrates that microalloying with Nb ($\leq 0.03\%$) in combination with increased Al levels up to 0.10% promotes both AlN and Nb(C,N) precipitation, but also results in a significantly higher content of free N at 900 °C than by Ti microalloying. However, it is significant that in the Nb plus Al steel the content of dissolved N is below the solubility limit for the undesired development of B nitrides. Therefore, like Ti, this microalloy combination can be used to protect B, but it also has the positive effect of avoiding the formation of coarse TiN precipitates which can be detrimental to toughness. In steelmaking a well controlled sequence of adding the microalloying elements into the liquid steel is necessary during the secondary metallurgy operation.

It is important to note that microalloying with Nb has practically the same effect as the addition of Ti. Additional analytical investigations of the extracted phases showed that about 90% of the entire B content exists in solid solution in the steel, and this is true when either Ti or Nb is used as the microalloy addition. However, due to the lower formation temperatures of the AlN and Nb(C,N) particles in the Nb microalloyed steel, a substantially finer particle dispersion exists compared to the TiN precipitates in the Ti microalloyed steels, with a correspondingly more favourable effect on the material properties, as shown in Figure 3.

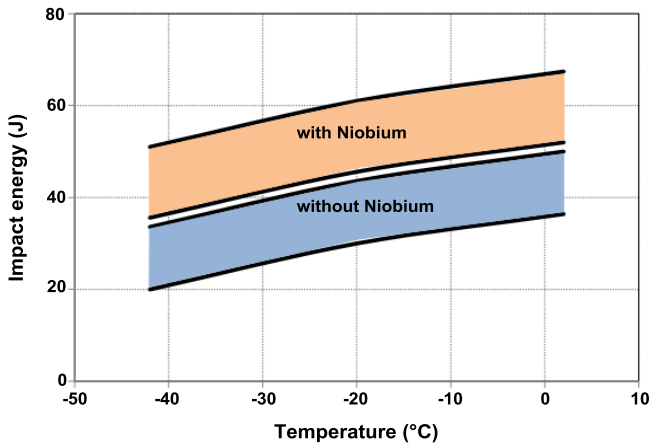


Figure 3. Effect of niobium on the Charpy impact toughness.

Microstructure

Hardness is a vitally important property for controlling the wear behaviour of the special structural steels and this is adjusted by control of the production process and selection of the appropriate chemical composition to produce the desired microstructure. The hardness is determined by the carbon content which remains dissolved in the martensitic matrix after the quench, however, the formation of a very small packet size of lath-like martensite of $<10\ \mu\text{m}$ is the basic precondition for optimum wear resistance. An important characteristic of lath martensite is the arrangement of the individual laths at various angles to each other, as shown in Figure 4(a) in a scanning electron microscope (SEM) image. Precipitated within this lath structure are fine carbides, which are found by analysis to be cementite $(\text{Fe,Mn,Cr,Mo})_3\text{C}$ or ultra-fine NbC particles, as shown in Figure 4(b). These carbides can contain up to 5% Mn, Cr and especially Mo. The addition of Mo in wear resistant steels is of great importance for attaining the required hardness and for the stability of the carbides. The carbides have a high hardness of $>1000\ \text{HV}$ and, owing to their volume fraction and extremely fine distribution, they not only contribute to the high hardness of the martensitic matrix, but are also a significant factor in ensuring high wear resistance, as they are responsible for additional strengthening of the microstructure which helps to prevent crack formation. The volume percentage of hard carbides and the martensite packet size can be controlled based on the steel composition, the rolling process and the heat treatment. Detailed microstructural investigations during the wear process for these steels are in progress.

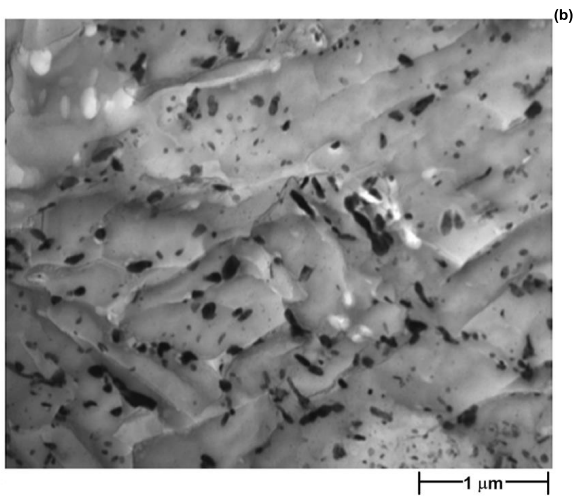
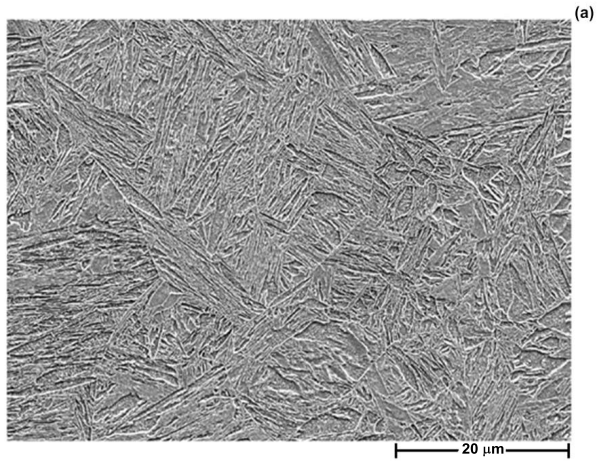


Figure 4. SEM images of the microstructure; (a) martensitic lath structure, (b) precipitated carbides.

Properties of Wear Resistant Steels

Wear resistant steels are well defined regarding their hardness. Table II provides an overview of wear resistant special structural steel plates, including delivery condition, hardness and typical CET range. In plate thicknesses up to 100 mm, the characteristic alloying elements of the steels are Mn, Cr, Mo and Ni at a C content up to 0.38% combined with microalloying elements like Nb.

Table II. Wear Resistant Steels and Properties

| Steel grade | Delivery condition | Hardness [HBW] | Thickness [mm] | Typical CET range | Special features | | |
|-------------|--------------------|----------------|----------------|-------------------|--------------------------|---------------------|-----------------------------|
| | | | | | Guaranteed core hardness | Min. CVN properties | Others |
| XAR® 300 | N | 270 - 340 | 4 - 50 | 0.38 – 0.43 | | | |
| XAR® 400 | Q(+T) | 370 - 430 | 4 - 100 | 0.26 – 0.38 | ✓ | ✓ | |
| XAR® 450 | Q(+T) | 420 - 480 | 4 - 100 | 0.30 – 0.43 | ✓ | ✓ | |
| XAR® 500 | Q(+T) | 470 - 530 | 4 - 100 | 0.39 – 0.46 | ✓ | | |
| XAR® 600 | Q(+T) | 550 - 630 | 5 - 50 | 0.52 – 0.56 | | | |
| XAR® HT | Q+T | 310 - 370 | 40 - 100 | 0.37 – 0.39 | | ✓ | |
| XAR® 400W | Q+T | 360 - 430 | 4 - 40 | 0.39 – 0.42 | | | Heat resistant up to 400 °C |

N - Normalised

Q(+T) – Quenched or Quenched and tempered depending on thickness and required properties

Q+T – Quenched and Tempered

CET – Carbon Equivalent

CVN – Charpy V notch toughness

HBW – Brinell Hardness

Influence of Alloying Elements on Through-thickness Hardness of the Plate

The hardness of the plate in the near-surface area is important, but the through-hardening properties of the steel also need to be considered. The through-hardening behaviour of the steel depends mainly on the alloy content and on the retardation of the diffusion-controlled transformations. Through-thickness hardenability depends to a lesser extent on the quenching intensity, especially in the case of very thick plates where the heat dissipation from the plate core is controlled exclusively by thermal conduction. Therefore, the more transformation-resistant the steel is owing to its chemical composition, the more likely is complete through-thickness hardening of the steel.

Mo, together with other elements such as Ni, plays an important role in allowing longer cooling times, whilst still achieving the desired core microstructure and thus boosting the achievable hardness in the core of the plate. Additionally, Mo promotes the fine grained structure of the steels and increases the yield strength.

Increased through-thickness hardenability improves the wear resistance significantly, especially in the case of abrasive wear and in applications leading to wearing out of the plate over the thickness of the cross-section. Investigations have shown that comparisons of two plates with nominally the same surface hardness, but with different core hardness profiles, show lifetime differences equal to or greater than 10%.

Mo, as with other elements such as Ni, is expensive and therefore, it is a basic necessity to be aware of the advantages of Mo alloyed steels with regard to the intended application. Through-hardened steels alloyed with Mo not only offer longer component lifetimes due to higher wear resistance as the plate becomes thinner due to wear but also reduce very expensive downtimes. Bearing in mind these important positive aspects, the higher costs of the material are quickly offset.

Wear Behaviour of Wear Resistant Steel Grades

In the most important applications for wear resistant steels, the characteristic wear type is ploughing leading to abrasive wear. Thereby, usually the plate surface gets scratched when exposed to an abrasive material, such as sand or other minerals and is finally removed - this wear mechanism is called abrasion.

A high material hardness is one important factor for promoting good wear resistance. Furthermore, a high material toughness improves the wear resistance and thus reduces the material loss by changing the wear mechanism from micro-ploughing to micro-machining.

Prior to looking at wear applications using wear resistant plates, it is advantageous to first have a look at the wear mechanism. In describing the mechanism, the tribological system is important. It is made up of different components - the base body, the counter body, ambient media, as well as structural conditions. To understand the wear process, not only one or two components are important: the whole system is relevant for each individual application.

The wear mechanism itself can be characterized by three zones: a lower shelf with low wear rates, an upper shelf with high wear rates and the associated transitional range, Figure 5. The key factor to describe abrasive wear is the hardness relationship, H_p , between the interacting wear components. If the hardness of the counter material is low in relation to the hardness of the plate, comparatively low wear occurs and the actual hardness of the plate does not make much difference and only becomes significant in the long term. With a similar or even higher hardness of the counter material compared to the plate, wear rates increase dramatically and even small differences in the hardness relationship may play an important role for controlling the lifetime of the plate. In the mining industry, for example, almost all wear applications will be found in the transitional or upper shelf zone because the abrasive's hardness is usually close to or higher than the hardness of the plate.

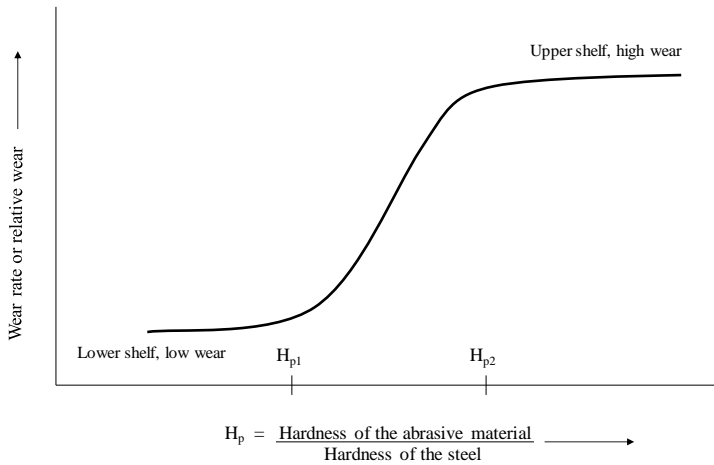


Figure 5. Schematic characterization of the wear mechanism.

From this point of view it becomes clear that hardness variations within the plate, especially from surface to core, can influence the wear resistance and thus the lifetime of the component. Different core hardness values will influence the lifetime of the component, such that as wear takes place and exposes new material, if the core hardness is higher then the increase in wear rate will be minimized and the lifetime of the component prolonged compared to a plate with a low core hardness.

Lifetime Estimation

To take the aspects described above into account, TKSE has developed a new calculation model, based on field and laboratory test results, for estimating wear behaviour and calculating the benefits to lifetime of a through-hardened plate manufactured at slightly higher costs compared to a non-through-hardened plate. A calculated example is given in the following section for plates with equal surface hardness but different core hardness profiles.

The surface hardness of both plates was 525 HV (~ 500 HB), while steel A has a core hardness of 450 HV and steel B has a core hardness of 495 HV, as shown in Figure 6. The starting thickness of the plates is taken as 90 mm and the replacement thickness of the plate shall be 15 mm. Sand with a hardness of around 750 HV has been selected as the abrasive material. By using the plate until a 15 mm residual thickness, the lifetime of the more through-thickness hardened plate B exceeds the less through-thickness hardened plate A by ~ 13%, Figure 7 - a remarkable lifetime difference and an important factor when looking at maintenance, downtimes and production loss.

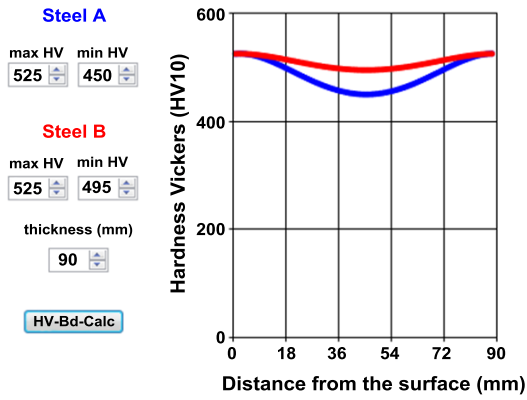


Figure 6. Specified plate hardness.

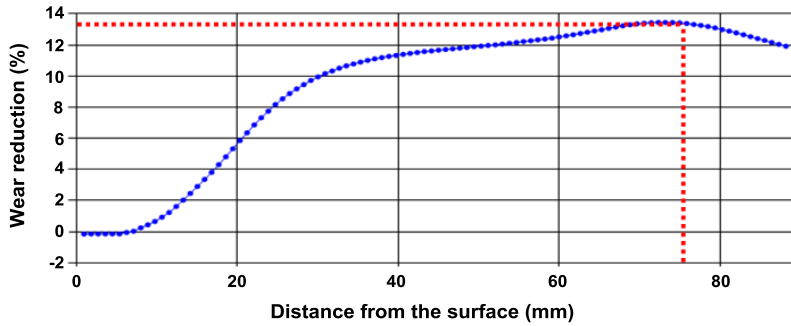


Figure 7. Resulting wear increase/decrease.

Field Test in a Semi-autogenous Grinding Mill (SAG Mill)

In order to verify the positive effects of the Nb-microalloying concept on the wear behaviour as compared to Nb-free steel grades, comparative field tests in a SAG-Mill have been carried out.

SAG-mills are used in raw materials processing to reduce the size of ore by impact and abrasion. Lifting bars carry larger rocks and grinding balls to the side of the mill whereupon they drop down on to the feed. As a consequence, the ore is reduced in size. However, depending on the mills' operating parameters (ball charge, ore charge, temperature, etc.) lifting bars are heavily exposed to abrasion and impact wear. The lifetime of lifting bars greatly affects the overall mill performance; thus manufacturers, as well as operators, aim to maximize the durability of the former by choosing material with high impact and abrasive wear resistance.

In this field test, four test bars, two of them XAR[®] 500, the others a competitor's material (Nb-free), offering the same hardness level of 500 HB, were installed in the middle ring of the shell of a SAG-mill which was operating in Canada. After 3,306 hours of operation and a material throughput of more than 935,000 tons, the bars were removed and the worn-off areas on the cross sections were measured. Figure 8 presents the results of the contour measurements. The XAR[®] 500 plate had lost 151.00 cm² on the cross section versus 153.86 cm² from the competing material, accounting for a difference of 1.9% on total wear. Even though the difference in wear appears to be very low, it should be noted that the hardness values of both tested materials are at the same level of 500 HB. The only difference was the different microalloying concept.

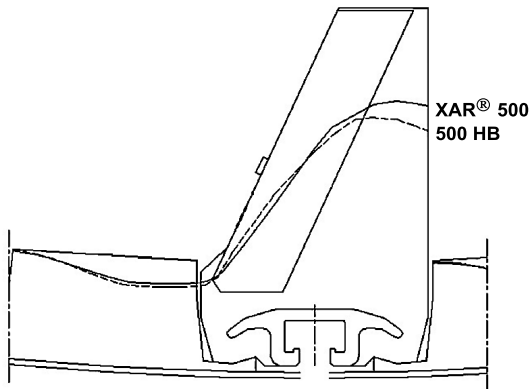


Figure 8. Cross section of lifting bars (initial and after operation).

As a result, the field test in the SAG-Mill verified the positive effect of a Nb-microalloyed concept on the wear behaviour. In this context, considering the lifetime of a lifting bar and the downtimes caused by the exchange of these components, any service time extension leads to an economic benefit.

Processing Properties of Wear Resistant Steel Grades

While mechanical properties such as high hardness and toughness levels are essential to improve the wear characteristics of wear resistant steel grades, providing suitable processing properties (weldability, cutting, formability, etc.) are often equally important for the manufacturer of wear resistant components or products. A certain minimum carbon content is vital to achieve the desired hardness levels in wear resistant grades. However, an increasing carbon content also leads to the necessity for preheating prior to welding or cutting, which has to be carried out to reduce the risk of cold cracking and excessive hardening of the cut edge or weld seam.

Thermal cutting and welding operations are sometimes conducted on-site, for example, in surface mining, limiting the availability of the appropriate processing conditions. One of the main objectives in the development of wear resistant steel grades was to optimize the chemical compositions of these grades by reducing the alloying content and consequently the carbon equivalent. Table II provides an overview of the typical carbon equivalent ranges of wear resistant steel grades produced by the Heavy Plate Unit of ThyssenKrupp Steel Europe. Table III shows the recommended preheating temperatures to minimize the risk of cold cracks during thermal cutting, as an example. Preheating is generally necessary for CET values over 0.32% or for increasing plate thicknesses. Recent developments in the production of wear resistant steel grades have enabled the use of lower CET values; thus facilitating welding/cutting with reduced or even without preheating for higher plate thicknesses. As a result, manufacturers are able to make significant savings in terms of costs and processing times.

Table III. Preheat Temperatures for Flame Cutting of Wear Resistant Steel Grades

| Steel grade | Plate thickness (mm) | | | | | | | | | | | | | | | |
|-------------|----------------------|--------|-----|--------|-----|--------|--------|--------|--------|--------|-----|-----|-----|-----|-----|---------------|
| | ≤5 | ≤10 | ≤15 | ≤20 | ≤25 | ≤30 | ≤35 | ≤40 | ≤45 | ≤50 | ≤55 | ≤60 | ≤65 | ≤70 | >70 | |
| XAR® 300 | | | | - | | | | 75 °C | 100 °C | | | | | | | Not available |
| XAR® 400 | | | | | | - | | | | | | | | | | 75 °C |
| XAR® 450 | | | | - | | | | 75 °C | | 100 °C | | | | | | 125 °C |
| XAR® 500 | | | - | | | | 100 °C | | | 125 °C | | | | | | 150 °C |
| XAR® 600 | - | 100 °C | | 150 °C | | 175 °C | | 200 °C | | | | | | | | |

Outlook and Further Developments

For further developments, a more detailed knowledge regarding dependencies between steel properties and wear behaviour is increasingly important. Methods for mathematical modelling of the wear behaviour of wear resistant structural steels as a function of the material properties and the environment are advantageous in supporting the selection of materials for wear applications. The development of mathematical models for computational estimation of the wear behaviour of XAR steels in relation to material and counter-material properties is therefore the subject of current research. Initial model developments have since found their way into practice like the aforementioned tool to consider through-thickness hardness of the wear plates.

To improve the wear resistance further, the use of multi-layer steels consisting of high-hardness outer layers and a softer more flexible inner layer can be considered. The wear resistant steel grade TriWEAR[®], Figure 9, combines both high wear resistance and good toughness and therefore improves the lifetime of components such as screen bars or hammer crushers with resulting significant economic benefit.



Figure 9. Multi-layer wear resistant steel.

Conclusions

Modern wear resistant steels with surface hardness levels up to 600 HB widely use alloying elements C, Mn, Cr and Ni, supplemented by additions of Mo and especially Nb. Mo helps to improve the hardenability of the steels, especially in thicker sections, and Nb significantly improves the toughness by facilitating the control of the austenite structure and the final martensitic microstructure.

To judge the benefits and to find the best possible alloy for an individual wear application, TKSE has developed a calculation tool, based on field and laboratory tests, with which it is possible to rate the technical benefits of high priced alloying elements against the cost factor.

A field test involving lifting bars in a SAG-Mill verified the positive effect of a Nb-microalloyed concept on the wear behaviour.

Hardness and toughness are the two basic demands of a wear resistant steel, however it is difficult to improve both of these properties, as generally improving one of them has a deleterious effect on the other. New developments involving multi-layer steels combining a tough inner layer with very hard outer layers are the subject of current research and one such wear resistant steel grade, TriWEAR[®], is showing very promising initial results. More detailed results will be shown in the future.

THE ROLE OF NIOBIUM FOR THE DEVELOPMENT OF WEAR RESISTANT STEELS WITH SUPERIOR TOUGHNESS

A.S. Schneider, J.L. Cayla, C. Just and V. Schwinn

AG der Dillinger Hüttenwerke, Research, Development and Plate-Design,
P.O. Box 1580, 66748 Dillingen/Saar, Germany

Keywords: Niobium, Direct Quenching, Wear Resistant Steel, Recrystallization, Strength, Plate, Charpy Toughness, Finish Rolling Temperature, Hardness, EBSD, Microstructure, Grain Size

Abstract

Wear resistant steels are commonly designed to have a high hardness and at the same time good weldability due to a low alloy content. The high hardness is achieved by quenching the material to a martensitic microstructure, which requires systematic alloying with Mn, Cr, Ni and Mo. However, even for wear resistant steels, a high toughness may be advantageous, as it not only ensures good impact resistance, even at sub-zero temperatures, but can enhance the wear resistance by causing a change in the wear mechanism. Besides a high level of process-based steel cleanliness, microalloying with Nb provides the basis to enhance the toughness of the steel. The objective of this paper is to present a selected study of how microalloying with Nb in combination with a well-adapted process route can be used to obtain wear resistant steels with a superior balance of toughness and hardness.

Introduction

Based on their high hardness and low-to-medium C content, wear resistant steels exhibit an optimum combination of wear performance and workability. Typically, wear resistant steels are available with hardness levels varying from 300 to 600 HB and are used in the form of heavy plates or hot rolled strip. The high hardness in these steels is realized by a quenching treatment leading to a fully martensitic microstructure. To obtain a uniform martensitic structure or hardness across the entire plate thickness, within achievable quenching rates, the steel has to be alloyed with carbon and other elements, such as Mn, Cr, Ni and Mo. The quenching treatment can be either carried out off-line, via the conventional reheating and quenching (RQ) route or achieved by direct quenching (DQ) after hot rolling using in-line water cooling units.

The DQ process has several advantages over the RQ process. For example, the production costs and time can be significantly reduced by eliminating the additional reheating and cooling step. Furthermore, direct quenching immediately after the hot rolling allows for some control of the austenite structure prior to transformation. It is well known that the deformation of austenite refines the post-transformation products causing an increase of strength and toughness [1-5]. In addition, due to the higher austenitization temperature relative to the RQ process, even microalloying elements such as Nb can be dissolved in the DQ process, which results in a higher hardenability [4]. Accordingly, the desired mechanical properties can be achieved with a leaner chemistry and the content of costly alloying elements can be reduced in steels produced via

direct quenching. Additionally, the reduction of the alloying elements is beneficial for the weldability and the formability of the steel.

The structure of the austenite in the DQ process and thus the mechanical properties strongly depend on the specific hot rolling parameters. The most critical parameter in this respect is the finish rolling temperature (FRT). If the finish rolling temperature is significantly above the non-recrystallization temperature (T_{nr}), a fully recrystallized austenite structure is obtained. This process is also referred to as hot rolling (HR). In contrast, if the rolling is performed at a lower temperature, only slightly above T_{nr} , grain growth is limited. Therefore, this process, referred to as recrystallized-controlled rolling (RCR), results in an austenite structure with fine and equiaxed grains. Nevertheless, because rolling is completed close to T_{nr} , a deformation substructure could be present in the steel. In the case of controlled rolling (CR), the FRT is lower than T_{nr} . As a consequence, the austenite grains are work hardened and elongated in the rolling direction. In the literature this structure is termed as a pancake microstructure.

Previous studies have shown that CR-DQ leads to a superior balance of strength and toughness compared to HR-DQ and RQ [3,5]. However, this is only true for steels with relatively large amounts of alloying elements, in which martensite formation occurs upon cooling despite the fine and heavily deformed austenite structure. The high strength in these steels is attributed to the refined post-transformation microstructure and the inheritance of the austenite deformation substructure in the martensitic phase, ie. the ausforming effect [4]. The improvement of toughness can also be explained by the refinement of the martensitic structure [4]. Furthermore, it has been suggested that the superior toughness is related to a crystallographic texture developed in the austenite prior to quenching, which can lead to delaminations or splitting in the Charpy specimens [2,3]. This has the beneficial effect of reducing the triaxial stress state at the crack tip and accordingly shifts the Charpy impact toughness transition temperature to lower values [6].

So far, only a few studies have investigated the effect of the CR-DQ process on the properties of wear resistant steels. To avoid the low ductility problems associated with fully martensitic microstructures in wear resistant steels with overall hardness levels above 500 HB, Kinnunen et al. performed rolling experiments using direct quenching from different final rolling temperatures [7]. The purpose of this study was to increase the toughness of the martensitic structure by incorporating a small amount of soft ferrite. However, their results indicated that the steel containing martensite and ferrite had a poorer abrasion resistance than the fully martensitic reference steel, which was attributed to the decrease in hardness with increasing ferrite content. Song et al. studied the microstructure and mechanical properties of a wear resistant steel with a C content of 0.17 wt.% produced via DQ and conventional RQ [8,9]. For a quenching temperature of 950 °C, in both processes, they observed superior mechanical properties for the DQ process compared to the RQ process. However, the hardly elongated grains visible in their optical micrographs indicate that rolling was completed at a temperature only marginally below T_{nr} .

Although these studies demonstrate the potential of the CR-DQ process, in both cases the rolling parameters were not chosen to optimize strength and toughness. In addition, as in most other studies on direct quenching, rolling and quenching were performed on a laboratory scale using plates with a length of not more than 1-2 m. Therefore, we investigated the influence of CR-DQ on the mechanical properties of wear resistant steel plates produced on a full-scale plate mill with lengths of several tens of meters. The uniformity of properties was assessed by testing the head and tail positions of each plate. To increase strength and toughness, FRTs significantly below T_{nr} were evaluated.

Experimental

In this study, three continuously cast slabs with an initial thickness of 290 mm were rolled to a final thickness of 20 mm and direct quenched to room temperature using a Mulpic cooling device. Depending on the exact dimensions of the slabs, these plates had lengths varying from 22-28 m in the rolled condition.

The chemical composition of the steel is given in Table I. The basic heat contains approximately 0.15 wt.%C, 0.3 wt.%Si, 1.3 wt.%Mn and a small amount of Mo. In addition, the steel was microalloyed with Nb for austenite grain size control during processing. Nb is also crucial for the CR-DQ process, as it increases the T_{nr} and thus enables rolling in a temperature interval between Ar_3 and T_{nr} .

Table I. Chemical Composition of the Investigated Steel

| Element | C | Si | Mn | Additional alloys |
|---------|-------|-----|-----|-------------------|
| wt.% | <0.15 | 0.3 | 1.3 | Mo, Nb |

Before rolling, the slabs were reheated at 1200 °C for several hours in a pusher furnace. The rolling included roughing passes at a high temperature to a constant intermediate thickness, a hold time in air and a final series of passes in a predefined temperature range close to the designated FRT. During hot rolling, the condition of the austenite was varied by applying three different FRTs with respect to the T_{nr} . The T_{nr} of the steel was calculated to be approximately 950 °C according to the equation developed by Boratto et al. [10]. To realize a fully recrystallized austenite structure before quenching, one plate was finish rolled at a temperature above the theoretical T_{nr} . This procedure will hereafter be referred to as hot rolling. In addition, two plates were controlled rolled at temperatures below T_{nr} . While for one of these plates rolling was completed only a few degrees below T_{nr} ($FRT < T_{nr}$), for the other plate the FRT was significantly below T_{nr} ($FRT \ll T_{nr}$).

The structure of the samples was examined by light optical microscopy and electron backscattered diffraction (EBSD). The metallographic samples were taken from both ends (head and tail) of each plate with the investigated cross-section parallel to the rolling direction. All samples were mechanically ground and polished by a conventional metallographic procedure. For the microstructural characterization in the optical microscope, the polished samples were etched in a 5% nital solution, while specimens for EBSD were electropolished using a Struers

electrolyte. The EBSD patterns were collected in a scanning electron microscope (Zeiss Supra VP 55) at an acceleration voltage of 25 kV and a working distance of 15 mm. The parent austenite grain structure was automatically reconstructed from the EBSD data by applying the ARPGE software [11]. This software uses an algorithm based on the general crystallographic relationship between martensite/bainite to determine which orientations are directly inherited from a unique parent grain (austenite).

Mechanical tests included measurements of hardness, tensile properties and impact toughness. As for the microstructural characterization, these tests were performed on samples taken from the head and the tail positions of each plate. For the tensile tests, full thickness flat tensile specimens were used and tested in accordance with the ISO 6892-1 specification. Charpy impact tests were conducted using standard V-notch samples as per the ISO 148-1 specification. The Charpy specimens with a cross-section of 10 x 10 mm were machined 2 mm beneath the surface in both the longitudinal and transverse directions of the 20 mm thick plates. The Charpy V-notch impact energy was determined at the following temperatures: -100 °C, -80 °C, -60 °C, -40 °C, -20 °C and 0 °C.

To assess the hardenability of the alloy for the applied rolling conditions, Vickers hardness profiles were determined across the thickness of the plates. The indents were performed with a maximum load of 100 N and a step size of 2 mm.

Results

Figure 1 shows representative engineering stress-strain curves of samples taken from both ends of the plates finish rolled at different temperatures with respect to T_{nr} . In all cases, the plates exhibit a similar stress-strain behavior at the head and the tail positions as well as a continuous transition from elastic to plastic deformation. Depending on FRT, the ultimate tensile strength of the plates is in the range of 1200-1350 MPa and the strain to failure varies between 7.7% and 8.9%. The highest ultimate tensile strength, but also a slightly smaller strain to failure than for the other two plates is observed for the plate finish rolled at the lowest temperature. Despite different FRTs, the other two plates, finish rolled at the intermediate and at the highest temperature, demonstrate similar ultimate strength and strain to failure values.

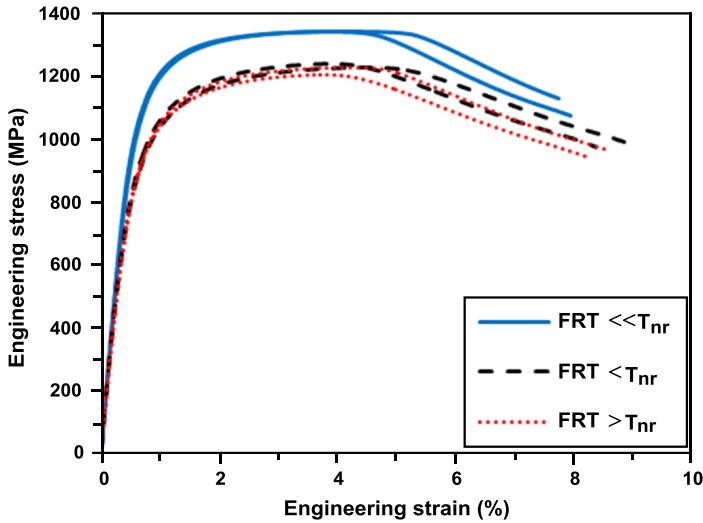


Figure 1. Representative engineering stress-strain curves of samples taken from the head and the tail positions of the plates finish rolled at different temperatures with respect to T_{nr} . For each plate, one curve is shown for the head and one for the tail position.

Charpy V-notch transition curves for samples oriented in the longitudinal and the transverse direction of the three plates are shown in Figure 2. Each data point in the plot represents the mean value of six individual Charpy V-notch tests performed on three samples from the head and three from the tail position of each plate. The small standard deviation represented by the error bars indicates that the measured impact energy is not significantly affected by the sample position, i.e. is almost the same at both ends of the plates. However, it can be seen that the impact energy strongly depends on FRT and sample direction. For samples oriented in the transverse and the longitudinal direction, the impact energy increases with decreasing FRT. This is true for the entire range of test temperatures except at a test temperature of $0\text{ }^{\circ}\text{C}$, for which the plates finish rolled at temperatures close to T_{nr} exhibit virtually the same impact energy.

A comparison between Figures 2(a) and (b) further indicates that the longitudinal sample direction leads to higher impact energies than the transverse direction. However, this effect is only pronounced for the plate with the lowest FRT. For example, at a test temperature of $0\text{ }^{\circ}\text{C}$, the impact energy of this plate measured in the longitudinal directions is a factor of two larger than that measured in the transverse direction. In contrast, for the other two plates, the impact energy for both directions differs by only a few Joules.

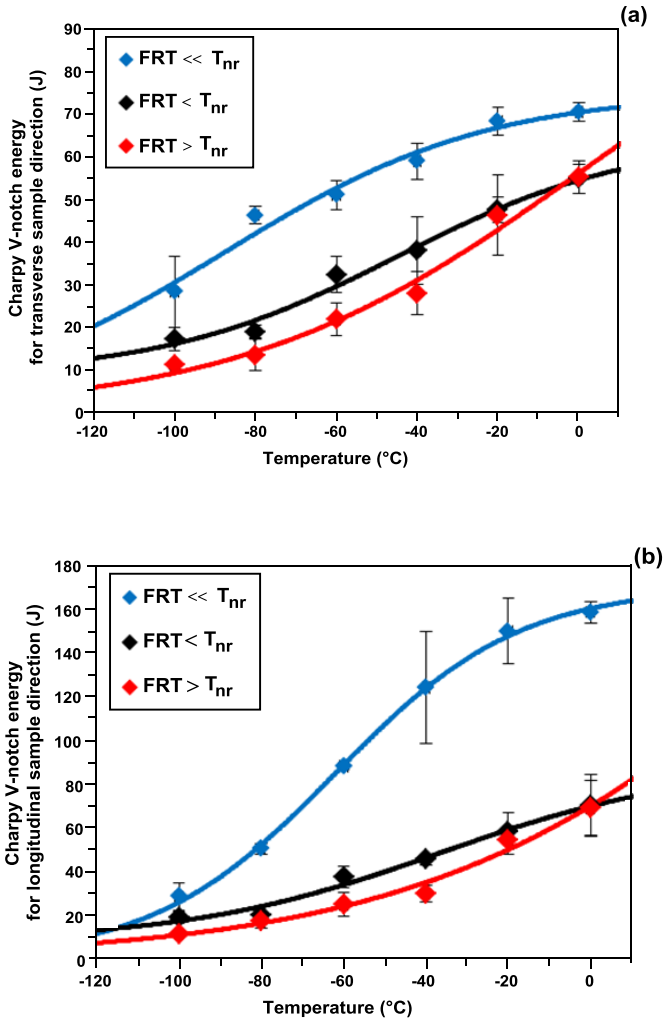


Figure 2. Charpy V-notch transition temperature curves for samples taken in the transverse (a) and in the longitudinal (b) directions of the three plates finish rolled at temperatures above and below T_{nr} . In the interest of clarity, each data point in the plot represents the mean value of six Charpy V-notch tests performed on three samples from the head and three from the tail position of each plate. The error bars represent one standard deviation.

In Figure 3, the single values of the Charpy V-notch energy measured at $-40\text{ }^{\circ}\text{C}$ in the transverse direction are plotted as a function of the proof stress, $R_{p0.2}$. From this plot it can be deduced that the best combination of strength and toughness is obtained for the plate finish rolled at the lowest temperature. With a proof stress of more than 1100 MPa this plate demonstrates impact energies in the range of $50\text{--}70\text{ J}$ at $-40\text{ }^{\circ}\text{C}$ for the transverse orientation. For the other two FRTs, lower proof stress and impact toughness values are observed. However, it is interesting to note that these plates show a very similar combination of strength and toughness despite different FRTs.

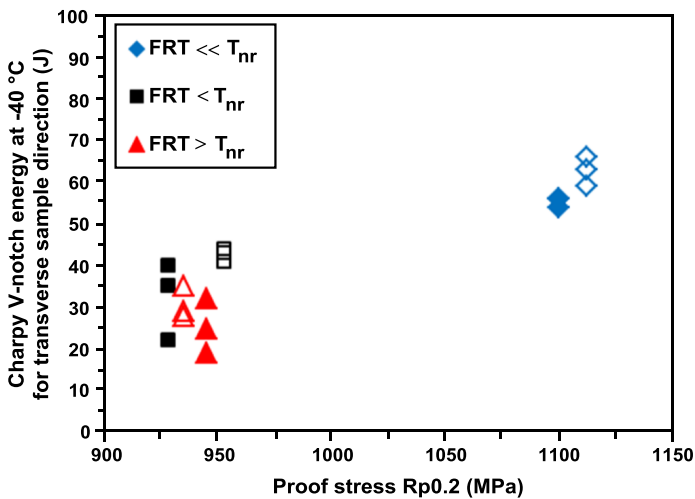


Figure 3. Single values of the Charpy V-notch impact energy measured at $-40\text{ }^{\circ}\text{C}$ for the transverse direction as a function of the proof stress $R_{p0.2}$. Filled symbols represent the head position and open symbols the tail position of the plates.

To examine the effect of FRT on the hardenability of the plates, Vickers hardness profiles measured at the head and tail plate positions are plotted in Figure 4. For all three plates, the hardness is relatively constant across the through-thickness direction and in the region of $400\text{ HV }10$, as expected for a martensitic steel with a C content of approximately 0.15% . The plate finish rolled at the lowest temperature displays higher hardness values than the other two plates. Furthermore, it can be seen that the hardness profiles at the head and the tail positions are very similar. For example, for the plate with the intermediate FRT, the mean hardness at both ends differ by less than $6\text{ HV }10$.

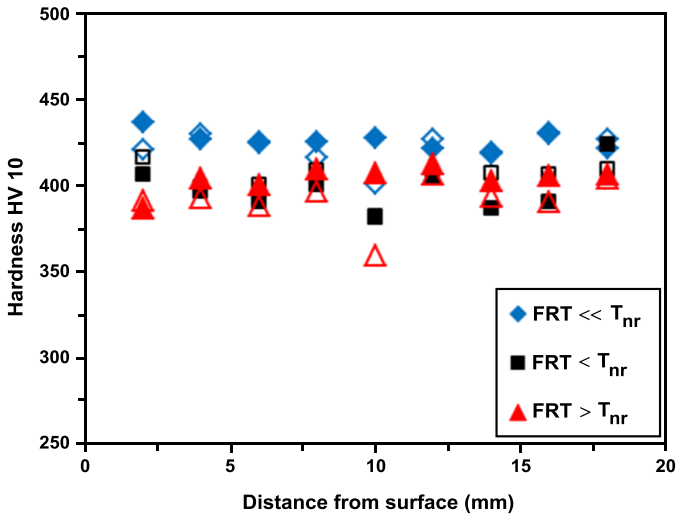


Figure 4. Vickers hardness profiles. Filled symbols represent the head position and open symbols the tail position of the plates.

Noticeable differences in the microstructure are observed depending on the FRT. This is highlighted in Figure 5, which shows optical micrographs of the surface, the quarter and the mid-thickness positions of the three plates. As the same microstructure was observed at both ends of the plates, only micrographs originating from the tail positions are presented. A relatively uniform microstructure, consisting of martensite and bainite, is visible for all plates throughout the plate thickness. Although not quantified, it seems that the bainite content increases slightly with decreasing FRT. A comparison of the micrographs further indicates that with decreasing FRT the microstructure becomes finer and elongated in the rolling direction for the lowest FRT.

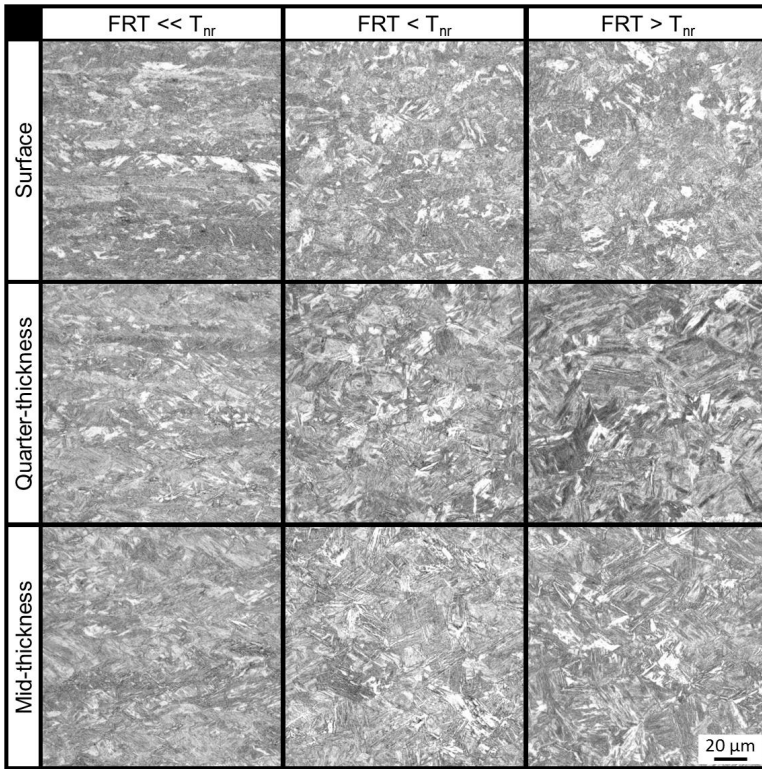


Figure 5. Light microscope images showing the microstructure at the surface, the quarter and the mid-thickness positions of the investigated plates.

To obtain additional insights into the microstructure prior to and post transformation, EBSD measurements were performed at the quarter-thickness positions of the plates and used to reconstruct the parent austenite structure. Consistent with the optical micrographs, the inverse pole figure (IPF) maps and the reconstructed austenite structure in Figure 6 reveal that with decreasing FRT the microstructure changes from coarse and fully recrystallized to fine and pancaked.

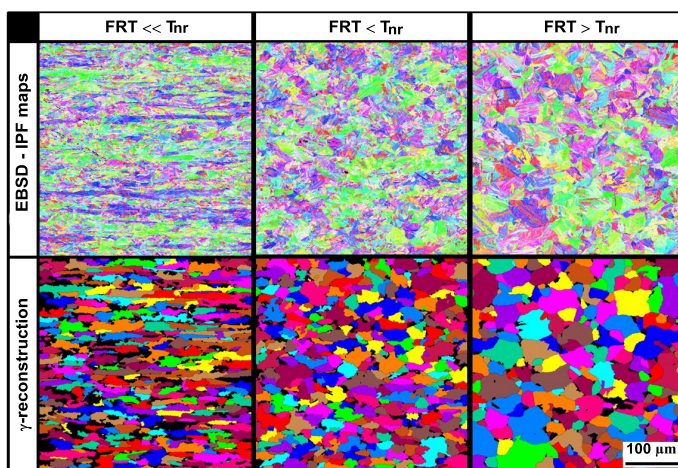


Figure 6. EBSD inverse pole figure (IPF) maps and austenite (γ) reconstruction of the microstructure at quarter-thickness of the three plates finish rolled at different temperatures.

From the reconstructed austenite structure, the mean values of the equivalent diameter, as well as the Feret ratio, i.e. the ratio between the minimum and the maximum Feret diameter or shortest and longest grain axis, were calculated and are listed in Table II. It can be seen that by decreasing the FRT in the tested range, the austenite grain size decreases from 25 μm to 16 μm . In addition, Feret ratios smaller than one indicate an elongation of the grains in the rolling direction for all three plates. While the stretching of the austenite grains with Feret ratios of 0.55-0.65 is relatively small for the plates finish rolled at temperatures close to T_{nr} , the Feret maximum (long axis) of the austenite grains in the plate finish rolled at the lowest temperature is, on average, 2.7 times larger than the Feret minimum (short axis).

Table II. Mean Values of Equivalent Diameter and Feret Ratio for the Three Plates Finish Rolled at Different FRT

| | FRT << T_{nr} | FRT < T_{nr} | FRT > T_{nr} |
|----------------------------|---|-------------------------------------|-------------------------------------|
| Diameter (μm) | 15.6 | 18.5 | 25.0 |
| Feret ratio | 0.37 | 0.55 | 0.64 |

The misorientation angle distributions from the EBSD measurements are shown in Figure 7. As expected for a martensitic/bainitic microstructure, the distributions display a pronounced peak at 60° and a smaller peak at around 53° for the three plates. Interestingly, the intensity of the peak at a misorientation angle of 60° , i.e. the portion of high angle grain boundaries characteristic for martensite and lower bainite, decreases with decreasing FRT.

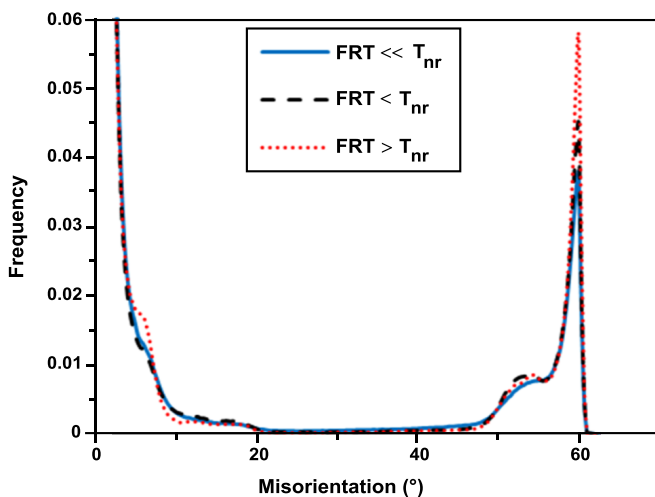


Figure 7. Grain boundary misorientation angle distribution of the investigated samples.

Discussion

In the production line used for the current study, the cooling intensity for direct quenching is regulated by the water flow rate and the speed with which the plates are moved through the cooling device [12]. For plates with lengths of several tens of meters, the limited speed of motion might result in a certain time lag between the cooling of the head and the tail positions of the plates. Due to the longer time interval before quenching of the tail with respect to the head position, microstructural differences might arise between the ends of the plates. Depending on temperature and rolling history, recovery, recrystallization and grain growth might occur and affect the austenite structure before quenching. Furthermore, if the cooling start temperature at the tail of the plates drops below A_{r3} , ferrite transformation might be promoted, which is more critical at low FRTs.

For the tested plates, uniform properties and microstructures were observed at the head and the tail positions indicating that these effects can be neglected for the production parameters and alloy composition used. This is partly related to the fact that due to the high hardenability and relatively small plate thickness the tested plates needed a relatively short cooling time and thus were moved at a high speed through the cooling device. In addition, the Nb microalloying in the alloy used retards recrystallization and grain coarsening.

The highest hardness as well as the best balance between strength and toughness was observed for the plate finish rolled at the lowest temperature, i.e. at a temperature significantly below T_{nr} . With an average hardness of approximately 425 HV throughout the thickness this plate exhibits an average impact toughness of approximately 60 J for the transverse and 125 J for the longitudinal sample direction at a test temperature of $-40\text{ }^{\circ}\text{C}$. These impact toughness values are much higher than those of the other two plates finish rolled at higher temperatures or conventional RQ plates of the same chemistry, which have a guaranteed V-notch toughness of 30 J at $-40\text{ }^{\circ}\text{C}$ for the longitudinal sample direction.

Several factors account for the enhanced toughness of the plate finish rolled at the lowest temperature. First of all, transformation from work-hardened austenite effectively refines the resulting martensitic/bainitic microstructure, because, if hardenability is high enough, additional dislocations and deformation bands can assist the nucleation of these transformation products upon cooling [4]. As a consequence, the critical packet size for brittle fracture decreases leading to the improvement of toughness. Other effects that might contribute to the superior toughness are the shortening and the randomization of the martensite laths due to the ausforming effect as well as a specific crystallographic texture causing splitting behavior in the Charpy specimens [2,3,6].

It is interesting to note that despite the obviously finer martensite microstructure visible in the optical micrographs and the EBSD maps, the plate finish rolled at the lowest temperature shows a slightly smaller portion of high angle grain boundaries, characteristic for the martensitic structure, than the other two plates finish rolled at higher temperatures. Two factors may account for this effect: (1) Compared to the other two plates, a higher portion of random grain boundaries or misorientation angles, related to the parent austenite structure, is detected in the EBSD scan of the plate finish rolled at the lowest temperature, due to its finer austenite grain size. Consequently, the portion of high angle boundaries, characteristic for lower bainite and martensite, is reduced in this plate in comparison to the other two plates. (2) The hardenability of the steel might not be sufficient to completely suppress diffusion controlled transformations at the lowest FRT, where the deformation substructure promotes the nucleation of ferrite and granular bainite. Thus, the microstructure might contain other constituents besides lower bainite and martensite thus reducing the fraction of high angle grain boundaries in the plate finish rolled at the lowest temperature. In contrast, the less work-hardened austenite structure with a larger grain size in the plates finish rolled at higher temperatures favors the formation of martensite and lower bainite, explaining the higher peak at 60° in the corresponding misorientation angle distributions. However, to account for the high hardness/strength of the plate with the lowest FRT, it has to be assumed that the contribution from the softer microstructural constituents such as ferrite and granular bainite is small and overcompensated by the ausforming effect, i.e. the strength/hardness increment related to the inheritance of the austenite dislocations in the transformed microstructure.

Although the average austenite grain size of the plate finish rolled at the intermediate temperature is only slightly larger than that of the plate finish rolled at the lowest temperature, it exhibits significantly lower impact toughness values. This shows that the reduction of the austenite grain size alone does not cause the improvement of toughness observed for the CR-DQ plate.

Furthermore, it is worthwhile noting that for the plate with the intermediate FRT the elongation of the austenite grains in the rolling direction is not too different from the plate finish rolled at a temperature above T_{nr} . Accordingly, it has to be assumed that the actual T_{nr} is lower than the theoretical T_{nr} calculated according to the equation by Boratto et al. [10], which is a reasonable assumption as this equation does not consider deformation due to rolling. Therefore, the microstructure of this plate might be more representative of a RCR process instead of a CR process. However, due to its fine grain size this plate still demonstrates comparable impact toughness values to the RQ counterparts. This is in contrast to most other studies on direct quenching, in which RQ plates generally show a higher impact toughness than RCR plates [3]. A possible explanation for this discrepancy is the Nb microalloying of the heat used for the current study, which drastically limits grain growth during hot processing.

Conclusions

Using the example of wear resistant steels, this study has shown, from a practical point of view, the importance of Nb microalloying in direct quenching. Firstly it guarantees, even for long plates, a uniform microstructure along the full plate length when the process route is optimized. Further, by increasing the T_{nr} it enables hot rolling in a temperature interval between T_{nr} and A_{r3} , which is crucial to obtain the desired microstructure and for the improvement of the mechanical properties related to low FRTs. Finally, during hot processing it limits the austenite grain growth leading to acceptable toughness levels even for higher FRTs.

References

1. K.A. Taylor and S.S. Hansen, "Structure and Properties of Some Directly-Quenched Martensitic Steels," *Proceedings of the International Symposium on Accelerated Cooling of Rolled Steel*, ed. G.E. Ruddle and A.F. Crawley (Pergamon Press, 1987), 85-101.
2. K.A. Taylor and S.S. Hansen, "Effects of Vanadium and Processing Parameters on the Structure and Properties of a Direct-Quenched Low-Carbon Mo-B Steel," *Metallurgical Transactions A*, 22 (1991), 2359-2374.
3. R.K. Weiss and S.W. Thompson, "Strength Differences between Direct-Quenched and Reheated-and-Quenched Plate Steels," *Physical Metallurgy of Direct-Quenched Steels*, ed. S.W. Thompson, K.A. Taylor and F.B. Fletcher (TMS, 1993), 107-138.
4. K. Okamoto, A. Yoshie and H. Nakao, "Physical Metallurgy of Direct-Quenched Steel Plates and its Application for Commercial Processes and Products," *Physical Metallurgy of Direct-Quenched Steels*, ed. S.W. Thompson, K.A. Taylor and F.B. Fletcher, (TMS, 1993), 339-405.
5. N.C. Muckelroy, K.O. Findley and R.L. Bodnar, "Microstructure and Mechanical Properties of Direct Quenched Versus Conventional Reaustenitized and Quenched Plate," *Journal of Materials Engineering and Performance*, 22 (2013), 512-522.
6. B.L. Bramfitt and A.R. Marder, "A Study of the Delamination Behaviour of a Very Low-carbon Steel," *Metallurgical Transactions A*, 8 (1997), 1263-1273.

7. E. Kinnunen et al., "Development of a New Direct Quenched Abrasion Resistant Steel," *International Journal of Metallurgical Engineering*, 2 (2013), 27-34.
8. H. Song et al., "Impact Toughness of an NM400 Wear-Resistant Steel," *Journal of Iron and Steel Research, International*, 20 (8) (2013), 72-77.
9. H. Song et al., "Effect of Direct Quenching on Microstructure and Mechanical Properties of a Wear-resistant Steel," *Acta Metallurgica Sinica*, 26 (4) (2013), 390-398.
10. F. Boratto et al., "Effects of Chemical Composition on the Critical Temperatures of Microalloyed Steels," *Proceedings of the International Conference Physical Metallurgy of Thermomechanical Processing of Steels and Other Metals*, Tokyo, Japan, (Thermec-88, ISIJ International, 1988), 383-390.
11. C. Cayron, "ARPG: A Computer Program to Automatically Reconstruct the Parent Grains from Electron Backscatter Diffraction Data," *Journal of Applied Crystallography*, 2007, no. 40:1183 – 1188.
12. A. Streisselberger et al., "Use of the Mulpic Cooling Equipment for the Production of High Strength Steel Plates," *Physical Metallurgy of Direct-Quenched Steels*, ed. S.W. Thompson, K.A. Taylor and F.B. Fletcher (TMS, 1993), 407-421.

HIGH PERFORMANCE ABRASION RESISTANT STEEL PLATES USING MICROALLOYING TECHNOLOGY FOR GRAIN REFINEMENT

N. Takayama¹, A. Ohmori¹, Y. Murota² and K. Araki³

¹Steel Research Lab., JFE Steel Co., 1-1 Minamiwatarida-cho, Kawasaki, 210-0855, Japan

²East Japan Works, JFE Steel Co., 1-1 Ogishima, Kawasaki, 210-0868, Japan

³Head Office, JFE Steel Co., 2-2-3 Uchisaiwaicho, Chiyoda-ku, Tokyo, 100-0011, Japan

Keywords: Abrasion Resistance, Wear Resistance, Low Temperature Toughness, Niobium, Microalloying, Grain Refinement, Hydrogen Embrittlement, Weldability

Abstract

In recent years, many additional material properties, such as weldability, low temperature toughness and resistance to delayed fracture, are required for abrasion resistant steel plates. However, all of these material properties usually show a trade-off relationship with strength and hardness. In response to these requirements, JFE steel has developed a series of high performance abrasion resistant steel plates known as the EVERHARD™ LE series. The improved properties of these steels are discussed within this paper.

The effects of prior austenite grain size on the microstructure and properties of abrasion resistant steel plates were investigated and the results are presented and discussed in this paper. Microalloying technology, including the use of Nb, promotes austenite grain refinement during processing which produces a finer martensitic microstructure in the final product. As a consequence the low temperature toughness and resistance to hydrogen embrittlement are improved in the newly developed steel plates. The EVERHARD™ LE series can be supplied with a guaranteed Charpy impact toughness at -40 °C. Crack-free welding of the EVERHARD™ LE steels can be readily achieved by careful control of the consumable and the preheat temperatures.

Introduction

The requirements of steel plates for the mining and processing industry include excellent wear resistance against the abrasion effects caused by ore, rock or sand. Abrasion of steel plates is affected by surface hardness [1-5] and abrasion conditions such as the abrasive materials being handled and the local environment. Even though the abrasion resistance of the steel is improved by a dispersion of hard particles [6], such as carbides and retained austenite [7], surface hardness is the most important factor affecting the abrasion resistance of the steel. In order to increase the hardness of the steel plates, quenching is often used to produce a martensitic microstructure [8]. However, to obtain sufficient hardenability in thick plates, it is necessary to add alloying elements, depending on the plate thickness, and the increasing hardenability potentially leads to a deterioration of low temperature toughness and weldability. Additionally, requirements for the steel plates for use in construction and industrial machinery have diversified, for example, securing low temperature toughness to enable use in cold climates and improved weldability by lowering the required preheating temperature are the major aspects for expanding the application

of abrasion resistant steels. Furthermore, hydrogen delayed fracture can be a possible failure mode when high strength steel with a tensile strength level of over 1000 MPa is used in wet or corrosive environmental conditions. Therefore, low temperature toughness, weldability and resistance to hydrogen embrittlement should be the primary issues to be addressed in developing abrasion resistant steel plate.

Considering an application of the abrasion resistant steels in the mining and processing industry, higher hardness is the essential material property. Therefore, a martensitic microstructure, which is obtained by a quenching treatment, is the starting point for material design. However, only increasing the hardness may result in reducing the toughness and resistance to hydrogen cracking of the steel. One of the key technologies to improve the properties is grain refinement with microalloying elements. Chemical compositions and plate manufacturing conditions are precisely controlled to avoid grain coarsening.

The authors reported [9] that grain refinement using NbC precipitation improved low temperature toughness and resistance to hydrogen embrittlement in HB 500 class abrasion resistant steel plates. Based on those results, JFE steel has developed a series of high performance abrasion resistant steel plates, EVERHARD™ LE series, with a good balance of hardness, toughness and weldability. In this paper, the effects of prior austenite grain size on these properties in abrasion resistant steel plates are presented [9,10] and the features of the EVERHARD™ LE series are introduced [11].

Experimental Procedures

Materials with Fine Prior Austenite Grains

HB 500 class abrasion resistant steel plates were used for the development program. Table I shows the chemical compositions of the steels. Two types of chemistries were used for obtaining different microstructures. Both steels contain approximately 0.3 wt.% carbon and several alloying elements to obtain sufficient hardenability, but additions of the microalloying elements such as Nb and Ti are different in the two steels. 25 mm thick steel plates were produced with application of a heat treatment. The concepts used for obtaining a fine microstructure are shown in Figure 1. Microalloying elements, such as Nb, Ti and V, contribute to the refinement of the austenite grains through a solute drag effect and a pinning effect by carbide precipitates. Furthermore, the dissolution of these elements in austenite also affects hardenability. Based on an alloy design that is capable of obtaining these effects, plate manufacturing parameters such as slab reheating temperature, controlled rolling and heat treatment were optimized to achieve a fine microstructure.

Table I. Chemical Compositions of Steels (wt.%)

| | C | Si | Mn | P | S | Nb | Others | Ceq |
|---------------------------|------|------|------|-------|-------|------|-------------|------|
| Conventional steel | 0.30 | 0.29 | 1.08 | 0.009 | 0.002 | - | V, Ti, etc. | 0.55 |
| Developed steel | 0.29 | 0.28 | 1.25 | 0.009 | 0.003 | 0.02 | V, Ti, etc. | 0.54 |

$$Ceq=C+Mn/6+(Cu+Ni)/15+(Cr+Mo+V)/5$$

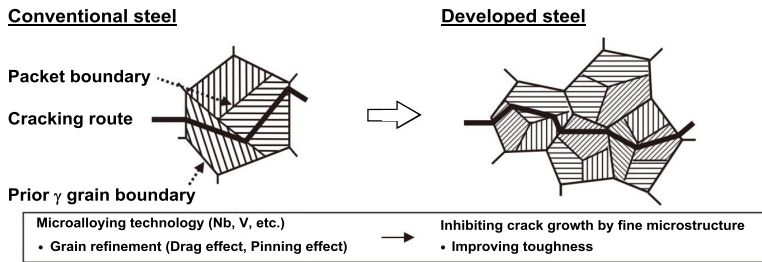


Figure 1. Schematic illustration of austenite grain refinement with microalloying technology.

Figure 2 shows photomicrographs of the prior austenite grains for the conventional abrasion resistant and the developed steels. By applying the above-mentioned austenite grain refining technologies, prior austenite grains, which were conventionally coarse, with a size of the order of 40–50 μm , were successfully refined to approximately 20 μm or less.

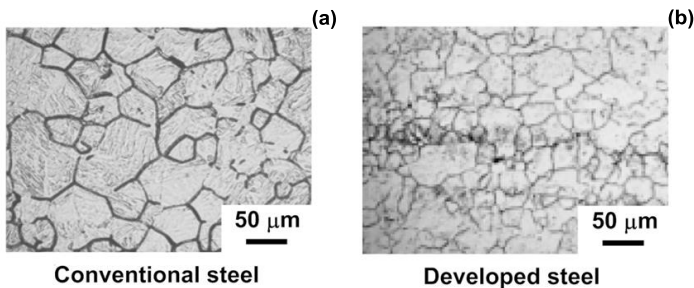


Figure 2. Prior austenite grains of; (a) conventional and (b) developed steel.

Procedures for Material Evaluation

Low temperature toughness was evaluated by Charpy impact tests conducted at $-40\text{ }^{\circ}\text{C}$. Standard V notch specimens were used. Longitudinal Charpy specimens were machined from the quarter thickness position and parallel to the rolling direction of the steel plate.

Resistance to hydrogen embrittlement was evaluated by testing hydrogen charged tensile specimens. Round bar tensile specimens with a gauge length of 6.0 mm in diameter and 70 mm in length were machined from the mid-thickness location of the steel plates. Hydrogen charging was conducted by immersing the specimen into an aqueous 5% ammonium thiocyanate solution with different immersion times of 0.5 to 2 hours at $50\text{ }^{\circ}\text{C}$. Immediately after hydrogen charging, the specimens were immersed in liquid nitrogen at $-196\text{ }^{\circ}\text{C}$ for an hour. Subsequently, a tensile test was conducted at a constant crosshead speed at 5 mm/min to fracture at ambient temperature. Additionally, another specimen prepared under the same hydrogen charging conditions was

subjected to hydrogen analysis. Diffusible hydrogen in the specimen was measured by hydrogen thermal desorption analysis using a gas chromatograph at a heating rate of 200 °C/hour.

Results and Discussion

Improvement of Low Temperature Toughness

For the use of abrasion resistant steels in cold climate regions, steels need to have sufficient toughness to prevent brittle fracture of the machine parts. Therefore, for the development of the improved HB 500 steel we set the target material Charpy impact toughness at a low temperature of -40 °C. Table II shows the surface hardness of the developed and conventional steels using the Brinell Hardness Test. Surface hardness of the steels was decisively controlled by C content for fully martensitic microstructures.

Table II. Surface Hardness of Developed Steel and Conventional Steel from Brinell Hardness Test

| | HBW 10/3000 | | | | | Ave. |
|---------------------------|------------------|-----|-----|-----|-----|------|
| | Individual value | | | | | |
| Conventional steel | 499 | 507 | 518 | 514 | 503 | 508 |
| Developed steel | 501 | 495 | 501 | 507 | 504 | 502 |

Reducing prior austenite grain size, resulting in a fine packet size, is quite effective [7] in improving the Charpy impact toughness. Figure 3 shows the Charpy energy values at -40 °C of the developed and conventional steels. Even with very high surface hardness levels, the Charpy toughness of HB 500 was improved significantly by refinement of the prior austenite grains.

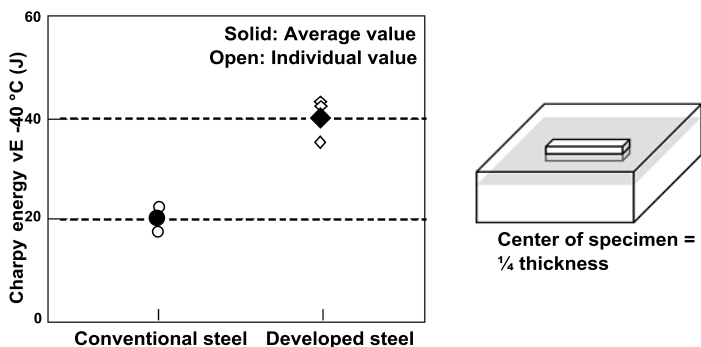


Figure 3. Charpy energy at -40 °C of developed and conventional steel.

Improvement of Resistance to Hydrogen Embrittlement

Figure 4 shows the relationship between diffusible hydrogen content and resistance to hydrogen embrittlement of the developed and conventional steels. The resistance to hydrogen embrittlement was evaluated by the safety index of the hydrogen embrittlement resistance given as $R1/R0 \times 100$ (%), where $R0$ and $R1$ represent the reduction in area of the uncharged specimen and the charged specimen, respectively. As shown in Figure 4, the resistance to hydrogen embrittlement of the developed steel is good compared to the conventional steel.

Figure 5 shows scanning electron microscope (SEM) micrographs of fracture surfaces of the hydrogen charged specimens. The conventional steel shows intergranular fracture. On the other hand, the developed steel shows quasi-cleavage fracture. The resistance to hydrogen cracking of the developed steel is improved by suppression of intergranular fracture which results from the refinement of the prior austenite grains and the consequential refinement of the martensitic microstructure.

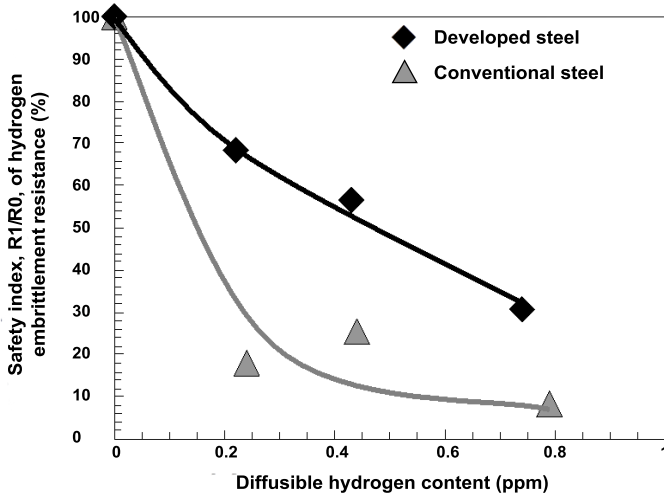


Figure 4. Resistance to hydrogen cracking of developed and conventional steel.

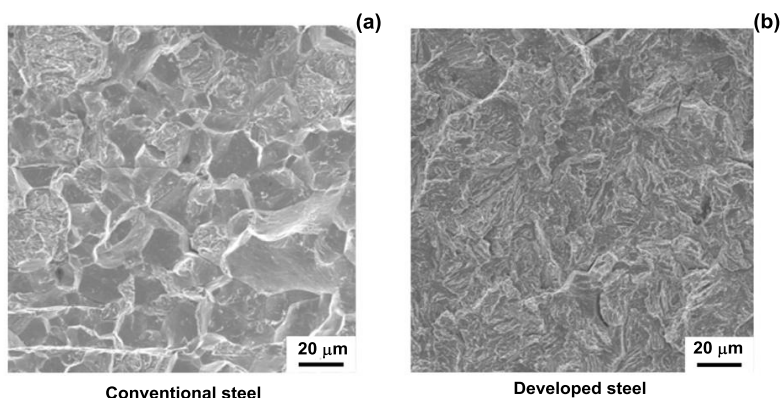


Figure 5. SEM micrographs of tensile test fracture surfaces after hydrogen charging by immersing in aqueous 5% ammonium thiocyanate solution for half an hour.

Application of EVERHARD™ LE Series

Grade Variants and Features

The microalloying technology for microstructural refinement described above was applied in the development of JFE steel's high performance abrasion resistant steel plates, named EVERHARD™ LE series. The product grades and features of the LE series are shown in Table III together with data for the conventional steels. In the conventional "Standard Series", surface hardness is guaranteed by the alloy design and special heat treatment. In the "LE Series", low temperature toughness at -40 °C is also guaranteed by grain refinement through the use of microalloying technology including Nb. The guaranteed toughness enables the use of the LE series in arctic climates and also improves safety against external impact and forming by cold bending. In Table III, the numbers showing hardnesses of (400, 450, 500) represent the median values of the surface hardness range.

Because low temperature toughness tends to decrease as plate thickness increases, there was a limit to plate thickness with the conventional technology. However, in response to requests for heavier gauges for larger scale buckets or vessels, the maximum thickness of EVERHARD C400LE was increased from the conventional 32 to 60 mm, and a new product EVERHARD C450LE (maximum thickness: 50.8 mm) was developed. An increase in maximum thickness of EVERHARD C500LE from 32 to 50 mm is also under consideration.

Table III. JFE Steel’s Abrasion Resistant Steel Plates EVERHARD™ Series

| Series | Features | EVERHARD Products | Grade | Surface hardness (HB) | Thickness (mm) | Charpy absorbed energy at -40 °C vE-40 (J) |
|----------|---|-------------------|--------|-----------------------|----------------|--|
| Standard | Basic EVERHARD™ Basic alloy-design for economical and easy-welding fabrication | EVERHARD C340 | HB 340 | 340±30 | 38-160 | - |
| | | EVERHARD C400 | HB 400 | 400±30 | 6-101.6 | |
| | | EVERHARD C450 | HB 450 | 450±30 | 6-101.6 | |
| | | EVERHARD C500 | HB 500 | 500±40 | 6-101.6 | |
| | | EVERHARD C550 | HB 550 | 550±40 | 6-32 | |
| LE | Low temperature service Sufficient toughness at -40 °C | EVERHARD C400LE | HB 400 | 400±30 | 6-60 | ≥27 J (≥12) |
| | | EVERHARD C450LE | HB 450 | 450±25 | 6-50.8 | ≥27 J (≥12) |
| | | EVERHARD C500LE | HB 500 | 500±40 | 6-32 | ≥21 J (≥12) |

The relationship between the surface hardness and abrasion resistance of the EVERHARD™ series is shown in Figure 6. Abrasion resistance is expressed by the weight loss ratio comparing the EVERHARD grade with a standard 400 MPa class mild steel in the rubber wheel abrasion test carried out in accordance with ASTM G65. The abrasion resistance of “Standard” and “LE series” shows a comparable dependence on hardness. The abrasion resistance of the HB 400 grade is approximately three times that of mild steel, and HB 450 and HB 500 class steels have outstanding abrasion resistance, approximately four and five times higher than mild steel respectively.

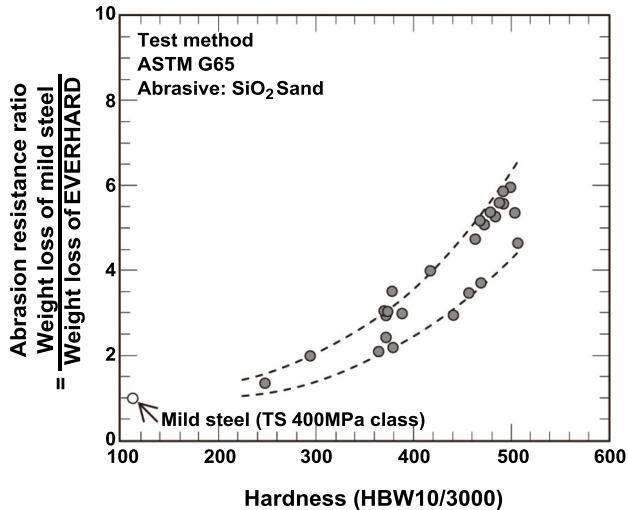


Figure 6. Relationship between hardness and abrasion resistance. The two lines represent the scatter band of results.

Weldability

High hardness, high strength steel plates generally display high sensitivity to low temperature cracking due to welding. In contrast, crack-free welding is possible with EVERHARD™ grades with the use of controlled welding conditions. Low temperature cracks occur in weld metal or heat affected zone (HAZ) when these regions are embrittled by the penetration of hydrogen into the steel as a result of the welding process. However, this type of crack can be prevented by selection and control of welding consumables, etc. together with a correct application of preheating. For example, the recommended preheating temperatures for the “LE series” are shown in Table IV. These preheat values are based on the results of y-groove weld cracking tests (JIS Z 3158, JIS: Japanese Industrial Standards) and on evaluation of the steel chemical compositions for SMAW (shielded metal arc welding) using an ultra-low hydrogen welding electrode, and GMAW (gas metal arc welding) using a solid wire. Whereas these are examples in which restraint is comparatively large, it is also possible to simplify welding work by relaxing the preheating temperature corresponding to the restraint intensity in practical welding situations.

Table IV. Preheating Temperature Guideline for EVERHARD™ Series

| Brand name | Welding method | Thickness(mm) | | | | | | | | | |
|-----------------|----------------|------------------|-------|--------|--------|--------|----|----|----|----|-------|
| | | 10 | 20 | 30 | 40 | 50 | 60 | 70 | 80 | 90 | 101.6 |
| EVERHARD-C400 | SMAW | 50°C | 75°C | 100°C | >125°C | | | | | | |
| | GMAW | Room temperature | | 50°C | >75°C | | | | | | |
| EVERHARD-C450 | SMAW | 75°C | 125°C | | >125°C | | | | | | |
| | GMAW | Room temperature | 75°C | 100°C | >100°C | | | | | | |
| EVERHARD-C500 | SMAW | 125°C | 175°C | >175°C | | | | | | | |
| | GMAW | Room temperature | 75°C | 125°C | >125°C | >150°C | | | | | |
| EVERHARD-C400LE | SMAW | 75°C | 100°C | 125°C | | | | | | | |
| | GMAW | Room temperature | | 75°C | >75°C | | | | | | |
| EVERHARD-C450LE | SMAW | 75°C | 125°C | >125°C | | | | | | | |
| | GMAW | Room temperature | 75°C | 100°C | | | | | | | |
| EVERHARD-C500LE | SMAW | 125°C | 175°C | | | | | | | | |
| | GMAW | Room temperature | 75°C | 125°C | | | | | | | |

Room Temperature
 50°C
 75°C
 >75°C

100°C
 >100°C
 125°C
 >125°C

>150°C
 175°C
 >175°C

Conclusions

Conventional abrasion resistant steels are usually designed to have a high surface hardness with minimal attention being paid to the toughness of the steel. However, as the applications for such steels become more severe, eg. use in colder climates, it has become necessary for steels to be developed with a guaranteed toughness requirement and improved resistance to hydrogen embrittlement.

The effects of prior austenite grain size control on the properties of quenched abrasion resistant steel plates were investigated with the aim of improving the steel toughness and resistance to hydrogen embrittlement by refinement of the final martensitic microstructure. The results are summarized as follows:

1. The inclusion of Nb in the alloy design resulted in a refined austenite grain size prior to quenching and a refined martensitic microstructure in the final quenched product.
2. Fine martensitic microstructures resulted in improved low temperature toughness and resistance to hydrogen embrittlement even for the higher hardness grades typically used as abrasion resistant steels.
3. Abrasion resistant steel plates of HB 400-500 class with fine microstructures, named the EVERHARD™ LE series, were developed utilizing Nb microalloying for microstructure control. They exhibit excellent low temperature toughness, resistance to hydrogen embrittlement and improved weldability while maintaining a high surface hardness for good abrasion resistance.

References

1. E. Rabinowicz, L.A. Dunn and P.G. Russell, "A Study of Abrasive Wear Under Three-Body Conditions," *Wear*, 4 (5) (1961), 345-355.
2. G.K. Nathan and W.J.D. Jones, "Influence of the Hardness of Abrasives on the Abrasive Wear of Metals," *Proceedings of Institution of Mechanical Engineers Part 3*, 181 (315) (1966), 215-221.
3. M.M. Khrushov, "Principles of Abrasive Wear," *Wear*, 28 (1) (1974), 69-88.
4. W. Yan, L. Fang, K. Sun and Y. Xu, "Effect of Surface Work Hardening on Wear Behavior of Hadfield Steel," *Material Science and Engineering A*, 460-461 (2007), 542-549.
5. Q.L. Wang and P.E. Xu, "Wear of Alloy in Silica Sand Slurry," *Wear of Materials*, (1985), 671-676.
6. K. Ueda, N. Ishikawa and Y. Murota, "Influence of Matrix Structure and Hard Carbide on Abrasive Resistance of Steel Plates," *Materials Science Forum*, 706-709 (2012), 2342-2347.

7. F. Bouchaud et al., “New Wear-Resistant Steel Creusabro Dual” (Paper presented at the International Symposium on the Recent Developments in Plate Steels, Winter Park, Colorado, 20-22 June 2011), 93-101.
8. T. Sadasue et al., “Development of Abrasion Resistant and High Strength Steels with Improved Low Temperature Toughness and Weldability for Construction Equipment and Industrial Machines,” *Materia Japan*, 42 (42) (2003), 145-147.
9. M. Murota, T. Abe and M. Hashimoto, “High Performance Steel Plates for Construction and Industrial Machinery Use” (Report No. 5, JFE Steel Corporation, 2005, 60-65).
10. S. Miura et al., “Improvement of Low Temperature Toughness and Resistance to Hydrogen Cracking of HB500 Class Abrasion Resistant Steel by Grain Refinement” (Paper presented at Materials Science and Technology (MS&T) 2012, Pittsburgh, Pennsylvania, 7-11 October 2012), 1202-1209.
11. “JFE Steel’s Abrasion-Resistant Steel Plates EVERHARD™” (Report No. 20, JFE Steel Corporation, 2015).

WEAR- AND CORROSION-RESISTANT STEELS CONTAINING NIOBIUM CARBIDE

M. Seifert¹, S. Huth^{1,2}, S. Siebert¹ and W. Theisen¹

¹Ruhr-Universität Bochum, Chair of Materials Technology,
Universitätsstr. 150, Bochum, 44801, Germany
²now at Hilti AG, Corporate Research & Technology,
Feldkircherstr. 100, Schaan, 9494, Liechtenstein

Keywords: Niobium Carbide, Martensitic Stainless Steels, Bearing Steels, PM Steels, Steels for Polymer Industry, Thermodynamic Equilibrium Calculations, Diffusion Alloying, Manufacturing

Abstract

Niobium, like titanium and vanadium, forms super-hard mono-carbides (MC) which remain relatively pure in Fe-base alloys on account of their low solubility for other metallic alloying elements. Because the super-hard mono-carbides have a higher hardness than the precipitated chromium carbides commonly used in wear-resistant alloys, they are suitable as alternative hard phases.

This paper deals with new wear- and corrosion-resistant steels containing niobium carbide that were produced by ingot and powder metallurgy (PM) for use as plastic mould and bearing steels. Based on equilibrium calculations by CALPHAD (CALculation of PHase Diagrams) methods, the microstructures developed during the production of these steels were analysed, and the results are discussed with respect to important properties such as abrasive wear and corrosion resistance. Alloys can be produced by precipitation of primary niobium carbides of the MC type, which are embedded in a martensitic metal matrix that can be subjected to secondary hardening. Because of the high affinity of niobium for carbon, the formation of chromium carbides can be suppressed even in high-chromium alloys, thus leaving chromium contents of more than 12 wt.% in the metal matrix as are required to impart corrosion resistance. This allows the production of stainless, wear-resistant cold-work tool steels for the food processing and pharmaceutical industries, as well as corrosion-resistant bearing steels.

Introduction

It is commonly known that martensitically hardenable Fe-Cr-C alloys with a considerable amount of carbides show good resistance to abrasive wear [1,2]. One group among these alloys is tool steels with a carbon content up to 2 wt.%. Above a critical carbon content, eutectic carbides form during solidification. These can be iron-rich M_3C , or chromium-rich M_7C_3 if the chromium content is high enough. The eutectic network tends to be coarse. Additionally, the carbide morphology is unfavourable and the amount increases with increasing carbon content. A high amount of coarse carbides is positive for the wear resistance, but impairs the ductility and the fracture toughness. This becomes worse if the eutectic content is so high that it forms a network that surrounds the more ductile metal cells, which leads to pre-defined crack paths [3]. In general, hard phases are able to reduce abrasive wear, if they are harder than the abrading

particles. Thus, for many applications, the carbides mentioned above are too soft and harder carbides would be preferred [4].

This can be improved by alloying steels with certain amounts of vanadium, niobium or titanium. These form MC type carbides with a hardness >2200 HV that precipitate primarily from the melt, even for alloying comparatively small amounts of these refractory metals [2,5]. Depending on the alloying content, this may lead to very large carbides [2]. Among these elements, niobium is the most promising element for several applications: it has almost no solubility in the iron matrix and thus does not contribute to secondary hardening [6,7]. This means that the amount of NbC and carbon needed for precipitation can be adjusted quite precisely. Furthermore, NbC precipitates have a lower solubility for the main alloying elements such as chromium and molybdenum than comparable carbides like TiC and VC. This means that higher amounts of those alloying elements remain dissolved in the matrix. This is especially interesting for corrosion-resistant steels that also require a considerable wear resistance, eg extruders in the polymer industry or cutting tools in the food industry [8 and references therein], because there is no chromium depletion around NbC.

The alloying strategy for martensitic stainless steels with good wear resistance is complex because these properties are somewhat contradictory. As in hardenable tool steels, hardness and wear resistance require a certain amount of carbon, and the corrosion resistance is in need of at least 10.5 wt.%Cr dissolved in the matrix [9]. As mentioned above, chromium is usually also required to precipitate carbides and so the alloying content of chromium has to be increased. This is only possible up to a certain amount because chromium stabilises ferrite and thus hinders martensitic transformation at very high amounts. Even though these three key properties can be adjusted within a wide range by an adequate heat treatment, there is only a limited possibility to keep all of them at a high level. As already mentioned, niobium can help to retain more chromium in the matrix and depress the well-known depletion around chromium-rich carbides [10,11].

The size of primary NbC precipitates is disadvantageous, not only for forging, but probably also for the corrosion resistance in some applications, eg for pitting corrosion. Adequate manufacturing routes for steels containing a high amount of NbC thus have to be developed. In this study, we focus on a new powder metallurgical manufacturing route that leads to two different concepts for corrosion- and wear-resistant steels. One of these is aimed at applications in the polymer industry, the other is being developed for bearings in sea water environments.

Martensitic Stainless PM Steels with Enhanced Wear and Corrosion Resistance

Development

The basic alloy system of this corrosion-resistant cold-work tool steel is Fe-Cr-Nb-Mo-C. As already mentioned, a chromium content of at least 10.5 wt.% is sufficient to ensure corrosion resistance [9] because chromium then transfers its passivation ability to the iron matrix [12]. This leads to the formation of a Cr₂O₃ layer that isolates the metal from the surrounding medium. If the corrosion resistance has to be high, the proportion of carbon and chromium has to be adjusted so that chromium-rich carbides are avoided. These withdraw chromium from the matrix, thus the

Cr content in it is reduced. Furthermore, a zone with a strong chromium depletion surrounds the carbides [10,11], which is especially detrimental for resistance against pitting corrosion.

The niobium content can be more or less arbitrarily adjusted to the intended content of NbC. In corrosion-resistant steels, the carbon content has to be balanced to: (i) form the intended amount of NbC, (ii) avoid chromium-rich carbides and (iii) achieve a hardenable matrix, i.e. a sufficient amount of carbon has to be dissolved in the matrix at the austenitisation temperature (T_{AUS}). After an adequate heat treatment, this will lead to NbC precipitates embedded in a stainless martensitic matrix [13].

Molybdenum is added to further increase the corrosion resistance, especially against pitting corrosion. There are ongoing discussions on how molybdenum actually increases the corrosion resistance in steels and it seems to be clear that it only shows its positive effects in combination with a sufficient amount of chromium [14–17]. At higher contents, molybdenum tends to segregate, which might lead to the precipitation of molybdenum-rich M_6C [1]. Naturally, these features are unwanted in stainless steels.

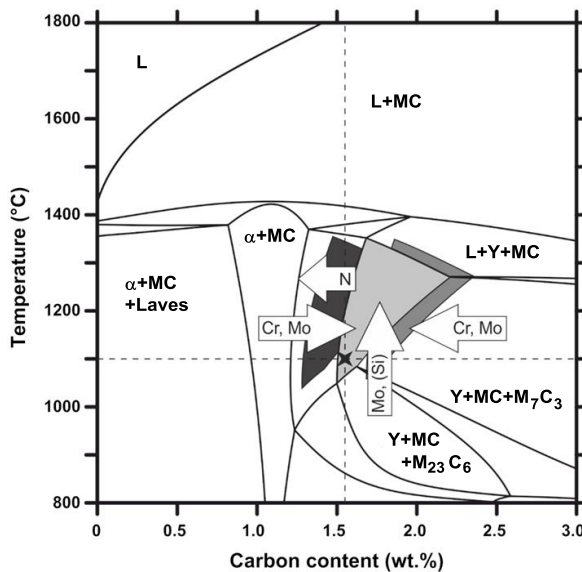


Figure 1. Quasi-binary phase diagram of the Fe-12Cr-10Nb-2Mo system depending on the carbon content (L=liquid, MC=NbC, α =Ferrite, γ =Austenite). The target phase field, γ +MC, is coloured in light grey. The influence of less and more niobium is shown by the shift of this phase field to lower carbon contents (9 wt.%Nb, dark grey) and to higher carbon contents (12 wt.%Nb, medium grey), respectively. The arrows indicate the influence of the addition of chromium, molybdenum, nitrogen and silicon on the target phase field. The dashed lines indicate a possible austenitisation temperature of 1100 °C for a carbon content of 1.55 wt.%.

These considerations led to a steel with 12 wt.%Cr, 10 wt.%Nb and 2 wt.%Mo [18,19]. A phase diagram calculated with the commercial software Thermo-Calc Version S in combination with the database TCFE7 is shown in Figure 1. The target phase field for a corrosion-resistant martensite containing only NbC is γ +MC coloured in light grey. The influence of different niobium contents is shown by the shift of this phase field, ie lower contents require less carbon (dark grey), higher contents require more carbon (medium grey). Arrows depict the influence of adding other alloying elements. Chromium and molybdenum clearly reduce the size of the γ +MC phase field because they both stabilise the ferrite and also lead to chromium-rich carbides. At higher amounts of molybdenum, ie above ≈ 3 wt.%, precipitation of M_6C becomes possible, which shrinks the target field from the bottom. Nitrogen, introduced either by atomisation with nitrogen gas or intentional alloying, widens the γ +MC field in the direction of lower carbon contents, whereas the right boundary remains constant. Manganese and silicon do not have any distinct influence on this alloy for contents usually introduced in the scrap used for melting the steel [18]. However, an unfavourable combination of too much silicon with certain amounts of chromium and molybdenum will lead to the stabilisation of M_6C , which shrinks the target phase field as already mentioned. It is obvious that a T_{Aus} of at least 1100 °C is necessary to safely hit the γ +MC phase field (see the dashed line). Even at 1100 °C, the possible carbon content is fairly limited at around 1.5–1.7 wt.% (dashed line indicates 1.55 wt.% in Figure 1). Lower austenitisation temperatures, as well as excessive carbon contents, would lead to the precipitation of chromium-rich carbides. However, this would probably be beneficial for applications demanding enhanced wear resistance [18]. A much higher T_{Aus} would lead to more retained austenite (RA) due to the higher difference in temperature and to coarsening of the microstructure [1]. The general hardenability of steels can be estimated by calculating the martensite-start temperature (M_s) and taking account of the composition of the matrix at T_{Aus} . This can be achieved using Equation 1, which was developed by Andrews [20] and subsequently modified by Kung and Rayment [21] and Berns and Krasokha [22] (composition in wt.%):

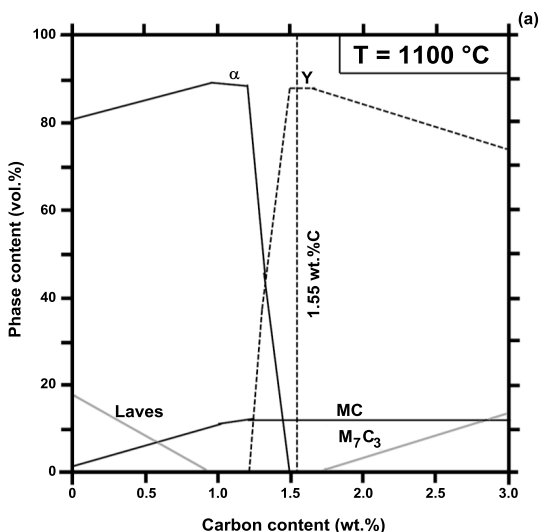
$$M_s = 539 - 423 \cdot (C+N) - 30.4 \cdot Mn - 17.7 \cdot Ni - 12.1 \cdot Cr - 7.5 \cdot Mo - (7.5 \cdot Si + 10 \cdot Co) \quad (1)$$

Figure 2 shows three equilibrium calculations at a possible T_{Aus} of 1100 °C and displays valuable information for the design of this steel. Figure 2(a) visualises the content of the stable phase depending on the carbon content. Besides the information gathered from Figure 1, the content of MC within the γ +MC-field can be estimated to be about 12 vol.%, which remains constant for higher carbon contents. Furthermore, the amount of MC, and with it the carbon content, stays almost constant with rising temperature (not shown here) owing to the low solubility of NbC in the matrix [23]. Figure 2(b) shows the atomic composition of the MC with increasing carbon content. According to the employed database, it can clearly be seen that the MC phase is almost purely Nb(C,N) for a carbon content of 1.55 wt.%. Only very small amounts of chromium, molybdenum and iron are dissolved in the MC. However, their amount slightly increases with increasing carbon content. Figure 2(c) shows the composition of the matrix with increasing carbon content. The x axis is scaled only from 1.0 to 3.0 wt.%C because the austenite is not stable below ≈ 1.2 wt.%, as shown in the diagram. For a carbon content of 1.55 wt.%, the matrix contains about 0.35 wt.%C, which is sufficient for a high hardness [1]. Additionally, the highest amounts of chromium (≈ 13.2 wt.%) and molybdenum (≈ 2.4 wt.%) are dissolved in the matrix at the intended carbon content of 1.55 wt.%. This leads to a pitting resistance equivalent number (PREN) of 21.4. The PREN is commonly used to estimate the resistance of a steel against pitting

corrosion or to at least to compare different steels. It is calculated using Equation 2 (in wt.%) [24,25]. The matrix contains almost no niobium or nitrogen.

$$\text{PREN} = \text{Cr} + 3.3 \cdot \text{Mo} + 20 \cdot \text{N} \quad (2)$$

Although Figure 2 indicates that no nitrogen is dissolved in the matrix, about 0.12 wt.% was detected experimentally [18]. This seems to be an inconsistency in the database used for the calculation. However, presumably the PREN is the only property that would differ slightly due to this. The nitrogen content in the Nb(C,N) is replaced by carbon, leading to a decreased carbon content in the matrix [26]. Nitrogen dissolved in the matrix has a positive influence on the PREN. Additionally, it contributes to the hardenability of the steel [27].



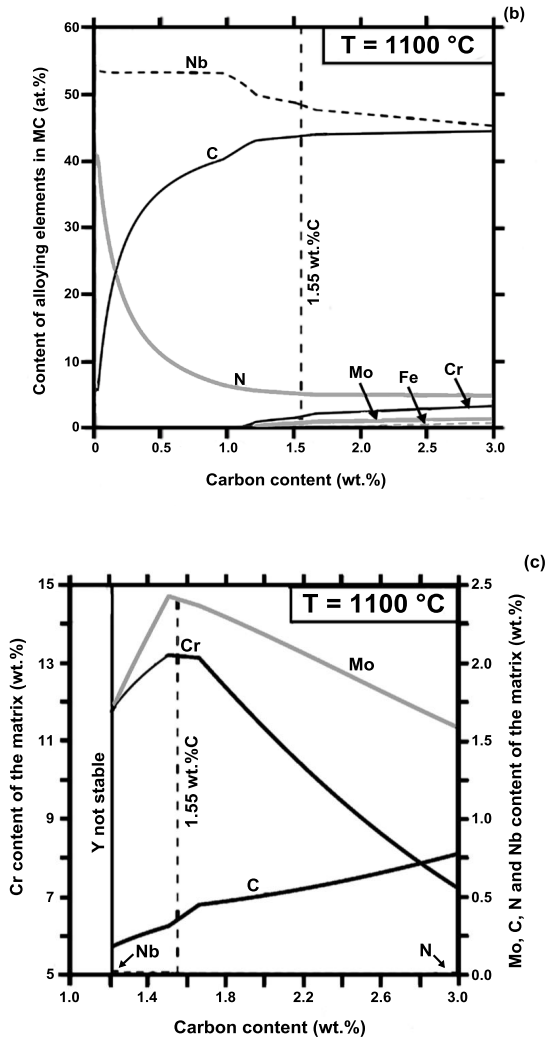


Figure 2. Different equilibrium properties at 1100 °C depending on the carbon content calculated with Thermo-Calc. The dashed line indicates a carbon content of interest for this study; (a) Phase content in vol.%, (b) Composition of the NbC, (c) Composition of the matrix. The x axis in (c) is scaled only from 1.0 to 3.0 wt.%C because the austenite is not stable below ≈ 1.2 wt.%, which is also shown in the diagram.

Figure 1 shows that the liquidus temperature of the NbC for the intended carbon content is higher than 1800 °C in this system. This means that these would precipitate directly from the melt at a very early stage of solidification. Huge carbides comparable to those in Figure 3(a) would be the consequence of this [2]. However, for rapid solidification, eg in welding seams, a fine dispersion of NbC is achievable, as can be seen in Figure 3(b) for a hardfacing alloy, which also clearly shows the martensitic structure of the matrix. A possible way to obtain a comparable microstructure is provided by powder metallurgy. However, in a melt conventionally designed for atomisation, the NbC would grow as large as mentioned above and would thus clog the nozzle and the atomisation would stop [28]. A possible way to overcome this is a process route called diffusion alloying [18,29,30].

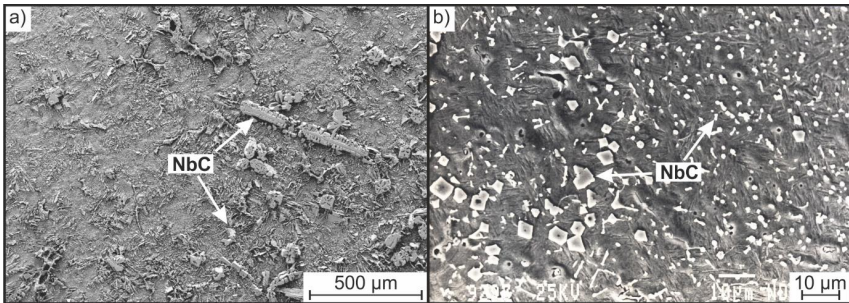


Figure 3. Different morphologies of NbC; (a) huge NbC in alloy G-X130NbCrMoW6-4-2-2 in the as-cast condition, (b) fine dispersion of NbC, comparable to a powder metallurgical microstructure, in hardfacing alloy X120NbCrMoV6-5-2-1.

Diffusion Alloying

Diffusion alloying is based on the idea of atomising a melt that is free of carbon. The resulting carbon-free powder can be mixed with a variable amount of interstitial elements, ie carbon, nitrogen or boron, from a gaseous or solid donor [30]. Consequently, different alloying concepts can be obtained with one base powder, leading to a higher corrosion resistance or wear resistance. The steels under investigation in this study were mixed with graphite, which ideally completely covers the surface of all powder particles after mixing.

The actual process of alloying the carbon-free powder with carbon takes place subsequently during hot isostatic pressing (HIP). At a high pressure of about 100 MPa and typical temperatures of about 1150 °C, the graphite presumably reacts with the oxygen contained in the surface oxides of the steel to form CO and/or CO₂ [18]. This gas phase distributes the carbon uniformly throughout the steel via the pores that initially represent an open porosity. Thus, the process of alloying actually takes place via the gas phase. Due to the high temperature, the carbonization step finishes after a few minutes. Although this cannot really be proven yet, other studies appear to support this theory [32]. The process route of diffusion alloying, including the HIP process, is shown schematically in Figure 4.

To improve the resistance to coarse abrasive wear, additional large NbC particles can be mixed into the powder of the existing alloying concept [13]. Such additions significantly change neither the composition of the matrix nor that of the NbC during diffusion alloying. Depending on the application, the content of admixed NbC can be varied like the content of carbon without losing the intended corrosion resistance.

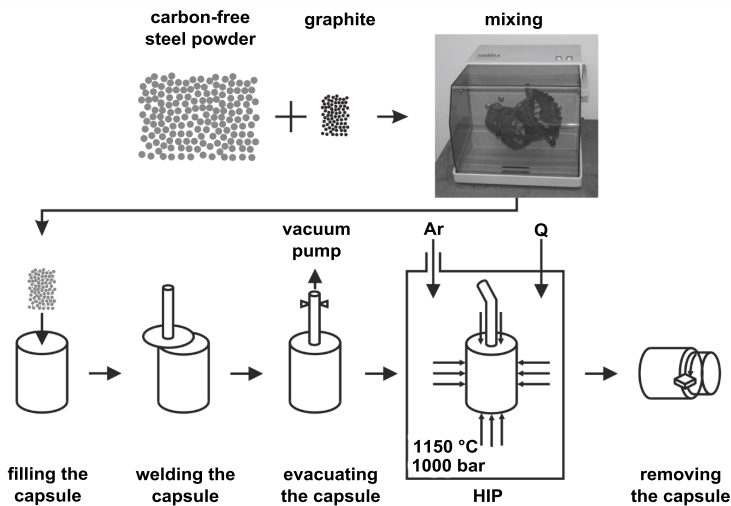


Figure 4. Schematic sequence of diffusion alloying including the HIP process, where Q indicates heat (according to [31]).

Experimental

Heat Treatment. Tempering curves were determined with specimens that were prepared after HIP, austenitised at 1100 °C for 30 minutes and quenched in oil. As indicated in Figure 1, this should lead to a microstructure free of chromium-rich carbides. In conjunction with the information shown in Figure 2, it can be concluded that virtually all the chromium and molybdenum are dissolved in the matrix. Subsequent tempering was conducted sequentially at 150, 200, 300, 400, 450, 500, 520, 540, 560, 580 and 600 °C for two hours each. The Vickers hardness was measured with a load of 294.1 N (HV 30). At least five indents per specimen were measured to enable the calculation of a mean value and a standard deviation.

Wear Tests. The wear resistance was measured using pin-on-grinding paper tests. The specimens were quenched and tempered at the secondary hardness maximum (SHM) to obtain their maximum wear resistance. They were used in the testing rig as a slowly rotating cylinder that was moved along a meandering path across a grinding paper without any overlaps. A schematic illustration of this test is shown in Figure 5, including the area of the specimen (A), the normal

force F_N applied to the specimen, its rotational speed ω and the feed rate v of the grinding paper, ie the table. Flint (SiO_2) with a mesh size of 220 and 80 as well as corundum (Al_2O_3) with a mesh-size of 220 were used as abrasive grinding papers. The mass loss Δm , the density ρ and the length of the wear track l were determined for the calculation of the wear resistance, W_R , using Equation 3. Additionally, scratch tests were performed using the same abrasive for a better understanding of the effective wear mechanisms.

$$W_R = \frac{\rho \cdot A \cdot l}{\Delta m} \quad (3)$$

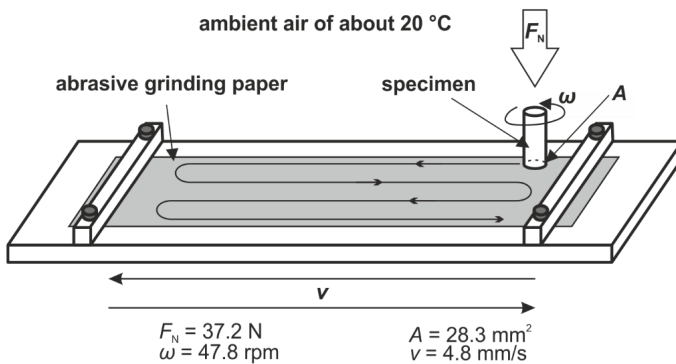


Figure 5. Schematic illustration of the pin-on-grinding paper test. The grinding paper is flint (SiO_2) of mesh size 220 and 80 or corundum (Al_2O_3) with a mesh size of 220. The area A of the specimen is given in the caption as well as the normal force F_N applied to the specimen, the rotational speed ω of the specimen and the feed rate v of the grinding paper (table).

Corrosion Tests. The corrosion resistance was tested in the as-quenched condition for $T_{\text{Aus}} = 1100 \text{ }^\circ\text{C}$. After this heat treatment, a wire was spot-welded onto the rear face of the specimens to provide an electrical contact. The specimens were then embedded in a polymer resin and ground on SiC emery paper of mesh size 1000. To avoid crevice corrosion, the gap between the specimen and the resin was covered with a commercially available lacquer. The exposed conductive surface of the specimens was subsequently measured.

These specimens were used as the working electrode in the corrosion cell. The other components of the cell are a counter electrode of platinum and a calomel reference electrode (Hg_2Cl_2 , +244 mV to the standard hydrogen electrode (SHE)). The latter is inserted in a separate glass vessel that is connected to the cell by a salt bridge that ends in a Haber-Luggin capillary directly in front of the surface of the specimen. A porous frit is used in the salt bridge to avoid contamination by the cell electrolyte. All three electrodes are connected to a potentiostat of type PGP 201 or PGZ 301 (from Voltalab, now Radiometer Analytical) that is connected to a PC. A gas outlet tube is also inserted into the cell. The electrolyte was either 0.5 molar (5%) sulphuric acid (H_2SO_4 , uniform surface corrosion) or 0.6 molar (3%) sodium chloride (NaCl , pitting

corrosion), respectively. The test setup is schematically shown in Figure 6, in which the electrolyte is coloured in grey.

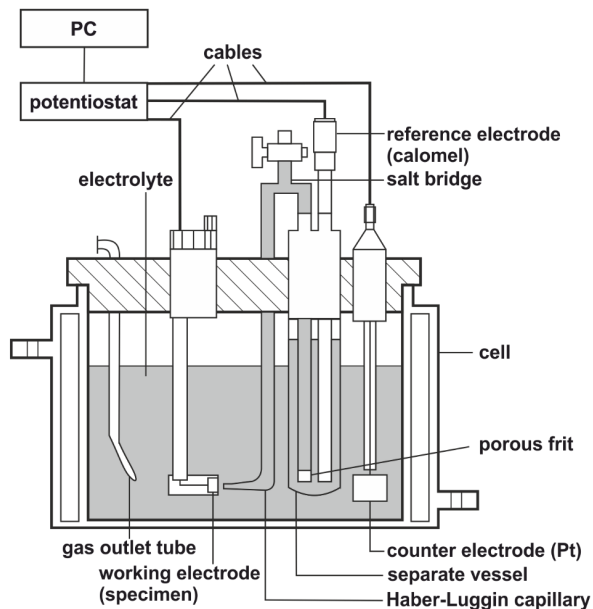


Figure 6. Schematic illustration of the corrosion test setup used to measure potentiodynamic polarisation curves. The electrolyte – either H_2SO_4 or NaCl – is coloured in grey.

Before starting the experiment, the electrolyte was purged with gaseous nitrogen for 30 minutes to remove most of the oxygen. The specimen was then cathodically polarised for 60 seconds at -1 to -1.5 V/SHE to clean the surface and at least to partially eliminate the oxide layer on the surface. This step was followed by the measurement of the open circuit potential (OCP) for 30 minutes. Meanwhile, the oxide layer reformed due to the remaining oxygen in the electrolyte. Subsequently, the potentiodynamic polarisation curve was recorded starting at 10 mV below the OCP with a potential step rate of 600 mV/h. The tests were performed at least twice to confirm reproducibility [33]. The measured potentials are given with respect to SHE. From these curves, different characteristic values were evaluated, such as the passive current density and different passivation potentials for H_2SO_4 and a threshold potential for NaCl indicating pitting corrosion. This latter was evaluated at the potential above which the current density remained higher than $100 \mu\text{A}/\text{cm}^2$ [34,35].

Results and Discussion

Alloy Composition. Preliminary investigations revealed that the calculations based on Thermo-Calc somehow led to incorrect results. Although the target phase field of γ +MC was reached, this was at considerably lower carbon contents than assumed [18]. Thus, the actual corrosion-resistant cold-work tool steel, named PSH1 below, does not contain 1.55 wt.%C, but 1.4 wt.%C. Its composition in wt.% is shown in Table I. All other calculations seem to be valid in the range of this carbon content. The other alloy in this study is a metal matrix composite (MMC) containing PSH1 admixed with 10 vol.%NbC, Table I. This alloy is named MMC in the following. Its carbon content is 1.5 wt.%, which is slightly higher than that of PSH1.

Table I. Composition of the Investigated Alloys (wt.%). Content of admixed NbC (vol.%)

| | Fe | Cr | Nb | Mo | C | N | Mn | Si | Vol.% NbC |
|-------------|------|------|------|-----|-----|-----|-----|-----|-----------|
| PSH1 | bal. | 11.8 | 10.6 | 2.3 | 1.4 | 0.2 | 0.4 | 0.4 | -/- |
| MMC | bal. | 11.8 | 10.6 | 2.3 | 1.5 | 0.2 | 0.4 | 0.4 | 10 |

Hardness and Microstructure. The microstructures of the as-quenched specimens are shown in Figure 7, which were taken with a scanning electron microscope (SEM) type GEMINI LEO 1530 VP. The fine dispersion of NbC that precipitated during diffusion alloying is obvious in PSH1, Figure 7(a). Their diameter is in the range of 1 – 3 μm , which is even smaller than in the hardfacing alloy shown in Figure 3(b). Figure 7(b) shows the microstructure of the MMC with admixed NbC. Although the precipitated NbC are still finely dispersed here, the distribution of the coarser admixed NbC is not totally homogeneous. Their diameter is about 10 μm , ie they are one order of magnitude larger. This should have a positive effect on the wear resistance of this material.

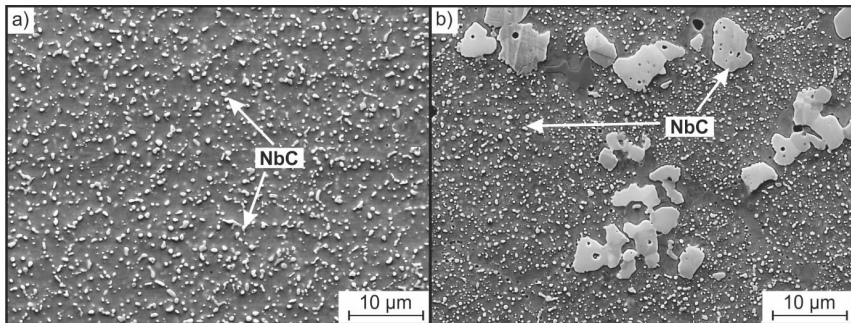


Figure 7. SEM images of the microstructure of; (a) PSH1 and (b) MMC [18] after HIP in the as-quenched condition ($T_{\text{Aus}} = 1100\text{ }^{\circ}\text{C}$). The finely dispersed NbC that precipitated during diffusion alloying have a diameter in the range of 1–3 μm and are thus even smaller than in the hardfacing alloy, Figure 3(b). The admixed NbC in the MMC are considerably larger (about 10 μm in diameter). Their distribution is not totally homogeneous.

Figure 8 shows the tempering curves for both investigated alloys. It is obvious that both reach almost the same hardness after quenching from $T_{Aus} = 1100\text{ }^{\circ}\text{C}$. This seems reasonable with respect to their very similar compositions. The slightly higher hardness of the MMC, ie 730 HV 30 in comparison to 710 HV 30, should be the result of the slightly enhanced carbon content in combination with the admixed NbC. Both steels contain small amounts of RA after quenching. According to Equation 1, its content should increase with increasing carbon content. However, the matrix of MMC might also be slightly depleted in chromium, which could compensate for the higher carbon content [13]. The increase in hardness of PSH1 to 750 HV 30 for tempering at 150 $^{\circ}\text{C}$ could be due to the precipitation of small Fe_2C [36–38]. This could over-compensate the loss in hardness due to tempering at low temperatures, by a decrease in the internal stresses [1].

Both steels exhibit a SHM at 520 $^{\circ}\text{C}$ that is associated with the high amount of molybdenum and chromium dissolved in the metallic matrix [13]. In this case, the PSH1 reaches 700 HV 30 and the MMC reaches 770 HV 30. The SHM of the MMC is considerably more pronounced owing to its higher carbon content. This increase in hardness can be explained by the precipitation of M_2C that is rich in chromium and molybdenum [39]. Niobium does not contribute to the SHM due to its low solubility in the steel matrix [6,7].

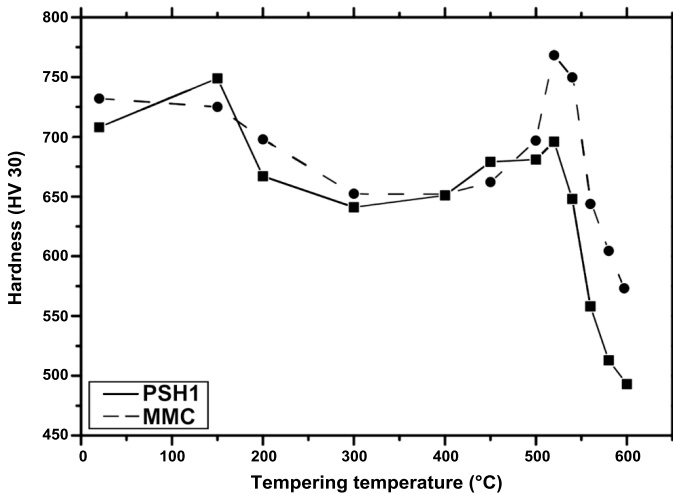


Figure 8. Tempering curves for the two investigated alloys PSH1 and MMC in the range from room temperature to 600 $^{\circ}\text{C}$ for hardening from 1100 $^{\circ}\text{C}$. The as-quenched hardness of both steels is comparable. The SHM is reached for tempering at 520 $^{\circ}\text{C}$ with MMC and achieves a higher hardness than PSH1.

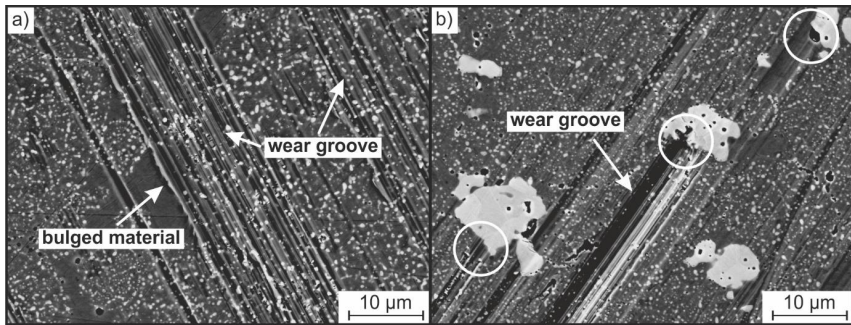


Figure 9. SEM images of worn surfaces of a) PSH1, b) MMC after scratch tests with flint 220. The wear grooves and bulged material at the edge of the grooves are obvious in PSH1. In the MMC, sections of the wear groove indicated by circles show where the abrasive particles were stopped or deflected.

Wear Resistance. Figure 9(a) shows a SEM image of a worn surface of PSH1 after a scratch test against flint 220. The wear groove caused by the abrasive is obvious. In PSH1, the precipitated NbC are the only hard phases in the microstructure. These are much smaller than the abrasive grains and are thus chipped out with the matrix, which is in good agreement with the findings of Axén and Zum Gahr [40]. Whereas the main wear mechanism is micro-cutting, the edges of the groove show very little micro-ploughing, as indicated by bulged material. The precipitated NbC do efficiently support the matrix in a way that the wear grooves are reduced. This view is corroborated by areas that do not contain NbC in which the wear grooves appeared to be deeper and wider, indicating their positive influence due to two-phase hardening of the matrix [13,18]. This can also be explained by a theory proposed by Axén and Zum Gahr, who correlated a decrease in abrasion with a decrease in the free matrix length between carbides [40]. This in turn correlates with a decrease in size and an increase in the number of hard phases [13], both of which are favoured by the manufacturing route performed for the steels in this study, ie diffusion alloying. Some parts of the wear groove indicate that the NbC grooved the abrasive flint particles [13,18]. Because the hardness of flint is considerably lower than that of NbC, this is in good agreement with [40].

The SEM image in Figure 9(b) depicts the effect of admixed niobium carbides on the wear behaviour of the MMC in a scratch test against flint 220. Even though the admixed NbC in this part of the microstructure are somehow smaller than those in Figure 7, they are able to stop or at least deflect the abrasive flint particles, which is indicated by circles in the image. Obviously, this leads to reduced dimensions of the wear grooves in comparison to those in PSH1. This can be correlated with the increased size of the hard phases, which leads to a change in the mechanism of wear protection from matrix hardening to deflecting the wear path [13,18]. Sometimes the large admixed carbides are broken due to micro-cracking. This might be explained by the minor support of the matrix that is actually soft in comparison to the NbC. This can cause plastic deformation at the edges of the large NbC, which leads to cracks due to their low toughness [13]. The addition of NbC to PSH1 thus leads to a far better resistance against coarse abrasive wear, which opens other fields of applications for this alloy [18].

In general, both alloys show the highest wear resistance against flint 220, followed by flint 80 and corundum 220 [13,18]. The considerably larger particles of flint 80 have a negative influence on the wear resistance, especially for the MMC. This is because the effect of larger carbides decreases with increasing abrasive particle size. For PSH1, the wear rate remains almost constant because the size of the abrasive particles in flint 220 is already much larger than that of the precipitated NbC. Thus, no further degradation is observed [13]. The abrasive wear of corundum is lowered but not stopped, as shown for flint 220. Many of the admixed NbC show crack networks and most of them are subject to micro-cutting. Some NbC are even gouged out of the matrix. This is in agreement with [40] because the hardness of corundum and NbC is similar.

One possible application for corrosion-resistant cold-work tool steels such as the PSH1 and the MMC in this study is for processing of polymers [13]. Here, abrasion is the main wear mechanism. Naturally, the actual wear behaviour in a certain application and in an experiment differs for several reasons. Additionally, the pin-on-grinding paper test does not include inter-dependencies such as corrosion or tribochemical reactions. However, the results of PSH1 and MMC were compared to those obtained with other alloys subjected to the same testing procedure. This is shown in Figure 10 for the alloys 1.4112 (X90CrMoV18, AISI 440B), Böhler M390 (X190CrVMo20-4-1), 1.2379 (X155CrVMo12-1, AISI D2) and Ni-Hard IV (G-X300CrNiSi9-5-2, EN-JN2049) for testing against flint 80. All materials were tested in the quenched and tempered condition, for which they reach their maximum wear resistance. The 1.4112 alloy is a conventionally cast corrosion-resistant cold-work tool steel containing coarse chromium-rich carbides. Böhler M390 is a powder metallurgical corrosion-resistant tool steel containing a high amount of chromium-rich carbides together with 2-3 vol.% VC that are finely dispersed in the martensitic matrix. The 1.2379 alloy is not corrosion-resistant but is only a wear-resistant cold-work tool steel containing coarse chromium-rich, as well as vanadium-rich carbides. Ni-Hard IV is a white cast iron with a high wear resistance due to its high hardness and coarse chromium-rich carbides. It is obvious that the PSH1 almost reaches the level of the common comparable alloy M390 [18,41]. However, the wear resistance of the MMC is superior to all other tested alloys [2].

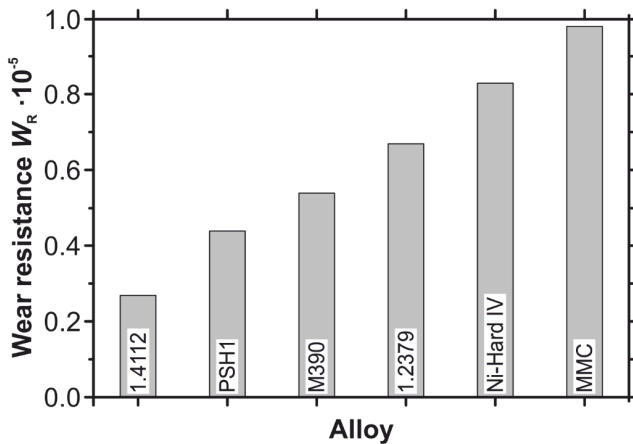


Figure 10. Comparison of the wear resistance W_R of PSH1 and MMC with 1.4112 (X90CrMoV18, AISI 440B), Böhler M390 (X190CrVMo20-4-1), 1.2379 (X155CrVMo12-1, AISI D2) and Ni-Hard IV (G-X300CrNiSi9-5-2, EN-JN2049). Whereas W_R of PSH1 is slightly below the level of the comparable corrosion-resistant cold-work tool steel M390, the MMC is superior to all other tested alloys, including the white cast iron Ni-Hard IV. All alloys were quenched and tempered at the SHM to obtain their maximum wear resistance.

Corrosion Resistance. Figure 11 shows representative potentiodynamic polarisation curves of the tested alloys (PSH1: solid line, MMC: dashed line) in comparison with the Böhler M390 (grey dotted line). This steel was quenched from 1150 °C as is standard in the industry. Figure 11(a) shows that the passive current density, ie the lowest current density in the plateau region, is below $10 \mu\text{A}/\text{cm}^2$ and thus much lower than that of M390 (about $50 \mu\text{A}/\text{cm}^2$). This indicates a high resistance to uniform surface corrosion. The passivation potential, represented by the first peak, and the OCP are almost the same for all three steels. The second peak in the curve of the M390 at about 200 mV/SHE is suggested to be the potential at which the matrix close to chromium-rich carbides is corroded because its chromium content is lower than that of the surrounding matrix [10,11]. This peak is missing for PSH1 and MMC because they do not contain any chromium-rich carbides. The small peak at about 600–700 mV/SHE is ascribed to corrosion of the mono-carbides, ie VC in M390 and NbC in PSH1 and MMC [12,42–45]. This peak appears for all three steels because they all contain such carbides. The transpassive region, represented by the sudden increase in current density at high potentials [12], of PSH1 and MMC starts at a considerably higher potential than that of M390 [41,42]. In combination with the missing second peak, this leads to a broad passive region between the passivation potential and the transpassive region. This is said to be favourable for a high corrosion resistance [42,46]. Thus the positive effect of NbC on the corrosion resistance of the newly developed steels is obvious from the measured curves.

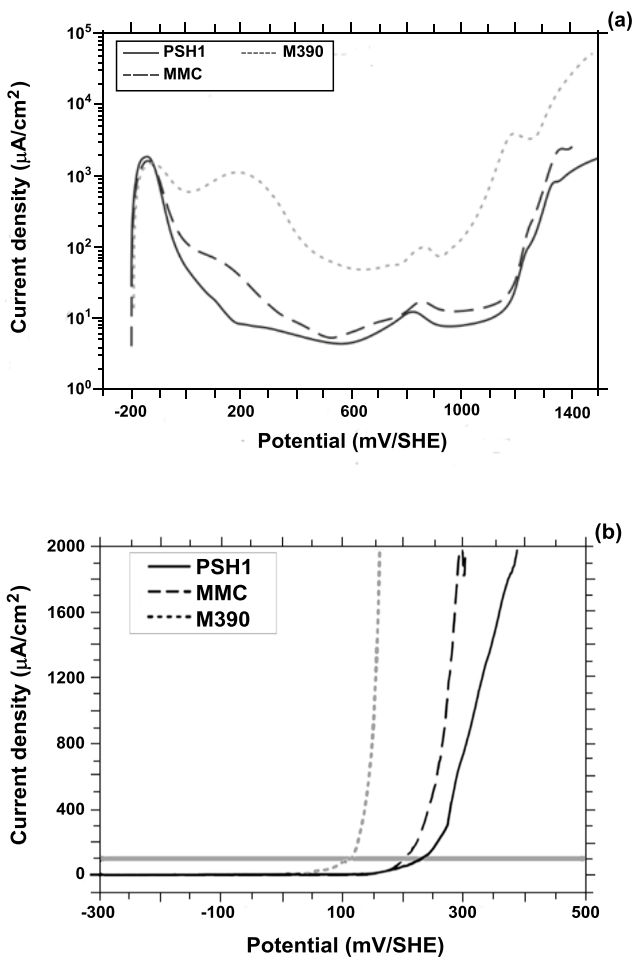


Figure 11. Representative potentiodynamic polarisation curves for PSH1 (solid line) and MMC (dashed line) in comparison with Böhler M390 (grey dotted line); (a) in H_2SO_4 and (b) in NaCl . PSH1 and MMC were quenched from $1100\text{ }^\circ\text{C}$, whereas T_{Aus} was $50\text{ }^\circ\text{C}$ higher for the M390 as in the standard in the industry. Figure 11(a) shows that the current density of the plateau region is considerably lower for PSH1 and MMC than for M390. Additionally, the plateau is broader. Both aspects indicate a better corrosion resistance for the newly developed steels. Figure 11(b) shows that PSH1 has the highest resistance against pitting corrosion followed by MMC and M390.

The corrosion behaviour in sulphuric acid is of interest for applications in the polymer industry. However, these steels could also be used in sea water environments as shown in the potentiodynamic polarisation curves measured in NaCl in Figure 11(b). The horizontal line at $100 \mu\text{A}/\text{cm}^2$ represents the threshold value defined above. Obviously, the common steel M390 shows the lowest corrosion resistance because the steep increase in current density, which indicates the onset of pitting corrosion, is located at the least noble potential (about 105 mV). It is followed by MMC (≈ 200 mV) and PSH1 (≈ 230 mV), where the latter shows a slightly nobler potential than the former. However, the steep increase of the curves starts at much lower potentials than in H_2SO_4 . This can be attributed to the pitting corrosion mechanism, which is much more sensitive to chromium depletion and inhomogeneities than uniform surface corrosion [24,47,48].

This behaviour is generally consistent with theory. The M390 is more prone to pitting corrosion owing to its lower molybdenum content, which is regarded as being especially effective in preventing pitting [15,17,49]. Additionally, the chromium-rich carbides lead to zones depleted of chromium, which act as starting points for pitting corrosion [10,11]. The difference between the pitting behaviour of PSH1 and MMC is small, but worthy of note. Since the matrix composition of both steels is the same, this difference has to be attributed to the admixed NbC. These are about one order of magnitude larger than the precipitated ones. As mentioned above, pitting corrosion in general is sensitive to inhomogeneities. This increases with increasing size of the inhomogeneities [50]. Thus, the MMC is more prone to pitting than PSH1.

Martensitic Stainless PM Bearing Steels for Extreme Loading and Lubrication Conditions

Development

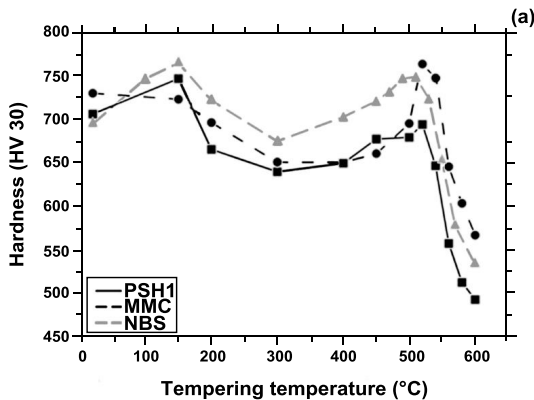
The new steels discussed above contain at least 10 vol.% carbides. This is not favourable for most bearing steels. One of the standard bearing steels is 1.3505 (100Cr6, AISI 52100), which contains about 2–3 vol.% after an adequate heat treatment. These are beneficial for the wear resistance in bearing lifetime tests [51]. Thus, the aim is to develop new steels with a carbide content of below 5 vol.%. However, as mentioned above, manufacturing by means of diffusion alloying allows almost arbitrary adjustment of the carbide content of PSH1 to the required value. Thus, a steel of similar composition to PSH1, but with a considerably lower amount of niobium would be an appropriate bearing steel. For a higher resistance to sea water, which can be simulated with NaCl [33], Equation 2 indicates that more chromium and molybdenum should be useful. However, because both elements stabilise ferrite, additional elements are required for the stabilisation of austenite. The newly developed steel is designated below as NBS (new bearing steel). The hardness of bearing steels has to be higher than 650 HV. The fine dispersion of carbides together with the generally fine microstructure of a PM steel should be beneficial for this application, not least for the necessary hot working processes in manufacturing. The final composition of the investigated steel is not given here for reasons of confidentiality.

Experimental

The experimental work was performed in accordance with the work described above, but in addition, the steel was forged after HIP. However, the heat treatment had to be adjusted to the new steel resulting in a slightly higher T_{Aus} , as well as slightly different tempering temperatures. The hardness was measured for several T_{Aus} and carbon contents. This led to the final adjustment of the desired carbon content and thus the amount of carbides, which is again not given here. A high resistance to abrasive wear is beyond the scope of most bearing steels. Thus, no wear tests were performed. However, tribocorrosion tests might be of interest for the NBS. Of course, the alloying concept could be favourable for wear-resistant bearing steels, eg for highly grease-lubricated bearings in heavily contaminated environments, such as those that apply for bucket-wheel excavators.

Results and Discussion

Hardness and Microstructure. Figure 12(a) shows a tempering curve of the NBS (grey dashed line) after quenching from an adequate T_{Aus} in comparison to PSH1 (solid line) and MMC (black dashed line). The hardness is in the range of that of PSH1 and MMC and even slightly above it. Thus, the hardness of the NBS considerably exceeds the required value of 650 HV. Good corrosion resistance should be obtained for tempering at low temperatures, ie up to 200 °C [52], whereas tempering at the SHM (at 520 °C) should increase the wear resistance. Figure 12(b) shows the microstructure of the NBS. The only carbides are NbC and their amount is obviously reduced compared to PSH1 and MMC, Figure 7. Some carbides seem to be accumulated and elongated in the vertical direction. This is due to the forging process, which elongates the carbides in the forging direction. In addition, the NbC is finely dispersed in the martensitic matrix. The black spots in the matrix are oxides and not pores.



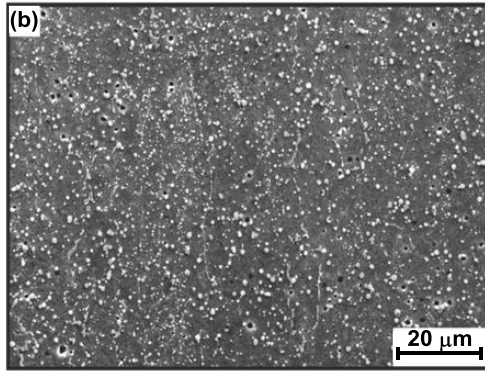


Figure 12. (a) Tempering curve of NBS (grey dashed line). Its hardness is in the range of that of PSH1 (solid line) and MMC (black dashed line) and well above 650 HV. (b) Microstructure of the new bearing steel. As intended, the content of NbC is reduced in comparison to PSH1 and MMC.

Corrosion Resistance. Figure 13 shows representative potentiodynamic polarisation curves of the NBS (grey dashed line) in comparison to those curves already shown in Figure 11. Obviously, its corrosion resistance is higher than that of the common steel M390, but lower than that of PSH1 and MMC. The curve shows a peak at about 200 mV/SHE indicating chromium-rich carbides in the matrix. It might also be attributable to chromium depletion around the oxides found in the matrix, Figure 12(b). Whereas those shown above are fairly small, considerably larger oxides (20–30 μm) were also found to some extent. These need to be addressed upon moving from the current model alloy to industrially applicable material. These could also be detrimental for the general corrosion resistance, ie the higher passive current density of the plateau region [53]. The passivation peak of the NbC at about 600–700 mV/SHE is missing or is only indistinct. This might be due to the lower amount of NbC than in PSH1 and MMC, in combination with the higher passive current density. However, the plateau is still broader than that of the M390, indicating a better corrosion resistance [42,46]. Furthermore, the corrosion resistance of the NBS is higher than that of the other tested alloys (≈ 260 mV). This can be attributed to the higher amount of chromium and molybdenum in this steel, in comparison to PSH1 and MMC [15,17,49]. However, the difference is comparatively small with respect to the differences in the contents of chromium (2 wt.%) and molybdenum (1 wt.%). This might be attributable to the existence of oxides in the NBS, which additionally lower the resistance to pitting corrosion [53]. Thus, the amount of oxides in the NBS has to be lowered to further improve its corrosion resistance. This would also be beneficial for the bearing lifetime with regard to improved wear resistance.

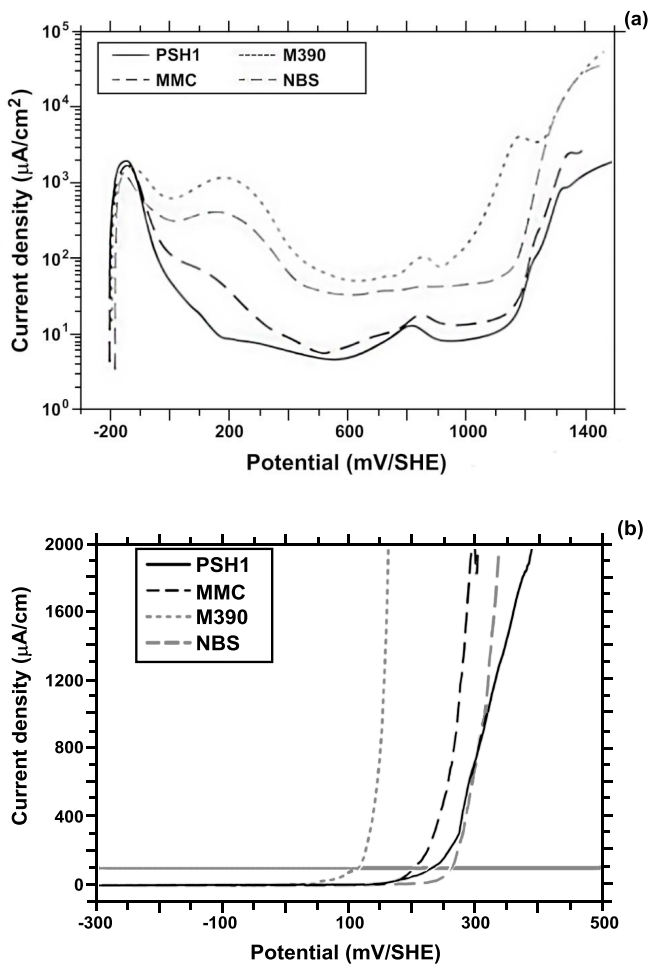


Figure 13. Representative potentiodynamic polarisation curves for NBS (grey dashed line) compared to the curves shown in Figure 11; (a) in H₂SO₄ and (b) in NaCl. The NBS was tested in the as-quenched condition that is comparable to the other three steels. In H₂SO₄, the corrosion resistance of the NBS is higher than that of M390, but lower than that of PSH1 and MMC. In NaCl the NBS shows the highest corrosion resistance of all four alloys.

Conclusions

The present study deals with the development of corrosion-resistant tool steels for the polymer and bearing industries. Diffusion alloying is introduced as a new way of manufacturing niobium-rich steels. The main conclusions are:

1. Diffusion alloying can be used to produce niobium-rich steels without huge primary NbC in the microstructure. In fact, a fine dispersion of NbC with a size of about 1-3 μm will result after HIP.
2. With diffusion alloying, the content of hard phases can be almost arbitrarily adjusted by admixing different amounts of carbon. Thus, steels with a high corrosion resistance, as well as a high wear resistance can be produced from the same steel powder. Furthermore, a metal matrix composite can easily be produced by admixing additional hard phases such as NbC.
3. The highest corrosion resistance is expected for quenching from the γ +MC phase field because the NbC contains only small amounts of chromium and molybdenum, which thus remain dissolved in the matrix.
4. All investigated steels show a high hardness and wear resistance. The resistance of the MMC against coarse abrasives is even higher than that of the white cast iron Ni-Hard IV.
5. The resistance of all investigated steels against uniform surface corrosion and pitting corrosion is considerably higher than that of a comparable common steel.
6. The development of a corrosion-resistant powder-metallurgical bearing steel containing NbC was possible by adjusting the alloying system. The hardness and corrosion resistance of this steel seem to be promising for possible applications in sea water environments, although further development is necessary.

Acknowledgements

Parts of this contribution were financed by the industrial partner Böhler Edelstahl GmbH & Co KG. Others were part of a joint research project (reference no. 03ET1072D) funded by the Federal Ministry for Economic Affairs and Energy. The authors gratefully acknowledge financial support by the BMWi.

References

1. H. Berns and W. Theisen, *Ferrous Materials – Steel and Cast Iron* (Springer Verlag, 2008).
2. W. Theisen, S. Siebert and S. Huth, “Wear Resistant Steels and Casting Alloys Containing Niobium Carbide,” *Steel Research International*, 78 (12) (2007), 921-928.
3. W. Theisen, *Bearbeiten verschleißbeständiger Legierungen aus werkstofftechnischer Sicht* (VDI, Düsseldorf, 1997).

4. H. Berns, ed, *Hartlegierungen und Hartverbundwerkstoffe: Gefüge, Eigenschaften, Bearbeitung, Anwendungen* (Springer Berlin Heidelberg, 1998).
5. G.C. Coelho, J.A. Golczewski and H.F. Fischmeister, "Thermodynamic Calculations for Nb-containing High-speed Steels and White-cast-iron Alloys," *Metallurgical and Materials Transactions A*, 34A (2003), 1749-1758.
6. F. Heisterkamp and S.R. Keown, "Niobium in High-speed Tool Steels," *Processing and Properties of High Speed Tool Steels: Proceedings of a Symposium by the Ferrous Metallurgy Committee of The Metallurgical Society of AIME at the 109th AIME Annual Meeting*, ed M.G.H. Wells and L.W. Lherbier (Las Vegas, NV: The Metallurgical Society of AIME, 1980), 104-123.
7. S. Karagöz and H.F. Fischmeister, "Niobium-alloyed High-speed Steel by Powder-metallurgy," *Metallurgical Transactions A*, 19 (6) (1988), 1395-1401.
8. C. Kerschenbauer et al., "PM Plastic Mould Steels," *The Use of Tool Steels: Experience and Research: Proceedings of the 6th International Tooling Conference*, ed J. Bergström et al., (Karlstad University, Motala Grafiska AB, Motala, 2002), 293-301.
9. DIN EN 10088: "Nichtrostende Stähle," Beuth Verlag, 2005.
10. H. Schüller, P. Schwaab and W. Schwenk, "Die Potentialabhängigkeit der interkristallinen Korrosion eines angelassenen austenitischen Chrom-Nickel-Stahls," *Archiv für das Hüttenwesen*, 33 (12) (1962), 853-862.
11. A. Bäumel et al., "Deutung der Ursachen der interkristallinen Korrosion von nichtrostenden Stählen in Zusammenhang mit der Chromverarmungstheorie," *Corrosion Science*, 4 (4) (1964), 89-103.
12. G. Herbsleb, "Der Einfluß von Legierungselementen auf das Passivierungsverhalten nichtrostender Stähle," *VDI-Zeitschrift*, 123 (12) (1981), 505-511.
13. S. Huth, N. Krasokha and W. Theisen, "Development of Wear and Corrosion Resistant Cold-work Tool Steels Produced by Diffusion Alloying," *Wear*, 267 (2009), 449-457.
14. R.F.A. Jargelius-Petterson and B.G. Pound, "Examination of the Role of Molybdenum in Passivation of Stainless Steels Using AC Impedance Spectroscopy," *Journal of the Electrochemical Society*, 145 (5) (1998), 1462-1469.
15. J.N. Wanklyn, "The Role of Molybdenum in the Crevice Corrosion of Stainless Steels," *Corrosion Science*, 21 (3) (1981), 211-225.
16. M. Urquidi and D.D. Macdonald, "Solute-vacancy Interaction Model and the Effect of Minor Alloying Elements on the Initiation of Pitting Corrosion," *Journal of the Electrochemical Society*, 132 (3) (1985), 555-558.

17. R.C. Newman, "The Dissolution and Passivation Kinetics of Stainless Alloys Containing Molybdenum - II. Dissolution Kinetics in Artificial Pits," *Corrosion Science*, 25 (5) (1985), 341-350.
18. S. Huth, "Entwicklung neuer pulvermetallurgischer Stähle für Anwendungen unter Verschleiß- und Korrosionsbeanspruchung" (Ph.D. thesis, Ruhr-Universität Bochum, 2009).
19. W. Theisen et al, "Verschleißbeständiger Werkstoff," Austrian Patent No. AT 507 215 B1 2010-03-15, (2009), held by Böhler Edelstahl GmbH & Co KG.
20. K.W. Andrews, "Empirical Formulae for the Calculation of Some Transformation Temperatures," *Journal of the Iron and Steel Institute*, 203 (7) (1965), 721-727.
21. C.Y. Kung and J.J. Rayment, "An Examination of the Validity of Existing Empirical Formulae for the Calculation of Ms Temperature," *Metallurgical and Materials Transactions A*, 13A (1982), 328-331.
22. N. Krasokha and H. Berns, "Study on Nitrogen in Martensitic Stainless Steels: Studie über Stickstoff in Martensitischen Rostfreien Stählen," *HTM*, 66 (3) (2011), 150-164.
23. V. Raghavan, "C-Fe-Nb (Carbon-Iron-Niobium)," *Journal of Phase Equilibria*, 24 (1) (2003), 57-61.
24. J.N. Bernauer, "Einfluss von Kohlenstoff als Legierungselement in stickstofflegierten Chrom-Mangan-Stählen" (Ph.D. thesis, ETH Zürich, 2004).
25. J.N. Bernauer (2004) Einfluss von Kohlenstoff als Legierungselement in stickstofflegierten Chrom-Mangan-Stählen, Zürich.
26. S. Huth and W. Theisen, "High Nitrogen PM Tool Steels Containing Niobium," *Proceedings of 10th International Conference on High Nitrogen Steels*, ed A.G. Svyazhin, V.G. Prokoshkina and K.L. Kosyrev (MISIS, Moscow, 2009), 90-95.
27. V.G. Gavriljuk and H. Berns, *High Nitrogen Steels: Structure, Properties, Manufacture, Applications* (Springer Berlin, 1999).
28. F. Jeglitsch, "Niobium in Tool Steels and Cemented Carbides," *Niobium Science and Technology: Proceedings of the International Symposium Niobium 2001*, ed Niobium 2001 Limited (Orlando, FL, 2001), 1001-1039.
29. T. Schneiders, "Neue pulvermetallurgische Werkzeugstähle" (Ph.D. thesis, Ruhr-Universität Bochum, 2005).
30. H. Berns, "Verfahren zur Herstellung von PM-Hartlegierungen (Process for the Production of PM Hard Alloys)," German Patent No. DE 42 35 148 C1 (1992).

31. S. Huth, "Entwicklung neuer pulvermetallurgischer Stähle für Anwendungen unter Verschleiß- und Korrosionsbeanspruchung" (oral presentation of Ph.D. thesis, Ruhr-Universität Bochum, 2009).
32. S. Huth et al., "Oxide Reduction during Carburization Nb-rich Tool Steel Powders for Diffusion Alloying," *Euro PM: Congress & Exhibition*, ed European Powder Metallurgy Association (Shrewsbury, 2012), 507-512.
33. DIN 50905-1: "Korrosionsuntersuchungen - Grundsätze," Beuth Verlag, 1987.
34. ASTM International G 150-99: "Standard Test Method for Electrochemical Critical Pitting Temperature Testing of Stainless Steel," ASTM, 2006.
35. M. Vayer, I. Reynaud and R. Erre, "XPS Characterisations of Passive Films Formed on Martensitic Stainless Steel: Qualitative and Quantitative Investigations," *Journal of Materials Science*, 35 (35) (2000), 2581-2587.
36. D. Peckner and I.M. Bernstein, *Handbook of Stainless Steels* (McGraw-Hill, New York, 1977).
37. H. Berns, G. Siekmann and I. Wiesenecker, "Gefüge und Bruch vergüteter Federstähle: Gefüge und Bruchmorphologie," *Draht*, 35 (5) (1984), 247-252.
38. H.K.D.H. Bhadeshia and R.W.K. Honeycombe, *Steels: Microstructure and Properties*, (Elsevier/Butterworth-Heinemann, Amsterdam, 2006).
39. H.F. Fischmeister, S. Karagöz and H. André, "An Atom Probe Study of Secondary Hardening in High Speed Steels," *Acta Metallurgica*, 36 (4) (1988), 817-825.
40. N. Axén and K. Zum Gahr, "Wear of TaC and TiC Steel Composite Hardfacings by Soft and Hard Abrasives," *Materialwissenschaft und Werkstofftechnik*, 23 (10) (1992), 360-367.
41. S. Huth et al., "Novel Corrosion- and Wear-resistant PM Plastic Mould Steels Containing NbC," *Proceedings of the 8th International Tooling Conference: Tool Steels - Deciding Factor in Worldwide Production*, ed P. Beiss et al. (Aachen, Verlag Mainz, Wissenschaftsverlag, 2009), 425-435.
42. S. Huth, H. Hill and W. Theisen, "Corrosion of Stainless PM Tool Steels: Interpretation of Current Density Potential Curves in Acid Environments," *HTM*, 65 (4) (2010), 195-200.
43. S. Süry and T. Geiger, "Einfluß der Wärmebehandlung auf den Verlauf der Stromdichte-Potential-Kurven bei einem 13%-igen Chromstahlguss," *Werkstoffe und Korrosion*, 20 (8) (1969), 665-672.

44. A. Sehgal, B.G. Ateya and H.W. Pickering, "Hydrogen Evolution and Absorption within Grain Boundary Grooves in Sensitized Stainless Steel under Condition of Anodic Polarization," *Journal of the Electrochemical Society*, 142 (10) (1995), L198-L200.
45. W.K. Kelly, R.N. Iyer and H.W. Pickering, "Another Grain Boundary Corrosion Process in Sensitized Stainless Steel," *Journal of the Electrochemical Society*, 140 (11) (1993), 3134-3140.
46. H. Kaesche, *Corrosion of Metals: Physicochemical Principles and Current Problems* (Springer Verlag, 2003).
47. H.J. Cleary and N.D. Greene, "Corrosion Properties of Iron and Steel," *Corrosion Science*, 7 (7) (1967), 821-831.
48. Y. Tan, "Understanding the Effects of Electrode Inhomogeneity and Electrochemical Heterogeneity on Pitting Corrosion Initiation on Bare Electrode Surfaces," *Corrosion Science*, 53 (5) (2011), 1845-1864.
49. P. Schmuki, "From Bacon to Barriers: A Review on the Passivity of Metals and Alloys," *Journal of Solid State Electrochemistry*, 6 (2002), 145-164.
50. G.T. Burstein and G.O. Ilevbare, "The Effect of Specimen Size on the Measured Pitting Potential of Stainless Steel," *Corrosion Science*, 38 (12) (1996), 2257-2265.
51. H.K.D.H. Bhadeshia, "Steels for Bearings," *Progress in Materials Science*, 57 (2) (2012), 268-435.
52. M. Seifert et al., "Corrosion Properties of a Complex Multi-phase Martensitic Stainless Steel Depending on the Tempering Temperature," accepted for publication in: *Materials and Corrosion*, DOI:10.1002/maco.201508229.
53. E. Klar and P. Samal, *Powder Metallurgy Stainless Steels: Processing, Microstructures, and Properties* (Materials Park, OH: ASM International, 2007).

MODERN PRE-HARDENED TOOL STEELS

P. Hansson

SSAB Special Steels, Oxelösund, Sweden

Keywords: Tool Steel, Mould, Manufacturing Time, Milling, Surface Engineering, Nitriding

Abstract

Traditional pre-hardened tool steel has been available in the market for decades and is commonly delivered to hardness levels up to approximately 380 HBW (40 HRC). Clean steel manufacturing has seen rapid development during recent decades and has, in combination with improvements in hard machining, provided steel producers the option to design and manufacture very clean pre-hardened engineering and tool steels. This has led SSAB to develop a family of new pre-hardened steels, Toolox, which utilise clean steelmaking practice to minimize inclusion content and continuous casters equipped with soft reduction to control and minimize segregation levels. These modern tool steels are delivered at nominal hardness levels in the range 300 to 450 HBW. The Toolox grades are also microalloyed with niobium to control austenite grain size during heat treatment steps and thereby control and increase the steel impact toughness.

The Toolox grades show very high dimensional stability in machining which enables higher cutting speeds to be used when compared with traditional steels of equivalent hardness and strength. Mould and die making, as well as engineering component manufacturing, are thereby simplified, since there is no need for additional heat treatments which results in reduced lead times and costs.

Additionally, use of effective heat treatment facilities enables the steel producer to choose lean chemistries for the target hardness level. The new chemical compositions provide benefits such as enhanced ductility, high thermal conductivity and improved machinability. Furthermore, such new steels are suitable for surface engineering to develop the desired mould surface properties.

Examples are given in this paper showing the advantages of using the Toolox steels, compared to conventional grades for machining operations, and a model is introduced for determining relative life spans of components subject to wear, depending on the hardness regimes of the interacting bodies. This allows, for example, the determination of the required steel surface hardness to minimize the effect of wear on moulds.

Introduction

Tool steel is essentially a wear resistant steel having a different set of properties compared with grades commonly used in earth moving/mining applications, etc. The main difference is whether the steel grades are developed to possess good welding properties, or developed to have good machinability and very high dimensional stability in the machining operation. Tool steels also require very high cleanliness to enhance their polishing properties. Inclusions have to be kept below 25 microns in size while keeping the area fraction of inclusions as low as possible. Figure 1 gives a summary of different applications/required steel properties.

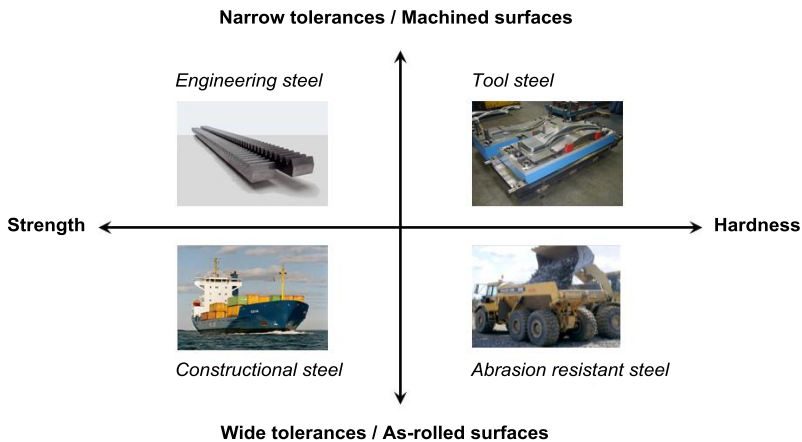


Figure 1. Common steel grade application areas.

Abrasion resistant steels commonly have low alloy contents and are tempered at low/intermediate temperatures to enhance their welding and toughness properties and are usually not suitable in applications exposed to elevated temperatures. However, the newly developed pre-hardened tool steels, Toolox, also offer attractive properties at elevated temperatures. These grades can be used at temperatures up to 590 °C without back-tempering, making them attractive as regular abrasion resistant steels in components which face abrasive wear at elevated temperatures, ie coking plants, slag handling buckets, etc.

When manufacturing, moulds having a surface hardness above approximately 380 HBW/ 40 HRC, soft-annealed tool steels are traditionally the common choice. Depending on which kind of plastic is being moulded, the mould is generally heat treated to a hardness of 45-55 HRC. This heat treatment is not only time consuming, but also generates dimensional distortions due to the phase transformations which take place during the thermal cycle, which have to be corrected after the final heat treatment. Furthermore, the risk for cracks occurring in the mould during quenching must be taken into account.

Modern pre-hardened tool steels, Toolox 33 (300 HBW), Toolox 40 (380 HBW) and Toolox 44 (450 HBW/~45 HRC), offer two major advantages:

- Shorter lead times are possible from ordering of a mould until its delivery;
- The mould has known mechanical properties.

These points arise as there is no need for heat treatment during the mould/die manufacturing and that SSAB issues a certificate showing the exact mechanical properties for each plate produced.

Steel Production and Chemical Composition

Steel shops equipped with effective secondary metallurgy can produce super-clean liquid steel, ie very low levels of tramp elements, in combination with extremely low inclusion contents. The critical part in the steel production cycle is the solidification phase of the liquid steel which needs to be controlled so as not to ruin the steel properties. Continuous casters equipped with integrated controlled-soft-reduction zones, enable very tight control of the steel solidification. The centreline segregation, commonly occurring in conventional casters, can be eliminated when a modern casting machine is used [1]. Figure 2 shows results where slabs of high-sulphur steel have been cast with/without Controlled Soft Reduction (CSR). These trials clearly show the potential of CSR to counter the movement of interdendritic liquid and thus inhibit macro-segregation.

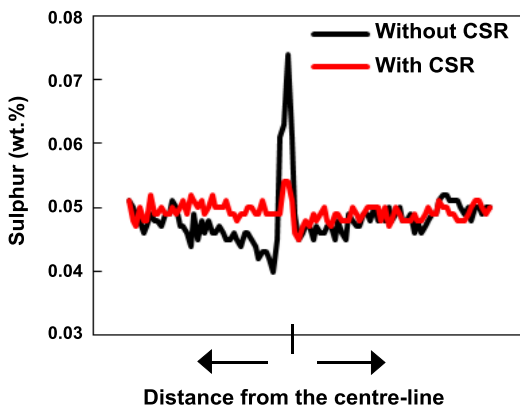


Figure 2. Sulphur segregation at slab centreline.

Furthermore, the steel melting shop has to protect the liquid steel from atmospheric exposure during the casting sequence in order to avoid oxygen pick-up. Protection of the casting is, in this case, by the use of ceramic tubes in the tapping sequence, from ladle into tundish and from tundish into mould, which guarantees an extremely low inclusion content in the solidified steel. The Toolox grades given in Figure 3 are cast with the use of a protected casting system.

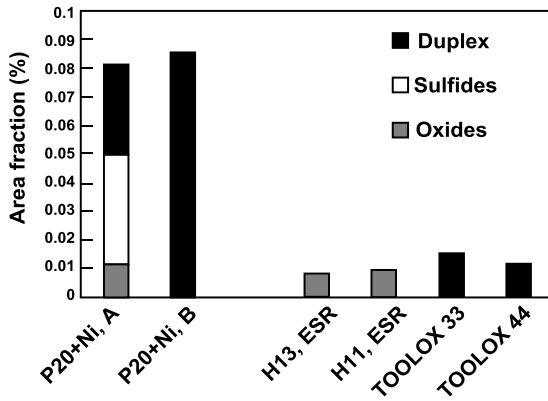


Figure 3. Steel inclusion contents, plate centre position.

Effective heat treatment facilities enable the steel producer to choose leaner chemical compositions when designing pre-hardened steels. When compared with traditional tool steels of equal hardness, P20, P20HH and H13, see Table I and II, the pre-hardened new type steel grades have very lean chemical compositions, which is beneficial to thermal conductivity. In this comparison, the maximum sulphur and phosphorus contents permitted for Superior H13 have been chosen. The Toolox grades are also microalloyed with niobium to control the austenite grain size during the heat treatment steps and thereby control and increase the steel impact toughness. The Superior H13 is normally delivered in the ESR-remelted condition, ie having microsegregation and cleanliness levels comparable with CSR-cast steel, see also Figure 3.

Table I. Typical Chemical Compositions. (wt.%)

| | Toolox 33 | Toolox 40 | P20/P20HH |
|----|------------------|------------------|------------------|
| C | 0.23 | 0.28 | 0.38 |
| Si | 1.10 | 1.15 | 0.30 |
| Mn | 0.80 | 0.60 | 1.45 |
| S | ≤0.002 | ≤0.002 | ≤0.035 |
| P | ≤0.010 | ≤0.010 | ≤0.035 |
| Cr | 1.20 | 1.22 | 2.0 |
| Mo | 0.30 | 0.50 | 0.20 |
| Ni | - | 0.70 | - |
| Nb | 0.015 | 0.015 | |
| V | 0.10 | 0.12 | - |

Table II. Typical Chemical Compositions. (wt.%)

| | Toolox 44 | H13 |
|----|------------------|------------|
| C | 0.32 | 0.40 |
| Si | 1.10 | 1.00 |
| Mn | 0.80 | 0.40 |
| S | ≤0.002 | ≤0.003 |
| P | ≤0.010 | ≤0.015 |
| Cr | 1.35 | 5.30 |
| Mo | 0.80 | 1.30 |
| Ni | 0.70 | - |
| Nb | 0.015 | |
| V | 0.14 | 0.90 |

Machining Properties

Pre-hardened tool steels must possess good machining properties in combination with excellent dimensional stability to ensure a straight-forward mould/die manufacturing process. Thereby, the mould/die-maker can exclude the stress relieving step in his manufacturing process and reduce lead time.

The machining properties of steel are partly governed by the carbide contents/distributions in the steel matrix. Chandrasekaran et al. [2] have studied the relationship between carbide amount in the steel matrix and machinability with the use of flat milling tests. The studied grades were Toolox 33 and the European grade W.Nr. 1.2312 (P20+S).

The constants in Taylor's equation ($Vt^n=C$ where V is the cutting speed, t is the tool life and C and n are constants), see Table III, were established using the following test setup:

- Cutting head, Sandvik Coromill 200 Ø 80 mm;
- Cutting insert, Sandvik GC 1025;
- Feed = 0.15 mm/tooth;
- $a_p = 2$ mm;
- Cutting width = 60 mm.

The cutting insert edge was defined to be worn out when reaching a flank wear, v_b , of 0.3 mm.

Table III. Constants in Taylor's Equation Evaluated for the Actual Test Setup

| Grade | n | C |
|----------------------|----------|----------|
| W.Nr. 1.2312 (P20+S) | 0.16 | 476 |
| Toolox 33 | 0.21 | 669 |

The maximum possible cutting speeds for 10, 30 and 45 minutes cutting edge life, calculated using the above data are given in Table IV.

Table IV. Calculated Maximum Cutting Speeds

| Grade | V _{10 min} (m/min) | V _{30 min} (m/min) | V _{45 min} (m/min) |
|----------------------|--------------------------------|--------------------------------|--------------------------------|
| W.Nr. 1.2312 (P20+S) | 329 | 276 | 258 |
| Toolox 33 | 412 | 327 | 301 |

The costs for each manufacturing step, for a component such as that shown in Figure 4, are compared in Table V. The components were made of Toolox 33 and W.Nr. 1.2312 (P20+S) respectively.



Figure 4. Component made for cost comparison. Size 120 x 1200 x 900 mm.

Table V. Cost Comparison for Manufacture of Component Shown in Figure 4

| | W.Nr. 1.2312 | Toolox 33 |
|-------------------|---------------|---------------|
| Steel cost | 719 € | 726 € |
| Machining | 4960 € | 3930 € |
| Stress relieving | 191 € | - |
| Grinding | 260 € | 70 € |
| Total cost | 6130 € | 4726 € |

The comparison in Table V shows that a substantial cost reduction, 1404 €/23%, was achieved when choosing Toolox 33 steel to manufacture the component, this was due to:

- faster milling;
- no need for stress relieving;
- machining in only one set-up.

In fact, if the customer had got the W.Nr. 1.2312 blank for free he would still have had a higher total production cost when compared with the total cost of making the component from Toolox 33.

Furthermore, the component manufacturer had to add approximately two days lead time for the stress relief operation when manufacturing the component from W.Nr. 1.2312.

The Hoffmann Group [4] has carried out a comparison which shows the actual time required for each machining step when milling a given cavity in H11 and Toolox 44 respectively, see Table VI. The H11 component was heat treated to a hardness level of 45 HRC in the manufacturing cycle, which in this case required three days lead time.

Table VI. Process Time Required in Each Machining Step

| | H11 | Toolox 44 |
|---------------|-----------------|------------------|
| Roughing | 00:53:38 | 01:21:40 |
| Pre-finishing | 01:43:37 | - |
| Finishing | 05:14:02 | 05:14:02 |
| Total | 07:51:17 | 06:35:42 |

The study shows a machining time reduction of 16% when choosing a pre-hardened tool steel.

The lead time reduction, thanks to the elimination of heat treatment, needs to be added to the machining time saving, to give an overall picture of the benefit of using the pre-hardened steel.

Mould Service Life Span

Abrasive wear is the dominating wear mechanism in moulding, except for mechanical damage of the moulds/dies. SSAB has developed a wear model [5] pertaining to the description of relative lifetimes of components having different surface hardness levels when subject to abrasive wear. The model is based on two main wear regimes, an aggressive and a soft one. The relative hardness, see Equation 1, is employed to determine the prevailing wear regime.

$$HV_{rel} = HV_{abrasive\ medium} / HV_{mould\ surface} \quad (1)$$

At relative hardness values above 1.6, an aggressive, chip-cutting, wear regime dominates the abrasive wear, resulting in low mould service life length. To obtain a long mould service life, the relative hardness should be well below 1.6 where a soft wear regime, ploughing, prevails. The transition between the wear regimes takes place when the relative hardness equals 1.6. It should be noted that in reality the transition takes place over a hardness range, which depends on the actual wear system. See also Figure 5.

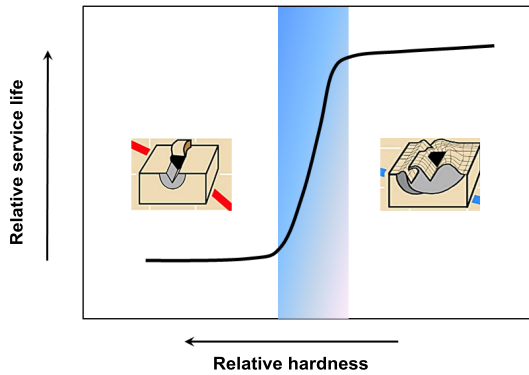


Figure 5. Prevailing wear regimes with respect to the relative hardness.

Using this model, the required mould surface hardness, when moulding a glass-fibre reinforced nylon component, has been determined. The glass-fibre, approximately 1200 HV, governs the actual wear system. The original mould was made of tool steel, W.Nr. 1.2358, heat treated to 55 HRC. This mould, however, showed too short and unpredictable mould lifetimes.

When determining the required mould surface hardness, W.Nr. 1.2311 (300 HBW) was chosen as the reference material and given a relative mould life span of one. The calculated relative service lives for different mould surface hardness levels are given in Table VII. The calculation shows that a minimum mould surface hardness of approximately 660 HV (~60 HRC) is required to ensure the mild abrasive wear mode prevails. A safety margin has to be added and the actual mould surface hardness was chosen to be 65 HRC. An increase in mould surface hardness from 55 HRC to 65 HRC thereby increases mould service life by approximately a factor of six times.

Table VII. Comparison of Relative Mould Service Life

| | Relative mould service life |
|------------------------------|------------------------------------|
| P20 (300 HBW) | 1 |
| Toolox 44 (450 HBW) | 4 |
| W.Nr. 1.2358 (55 HRC) | 6 |
| Toolox 44, nitrided (65 HRC) | 35 |

It was decided to manufacture a new mould in Toolox 44 and to nitride its surface to ensure the soft abrasive wear mode in continuous component production. Directly after mould manufacturing, ie before nitriding, a couple of test runs of ~50-100 components were carried out to check the final product dimensions. The mould was thereafter nitrided and the serial production started. The actual mould was, in this case, used both as a try-out-tool (before nitriding), as well as a serial production mould (when nitrided). Costs and lead times were drastically reduced thanks to elimination of manufacturing of separate try-out-moulds and production moulds.

Die Life Span in Stamping

Die life span is usually governed by adhesive wear in stamping. One of the paramount questions to answer is: which die matrix properties are required in combination with the necessary properties/conditions on the active die/sheet surfaces to achieve long die life span and also to increase the time elapsed between routine maintenance.

Usually, the die steel surface hardness has been the dominant parameter when judging the die performance, while only minor attention has been paid to the die matrix toughness. Modern steel making technology, however, enables steel manufacturing of tool steels with much improved toughness when compared with traditional grades. Traditional tool steels used in stamping dies usually have a toughness of around 5-6 J (Charpy V) at room temperature.

A study was carried out to evaluate the influence of surface-engineered layer properties when stamping Extra High Strength Steel (EHSS) samples, 1.95 mm, DP600. The results are summarized in Table VIII.

Table VIII. Relative Die Life Span

| Die steel | Die surface condition | Relative life span |
|-----------------------------|-----------------------|--------------------|
| W.Nr. 1.2358 | 55 HRC/Ra = 0.2 | 1 |
| Toolox 44 | 45 HRC/Ra = 0.2 | 0.9 |
| Toolox 44, plasma nitrided | 65 HRC/Ra = 0.2 | 13 |
| W.Nr. 1.2358, Duplex coated | ~70 HRC/Ra = 0.1 | >>13 |
| Toolox 44, Duplex coated | ~70 HRC/Ra = 0.1 | >>13 |

Ra (μm)

In the actual test set up, the criterion of a successful test was 50,000 stamped samples. Only the duplex coated dies fulfilled this actual criterion. This shows that as long as the die matrix has a sufficiently high yield strength to ensure operation in elastic mode, then the surface engineered layer governs the die life length.

Dies Operating at Elevated Temperatures

Applications where the tool mould/die is exposed to elevated temperatures (die-casting, aluminium extrusion, etc.), put additional demands on the tool steel. In such applications, strength and toughness at elevated temperatures are of interest, in combination with as high a thermal conductivity as possible in the tool steel. High die steel strength and impact toughness properties at elevated temperatures lower the risk for heat checking to occur. Also thermal conductivity influences the heat checking risk. This can be reduced by use of tool steels having high thermal conductivity. The thermal load on the die can be described by the following equation.

$$\sigma = C\alpha E\Delta T \quad (2)$$

Where E is Young's Modulus, α is mean coefficient of expansion, ΔT is the temperature difference and C is a constant. High thermal conductivity reduces the temperature peak and thereby the thermal load on the die. Furthermore, high thermal conductivity in a die can give higher cooling rates in the solidifying metal, thereby producing smaller dendrite arm spacings and enhanced mechanical properties, notably higher strength, of the cast component [6].

Conclusions

SSAB has developed a family of pre-hardened tool steels, Toolox, which are produced at nominal hardness levels in the range 300 to 450 HBW. These steels are microalloyed with niobium for grain size control and are made with a carefully controlled steelmaking practice to ensure good cleanness and with the use of soft reduction during casting to minimize segregation.

These steels can be used to reduce mould manufacturing time as transport to/from heat treatment and also the heat treatment itself are no longer needed during mould manufacture, giving substantial savings in mould cost and manufacturing lead time.

Surface engineering is an attractive method to optimize the abrasive/adhesive wear properties needed for enhanced mould/die life and Toolox steels are suitable for such processes (nitriding, PVD coating, etc).

A machining trial reported in the current study has shown the benefits of using Toolox grade 33 compared to a European grade W.Nr. 1.2312 in terms of maximum possible cutting speeds and elimination of a stress relieving heat treatment. The study also showed a reduction in overall component cost and a 16% reduction in time to manufacture.

SSAB has developed a wear model to describe the relative life span of components having different surface hardness levels which are subject to abrasive wear. The model can be used to determine the optimum mould hardness level needed, depending on the application, to ensure minimum wear. The model was used to determine the mould hardness required to mould a glass fibre of approximate hardness 1200 HV and a subsequent trial carried out using nitrided Toolox 44 showed very large improvements in mould life.

In some applications the tool steel mould is subjected to elevated temperatures which introduces the risk of heat checking. The Toolox grades with improved strength, toughness and thermal conductivity are suitable for such applications.

References

1. A. Lagerstedt and H. Fredriksson, *Stränggjutning av verktygsstål*. ISBN KTH/MG-UND-02/01-SE, TRITA-MG 2002:01. In Swedish. <http://www.worldcat.org/title/stranggjutning-av-verktygsstal/oclc/186489815>
2. H. Chandrasekaran et al., "Milling of Prehardened Mould Steels – Role of Microstructure on Machinability and Tool Wear," *Proceedings of 7th International Tooling Conference*, Politecnico di Torino, 623-630.

3. Hasco Hasenclever Gmbh, Private communication.
4. Hoffmann Group, Private communication.
5. WearCalc, SSAB.
6. New Die Steels, NADCA Course, November 2014.

DEVELOPMENT OF Nb-BEARING HEAVY STEEL PLATES WITH ULTRA HIGH STRENGTH AND EXCELLENT TOUGHNESS

Zhao Sixin¹, Ding Jianhua¹, Yao Liandeng¹, Zhang Yongqing² and Guo Aimin²

¹Research Institute, Baoshan Iron & Steel Co. Ltd., Shanghai, China

²CITIC Metal Co. Ltd., Beijing, China

Keywords: Heavy Plate, Ultra High Strength, Toughness, Direct Quenching, Direct Quenching and Tempering, Niobium, Mechanical Properties, Delayed Fracture, Weldability

Abstract

Large engineering machinery is widely used all over the world and the market is still growing. Therefore, the demand for high strength and ultra-high strength steel plates with good toughness is increasing. To satisfy this need, Baosteel has developed Nb-bearing high strength heavy plates with high toughness and good weldability by direct quenching (DQ) or direct quenching and tempering (DQ+T) processes. With Nb/Nb+Mo microalloying, heavy plates with yield strengths from 690 to 1150 MPa were developed. The microstructures of these steel plates were composed of bainitic ferrite plates with 0.1~1.5 μm thickness and martensite-austenite constituent decorating the boundaries of the bainitic ferrite plates. Spherical cementite precipitates were observed at the bainitic ferrite boundaries after the tempering process. It was found by instrumented impact experiments that the steel plates exhibited good crack arrest properties at -40 °C. Steel plates with yield strengths of 690/890/1150 MPa, for which the C contents are less than 0.11% and carbon equivalents are less than 0.59%, have excellent weldability. These steels are commercially produced and already widely used in the mining industry.

Background

Construction and machinery equipment used in the engineering sector, such as truck cranes, concrete mixers and hydraulic supports for coal mining are growing in size and being used in increasingly severe working conditions. Therefore, the demands for high strength steel plates with excellent toughness are growing accordingly. Heavy steel plates with good weldability, good ability to arrest cracks and high resistance to delayed fracture, are expected by the market. Steel plates with improved performance were developed to meet the market demand [1-3].

In recent years, coal has accounted for about 70% of China's primary energy production and consumption. In order to improve productivity and decrease accidents, mining machinery, such as hydraulic supports, has been an area of rapid development. For coal mine machinery, steel accounts for 95% of total equipment weight. According to the available statistics, every 100 million tons of coal produced would consume about 60,000 to 80,000 tons of steel plates.

Baosteel has developed Nb bearing Q690CF, Q890CF and Q1150 steels to meet these needs. Heavy plates of Q690, Q890 and Q1150 have minimum yield strengths of 690 MPa, 890 MPa and 1150 MPa respectively. By refinement of bainitic ferrite plates and a uniform dispersion of martensite-austenite constituent or cementite, heavy plates show high -40 °C toughness, and

good resistance to delayed fracture. Furthermore, the developed steel plates show excellent weldability due to the low C content (<0.11%) and low carbon equivalent.

This paper aims to introduce the development of these Nb-bearing heavy plates and then describes the applications of these plates in the coal mining industry.

Nb-bearing High Strength Heavy Plate

Concepts of Nb-bearing Materials Design

To obtain high strength and good weldability, steel plates with Nb/Nb-Mo and low C content were developed. The austenite grains of continuously cast slabs are refined by Ti and Al addition. Therefore, the complex interaction of Nb, Ti, Al, Mo and C, N, O should be considered before designing new steel plate compositions. Figure 1 shows that oxides of Al, Ti and Mg are formed at higher temperatures. Consequently, carbides and nitrides of Ti are formed in the temperature range 1000-1350 K followed by precipitation of NbC and NbN. To maximize the effects of Nb, an optimized Ti amount should be added to form carbides and nitrides whilst avoiding formation of coarse TiN precipitates which are detrimental to fatigue and fracture properties.

Figure 2 shows Nb contents in austenite and precipitates for different total Nb and C contents under thermodynamic equilibrium conditions. It is obvious that the contents of Nb in austenite and precipitates increase with total Nb content. Complex precipitates consume more Nb at high C contents. It is well known that Nb in austenite increases the recrystallization temperature. Sufficient Nb in austenite is beneficial to obtain fine austenite grains through dynamic recrystallization. Furthermore, a fine final microstructure can be produced from a fine austenite microstructure which can support more bainitic ferrite nucleation sites.

From the above discussion, Nb, C and Ti contents need to be optimized for producing heavy plates with a fine microstructure. Ti was added to form TiN and Ti_xO_y for consuming N and O. To obtain the optimum amount of Nb in austenite, Nb and C contents were optimized. At the same time, the C content was determined from consideration of the thermodynamics of bainite transformation and bainitic ferrite growth kinetics. Coupling the above theoretical analyses, high strength steel plates with good toughness and weldability were developed.

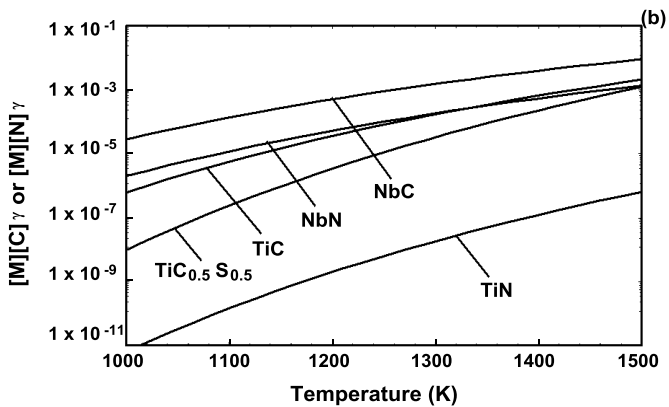
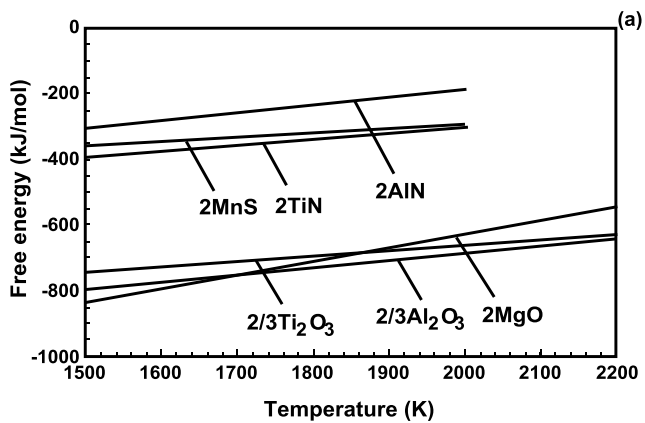


Figure 1. Oxides, carbides and nitrides formed at different temperatures; (a) Chemical driving force of compounds at high temperature, (b) Solubility of carbides and nitrides of Nb, Ti in austenite (S: 0.003wt.%) [4].

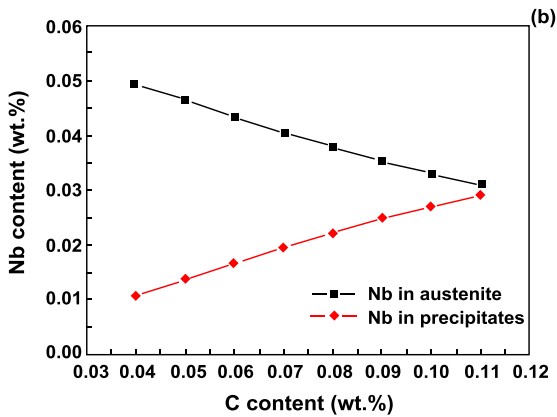
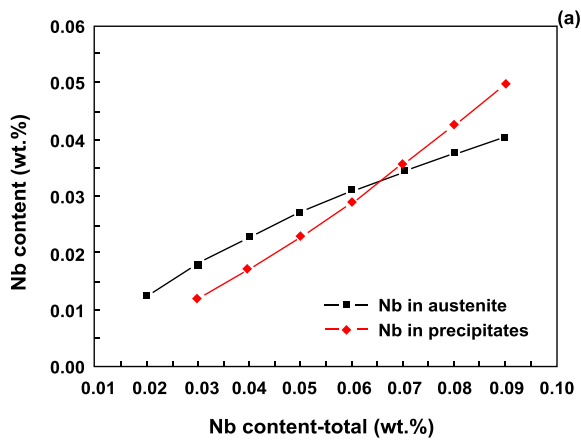


Figure 2. Nb contents in austenite and precipitates at different Nb total contents and C contents (austenized at 1200 °C); (a) Nb in austenite and precipitates at different Nb total content (0.11%C-0.03%V-0.02%Ti-0.0040%N-x%Nb), (b) Nb in austenite and precipitates at different carbon contents (0.06%Nb-0.03%V-0.02%Ti-0.0040%N-x%C) [5].

Chemical Composition

Chemical compositions and carbon equivalents of the developed heavy plates are shown in Table I. Using the calculation method mentioned above, the Nb content in austenite should be 0.035%, 0.040%, 0.036% and 0.037% in Grade Q690CF, Q690HP, Q890CF and Q1150 heavy plates respectively. For studying the effects of Nb on the high strength heavy plates' mechanical properties, steel plates without Nb were also studied. Mo provides 20-30 kJ/mol solute drag energy to diffusional transformation boundaries, whereas Ni and Mn provide 8 kJ/mol [6-8]. This means that the effect of Mo on diffusional phase boundary mobility is 3-4 times as large as that of Mn and Ni according to the thermodynamics. Thus, fine microstructures can be obtained by optimizing the content of Mo which can restrain the diffusional growth mechanism.

The Carbon Equivalents (CEVs) of the developed steels are no more than 0.43%, 0.56% and 0.58% for Q690CF, Q890CF and Q1150 steel plates, respectively. Moreover, heavy plates with yield strengths exceeding 690 MPa can be welded without preheat if the carbon equivalent is no more than 0.39%, as for the Q690HP variant in Table I. The plate thickness range is 12.0-40.0 mm for yield strengths of 690 MPa/890 MPa heavy plates and is 15.0-40.0 mm for a yield strength of 1150 MPa heavy plates.

Table I. Chemical Composition and Carbon Equivalent of Developed Steels (wt.%)

| Grade | C | Si | Mn | P | S | Nb | Mo | Others | CEV max. | Nb in austenite (austenitized at 1200 °C) |
|---------|-------|------|------|-------|-------|-------|------|---------------|----------|--|
| Q690CF | 0.060 | 0.30 | 1.83 | 0.010 | 0.002 | 0.045 | --- | B,Ni,Al,Ti | 0.43 | 0.035 |
| Q690HP* | 0.055 | 0.20 | 1.78 | 0.010 | 0.001 | 0.050 | --- | B,Ni,Al,Ti | 0.39 | 0.040 |
| Q890CF | 0.085 | 0.30 | 1.90 | 0.008 | 0.001 | 0.055 | 0.26 | Cr,B,Ni,Al,Ti | 0.56 | 0.036 |
| Q1150 | 0.095 | 0.30 | 1.95 | 0.008 | 0.001 | 0.060 | 0.34 | Cr,B,Ni,Al,Ti | 0.58 | 0.037 |

CEV=C+Mn/6+(Cr+Mo+V)/5+(Ni+Cu)/15

* Q690HP with 12.0-40.0 mm thickness can be welded without preheat.

Manufacturing Process and Fine Microstructure

Heavy plates with high tensile strength are generally manufactured by DQ/DQ+T or reheat quenching and tempering (RQT) processes. In the case of DQ, heavy plates are quenched directly after controlled rolling. As far as the DQ process is concerned, austenite grain refining by dynamic recrystallization and a high dislocation density were introduced during hot rolling. Thus, the density of nucleation sites for new phases is increased. The growth of plate-like bainitic ferrite, controlled by a diffusional process, is restrained by the use of higher cooling rates and lower finish cooling temperatures. Fine bainitic ferrite plates are formed because the nucleation site density is higher and growth rate is lower. The C concentration of residual austenite (RA) increases during RA transformation to martensite-austenite (MA) constituent. Thus, comparing with reheat quenching, we can produce heavy plates with the same carbon equivalent and higher tensile strength, or the same tensile strength and lower carbon equivalent, by using the controlled rolling and DQ process.

Microstructures of steel plates with minimum yield strength 690 MPa, produced by the DQ process with average cooling rates of 20 °C/s and 30 °C/s are shown in Figure 3 [9]. The microstructure of the 690 MPa heavy plates is composed of bainitic ferrite with MA constituents decorating the boundaries of the bainitic ferrite plates after DQ processing. Bainitic ferrite plates become finer at higher cooling rates. TEM micrographs of 690 MPa steel plates produced by direct quenching (cooling rate 20 °C/s) followed by tempering at different temperatures are shown in Figure 4 [9]. MA constituents decomposed during the tempering process.

FESEM of 890 MPa plates after DQ and DQ+T are shown in Figure 5. TEM micrographs of 1150 MPa steel plates after DQ, DQ+T are shown in Figure 6. For 1150 MPa grade steel plates, the thickness of sub-units of bainitic ferrite plates is nearly 0.1-0.5 μm. Spherical cementite precipitates at the bainitic ferrite boundaries are found after the tempering process.

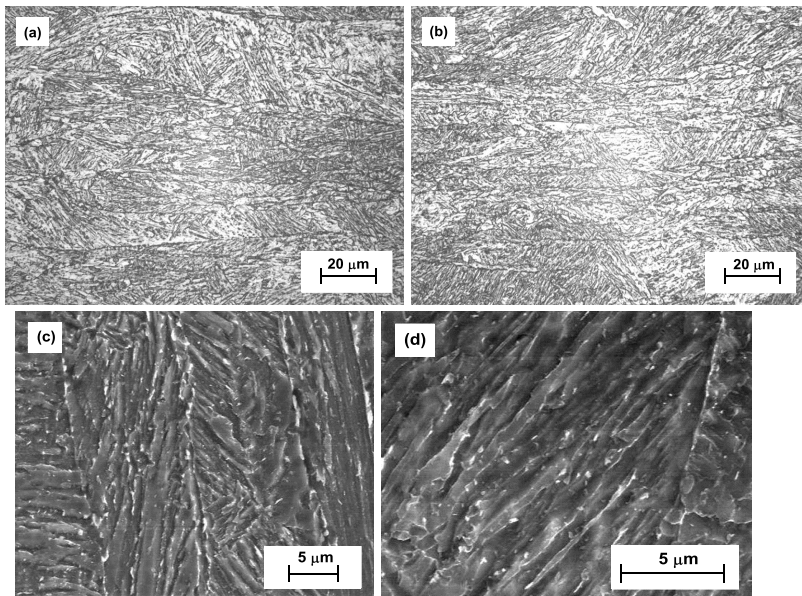


Figure 3. Microstructure of steel plates with minimum yield strength of 690 MPa produced by DQ with;
(a) average cooling rate 20 °C/s (optical micrography), (b) average cooling rate 30 °C/s (optical micrography), (c) average cooling rate 20 °C/s (FESEM), (d) average cooling rate 30 °C/s (FESEM) [9].

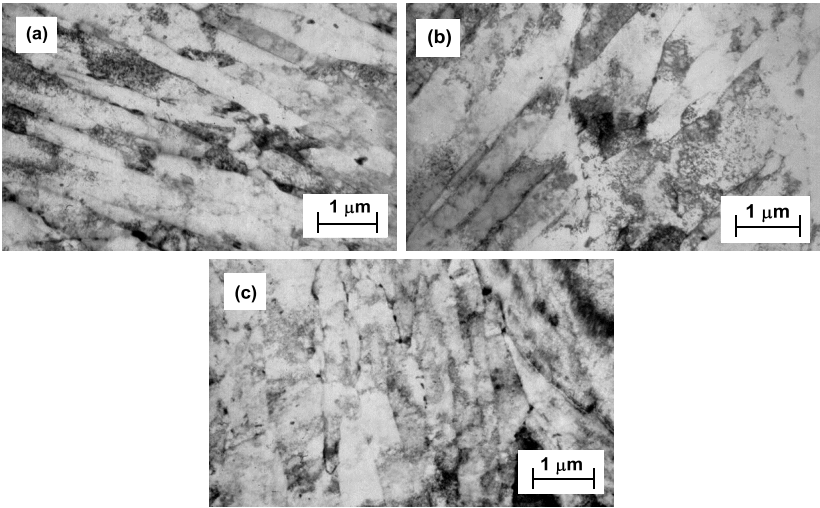
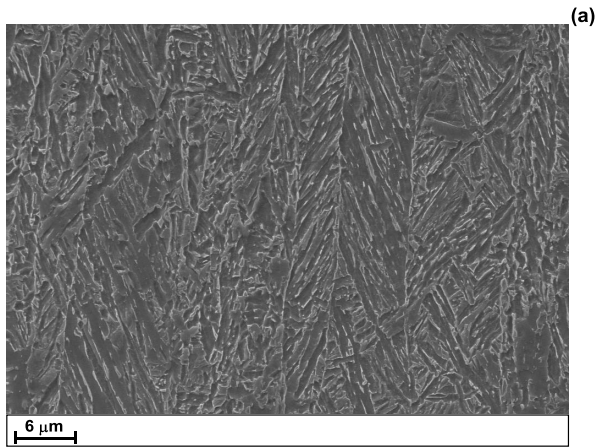


Figure 4. TEM micrographs of steel plates with yield strength 690 MPa produced by direct quenching (cooling rate 20 °C/s) followed by tempering at different temperatures; (a) 610 °C, (b) 630 °C, (c) 650 °C [9].



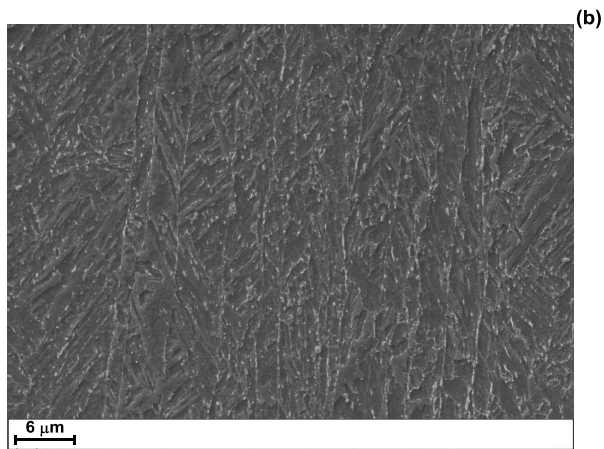


Figure 5. FESEM micrograph of 890 MPa yield strength steel plates; (a) DQ, (b) DQ+T.

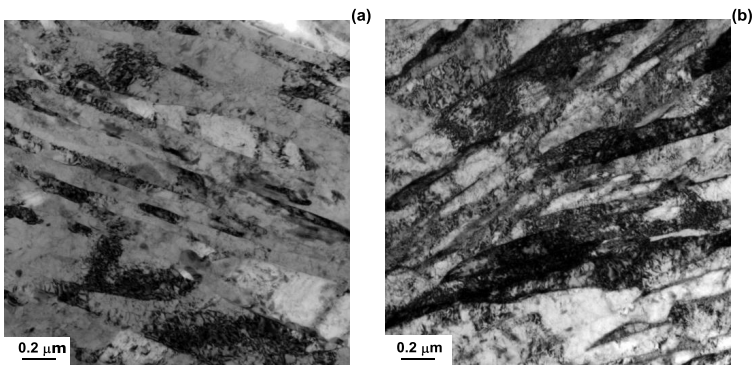


Figure 6. TEM micrographs of 1150 MPa yield strength steel plates; (a) DQ, (b) DQ+T.

Mechanical Properties

The mechanical properties of heavy plates with yield strengths 690/890/1150 MPa are shown in Table II. It can be seen that the developed steels have high yield strength, good low temperature toughness and elongation. Figure 7 shows the effects of finish rolling temperature on tensile strength and $-40\text{ }^{\circ}\text{C}$ Charpy V-notch impact energy. At higher finish rolling temperatures, aggregation of boron at grain boundaries restrains the austenite decomposition and increases the depth of hardenability. Moreover, surface ferrite may be formed at lower finish rolling temperatures which reduces the tensile strength. The dislocation density in austenite is increased by ausforming at lower temperatures. Thus, a fine microstructure can be formed which increases

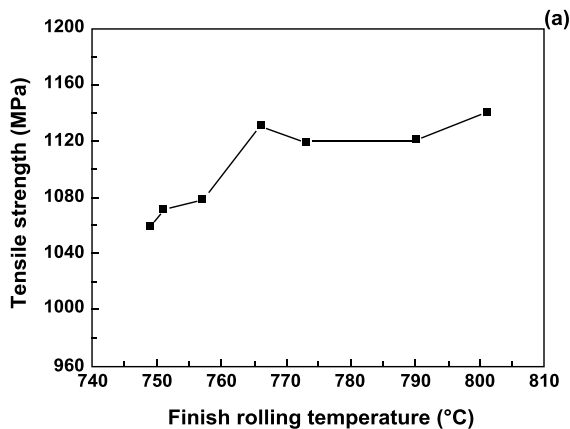
the low temperature impact toughness.

Figure 8 shows the results of instrumented impact energy tests and impact fracture morphology [9]. The formation and propagation work of cracking are the energy absorbed by the specimen before and after the maximum load. Heavy plate with a yield strength of 690 MPa has good crack arrest properties as propagation work of cracking values are 168 J, 190.5 J and 179 J at 0 °C, -20 °C and -40 °C respectively. Impact fracture exhibits the ductile mechanism as the fracture surface has many tiny and uniform dimples. Dynamic yield strengths are 879 MPa, 903 MPa, 927 MPa and dynamic tensile strengths are 1093 MPa, 1132 MPa, 1152 MPa at 0 °C, -20 °C and -40 °C, respectively, Table III. It seems that the work hardening effect is more significant at lower temperatures.

Effects of Nb on low temperature impact energy of the developed steels are shown in Figure 9. It is obvious that the low temperature impact energies of heavy plates are improved by the Nb addition.

Table II. Mechanical Properties of 690/890/1150 MPa Heavy Plates

| Grade | Yield strength(YS) MPa | Tensile strength(TS) MPa | Elongation % $L_0=5.65\sqrt{S_0}$ | Akv -40 °C J |
|--------|---------------------------|-----------------------------|--------------------------------------|-----------------|
| Q690CF | 750 | 845 | 21 | 260 |
| Q890CF | 985 | 1120 | 16 | 187 |
| Q1150 | 1180 | 1280 | 12 | 115 |



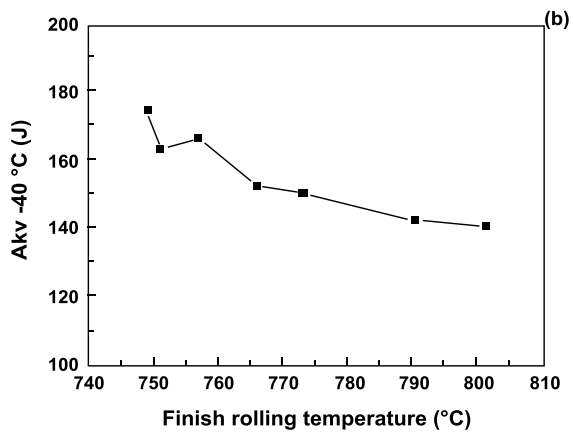
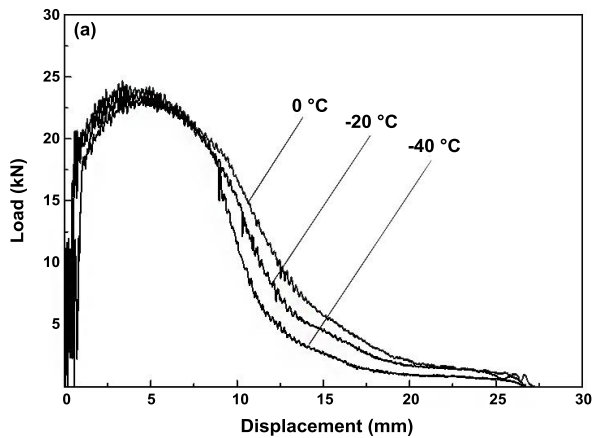


Figure 7. Effect of finish rolling temperature on; (a) tensile strength, (b) -40 °C Charpy V-notch impact energy of Q890CF.



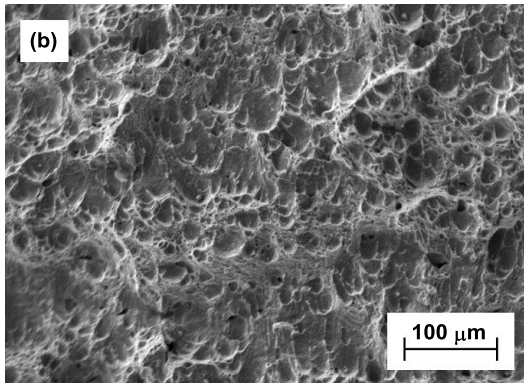


Figure 8. Instrumented impact results of steel plate (690 MPa) produced by DQ with cooling rate of 20 °C/s and tempered at 630 °C; (a) displacement - load curves, (b) fracture morphology [9].

Table III. Formation and Propagation Work of Micro-cracking and Dynamic Strength of Steel Plates Produced by DQ with Average Cooling Rate of 20 °C/s and Tempered at 630 °C [9]

| Temperature °C | Formation work of crack J | Propagation work of crack J | A_{kv} J | F_{yd} kN | σ_{yd} MPa | F_{max} kN | σ_{bd} MPa |
|----------------|---------------------------|-----------------------------|------------|-------------|-------------------|--------------|-------------------|
| 0 | 93 | 168 | 261 | 18.82 | 879 | 23.40 | 1093 |
| -20 | 62.5 | 190.5 | 253 | 19.32 | 903 | 24.24 | 1132 |
| -40 | 62 | 179 | 241 | 19.85 | 927 | 24.65 | 1152 |

F_{yd} : yield load; σ_{yd} : dynamic yield strength; F_{max} : maximum load; σ_{bd} : dynamic tensile strength

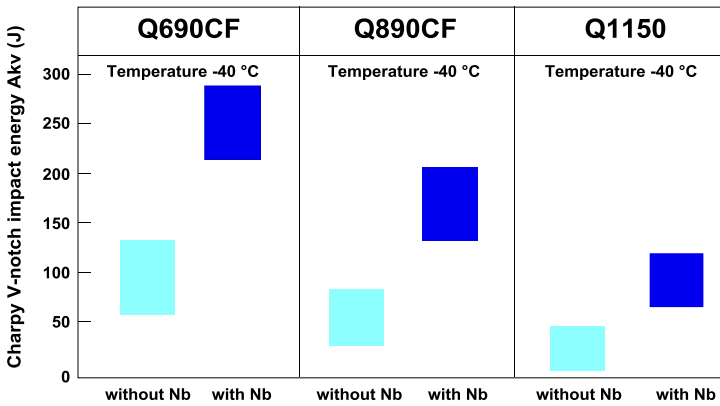


Figure 9. Effects of Nb on toughness of DQ+T high strength heavy plates.

Delayed Fracture

Delayed fracture of ultra high strength steel plates is caused by aggregation of hydrogen at dislocations and micro-cracks. The dislocation density is usually higher in ultra-high strength steel plates because these tend to employ lower temperature deformations. Thus, delayed fracture may occur because of the hydrogen aggregation phenomenon. To ensure their safety of application, high strength steel plates, as are used to build large items of machinery, should have good resistance to delayed fracture.

Delayed fracture properties were evaluated by low strain-rate tension and four-point bending experiments. For the low strain-rate tension experiments, specimens were immersed in 3.5% NaCl+HCl solution which has a pH value of 3.5. Delayed fracture susceptibility can be indicated by comparing the fracture times of the specimens in air and in solution under a strain rate of 1.0×10^{-6} /s. These results are shown in Table IV. The ratios of fracture time in solution and air, T_s/T_a , are 0.977, 0.968 and 0.965 for Q690CF, Q890CF and Q1150, respectively. The four-point bending experiments were carried out by loading specimens which were immersed in 0.1 mol/L HCl solution to 80% yield stress. The final thicknesses of the specimens were measured after 360 hours. These results are shown in Figure 10 and Table V. The thickness reductions of Q690CF, Q890CF and Q1150 were 0.07 mm, 0.12 mm and 0.16 mm, respectively. It can be seen that the developed high strength heavy plates have high resistances to delayed fracture. The microstructure of the developed heavy plates, Figures 4-6, is composed of fine bainitic ferrite plates and MA/cementite decorating the bainitic ferrite plate boundaries. Therefore, this suggests that the resistance to delayed fracture is enhanced because hydrogen may be trapped harmlessly by fine cementite and MA.

Table IV. Fracture Time of Low Strain-rate Tension Specimens

| Grade | D (diameter) mm | T _a h | T _s h | T _s /T _a |
|--------|--------------------|---------------------|---------------------|--------------------------------|
| Q690CF | 6.45 | 61.3 | 59.9 | 0.977 |
| Q890CF | 6.45 | 62.4 | 60.4 | 0.968 |
| Q1150 | 5.63 | 48.9 | 47.2 | 0.965 |

T_a: Fracture time in air; T_s: Fracture time in solution



Figure 10. Specimens after four-point bending test 360 h.

Table V. Four-point Bending Test Results of Q690CF/Q890/Q1150

| Specimen | Distance between internal bending points mm | Loading parameter % of yield strength | Original thickness mm | Final thickness mm | Thickness reduction mm |
|----------|---|---------------------------------------|-----------------------|--------------------|------------------------|
| Q690CF | 27.5 | 80% | 3.53 | 3.46 | 0.07 |
| Q890CF | 27.5 | 80% | 3.48 | 3.36 | 0.12 |
| Q1150 | 27.5 | 80% | 3.54 | 3.38 | 0.16 |

Weldability

Welding parameters and mechanical properties of welded joints are shown in Table VI. Welded joints of the developed heavy plates have good tensile strength and high Charpy V-notch energy at low temperature. Moreover, steel plates of Q690HP (yield strength 690 MPa) can be welded without preheating due to low carbon content and CEV.

Oblique Y type groove welding crack experiments were carried out on Q1150 plate. Experimental parameters and results are shown in Table VII and Table VIII. The surface or root crack ratios were calculated by (total length of surface (root) cracks/total length of welding line) x 100%. The crack ratio of the section is calculated by (total height of cracks at section/minimum thickness of welding line) x 100%. The crack ratios are average values of five specimens in one welding sample. The morphology of an oblique Y type groove welding crack sample section is shown in Figure 11. Although under severe welding conditions, heat affected zone cracking of Q1150 can be eliminated by preheating at ≥ 100 °C.

Table VI. Welding Parameters and Mechanical Properties of Welded Joint (GMAW)

| Grade | Thickness mm | Heat input kJ/mm | Preheat temperature °C | Interpass temperature °C | TS MPa | Fracture position | Charpy impact energy | |
|--------|--------------|------------------|------------------------|--------------------------|--------|-------------------|----------------------|--------------|
| | | | | | | | Location | Akv -40 °C J |
| Q690CF | 40 | 1.7 | 75 | ≤200 | 840 | Weld metal | HAZ | 228 |
| Q890CF | 40 | 1.5 | 75-150 | ≤200 | 1010 | Weld metal | HAZ | 146 |
| Q1150D | 25 | 1.2 | 100-175 | ≤200 | 1069 | Weld metal | HAZ | 82 |

Table VII. Oblique Y Type Groove Welding Crack Experimental Parameters for Q1150 (25 mm thick)

| Grade | Welding current A | Welding voltage V | Preheating temperature °C | Protective gas | Gas flow L/min |
|-------|-------------------|-------------------|---------------------------|---------------------------|----------------|
| Q1150 | 220-280 | 24-32 | 100, 125, 150 | 80%Ar+20% CO ₂ | 14-22 |

Table VIII. Oblique Y Type Groove Welding Crack Results for Q1150

| No. | Preheating temperature °C | Gap mm | Crack ratio of surface % | Crack ratio of section % | Crack ratio of root % |
|-----|---------------------------|-----------|--------------------------|--------------------------|-----------------------|
| 1-1 | 150 | 1.95-1.97 | 0 | 0 | 0 |
| 1-2 | 150 | 1.97-1.97 | 0 | 0 | 0 |
| 2-1 | 125 | 1.95-1.96 | 0 | 0 | 0 |
| 2-2 | 125 | 1.95-1.96 | 0 | 0 | 0 |
| 3-1 | 100 | 1.95-1.95 | 0 | 0 | 0 |
| 3-2 | 100 | 1.96-1.96 | 0 | 0 | 0 |
| 4-1 | 100 | 2.08-2.10 | 0 | 0 | 0 |
| 4-2 | 100 | 2.12-2.14 | 0 | 0 | 0 |



Figure 11. Section of Oblique Y type groove welding crack sample (preheating 150 °C).

Applications

High Performance Heavy Plates for Coal Mine Equipment

The developed heavy plates have improved performance and less alloying content, as shown above. Moreover, production time was reduced because there was no need for the reheat process. Steel heavy plates developed by Baosteel are widely used for coal mine equipment, such as hydraulic supports. Figure 12 shows a comparison of manufacturing cost for the developed steels and conventional heavy plates.

The coal mining supports are manufactured by an engineering company, then transported to a mine and installed at several hundred meters underground. To facilitate the transport and installation operations, developed higher strength steels with thinner gauge are used to decrease the weight of the supports. More recently, Nb-bearing heavy plates Q890CF and Q1150D, developed by Baosteel, have been used in the main structure of mine hydraulic supports. For support ZFY18000/28/53D, Table IX shows that total weight reduces by 10% and steel weight reduces by 15% through replacing conventional steel by the developed Nb-bearing heavy plates, Figure 13.

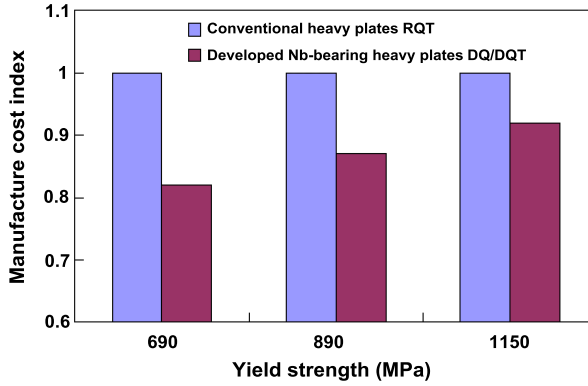


Figure 12. Comparison of manufacturing costs of conventional heavy plates (RQT) and developed Nb-bearing heavy plates (DQ/DQT).

Table IX. Lightweight Design of Mine Hydraulic Support ZFY18000/28/53D

| Structure | Yield strength (Conventional heavy plate → Developed Nb-bearing heavy plate) MPa | Thickness (Conventional heavy plate → Developed Nb-bearing heavy plate) mm |
|-------------|---|---|
| Top beam | 690→890 | 30→25 |
| Pedestal | 690→890 | 40→30 |
| Shield beam | 690→890 | 30→25 |
| Push rod | 890→1150 | 30→25 |

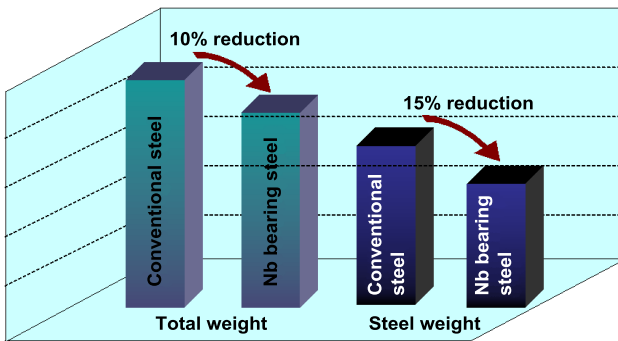


Figure 13. Total and steel weight reduction of mine hydraulic support ZFY18000/28/53D through replacing conventional steel by developed Nb-bearing steel heavy plates.

Welding of Q690HP Heavy Plates with No Preheat.

Conventional heavy plates with high yield strength such as 690 MPa generally should be preheated before welding to decrease the hardness of the Heat Affected Zone (HAZ) and avoid welding cracks. To reduce the labor intensity and welding cost, Nb-bearing heavy plate Q690HP with thickness 40 mm, which can be welded without preheating, was developed. Table X shows the welding parameters and welded joint mechanical properties of Q690HP. Shield beams of mine hydraulic supports are now manufactured with Q690HP. It is obvious that Q690HP has a good market potential due to its cost saving potential.

Table X. Welding Parameters and Welded Joint Mechanical Properties of Q690HP

| Grade | Heat input kJ/mm | Preheat temperature °C | Interpass temperature °C | TS MPa | Fracture position | Charpy impact energy | |
|--------|---------------------|------------------------------|--------------------------------|-----------|----------------------|----------------------|-----------------|
| | | | | | | Location | Akv -40 °C J |
| Q690HP | 1.5-1.9 | Room temperature (≥10) | 130-180 | 835 | Weld metal | HAZ | 237 |

Conclusions

Baosteel has developed Nb bearing high strength heavy plates with high toughness and good weldability by direct quenching (DQ) or direct quenching and tempering (DQ+T) processes. The C content was varied from 0.055 to 0.095% according to the desired strength and Nb content from 0.045 to 0.060%. With Nb/Nb+Mo microalloying, heavy plates with yield strengths from 690 MPa to 1150 MPa were developed. The microstructures of these steel plates were composed of bainitic ferrite plates with 0.1~1.5 μm thickness and martensite-austenite constituent decorating the boundaries of the bainitic ferrite plates.

With this development of Nb/Nb+Mo-bearing Q690CF, Q690HP, Q890CF and Q1150D grades, Baosteel has expanded its heavy plate products series. These steels show high/ultra-high strength, good low temperature toughness, high crack arrestability, high resistance to delayed fracture and excellent weldability. Moreover, Q690HP with thicknesses ranging from 12.0-40.0 mm can be welded without preheat. In recent years, these products have become widely used in large machinery such as hydraulic supports in mines. In light of this, we expect the demand for these steels in large machinery, such as automobile cranes, crawling cranes, concrete mixers and mining trucks to expand.

References

1. N. Shikanai, S. Mitao and S. Endo, "Recent Development in Microstructural Control Technologies through the Thermo-mechanical Control Process (TMCP) with JFE Steel's High Performance Plates" (Report No.11, JFE Steel Corporation, 2008), 1-6.
2. W-S. Chang, "Microstructure and Mechanical Properties of 780 MPa High Strength Steel Produced by Direct-quenching and Tempering Process," *Journal of Materials Science*, 37 (2002), 1973-1979.
3. R.D.K. Misra et al., "Microstructural Evolution in a New 770 MPa Hot Rolled Nb-Ti Microalloyed Steel," *Materials Science and Engineering: A*, 394 (1-2) (2005), 339-352.
4. S. Zhao and L. Yao, "Precipitation Behaviour of Ti in Ti and Nb-Ti Microalloyed High Strength Steel," *Transactions of Materials and Heat Treatment*, 31 (2010), 71-79.
5. S. Zhao, "The Relationship of Nb in Austenite and Total Nb Content at Different Austenization Temperature". (Report, Baoshan Iron & Steel Co., Ltd., 2014), 1-15.
6. K.M. Wu, M. Kagayama and M. Enomoto, "Kinetics of Ferrite Transformation in an Fe-0.28mass%C-3mass%Mo Alloy," *Materials Science and Engineering: A*, 343 (2003), 143-150.
7. K. Oi, C. Lux and G.R. Purdy, "A Study of the Influence of Mn and Ni on the Kinetics of the Proeutectoid Ferrite Reaction in Steels," *Acta Materialia*, 48 (9) (2000), 2147-2155.
8. M. Enomoto, "Influence of Solute Drag on the Growth of Proeutectoid Ferrite in Fe-C-Mn Alloy," *Acta Materialia*, 47 (13) (1999), 3533-3540.
9. S. Zhao and L. Yao, "Development of 780 MPa Steel Plate by Direct Quenching and Tempering Processes," *Transactions of Materials and Heat Treatment*, 32 (3) (2011), 95-102.

ABRASION RESISTANT METALLIC ALLOYS FOR THE MINING INDUSTRY

E. Albertin¹ and A. Sinatora²

¹Institute for Technological Research of São Paulo State, Metallurgy Division, São Paulo, Brazil

²University of São Paulo, Surface Phenomena Laboratory, Department of Mechanical Engineering, São Paulo, Brazil

Keywords: Abrasion, Abrasion Resistant Materials, Mining, Niobium

Abstract

In the mining industry, abrasion is the most significant wear mechanism. The resistance to abrasion is a property that must be combined with other material properties, such as toughness and corrosion resistance. In the crushing, grinding and material handling operations, the most relevant wear resistant materials are steels and cast iron.

Pearlitic and martensitic steels compete in applications, such as lifters and liners for SAG mills. Martensitic steel can also be the material choice for large balls for SAG mills, chutes and wear plates for heavy trucks. Austenitic manganese steel remains the proper choice for jaws or cone crushers. In applications with lower impact demands, high chromium cast irons are widely used for balls and liners. All these materials are subjected to increasingly higher stresses as the size of all such equipment is increasing over time.

The wear performance of such steels has been improved by refining the pearlite, increasing the hardness of martensite and increasing the work hardening of austenite. In cast iron, the approach has been to optimize the matrix hardness and adjust the carbide content according to the application.

Niobium has been investigated in the improvement of wear resistance due to its multiple effects; Niobium can harden pearlite due to grain refinement, it can harden the martensite due to precipitation hardening and can form very hard NbC carbides from the melt.

This paper critically reviews the literature with regard to improvement of the abrasive wear resistance of pearlitic, martensitic and austenitic steels, and high chromium cast irons. This paper also presents test results obtained from different materials containing niobium, with the aim of ranking them for applications where abrasion is the predominant wear mechanism.

Introduction

Abrasion in the mining industry is the wear mode that reduces the thickness, diameter and height of components used to crush, grind, sieve, store and transport mineral goods. The main consequences of abrasion are safety and environmental risks, as well as decreasing efficiency, increasing energy losses, increasing the maintenance time, and thus losses in production and productivity.

Engineers look for simple abrasion models to predict thickness, diameter, height, mass, noise or any other variable that would allow them to know within a certain margin of uncertainty when to replace the parts subject to abrasion. A graphical description that relates abrasion models and life of wear parts is presented in Figure 1.

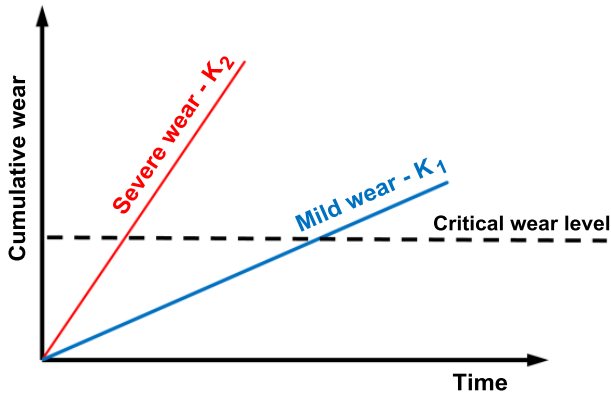


Figure 1. Cumulative wear vs time. When the cumulative wear intercepts the critical wear level the wear part needs to be replaced. Holmberg [1].

In Figure 1, both the severe and mild wear cases were drawn as straight lines, which is the case in a large number of abrasion phenomena. K is the gradient of the straight lines in Figure 1 and therefore, it expresses the intensity of abrasion, being greater for the severe wear case (K_2) than for the mild wear case (K_1). The well-known abrasion model proposed by Rabinowicz tries to estimate the mass loss based on applied load, material hardness and abrasive particle geometry, as in Equation 1 [2].

$$Q = k_i \frac{W}{H} \quad (1)$$

where:

Q is the cumulative mass loss (kg),

W is the normal force (applied load) (N),

H is the abrasion resistant material hardness (Pa), and

k is a constant related to the abrasive geometry (kg/m^2).

The first outcome from Figure 1 and Equation 1 is that there are simple (linear) and useful predictive models to be used in maintenance planning to estimate the replacement time for components. Graphs for mild and severe wear conditions can be easily obtained in the laboratory. The challenge of how to link laboratory studies and service performance in order to predict component life will be scrutinized in a later paper in this conference [3].

A second consequence is that, in order to increase service life of an abrasion resistant component, represented by the elapsed time until the straight line intercepts the critical wear level, it is necessary to “push” the constant K from K_2 to K_1 . The terms “severe” and “mild”, from Figure 1, are more properly defined in connection with the abrasion mode of wear in Table I, from Gates [4]; it is possible to associate the constant K to some variables of the tribosystem.

Table I. Proposed Severity-based Classification for Abrasive Wear [4]

| Typical Situations | Abrasive Wear Mode | | |
|---------------------|--|---|--|
| | Mild | Severe | Extreme |
| Particle size | Small | Moderate | Large |
| Constraint | Unconstrained | Partially constrained by counterface | Strongly constrained |
| Particle shape | Rounded | Sharp | Sharp |
| Contact stress | Low – insufficient to fracture particles | Moderate – sufficient to fracture particles | Very high – may cause macroscopic deformation or brittle fracture of material being worn |
| Dominant mechanisms | Microplowing | Microcutting | Microcutting and/or microfracture |
| Equivalent terms | • Low-stress abrasion | • High-stress abrasion | • Gouging abrasion |
| | • Scratching abrasion | • Grinding abrasion | |
| | • Low-stress three-body | • High-stress three-body | • High-stress two-body |
| | | • Low-stress two-body | |

Increasing abrasive particle size, abrasive sharpness and the external load lead to microcutting abrasion micromechanism, promoting, therefore, the severe abrasion regime (K_2). Increasing the abrasive hardness will also act to promote the severe abrasion mode. Small abrasive grains, rounded grains and low loads, promote the micromechanism of microplowing and, therefore, the mild abrasion regime (K_1).

An increase in the material hardness will contribute to reducing the constant K. However, it is well known that the behavior of an abrasion resistant material does not depend solely on its own hardness but also on the hardness of the abrasive media. This concept is expressed in Figure 2, from Zum Gahr [5].

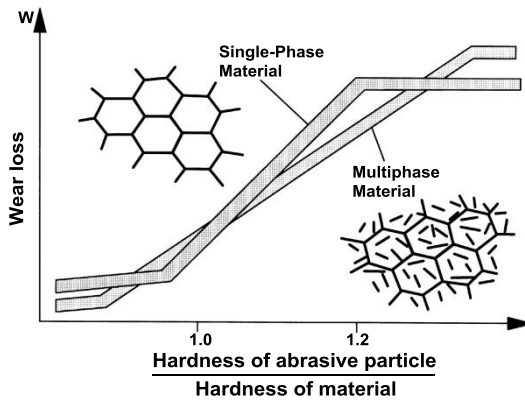


Figure 2. Schematic representation of wear regimes as a function of the relationship between the hardness of abrasive particles and the hardness of the abrasion resistant material. Adapted from Zum Gahr [5].

The Effect of Hardness on Abrasion

To investigate the mild and severe abrasion regimes, several steels and cast irons were studied in laboratory, pin on disc, abrasion tests. Table II summarizes the most relevant data for the materials. Figures 3(a), (b) and (c) are representative microstructures of the cast irons tested and Figures 4(a) and (b) present the wear and friction data.

Table II. Summary of Heat Treatments and Microstructures of the Tested Materials. Pintaúde, et al [6]

| Material | Heat Treatment | Expected Microstructure |
|-----------------|---|---|
| 52100 steel | Oil-quenched after holding at 900 °C for 60 min, tempering at 500 °C for 24 h | Tempered martensite + M ₃ C carbides |
| 1070 steel | Water-quenched after holding at 860 °C for 60 min, tempering at 250 °C for 50 min. | Tempered martensite |
| Ductile iron | Oil-quenched after holding at 860 °C for 60 min, double tempering at 370 °C for 90 min plus 60 min, and sub-zero treatment, maintaining in liquid nitrogen for 120 min. | Tempered martensite + graphite nodules |
| White cast iron | Annealing at 700 °C for 8 h. Air-quenched after holding at 1000 °C for 40 min. | Martensite + M ₇ C ₃ carbides |
| Multicomponent | Double tempering at 550 °C for 180 min. Air-quenched after holding at 1000 °C for 40 min. Double tempering at 600 °C for 240 min plus 180 min | Tempered martensite + (MC + M ₂ C) carbides + secondary precipitates |

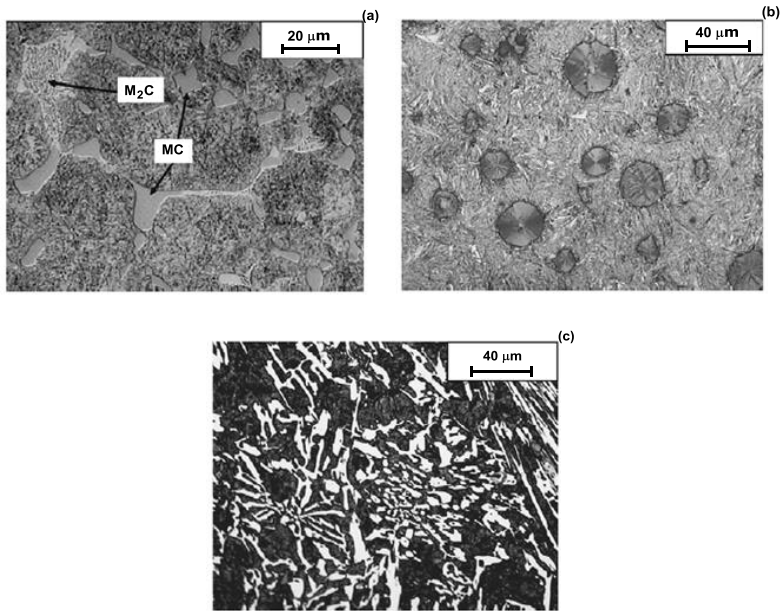
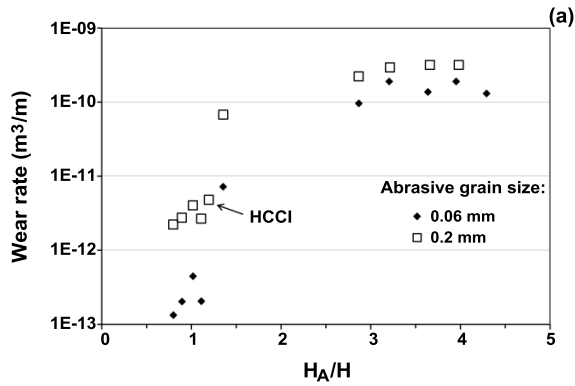


Figure 3. Microstructure of tested cast irons; (a) multicomponent cast iron, martensite + MC and M₂C carbides, (b) ductile cast iron, martensite + graphite nodules and (c) high-chromium cast iron, martensite + M₇C₃ carbides. Pintaúde, et al [6].



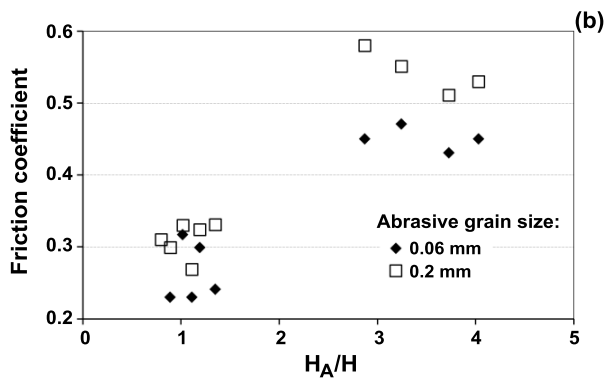


Figure 4. (a) Relationship between wear rate (m^3/m) and the ratio of the abrasive hardness (H_A) and material bulk hardness (H) and (b) friction data. Single phase materials. Pintaúde et al. [6]. (HCCI: high Cr cast iron.)

The wear rate increased by approximately three orders of magnitude with increasing H_A/H . The abrasive grain size played a more significant part in the tests where the lower abrasion rates were measured. Two levels of friction coefficient were observed: from 0.2 to 0.3 and from 0.4 to 0.6, approximately. Lower wear rates and lower friction coefficients were associated with smaller abrasive grain sizes and with the prevalence of microplowing instead of microcutting.

To reduce the wear rates, the H_A/H ratio must be decreased. Most of the time the abrasive hardness cannot be chosen since it depends on the mineral being mined. Therefore, the increase in the material hardness is the main factor to be engineered in Figure 4, to reduce abrasion.

The hardness of single-phase material with martensitic matrices is limited to the tempered hardness of martensite and the compromise between hardness and toughness necessary for optimum behavior in service. Therefore, a series of high chromium cast irons (HCCI) with M_7C_3 carbides and with austenitic and martensitic matrices, as well as cast high speed steels (MCI), quenched and tempered, were investigated with a pin on disc experimental set-up. The wear rate and the friction data are presented in Figure 5 [7]. Composition data for these alloys are depicted in Table III.

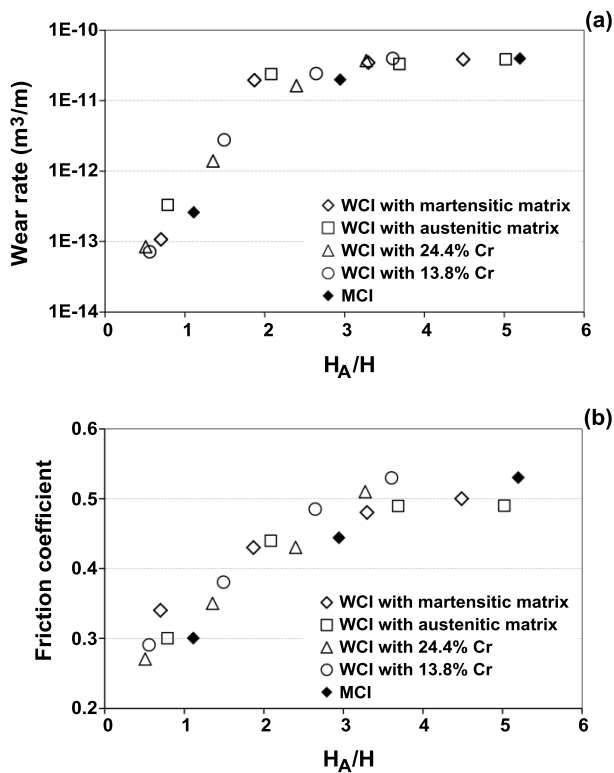


Figure 5. (a) Relationship between wear rate (m^3/m) and the ratio of the abrasive hardness (H_A) and material bulk hardness (H) and (b) friction data. Hard second-phase materials. Coronado et al. [7].

Table III. Composition (% wt.) of the Hard Second Phase Materials. Coronado et al. [7]

| Material | Cr | C | Si | Mn | S | Mo | Ni | Nb + Ti |
|------------------|-----------|---------|------------|------------|-------|------------|-----------|---------|
| WCI 13.81 wt.%Cr | 13.81 | 5.06 | 0.27 | 0.42 | 0.005 | - | - | - |
| WCI 24.41 wt.%Cr | 24.41 | 3.14 | 0.36 | 0.36 | 0.013 | - | - | - |
| MCI | 1.4 – 2.1 | 3 – 3.6 | 0.5 – 1.25 | 0.45 – 1.3 | 0.005 | 0.25 – 0.7 | 4.1 – 4.8 | 3 |

The wear rates varied by approximately three orders of magnitude, as already shown in Figure 4 for single phase materials. The friction coefficient increased steadily from 0.2 to 0.6, approximately. As in the previous series of tests, the lower wear rates and lower friction coefficients were associated with the prevalence of microplowing instead of microcutting.

The wear regions, predicted in Figure 2, are experimentally revealed in Figures 4(a) and 5(a), as well as the transition between the two wear regimes. For the materials with large and hard second phases, Figure 5(a), the severe wear region has lower wear rates than materials without large hard second phases, as also predicted in Figure 2.

There are also some differences between Figures 2 and 4. The end of the severe region and the beginning of the transition to the mild one occurs in Figure 2 at a value of H_A/H of 1.2. This is based on the predictions of Torrance [8], where the indentation stresses of a perfectly rounded particle were used to calculate the minimum hardness differences (20% in this case) necessary for a hard body to penetrate a soft one. A second condition, assumed in Figure 2, is that the materials have elasto-plastic behavior; that means they do not work harden as they are worn out, or in other words, that during the wear process they keep their original bulk hardness. The abrasives in the tests in Figure 4 were sharp instead of rounded and work hardening occurred as will be seen later. Therefore, the transition regions on the experimental curves are displaced to greater values of H_A/H , in comparison with the Zum Gahr model.

Both Figures 4(a) and 4(b) show that the reduction in the abrasion with reduced H_A/H is less pronounced in the severe wear region, that is, a great increase in material hardness is necessary to result in a small reduction in the abrasion rate. On the contrary, if the wear occurs in the transition region, a small increase in the hardness of the abrasion resistant material results in a large decrease in the wear.

These conclusions are of importance in the evaluation of results of laboratory wear tests. An analysis of the real tribosystem is, therefore, necessary in order to adjust the severity of the laboratory tests to the field conditions. If the field tribosystem promotes abrasion in the mild regime or in the transition region, the laboratory test cannot be performed with hard abrasives (tests in the upper plateau of the graphs). With such a test configuration, the abrasion resistance increase might be considered unimportant or uneconomical, since with this test condition, with high wear rates, the effect of increasing the abrasive's hardness is intrinsically small.

Figures 4(a) and 5(a) allow us to predict that for abrasion in the severe regime, the increase in abrasion resistance attainable with the addition of a hard second phase will be as large as one order of magnitude (from $k = 10^{-10} \text{ m}^3/\text{m}$ in Figure 4(a) to $k = 10^{-11} \text{ m}^3/\text{m}$ in Figure 5(a) for a constant material hardness. As a consequence, to further improve wear resistance, it will be necessary to add second hard phases and to increase the bulk hardness to reach the transition region of the graphs. The increase of the bulk hardness for wear plate material, steels and weld deposits, Figure 6, was studied in dry rubber wheel testing (RWAT).

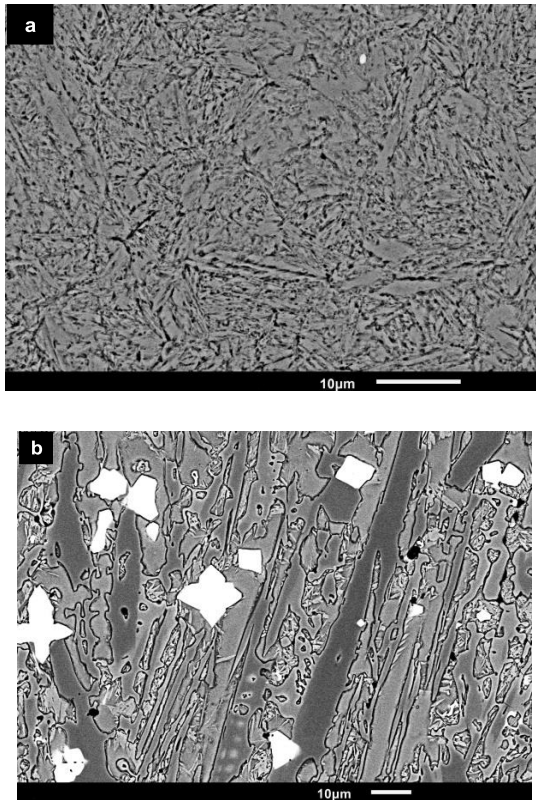


Figure 6. (a) Martensitic Q & T steel, (b) Weld deposit. M_7C_3 carbides, NbC carbides in an austenitic matrix.

As expected, the increase in hardness reduced the wear coefficient for both sets of materials. It is apparent that the gradient of the abrasion data for steel, K_2 , is greater than for the weld deposits K_1 . The RWAT abrasion tests were performed with silica sand (1000 to 1200 HV), H_A/H in the range of ~8.7 to 1.5 and the effect of the relative hardness is shown in Figure 7(b).

This figure shows that possibly there is a mild to severe wear transition similar to those shown in Figures 2, 4 and 5 for three-body abrasion tests. There remains a question: how to compare two-body and three-body wear rates or wear coefficients?

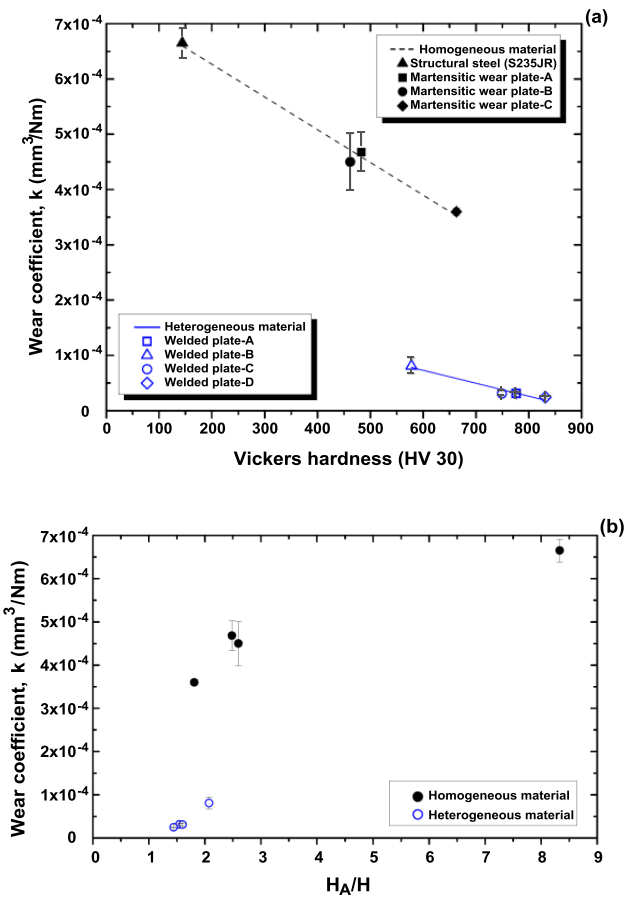


Figure 7. Wear coefficient for materials without big hard second phase, dashed line, and for materials with big hard second phase, solid line. RWAT, silica sand # 100, 130N; (a) Wear x Hv, (b) Wear x H_A/H . Penagos, Tressia and Sinatora [9].

It is also remarkable in Figure 7(a) that a hypothetical single phase material with a hardness of 600 HV would have a wear coefficient of approximately $4.0 \times 10^{-4} \text{ mm}^3/\text{Nm}$ and the addition of a second hard phase would increase its wear resistance, bringing the wear coefficient to $0.8 \times 10^{-4} \text{ mm}^3/\text{Nm}$, a fivefold decrease. However, if, simultaneously to the addition of the second hard phase, the bulk hardness had been increased to 830 HV, the abrasion coefficient would be reduced to $0.25 \times 10^{-4} \text{ mm}^3/\text{Nm}$, one order of magnitude increase of the abrasion resistance. The same

tendency for cast materials with hard second phases is observed in Figure 8. Those trends were already observed in Figures 2 and 4.

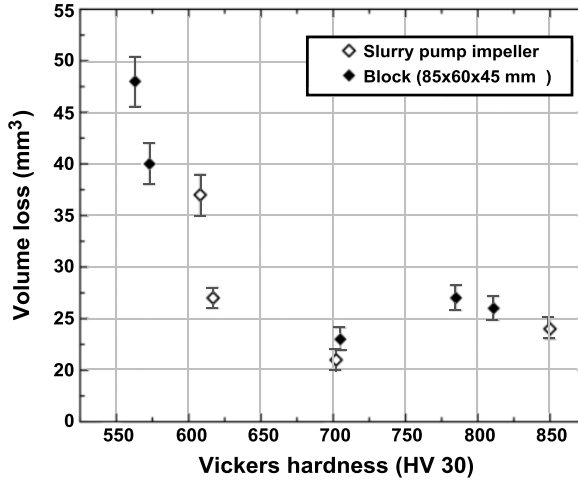


Figure 8. Volume loss for cast materials with large hard second phase, RWAT, silica sand # 50, 130 N. Penagos and Sinatora [10].

After considering the approach to reduce abrasion based on hardness, let us consider some effects not directly connected to hardness.

The Effect of Other Parameters on Abrasion

Microstructure

In order to study the effect of microstructure refinement, white cast iron alloy blocks were cast in a sand mold with a chill plate, as shown in Figure 9. Alloys with 0.6%Nb had their abrasion resistance compared, after quenching and tempering procedures, in a pin on disc and in the dry RWAT test [11].

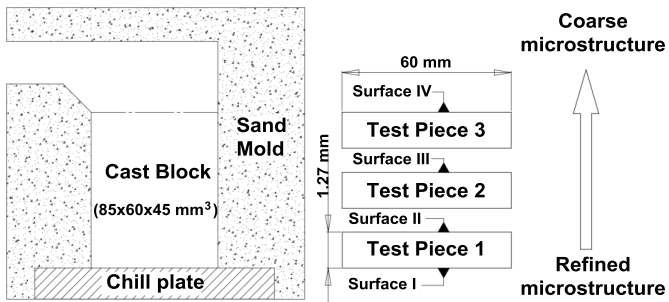
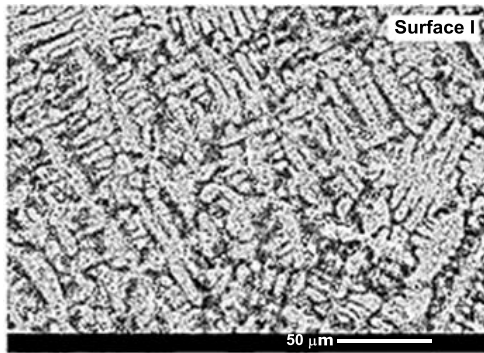


Figure 9. Experimental set-up to change carbide spacing (mean free path) of 2.8%C, 18.8%Cr and 0.6%Nb white cast iron.

The casting plus heat treatment procedure resulted in a peculiar match of carbide spacing and hardness. Figure 10 shows that there was a pronounced grain refinement, and quantitative metallography showed that at the two surfaces closer to the chill plate, the carbide spacing decreased significantly. The two other surfaces had similar austenitic grain size and carbide spacing. As the carbide spacing increased, the width of the carbides also increased. The bulk and microhardness, however, were quite similar for the three samples nearer the chill plate, as shown in Table IV.



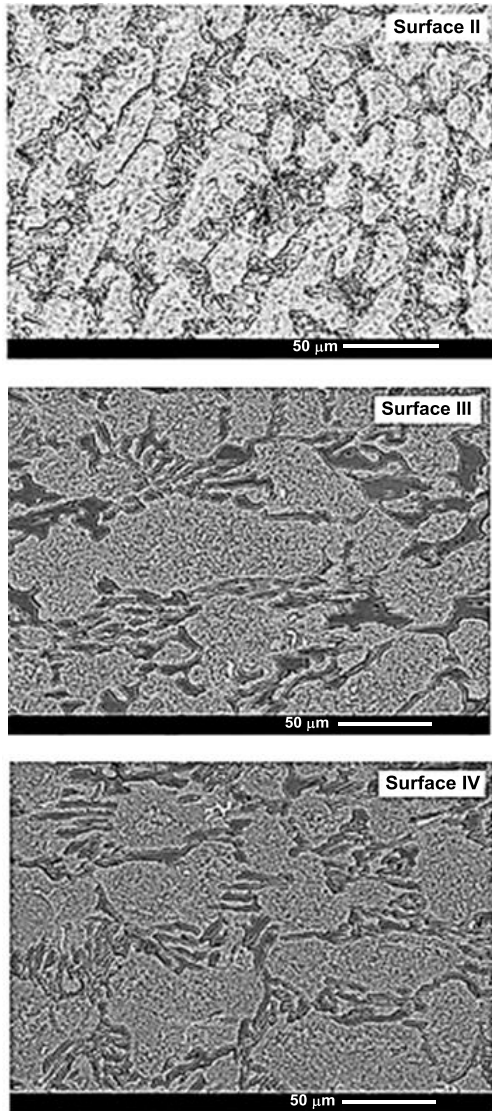


Figure 10. Micrographs of the 2.8%C, 18.8%Cr. Martensite + eutectic of martensite + M_7C_3 carbide.

Table IV. Hardness of Materials and Phases

| Test Surface | Material Macrohardness HV 30 | Matrix Microhardness HV 0.1 | M ₇ C ₃ Hardness HV 0.25 |
|--------------|------------------------------------|-----------------------------------|---|
| I | 806 ± 3 | 760 ± 19 | - |
| II | 811 ± 8 | 752 ± 43 | - |
| III | 802 ± 4 | 728 ± 9 | 1473 ± 253 |
| IV | 784 ± 8 | 708 ± 12 | 1437 ± 300 |

As a consequence of the increase in carbide spacing and in carbide coarsening, there was an abrasion reduction of more than 30% for both pin on disc and dry RWAT tests when the two slices near the surface were compared, Figure 11.

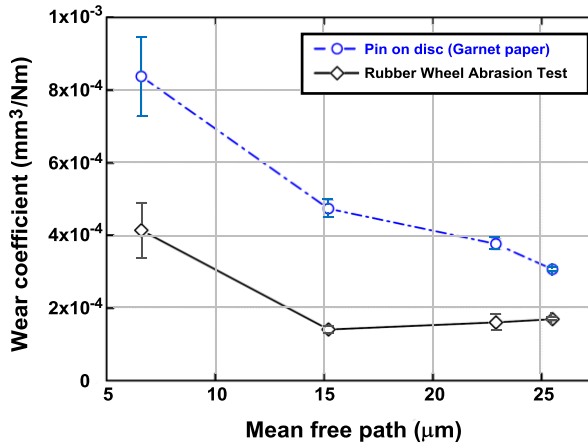


Figure 11. Wear coefficient as a function of carbide spacing. Pin on disk abrasive garnet. Dry RWAT, silica 2.8% C, 18.8% Cr, and 0.6% Nb alloy.

This result is probably due to the more effective barrier exerted by the thicker carbides as is to be seen in Figure 12. The thicker carbides were able to resist cracking and therefore, were able to restrain the width of the abrasion marks when compared with samples with thinner and less spaced carbides.

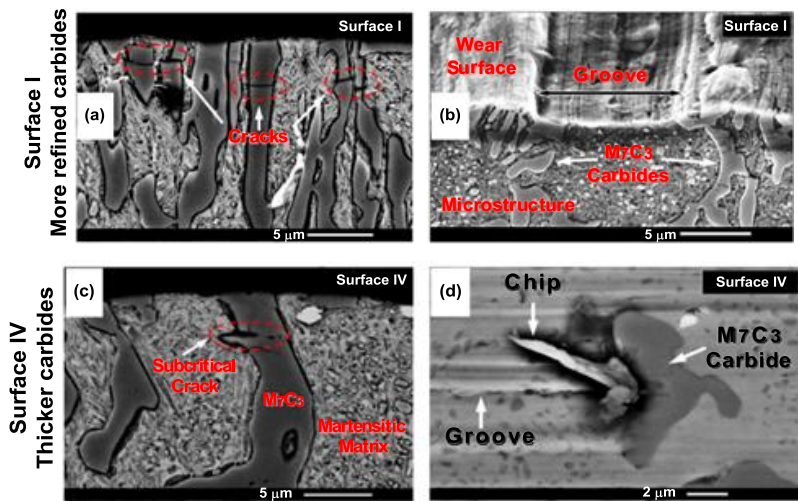


Figure 12. (a) Subsurface microstructure of thinner carbides for the more refined structure, (b) subsurface microstructure and taper section for the more refined structure (surface I), (c) subsurface microstructure and (d) wear surface for thicker carbides. Note that thicker carbides are less susceptible to cracking and fracture and can occasionally act as a barrier to abrasive grit, resulting in a higher wear resistance. Penagos et al [11].

The comparison of abrasion results for the base alloy and the alloy with 0.6%Nb from dry RWAT tests is shown in Figure 13. No significant hardness change was measured for equivalent samples. Besides that, it is noticeable that the carbide coarsening reduced the abrasion, a promising effect of niobium that is under investigation.

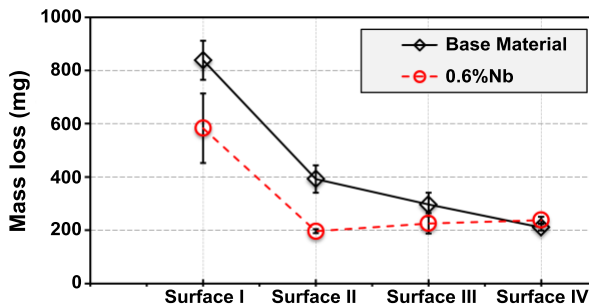


Figure 13. Mass loss, dry RWAT, 130 N, # 100, 2.8% C, and 18.8% Cr, without and with 0.6%Nb alloy.

Another example where the microstructural parameters prevailed over the hardness effect was detected in a series of high carbon, high speed steels containing niobium (compositions presented in Table V). For these alloys, the carbon content was adjusted, providing extra carbon as the niobium content was increased, in order to keep the same carbon content in the matrix [12].

Table V. Chemical Composition of the HSS-Nb Alloys

| Alloys | Chemical Composition (wt.%) | | | | | | |
|---------|-----------------------------|------|------|------|------|------|------|
| | C | Cr | Mo | W | V | Nb | Ti |
| Nb0 | 0.51 | 4.18 | 3.27 | 1.91 | 0.97 | - | - |
| Nb2.5 | 0.81 | 3.94 | 3.32 | 2.33 | 0.92 | 2.52 | - |
| Nb2.5Ti | 0.81 | 3.94 | 3.09 | 2.23 | 0.91 | 2.81 | 0.11 |
| Nb5 | 1.05 | 3.81 | 3.33 | 2.83 | 0.92 | 5.73 | - |
| Nb5Ti | 1.07 | 3.80 | 3.07 | 2.56 | 0.92 | 5.73 | 0.09 |

All cast samples were annealed (700 °C, 5 h, furnace cooling). The entire test pieces were heat treated through quenching (austenitization at 1100 °C, 2 h, still air cooling) and double tempering (500 °C, 2 h, still air cooling). For all the alloys, resultant bulk hardness ranged from 680 to 740 HV 30, while matrix microhardness ranged from 630 to 700 HV 0.1. The relevant microstructures are shown in Figure 14.

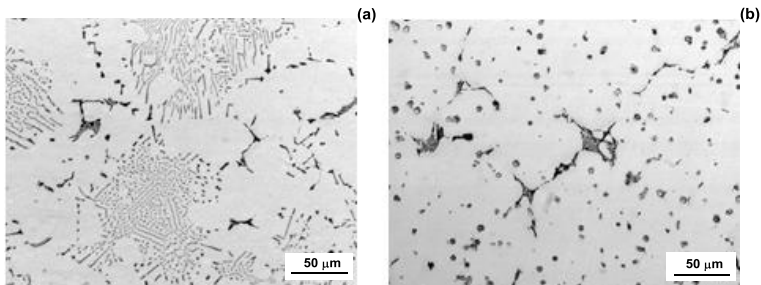


Figure 14. Distribution and morphological details of the eutectic carbides in the microstructure of the HSS-Nb alloys Nb2.5 (a), and Nb2.5Ti (b) [12].

The alloy without Nb (Nb0) was cast with the same matrix composition as the other four alloys, but without carbides. The effect of the hard carbides is apparent since the Nb0 alloy showed the highest wear coefficient, evaluated through dry RWAT using hematite as the abrasive, Figure 15. Examination after the test revealed that the carbides of the alloys Nb5 and Nb5Ti suffered cracking resulting in higher wear coefficients than for Nb2.5 alloys.

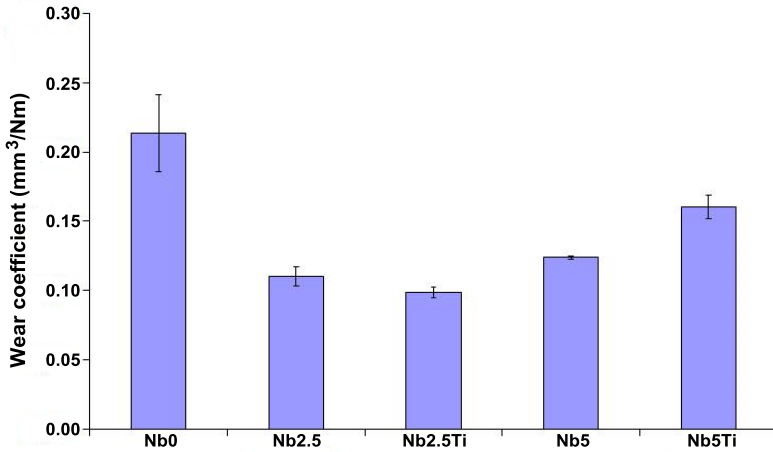


Figure 15. Wear coefficient of the HSS-Nb alloys. RWAT: 130 N, 200 rpm, 30 min, hematite (-210 μm +105 μm ; 860 HV 0.1) [12].

The Nb2.5 alloy showed Chinese script-like eutectic NbC carbides in the form of eutectic cells, while the Nb2.5Ti alloy contained polygonal divorced NbC carbides. Microstructural examination after the wear test showed that for the abrasion tests performed with hematite, just part of the Chinese script carbide was pulled out along with the matrix in the Nb2.5 alloy. Moreover, the polygonal divorced carbides of the Nb2.5Ti alloy were not pulled out, even when the matrix was severely worn, as shown in Figure 16.

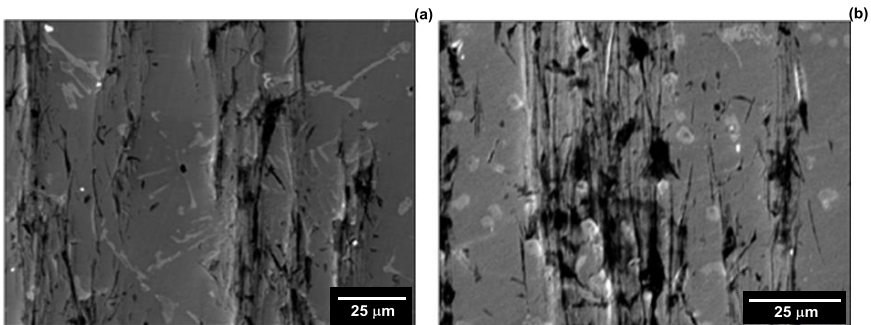


Figure 16. Details of the worn test piece of the Nb2.5 alloy (a) and the Nb2.5Ti alloy (b). SEM – back-scattered electrons [12].

A microstructural analysis was attempted to rationalize the abrasion behavior of those alloys, noting a clear relationship with carbide perimeter, as shown in Figure 17. Further investigation might confirm a linear correlation between carbide perimeter and wear coefficient, as well as indicate whether the result for Nb₂.5Ti alloy is actually a minimum.

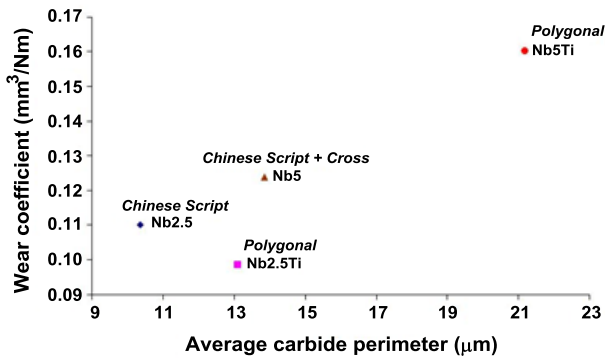


Figure 17. Relationship between wear coefficient and average NbC carbide perimeter [12].

Carbon Content

Apart from the microstructure, some results also show a correlation between the carbon content of the alloys and their abrasion resistance. Figure 18 presents data from ongoing research on the abrasion resistance of 13% manganese steel (Hadfield) with similar bulk hardness, used in crushing operations at mines.

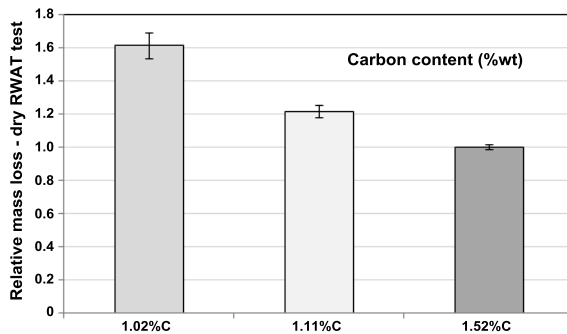


Figure 18. Relationship between the relative mass loss (reference material ASTM H13 steel 514 ± 5 HV) and carbon content of manganese steel, with coarse abrasive particle size. Dry RWAT, silica (+300 – 600 μm, 130 N, 10 min) [13].

The decrease in mass loss with increasing carbon content was confirmed by dry and wet rubber wheel abrasion tests, performed on the alloys with the largest differences of carbon content; results shown in Figure 19.

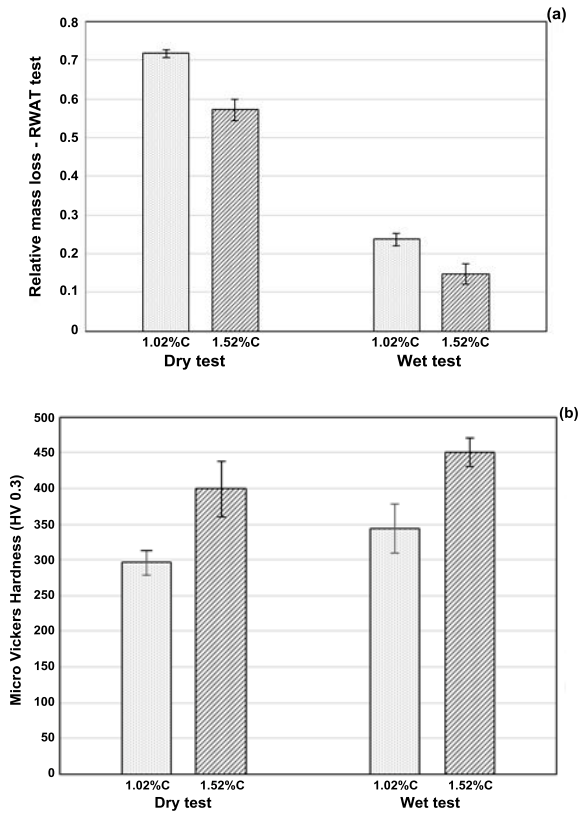


Figure 19. Relationship between the relative mass loss (reference material ASTM H13 steel 514 ± 5 HV) and carbon content of manganese steel, with fine abrasive particle size. Dry RWAT, silica ($\sim 300 + 150 \mu\text{m}$, 130 N, 10 min) [13].

The effect of increasing carbon content was the same for both dry and wet tests, as was observed with the large abrasive grain size ($600 -v- 150 \mu\text{m}$) in Figure 18. After dry and wet abrasion tests, measurements showed that surface hardness was higher for the high carbon steel. Therefore, it is hypothesized that the higher carbon content has promoted a more intense work hardening for the high carbon alloy than for the low carbon one and that resulted in lower mass loss of the high carbon alloy in the three test conditions.

The paper of Diesburgh and Borik [14], presents supportive information about such findings regarding the abrasion resistance of manganese steels. The authors performed a series of jaw crusher tests on nine Hadfield steels for which chemical compositions, hardness and wear results are displayed in Tables VI and VII where the gouging wear ratio is the ratio between the mass losses of a sample and the mass loss of a reference material.

Table VI. Chemical Composition of Hadfield Steels, wt.%

| Code No. | Materials | Element, % | | | | | | | | |
|----------|-------------|------------|-------|------|----|----|------|---|---|--------|
| | | C | Mn | Si | Cr | Ni | Mo | P | S | Other |
| 40 | 12Mn-1Mo | 0.65 | 12.74 | 0.51 | - | - | 0.96 | - | - | |
| 41 | 12Mn | 0.93 | 12.97 | 0.5 | - | - | - | - | - | |
| 42 | 12Mn-1Mo | 0.93 | 12.0 | 0.5 | - | - | 1.0 | - | - | |
| 43 | 12Mn-1Mo | 1.09 | 12.5 | 0.5 | - | - | 0.94 | - | - | |
| 44 | 12Mn | 1.10 | 12.5 | 0.5 | - | - | - | - | - | |
| 45 | 12Mn | 1.24 | 12.5 | 0.5 | - | - | 0.05 | - | - | |
| 46 | 12Mn-1Mo-Ti | 1.26 | 12.5 | 0.5 | - | - | 0.96 | - | - | 0.25Ti |
| 47 | 12Mn-1Mo-Ti | 1.29 | 12.5 | 0.5 | - | - | 0.94 | - | - | 0.18Ti |
| 48 | 12Mn-1Mo-Ti | 1.29 | 12.5 | 0.5 | - | - | 1.02 | - | - | 0.13Ti |
| 49 | 12Mn-1Mo-Ti | 1.31 | 12.5 | 0.5 | - | - | 0.92 | - | - | |

- Not analyzed

Table VII. Hardness, Wear Results and Impact Energy of Hadfield Steels

| Code No. | Type of Steel | HB | Charpy V-notch Energy (ft-lb) | Charpy V-notch Energy (J) | Gouging Wear Ratio | Weight Loss (g) | Principal Components of Microstructure * |
|----------|---------------------|-----|-------------------------------|---------------------------|--------------------|-----------------|--|
| | | | | | | Pin | |
| 40 | 12Mn-1Mo (0.65C) | 191 | 88 | 119 | 0.42 | - | A |
| 41 | 12Mn (0.95C) | 185 | 102 | 138 | 0.33 | 0.0871 | A |
| 42 | 12Mn-1Mo (0.95C) | 188 | 53 | 72 | 0.32 | - | A,P |
| 43 | 12Mn-1Mo (1.09C) | 192 | 107 | 145 | 0.29 | 0.0821 | A |
| 44 | 12Mn (1.1C) | 199 | - | - | 0.28 | - | A |
| 45 | 12Mn (1.25C) | 198 | 59 | 80 | 0.21 | - | A |
| 46 | 12Mn-1Mo-Ti (1.25C) | 201 | 53 | 72 | 0.21 | - | A |
| 47 | 12Mn-1Mo-Ti (1.3C) | 204 | 64 | 87 | 0.22 | - | A |
| 48 | 12Mn-1Mo-Ti (1.3C) | 201 | 57 | 77 | 0.22 | - | A |
| 49 | 12Mn-1Mo-Ti (1.3C) | 199 | 25 | 34 | 0.21 | - | A |

* A - austenite, P - pearlite

The relative mass loss data from the jaw crusher tests from Table VII are plotted in Figure 20 [14]. The decrease of abrasion losses with increasing carbon content, foreseen in the limited results from Figures 18 and 19, was confirmed with this larger number of experiments and in a quite distinct tribosystem, more related to the application where those alloys are used.

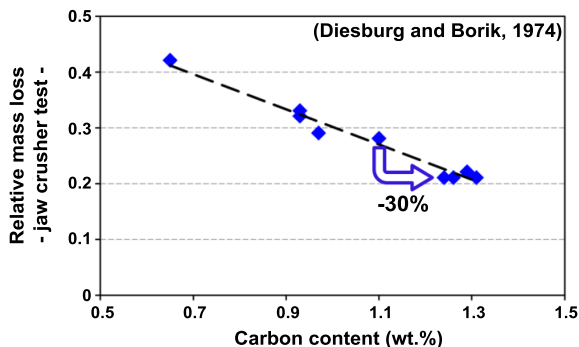


Figure 20. Relationship between the relative mass loss and carbon content of manganese steel. Jaw crusher tests [14].

Increasing the (dissolved) carbon content from 1.05 to 1.35%, ie. the bottom and upper limit of the ASTM class “C” manganese steel standard, resulted in a decrease in the relative mass loss from 0.28 to 0.20, approximately 30%. Each 0.1% of carbon resulted in a 10% increase of abrasion resistance. The effect of carbon in Figures 18 and 19 is around 7% per 0.1% carbon. This achievement was not highlighted by the authors at the time of the publication [14].

Environment

The last of the effects, not directly connected to hardness, is the effect of the environment, as presented in Figure 21.

Two distinct tendencies can be seen in Figure 21. As the abrasive particle size increased, the abrasion also increased, at first strongly, as the abrasive grain size increased from 0.15 to 0.60 mm. After that, the increase in abrasion occurred at a lower rate. The second trend is that the abrasion was more intense at lower pH values for all the grain sizes. The decrease in the abrasive wear rate from the lowest to the highest pH lies on the range ~20 to 80% depending on the abrasive particle size, an effect that may be more pronounced than some of the hardness and microstructural effects studied before in this paper. The reason for this behavior is not yet fully understood.

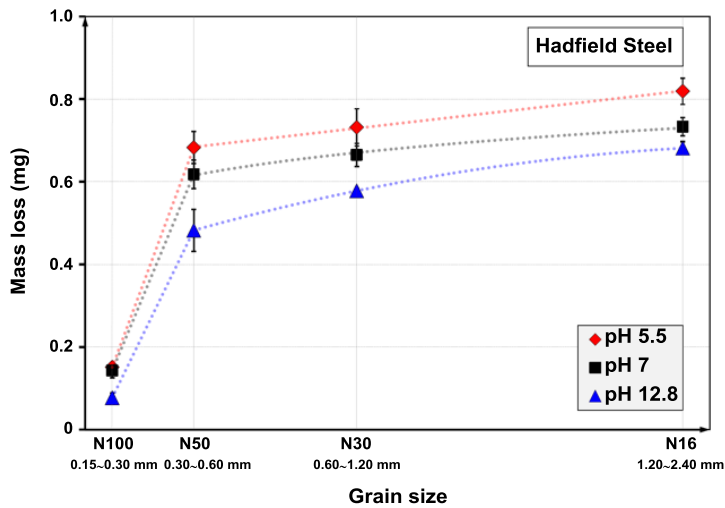


Figure 21. Relationship between abrasive grain size, pH and mass loss of manganese steel. Wet RWAT, (Hadfield composition: 1.11%C, 14.2%Mn and 1.81%Cr). Tressia [15].

Conclusions

The relationship between laboratory tests and field performance is a complex subject still open to discussion and investigation. However, the results show clearly that laboratory wear tests performed under test conditions more severe than those found in field service will underestimate the benefits of improving material hardness. Since this improvement is achieved at higher costs, the benefits can be underestimated as a consequence of severe conditions of the laboratory test.

Relatively small hardness decreases due to casting, welding, and heat treatment variations will strongly reduce the abrasion resistance of the components that are used in the transition region between mild and severe wear. In other words, transferring laboratory results to field operations requires careful follow-up, in order to assure that sound and reliable materials like the ones tested in a laboratory will be applied to each piece of equipment.

Hardness and hard, large phases are key factors to produce high abrasion resistant materials.

Niobium plays a decisive role in increasing abrasion resistance of materials for the mining industry. The shape, size and distribution of niobium carbides need to be engineered to achieve the maximum effect.

Acknowledgements

The authors acknowledge the companies CBMM (Companhia Brasileira de Metalurgia e Mineração), ThyssenKrupp Fördertechnik Latino Americana and Vale for supporting research activities. A special thanks to researchers in the area of abrasion that have been part of the Surface Phenomena Laboratory: Luiz Alberto Franco, Gustavo Tressia de Andrade, Jimmy Penagos, Juan Ignacio Pereira, Paulo Machado, Marcos Henrique Ara, Giuseppe Pintaúde, John Jairo Coronado, Marcio Matos Santos, Felipe Gustavo Bernardes, Sara Aida Rodríguez Pulecio and Leonardo Villabón.

References

1. K. Holmberg, "Reliability Aspects of Tribology," *Tribology International*, 34 (12) (2001), 801–808.
2. E. Rabinowicz, L.A. Dunn and P.G. Russell, "A Study of Abrasive Wear Under Three-body Conditions," *Wear*, 4 (5) (1961), 345-355.
3. J. Gates, "The Challenge of Accurate Prediction of Industrial Wear Performance from Laboratory Tests," Paper presented at the International Symposium on Wear Resistant Alloys for the Mining and Processing Industry, Campinas 2015.
4. J.D. Gates, "Two-body and Three-body Abrasion: A Critical Discussion," *Wear*, 214 (1) (1998), 139-146.
5. K. Zum Gahr, *Microstructure and Wear of Materials* (Amsterdam, The Netherlands: Elsevier Science Publishers B.V., 80-131, 1987.
6. G. Pintaude et al., "Mild and Severe Wear of Steels and Cast Irons in Sliding Abrasion," *Wear*, 267 (1-4) (2009), 19-25.
7. J.J. Coronado, S.A. Rodríguez and A. Sinatora, "Effect of Particle Hardness on Mild-severe Wear Transition of Hard Second Phase Materials," *Wear*, 301 (1-2) (2013), 82-88.
8. A.A. Torrance, "An Explanation of the Hardness Differential Needed for Abrasion," *Wear*, 68 (2) (1981), 263-266.
9. J.J. Penagos, G. Tressia and A. Sinatora, "Abrasive Wear Tests on Materials used for Wear Plates" (Surface Phenomena Laboratory Technical Report TK 03-1-001-Rev0 for ThyssenKrupp Fördertechnik Latino Americana - TKFLA, 2014).
10. J.J. Penagos and A. Sinatora, "The Effect of Structure Refinement and Niobium Addition on Abrasion Resistance of White Cast Irons used for Slurry Pump Impellers" (Surface Phenomena Laboratory Technical Report NB01-2-003-Rev0 for CBMM - Companhia Brasileira de Metalurgia e Mineração, 2013).

11. J.J. Penagos et al., “Structure Refinement Effect on Two and Three-body Abrasion Resistance of High Chromium Cast Irons,” *Wear*, (doi:10.1016/j.wear.2015.03.020) (2015).
12. P.F. Silva and M. Jr. Boccalini, “Abrasive Wear of Nb-alloyed High Speed Steels,” *Proceedings of the First International Brazilian Conference on Tribology*, Rio de Janeiro, Brazil, 26 November 2010.
13. P. Machado and A. Sinatora, “Abrasive Wear Tests on Hadfield Steels Extracted from Field Samples” (Surface Phenomena Laboratory Technical Report VL0X-1-001-Rev0 for VALE, 2015).
14. D.E. Diesburg and F. Borik, *Optimizing Abrasion Resistance and Toughness in Steels and Irons for the Mining Industry*, (Materials for the Mining Industry Vail Co. Climax Molybdenum Co., 1974). 15-42.
15. G. Tressia, “Abrasion Resistance of Hadfield Steel for Crushers–Effect of the Abrasive Grain Size on pH” (Master Degree Dissertation, 2015), 127.

EFFECTS OF NIOBIUM ADDITIONS ON THE PROPERTIES AND LIFE CYCLE OF STEELS FOR HOT WORKING TOOLS

F. Hippenstiel

BGH Edelstahl Siegen GmbH, Siegen, Germany

Keywords: Hot Work Steel, Microalloying, Hardness, Toughness, Wear Resistance,
Forging Tools

Abstract

Mechanical, thermal, and chemical loads influence the life cycle of hot working tools. For economic hot forming processes, tools and dies are made from classical hot work steels of the CrMoV and NiCrMoV steel groups. The CrMoV steels, with a secondary hardening effect, are mainly used in the die-casting industry and as high stressed dies in drop forging presses. Hammer dies have a higher demand on toughness, so NiCrMoV grades are used. In every case, tool properties depend on the steelmaking processes and the final heat treatment. Increasing demands on tools are created by changes in process technologies, such as using bigger tools and dies or critical cavity geometries. In this case, there is a need for a further optimization of classical tool steels in view of the toughness behavior. This paper shows one way to increase mechanical-technological properties through small additions of niobium that lead to a higher toughness of existing steels grades. Thus, microalloying can be used for alloy design of new hot work steels.

Introduction

An essential function of any hot work steel is the capacity to retain sufficient hardness at working temperature during forging or casting. High hardness is best for resisting wear, but this can lead to premature cracking of the tool. If the hardness of the selected steel is too low, the steel will rapidly erode under working conditions and lack thermal stability. In addition, selection of hot work steels has to include the complexity of the mechanical, thermal, and chemical loads and the expected life cycle (number of forgings to be produced). Prime requirements can be summarized as follows:

- Good machinability (most steels for forging tools will be supplied in the pre-hardened condition);
- Resistance to the mechanical and thermal stresses without fracture in service;
- High life cycle (high number of produced forgings without losing shape);
- Low tool costs over the whole supply chain from steel to final product [1].

Appropriate people in the forge shop, adequate production facilities and the correct tool steel are the basics for a successful hot forming process. Forge masters have faced new challenges given by increasing demands on product sizes, new high strength pre-material for hot deformation, and more complex component geometries. An example for such new challenges is given in Figure 1 [2].



Figure 1. Example of a complex forging. (a) Die tool, (b) aluminum forging for an airplane [2].

For a higher tool life cycle, the use of a perfect tool steel is a precondition. The main requirements on material characteristics are listed as follows:

- Homogeneous microstructure (uniform distribution of carbides, low segregation);
- High cleanliness (and residual non-metallic inclusions have to be shape-controlled);
- Low content of sulfur and phosphorus.

By fulfilling these requirements, a higher toughness level in the hardened condition is expected. In addition, the correct heat treatment to attain the desired working hardness, surface treatment (if required), and maintenance of the tool during production are responsible for a high tool life. Figure 2 shows the load conditions affecting the hot working steel during drop forging [2].

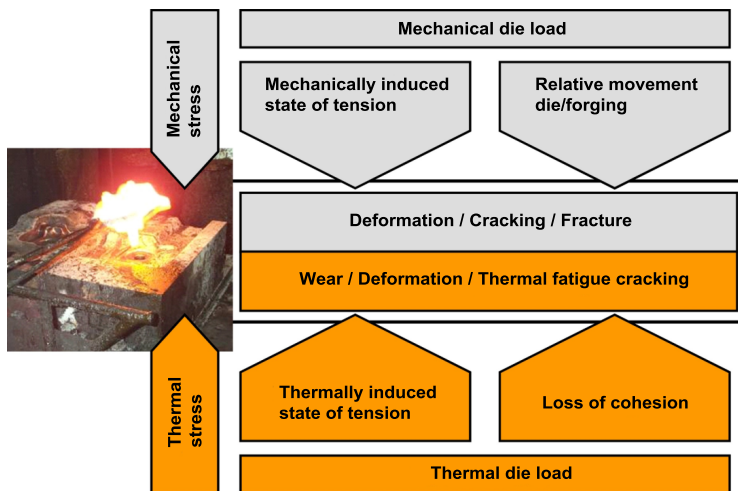


Figure 2. Load condition of a forging tool [2].

The task of a tool steel producer, therefore, is to contribute to extending the life cycle of the tool by modification of existing tool materials, or developing new alloying concepts.

Production of Hot Work Steels and Alloying Principles

The classic route for producing tool steels, like hot work steel, is the electric arc furnace process. Scrap is melted down using electrical energy to first produce crude steel, which then undergoes further treatment and refining by secondary metallurgy in a ladle furnace and degassing station. In most cases, the steel is also deep desulfurized in secondary metallurgy, and then poured by ingot casting or continuous casting for further processing. One of the most important steps is metal forming using the correct hot rolling and forging processes. Much of the steel used for tool and mold making is made from rolled billets. Larger dimensions are produced by forging. After forming, the steel manufacturer carries out a suitable heat treatment, which may be either a preliminary heat treatment prior to machining, or a final heat treatment in the case of pre-hardened tool steels. Figure 3 shows the process route for manufacturing as-forged dimensions [3].

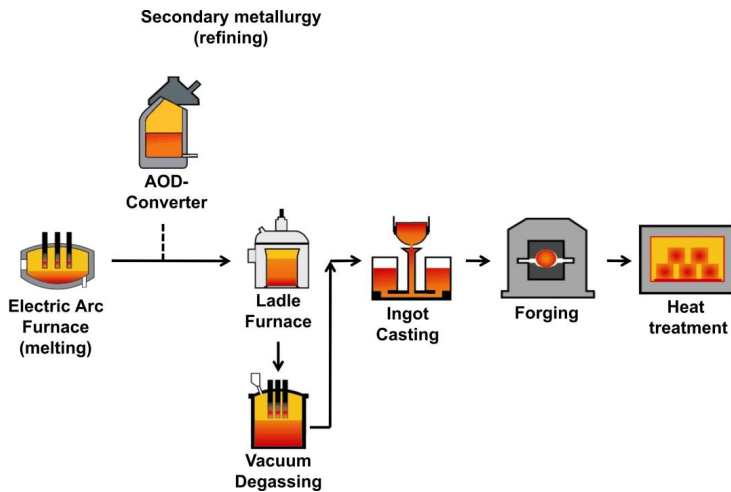


Figure 3. Process route for manufacturing forged tool steels.

In addition to conventional steelmaking, there are also special metallurgical processes available. These technological solutions are mostly combined with the established traditional methods of steelmaking and applied metallurgy. Special melting processes, such as electro slag remelting (ESR) or vacuum arc remelting (VAR), achieve very fine solidification structures because of the increased local solidification speeds associated with these processes. They also reduce the incidence of non-metallic impurities, sometimes introduced from the pre-melt, which can have an influence on the final toughness, as shown in Figure 4 [3].

Over the years, requirements of hot work steels have been increasing, especially for die casting tools. To follow customer demands, steel makers have been carrying out a lot of process improvement in steel melting, and in heat treatment of the slabs and ingots, as well as heat treatment of the produced hot work steels. The latest results of process improvement are low content of tramp elements in the steel to protect against embrittlement during service [4]. The measures are very expensive, so that the steel user has to balance performance requirements, steel costs and the expected life cycle of the tools.

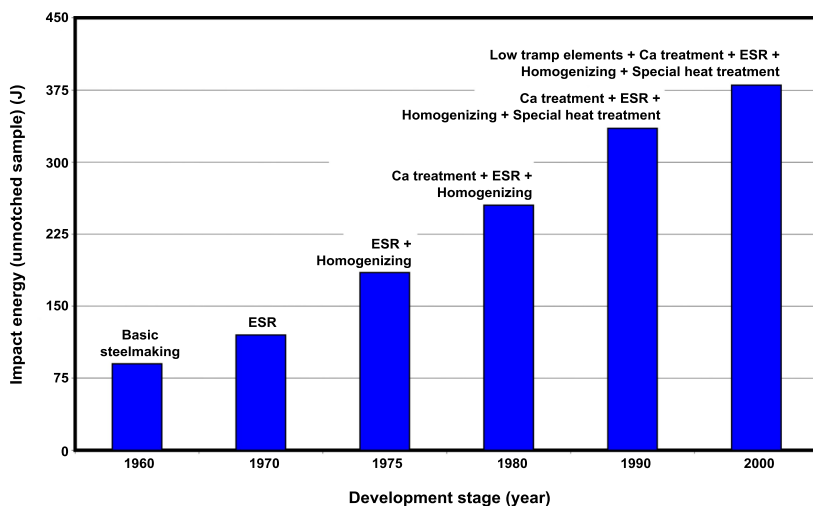


Figure 4. Measures in production of hot work steels to fulfill highest material toughness requirements [4].

The selected alloying design of hot work steel has a significant influence on the properties and the life cycle of the tools. Table I gives an overview of hot work steels according to the DIN EN ISO standard 4957 [5].

Table I. Major Hot Work Steels for Forging Dies According to DIN EN ISO 4957, wt.% [5]

| Steel grade | Standard | | C | Si | Mn | Cr | Mo | Ni | V | Application |
|--------------|----------|------|------|------|------|------|------|------|------|-------------------------|
| 55NiCrMoV7 | 1.2714 | min. | 0.50 | 0.10 | 0.60 | 0.80 | 0.35 | 1.50 | 0.05 | Hammer dies, die holder |
| | | max. | 0.60 | 0.40 | 0.90 | 1.20 | 0.55 | 1.80 | 0.15 | |
| 32CrMoV12-28 | 1.2365 | min. | 0.28 | 0.10 | 0.15 | 2.70 | 2.50 | - | 0.40 | Press dies |
| | | max. | 0.35 | 0.40 | 0.45 | 3.20 | 3.00 | - | 0.70 | |
| X37CrMoV5-1 | 1.2343 | min. | 0.33 | 0.80 | 0.25 | 4.80 | 1.10 | - | 0.30 | |
| | | max. | 0.41 | 1.20 | 0.50 | 5.50 | 1.50 | - | 0.50 | |
| X38CrMoV5-3 | 1.2367 | min. | 0.34 | 0.30 | 0.30 | 4.80 | 2.70 | - | 0.40 | |
| | | max. | 0.40 | 0.50 | 0.50 | 5.20 | 3.20 | - | 0.60 | |
| X40CrMoV5-1 | 1.2344 | min. | 0.35 | 0.80 | 0.25 | 4.80 | 1.20 | - | 0.85 | |
| | | max. | 0.42 | 1.20 | 0.50 | 5.50 | 1.50 | - | 1.15 | |

Mainly, performance of the different steel concepts is influenced by the carbon content and by alloying with chromium, manganese, silicon, molybdenum, nickel, and vanadium. Increasing the carbon content will cause an increase in the strength and in the hardenability, but toughness will be reduced. The effect of the other alloying elements on properties of hot work steel is given in Table II.

Table II. Effect of Alloying Element on Properties of Hot Work Steel

| Property | Si | Mn | Cr | Mo | Ni | V |
|-------------------|----|----|----|----|----|----|
| Wear resistance | - | - | + | ++ | - | ++ |
| Hardenability | + | + | ++ | + | + | + |
| Toughness | - | ± | - | + | + | + |
| Thermal stability | + | ± | + | ++ | + | ++ |

In practice, hot work steels using the CrMoV alloying concept show inadequate toughness and low thermal conductivity, but a high heat and wear resistance. In comparison, the NiCrMoV steel concept shows better toughness properties driven by the high nickel content, but the wear resistance is lower. This results from a lower content of carbide-forming elements, such as chromium, molybdenum and vanadium.

Classical hot work steels of the CrMoV group show, during tempering in a temperature range of 400 to 550 °C, a secondary hardness maximum due to generation and then coarsening of precipitates (carbides) during tempering. Figure 5 compares a tempering diagram of the grade X40CrMoV5-1 with steel grade 55NiCrMoV7. This latter steel shows a normal tempering curve, comparable with classical quenched and tempered steels.

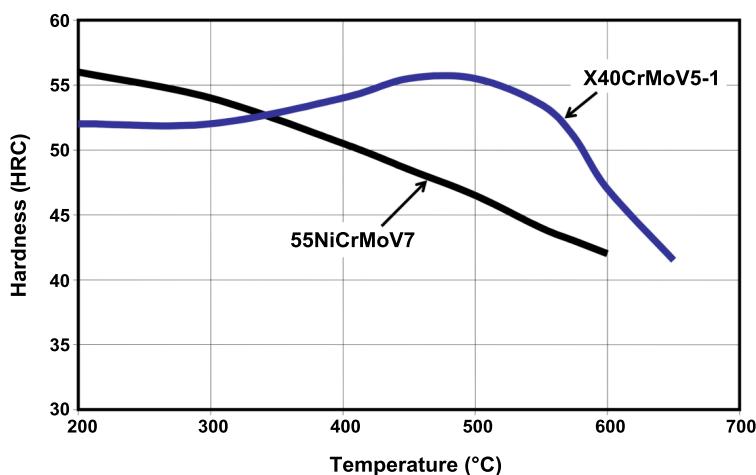


Figure 5. Tempering diagram of the hot work steels 55NiCrMoV7 and X40CrMoV5-1.

To extend the life cycle of hot work steels, improvement of the thermal fatigue behavior is necessary. Due to the relationship between grain size and toughness of the material, controlling grain size and preventing grain coarsening during heat treatment is a possible option. Figure 6 shows the effect of toughness and grain size; coarse grains cause premature crack formation and result in material pitting, Figure 6(a). Finer grains lead to fine incipient cracking with no material pitting, Figure 6(b).

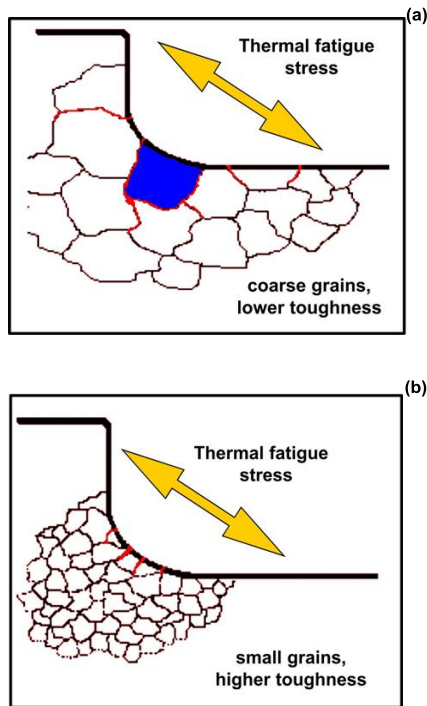


Figure 6. Effect of material toughness and grain size on thermal cracking of tools [6].

Effect of Niobium Additions on Properties and Life Cycle

Niobium is an element with high affinity for carbon and forms very stable carbides. Therefore, it is well suited as a carbide forming alloying element in the production of tool steels. In many cases, niobium is added to hot work steels in a range up to 0.20 wt.%. The target of such microalloying is to inhibit austenitic grain growth during heat treatment. Furthermore, an investigation to reduce vanadium content in X40CrMoV5-1(AISI H 13) to 0.5 wt.% and add 0.1 wt.% niobium has been carried out. The modified grade shows the same properties as H13 grade with 0.95 wt.% vanadium, but production costs are lower and the austenite grain size is finer. A similar alloying concept according to this described design has found industrial application in the die casting industry [7-9].

Furthermore, smaller additions of niobium support the enhancement of properties of hot work steels. One example is given by microalloying heavy-duty forgings of a NiCrMoV steel, due to increasing demands in terms of quality. In order to convert raw ingots into high-quality forged products with uniform properties, it is necessary to control grain size during the whole manufacturing process. A significantly finer ferrite grain leads to better testability of heavy-duty forgings by ultrasonic inspection and for adjusting the mechanical-technological characteristics. Figure 7 shows results of the calculated and measured grain size of a forged hot work steel block. The NiCrMoV steel with a high content of precipitates, Heat B, was microalloyed with niobium. It is evident that the melt with a small niobium addition shows a finer grain size in the simulation by the BGH Edelstahl software MICDEL, as well as in metallographic investigations in the central position of the forged and heat treated bar. In principle, improvement of microstructure of heavy-duty forgings made of hot work steels is possible by microalloying [10].

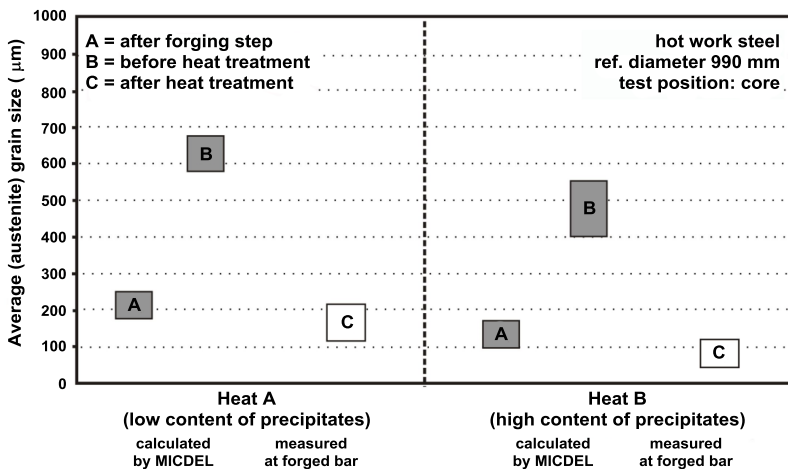


Figure 7. Calculated and measured grain sizes of a forged hot work steel block with different amount of precipitates [10].

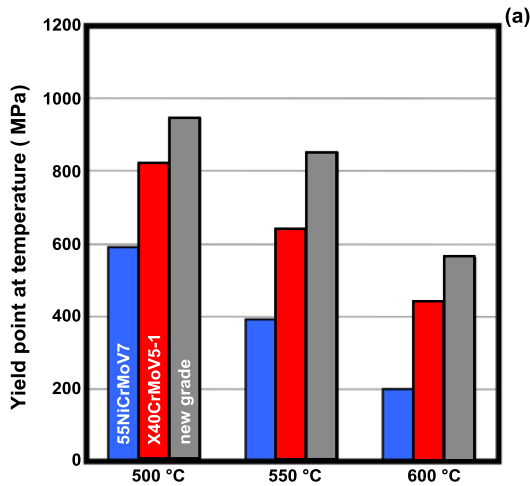
Another example of the use of niobium in hot work steels is the possibility to create a new steel type [2,11,12]. The idea behind the development was to combine the positive properties of the CrMoV and NiCrMoV steel groups, ie. toughness combined with wear resistance. The chemistry of the new grade is given in Table III.

Table III. Alloying Concept of New Hot Work Steel Grade, target analysis, wt.% [11]

| C | Si | Mn | Cr | Mo | Ni | V | Nb |
|------|------|------|------|------|------|------|------|
| 0.35 | 0.25 | 0.50 | 2.70 | 1.00 | 0.65 | 0.20 | 0.04 |

In practical use, the new steel shows very good properties with regard to the state-of-the-art tools. This behavior is conferred by a very good thermal conductivity, high temperature yield strength and good toughness. The life cycles of the tools made with this new steel grade exceed those from the hot work tool steel X40CrMoV5-1 and therefore, the development represents an economical alternative. Yield strength and toughness of the new grade, in comparison with the classical hot work steel 55NiCrMoV7 and X40CrMoV5-1, are given in Figure 8.

During the development of this steel grade, Thermo-Calc calculations of precipitation have been carried out which show the existence of carbides at significantly higher temperatures for the niobium alloyed variant, when compared to the niobium free steel. In the range of usual tempering temperatures, the quantity of secondary hardening carbide is higher compared to grade X40CrMoV5-1. This explains the results of the new steel grade in mechanical-technological tests and the reported behavior and life cycle of tools in the field [11].



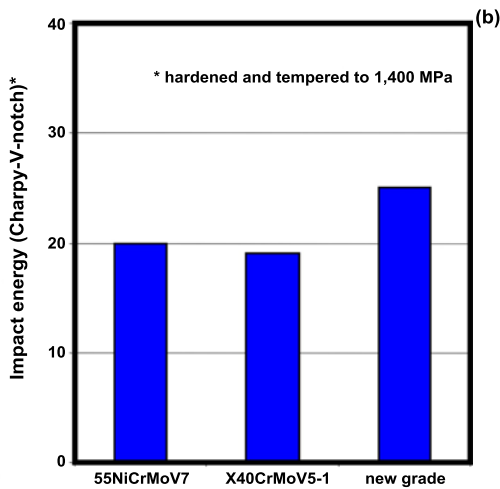


Figure 8. Yield strength and toughness of a new Nb microalloyed hot work steel in comparison to classical grades; (a) Yield strength, (b) Charpy toughness [12].

A special application of this hot work tool steel is the so-called mandrel bar for production of seamless rolled tubes. In general, the steel X40CrMoV5-1, or slight variations, is used; the strength is adjusted to about 1150 MPa. In addition, there are relatively high toughness demands. A variety of measures has been attempted over the years to increase the toughness.

By adding niobium, toughness should be improved. A pilot industrial heat has been cast and the steel bars for mandrels have been produced under the same process condition as for steel bars without niobium. Figure 9 shows the results of the mechanical testing of steel bars for mandrels with dimensions from Rd. 200 to 300 mm with the same heat treatment parameters, compared with the results of a melt modified with niobium. It is shown in this example, that toughness is somewhat higher in the niobium steel than in the classical steel. It is now to be tested whether the improvement in the toughness can be reproduced.

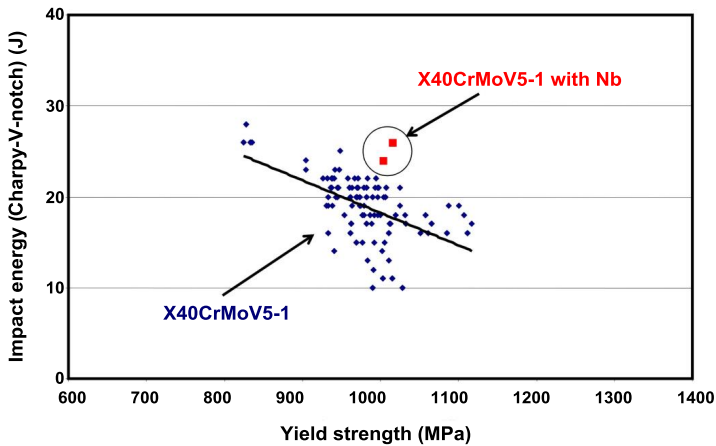


Figure 9. Results of mechanical testing steel bars in X40CrMoV5-1 for mandrels, toughness versus yield strength, in comparison with results for a Nb modified heat of the same grade.

Conclusions

In the selection of hot work tool steels, it is necessary to pay attention to balancing working hardness and toughness. Toughness influences the tool wear and thus, overall costs. It is possible to influence the grain sizes of hot work tool steels through additions of niobium. During heat treatment, grain coarsening is reduced due to the presence of niobium carbides. This should be reflected in improved toughness behavior.

Accordingly, a pilot industrial heat has been cast and the steel bars for mandrels have been produced under the same process condition, as for those without niobium. For an equivalent strength, the Nb-containing bars indeed exhibited superior toughness as expected. Further work is in progress to confirm the reproducibility of this effect.

This mode of action of niobium could be used to develop new steel grades, as well as optimizing existing steel grades.

References

1. Confederation of British Forgers: Codes of best forging practice, Selection of die steels, 1996.
2. P. Vetter and F. Hippenstiel, "High-Performance Die Steels for Creating New Customer Values," (Paper presented at the 20th International Forging Congress IFC, Hyderabad, 2011), 251-254.
3. F. Hippenstiel, "Plastic Mold Steels," in G. Menning und K. Stoeckhert, *Mold-Making Handbook*, 3rd Edition, (Hanser, 2013).

4. F. van Soest, C. Ernst and D. Duh, Stand der Technik bei den Werkzeugstählen, Präsentation Seminar Dr. Sommer Werkstofftechnik, Issum, 04.05.2009.
5. DIN ISO EN 4957 Werkzeugstähle – Tool steels.
6. P. Vetter, Presentation Hot Work Steel, 2000.
7. F. Jeglitsch, Niobium in Tool Steels, Part I, BHM, 146. Jg. (2002), Heft 3, 50-60.
8. F. Jeglitsch, Niobium in Tool Steels, Part II, BHM, 146. Jg. (2002), Heft 5, 151-158.
9. K. Hulka and J.R.C. Guimaraes, *The Role and Emerging Use of Niobium in Tool Steels*, (Brazil, CBMM, 1993).
10. F. Hippenstiel and P. Vetter, “Manufacturing Tool Steels for Large Moulds and Dies - A Challenge for the Steel Industry,” (Paper presented at the 7th International Tooling Conference Tool 2006, Turin, 2006), 371-377.
11. D. Bockholt, D. Caliskanoglu and P. Vetter, “A New High-performance Die Steel for the Forging Industry,” (Paper presented at the 9th International Tooling Conference Tool 2012, Leoben, 2012), 183-190.
12. Patent application EP2535430A2, 2011.

THE CHALLENGE OF ACCURATE PREDICTION OF INDUSTRIAL WEAR PERFORMANCE FROM LABORATORY TESTS

J.D. Gates¹, P.J. Bennet², L.J. McInnes² and B.R. Tunstall³

¹AMPAM (Advanced Materials Processing and Manufacturing), The University of Queensland, St. Lucia, Qld 4072, Australia

²UQMP (UQ Materials Performance), The University of Queensland, St. Lucia, Qld 4072, Australia

³School of Mechanical and Mining Engineering, The University of Queensland, St. Lucia, Qld 4072, Australia

Keywords: Low Stress Sliding Abrasion, High Normal Stress Abrasion, Martensitic Steels, White Cast Irons, Ball Mill Abrasion Test, Sliding-bed Abrasion Test, Field-laboratory Correlation

Abstract

Several plant wear trials and several laboratory test methodologies are described and analysed. Each example is evaluated in terms of its success (or lack thereof) in yielding useful quantitative performance data for candidate wear-resistant materials. Field trials are challenging, though if performed with sufficient care and resources they can yield useful quantitative data. To be useful, a laboratory test must satisfy several performance criteria, notably: It should simulate with reasonable fidelity both the macro-mechanics and micro-mechanics of the conditions present in the field; it should be validated against field trials and confirmed to produce accurate quantitative performance predictions for various classes of materials; it should not be excessively sensitive to precise set-up conditions; and it should provide reasonable data productivity and statistical quality. Rather than attempting to break down a complex industrial wear process into its individual component mechanisms and “engineer” each of these mechanisms in the laboratory, fidelity is more likely to be achieved by a mechanically simple device that preserves the natural complexity of the industrial wear process.

In the process of the case studies, commentary is given on two key modes of abrasive wear, namely high normal stress abrasion (HNSA) and low stress sliding abrasion (LSSA). An important lesson from this analysis is the fundamental observation that LSSA does not equate to low wear rates; indeed, the highest wear rates observed industrially are from LSSA, due to the dominance of tangential sliding and high tonnage throughputs. The nature of LSSA is such that materials selection has the capacity to achieve much greater percentage improvements in component service life than is possible in HNSA situations. The proposed new generation of field-validated laboratory tests will provide confidence to invest in the development of superior wear-resistant materials. One promising class of wear-resistant casting alloy is a “double composite” in which niobium-rich carbides provide additional reinforcement to a conventional chromium carbide eutectic cast iron.

Introduction and Aims

Materials Selection for Mining and Minerals Processing Plant

The operators of mining and mineral processing plant face a difficult challenge when selecting the best wear-resistant material for each item of equipment at their site. Experience demonstrates that there is no single material that performs well in every situation. For example, alloys that perform well in slurry pumps are not necessarily the best alloys for ball mill liners or ore chutes. Similarly, alumina-based ceramics might perform reasonably well in some ore chutes, but would not be expected to perform well in ball mills or ground-engaging tools. These differences in the relative performance of candidate wear-resistant materials are due to the different ways in which their microstructures respond to the operative wear modes in these different applications.

Selection of the best or most cost-effective wear-resistant material or product relies upon an understanding of the factors that control the relative performance of the various candidate classes of materials in different wear modes. Moreover, even when armed with such specialist understanding, it is not possible to reliably predict the best material from first principles or general experience alone; appropriate wear tests must be performed utilising the target ore. This is because wear mode is not a simple function of the macro-mechanics of the industry operation, but is strongly influenced by the mineralogy and other properties of the ore.

The requirement for physical tests to be performed raises the need for access to reliable test methodologies. In principle, the gold standard for data generation is a full-scale plant trial or field trial. However, full-scale plant or field trials are expensive, time consuming and carry considerable risk. Moreover, wear rates in the plant can be affected by variable characteristics of the ore stream, and it can take a very long time to collect statistically reliable data. On the other hand, plant operators are justifiably suspicious of the predictions from laboratory tests, which have often been demonstrated to have poor predictive ability.

Aims and Strategies

The objective of the authors' research is to develop new laboratory abrasive wear test methods that are superior to some of the commonly used tests that have been shown to be flawed. Any proposed new laboratory test in this field should satisfy all of the following criteria:

- It should reproduce or simulate, with reasonable fidelity, the actual abrasive wear conditions that are present in the field - notably the ore itself and the contact mechanics;
- It should be validated against empirical trials in the field, and confirmed to produce comparable quantitative relative performance data for different wear-resistant materials;
- It should not be excessively sensitive to precise set-up conditions;
- It should provide reasonable data productivity and statistical quality.

The first criterion above mentions the "ore", that is, the abrasive substance that will be encountered in the plant. Perhaps the most important single requirement for any abrasive wear test is that it must use the same abrasive medium as will be encountered in the target industry operation. It is well established that abrasive wear resistance is not a fundamental material

property; it is a system property. This principle is so important, but so often forgotten, that it is worth quoting M.A. Moore [1] on the subject: “In selecting and specifying laboratory wear tests, attention must be paid to the fact that wear performance is systems related, depending not only on materials properties, but also on the characteristics of the abrasive, sliding and loading conditions.” Predictions of industry performance based on laboratory tests using some idealised abrasive substance are very likely to be misleading. This phenomenon will be illustrated in some of the case studies presented in this paper.

Rather than attempting to break down a complex industrial wear process into its individual component mechanisms and “hard-engineer” each of these mechanisms in the laboratory, the first criterion above is more likely to be satisfied by a device that “preserves the natural complexity” of the industrial wear process. The most successful laboratory tests will be those that are mechanically simple at an external macroscopic scale, but are permitted to sustain complex conditions at the internal microscopic scale. This microscopic complexity is what occurs in industrial service, and efforts to simplify it or apply hard controls to the individual component mechanisms are more likely to introduce errors than to achieve useful outcomes.

Controlled experiments can still be carried out in such externally simple, internally complex test devices, by a “subtraction” principle more so than by an “addition” principle. For example, if it is desired to assess the contribution of corrosion mechanisms to an industrial wear environment, the researcher can attempt to “subtract” the corrosion component by a variety of means, such as removing oxygen, removing electrolytes, use of inhibitors, replacing water by inert fluids, use of corrosion-resistant materials, and combinations of these measures. The corrosion component in the natural environment can be assessed by observing the reduction in the total wear rate that occurs when these measures are taken. The interpretation of the results may not be simple, but such experiments are likely to be more illuminating than tests in which the rate of corrosion is measured in some idealised test that bears no resemblance to the service environment.

This paper will present a number of case studies, sourced both from published literature and from the authors’ own work, to illustrate the comparisons between field performance data and the data from various laboratory abrasive wear tests. The ultimate aim is to encourage the wear research community to move from simplistic laboratory tests, which do not reproduce plant conditions and hence cannot predict plant performance, towards a new generation of laboratory or pilot-scale tests that do reproduce plant conditions with reasonable fidelity and can predict plant performance with reasonable accuracy.

Levels of Correlation between Laboratory and Field Performance

In assessing the correlation between laboratory abrasion test data and plant wear data, four levels of correlation fidelity (and hence predictive ability) should be considered, as follows:

1. Rank correlation, or monotonic increasing correlation: If material A wears faster than material B in the laboratory test then the same ranking should be observed in the plant;
2. Linear correlation: A plot of wear rates for various materials in the field or plant versus their wear rates in the laboratory should show an approximately linear form;

3. Quantitative relative correlation, or unit slope correlation: If material A wears for example 60% faster than material B in the laboratory test, then a similar relative wear rate should be observed in the plant. That is, a plot of relative wear rates in the plant versus relative wear rates in the laboratory should show a linear form with a slope of approximately 1;
4. Quantitative absolute correlation - if a material experiences a wear rate in the laboratory test of for example 10 g/MJ then a similar wear rate should be observed in the plant.

Level 1 correlation is clearly inadequate, since it does not provide sufficient information to determine the most cost-effective material to use for a given target application. Swanson [2] described both level 2 correlation (expressed as a “linear correlation between the relative wear rates (or resistances) measured in the laboratory and the field”) and level 4 correlation (expressed as “the wear coefficient, K , in the abrasive wear equation, producing similar results in both the field test and the laboratory test”). Swanson did not consider the possibility of a level of correlation intermediate between levels 2 and 4; but in the opinion of the current authors, level 3 correlation should usually be sufficient, since it can determine the most cost-effective material for a given application. Moreover, if the plant wear rate for a benchmark material is available, then a level 3 correlation can even permit prediction of the absolute wear rate for a new material. Full level 4 correlation is only required when attempting to predict operating costs for a plant that is yet to be built.

Case Studies from Literature

Scarcity of Field Performance Data

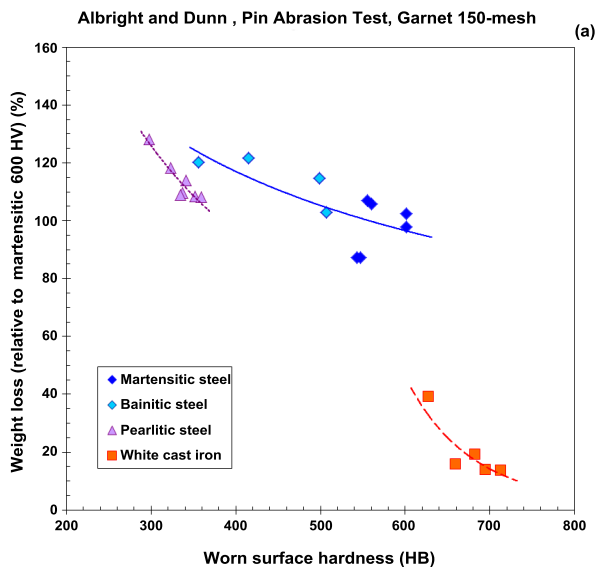
Because plant trials are difficult and expensive to perform, and since confounding variables often render the resulting data questionable, relatively few published studies exist that provide credible plant data. Even more scarce are studies in which credible plant data are correlated with systematic laboratory data for the same or comparable alloys. One of the main aims of the current study is to present some examples of published studies in which this challenging task has been carried out successfully.

Industrial Ball Mill Trial – Albright and Dunn 1983

One of the most detailed and fruitful plant trials that the current authors are aware of was that performed by Albright and Dunn [3]. The plant trial was performed in two nominally identical grate-discharge ball mills, each 2.9 m diameter and 2.4 m long. Each mill was lined with 20 integral-lift shell liners, 1040 mm long and 430 mm wide. The liners had a relatively shallow triple-wave profile, 83 mm thick at the peak and approximately 52 mm at the trough. A total of 40 liners were cast from 22 different alloys and distributed between the two mills. The mills were fed with ore from the Climax Molybdenum mine in Colorado U.S.A., consisting primarily of quartz and granite with a small proportion of MoS_2 . The two mills were operated with nominally identical ore feed type and tonnage throughput, until perforation of the least abrasion-resistant liners after approximately 4800 hours operation.

To achieve a useful comparison with the plant data, Albright and Dunn were aware of the need to select a laboratory test that would produce a wear mode matching that of the plant environment. They judged that the grinding mill environment would be characterised by high stress abrasion, as opposed to either low stress abrasion or gouging abrasion. They then stated that “it is widely agreed that the laboratory pin type test provides reasonable insight into the behavior of materials under conditions of high-stress grinding abrasion.” This “widely agreed” view will be subjected to critique in the current paper.

Albright and Dunn plotted mill trial mass loss and pin test mass loss, both against liner hardness and against carbon content. After converting the raw mass loss values into a dimensionless relative wear rate (relative to the average wear rate of several martensitic steels with average hardness 600 HV), Gates et al. [4] replotted the data on similar axes, but identified the specific alloy class for each graph point as either pearlitic steel, bainitic steel, martensitic steel or white cast iron. From these plots, Gates et al. pointed out that there was a significant difference between the form of curve produced by the mill trial and that produced by the pin abrasion test. For convenience, these graphs (Figure 2 of the 2007 paper [4]) are reproduced, in slightly modified form, as Figure 1(a) and (b) below. Unlike the 2007 paper, which converted Albright and Dunn’s Brinell hardness values to Vickers, the charts here use the original Brinell values. Another difference is that the graphs below use Albright and Dunn’s values for the “worn surface” hardness, whereas the 2007 paper used their “shell surface” values. In contrast to what is sometimes found as a result of work-hardening effects, in this case the worn-surface hardness values are mostly somewhat lower than those measured near the original surface, because the advanced wear reveals the softer core of the casting.



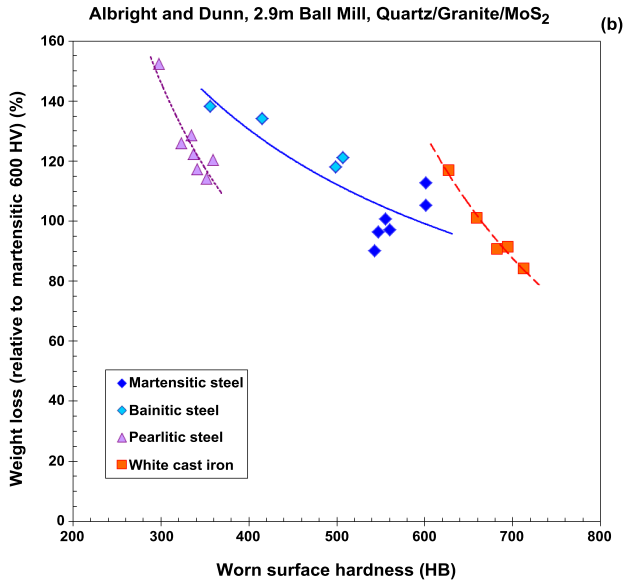


Figure 1. Re-plot of data extracted from Albright and Dunn 1983 [3] (similar to those presented in Figure 2 of Gates et al. 2007 [4]). After identifying the four alloy classes, wear rate relative to martensitic steel of hardness 600 HV is plotted against worn surface hardness.

Explicitly identifying the four alloy classes in the graphs provides a clearer view of the factors controlling wear performance than can be discerned from Albright and Dunn’s original graphs. It can be seen, for example, that the pearlitic steels provide better performance (lower wear rates) than their low hardness would have predicted, if one was judging from experience with martensitic, bainitic and tempered martensitic steels.

In the pin abrasion test, as shown in Figure 1(a), the white cast irons show very much lower wear rates than the martensitic steels. The bulk hardness of the white cast irons (average 675 HB) is somewhat higher than that of the martensitic steels (average 568 HB), but the dramatic improvement in wear performance is far greater than can be explained by bulk hardness alone. Gates et al. 2007 [4] argued that the performance advantage is due to the well-documented “particle-reinforced composite effect.” The network of very hard chromium-rich M_7C_3 carbides in the white cast iron very effectively protects the matrix and provides abrasion resistance much greater than would be predicted by bulk hardness alone.

However, in the ball mill plant trial, as shown in Figure 1(b), the white cast irons do not show any significant benefit compared to the martensitic steels. Evidently, the carbide network is no longer providing a significant protective effect. It can readily be demonstrated that this loss of

the protective effect is due to the introduction of micro-fracture wear mechanisms in the brittle carbides under the conditions of the industrial ball mill.

Many authors have attempted to explain this micro-fracture as being due to the effect of “impact” in the industrial mill. However, Gates and co-workers [4,5] demonstrated that the micro-fracture does not require “impact”, being easily shown to occur in small laboratory ball mills operated in sliding mode, hence without significant impact. The authors argued that the micro-fracture is simply characteristic of “high stress abrasion” conditions. They argued that high stress abrasion requires only two conditions to be satisfied:

- A rigid metal counterface that acts to crush the abrasive particles into the wearing surface with significant force;
- An abrasive mineral that has sufficient strength (hardness and fracture toughness) to *transmit* the contact force from the counterface to the wearing surface so as to cause micro-fracture of the reinforcing particles.

The comparison between industrial plant trial behaviour and laboratory abrasion test behaviour can be further elucidated by plotting the wear rates from the two tests directly against each other, rather than by plotting each separately against hardness. Albright and Dunn [3] provided such a direct comparison in Figure 8 of their paper - plotting pin test mass loss against mill trial mass loss. A similar method of presentation has been used in Figure 2 below, plotting dimensionless relative wear rates and again identifying the four alloy classes.

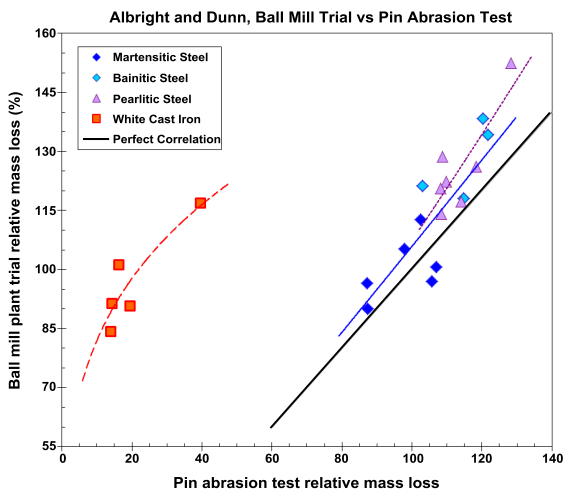


Figure 2. Re-plot of data extracted from Albright and Dunn [3]. Directly compares wear rates from the industrial ball mill trial (grinding quartz and granite) against those for the same alloys in the pin abrasion test (using 150-mesh garnet cloth).

If we consider only the steel liner alloys, the correlation between the laboratory test and the plant trial appears to be quite good. Within the 17 steels, rankings are largely preserved between the two tests (within a reasonable statistical scatter), and indeed the correlation appears close to linear. Hence, the pin abrasion test achieves at least “level 2” correlation with the mill trial. Continuing to focus on the steel data, it can be seen that there is a reasonably good match between the quantitative relative wear rates in the two tests. For example, the ratio of the worst-performing steel (pearlitic steel, alloy H) to the equal-best performing steel (martensitic steel, alloy C) is 1.47 in the pin abrasion test and 1.69 in the mill trial. This means that the pin test predicts that the hard martensitic steel will out-perform the soft pearlitic steel by 47%, and in the industrial mill trial the actual benefit is slightly greater, at 69%. Although this is not perfect agreement (the slope of the curve deviates from unity), it is far better than is often achieved by laboratory tests, and might reasonably be judged to achieve “level 3” correlation.

However, if we now turn our attention to the white cast irons, and consider their performance compared to steels of comparable bulk hardness, we can see that the correlation breaks down. The marked difference in behaviour between the two groups can be discerned by comparing the ratio of wear rate of the martensitic steels taken as a group to that of the white cast irons taken as a group. In the pin abrasion test, this ratio is 4.8, but in the mill trial the ratio is only 1.03. Thus, the pin test predicts that white cast irons will give approximately 380% improvement in service life compared to steels, but in the mill trial the white cast irons give negligible improvement. This dramatically demonstrates the inadequacy of the pin abrasion test in predicting plant behaviour. The difference is best understood in terms of a difference in wear mode. In the industrial ball mill environment, with an ore with high quartz content, the wear mode is clearly high stress abrasion, such that particle-reinforced composite alloys provide no significant benefit over homogeneous alloys of comparable bulk hardness. By contrast, the pin abrasion test with garnet abrasive is clearly manifesting a low stress abrasion mode.

This finding is in stark contrast to the widespread view, as articulated by Albright and Dunn, that the pin abrasion test simulates high-stress abrasion. Such a view persisted into later publications, such as those by Hawk, Tylczak and co-workers [6,7] which state that the pin-on-drum test “involves high-stress two-body abrasive wear.” The fallacy of this traditional view of the pin abrasion test has been thoroughly demonstrated by Gates et al. 2007 [4].

A comparison between Figure 1 and Figure 2 reveals that, within the steels, the wear rates in the two test types correlate better with each other than they do with measured hardness. This is an illustration of the fact that wear resistance is not controlled simply by hardness but is significantly affected by the details of the microstructure.

As noted above, if attention is restricted to steels, ie excluding particle-reinforced composites, then the correlation between the pin abrasion test and the ball mill plant trial appears quite good. Indeed, within this restricted set of materials, the test appears to achieve level 3 quantitative relative correlation with a slope very close to 1.

For researchers who have access to the traditional pin abrasion test in one of its forms, it may be tempting to take a view that, so long as comparisons are drawn only between alloys within a given class, the pin test can provide reliable correlation with service performance. Precisely such

a concept was suggested by Hawk et al. [6], who wrote "... given the high degree of scatter in wear data, a functional relationship between data from different wear tests may not emerge. However, trends within classes of alloys (such as hardened martensitic steels) will be present, and good/poor performers will stand out." Taken at face value this might be a true statement. However, a laboratory test that is only able to compare materials within a single specific class, and which provides clearly erroneous predictions about other material classes, must be treated with suspicion. At best, such a test should be regarded as having "very limited applicability". In the opinion of the current authors, it is more appropriate to deem the pin test as "unsuitable" for evaluating materials for comminution environments, because it produces a completely different wear mode.

In conclusion, it has been demonstrated that the pin abrasion test does not represent high stress abrasion in any industrially meaningful sense. Consequently, for the prediction of performance in comminution environments, tests should be sought that simulate the industry wear conditions with greater fidelity.

Agricultural Tools - M.A. Moore 1987 and Bialobrzaska 2015

Moore [1] discussed the principles by which a suitable laboratory test might be selected to simulate a given service environment, and hence predict the relative performance of candidate wear-resistant materials. He divided laboratory wear tests into two main categories, according to whether the abrasive particles are loose or fixed. In each of these categories he listed four test types, depending on the contact geometry and nature of the motion (such as circular motion on a rotating flat plate, reciprocating motion on a flat plate, linear motion on a belt, linear motion on the cylindrical surface of the tyre on a rotating wheel, etc.). We regard some of these as so closely equivalent that they do not require separate consideration. In particular, in the case of tests involving the rubbing of the initially flat end of a pin specimen on bonded abrasive cloth, it should be of minimal consequence whether the motion is achieved by circular motion of a flat plate (pin-on-disk test), rotation of a cylinder (pin-on-drum test), or by reciprocation of a flat table (pin-on-plate test). On the other hand, we regard two of Moore's eight listed categories as requiring subdivision, since they have differences that significantly alter their behaviour. These are the loose abrasive tests which Moore described as "Pin-on-Disc or Ring-on-Disc" and as "Rubber (or Steel) Wheel."

In accordance with our understanding of the factors likely to have a significant effect on the relative performance of different wear-resistant materials, we suggest that Moore's eight laboratory test types should be re-grouped into six categories as follows:

- Fixed 1 - Grinding Wheel Abrasion Test, using solid bonded grinding wheel;
- Fixed 2 - Pin Abrasion Test, or more precisely Pin-on-Bonded-Abrasive Test, using bonded abrasive cloth (pin-on-disk, pin-on-drum, pin-on-plate);
- Loose 1 - Pin-on-disk (and potentially pin-on-plate) test converted to an abrasive wear test simply by spreading loose abrasive particles onto the flat surface and assuming that some of the abrasive particles will enter the planar contact zone;

- Loose 2 - Steel Wheel Abrasion Test (and potentially Ring-on-Disk and Four-Ball Micro-abrasion Tests), with either a block specimen held against the rim of a rotating steel wheel or other tapering contact geometries, such that the loose abrasive particles are fairly reliably entrained into the tapering contact zone;
- Loose 3 - Rubber Wheel Abrasion Test, with block specimen held against the rim of a rotating rubber-tyred wheel, such that the loose abrasive particles are reliably entrained into the tapering contact zone;
- Loose 4 - A test described as “Abrasive Tank or Bin”, which Moore did not describe in more detail but which is likely to have consisted of rod specimens tracing a circular path through a stationary container of abrasive or, equivalently, stationary rods in a rotating container.

Analysis of example data from tests of the type designated Loose 1 and Loose 2 suggests that tests of this type are seriously problematic, because the wear rate is a strong function of the effectiveness with which the abrasive particles are entrained into the contact zone. Tests of the type Loose 1 are likely to be irretrievably unreliable, because there is no physical reason why the abrasive should be reliably or consistently entrained into the tight planar contact zone. Even in the somewhat better Loose 2 contact geometry, it has been demonstrated that the effectiveness of entrainment and the velocity and mode of particle motion through the contact zone is strongly affected by the relative hardness of the specimen and the counterface. Gore and Gates [8] provided a detailed demonstration of how this “differential friction effect” can lead to highly misleading predictions of the relative performance of alloys. For example, a high speed tool steel with a hardness of 880 HV was measured to have a wear rate comparable to that of aluminium with a hardness of only 80 HV — a result that is unlikely to be reproduced in any field environment.

Tests of the type designated Loose 3 and Loose 4 can be regarded as producing low stress abrasion wear modes, whereas those of type Loose 1 and Loose 2 can be regarded as producing high stress abrasion. For this reason, tests of the type Loose 2, commonly known as the Steel Wheel Abrasion Test (SWAT), are gaining popularity among comminution researchers. However, because of the differential friction effect as discussed above, there are severe reservations about the reliability of predictions from this test. In a paper from the authors from 2007 [4], the Ball Mill Abrasion Test (BMAT) is proven to be a greatly superior laboratory test for the prediction of performance for comminution environments, however, in 1987 Moore was not aware of the BMAT.

Very limited data have been published for tests of the type Fixed 1 or Loose 4. The most commonly used laboratory abrasive wear tests are of types Fixed 2 (Pin Abrasion Test) and Loose 3 (Rubber Wheel Abrasion Test).

In seeking a laboratory test to simulate the wear of agricultural tools when cultivating stony soils, Moore judged that a test with fixed abrasive was more appropriate than one with loose abrasive. He cited evidence from previous research which had shown that, for typical soil particle size distributions, the wear of agricultural tools tended to be dominated by interactions with stones in the size range 19 to 38 mm. Analysis of load-time history indicated that the most important interactions were not the transient impact events, when a tool first strikes a stone (2 to 250 MPa but less than 1 ms in duration), but rather the more sustained interactions where the tool pushed

the stones through the surrounding soil and the stones would thus slide across the tool surface (0.5 to 2.0 MPa but sustained for 0.5 to 5 s duration). Because the stones are somewhat constrained in the soil matrix, Moore reasoned that an appropriate laboratory test would have a stiff counterface with fixed abrasive - to simulate abrasion of the tool either by the stone surface itself or by finer grit particles trapped between the stone and the tool.

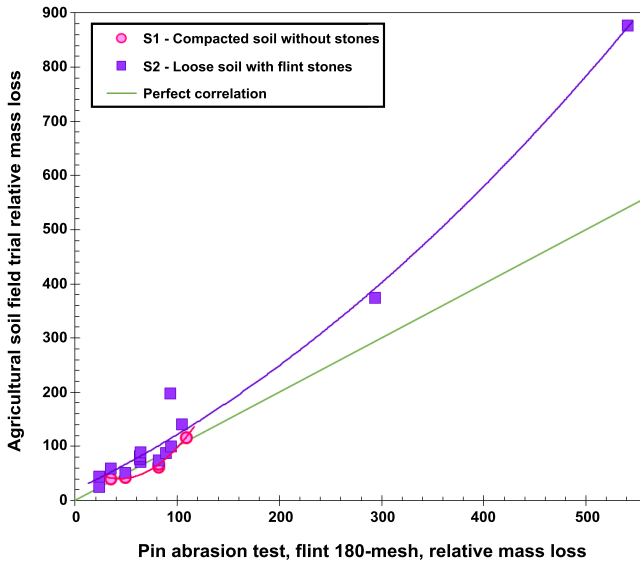
Thus, Moore used a test of type Fixed 2, pin-on-disk with bonded flint abrasives in various particle sizes. He compared data from this laboratory test against data from field trials in soils with various stone contents. The relative wear resistance data from Moore's Figures 6 and 7 has been converted to relative wear rate, and the results are presented in Figure 3(a) and (b) below. Over a reasonable range of alloys and soil types, the data show a credible correlation.

This correlation between the pin abrasion test and wear of tools in agricultural field trials should be considered in light of what can be understood about the wear conditions in the field trial. Moore considered that the abrasive asperities on the stones were constrained, and that finer grit particles were "firmly trapped" between the stone and tool surfaces. However, it should not be thought that this represents high stress abrasion in the way that a comminution operation does. Compared to the metallic grinding media in a ball mill, the 19-38 mm stones are relatively light, and their rough surfaces could not be expected to crush the grit particles into the tool surface as strongly as occurs in such a mill. The empirical evidence from data such as Albright and Dunn [3] and other data cited by Gates et al [4] indicates that the Pin Abrasion Test is more representative of low stress abrasion than high stress abrasion, and Moore's agricultural field trials are consistent with this view.

The data presented in Figure 3(a) and (b) achieve at least level 2 (linear) correlation, and could be judged to represent a tolerable level 3 (quantitative relative) correlation. In some regions, the slope of the empirical curve deviates significantly from the ideal value of 1, which must represent differences between the laboratory and field wear modes, but we do not have enough information about the wear-resistant materials or details of the field conditions to permit any more than speculative suggestions regarding the causes of these deviations. It was illustrated by the Albright and Dunn case study that the greatest value is obtained from a field trial when the different classes of wear-resistant materials are clearly identified in the data presentation, and failure to do so risks obscuring important information.

(a)

M.A. Moore Fig.6, Agricultural Soil Trial vs Pin Abrasion Test



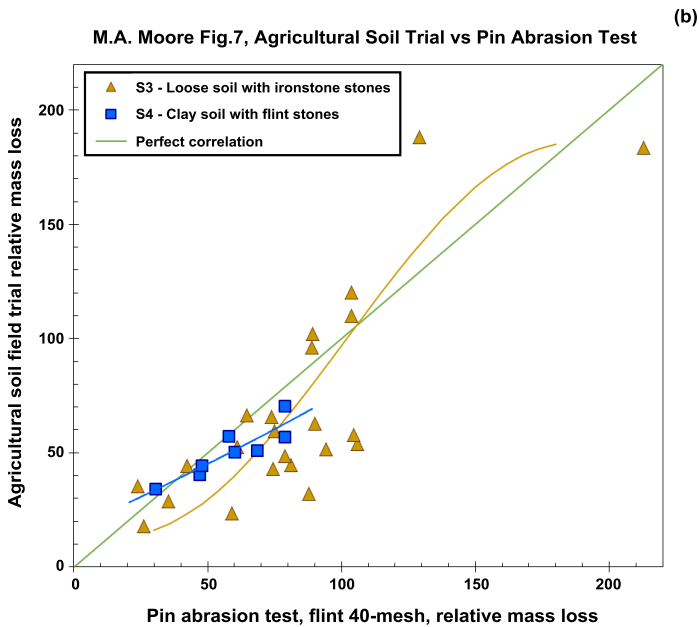


Figure 3. Re-plotted data from Moore 1987 [1] directly comparing wear rates from agricultural field trials against those for the same alloys in the pin abrasion test; (a) using 180-mesh flint, (b) using 40-mesh flint.

Another correlation between laboratory test data and wear measured in an agricultural tool field trial has recently been published by Bialobrzeska and Kostencki [9]. The field trials were performed in cultivated soils largely free of stones. The laboratory tests used the Rubber Wheel Abrasion Test. From the absolute mass loss values presented in their Figure 12, we have calculated relative wear rates and these are presented in Figure 4 below.

On face value Figure 4 could be characterised as showing an adequate level 1 (rank) correlation and perhaps level 2 (linear) correlation, but fall short of a credible level 3 (quantitative relative) correlation because the slope of the empirical curve is much greater than 1. However, it is probably more accurate to observe that the range of wear-resistant materials tested was simply too limited to permit any useful conclusions to be drawn about the quantitative nature of the correlation between laboratory and field performance. All four of the materials used by Bialobrzeska and Kostencki were low-to-medium carbon (0.28-0.37%C) low-alloy steels with hardness in the range 44 to 50 HRC. While such a study might have value for the selection of a specific steel for a given application, it lacks the breadth to be capable of elucidating more widely applicable principles of laboratory-field correlations.

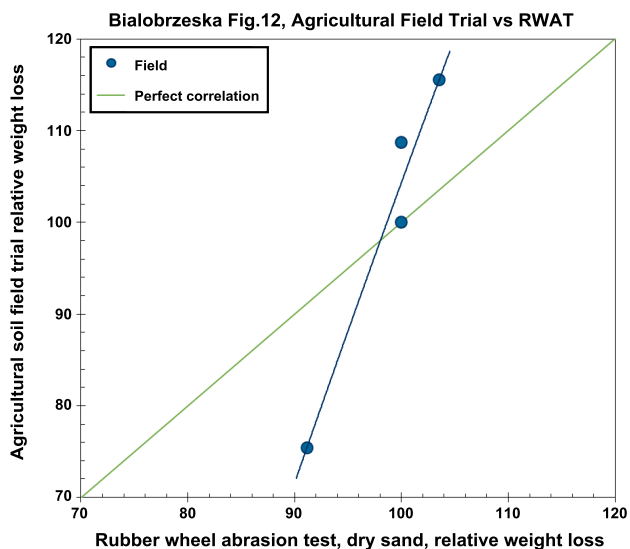


Figure 4. Re-plotted data from Bialobrzaska and Kostencki 2015 [9], directly comparing wear rates from an agricultural field trial against those for the same alloys in the rubber wheel abrasion test.

The BMAT – A Better Test for High Stress Abrasion

Past Usage of Laboratory Ball Mills

Laboratory ball mills are widely used to assess the comminution characteristics of ores. Well-known early descriptions of the use of a laboratory ball mill for this purpose were those by Bond and co-workers in the 1930s [10,11]. However, in the 1950s when Bond wanted to measure the abrasiveness of ores, he did not measure the wear of either balls or liners in a laboratory ball mill. Instead, Bond used a completely different apparatus, measuring the wear of a steel paddle driven by a moderately high-speed rotor (paddle tip velocity 7.2 ms^{-1}), striking falling ore particles inside a co-rotating drum [12]. Although it does cause breakage of the ore particles, the paddle-in-drum device lacks any metal counterface to crush the abrasive particles into the wearing surface, and it bears little relationship to a ball mill. Those of Bond's papers that we have reviewed do not explain why he chose the paddle-in-drum device, other than to say that it was adopted "after several other devices had been tried ... and rejected for various reasons" [12].

Although it would seem logical to do so, relatively few researchers have used laboratory ball mills to measure the wear resistance of alloys for either grinding media or mill liners. Those who have done so, or who refer to others having done so, include the following:

J.J. Moore and co-workers [13,14] used a ceramic-lined laboratory ball mill, 203 mm in diameter, operated in batch mode. They described their tests as “laboratory marked ball wear tests.” The term “marked ball wear test” (MBWT) is more commonly used in relation to industrial plant trials rather than laboratory tests, but in principle the methodology can be used in any sized mill. Its significance is the fact that the tests are performed with specimens of several different alloys exposed simultaneously [15] - a very useful feature. Moore’s specimens were 26 mm diameter balls in a wide range of alloys - 0.2%C mild steel, 0.9%C low-alloy tempered martensitic steel, 1.1%C martensitic stainless steel, and three different white cast irons. In many of the tests the abrasive used was quartz with up to 10% pyrrhotite, while other tests were performed using a variety of natural ores. The mineral and chemical environments were manipulated in such a way as to permit identification of contributory wear mechanisms, notably corrosion. They stated that a plant trial was also performed in a SAG mill of diameter 8.2 m, but no quantitative data were presented and it is probable that only a single alloy was used.

Iwasaki, J.J. Moore and Lindeke [16] used laboratory and pilot-scale ball mills of diameters between 203 mm and 1067 mm to explore the effect of mill diameter (and also ball diameter) on grinding media wear rates and mineral grinding performance. They used laboratory mills of diameters between 203 and 914 mm operated in batch mode, and pilot-scale mills of diameters between 305 and 1067 mm operated in continuous open-circuit mode. The focus was on the measurement of absolute values of wear rate, for purposes of understanding the scale-up from laboratory to industrial plant. No comparisons were made between the performance of different media alloys.

Chandrasekaran, Natarajan and Kishore [17] used a laboratory ball mill, 200 mm diameter × 200 mm long, operated in batch mode. The specimens were 30 mm diameter forged low-alloy steel balls. Only a single alloy composition was used, but 15 different heat treatments were applied to give a range of microstructures, including pearlite, martensite, tempered martensite, and bainite. Individual alloys were marked using shallow grooves cut by an abrasive wheel. The abrasive was quartzite, and tests were performed dry. Batch test interval duration was two hours, and a total of three such test intervals were used to evaluate performance. Thirumalaisamy and Kishore [18] also used a laboratory ball mill to conduct “marked ball wear test” experiments on the effect of abrasive feed volume on the absolute value of wear rate. They interpreted the resulting data as evidence for a combination of “impact” and “abrasion” wear mechanisms (although this interpretation has been questioned by Gates et al. [4]).

Radziszewski and co-workers [19-21] used a laboratory ball mill as part of their methodology for assessing the rates and component mechanisms of wear in tumbling mills. However, rather than using it as their primary wear testing device, they used it mainly to assess the corrosion component of the total media wear rate. To measure the abrasive wear component, they elected to use a steel wheel abrasion test of the type that had been explored by Gore and Gates [8], based upon the ASTM G65 rubber wheel abrasion test but replacing the rubber-tyred wheel with a solid steel wheel.

Chenje et al. [22] used a laboratory ball mill 450 mm diameter × 450 mm long, operated in batch mode. The specimens were 60 mm diameter cast balls. Three balls each of five different alloys (low-alloy steels and chromium cast irons) were exposed to the test simultaneously. To

distinguish between the alloys, each ball was marked using shallow grooves cut by an angle grinder. The abrasive was granite, and tests were performed wet with 65% solids. Batch test interval duration was five hours, and a total of 16 such test intervals were used in order to evaluate the relative performance of the alloys.

Albertin and Sinatora [23] used a 400 mm diameter laboratory ball mill to compare the wear performance of a variety of white cast iron alloys, varying both carbide volume fraction and matrix microstructure. The specimens were 50 mm diameter balls, and the different alloys were exposed simultaneously to the wear environment. Three different abrasives were used — quartz sand, hematite, and a phosphate rock. The tests were conducted in a closed-circuit continuous feed mode for a total of 200 hours exposure. This probably represents the most systematic and industrially-relevant use of the ball mill abrasion test that has been published to date. Albertin and Moraes [24] also used a pilot-scale ball mill to evaluate the performance of 60 mm grinding balls made from various steels and white cast irons when milling coal. The mill was operated in batch mode, but renewing the abrasive every ten hours to a total of 70 hours exposure.

Gates first used a laboratory ball mill for the purposes of abrasive wear testing of alloys in 2001 [25]. Gates and co-workers [4,26-41] have used this apparatus and methodology for a variety of experiments, using mills of various diameters between 300 mm and 1800 mm operated in batch mode. Most of their work has focussed on assessing the factors controlling the relative performance of wear-resistant materials spanning different microstructure classes (as well as numerous specific alloys and heat treatments within a given class). A feature of their work has been critical evaluation of common interpretations about the effect of “impact” in determining the relative performance of different classes of wear-resistant materials.

The recent review by Aldrich [42] is ambiguous in regard to the possible use of laboratory ball mills for measurement of wear rates. Although Aldrich initially lists the marked ball wear test within a section on laboratory testing techniques, the methods described for marking the different media samples are those which, to our knowledge, have been used only for industrial MBWT trials. Moreover, the section refers to placing the test balls into an “operating mill” and retrieving them for mass loss determination “when the mill is down for scheduled maintenance” - comments which presumably have relevance only to industrial mills. Aldrich does not cite any published studies in which MBWTs have been used in the laboratory, but elsewhere cites two papers by Sepulveda [15,43] both of which are concerned explicitly with trials conducted at full scale, not in the laboratory.

Advantages of the BMAT

Previous experience with the ball mill abrasion test indicates that, for the purpose of assessing the performance of wear resistance of materials for comminution environments, it has several advantages over alternative laboratory test devices that have been proposed for this duty. These advantages are:

- There is no difficulty ensuring that the abrasive medium enters and passes through the contact zone between the specimens and counterface bodies - this occurs naturally and indeed inevitably;

- It is able to accommodate essentially any mineral ore or other abrasive medium, in a wide range of particle sizes relevant to industrial service. The measured values of relative wear rates between alloys are not sensitive to the exact abrasive particle size;
- Without the necessity for any complex engineering measures, qualitatively the abrasive particle and counter-body kinematics and contact mechanics in the BMAT naturally match those in an industrial ball mill quite closely;
- Its design facilitates simultaneous exposure of multiple specimens without difficulty - for example, we have frequently performed tests in 500 mm and 600 mm diameter ball mills in which more than 100 individual specimens were tested simultaneously. This contrasts strongly with most standard laboratory tests, which are usually restricted to exposure of between one and three specimens at a time. This feature not only improves productivity but facilitates experimental control and removes the need for careful maintenance of supplies of “standard” consumables;
- As demonstrated by J.J. Moore, the test parameters can readily be manipulated in such a way as to identify and quantify the various component damage mechanisms that contribute to the overall wear rate;
- It is very versatile. A variant on the BMAT, known as the ball mill edge chipping test (BMECT), can also assess the resistance of alloys to small-scale fracture phenomena (chipping at features such as forging laps) - and does so more efficiently than alternative tests such as the Charpy impact test. Another variant, the ball mill impact-fatigue test (BMIFT), can assess the resistance of alloys to impact-fatigue spalling, in much the same way as the dropped ball test (DBT) [44] though at lower energies;
- The apparatus is mechanically simple, robust, and low cost;
- It has been found that the relative wear rates between specimens of different materials have excellent reproducibility, without requiring any arduous controls. With somewhat more careful attention to test conditions, the absolute values of wear rate are also reasonably reproducible within a given batch of abrasive;
- Finally, as will be shown below, if the conditions are set up with sufficient care, the BMAT can achieve level 4 (quantitative absolute) correlation with plant wear rates.

Given these advantages, it becomes difficult to understand why researchers would persist with unrepresentative bench-top abrasive wear tests when attempting to evaluate wear-resistant alloys for comminution operations. We are not suggesting that the BMAT reproduces every aspect of damage mechanisms in large industrial mills; it lacks the ability to reproduce the larger-scale fracture-related consumption mechanisms associated with high impact energies in large industrial mills, hence the BMAT needs to be supplemented by a high energy impact test in those cases. However, for the abrasive and corrosive wear components it is difficult to discern advantages in other more idealised laboratory tests. The quality of the BMAT’s predictive ability for industrial ball mill wear rates will be discussed in the case study below.

Like all laboratory tests the BMAT is limited by its size, and questions of scale-up will require further research. However, the above listed advantages indicate that the BMAT is an order of magnitude superior to traditional bench-top laboratory tests. Ultimately, if the intention is to simulate a ball mill, then it is appropriate to use a ball mill.

Level 4 (Absolute) Correlation from Ball Mill Abrasion Test

Newmont Asia Pacific commissioned the authors to develop a methodology by which the absolute values of grinding media consumption rates in an industrial ball mill could be predicted from batch tests in a laboratory ball mill [28,32].

The simplest quantity by which the wear rate of grinding media can be expressed is total mass loss per unit time, in units such as kg/h. Since the primary performance measure of an industrial mill is the rate of production of ore of a desired product particle size distribution, it is industrially more useful to express media wear rate in terms of mass loss per mass of ore ground, in units such as kg/t. Giblett and Seidel [45], however, have found it most useful to express wear rate in terms of mass loss per grinding energy [43,46,47], in units such as kg/kWh or g/MJ. This quantity is sometimes designated the “specific consumption rate”.

To facilitate development of the methodology, Newmont provided us with two key resources:

- Detailed historical data for the rates of consumption of steel grinding media in the ball mills in three of Newmont’s gold ore processing plants, along with detailed milling parameters, such as operating power draw, grinding energy consumed per mass of ore ground, and the measured Bond Work Index values for the ores;
- Supplies of well-characterised ores from each of these sites, sufficient to perform a substantial number of experiments on the effects of laboratory mill setup parameters on test outcomes.

The development of the methodology involved the following steps:

1. Using carefully prepared samples of a well-characterised ore (from Newmont’s Tanami plant), determine the combination of mill setup parameters required to achieve a reliable match between the P80 (80% passing size of the mill product) of the batch mill test and that of the plant mill;
2. Using the known Bond Work Index of the reference ore, assess the effective grinding energy input per mass of ore ground from the measured feed and product particle sizes (F80 and P80);
3. Measure the wear rate for the standard commercial martensitic steel media grade, expressed as specific consumption rate (media mass loss per unit grinding energy input);
4. Measure the specific consumption rate for an alternative (softer) steel media grade;
5. Assess the sensitivity of the measured specific consumption rate values to variations in test parameters, such as test duration and feed F80 (both of which affect the batch product P80 and may cause it to deviate from the plant P80 value);
6. Measure the wear rates produced by two other Newmont ores (KCGM Fimiston and Jundee);
7. Assess the merits of alternative methods of determining the specific energy input for each test (Bond approach versus Levin approach).

The methods and results were presented at the Comminution '12 conference [32], and a more detailed paper is being prepared for submission for journal publication. Only a brief summary of the methods and outcomes will be presented here. Table I summarises the input parameters used to set up the test.

Table I. Tanami Plant and Laboratory Parameters

| Parameter | Units | Plant | Laboratory |
|---|--|-------|--------------|
| Mill diameter | m | 5.5 | 0.30 |
| Mill rotation speed | r/min | | 52 |
| Ball charge mass | kg | | 18.1 |
| Ore feed 80% passing size (F80) | mm | 10700 | 3394 |
| Product % passing size (P80) | mm | 181 | 181 (target) |
| Bond Work Index of ore | $\mu\text{m}^{0.5}\cdot\text{MJ}/\text{t}$ | 76.9 | |
| Grinding energy per mass of ore ground | MJ/t | 49.7 | 43.9 |
| Batch ore feed mass | kg | | 2.72 |
| Batch test duration | min | | 15.1 |
| Grinding energy for standard test | MJ | | 0.119 |
| Mill power draw | kW | 4706 | 0.132 |
| Mill power constant = energy per revolution | J/r | | 153 |

During the first phase of the work, the grinding energy associated with each test was back-calculated from the Bond Work Index and the measured F80 and P80. Since the product P80 is used in the calculation of grinding energy, variations in P80 have the potential to influence the measured value of wear rate expressed as mass loss per grinding energy. In order to explore the sensitivity of the specific consumption rate measurements to variations in P80 either side of the target value, various experiments were conducted in which the product P80 was manipulated via a number of different primary input variables, such as test duration, ore feed volume, ball diameter and mill rotation speed.

Figure 5 presents one of the data sets collected during the research, in which ball charge mass loss and product particle size distribution were measured as a function of test duration, for a constant feed volume of Tanami ore. Naturally, increasing test duration causes an increase in mass loss and a decrease in product particle size. The measured specific consumption rate appears to decrease slightly as a function of increasing test duration. However, it should be noted that the scale is fairly fine, and the value of specific consumption rate is changing by less than 20% for a 90% change in test duration — hence the measurement does not seem overly sensitive to this input parameter.

The sensitivity (or conversely the robustness) of the technique can be most readily assessed by plotting mass loss and specific consumption rate directly against P80. Such a graph is shown in Figure 6 for the same raw data as in Figure 5. Neglecting the single outlier value, it appears that the measured values of specific consumption rate are insensitive to P80 over a range of P80

values from about 120 μm to 230 μm . The main conclusion from the research program was that the methodology was capable of providing reproducible values of specific consumption rate so long as the product P80 from the batch test was within $\pm 50 \mu\text{m}$ of the plant P80 — a target that is not unreasonably difficult to achieve.

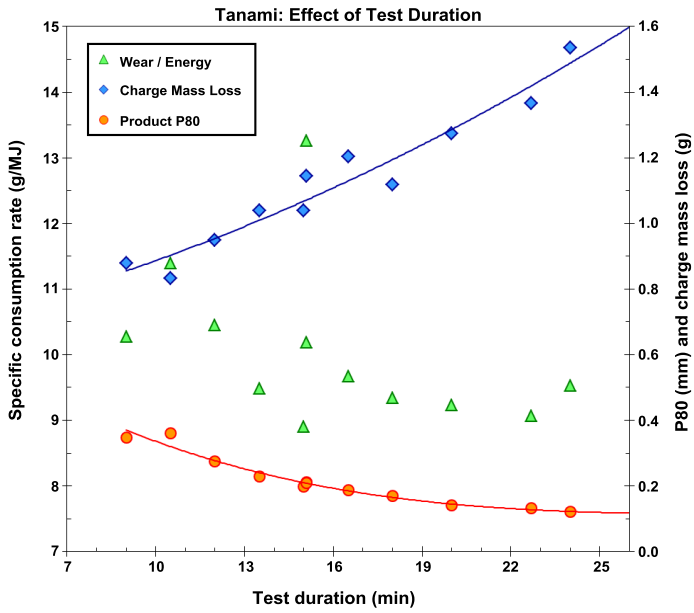


Figure 5. Effect of test duration on 80% passing size of product (secondary axis), charge mass loss (secondary axis), and specific consumption rate (primary axis).

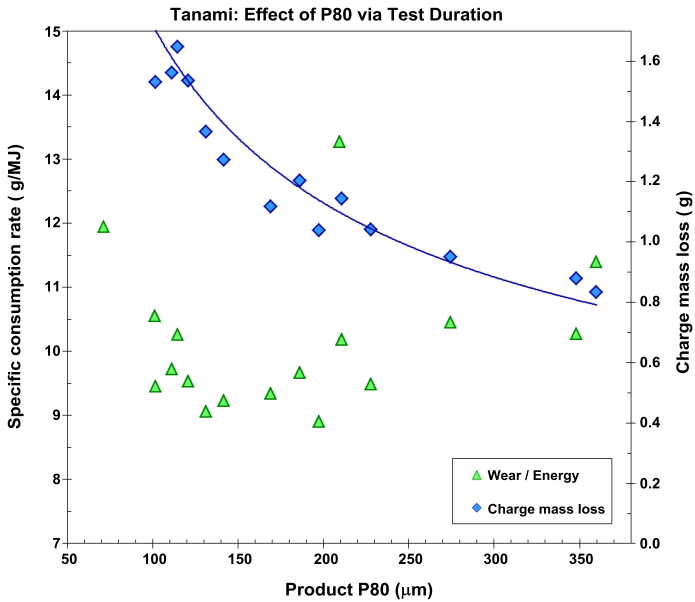


Figure 6. Effect of P80 (varied via test duration) on charge mass loss (secondary axis) and specific consumption rate (primary axis).

Once the methodology was established, it was possible to use the technique to measure the specific consumption rate for the standard grinding media and compare these with the corresponding values from the plant. Table II provides a summary of the primary outcomes of these measurements and comparisons. For the three ores, the table shows a very good match between the specific consumption rate as measured in the laboratory test and that experienced in the plant. For the well-characterised Tanami ore, the error between laboratory prediction and actual plant wear rate is less than 10%. For the two less well characterised ores, the error is no more than 20%.

Table II. Correlation Between BMAT Predictions and Plant Media Consumption Rates

| | | Plant | Laboratory | Error | Laboratory |
|-------------------------------|------|-------|------------|-------|------------|
| | | | H70 balls | | H60 balls |
| Tanami, The Granites | | | | | |
| Charge mass loss per test | g | N/A | 1.26 | | 1.44 |
| Mass loss per mass ore ground | g/kg | 0.47 | 0.46 | -2% | 0.53 |
| Specific consumption rate | g/MJ | 9.2 | 10.1 | 9% | 12.5 |
| KCGM, Fimiston | | | | | |
| Charge mass loss per test | g | N/A | 1.52 | | |
| Mass loss per mass ore ground | g/kg | 0.19 | 0.56 | 192% | |
| Specific consumption rate | g/MJ | 8.3 | 10.0 | 20% | |
| Jundee | | | | | |
| Charge mass loss per test | g | N/A | 1.82 | | |
| Mass loss per mass ore ground | g/kg | 0.30 | 0.67 | 122% | |
| Specific consumption rate | g/MJ | 8.0 | 9.0 | 13% | |

The significance of these findings should not be underestimated. What has been developed is a laboratory test methodology that provides full level 4 correlation with plant wear rates. It can predict, within about 20%, the absolute values of wear rate in the plant; and can do so directly from first principles, without any empirical “calibration” factors.

It might be noticed in Table II that, for all three plants, the laboratory test slightly over-predicts the plant wear rate. This suggests that, despite its small size, the laboratory mill is successfully reproducing the important consumption mechanisms that occur in the much larger industrial ball mills. This indicates that “impact” or fracture-related consumption mechanisms are not significant in any of these three industrial mills.

Conceivably the slight over-prediction of consumption rate by the laboratory mill could be due to an excessive contribution from corrosion in the small batch mill - a possibility raised by Dodd and Dunn [48]. However, this small difference could also be influenced by a variety of other factors which might differ between laboratory and plant, such as, for example, the possibility of differences in abrasion resistance between the actual media being used in the plant and the batch of small-diameter media that was used for the laboratory tests. Such details can be explored in further research, but should not be permitted to divert our attention from the primary significance of these findings - which is that we have achieved level 4 correlation in a simple laboratory test apparatus.

Finally, it may be noted that when wear rate is expressed as mass loss per mass of ore ground, the laboratory test is much less successful in predicting plant wear rate. The prediction appears good for the Tanami ore, but poor for the KCGM and Jundee ores. Clearly, it is mass loss per grinding energy (specific consumption rate) which should be the focus of attention in further work.

The Importance of Low Stress Sliding Abrasion

Understanding the Difference between High Stress Abrasion and Low Stress Abrasion

Several different approaches to classifying abrasive wear have been suggested [49], and occasionally these conflict with each other [50]. The primary purpose of a wear classification scheme must be to guide mitigation measures (and if a proposed classification scheme cannot be demonstrated to provide useful guidance of this type then it is reasonable to question its value).

Such an explicit purpose for wear classification is offered in recognition of the fact that measures which may be successful in reducing the rate of wear in one wear mode, might actually increase the rate of wear in another wear mode. The most commonly cited example of this is when increasing hardness, rather than achieving the desired reduction in wear rate through reduction of indentation depth, instead precipitates a more damaging wear mechanism - from micro-ploughing to micro-cutting, or from micro-cutting to micro-fracture. Such a phenomenon can be understood in terms of the Archard wear equation in its form applicable to abrasive wear:

$$W = k_1 \cdot k_2 \cdot F \cdot v / H \quad (1)$$

where:

W is the wear rate, expressed as volume of material removed (and hence volume of debris created) per unit time;

k_1 is a dimensionless geometric constant indicating the sharpness of the abrasive particles - whereby, for a given value of contact force, a sharper particle (larger value of k_1) penetrates deeper into the material and creates an indentation with a larger cross-sectional area in planes perpendicular to the surface of the indented material;

k_2 is the ratio of the volume of material removed to the volume of the groove - bearing in mind that, in a ductile material, a groove can be created by a “micro-ploughing” mechanism in which material is merely displaced laterally, rather than by a “micro-cutting” mechanism in which material is directly removed from the surface as primary debris;

F is the normal contact force;

v is the tangential sliding velocity;

H is the hardness of the material being worn (expressed in units of contact force per projected area of indentation).

In abrasive wear occurring by a pure micro-cutting mechanism, the value of the coefficient k_2 should equal or approach 1, while in wear dominated by micro-ploughing mechanisms, k_2 is very much smaller than 1, (eg. perhaps 0.01). Hence, for a given value of indentation depth, micro-cutting is a much more damaging mechanism than micro-ploughing. In addition, if micro-fracture wear mechanisms occur, cracking and release of fragments from outside of the primary wear groove can result in a value of k_2 greater than 1, hence this is extremely damaging.

Excessive increases in the hardness of the material can decrease ductility and toughness and precipitate these detrimental transitions in wear mechanism. If this occurs, it is possible for the increase in hardness to cause an increase in wear rate instead of the intended decrease. Even if complete ranking reversals do not occur, these detrimental transitions in wear mechanism can

readily degrade the quantitative benefit achievable from a harder material and may thus reverse the cost-benefit balance.

A change in material hardness is not the only parameter that can influence wear coefficients. It has already been noted that more angular abrasive particles can lead to greater penetration depth for a given contact force, hence increasing the magnitude of the coefficient k_1 in the Archard equation. Sharp cutting edges may also promote more damaging wear mechanisms, thereby increasing the coefficient k_2 .

The possibility (indeed the frequent observation) of such reversals of cost-benefit balance is the reason why the distinction between high stress abrasion and low stress abrasion is of such great practical importance. We regard this as the most important single distinction to be made in any classification scheme governing sub-divisions of abrasive wear.

Among those authors who propose classification schemes involving a distinction between high stress abrasion (HSA) and low stress abrasion (LSA), most place the emphasis on contact stress in relation to fracture of the abrasive particles. It is usually proposed that the dividing line between HSA and LSA is determined by whether or not the abrasive particles fracture. Fracture of the abrasive particles generates fresh sharp cutting edges which, as described above, can lead to increases in both coefficients k_1 and k_2 in the Archard equation.

However, if particle fracture was sufficient to define HSA, then crushing of a soft, weak mineral such as talc would be regarded as HSA. This would clearly not be a useful conclusion to draw from a classification scheme. Gates et al. [4] demonstrated that particle fracture alone is not sufficient to create the kind of HSA conditions that lead to high wear rates in general and poor performance from particle-reinforced composite materials in particular. For these damaging conditions to arise, it is also necessary to satisfy two conditions: firstly that there must be a rigid counterface which pushes the abrasive particles into the wearing surface with significant force; and secondly that the abrasive mineral particles must be strong enough to transmit the forces from the counterface to the wearing surface and its microstructural elements. Thus, rather than “fracture” of the abrasive particles, almost conversely it is probably the “strength” of the abrasive mineral that is the strongest determinant of HSA conditions [29].

The Economics of Low Stress Abrasion – Misleading Nomenclature

Almost everything that is written about high stress abrasion versus low stress abrasion would tend to suggest that in HSA the wear rates are high and in LSA the wear rates are low. The nomenclature itself almost inevitably suggests this. If this inference were accurate, then economically it might be appropriate to invest resources primarily in HSA and to largely ignore LSA.

However, experience tells us that the highest industrial wear rates are in situations which we judge to be low stress abrasion - in live ore transfer chutes. “Live” transfer chutes are those in which rock-box designs are not employed and hence the ore flows through the transfer station in a continuous stream, creating near-continuous sliding against the liners rather than the tumbling action that occurs in a rock-boxed chute. A practical example has been seen in the inspection, by

the authors, of an iron ore chute (in 2000 at BHP Iron Ore's Finucane Island ore handling plant in Port Hedland, Australia) in which NiHard 4 white cast iron blocks, 75 mm in thickness, were wearing out within two weeks. Another example was a live chute passing copper-gold ore in Papua New Guinea in which 100 mm NiHard block liners were wearing out in as little as four days.

The empirical evidence available in the Port Hedland installation [51] indicated that the wear mode was low stress abrasion. For example, there was no evidence to suggest that the high wear rates in the NiHard castings were due to micro-fracture wear mechanisms in the brittle carbides, promoted by "impact" or other conditions in the chute. Rather, the evidence indicated that the high wear rates in the live chute were simply a function of the continuous sliding abrasive action and the high tonnage throughputs, exacerbated by some sub-optimal installation design features.

Improved Nomenclature

Ball mills and other comminution equipment in the mining industry commonly show the characteristic features of HSA, but wear rates approaching those described above for LSA in ore chutes have never been encountered by the authors. The reason that HSA does not typically produce such high wear rates is readily understood in terms of the $F \times v$ term in the Archard wear equation. The contact force F may be high, but the total wear rate may be quite low if the sliding velocity v is low.

This very simple observation serves to alert us to the fact that contact force is only one of the two input parameters that characterise the distinction between HSA and LSA. The accepted nomenclature for the two wear modes might encourage an emphasis on the F term and a neglect of the v term, but this can be misleading. It is suggested that the tribology community should consider a move to two-part descriptors, such as to remind the user that sliding velocity is at least as important as contact force.

In the past there was a practice in some circles (notably in the U.S. mining industry) to denote the HSA wear mode as "high stress grinding abrasion", or simply "grinding abrasion" [49,52]. The latter was suggested in reference to a type of industrial operation within which this wear mode frequently occurs, namely mineral grinding (comminution). In practice, nomenclature involving the words "grinding abrasion" has fallen out of favour. This might be in recognition of the ambiguity [50] of the word "grinding", which in addition to mineral comminution can also refer to machine workshop operations using bonded grinding wheels. When using grinding wheels, the sliding velocities are high and contact forces are low — the opposite of true HSA. There is an obvious risk that early-career researchers might assume that a grinding wheel would make a good laboratory test to simulate "grinding abrasion", and indeed such tests have been used [1]. It is preferable that the accepted nomenclature should not encourage such misconceptions.

The following two-part descriptors are recommended:

- “Low stress sliding abrasion” (LSSA) - emphasising the dominance of tangential sliding. This designation has considerable merit, since it conveys the limited ability to damage the microstructure and yet also conveys the sliding that can lead to high wear rates;
- “High normal stress abrasion” (HNSA) - emphasising the dominance of normal contact forces over tangential motion. Various alternative candidate designations that have been considered are discussed below.

For HNSA, alternative designations that have been considered or might be considered include high stress grinding abrasion (HSGA), high stress crushing abrasion or high stress comminution abrasion (HSCA). Although it might seem to have the virtue of elegant simplicity, the abbreviated term “crushing abrasion” is not recommended. It is questionable whether the empirical evidence supports the notion that jaw crushers produce a HSA wear mode. Currently, the wear mode in jaw crushers is denoted “gouging abrasion”, and ill-defined as this term might be, it will probably suffice pending further research. Instead of either “grinding” or “crushing”, the word “comminution” might better indicate the conditions involved in the wear mode currently being denoted HSA. If used in the two-part descriptor “high stress comminution abrasion,” it would probably convey most of the important aspects of this wear mode with minimal ambiguity. All of these designations retain the phrase “high stress” which can serve to focus attention on the need for a rigid counterface to achieve this characteristic wear mode. Choice of an ideal descriptor is worthy of ongoing attention from the tribology community, but the term high normal stress abrasion appears to have the most merit of those considered to date.

The most important lesson from the above discussion is the fundamental observation that low stress abrasion does not equate to low wear rates; indeed, the highest wear rates that are observed industrially are caused by low stress sliding abrasion. Irrespective of the nomenclature chosen, it is clear that, economically, LSA has just as much claim for allocation of resources as HSA does. Improved nomenclature is needed in order to convey this fact, and the new terms HNSA and LSSA will be used hereafter.

Materials Selection for Low Stress Sliding Abrasion

The nature of LSSA is such that materials selection has the capacity to achieve much greater improvements in component service life than is possible in HNSA. Gates et al. [4] showed that in HNSA the curve of wear rate versus hardness is very flat, and that most particle-reinforced composite alloys provide minimal benefit compared to homogenous alloys of comparable bulk hardness. Consequently, only relatively small incremental improvements in service life are achievable though the use of harder or “better” wear-resistant materials in such conditions. By contrast, in LSSA, the wear rate versus hardness curve is much steeper, and particle-reinforced composite alloys provide major benefits compared to homogeneous alloys.

Figure 10 shows the data from a plant trial conducted in the upper “hood” section of the iron ore chute mentioned above. This was one of two trials conducted in the Port Hedland ore transfer chute. These trials will be described in more detail below, but a clear outcome was to provide field confirmation of the concept stated in the above paragraph - that in LSSA environments, materials selection has the capacity to achieve major improvements in service life.

High Wear Rates from LSSA – Iron Ore Chute

The duty of an ore transfer chute is to “catch” a stream of ore discharged from the head pulley of one conveyer belt, re-direct it and load it evenly onto a second conveyer belt travelling in a different direction. It must achieve this task automatically and passively, without any human or mechanical intervention, using only momentum and gravity. Importantly, it must carry out this duty without interruption to the operation.

Two things which can create interruptions to production are changing out worn liners, and clearing blockages. Liner wear in chutes can often be very effectively managed by use of “rock-boxing” designs, in which a series of ledges trap some of the rock and fines. This minimises wear by two quite distinct mechanisms:

- For a significant proportion of the time that the ore stream is passing across the liner surfaces, it does not contact the metal but instead contacts the layer of trapped rock and fines. Effectively, the ore itself acts as a zero-cost, continuously self-renewing wear-resistant coating;
- The ledges alter the nature of the motion of the ore stream - from a unidirectional sliding motion to a tumbling motion.

In Australia’s Pilbara region iron ore operations, the ore becomes highly cohesive when damp. The disadvantage of rock-boxing designs is that the tumbling action encourages formation of blockages. In the wet season, in some transfer stations it was reported that large proportions of the week were consumed by clearing blockages with high-pressure hoses.

To address this problem, in 1999 BHP Iron Ore engaged Tasman Warajay Pty Ltd to provide a non-blocking “Controlled Flow” (live) chute for the CN40/CN42 transfer point at Finucane Island - shown in Figure 7. This transfer point handled the majority of the mid-size (lump, 6 to 40 mm) product of the plant, plus adhering fines (6 mm), and included a substantial recirculating load. At that time it carried an estimated average 1800 tonnes per hour, and plans were underway to increase production to 2000 tonnes per hour. If such a transfer point experiences a blockage, plant production stops. The value of lost ore production due to unplanned stoppages was at that time estimated at AU\$210,000 per hour.



Figure 7. CN40/CN42 transfer station at BHP Iron Ore’s Finucane Island operation in 2000, with Tasman Warajay “Controlled Flow” chute.

The live chute performed to specification in terms of its non-blocking characteristics, with blockage events falling to a small fraction of the number previously experienced. However, the chute became subject to significant down-time for replacement of wear liners. In the highest wear areas, any given liner plate needed to be changed out every 1 to 2 weeks. By comparison, traditional chutes at the site with extensive rock-boxing required relatively little maintenance, with typically three months between charge-outs of the fastest-wearing components. In essence, the blockage problem had been solved but a wear problem had been introduced. The current author, Gates, was engaged to investigate the reasons for the rapid wear and to recommend solutions [51].

From the viewpoint of plant production and overall profitability, in principle, wear should be a less serious problem than blockages, because the liner change-outs can be performed during scheduled maintenance periods, whereas blockages occur randomly, stopping production. The reported estimate of \$3,000 per week in maintenance costs might seem insignificant compared with \$210,000 per hour of lost production. Nevertheless, the high maintenance requirement was a problem to the company’s maintenance department at Finucane Island. Moreover, to enable the planned increase in productivity to 2,000 tonnes per hour, it was clearly necessary that maintenance shutdown intervals be longer than one week. At most sites it would be desired that maintenance shutdowns occur no more frequently than every three months, but at Finucane Island at that time it was conceded that four week intervals would be acceptable.

To achieve this goal it was necessary to find ways to increase component service life by a factor of four or more. Available information suggested that, if the operative wear mode was low stress sliding abrasion, then such an increase should be feasible. The goals for the project were as follows:

- Extend the period between liner change-outs to at least four weeks;
- Make the change-outs easier and quicker to perform;
- Accomplish the above objectives without re-introduction of blockages;
- Provide guidelines for the best liner products to use in different positions within the chute;
- Provide the information necessary for manufacturers of live chutes to successfully deploy this technology (previously highly successful in general bulk solids handling duty) in hard-rock mining operations.

The evidence collected from site, and subsequent laboratory investigations, enabled clear identification of the reasons for the high wear rates and maintenance burden experienced in the live chute by comparison with traditional chutes at the site. The reasons, and some resulting recommendations, are summarised below.

Problem 1, Lack of Rock-Boxing: Rock-boxing is remarkably effective in reducing metal wear, not only because it promotes impingement of incoming ore onto rock rather than onto metal, but also because it causes ore particles to tumble rather than slide across the metal. By removing the rock-boxing, wear rates will inevitably be higher. Recommendation: It is not practical to re-introduce rock-boxing to the subject chutes because this would destroy the controlled-flow and non-blocking characteristics. Instead, other solutions must be found to control wear rates to acceptable levels.

Problem 2, Monolithic Linings: Use of large-area monolithic linings, such as rolled and fabricated weld-overlay plate, leads to high maintenance costs, despite the fact that chromium carbide overlay plate itself offers good abrasion resistance. This is because perforation at a single point of high abrasion intensity requires replacement of the entire sheet. This represents an unacceptable maintenance burden, both because of the high cost of the replacement sheets and because of the time-consuming nature of the required on-site work. Recommendation: Segmented liners are recommended since they are faster to replace; but attention must be paid to avoiding preferential wear at joints and bolt recesses (see below).

Problem 3, Impingement Points: The point where a free-falling ore stream first impinges on the liner is a site of high wear. The site and laboratory investigations determined that this high wear was not caused by introduction of dynamic stress-wave micro-fracture wear mechanisms (as originally suspected), but simply because the deceleration vector provides a source of significant normal contact force F in conjunction with the substantial sliding velocity v . Recommendation: In view of the identified wear mode, it was viable to address the problem by use of available abrasion-resistant materials, such as high-alloy white cast irons with high volume fractions of chromium carbides.

Problem 4, Open Bolt Recesses: The primary reason for the poor outcomes of early attempts to use segmented liners was that these liners were weakened by open bolt recesses exposed to the ore flow. The preferential wear of the liner below each of these bolt recesses was obvious to the eye, and can be discerned in Figure 9 and Figure 11(a). The preferential wear persisted to a significant extent even when the bolt recesses were filled with hardened 4140 steel square-headed bolts, again shown in Figure 11(a). Recommendations: Either fill the bolt recesses with a material at least as wear-resistant as the liner block itself; or change the liner design to one with integral backing studs, avoiding through-bolting.

Problem 5, Sub-optimal Wear-resistant Alloys: NiHard 4 is an adequate but not outstanding wear-resistant alloy. NiHard castings (known on site as “billets”) may seem to have the advantage of lower cost than products such as Duaplate, but in view of down-time issues this saving in unit cost is probably false economy. Moreover, the benefit from the greater thickness of these “billets” is negated if the method of fastening means that they must be discarded after less than half of their thickness is used. Recommendation (a): Composite products such as Domite, Duablock and Duaplate use a mild steel backing plate to reinforce the abrasion-resistant alloy. This protects against gross brittle fracture, thus permitting the use of harder (potentially more brittle) alloys, with high volume fractions of chromium carbides, than would be feasible in a simple casting. Recommendation (b): Where thick through-bolted castings appear more favourable, in addition to addressing the problem of open bolt recesses as above, it is important to use alloys which simultaneously maximise abrasion resistance while maintaining adequate fracture toughness. Better performance than NiHard is offered by high-Cr-Mo white cast irons with tailored compositions and heat treatments. There is also scope for future alloy development for cast block products that will achieve even higher abrasion resistance — at least comparable with that of weld-overlay plates and without the inherent weakness introduced by relief-check cracking in the weld deposit.

Plant Wear Trial in Iron Ore Chute

The above recommendations were accepted by BHP Iron Ore and Tasman Warajay, leading to immediate commencement of plant trials to verify and optimise the proposed solutions.

As a temporary solution to the perforation of the original rolled Duaplate (a relatively thin chromium carbide weld overlay plate) in the upper “hood” section of the chute, cast NiHard 4 plates had been retrofitted over the remains of the original continuous lining. In the hood, liner change-outs are more difficult than in the spoon, due to accessibility problems. Heavy block liner castings would create occupational health and safety (OHS) concerns, and moreover their greater thickness may have created a geometric problem, given that they were being bolted over an existing liner.

In ore transfer chutes, the intensity of conditions varies sharply in both longitudinal and lateral directions, as can be discerned from the deeply worn recesses (associated with the freefall impingement zone) visible in Figure 9. Moreover, the location of the most intense wear zone has been observed to move with time - compare Figure 9(a) with Figure 9(b). Therefore, in order to compare candidate materials using a simultaneous exposure trial, it is necessary to use a type of planar array wear test design [7].

The two rows of retrofitted NiHard 4 plates that were in place at the time of the site inspection are shown in Figure 8. The NiHard plates had dimensions $445 \times 145 \times 32$ mm, and weighed approximately 15 kg. Such large plates are not ideal for a planar array wear test under these conditions, but at the time it was not feasible to manufacture an insert containing a larger number of smaller coupons. Given that a pattern of bolt holes already existed to suit the NiHard plates, it was recommended that this geometry be retained.

To improve the wear life, Duaplate segments of thickness 17 on 12 mm were selected and cut to the dimensions of the NiHard plates, with studs welded to the backing plate. It was predicted that the Duaplate would perform better than the NiHard 4, because of its high volume fraction of very hard chromium-rich carbides. The useful thickness of abrasion-resistant alloy in the two cases was comparable, since the NiHard plates can only be allowed to wear some 19 mm (in the vicinity of the bolt) before failure of the bolt becomes a danger.



Figure 8. Retrofitted NiHard 4 cast liner segments bolted to the original continuous lining in the upper “hood” section of a live chute in Port Hedland, Australia. The added plates were not sufficient to span the whole of the impingement zone at the entrance to the hood.

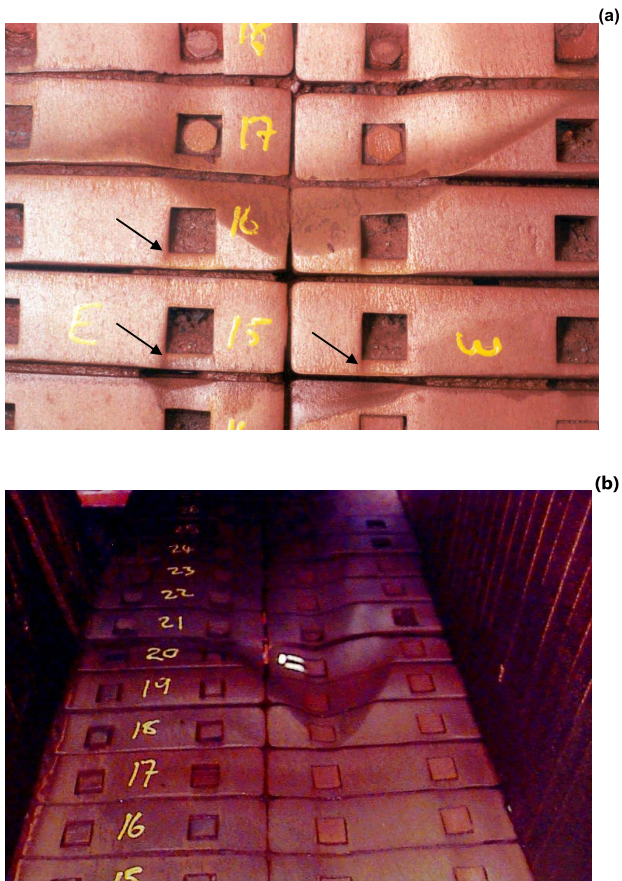


Figure 9. Cast liner blocks in the lower “spoon” section of the live chute; photographs taken at different times in 2000. Wear intensity varies strongly both longitudinally and laterally. Moreover, the point of maximum wear was seen to shift from week to week — compare location of high-wear zone in (a) with that in (b). In addition to intense wear at the freefall impingement point, preferential wear can also be discerned below (downstream from) the open bolt recesses.

The trial used a chequer-pattern of alternating liner plates in the two alloy products. No photograph was taken of the actual trial installation. Both installation and monitoring (weighing & Fabrication). As can be seen in Figure 10, the trial was successful in yielding quantitative information from which the relative performance of the two liner products could be assessed. The following features can be observed from Figure 10:

- The absolute values of wear rates were reasonably consistent between the two trial periods, and this is true for both materials;
- For the NiHard, the highest wear rate clearly occurs at row 7. However, for the Duaplate this does not appear to be a particularly high wear area. Given that these data come from simultaneous exposure of the two materials, this difference is somewhat surprising. The difference may be due to the two materials responding differently to ore impingement angle;
- Other than one outlier point at row 5 in the second exposure period, the data show the Duaplate to be clearly superior to the NiHard, in most locations offering between 3 and 5 times longer service life;
- However, the quantitative relative performance of the two materials varies strongly as a function of longitudinal position. It may be that high impingement angles near the entrance to the hood lead to less favourable performance from the Duaplate — either by encouraging micro-fracture of the brittle carbides, or by attacking the exposed edges of the relief-check cracks in the weld overlay. Unfortunately, it was not possible for us to inspect the installation or the used samples so as to directly assess such mechanisms.

Motivated by the outcomes of this trial, more Duaplate segments were ordered. In mid-December 2000, it was reported that the life of a given Duaplate liner in the high-wear areas was 10 to 12 weeks, compared with an average of three weeks with the NiHard 4. This 3- to 4-fold improvement confirmed the predictions from the trial wear-rate data.

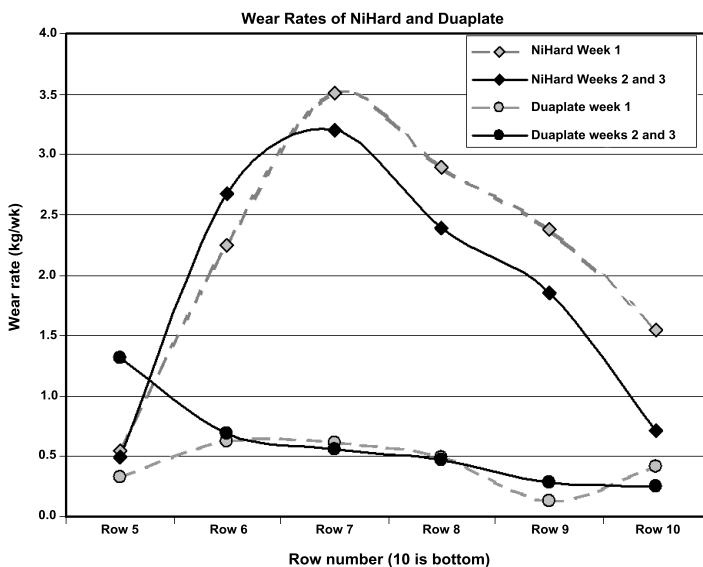


Figure 10. Wear rate measurements from plant trial in hood section of live chute passing iron ore at 1,800 tonnes per hour. Trial used planar array design with plate segments in two alloy products - cast NiHard 4 and Duaplate weld overlay.

The outcomes of this trial confirm and highlight the potential for improving equipment service life in LSSA environments, by the appropriate selection of wear-resistant products and by intelligent installation design. The importance of the latter point is highlighted by Figure 11, which shows the lower “spoon” section of the live chute at Port Hedland. The photographs show:

- The damaging effect of open bolt recesses with conventional hex-head bolts. The higher impingement angle at the downstream edge of the recess leads to high local wear rates, eventually leading to strong channelling of ore flow, creating a line of intense wear;
- The modest improvement obtained simply by use of high square-headed bolts made from hardened 4140 steel;
- The greater improvement obtained by use of Domite (brazed high Cr-Mo white cast iron) bolt caps.

The first Domite-capped bolts were installed in the week prior to the author’s site visit. As shown in Figure 11(b), the higher abrasion-resistance of the Domite resulted in it standing slightly proud of the NiHard, even after only one week of service. The Domite plugs were very successful in preventing preferential wear at the bolt recesses. The only preferential wear occurred where the narrow Domite piece was oriented axially so that did not fill the full width of the bolt recess - see middle-left bolt cap in Figure 11(b).

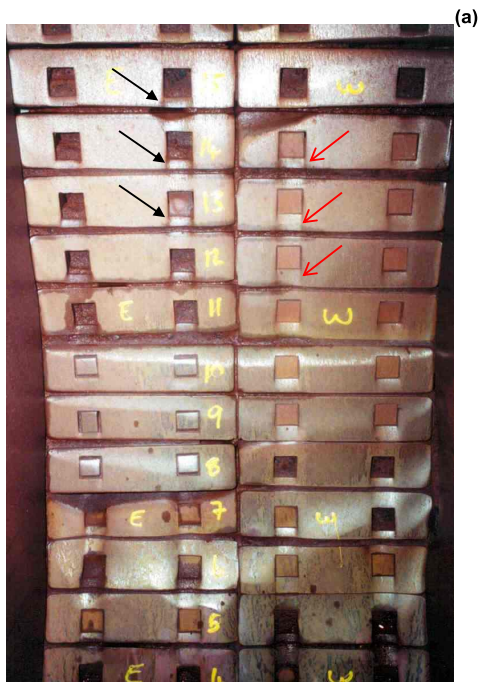


Figure 11. The lower “spoon” section of the live chute at Port Hedland. Shows the damaging effect of open bolt recesses ((a), black solid-headed arrows), the modest improvement obtained from hardened 4140 steel bolt caps ((a), red open-headed arrows), and the greater improvement obtained by use of white cast iron bolt caps (b).

A data-collection exercise was instigated in an attempt to quantify the increase in liner life attributable to use of the Domite-capped bolts by comparison with simple 4140 steel square-headed bolts. A total of six NiHard “billet” castings - three with 4140 bolts and three with Domite-capped bolts - were weighed on a weekly basis.

The results of this trial were ambiguous. Although in the majority of cases it appeared that the billets with Domite-capped bolts suffered less wear, there were anomalies due to the fact that the wear intensity in the spoon varies strongly with position, not only down the length of the spoon but also from east to west across the spoon. The protocol used for this trial had been designed to minimise the labour involved in removing, weighing and replacing billets each week, but in practice this protocol was a failure. A different protocol, involving larger numbers of billets installed in a chequer pattern, and weighed less frequently, was proposed for any future data-collection exercises, but was not implemented at that time.

Despite the failure to quantify the increase in billet life, direct observation of wear patterns made it clear that the Domite-capped bolts were a success. On the strength of these trials, BHP Iron Ore decided to order a large batch of Domite-capped bolts for use throughout the spoon. In mid-December 2000 the maintenance contractors reported that the wear in the spoon was under a good level of control:

- With open bolt recesses, the billet life at the positions of highest wear intensity had been only 1–2 weeks;
- With 4140 square-headed bolts this increased to 3–4 weeks;
- With Domite plugs it was reported that the life of any given billet was 10–12 weeks.

This satisfied the target four-fold increase in liner life, and extended the necessary maintenance intervals (for this section of the chute) to an acceptable level.

Seeking a Better Test for Low Stress Sliding Abrasion

Existing Tests for Low Stress Sliding Abrasion

For the reasons described above, low stress sliding abrasion is a highly fruitful area for research and development.

Opportunities to conduct field trials, such as those described in this paper, are rare. Even when opportunities do occur, the resulting statistics are often quite poor. Consequently, there is a powerful need for laboratory tests capable of providing reliable predictions of the relative service lives of candidate wear-resistant products.

The most commonly used laboratory test for low stress sliding abrasion is the rubber wheel abrasion test (RWAT). The RWAT does not appear to suffer from problems of the magnitude of those that beset the pin abrasion test (whereby the PAT produces a wear mode markedly different from that which it is purported to represent). Indeed, the RWAT has some significant benefits, since it unquestionably produces low stress sliding abrasion yet creates usefully high

wear rates, thus yielding a reasonably high rate of data production. However, it has four features which give cause for concern:

- Unless one is investigating the wear performance of pavements subject to abrasion by grit under the influence of rubber-soled shoes and vehicle tyres, then most industrial wear environments do not involve a rubber counterface. Admittedly, we do not have any definitive information to indicate that the rubber wheel introduces anomalies into the data, but in principle it seems unwise to introduce a feature which so clearly deviates from industrial conditions;
- At a practical level, the RWAT introduces significant limitations into the types of abrasive materials that are able to be used. It has repeatedly been demonstrated that mineral properties and particle shapes can significantly affect the relative performance of candidate wear-resistant materials; hence, it is of considerable concern that the RWAT is almost always operated with an idealised quartz sand abrasive;
- Because the ASTM G65 rubber wheel abrasion test only exposes one specimen at a time, it is critically important to maintain invariant conditions from test to test, year to year and laboratory to laboratory. This is challenging and somewhat expensive to achieve. Moreover, it can be very time-consuming to generate a statistically credible data set for a large number of candidate wear-resistant materials. In our laboratory, drawing upon our experience with the BMAT, we have a strong preference for tests that simultaneously expose large numbers of specimens. Simultaneous exposure removes the need for idealised “standard” abrasives, and confers the freedom to use the actual abrasives from any given end user’s site operations;
- There are some laboratory wear performance predictions from the RWAT that, as described below, appear questionable as to their quantitative (level 3) accuracy.

In 2002, the authors performed abrasive wear tests on competing commercial wear plate products used in underground ore chutes at BHP Billiton Cannington mine [53]. Three of the products were quenched-and-tempered martensitic steels and one was a chromium carbide weld overlay product (AS/NZS 2576 class 2360).

On the assumption that the chutes would involve low stress sliding abrasion, the rubber wheel abrasion test was selected. In recognition of the importance of the mineral type, the RWAT tests were performed both with quartz sand and with screened Cannington mine ore fines. The results are summarised in Table III.

Table III. Rubber Wheel Abrasion Test Data for Cannington Mine

| Abrasive Mineral: | | Sand | | | Cannington Ore | | |
|-------------------|----------|------------------|---------|------|------------------|---------|-------|
| Plate | Hardness | Weight Loss (mg) | | Life | Weight Loss (mg) | | Life* |
| Material | (HV) | Mean | Std Dev | (%) | Mean | Std Dev | (%) |
| Q+T Plate 1 | 442 | 35 | 2 | 100% | 343 | 9 | 100% |
| Q+T Plate 2 | 399-419 | 38 | 5 | 91% | 397 | 19 | 86% |
| Q+T Plate 3 | 387 | 71 | 7 | 49% | 506 | 11 | 68% |
| 2360 Overlay | 872 | 29 | 7 | 122% | 8.8 | 1.3 | 3900% |

* “Life” = relative wear resistance compared to (quenched and tempered) Q+T Plate 1. This only translates into relative service life if equal thicknesses of material are being compared.

The performance rankings of the four materials are the same in the two abrasive materials, with projected service life rankings, as follows: 2360 overlay > Q+T plate 1 > Q+T plate 2 > Q+T plate 3. These performance rankings match the measured hardness rankings (noting that the hardness readings were taken from the specimen face on which the wear tests were performed).

However, the two abrasives produced markedly different absolute values of wear rate in the RWAT. In the three martensitic steels, the wear rate in Cannington ore was some seven to ten times higher than for the same material tested in sand. For the hardfaced plate the opposite situation applies, with the wear rate in sand being some three times higher than that in Cannington ore. Such contrary behaviour is remarkable and requires explanation.

The two characteristics of an abrasive that are likely to affect the absolute wear rates in this way are the particle size and the particle angularity. In LSSA, coarser particles, and more angular (sharper) particles, both generally increase wear rates. The Cannington ore contains a proportion of coarser particles (up to 850 µm), and is certainly more angular than the quartz sand. However, it should not be assumed that the Cannington ore is inherently more abrasive than sand, since as already noted, on the hardfaced plate it produces lower wear rates than the sand does.

This contrary behaviour can be understood in terms of the interaction between the abrasive minerals in the ore and the hard particles in the weld overlay. Clearly, the minerals in the Cannington ore are not hard enough or strong enough to damage the chromium carbides in the hardfaced plate. This will remain true whether the particles are angular or rounded, large or small. Therefore, although the angularity of the Cannington ore makes it highly aggressive to martensitic steels, it does not render it particularly aggressive to the hardfaced plate. This is sufficient to explain the observed behaviour.

For the three martensitic steel plate materials, the relative wear resistances measured in the Cannington ore tests are not greatly different from those measured in the sand tests. The only significant difference is that the disadvantage of using the softer Q+T plate 3 compared to the two harder steels appears greater in sand than it does in Cannington ore.

In both abrasives, the hardfaced plate performs better than any of the martensitic steel plate materials. This confirms that with both abrasives the wear mode is LSSA, whereby the particle-reinforced composite alloy performs significantly better than the homogeneous steel. However, the difference is much greater in Cannington ore than in sand. In sand, the benefit of using the hardfaced plate appears modest, whereas in Cannington ore the measured increase in wear resistance is huge. Evidently, the nature of the Cannington ore creates a more extreme differential in performance between the two alloy classes.

These laboratory test results suggest that in Cannington ore the clad plate offers very much higher service life. In practice, the increase in service life may not be as great as the factor of ~39 suggested by the bottom-right cell in Table III. One factor in this respect is that the weld deposit does not constitute the full plate thickness of the clad plate, and even the total thickness may be less than that of the martensitic steel plate. Any raw performance ratio indicated by the wear test must be multiplied by the ratio of the usable thickness of hardfacing deposit to the usable thickness of martensitic steel plate.

More importantly for the current discussion is the question of whether it can be guaranteed that the wear mode in the rubber wheel abrasion test is identical to that in the intended field application. Will the clad plate really offer 39 times better wear performance (per thickness) in service? This is the type of question for which wear researchers should be diligently seeking answers.

Inner-circumference Sliding Bed Abrasion Test

In an attempt to address the above-described disadvantages of the rubber wheel abrasion test, the authors have expended considerable effort designing, constructing, trialling and sometimes abandoning new designs of laboratory test devices for low stress sliding abrasion. The new laboratory test for LSSA, denoted the “inner-circumference sliding bed abrasion test” (IC-SBAT), is the result of this process.

The criteria for developing a new design of laboratory test for LSSA included the following:

- First and foremost, it must be capable of accommodating the actual abrasive substance that is present in the field operation. This is not negotiable, since the mineral is the strongest single factor controlling relative performance of candidate wear-resistant materials;
- Secondly, it must reproduce with reasonable fidelity both the macro-mechanics and the micro-mechanics of abrasive-to-metal contact that are present in the field;
- It should avoid artificial devices such as rubber counterfaces or bonded abrasive products. Since these devices are not present in the field, they make it less likely that the laboratory test would be capable of reproducing the contact mechanics conditions of the industrial operation;
- The laboratory test should enable simultaneous exposure of multiple specimens. This provides the opportunity for one or more internal reference materials to be included in every test, which eliminates the traditional problem of the need to maintain strictly invariant abrasion intensity from test to test. It also improves data productivity and statistical quality;
- Finally, its design should seek to avoid the common situation in which specimen wear is dominated by leading-edge effects.

The last of these criteria warrants discussion. An example of an existing test which successfully avoids this problem is the rubber wheel abrasion test. The contact geometry is such that the wear scar is entirely contained within the flat face of the specimen and there are no significant leading-edge effects. By contrast, in most slurry-pot devices the measured specimen mass loss is strongly influenced by what occurs at exposed edges upon which the abrasive particles impinge. This may or may not be a fair representation of what occurs in service; but in such devices there is a concern that the measured wear rates may be unduly sensitive to the precise details of specimen preparation or installation, leading to the potential for erroneous results.

The “inner-circumference” design of the IC-SBAT is aimed at avoiding leading edge effects. The basic design is illustrated in Figure 12. The abrasive bed is driven past the stationary specimen array by paddles. Currently, the device has two specimen rings accommodating 22 specimens each, but there is capacity to increase to a larger number of rings. The wear intensity is not identical between the rings, but this can be accounted for by use of reference specimens.

The inner-circumference specimen array has the consequence that the leading edge of one specimen is protected by the trailing edge of the upstream specimen. Even if installation does not achieve complete protection, the sharp leading edges are somewhat recessed, out of the main flow stream. Consequently, the wear is concentrated on the flats of the specimens, so it becomes possible to assess the rate of thickness loss. The specimens shown in Figure 13(a) have been subjected to an IC-SBAT test and show no tendency for preferential wear on leading edges.

The device is very versatile, accommodating a wide variety of abrasive types, operation modes and speeds. Figure 12(b) shows the IC-SBAT loaded with 20 mm gravel for a sliding-bed abrasion test, while Figure 14 shows the device being operated in slurry erosion or wet particle erosion mode (IC-WPET). Figure 15 shows specimens after a relatively long-term (60 hour) test in IC-WPET mode. In the polyurethane specimen, Figure 15(b), there is preferential wear at the impingement zone, but this is located some 2 mm behind the leading edge. Impingement angle is of course very important in erosive wear, and we are currently working on design modifications that will allow the impingement angle to be manipulated.

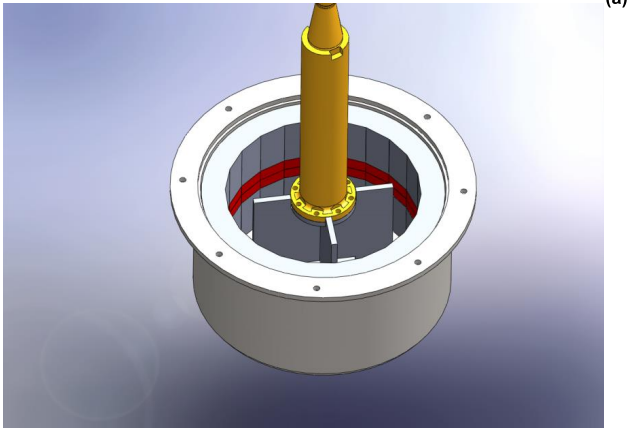


Figure 12. Key design features of the IC-SBAT (inner-circumference sliding bed abrasion test);
(a) Design drawing, (b) Constructed device ready for a test with 20 mm gravel.

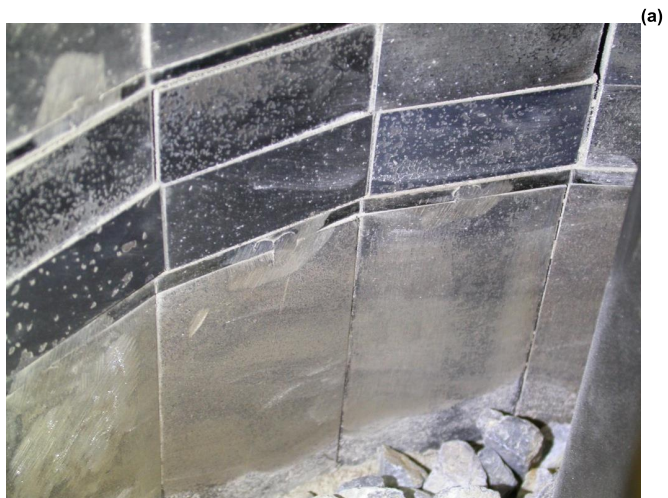


Figure 13. Different specimen sets installed in the IC-SBAT; (a) Mild steel specimens used for commissioning trials, (b) Polymeric wear-resistant materials, including polyurethanes and ultra-high molecular weight polyethylene, installed for a consultancy project.



Figure 14. Operation of the IC-SBAT device in wet particle erosion mode (IC-WPET).



(a)



(b)

Figure 15. Worn specimens after testing in the IC-SBAT device when operated in wet particle erosion mode (IC-WPET); (a) Stippled surface of mild steel specimen, due to erosion-corrosion (scale millimetres), (b) Polyurethane specimen showing impingement zone behind the leading edge (specimen 55×25 mm, particle flow from left to right).

Plant Trial Comparison for IC-SBAT

To date one plant trial has been performed in an attempt to correlate the IC-SBAT data with industrial wear rate data. The trial was in an Aran pug mill mixer at Karreman quarry in Brisbane, Australia. The trial was detailed and sustained, involving simultaneous exposure of six different white cast iron alloys, with at least ten paddle specimens of each alloy. The trial was run for 20 weeks, with approximately 100,000 tonnes of production throughput in each of the two parallel legs of the twin pug-mill mixing station.

Of the six paddle types compared, two were commercial paddles - one supplied by the original equipment supplier and one after-market replacement component. The other four paddle types were cast in a Brisbane foundry to our alloy specifications, aimed at achieving a wide variety of microstructure types within the generic high-Cr-Mo white cast iron alloy class. Figure 16 shows the CAD model for the experimental paddle castings and Figure 17 shows some of the resulting castings along with the commercial paddles.

The compositions of the six alloys are shown in Table IV. Alloy F contains the strong carbide formers niobium, vanadium and titanium, with a stoichiometric balance of surplus carbon above what would be required in the host white cast iron alloy. In the induction furnace, 2.4% niobium was added, but at that time (2010) there was no access to vacuum melting facilities. Oxidation led to loss of approximately two-thirds of both the niobium and the titanium that had been added.

Figure 18 shows two views of the pug mill, firstly during installation of the paddles and secondly during the course of the trial. Figure 19 shows two of the worn paddles. Many of the paddles were more extensively worn than these, but these were chosen for scanning electron microscope (SEM) examination as representing the stage of wear likely to dominate the life of the component.

The relative abrasive wear performance of the six alloys was measured in two laboratory tests, the RWAT and the IC-SBAT, for comparison with the pug mill trial results. In the RWAT the usual quartz sand was used, but the IC-SBAT used greywacke gravel from the quarry where the trial was conducted. The quantitative results are shown in Table V.

Scanning electron microscope images of the worn surfaces from the pug mill trial and from the IC-SBAT, at comparable magnifications and imaging conditions, are shown in Figure 20 and Figure 21. Figure 20 shows secondary electron images, emphasising the topography of the worn surface. The wear scars from the IC-SBAT and the pug mill environment are very similar. The abrasive particle motion appears to be predominantly sliding, but with some embedding. In both the pug mill and the IC-SBAT, the wear grooves are only semi-continuous. By contrast, in the RWAT the grooves were completely continuous and straight.

Figure 21 shows backscattered electron images, which provide atomic number contrast. These images enable assessment of the way in which the abrasive particles interact with the M_7C_3 reinforcing particles. Shown here is alloy B, the after-market paddles, which performed relatively poorly, apparently because the matrix was undesirably soft. There was only a small amount of cracking of the carbides, such that the wear mode appears to be predominantly low stress sliding abrasion. However, in this alloy and under these conditions the carbides are not providing very strong protection of the matrix.

The rank order of alloy performance is much the same in the two laboratory tests as in the plant trial. However, the quantitative RWAT results were poor at differentiating between the reference alloy (the OEM paddle A) and the three inferior alloys. The IC-SBAT provided a better match, but on these inferior alloys the pug mill was the most severe of the three tests.

In all three tests, alloy F, containing carbides of niobium, vanadium and titanium, provided the best wear resistance of the six alloys. The worn surface of this alloy is shown in Figure 22. It can be seen that the niobium-rich carbides stand proud - significantly more so than the chromium carbides do. Despite the relatively low volume fraction of these niobium-rich carbides, they are evidently having a protective effect for the host alloy around them. The complex alloy appears to be functioning as a kind of “double-composite”, with two different reinforcing phases. If the volume fraction of NbC particles was increased, it would seem probable that they would provide even more effective protection to the host alloy.

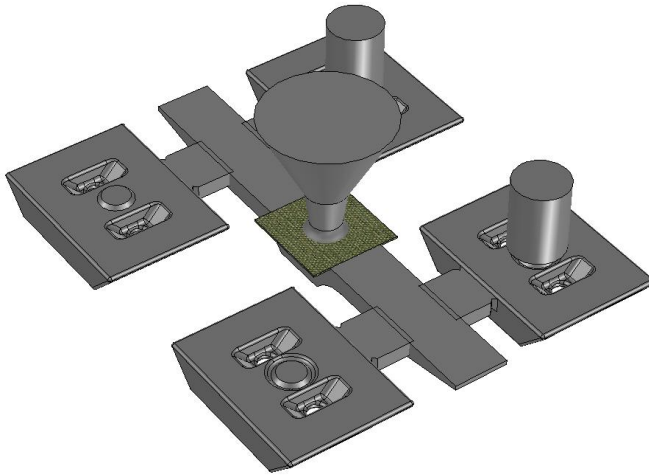


Figure 16. CAD model for the paddle castings that were manufactured in various white cast iron alloys for purposes of the pug mill trial.



Figure 17. Paddles ready for installation in the pug mill trial. Paddles A were the OEM paddles, B the after-market paddles, D and F were alloys cast for the purposes of the trial.



Figure 18. One leg of the pug mill; (a) during installation of the paddles and (b) at an inspection conducted during the course of the trial.

Table IV. Alloy Compositions of Commercial and Experimental Paddles in Pug Mill Trial

| Code | Description | C | Cr | Mo | Nb+V+Ti | CVF ₁ † | Ratio | Hardness |
|------|----------------------|---------|---------|---------|---------|--------------------|----------------------|----------|
| | | (mass%) | (mass%) | (mass%) | (mass%) | (vol%) | CrE ₁ /C‡ | (HV) |
| E | Stable austenite | 4.15 | 27.5 | 0.00 | — | 51 | 6.5 | 550 |
| B | After-market paddles | 3.45 | 29.6 | 0.06 | — | 43 | 8.4 | 522 |
| D | Reduced-CVF | 1.87 | 13.8 | 2.60 | — | 16 | 7.8 | 797 |
| A | OEM paddles | 3.38 | 27.2 | 0.00 | — | 41 | 7.8 | 666 |
| C | 17Cr-3Mo | 3.02 | 18.0 | 2.88 | — | 32 | 6.3 | 852 |
| F | 17Cr-3Mo + Nb,V,Ti | 3.59 | 16.7 | 3.13 | 2.7‡ | 34* | 5.7* | 897 |

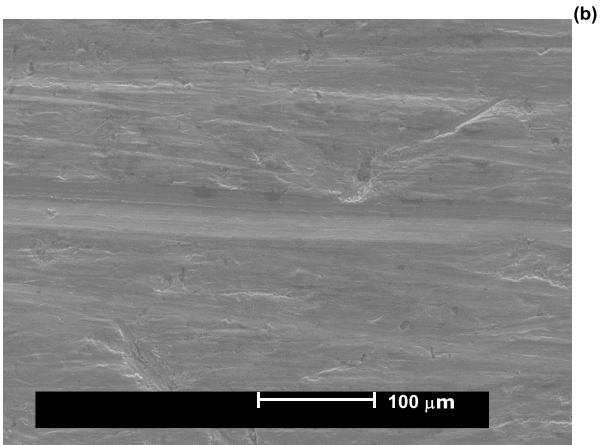
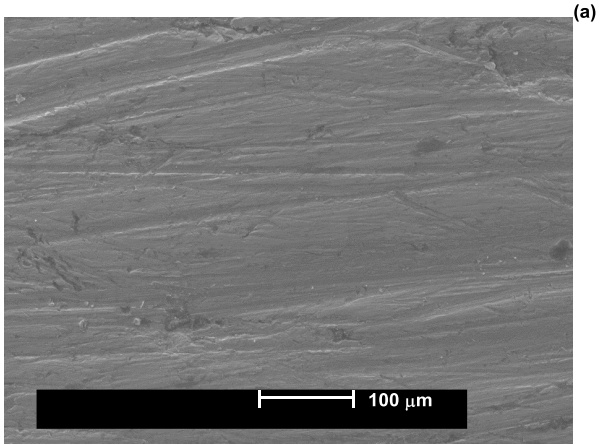
† Carbide volume fraction CVF normally calculated from Maratray's [54] formula, % carbides = 12.33(% C) + 0.55(% Cr) – 15.2. However here, both CVF₁ and ratio CrE₁/C are based upon a “chromium equivalent” CrE₁ = Cr + [(Mo–1.25)×52.0/95.9], where 1.25% was the average Mo content in the systematic series of 42 alloys used by Maratray and Usseglio-Nanot [55] to determine their empirical formula.

‡ Strong carbide former concentrations were planned to be 2.4%Nb, 1.3%V, 1.2%Ti, but air melting resulted in oxidation losses which reduced the levels to 0.85%Nb, 1.33%V, 0.47%Ti.

* In alloy F, the listed C, Cr and Mo compositions are as-analysed bulk levels, but the values of CVF₁ and CrE₁/C are the estimated values for the “host” alloy, after stoichiometric carbon removed from solution by Nb, V, Ti.



Figure 19. Worn paddles recovered after the pug mill trial, marked for cutting of samples for SEM examination of worn surfaces.



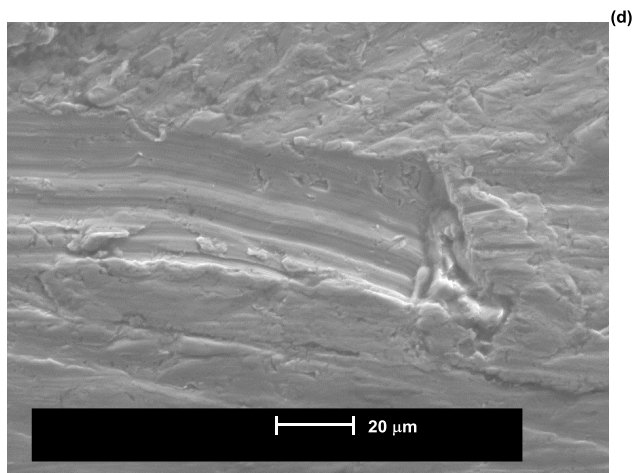
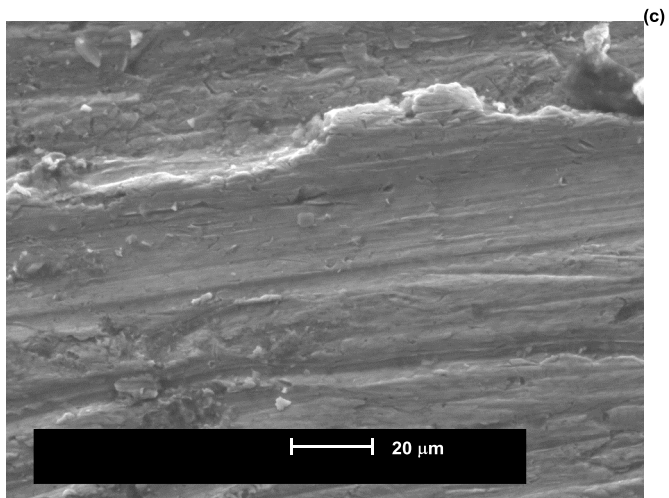
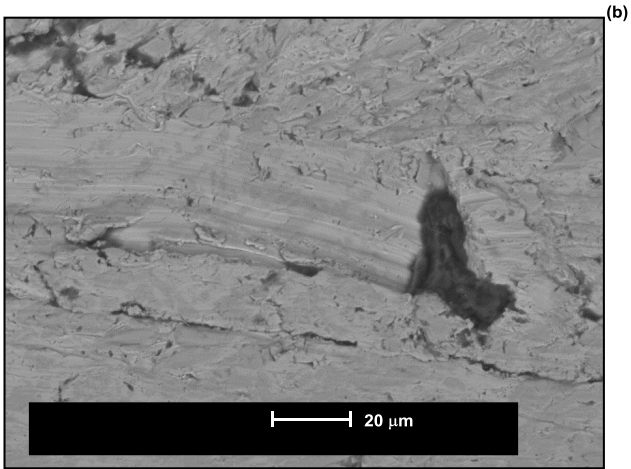
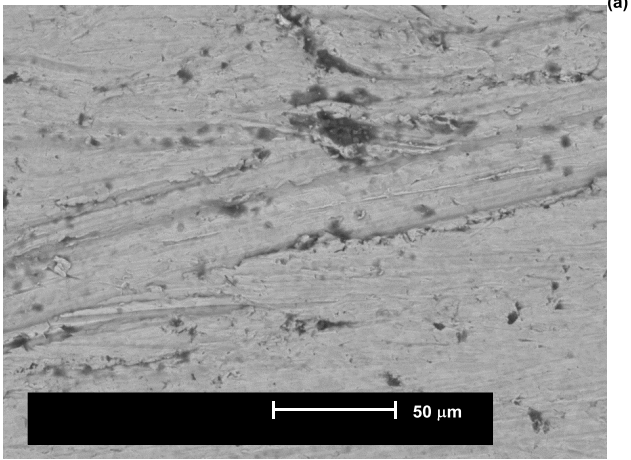


Figure 20. SEM secondary electron images comparing the worn surface characteristics from the pug mill trial with those from the IC-SBAT with the same greywacke abrasive; (a) Pug mill worn surface at low-medium magnification, (b) IC-SBAT worn surface at low-medium magnification, (c) Pug mill at medium-high magnification, (d) IC-SBAT at medium-high magnification.



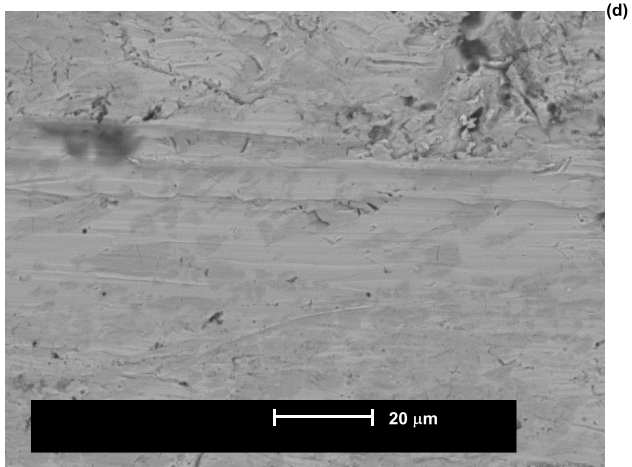
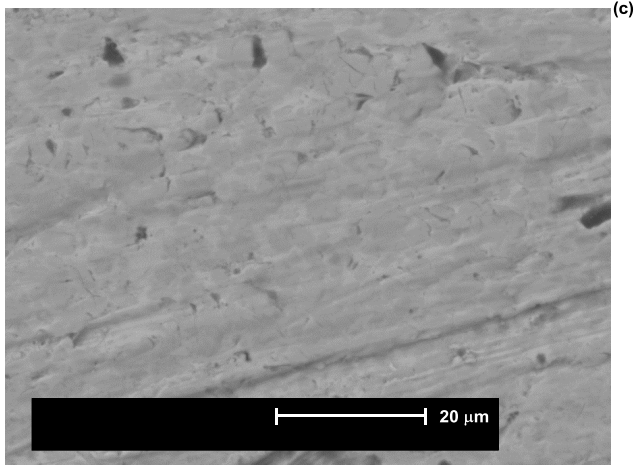


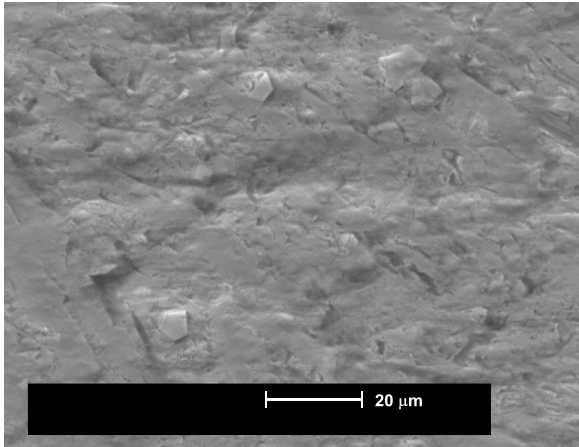
Figure 21. SEM backscattered electron images; (a), (b) Pug mill and IC-SBAT worn surfaces at medium-high magnification, (c), (d) Pug mill and IC-SBAT worn surfaces at high magnification.

Table V. Wear Data from Pug Mill Trial and Comparative Laboratory Tests

| Code | CVF ₁ † (vol%) | Ratio CrE ₁ /C† | Hardness (HV) | Relative Wear Life | | |
|------|------------------------------|-------------------------------|------------------|--------------------|---------|----------|
| | | | | RWAT | IC-SBAT | Pug Mill |
| E | 51 | 6.5 | 550 | 95 | 78 | 50 |
| B | 43 | 8.4 | 522 | 97 | 81 | 63 |
| D | 16 | 7.8 | 797 | 106 | 78 | 63 |
| A | 41 | 7.8 | 666 | 100 | 100 | 100 |
| C | 32 | 6.3 | 852 | 135 | 167 | 110 |
| F | 34* | 5.7* | 897 | 185 | 185 | 123 |

† See footnote † in Table IV.

* See footnote * in Table IV.



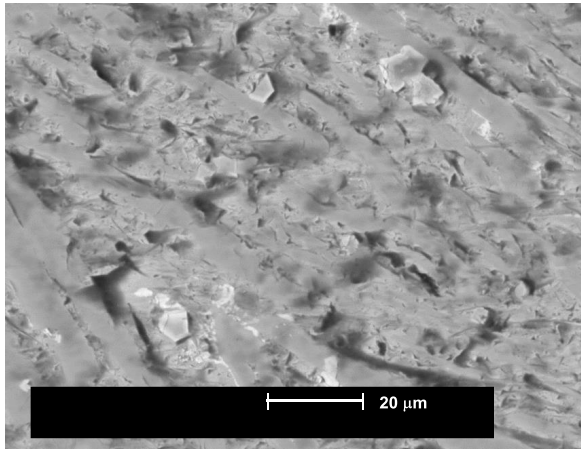


Figure 22. SEM images showing the worn surface of the NbVTi-bearing alloy F in the IC-SBAT with greywacke. The Nb-rich carbides stand proud of the matrix, and evidently provide a measure of protection to the host alloy despite their low volume fraction.

Summary of Field Trial Outcomes

Table VI provides a summary of plant trials that have been conducted, supplemented by a particularly fruitful study from the literature as reviewed in this paper. The right-hand columns show the levels of success that can be attributed to each trial, in terms of: whether quantitative performance data were successfully obtained; whether field-laboratory correlations were obtained; and whether the experimental wear-resistant material (if any) performed favourably.

It is commonly reported that a majority of the wear trials undertaken never yield quantitative data, because of lack of control or other practical problems. In light of this, it is remarkable that six out of seven trials conducted by the authors were successful in providing quantitative data.

The second success measure, that of field-to-laboratory correlation, can be regarded as the “holy grail” of tribological studies. The Newmont trial was especially remarkable in this respect, demonstrating that the laboratory ball mill abrasion test can achieve full level 4 correlation with plant wear data.

Table VI. Summary of Some Plant Trial Outcomes

| Site | Equipment | Alloys | QD† | FLC† | EMF † |
|------------------|------------------------|--|-----|------|-------|
| (Climax [3]) | Ball mill liners | Pearlitic steel, Martensitic steel, Various WCIs | (✓) | (✓) | – |
| Mount Isa Mines | Rod mill lifter bar | Pearlitic steel, Reduced-CVF WCI | ✓ | × | ✓ |
| Mount Isa Mines | SAG mill liner/lifters | Pearlitic steel, transformation-toughened WCI | × | × | × |
| Alcoa Pinjarra | SAG mill liner/lifters | Pearlitic steel, Martensitic steel | ✓ | ✓ | × |
| BHP Port Hedland | Transfer chute | NiHard 4, High-Cr-Mo WCI, Duaplate | ✓ | × | ✓ |
| Moranbah North | Tailings pipes | Mild steel, HDPE, experimental polymer | ✓ | × | × |
| Karreman Quarry | Pug mill paddles | 6 different WCIs | ✓ | ✓ | ✓ |
| Newmont Tanami | Ball mill balls | Martensitic steel (absolute wear rates) | ✓ | ✓✓ | – |

† QD = Quantitative data obtained; FLC = field-laboratory correlation obtained; EMF = Experimental wear-resistant material performed favourably.

Conclusions

This paper has analysed the challenges that are faced in predicting the field performance of wear-resistant materials. Attempts to predict long-term performance can be based either upon laboratory wear tests or on quantitative field trials, but both approaches require considerable care and critical analysis before they are likely to yield reliable predictions.

Four levels of correlation between laboratory and field data can be identified, namely 1) rank, 2) linear, 3) quantitative relative and 4) quantitative absolute correlation. To make rational economic decisions regarding materials selection, equipment operators require access to predictive data exhibiting at least level 3 correlation.

Site personnel are often sceptical about laboratory test data, and this paper has provided examples demonstrating that such reservations are well justified. Sometimes, in an effort to isolate and control individual aspects of the wear environment, laboratory tests become so idealised that they no longer represent industrial conditions in any substantive sense, and their predictions may be more misleading than useful. An alternative strategy is proposed whereby

mechanically simple laboratory test machines are permitted to preserve the natural complexity of the industrial environment. In such machines, the dominant wear mechanisms can be discerned indirectly by means of experiments in which key input parameters are systematically varied.

The paper has described two laboratory wear tests developed using this alternative strategy: the ball mill abrasion test (BMAT) for high stress abrasion as occurs in comminution environments; and the inner-circumference sliding bed abrasion test (IC-SBAT) for low stress sliding abrasion as occurs in ore chutes. The BMAT has been shown to be greatly superior to the “standard” pin abrasion test (PAT) that is often suggested (incorrectly) to simulate high stress abrasion. The BMAT easily achieves level 3 correlation, and with additional care can achieve level 4 correlation. The newly developed IC-SBAT shows promise for achieving level 3 correlation.

If performed with sufficient care and resources, field trials can yield useful quantitative data. However, to be sustainable in the longer term, research and development for wear-resistant materials requires access to laboratory tests that are intelligently designed and thoroughly validated against field performance. Armed with such tests, we will be in a position to evaluate a much wider range of candidate materials than could reasonably be evaluated in the field.

References

1. M.A. Moore, “Laboratory Simulation Testing for Service Abrasive Wear Environments,” *Wear of Materials 1987* (New York, NY: American Society of Mechanical Engineers, 1987), 673-687.
2. P.A. Swanson, “Comparison of Laboratory Abrasion Tests and Field Tests of Materials Used in Tillage Equipment,” *Tribology: Wear Test Selection for Design and Application*, ASTM STP 1199, ed. A.W. Ruff and R.G. Bayer (Philadelphia, PA: American Society for Testing and Materials, 1993), 80-99.
3. D.L. Albright and D.J. Dunn, “Wear Behaviour of Iron and Steel Castings for the Mining Industry,” *Journal of Metals*, 35 (11) (1983), 23-29.
4. J.D. Gates, et al., “The Meaning of High Stress Abrasion and its Application in White Cast Irons,” *Wear*, 263 (2007), 6-35.
5. G.J. Gore and J.D. Gates, “‘Impact-Abrasion’: Has its Time Come ... and Gone?,” *Materials Australia*, 32 (Jul/Aug 2000), 13-15.
6. J.A. Hawk et al., “Laboratory Abrasive Wear Tests: Investigation of Test Methods and Alloy Correlation,” *Wear*, 225-229 (1999), 1031-1042.
7. J.H. Tylczak, J.A. Hawk and R.D. Wilson, “A Comparison of Laboratory Abrasion and Field Wear Results,” *Wear*, 225-229 (1999), 1059-1069.
8. G.J. Gore and J.D. Gates, “Effect of Hardness on Three Very Different Forms of Wear,” *Wear*, 203-204 (1997), 544-563.

9. B. Bialobrzaska and P. Kostencki, "Abrasive Wear Characteristics of Selected Low-alloy Boron Steels as Measured in Both Field Experiments and Laboratory Tests," *Wear*, 328-329 (2015), 149-159.
10. W.L. Maxson, F. Cadena and F.C. Bond, "Grindability of Various Ores," *Transactions American Institute of Mining and Metallurgical Engineers*, 112 (1933), 130-146.
11. F.C. Bond and W.L. Maxson, "Grindability and Grinding Characteristics of Ores," American Institute of Mining and Metallurgical Engineers Technical Publication No. 888, 1938 (*Transactions American Institute of Mining and Metallurgical Engineers*, 134 (1939), 296).
12. F.C. Bond, "Metal Wear in Crushing and Grinding," *Chemical Engineering Progress*, 60 (2) (1964), 90-93.
13. A.K. Gangopadhyay and J.J. Moore, "The Role of Abrasion and Corrosion in Grinding Media Wear," *Wear*, 104 (1985), 49-64.
14. J.J. Moore, R. Perez, A. Gangopadhyay et al., "Factors Affecting Wear in Tumbling Mills: Influence of Composition and Microstructure," *International Journal of Mineral Processing*, 22 (1988), 313-343.
15. J.E. Sepúlveda, "Methodologies for the Evaluation of Grinding Media Consumption Rates at Full Plant Scale," *Minerals Engineering*, 17 (2004), 1269-1279.
16. I. Iwasaki, J.J. Moore and L.A. Lindeke, "Effect of Ball Mill Size on Media Wear," *Minerals and Metallurgical Processing*, 4 (2) (1987), 160-168.
17. T. Chandrasekaran, K.A. Natarajan and Kishore, "Influence of Microstructure on the Wear of Grinding Media," *Wear*, 147 (1991), 267-274.
18. C. Thirumalaisamy and Kishore, "Estimation of Abrasive and Impact Components of Overall Wear," *Materials Australia*, 32 (July/August 2000), 19-20.
19. P. Radziszewski, "Developing an Experimental Procedure for Charge Media Wear Prediction," *Minerals Engineering*, 13 (2000), 949-961.
20. P. Radziszewski, "Exploring Total Media Wear," *Minerals Engineering*, 15 (2002), 1073-1087.
21. P. Radziszewski et al., "Tumbling Mill Steel Media Abrasion Wear Test Development," *Minerals Engineering*, 18 (2005) 333-341.
22. T.W. Chenje, D.J. Simbi and E. Navara, "Relationship Between Microstructure, Hardness, Impact Toughness and Wear Performance of Selected Grinding Media for Mineral Ore Milling Operations," *Materials and Design*, 25 (2004), 11-18.

23. E. Albertin and A. Sinatora, "Effect of Carbide Fraction and Matrix Microstructure on the Wear of Cast Iron Balls Tested in a Laboratory Ball Mill," *Wear*, 250 (2001), 492-501.
24. E. Albertin and S. deMoraes, "Maximizing Wear Resistance of Balls for Grinding of Coal," *Wear*, 263 (2007), 43-47.
25. J.D. Gates, "Abrasion in a Vertical Roller Mill" (Report #40325 for Queensland Cement Limited, UQ Materials Performance, Oct 2001), 1-29.
26. Z. Hildebrand, "A New High-Stress Abrasion Testing Method" (B.Eng. thesis, The University of Queensland, Nov 2002).
27. J.D. Gates, "Alloy Development and Optimisation of Abrasion-Resistant White Cast Irons – Final Report on 2006-2007 R&D Project" (Report #40912 for Bradken, CAST Cooperative Research Centre, Mar 2008), 1-90.
28. J.D. Gates, "Grinding Media Wear Testing for Continuous Improvement Program – Phase 01" (Report #41133+41218 for Newmont Asia Pacific and Comsteel Grinding Media, CAST Cooperative Research Centre, May 2008), 1-11.
29. J.D. Gates et al., "Effect of Abrasive Mineral on Alloy Performance in the Ball Mill Abrasion Test," *Wear*, 265 (2008), 865-870.
30. A. Comino, "Effect of 'Impact' on the Performance of White Cast Irons Relative to Low-alloy Steels in Grinding Mills" (B.Eng. thesis, The University of Queensland, Oct 2009).
31. C. Blyth, "Effect of Impingement Angles on the Performance of White Cast Irons Relative to Low-alloy Steels in Grinding Mills" (B.Eng. thesis, The University of Queensland, Oct 2010).
32. J.D. Gates, "Grinding Media Wear Testing – Phase 02" (Report #41293 for Newmont Asia Pacific, CAST Cooperative Research Centre, Jul 2011), 1-46.
33. J.D. Gates, A.L. Giblett and R. Dunne, "Prediction of Plant Ball Mill Media Wear Rates from Laboratory Ball Mill Test Data" (Paper presented at Comminution '12, Cape Town, South Africa, Apr 2012).
34. L. Keen, "Effect of Tempering on Abrasion and Chipping of White Irons" (B.Eng. thesis, The University of Queensland, Oct 2012).
35. A.A. AbdulKadir, "The Ball Mill Edge Chipping Test (BMECT) for Evaluating Fracture Toughness of White Cast Irons" (B.Eng. thesis, The University of Queensland, Oct 2013).
36. I.T. Cheong, "Exploring the Ball Mill Impact-fatigue Test (BMIFT)" (B.Eng. thesis, The University of Queensland, Oct 2013).

37. P.J. Bennet and J.D. Gates, "Mill Media Research Phase 04 – Effect of Corrosion on Wear Performance of Cast Chrome-Iron vs Forged Low-Alloy Steel Media" (Report #41562-04 for Newmont Mining Corporation, AMPAM, Feb 2014), 1-48.
38. J.D. Gates, "Wear Performance of Grinding Media using BMAT with Kittilä (Finland) Ore" (Report #41942 for Metso Process Technology & Innovation, UQ Materials Performance, Jul 2014), 1-20.
39. J.D. Gates, "Wear Performance of Grinding Media in Cananea Ore and Preparations for Cananea Plant Trial" (Report #42011 for Metso Process Technology & Innovation, UQ Materials Performance, Sept 2014), 1-49.
40. B. Hadaway, "Understanding the Performance Characteristics of Commercial Grinding Media" (B.Eng. thesis, The University of Queensland, Oct 2014).
41. M. Goode, "Understanding the Relationship between Corrosion and Abrasion Consumption Mechanisms in Grinding Mills" (B.Eng. thesis, The University of Queensland, Oct 2014).
42. C. Aldrich, "Consumption of Steel Grinding Media in Mills – A Review," *Minerals Engineering*, 49 (2013), 77-91.
43. J. Sepulveda, B. DeArango and L. Wardell-Johnson, "Comparative Evaluation of Grinding Media Consumption Rates at Full Plant Scale" (Paper presented at SAG 2006, Vancouver, B.C., Canada, 2006), 1-18.
44. R. Blickensderfer and J.H. Tylczak, "A Large-scale Impact Spalling Test," *Wear*, 84 (1983), 361-371.
45. A. Giblett and J. Seidel, "Measuring, Predicting and Managing Grinding Media Wear" (Paper presented at SAG 2011, Vancouver, B.C., Canada, Sep 2011), 1-12.
46. J. Levin, "Observations on the Bond Standard Grindability Test, and a Proposal for a Standard Grindability Test for Fine Materials," *Journal of the South African Institute of Mining and Metallurgy*, 89 (1) (1989), 13-20.
47. M.C. Fuerstenau and K.N. Han, *Principles of Mineral Processing*, (Littleton, CO: Society for Mining Metallurgy and Exploration, 2003), 85.
48. J. Dodd et al., "Relative Importance of Abrasion and Corrosion in Metal Loss in Ball Milling," *Minerals and Metallurgical Processing*, 2 (4) (1985), 212-216.
49. J.D. Gates and G.J. Gore, "Wear of Metals: Philosophies and Practicalities," *Materials Forum*, 19 (1995), 53-89.
50. J.D. Gates, "Two-body and Three-body Abrasion: A Critical Discussion," *Wear*, 214 (1998), 139-146.

51. J.D. Gates, "Wear Liners for Iron Ore Chutes – Final Report" (Report #40274 for Tasman Warajay Pty Ltd, UQ Materials Performance, Dec 2000), 1-10.
52. H.S. Avery, "The Measurement of Wear Resistance," *Wear*, 4 (1961), 427-449.
53. J.D. Gates, "Wear Tests on Bisalloy 500 and Other Wear Plate" (Report #40557 for BHP Billiton Cannington Mine, UQ Materials Performance, Sep 2002), 1-16.
54. F. Maratray, "Choice of Appropriate Compositions for Chromium-Molybdenum White Irons," *Transactions of the American Foundrymen's Society*, 79 (1971), 121-124
55. F. Maratray and R. Usseglio-Nanot, *Atlas – Transformation Characteristics of Chromium and Chromium-Molybdenum White Irons*, (Paris, France: Climax Molybdenum S.A., 1970), 16

OPTIMIZED GEAR PERFORMANCE BY ALLOY MODIFICATION OF CARBURIZING STEELS FOR APPLICATION IN LARGE GEAR BOXES

Th. Tobie¹, F. Hippenstiel² and H. Mohrbacher³

¹FZG – Gear Research Centre, Technische Universität München,
Boltzmannstr. 15, 85748 Garching, Germany

²BGH Edelstahl Siegen GmbH, Siegen, Germany

³NiobelCon bvba, Swaenebeeklaan 5, 2970 Schilde, Belgium

Keywords: Gears, Gear Failures, Gear Performance, Case Carburizing Steels, Alloy Modifications, Molybdenum, Nickel, Niobium, Hardenability, Tempering Resistance, Grain Refinement, Toughness, Gear Testing, Gear Strength Values

Abstract

Both the tooth root and tooth flank load carrying capacities are parameters that decisively influence gear size, as well as gearbox design. The principal requirement of all modern gearboxes is to comply with the demands for steadily increasing power density and to simultaneously offer high reliability of their components. Consequently, the required performance spectrum of materials used for such components is very high. For larger gear sizes, the loads and stresses increase at both surface and sub-surface locations within the gear tooth. Thus, the material properties and particularly the strength, increase in importance at greater material depths below the surface.

The choice of appropriate alloying elements in high performance carburizing steels, in combination with an appropriate heat treatment, allows the adjustment and optimization of strength properties over the material depth. Thereby, the requirements of highly loaded, large gears can be met and a sufficiently high load carrying capacity provided.

This paper initially gives an overview of the main failure modes of case carburized gears resulting from material fatigue at the surface and subsurface locations. Furthermore, the underlying load and stress mechanisms, specifically in relation to the gear size, are discussed as these considerations principally define the required material properties. Subsequently, the principles of newly developed, as well as modified, alloy concepts for optimized gear steels with high load carrying capacity are presented. In particular, the impact of modification of the bulk alloying elements molybdenum, manganese and nickel, as well as that of the microalloying element niobium, was investigated. Furthermore, an evaluation of the relevant material properties of these modified steel grades and a comparison to typical reference grades for gears are presented.

In experimental work, the load carrying capacities of tooth root and flank were determined using a pulsator, as well as an FZG back-to-back test rig. The results demonstrate the effectiveness of these innovative, new alloy concepts. Furthermore, the test results are compared to the current state-of-the-art and benchmarked against established load carrying characteristics of gears manufactured from conventional reference steel grades.

Introduction

Power transmitting gears for modern gearboxes are nowadays nearly always made of case carburized steels, which are particularly suitable for withstanding high local stresses without suffering damage. The properties of the base material in combination with an adequate heat treatment are key factors to ensure a sufficiently high load carrying capacity, as well as a high reliability of the components over the required gearbox lifetime. Gears are generally case carburized to increase surface hardness, to improve wear resistance and to achieve high contact and bending strengths. The heat treatment involved in case carburizing is an exceedingly demanding process, requiring a high level of technical knowledge, as well as a profound understanding of the material characteristics.

Gears and gearboxes are used for a wide range of applications. For example, high-power wind turbines usually have a gearbox transforming the low speed rotor shaft rotation to a higher speed required by the generator. Approximately 85 percent of all windmills are equipped with a gearbox. Usually such gearboxes are designed as one- or two-stage planetary transmissions. These gearboxes have been gradually increasing in size over recent years owing to the up-scaling of individual turbine sizes. In combination with this growth in size, the economic and qualitative optimization of the entire manufacturing chain is of high importance. The gears in wind turbines are sometimes exposed to extremely high loads at the gear flanks and in the tooth root of the gear teeth, for example, during sudden changes of wind speed or hard stops. Many failures and breakdowns of wind turbines, accordingly, originate in the gearbox, leading to significant outages and replacement costs. The powertrain of a windmill accounts for approximately 25 percent of the total equipment cost.

In the mining industry, gears and gearboxes can be found in a variety of different applications along the entire process chain, such as conveyor drives for extraction, gearboxes for mill drive systems in the processing stage, or gearboxes for stackers/reclaimers and special trucks for the transportation process. Most of the gears in these applications have to transmit a high torque and are often subjected to demanding operating conditions and have to achieve a long service life. Consequently, large sized gears can be found in many of these products.

The general requirements for high performance gear components are a hard case providing adequate fatigue strength, as well as wear resistance and a tough core preventing brittle failure under high impact loads [1]. Accordingly, various alloy concepts, as well as thermomechanical and thermochemical treatments have been developed to achieve this property combination. Alloy concepts for medium- and large-size gear applications vary significantly in different markets owing to historical drivers (eg. automotive, machine building, military), and practical experience as well as local availability of alloying elements, Table I.

Table I. Major Carburizing Steel Grades for Medium- and Large-size Gears in Various Geographical Markets

| Steel Grade | Standard | | C | Si | Mn | P | S | Cr | Mo | Ni | Region |
|-------------|-------------------|------|------|------|------|-------|-------|------|------|------|-----------------|
| 20MnCr5 | EN 10084 (1.7147) | min. | 0.17 | - | 1.10 | - | - | 1.00 | - | - | Western Europe |
| | | max. | 0.22 | 0.40 | 1.40 | 0.035 | 0.035 | 1.30 | - | - | |
| 18CrNiMo7-6 | EN 10084 (1.6587) | min. | 0.15 | - | 0.50 | - | - | 1.50 | 0.25 | 1.40 | Western Europe |
| | | max. | 0.21 | 0.40 | 0.90 | 0.025 | 0.035 | 1.80 | 0.35 | 1.70 | |
| 15CrNi6 | EN 10084 (1.5919) | min. | 0.14 | - | 0.40 | - | - | 1.40 | - | 1.40 | France, Germany |
| | | max. | 0.19 | 0.40 | 0.60 | 0.035 | 0.035 | 1.70 | - | 1.70 | |
| 17NiCrMo6-4 | EN 10084 (1.6566) | min. | 0.14 | - | 0.60 | - | - | 0.80 | 0.15 | 1.20 | Italy, France |
| | | max. | 0.20 | 0.40 | 0.90 | 0.025 | 0.035 | 1.10 | 0.25 | 1.50 | |
| SAE 8620 | SAE J1249 | min. | 0.18 | 0.15 | 0.70 | - | - | 0.40 | 0.15 | 0.40 | North America |
| | | max. | 0.23 | 0.35 | 0.90 | 0.030 | 0.040 | 0.60 | 0.25 | 0.70 | |
| SAE 9310 | SAE J1249 | min. | 0.08 | 0.15 | 0.45 | - | - | 1.00 | 0.08 | 3.00 | North America |
| | | max. | 0.13 | 0.35 | 0.65 | 0.025 | 0.040 | 1.40 | 0.15 | 3.50 | |
| 20CrMnTi* | GB T 3077 - 1999 | min. | 0.17 | 0.17 | 0.80 | - | - | 1.00 | 0.00 | - | China |
| | | max. | 0.23 | 0.37 | 1.10 | 0.035 | 0.035 | 1.30 | 0.15 | 0.30 | |
| 20CrMnMo | GB T 3077 - 1999 | min. | 0.17 | 0.17 | 0.90 | - | - | 1.10 | 0.20 | - | China |
| | | max. | 0.23 | 0.37 | 1.20 | 0.025 | 0.035 | 1.40 | 0.30 | 0.30 | |
| SCM420 | JIS 64105 | min. | 0.18 | 0.15 | 0.60 | - | - | 0.90 | 0.15 | - | Japan |
| | | max. | 0.23 | 0.35 | 0.85 | 0.030 | 0.030 | 1.20 | 0.30 | - | |

*0.04-0.10%Ti

Carburizing steels must comply with the following key requirements in view of component properties and durability:

- Chemical composition/hardenability;
- Homogeneity/microscopic and macroscopic cleanliness;
- Mechanical properties (tensile strength, fatigue strength and toughness);
- Wear resistance, contact fatigue strength, bending strength and vibration resistance;
- High and uniform dimensional stability [2].

DIN EN 10084 and ISO 683-11 [3,4] specify the technical delivery conditions for carburizing steels. In addition to the classification and designation of the steel grades, production processes, property requirements (eg. hardenability ranges), testing and inspection procedures are also specified. As well as these general standards, many end users have issued proprietary delivery specifications, which describe particular demands (eg. austenite grain size) in more detail. This is a result of the many possible processing routes for the production of carburized components. Depending on the component requirements, different sequences of annealing, hardening and machining are used, Figure 1. For instance, when a high dimensional stability of the component is needed, pre-hardening is performed before, and stress relieving is performed after, machining. It is, hence, essential to take the entire process chain into consideration when optimizing the material. For the design of large-scale gearboxes, steel grades are commonly selected according to the requirements specified in DIN 3990/ISO 6336, part 5 [5,6]. Figure 2 indicates, as an example, the anticipated tooth root endurance strength of various steel alloys and heat treatment concepts. Within the strength ranges, in general three quality levels can be distinguished: grade ML stands for the minimum requirement; grade MQ represents requirements which can be met

by experienced manufacturers at moderate cost; grade ME represents requirements which must be aimed at when higher allowable stresses are desirable, Figure 2, (within each colored area the upper bound represents the strength level for ME requirements and the lower bound for ML requirements. The lines within the colored region represent the strength level for MQ requirements.) It is obvious that the highest strength values are achievable for case carburized gears of quality grade ME. The diagram relates an easily measurable property such as case surface hardness to a complex system property, such as the tooth root endurance strength. The fact that for a given surface hardness a rather wide range of tooth root endurance strength levels can be obtained, suggests that alloy composition, microstructure and thermochemical treatment have an extremely high impact on the actual gear performance. Another system property of high importance for gear durability is the resistance to gear flank failures, such as pitting, and micropitting, as well as tooth flank fracture. High contact pressure, the status of lubrication, material properties, microstructure and chemical composition influence these system properties. Also, with respect to the flank load carrying capacity, case carburized materials of the highest quality level (ME) typically show the highest achievable strength values.

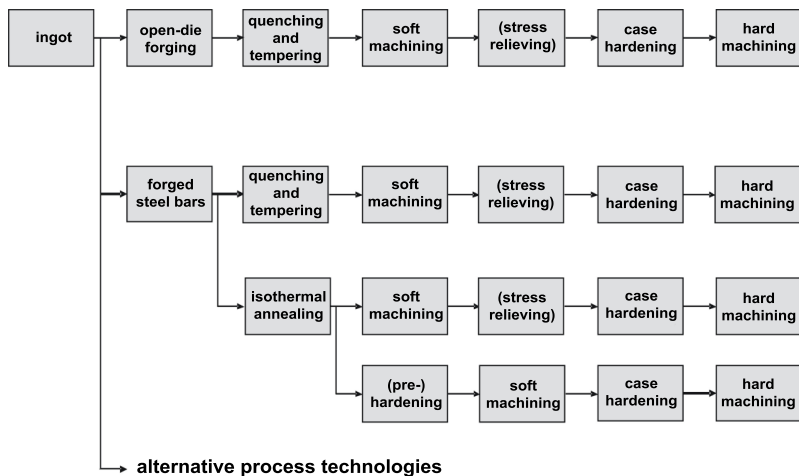
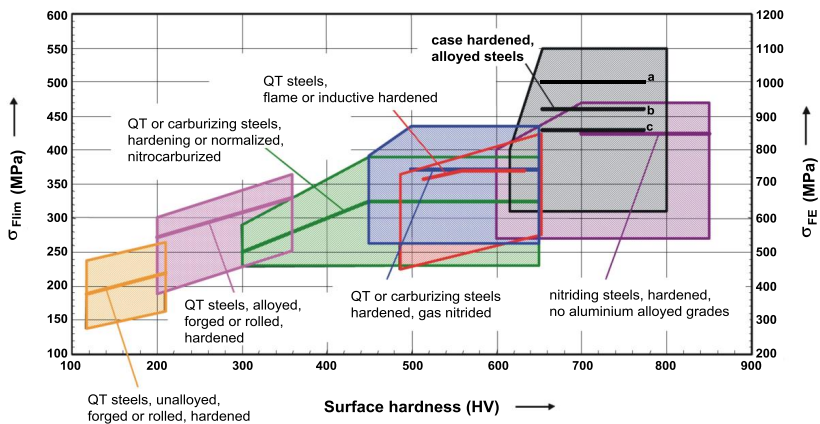


Figure 1. Typical processing routes for manufacturing of case hardened components.



- a Core hardness ≥ 30 HRC
- b Core hardness ≥ 25 HRC Jominy hardenability at $J = 12$ mm \geq HRC 28.
- c Core hardness ≥ 25 HRC Jominy hardenability at $J = 12$ mm $<$ HRC 28.

Figure 2. Tooth root load carrying capacity - allowable bending stress numbers according to ISO 6336-5 and indication of quality levels (ML, MQ, ME) [6].

For both vehicle and industrial transmissions, further optimization of gear steels towards better performance under demanding conditions is necessary. This is in part motivated by the need for reducing fuel consumption and emissions. In addition, a higher load bearing capacity is required at the surface in the near surface case, as well as at greater depths below the surface. A secondary target is to design efficient alloying concepts taking the entire processing route into consideration, including modified or innovative heat treatments. A fundamental way of dealing with these demands is to adjust the chemical composition of carburizing steels. In this respect, one can principally define two approaches. An economically driven approach aims at achieving a defined performance spectrum with a reduced alloy cost concept, whereas a performance driven approach targets superior properties at equal or moderately increased cost. The current work considers both approaches, focusing on modified molybdenum-based alloy concepts, including niobium microalloying. Thereby, innovative heat treatment conditions have also been tested.

Optimization Strategy for Carburizing Steels

Background: Gear Fatigue Failure Modes and Failure Mechanism

The gear load carrying capacity, in general, can be limited by different failure modes. Each failure mode is decisively influenced by the gear design, the material characteristics, the operating conditions and the gear lubricant performance. Nevertheless, each failure mode is influenced by different physical parameters and is subject to different failure mechanisms. For a specific gear design, a clear understanding of the underlying mechanism and the relevant load and stress conditions is required. This allows a material with optimum properties to be selected

to permit the gear to be manufactured with the required high load carrying capacity. Gear failures can basically be characterized as either material fatigue related failures or non-fatigue failure modes, which are primarily due to tribological problems in the lubricated contact zone. Furthermore, a differentiation of gear failures is possible depending on the failure initiation site, on the one hand with regard to the location on the gear - at the gear flank or in the tooth root area - and on the other hand with regard to the crack initiation site in the material volume - at the surface, in the case hardened zone or at greater material depth. This can result in different material property requirements in different areas. Figure 3 shows the main gear failure modes related to material fatigue.

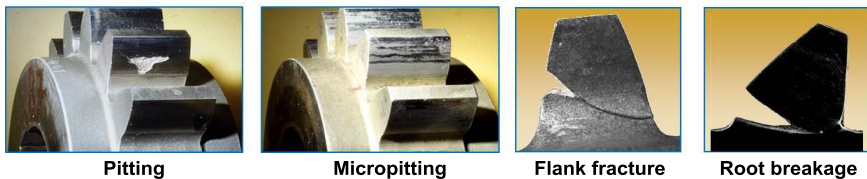


Figure 3. Main gear fatigue failure modes.

Pitting and tooth root breakage are the classical fatigue failure modes of gears. Both failure types are usually initiated at the surface or close to the surface and characterized by a crack that propagates further into the material. Whereas the pitting load capacity is strongly influenced by the Hertzian contact stresses in the gear contact zone, the tooth root strength is related to bending stresses in the root fillet. Differences in the nature of contact and bending stresses may result in different requirements regarding the material properties in relevant material areas, see also Figure 5.

Additionally, the failure mode of micropitting can influence the gear performance. Micropitting is most often observed on the surface of the loaded gear flank under unfavorable lubrication conditions. Nevertheless, micropitting is recognized as a fatigue failure mode but with crack propagation limited to the near surface material. Consequently, micropitting is influenced by the material characteristics specific to the surface and very close to the surface. Furthermore, the contact load at the flank surface also induces stresses at a greater material depth below the surface. If these stresses exceed the available local strength of the material, subsequent failures with crack initiation below the surface may arise. Such failures are referred to in the literature as tooth interior fatigue fracture (TIFF), tooth flank fracture or subsurface fatigue. As the load induced stresses at greater material depth increase with increasing gear size, the strength properties of the material at greater material depth gain more importance for larger gears.

The stress condition in a gear tooth is basically related to the tooth normal force acting in the gear contact zone which depends on the applied torque. This tooth normal force causes contact stresses at the gear flank and bending stresses especially in the root fillet, Figure 4. Further stresses arise depending on the gear geometry, the operating conditions and the manufacturing process.

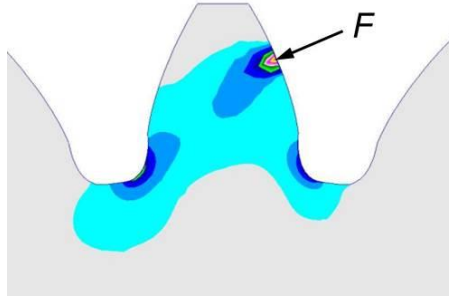
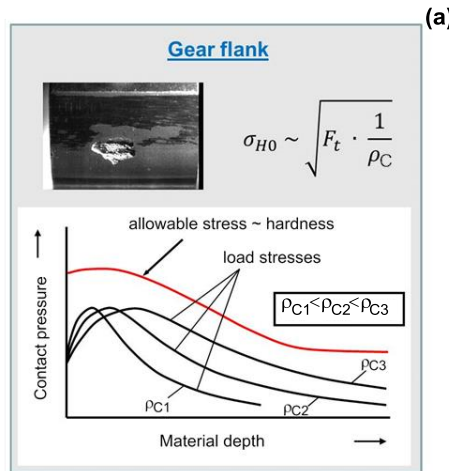


Figure 4. General stress condition inside a gear tooth (F – tooth normal force).

Basically, increasing the gear size allows transmission of a higher torque. Nevertheless, load induced stresses at greater material depth also increase with increasing gear size, even if the maximum stress value is comparable. Figure 5 clearly demonstrates the distribution of the relevant stresses over material depth for different gear sizes. It is obvious that with increasing gear size, expressed by the radius of curvature, ρ_C , for the gear flank, and the gear module, m_n , for the tooth root, an adjustment of the hardness profile is necessary. Consequently, with increasing gear size an increased case hardening depth is required. The influence of case hardening depth (CHD) on the pitting and bending strength of gears is shown in Figure 6.



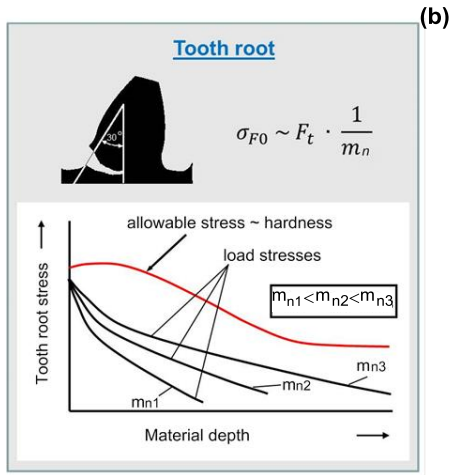
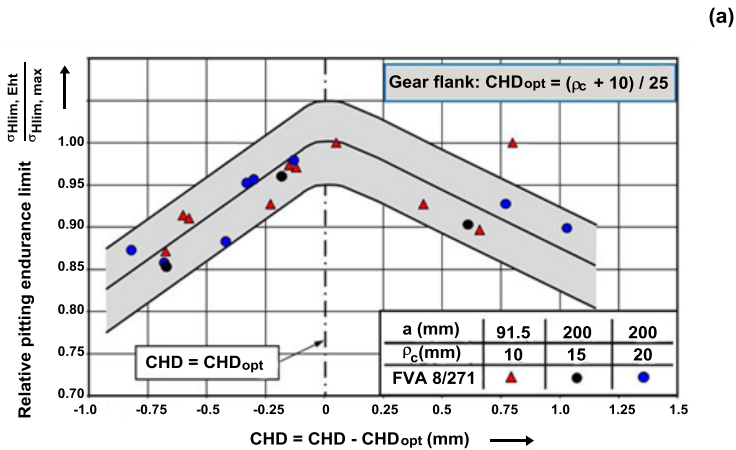


Figure 5. Principles of stress and strength condition depending on gear size; (a) at the gear flank, (b) at the tooth root [30] (σ_{H0} – nominal contact stress at pitch point, σ_{F0} – nominal tooth root bending stress, F_t – nominal tangential load).



(b)

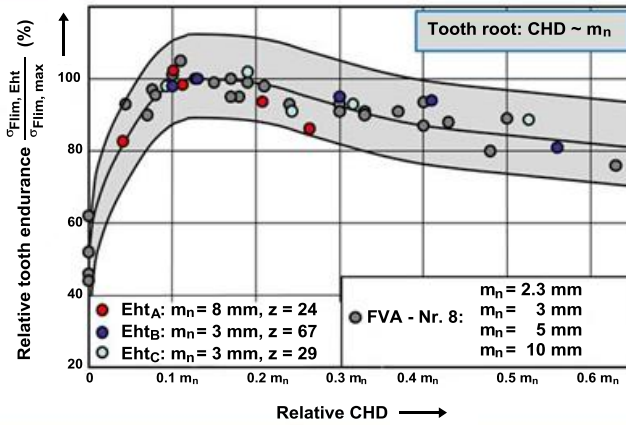
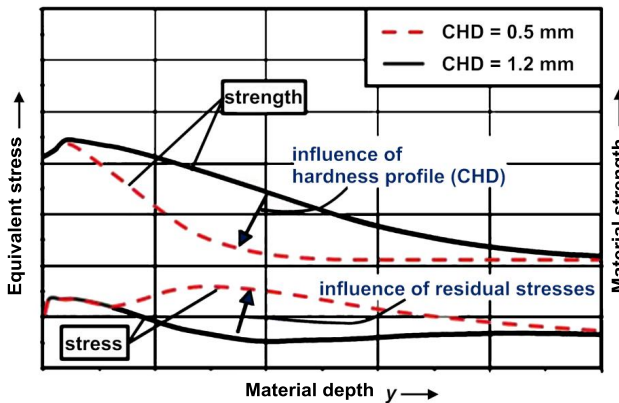


Figure 6. Influence of CHD on; (a) pitting and (b) bending strength of case carburized gears [31] (a – center distance; z – number of teeth; FVA 8/271 – relevant research project number of German research association FVA; Eht – old symbol for CHD).

The strong influence of CHD on the local material exposure A_{FB} , defined as the ratio of locally occurring equivalent stresses to locally available strength, of the gear flank is shown in Figure 7.

(a)



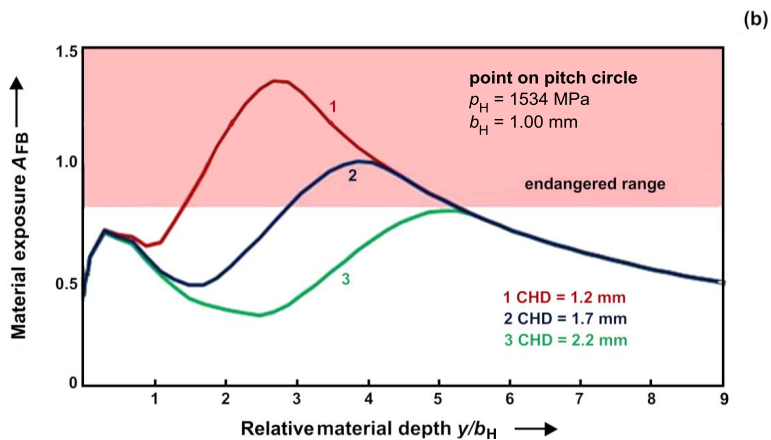


Figure 7. Influence of different CHD values on material exposure A_{FB} and risk of tooth flank fracture [30] (p_H – local Hertzian contact stress; b_H – local semi-Hertzian contact width).

As a different hardness profile also influences the residual stresses - compressive residual stresses are assumed in the complete case carburized layer - not only the material strength but also the equivalent stress distribution are influenced by different CHDs, Figure 7(a). Obviously, the ratio between local equivalent stress and local material strength is more critical with a smaller CHD and in this case is most unfavorable at a certain material depth that is close to the case-core interface. Consequently, CHD is not only an important parameter for pitting and bending strength of gears, but may also strongly contribute to minimizing the risk of crack initiation below the surface and thereby reduce the risk of failures due to tooth flank fracture, Figure 7(b). Furthermore, it is obvious that increasing the core strength of the gear material may contribute to reducing the risk of a failure initiation at greater material depth.

Requirements on Material Properties for Large Gear Sizes

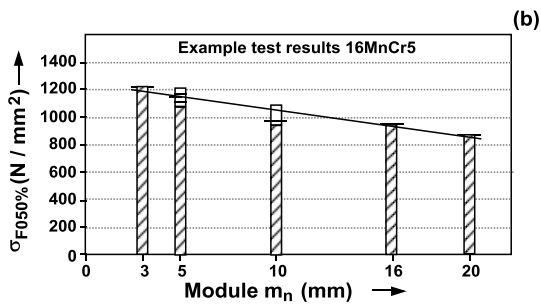
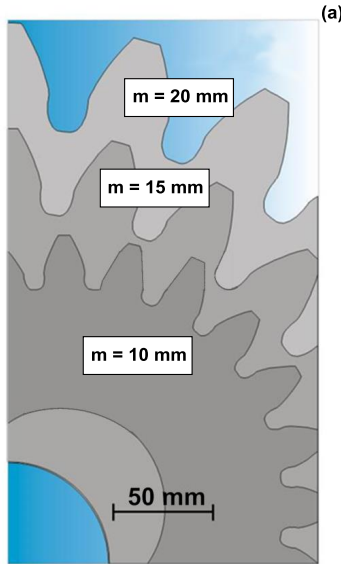
An increased case hardening depth required for large gear sizes correlates with an increased carburizing time. Longer carburizing times will affect the bulk material properties and may result in special demands on the material characteristics for large sized gears. Some major requirements for optimized materials with special regard to large gear applications are summarized below:

- Case Hardening Depth (CHD): adequate CHD is necessary to achieve the required fatigue strength in the case and at the core: effects shown in Figure 6 and Figure 7; the gear material has to be suitable for long heat treatment process times to achieve the high CHD required for large gears;

- Surface Hardness: a minimum surface hardness of 660 HV (58 HRC) is required according to existing standards in order to achieve allowable stress numbers for pitting and bending resistance of quality levels MQ and ME; higher surface hardness values do not increase fatigue resistance, but make machinability more difficult; in contrast, wear resistance of the surface typically increases with higher surface hardness;
- Core Tensile Strength and Toughness: increased core hardness is known specifically to influence the tooth root bending strength; higher core toughness allows higher core hardness for optimized root bending strength; furthermore, increased core strength and toughness are assumed to reduce the risk of tooth flank fracture damage. Gear steels with improved hardenability are required to achieve the desired properties for large gears;
- Microstructure and Grain Size: fine acicular martensite in the case hardened region and fine acicular martensite and bainite in the core are required for optimized load carrying capacities; fine grain size, especially ASTM 8 and finer, is known to positively impact gear flank and tooth root load carrying capacity; specific alloying additions are required to ensure grain size stability and a fine microstructure, even at long carburization process times;
- Residual Austenite: a certain amount of retained austenite in the case hardened region is assumed to be beneficial for micropitting load capacity and may also contribute to an improved pitting strength. This is due to the ductility of the residual austenite. Higher amounts of residual austenite may reduce case hardness and bending strength; up to 25% finely dispersed retained austenite is allowable according to existing gear standards;
- Cleanness: non-metallic inclusions are known to act as local stress raisers; depending on inclusion size and chemical composition, the gear load carrying capacity, especially in consideration of the risk of a crack initiation below the surface, may be influenced; as the highly stressed material volume increases with gear size, the probability of undesirable inclusions being located in critical material volumes is increased; consequently this results in high demands on cleanliness of gear material, especially for large gears;
- Area Reduction Ratio, Material Homogeneity and Intergranular Oxidation Depth: are further parameters that gain special importance for large gears; requirements according to existing gear standards have to be fulfilled even for larger gear sizes; intergranular oxidation can act as a fatigue fracture initiation site and may reduce the fatigue strength of the tooth;
- Hardenability: improved hardenability of the gear material is a basic requirement to achieve several of the above described properties for large gears.

Figure 8 demonstrates the influence of gear size on the tooth root bending strength. Basically, allowable stress numbers decrease with increasing gear size due to different size effects. Nevertheless, the results clearly demonstrate that, for large gear sizes, gear materials with higher hardenability (17CrNiMo6, 17NiCrMo14) achieve significantly higher bending strength values, compared to gear materials with lower hardenability (16MnCr5). The influence of material

hardenability on gear strength is higher at larger gear sizes. Consequently, appropriate alloying additions to achieve a high material hardenability and to ensure adequate material characteristics are essential for high performance carburizing steels, in order to meet the requirements of large sized gears and to provide a sufficiently high gear load carrying capacity.



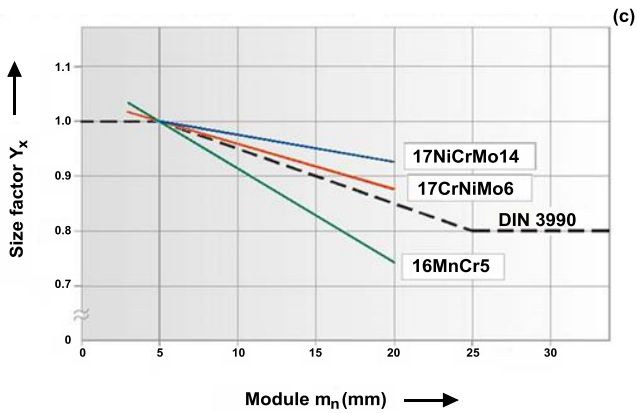


Figure 8. Influence of gear size on tooth root bending strength for gear materials with different hardenabilities; (a) examples of investigated test gears, (b) experimentally determined tooth root endurance limit for material 16MnCr5 depending on gear size, (c) experimentally determined size factor for tooth root bending strength for different gear materials [32] (m_n - gear module; Y_x - size factor for tooth root bending strength; $\sigma_{F0.50\%}$ - nominal tooth root bending stress at endurance life for 50% failure probability). Size factor is defined in DIN 3990-5 and ISO6336-5.

Steel grade 18CrNiMo7-6 (1.6587) has been selected as a performance reference material for the following investigations, since this grade currently is being widely used for demanding gear applications in Europe. The task was to modify the main alloying elements in such a way as to achieve either the same performance at lower alloy cost or better performance at similar alloy cost. The following approach is considered to be relevant in this respect:

- Improving hardenability;
- Increasing core tensile strength and toughness;
- Increasing fatigue strength in both case and core;
- Reducing quench distortion and thus detrimental tensile residual stresses;
- Improving microstructural stability to withstand elevated temperatures during manufacturing and service.

A fundamental way to deal with these issues is to adjust the chemical composition of the carburizing steel. Accordingly, the chemical composition of carburizing steels can be further developed to achieve the above goals using the following guidelines:

- Minimize intergranular oxidation → reduce Si, Mn, and Cr;
- Prevent MnS inclusions → reduce S, limit Mn;
- Prevent TiN inclusions → control Ti / N wt.% ratio close to 3.4;
- Improve hardenability → increase Mo;
- Minimize segregation → increase Mo and limit Mn levels

- Improve toughness → increase Ni and Mo;
- Refine and homogenize grain size → balance Nb, Ti, Al and N microalloying additions;
- Strengthen grain boundaries → reduce P and S, add Mo and Nb;
- Nano-precipitation to improve resistance to hydrogen embrittlement → add Nb.

Some developments of improved gear steels have focused on high nickel additions and reduced molybdenum content, Figure 9. Although this approach provides an elevated core strength and generally high toughness, the hardness in the near surface zone can be too low as nickel is a very efficient austenite stabilizer. On the other hand, raising the carbon and molybdenum contents, optionally in combination with microalloying elements, shifts the hardenability curve entirely upwards, thus providing a safety margin against local overloading. This second approach may lead to lower toughness, especially when the nickel content is reduced. However, refining and homogenizing the martensitic microstructure (packet size) can regain toughness. It was shown for 18CrNiMo7-6 that below an average martensite packet size of 20 μm the impact toughness strongly increases [10]. Since the packet size strongly correlates with the prior austenite grain size [10,11], control and refinement of the latter across the entire processing chain is an appropriate means of improving toughness.

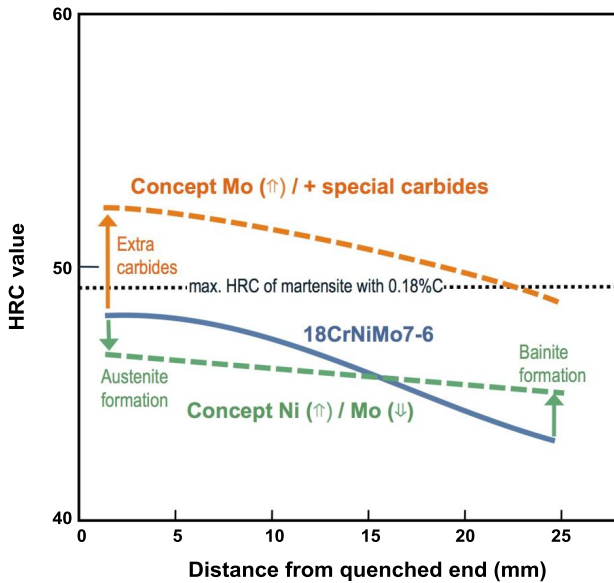


Figure 9. Effect of modified alloy concepts on the hardenability compared to the 18CrNiMo7-6 reference material.

Controlling Grain Size in Carburizing Steels

Many studies have indicated that prior austenite grain size control in carburizing steels can be effectively achieved by using niobium microalloying in combination with other microalloys, such as titanium, aluminum and nitrogen [12-19]. The alloying concepts developed have generally been aimed at refinement and homogenization of the grain size under standard case carburizing conditions. Furthermore, it has been demonstrated that high temperature carburizing becomes possible without violating grain size restrictions, thus allowing a faster furnace throughput. This is particularly beneficial when a larger case depth is required as in gears for trucks and heavy machinery. Additionally, a production concept for fine-grained carburizing steel has been developed based on an aluminum-free melt. This is to fully eliminate brittle alumina type inclusions which deteriorate toughness and fatigue resistance in the steel.

The restriction of grain coarsening is based on a pinning effect of precipitates on the austenite grain boundary. For efficient grain boundary pinning a suitable size and distribution of precipitates are necessary, which again depends on the prior thermochemical treatment, as well as the carburizing temperature. Above a critical carburizing temperature, the precipitates coarsen or dissolve and the pinning effect is lost. It appears to be most efficient to keep as much as possible of the microalloy content in solid solution prior to thermochemical processing, which can then precipitate as fine and homogeneously distributed particles during heating to the carburizing temperature. Niobium has the beneficial characteristic of low solubility in such steels, similar to titanium, providing temperature-stable precipitates. However, niobium has a lower affinity for nitrogen and contrary to titanium does not form coarse nitrides. Also, its precipitation kinetics are slower so that niobium remains in solution longer forming finer and more dispersed precipitates. It was also found that mixed precipitates of niobium, titanium and nitrogen are more resistant to dissolution at very high austenitizing temperatures. Therefore, a microalloy combination of low titanium (sub-stoichiometric to nitrogen) and niobium in the range of 0.03 to 0.1% has been proven to be most efficient.

Adding niobium in combination with titanium to the reference grade, 18CrNiMo7-6, has a marked effect on the grain size distribution as shown in Figure 10. Not only is the grain size generally much finer, but also the scatter band is narrower. The microalloyed variant safely avoids prohibited grain sizes despite the high carburizing temperature (1030 °C) and the long duration (25 hours). Similar good results of grain size stability have been obtained with modified variants of 25MoCr4 and 20CrMo5 grades, Figure 11. The niobium and titanium dual microalloyed 25MoCr4 variant reveals resistance to coarsening up to 1050 °C carburizing temperature, whereas the Nb-only microalloyed 20CrMo5 variant is stable up to 1000 °C. The data indicate that for very high carburizing temperatures, addition of multiple microalloys appears to increase the temperature stability of pinning precipitates. However, under standard carburizing conditions below 1000 °C, the Nb-only microalloyed concept exhibits a very fine austenite grain size with a moderate grain size scatter band.

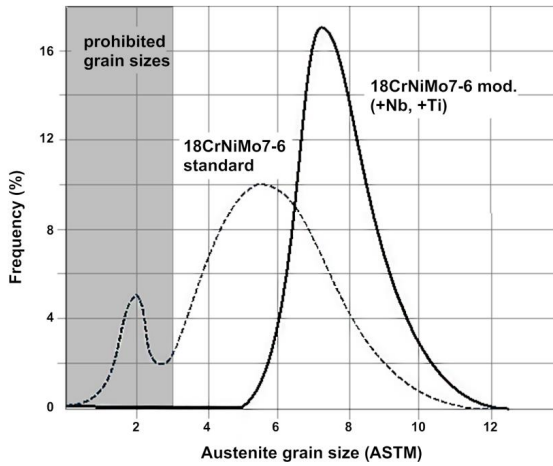


Figure 10. Grain size distribution of a Nb+Ti microalloyed 18CrNiMo7-6 (1.6587) heat compared to a conventional analysis (carburizing conditions: 1030 °C/25 h).

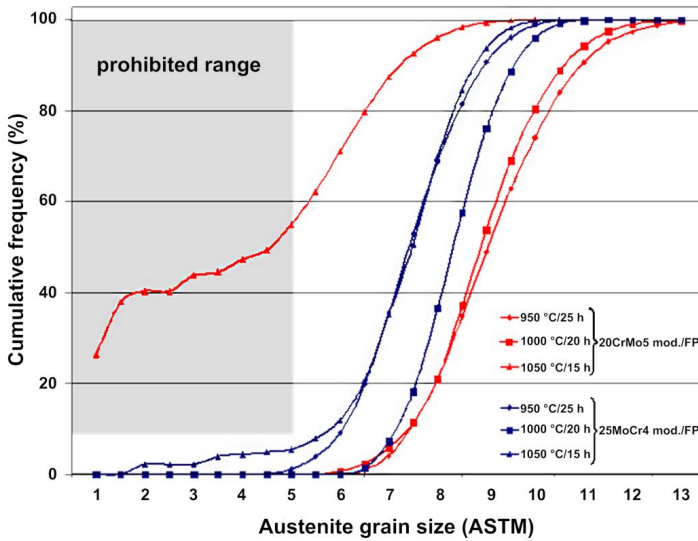


Figure 11. Grain size stability under various carburizing conditions for Nb-microalloyed 20CrMo5 (1.7264) and Nb+Ti microalloyed 25CrMo4 (1.7325).

The martensite–start temperature depends on the austenite grain size [20]. The smaller the austenite grain size, the lower is the martensite start temperature. In a mixed grain size structure transformation can occur locally at different temperatures. This situation will lead to the generation of residual stresses due to the volume change when the microstructure transforms from austenite to martensite. The earlier formed martensite islands cannot plastically accommodate the transformation volume change of the later formed martensite islands. Hence, the imbalance of elastic stresses causes a macroscopic distortion of the quenched component. It has been experimentally confirmed that a larger grain size scatter results in increased distortion, Figure 12 [21]. The distortion has to be corrected by straightening or hard machining. This is not only costly, but also reduces the thickness of the case carburized layer when performing hard machining. Furthermore, residual stresses are additive to the applied load stresses. Tensile residual stresses can cause premature failure, for instance under fatigue conditions.

Consequently, microalloying of case carburizing steel, leading to reduced grain size scatter as demonstrated above, is expected to reduce quench distortions. This could indeed be verified for components manufactured from the modified variant of 25MoCr4 (320 ppm Nb, 90 ppm Ti, 160 ppm N) shown in Figure 11. The material was continuously cast into bar. The bar was FP (ferrite/pearlite) annealed before cold extrusion and then again FP annealed. Carburization occurred at 980 °C for 195 minutes to a target case depth of 0.95 mm with a total furnace residence time of 400 minutes. The components were then quenched in an oil bath (Isorapid 277) and held at 60 °C. Subsequently, part distortion was characterized by roundness deviation measurements at five positions as shown in Figure 13. It is obvious that the microalloyed variant has much lower roundness deviation, as compared to the standard alloy. At each measuring position the deviation was reduced by approximately 50%, resulting in a similar reduction of rectification. The cost savings achieved by such reduced rectification by straightening or hard machining are likely to compensate for the cost of the microalloys. If the available equipment allows high temperature carburizing, significant process time savings can be realized. For instance, for producing a target case depth of 1.5 mm the total treatment cycle time can be reduced by 25 and 40 percent when the carburizing temperature is raised to 980 °C and 1030 °C, respectively, as compared to a standard carburizing temperature of 930 °C.

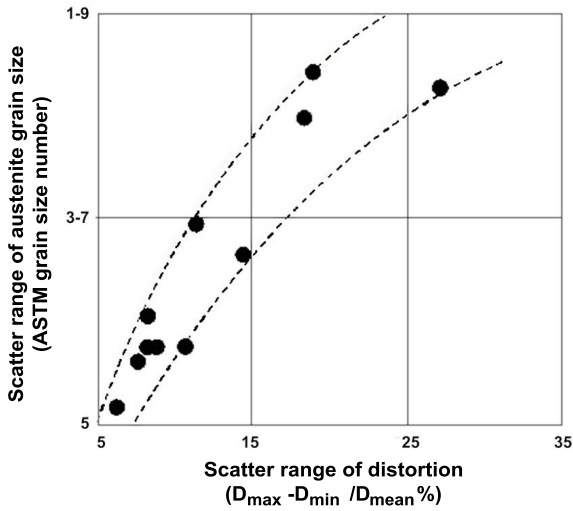


Figure 12. Dependency of distortion scattering after heat treatment on the mean prior austenite grain size scattering in the steel 16MnCr5 (1.7131) [21].

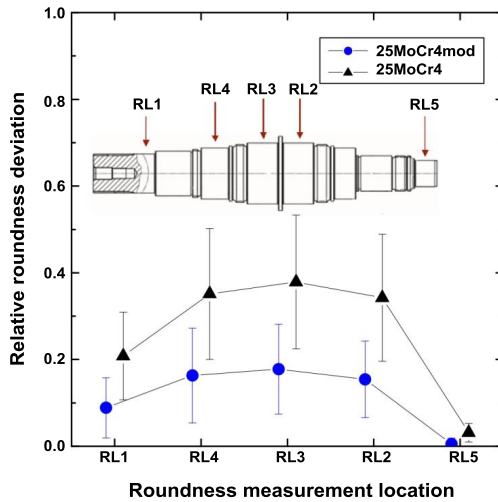


Figure 13. Roundness deviation of a heat-treated transmission shaft measured at five positions for standard 25MoCr4 (1.7325) and 25MoCr4 modified by Nb+Ti microalloying.

Increasing Hardenability and Tempering Resistance

As outlined above, it is of great interest to avoid a steep hardness gradient in the transition area from the case layer to the core material. Therefore, the hardenability of the alloy must be improved. Several alloying elements, besides carbon, contribute to hardenability, including molybdenum, manganese, chromium and nickel, as well as boron. For cost reduction reasons, alloys using higher manganese and chromium additions, eventually combined with boron microalloying have been favored for many gear applications. However, such reduced cost alloy concepts, although providing good hardenability, have limitations in terms of toughness and tempering resistance. Additionally, the limitation of intergranular oxidation requires manganese, chromium and silicon levels to be reduced. In some extreme cases, alloy producers have developed highly alloyed steels for those applications where transmission failure causes high replacement and outage costs. An example is 15NiMoCr10-4 (C:0.15%, Si:1.1%, Cr:1%, Mo:2% and Ni:2.5%), which is used in high end applications eg. in aerospace or Formula-1 gears. However, such steel requires special melting technology and is not widely available. Comparing this steel to another high-nickel steel (14NiCrMo13-4), the increase of the molybdenum content from 0.25% to 2.0% brings about a significant improvement of hardenability, surface hardness and tempering resistance [22], Figure 14. The high tempering resistance of the material brings two important advantages. Firstly, it allows duplex treatments, ie. the case hardened surface undergoes a second treatment such as Physical Vapour Deposition (PVD) coating or plasma nitriding (PN) to further increase the surface hardness. These treatments are usually performed in a temperature window of 300 to 500 °C. It is thus a prerequisite that the hardness obtained in the underlying material after quenching from the carburizing temperature is not degraded by the subsequent heating cycle. Secondly, many conventional case carburizing steel grades are restricted to a maximum operating temperature of 120 to 160 °C. A steel grade with high tempering resistance can be operated at higher temperatures without degrading. Elevated operating temperatures may occur for instance by frictional heating if the transmission gear box experiences lubrication problems.

Good tempering resistance in a typical gear steel base alloy can also be achieved with lower molybdenum additions as indicated in Figure 15. Even at levels of 0.5-0.7% a molybdenum addition provides good resistance against softening for tempering parameters (HP – Holloman parameter) up to around 16×10^3 . Resistance to softening at tempering parameters below 16×10^3 means that a secondary treatment at a temperature of 450 °C for up to 10 hours should be possible. This condition is typical for plasma nitriding.

Microalloying with niobium further enhances the tempering resistance, in a synergistic effect with molybdenum. Molybdenum and niobium have, to some extent, similar metallurgical effects. Both exert strong solute drag on grain boundaries as well as at dislocations [23] and also lower the activity of carbon [24]. These fundamental effects are evidenced by delayed recovery and/or recrystallization, as well as a reduced rate of pearlite growth, thus increasing hardenability. The solubilities of both elements in austenite are, however, very different. Molybdenum has a high solubility [25], whereas that of niobium is low [26]. Therefore, niobium precipitates as NbC particles at relatively high temperatures. Manganese, chromium and particularly molybdenum increase the solubility of niobium in austenite [27]. Accordingly, more niobium will be in

solution after quenching from the austenitizing temperature and thus available for fine precipitation during the tempering treatment, which acts to resist softening.

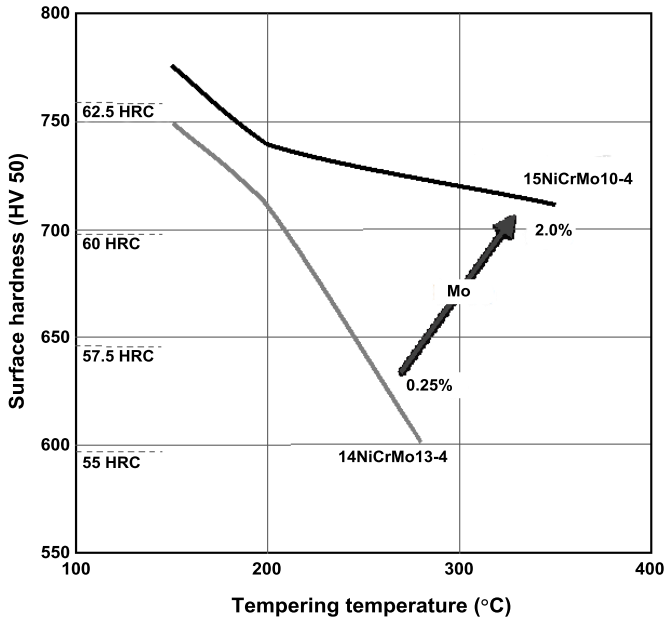


Figure 14. Surface hardness of the carburized layer in relation to tempering temperature and effect of increased molybdenum content.

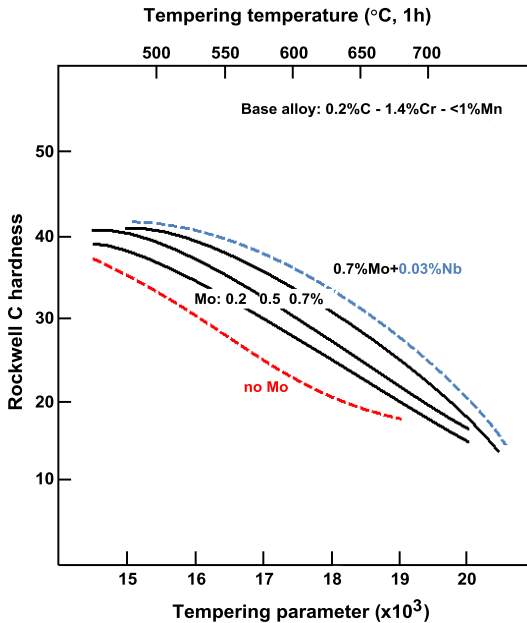


Figure 15. Effect of tempering resistance as a function of the molybdenum content and synergistic effect with niobium ($HP = T \times (20 + \log t) \times 10^{-3}$ [T in K, t in h]).

Modification and Testing of Carburizing Steels

Based on the individual and synergistic effects of alloying elements described above, the intended processing route and the desired property profile, two modified alloy concepts have been designed, Table II, for a full scale production trial including gear running tests. One of the alloy designs (concept V1) can be considered as a modified 20MnCr5 grade. It is aimed at producing a higher performance than that of 18CrNiMo7-6 at similar alloy cost. The content of carbon is increased for higher maximum hardness, while molybdenum and nickel are added for increased hardenability and tempering resistance. The other alloy design (concept V2) developed can be seen as a modified 20CrMo5 grade with added nickel, which has a lower total alloy cost than 18CrNiMo7-6, yet aiming for similar performance. In both concepts niobium microalloying is used for austenite grain size control. The mechanical properties of both novel case carburizing steels, obtained after heat treatment, indeed realize the desired property levels, Table III. The hardenability of concept V1 is superior to that of 18CrNiMo17-6, whereas that of concept V2 is within the hardenability range of the reference steel. After an austenitizing treatment at 880 °C for 2 hours followed by quenching in oil and holding at 180 °C for 2 hours concept V1 clearly shows better tensile and fatigue strength, while concept V2 nearly exactly matches the strength

of the reference grade. The toughness of both developed steels is lower than that of 18CrNiMo7-6 due to the reduced nickel content, yet remains at an acceptable level.

Table II. Chemical Composition of Developed Case Carburizing Steels

| Steel Grade | C | Si | Mn | Cr | Mo | Ni | Nb |
|-------------|------|------|------|------|------|------|------|
| Concept V1 | 0.26 | 0.12 | 1.46 | 1.23 | 0.54 | 0.91 | 0.03 |
| Concept V2 | 0.21 | 0.25 | 1.17 | 1.15 | 0.21 | 0.22 | 0.04 |

Table III. Mechanical Properties of Developed Case Carburizing Steels
(Hardened at 880 °C/2 h + Oil Quench/180 °C/2 h)

| Property | Concept V1 | Concept V2 | 18CrNiMo7-6 |
|--|------------|------------|-------------|
| Tensile strength, R_m (MPa) | 1758 | 1182 | 1182 |
| Impact energy, A_v (J) at RT | 47 | 55 | 80 |
| Rotating fatigue limit $\sigma_{(50\% @N=10^7)}$ (MPa) | 722 | 491 | 510 |
| Hardenability at 11 mm (HRC) | 51 | 44 | 41 |
| Hardenability at 25 mm (HRC) | 50 | 36 | 36 |

The heat treatment behavior of the developed alloys has been tested using a carburizing process at 1030 °C to a nominal case depth range of 0.95 to 1.2 mm. This depth requirement originated from the gear running tests to be executed with 5 mm module gears actually requiring 0.75 to 1.0 mm case depth. The additional case depth was intended to compensate for grinding losses during hard machining of the carburized gear. For determining the depth of the case layer, a limit hardness of 550 HV was defined according to ISO 6336-5. The target surface hardness was set at 670 HV as minimum. Additionally, secondary plasma nitriding treatments have been performed at 400 and 440 °C, respectively. Table IV summarizes the hardness data for the various pilot heat treatments. In the as-quenched condition, after carburizing, both grades fulfill the requirements. Both alloy concepts sustain a tempering treatment at 200 °C. Concept V2, however, does not retain sufficient hardness after the plasma nitriding treatment. On the contrary, concept V1, due to its increased tempering resistance, shows a very high surface hardness of around 1000 HV after plasma nitriding, whereas the core hardness is reduced. Nevertheless, a core hardness of more than 400 HV is still a high value. It thus appears that concept V1, with some further optimization, has the potential of fulfilling the case depth requirements at secondary treatment temperatures up to 440 °C. A slight increase of the molybdenum content towards 0.7%, Figure 9, and fine-tuning of the microalloy addition are thought to be the most promising way of achieving this.

Table IV. Hardness Characteristics after Various Heat Treatments

| Treatment after carburizing at 1030 °C | Concept V1 (20MnCr5 mod.) | | | Concept V2 (20CrMo5 mod.) | | |
|---|---------------------------|--------------|---------------------------|---------------------------|--------------|---------------------------|
| | Surface (HV 1) | Core (HV 10) | CHD _{50HV1} (mm) | Surface (HV 1) | Core (HV 10) | CHD _{50HV1} (mm) |
| As-quenched | 769 | 544 | 2.04 | 786 | 408 | 1.28 |
| Freezing -70 °C/2 h Tempering 200 °C/2 h | 717 | 505 | 1.53 | - | - | - |
| Tempering 200 °C/2 h | - | - | - | 672 | 430 | 1.20 |
| Plasma nitriding at 400 °C | 994 | 432 | 0.8 | 707 | 416 | 0.25 |
| Plasma nitriding at 440 °C | 1009 | 422 | 0.35 | 570 | 395 | 0.1 |

Operational performance of the developed steel grades (V1 and V2) was tested and benchmarked at FZG, TU München, Germany. The tooth root load carrying capacity was investigated in a pulsator rig, Figure 16. Investigations on the flank load carrying capacity were performed by running tests on a back-to-back gear test rig, Figure 17, according to DIN ISO 14635-1 [28]. The test gears for these investigations were case hardened after gear milling. Subsequent to case carburizing, the test gears were mechanically cleaned by shot blasting. The flanks, as well as the tooth roots of the test gears for the investigations on the tooth root bending strength, were not ground. The gear flanks of the test gears for the gear running tests were finally ground to a gear quality of $Q \leq 5$ (DIN 3962) and a surface roughness $R_a \leq 0.3 \mu\text{m}$. In order to reduce the effects of premature contact resulting from tip mesh interference due to elastic tooth deflections under load, profile modifications in the form of a tip relief were applied to the gears for the running tests.

For the experimental investigations on the tooth root bending strength, standard pulsator test gears with a gear module $m_n = 5 \text{ mm}$, number of teeth $z = 24$ and face width $b = 30 \text{ mm}$ were used. For the running tests, spur gears with a module $m_n = 5 \text{ mm}$, a gear ratio of 17/18 and a face width $b = 14 \text{ mm}$ were used. Both test gear types are typical of those used for the examination respectively of bending strength and pitting load capacity of case carburized gears and are in accordance with the requirements of ISO 6336 [6] for reference test gears.

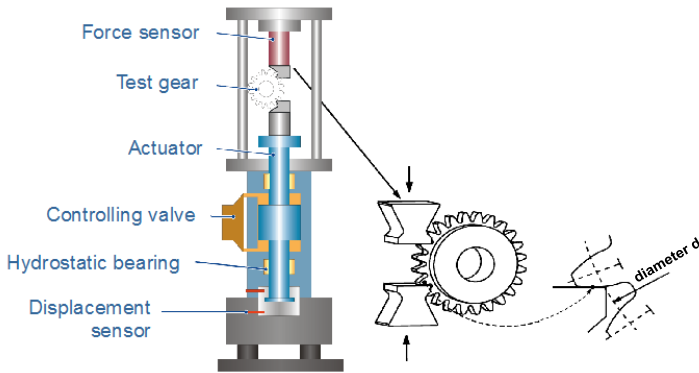


Figure 16. Schematic illustration of a pulsator test rig for investigation of the tooth root load carrying capacity.

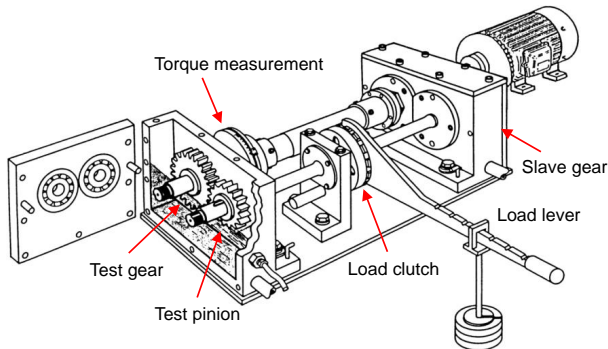


Figure 17. FZG standard back-to-back gear test rig for investigation of the flank load carrying capacity.

The tooth root load carrying capacity is one of the determining factors in gear design. Besides the strength of the material itself, the existing state of stress (load induced stresses and residual stresses) significantly influences the tooth root load carrying capacity. The mechanical cleaning procedure by shot blasting, as used in this test program, introduces compressive stresses in the sub-surface zone and is beneficial for fatigue resistance, see also Figure 18 [33]. The current tests were carried out under constant pulsating load and continued until the limiting number of load cycles (6×10^6) was reached or tooth root breakage occurred. For each alloy concept, a complete S-N curve was determined based on approximately 25 test points. The endurance strength level was determined using the “staircase method” based on at least 10 data points for each alloy concept. The pulsating load at the endurance limit was estimated for a failure

probability of 50 percent. The high-cycle fatigue part of the S-N curve was determined from approximately ten valid tests for each variant. The conversion of the pulsating load into the resulting tooth root stress was carried out according to DIN 3990 part 3 [5]. The allowable stress numbers for bending, σ_{Flim} and σ_{FE} , given in DIN 3990/ISO 6336 [5,6] are valid for standard reference test gears at standard test conditions in a gear running test and a failure probability of 1 percent. Therefore, the test results from the pulsator tests were converted to these conditions according to the state-of-the-art approaches.

The results obtained from these tests are shown in Table V. Case carburized alloy V1 (20MnCr5 mod.) clearly exhibits a higher tooth root bending strength than the case carburized alloy V2 (20CrMo5 mod.) as can be expected from the hardness characteristics. It has been established that surface hardened gears of high load capacity containing high residual compressive stresses in the surface layer due to shot peening, exhibit an increased risk of crack initiation below the surface [7]. In this respect, the cleanliness of the material has a decisive influence. Furthermore, it is assumed that the microstructure and especially the ductility of the surface layer are also relevant in determining the cracking behavior. Alloy V1 did not show sub-surface crack initiation.

Table V. Characteristics of the Determined S-N-curves Concerning Tooth Root Bending Strength for 50% Failure Probability as well as Nominal and Allowable Bending Stress Numbers

| Criterion | Concept V1 | Concept V2 |
|---|--|---|
| Nominal endurance tooth root bending stress for 50% failure probability (MPa) | 1368 | 1072 |
| Gradient of S-N curve at short fatigue life (50% failure probability) | 28.1 | 8.8 |
| Number of load cycles at inflection point (50% failure probability) | 2,048,078 | 436,884 |
| Nominal tooth root bending stress σ_{FE} (MPa) | 1134 | 885 |
| Nominal bending stress σ_{Flim} (MPa) | 567 | 442 |
| Cracking behavior in low-cycle fatigue range | Fractures with crack initiation at the surface | Fractures with crack initiation at the surface |
| Cracking behavior in high-cycle fatigue range | Fractures with crack initiation at the surface | Fractures with crack initiation below the surface |

In Figure 18 the determined nominal bending stress numbers are compared to the nominal tooth root bending stress levels according to DIN 3990/ISO 6336 [5,6] and to the test results from several batches of two case hardened Western European standard steels determined under comparable test conditions [33]. A further performance benchmark of both developed alloys against established case carburizing alloys is shown in Figure 19. In this graphic, the grey shaded area indicates the typical performance range of European state-of-the-art carburizing grades, see also Figure 18. Additionally, some international carburizing grades that were tested by the same method are indicated. Figure 18 and Figure 19 prove that alloy V1 ranks on top (quality level ME) of the property field of established alloys according to DIN 3990 [5] and performs better than many more highly alloyed steel grades, including the reference grade 18CrNiMo7-6. Alloy V2 compares well with the state-of-the-art alloys achieving quality level MQ.

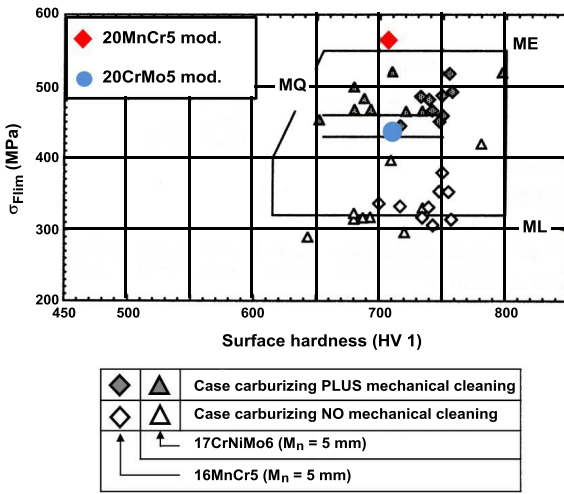


Figure 18. Comparison of the tooth root bending stress numbers of newly developed case carburized steels vs. strength levels of DIN 3990 and vs. results of reference steels determined under comparable test conditions [33].

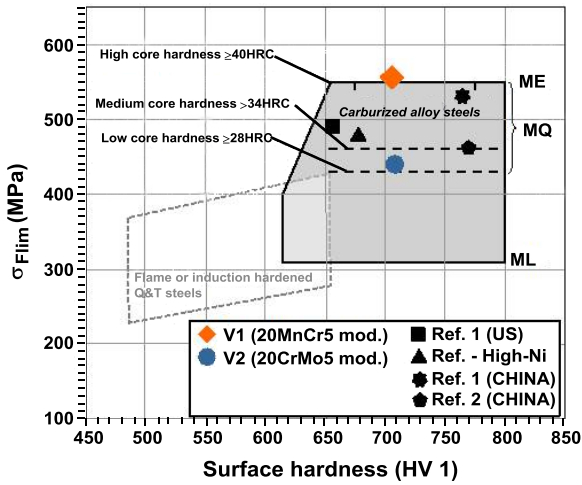


Figure 19. Comparison of the tooth root bending stress numbers of newly developed case carburized steels vs. some international case carburizing steels (see also Table I). (Note: Refs. 1 and 2 do not correspond to references in the current paper.)

In order to determine the pitting load capacity of the gear flank, repeated gear running tests in the high cycle, as well as the low cycle fatigue range were carried out [34]. The test rig was driven at a constant speed of 3000 rpm. All test runs were performed using oil spray lubrication (approx. 2 l/min into the tooth mesh) with FVA 3 + 4% Anglamol 99 (S-P-additive), a mineral oil of viscosity class ISO VG 100, and an oil temperature of 60 °C. Prior to each test run, a two-stage running-in period was performed. Under the described test conditions, six to eight test runs for each variant were scheduled at different load levels in order to determine the pitting load carrying capacity. The test runs were continued until either one of the failure criteria mentioned below was reached or the specified maximum number of load cycles was exceeded without failure. The test runs were regularly interrupted after a defined interval of load cycles in order to inspect the flank condition. According to the defined failure criteria, a test run was terminated when:

- Tooth breakage occurred;
- The flank area damaged by pitting exceeded about 4% of the working flank area of a single tooth or about 2% of the total working flank area;
- The mean profile deviation due to micropitting exceeded the limiting value of 15-20 μm ;
- A minimum number of 50×10^6 load cycles was reached without damage.

After every test run, the flank condition was evaluated and documented by means of digital photographs, Figure 20. During all test runs of alloy V2, micropitting was observed on the flanks of the test pinion and test gear. However, the limiting criterion of a profile deviation $f_m > 20 \mu\text{m}$ due to micropitting was not reached in any of the test runs. Normally, light micropitting leads to pitting failure at higher numbers of load cycles. Test gears made from alloy V1 indicated a significantly lower sensitivity to micropitting than the test gears made from alloy V2.

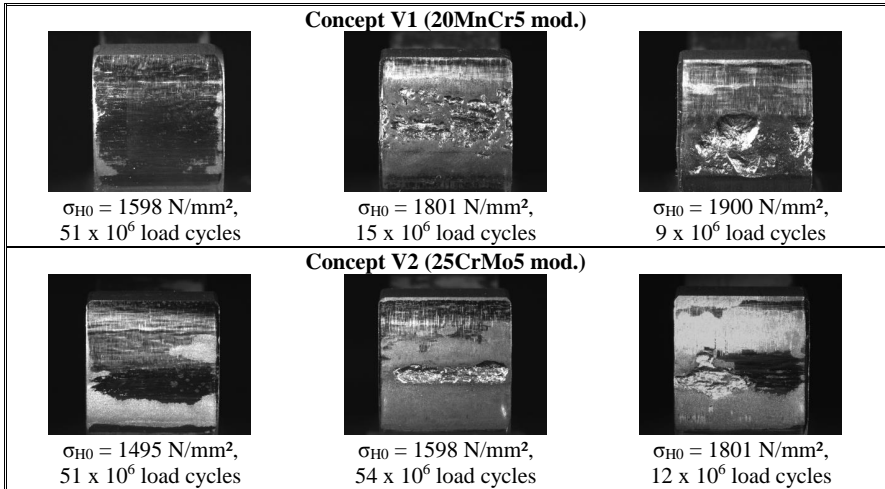


Figure 20. Examples of typical tooth flank condition at the end of the test runs for various nominal contact stresses σ_{H0} and load cycles

The gear running tests allow an approximate determination of the pinion torque at the endurance limit, as well as of the nominal contact stress number at the endurance limit for a failure probability of 50 percent. The allowable contact stress (σ_{Hlim}) representing the pitting load capacity with a failure probability of 1 percent is then calculated according to DIN 3990 [5]. Table VI summarizes the flank pitting load capacity limits determined for the two developed steel grades. A benchmark comparison of these data against the strength values for the different quality levels according to DIN 3990/ISO 6336, as well as for some reference data from literature [29] is shown in Figure 21. A further performance benchmark of both developed alloys against established case carburizing alloys is shown in Figure 22. Obviously, alloy V1 (20MnCr5 mod.) exhibits a very high pitting endurance limit and outperforms established alloys of quality level ME. The pitting endurance limit of alloy V2 (20CrMo5 mod.) is situated in the upper region of the established contact stress field for case hardened steels reaching quality level ME.

Table VI. Experimentally Determined Endurance Limit for Pitting

| Criterion | Concept V1 | Concept V2 |
|--|-------------------|-------------------|
| Nominal endurance strength for 50% failure probability (MPa) | 1699 | 1547 |
| Allowable contact stress (MPa) | 1793 | 1633 |

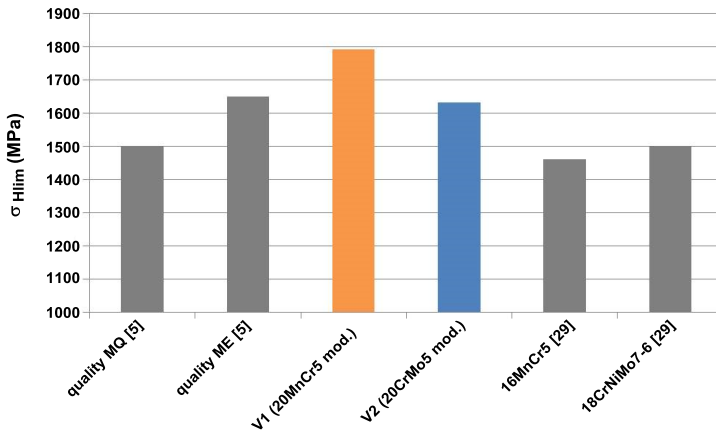


Figure 21. Comparison of determined pitting strength number of new case carburized steels vs. strength levels of DIN 3990 and literature data for reference steels.

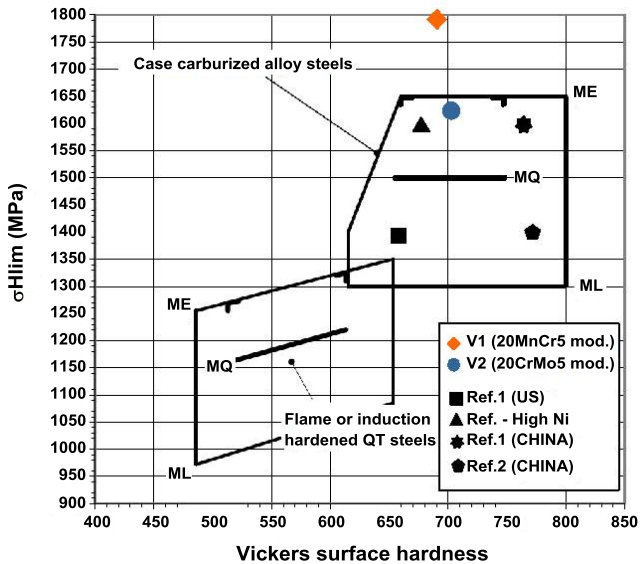


Figure 22. Comparison of pitting endurance strength number of new case carburized steels vs. strength levels of DIN 3990 and vs. some international case carburizing steels (see also Table I). (Note: Refs. 1 and 2 do not correspond to references in the current paper.)

The current results suggest that alloy V1 has the potential of providing an economically viable solution for highly loaded gears in heavy machinery and vehicles. Its use in vehicle transmission could enable downsizing of components, thus reducing weight. In larger transmissions, such as used in trucks and heavy machinery, its use could help avoid unexpected failure and promote extended warranty periods. The results from alloy V2 position it as a cost attractive alternative to the established premium grade 18CrNiMo7-6.

Conclusions

Recent and future application-driven demands challenge the performance of industrial and automotive gearboxes. Many parameters, such as material, heat treatment, gear design, machining and lubrication have to be considered for optimizing gearbox performance. In this paper the focus was on optimizing the alloy composition of case carburizing steels, particularly by the use of molybdenum and niobium as alloying elements.

Molybdenum alloying in case carburizing steels is established due to its strong hardenability effect. Yet, for alloy cost reasons, many attempts have been made in recent years to replace molybdenum fully or partially by other elements which increase hardenability.

The current results demonstrate, however, that molybdenum has several additional metallurgical benefits that are not provided by other hardenability enhancing elements.

Molybdenum significantly increases the tempering resistance, thus opening an opportunity for performing secondary heat treatments after case carburizing. The increased tempering resistance also makes gears less vulnerable to hot running in case of lubrication problems during operation.

It is also known that molybdenum enhances high angle grain boundary cohesion, thus obstructing intergranular crack propagation and hence retarding macroscopic damage.

Contrary to manganese, molybdenum does not have a strong tendency to segregate and it does not form inclusions. Furthermore, its use does not increase the sensitivity to intergranular oxidation, as is the case for manganese and chromium.

The present investigation has demonstrated that modifying standard alloys with a moderate addition of molybdenum (0.5-0.7 wt.%) can lead to significantly better performance in gear running tests compared with state-of-the-art alloys, including several high nickel steels.

Microalloying, and in particular the addition of niobium to case carburizing steels, has been gaining increasing interest over the years. The benefit is an improved control of grain size scatter at simultaneously reduced prior austenite grain size throughout the heat treatment processes. A finer and more homogeneous grain structure results in improved toughness, higher fatigue resistance and less distortion after heat treatment. Additionally, niobium further increases the tempering resistance provided by molybdenum, due to a synergistic metallurgical effect.

Recently, it has also become evident that grain refinement (prior austenite grain size) of martensitic steels by niobium microalloying, as well as its precipitation as nano-carbides, results in an increased resistance to hydrogen embrittlement.

These effects of microalloying with niobium gain increased importance, especially for highly loaded, large-size gears that require a greater case hardening depth and thus increased carburization times.

Based on the fundamental understanding of metallurgical effects of alloying elements in general, and molybdenum and niobium in particular, it is possible to modify existing case carburizing steels to give increased performance levels at acceptable alloy costs. It also becomes possible by applying innovative heat treatment processes to either increase production efficiency or performance.

References

1. F. Hippenstiel, K.-P. Johann and R. Caspari, "Tailor Made Carburizing Steels for Use in Power Generation Plants" (Paper presented at the European Conference on Heat Treatment 2009, Strasbourg, France).
2. H. Spitzer, W. Bleck and R. Flesch, Einsatzstähle – Normung und Entwicklungstendenzen, ATTT/AWT-Tagung Einsatzhärtung, 29/30 April 1998, Aachen, Tagungsband, 11-20.
3. DIN EN 10084:2008 Case Hardening Steels – Technical Delivery Conditions.
4. ISO 683-11, Edition 1987: Heat-treatable Steels, Alloy Steels and Free-cutting Steels, Part 11: Wrought Case-hardening Steels.
5. DIN 3990 1-5: Edition 1987:12, Calculation of Load Capacity of Cylindrical Gears; Endurance Limits and Material Qualities.
6. ISO 6336 1-5: Edition 2006/2003, Calculation of Load Capacity of Spur and Helical Gears - Strength and Quality of Materials.
7. N. Bretl et al., "Investigations on Tooth Root Bending Strength of Case Hardened Gears in the Range of High Cycle Fatigue," *Thermal Processing for Gear Solutions*, (September 2014), 52-59.
8. M. Uno, M. Hirai and F. Nakasato, "Effect of Alloying Elements on the Properties of Cr-free Carburizing Steels," *The Sumitomo Search*, 39 (September 1989), 33.
9. A. Stenico, "Werkstoffmechanische Untersuchungen zur Zahnfußtragfähigkeit einsatzgehärteter Zahnräder" (Ph.D. thesis, TU München, Germany, September 2007).

10. Chunfang Wang et al., "Effect of Microstructure Refinement on the Strength and Toughness of Low Alloy Martensitic Steel," *Journal of Materials Science and Technology*, 23 (5) (2007), 659.
11. S. Morito et al., "Effect of Austenite Grain Size on the Morphology and Crystallography of Lath Martensite in Low Carbon Steels," *The Iron and Steel Institute of Japan International*, 45 (1) (2005), 91.
12. B. Huchtemann and V. Schüler, Thyssen Technische Berichte, Heft 1/93 (1993), 97.
13. M. Kubota and T. Ochi, "Development of Anti-coarsening Steel for Carburizing," *Materials Science Forum*, 539-543 (2007), 4855.
14. M.J. Leap and E.L. Brown, "Effects of Composition and Processing on Development of Grain Coarsening Resistance in Cold Forged and Carburised Steel," *Materials Science and Technology*, 18 (9) (2002), 945.
15. T. Kimura and Y. Kurebayashi, "Niobium in Microalloyed Engineering Steels, Wire Rods and Case Carburized Products," *Proceedings of the International Symposium Niobium 2001*, Orlando, Florida, USA, (December 2 - 5, 2001) TMS, 801.
16. F. Hippenstiel, "Tailored Solutions in Microalloyed Engineering Steels for the Power Transmission Industry," *Materials Science Forum*, 539-543 (2007), 4131.
17. K.A. Alogab et al., "The Influence of Niobium Microalloying on Austenite Grain Coarsening Behavior of Ti-modified SAE 8620 Steel," *The Iron and Steel Institute of Japan International*, 47 (2) (2007), 307.
18. K.A. Alogab et al., "The Effects of Heating Rate on Austenite Grain Growth in a Ti-modified SAE 8620 Steel with Controlled Niobium Additions," *The Iron and Steel Institute of Japan International*, 47 (7) (2007), 1034.
19. K. Klenke, "Improved Performance by High Temperature Carburizing Shown by the Example of VW4521+Nb," *Proceedings of Steels in Cars and Truck 2008*, Verlag Stahleisen Düsseldorf, (2008), 173.
20. Hong-Seok Yang and H.K.D.H. Bhadeshia, "Austenite Grain Size and the Martensite-start Temperature," *Scripta Materialia*, 60 (7) (2009), 493.
21. A. Randak and R. Eberbach, HTM Härtereitechnische Mitteilungen 24 (1969) Heft 3/ Oktober, 201.
22. E. Dehner and F. Weber, "Experience with Large, High-Speed Load Gears," *Gear Technology* (www.geartechnology.com), (July 2007), 42.

23. F. Togashi and T. Nishizawa, "Effect of Alloying Elements on the Mobility of Ferrite/Austenite Interface," *Journal of the Japan Institute of Metals*, 40 (1) (1976), 12.
24. T. Tanaka and T. Enami, "Metallurgical Variables Involved in Controlled Rolling of High Tensile Steels and its Application to Hot Strip," *Tetsu-to-Hagané*, 58 (13) (1972), 1775.
25. E.J. Pavlina, J.G. Speer and C.J. Van Tyne, "Equilibrium Solubility Products of Molybdenum Carbide and Tungsten Carbide in Iron," *Scripta Materialia*, 66 (5) (2012), 243.
26. V.K. Lakshmanan and J.S. Kirkaldy, "Solubility Product for Niobium Carbide in Austenite," *Metallurgical Transactions A*, 15A (3) (March 1984), 541.
27. S. Koyama, T. Ishii and K. Narita, "Effects of Mn, Si, Cr and Ni on the Solution and Precipitation of Niobium Carbide in Iron Austenite," *Journal of the Japan Institute of Metals*, 35 (1971), 1089.
28. ISO 14635 Part 1: Gears – FZG Test Procedures – Part 1: FZG Test Method A/8, 3/90 for Relative Scuffing Load-carrying Capacity of Oils, 2000.
29. G. Niemann and H. Winter, *Maschinenelemente, Band II: Getriebe allgemein, Zahnradgetriebe - Grundlagen, Stirnradgetriebe*, (Berlin, Springer-Verlag, 1989).
30. Th. Tobie, B.-R. Höhn and K. Stahl, "Tooth Flank Breakage – Influences on Subsurface Initiated Fatigue Failures of Case Hardened Gears," *Proceedings of the ASME 2013 International Design Engineering Technical Conferences and Computers and Information in Engineering Conference*, Portland, Oregon, USA, (August 4-7, 2013), Paper No. DETC2013-12183.
31. Th. Tobie, *Zur Grübchen - und Zahnfußtragfähigkeit einsatzgehärteter Zahnräder* (Ph.D. thesis, TU München, Germany, 2001).
32. M. Steutzger, *Größeneinfluß auf die Zahnfußfestigkeit*, Forschungsvorhaben Nr. 162, Heft 529, Forschungsvereinigung Antriebstechnik e.V., Frankfurt am Main, 1997.
33. U. Weigand, *Werkstoff - und Wärmebehandlungseinflüsse auf die Zahnfußtragfähigkeit*. (Ph.D. thesis, TU München, Germany, 1999).
34. B.-R. Höhn et al., "FZG Rig-based Testing of Flank Load-carrying Capacity Internal Gears," *Gear Technology* (www.geartechnology.com), (June/July 2012), 60.

CUTTER RINGS WITH NON-UNIFORM NIOBIUM CARBIDE DISTRIBUTION FOR TUNNEL BORING

B. Feistritzer

FE&I - Forschung, Erfindungen & Innovationen, Waldschach 56c, 8505 St. Nikolai i.S., Austria

Keywords: Cutter Rings, Tunnel Boring, Niobium Carbide, Carbide Distribution, Disc Cutters, Centrifugal Casting, Carbide Separation

Abstract

Cutter rings made by centrifugal casting out of niobium alloyed steel were developed to be used in tunnel boring machines. The new material has great potential to replace conventional forged tool steel rings for cutting hard rock. Due to applying high centrifugal acceleration forces during the casting process, primary precipitated carbides with MC-structure are concentrated in the most wear affected zone of the cutter ring, thus leading to higher wear resistance of such rings. The carbide distribution across the cutter ring profile can be adjusted by production process parameters and the chemical composition of the melt.

Introduction

Tunnel boring machines (TBMs) have been used commercially to excavate the full face of tunnels simultaneously for over 100 years. To improve the performance in cutting hard rock, TBMs equipped with disc cutters were developed in the 1950s, and are still predominant for hard rock excavation [1]. These days, the working parts of disc cutters are high wear resistant cutter rings, mostly made of forged hot working tool steel, of up to 20 inches in diameter.

Replacing worn cutter rings is time consuming and so catastrophic failures of such cutters, under loads of up to 300 kN per ring, can lead to huge downtime costs [2]. Therefore, the tunnel boring industry is looking for new cutter rings, with higher wear resistance leading to lower maintenance.

To match these requirements, cutter rings were developed having a high amount of hard NbCs in the wear affected zone of the ring, and an inner, tough microstructure, with far fewer carbides, patent pending AT300/2013.

Production

The production of such cutter rings is based on the limited solubility of NbCs in an iron base melt, and in the segregation of such carbides to the outer diameter during centrifugal casting.

In order to form primary NbC particles in the melt, the quantity of niobium and carbon should exceed the solubility product of NbC in the melt. Because the solubility of NbC in an iron melt at normal melting temperatures is very small, the formation of primary carbides already starts with quite small quantities of niobium. The density of the formed particles is a little higher than the

density of the iron melt, and this leads to their outward migration under the influence of high centrifugal acceleration forces, applied during spin casting, Figure 1. The movement of the carbide particles stops if they get into a loose network with each other, resulting in a relatively homogeneous carbide rich layer at the outer surface of the casting. For best economic use of material and to reduce machining costs, the mold has been designed to enable net shape casting in the outer part of the ring.

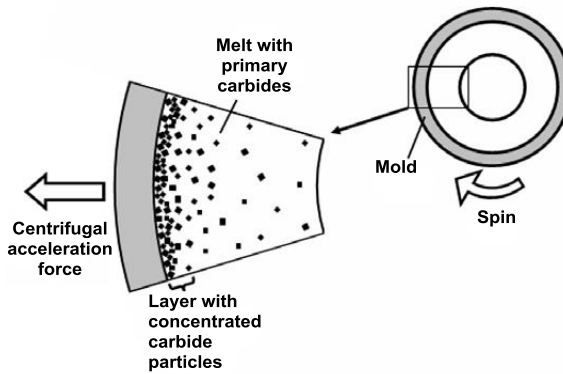


Figure 1. Formation of a layer with concentrated carbide particles during centrifugal casting.

The primary NbC can be formed in the iron base melt by adding carbon, or carbon containing alloys, to a niobium containing melt. It is also possible to add NbC directly into the melt, eg. in the form of Fe-NbC. The whole process must be controlled in such a way that the primary carbide particles, which are slightly heavier than the melt, have enough time to segregate outwards and to form the carbide rich layer, before they get stuck in the solidifying melt. Rapid cooling at the surface of the mold always leads to a layer containing less NbC next to the mold surface. The microstructure of the inner part of the ring consists of solidified residual melt with only a few primary and eutectic NbC particles. Depending on the chemical composition of the melt and on the subsequent heat treatment, other carbides can exist in this area or in the whole casting.

After casting, a heat treatment has to be applied in order to achieve the best properties of the matrix. Due to the high thermal stability of NbC, the formed particles are not affected by the treatment. Small additions of vanadium or titanium lead to mixed Nb-V-Ti carbides, resulting in different morphologies and properties of the primary carbide particles.

Microstructure and Properties

Figure 2 shows the principal design of commonly used cutter rings and their cross section. During boring, the outer cutting edge of the ring is pressed against the hard rock and breaks it into small pieces, which fall and grind onto the outer surfaces next to the edge. So the whole outer zone is the wear loaded part of the ring. A cross section of a cast cutter ring is shown in Figure 3. Due to etching of the polished sample surface, the carbide enriched zone is visible with the naked eye. It can be seen that the concentrated carbides are situated exactly in the wear affected area. A typical microstructure of the carbide rich area can be seen in Figure 4(a), while the inner zone is shown in Figure 4(b). The carbide volume fraction in the outer part lies typically between 20% and 40%, depending on the chemical composition of the melt and the production specifications. In this example, the angular carbide particles are pure NbC. The particles still have the structure that they had in the Fe-NbC, an alloy of iron and NbC, used as the NbC source to the base melt. Additions of vanadium or titanium lead to rounder carbide appearances, as shown in a deep etched sample containing Nb-V carbides, Figure 5 [3]. The carbides are connected to each other three-dimensionally, forming a robust network. Varying concentrations of niobium and vanadium in the carbides result in different brightness in the SEM picture.

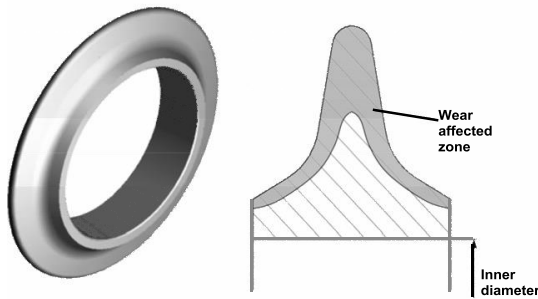


Figure 2. Design and cross section of commonly used cutter rings.



Figure 3. Cross section of cast cutter ring with carbide enriched layer.

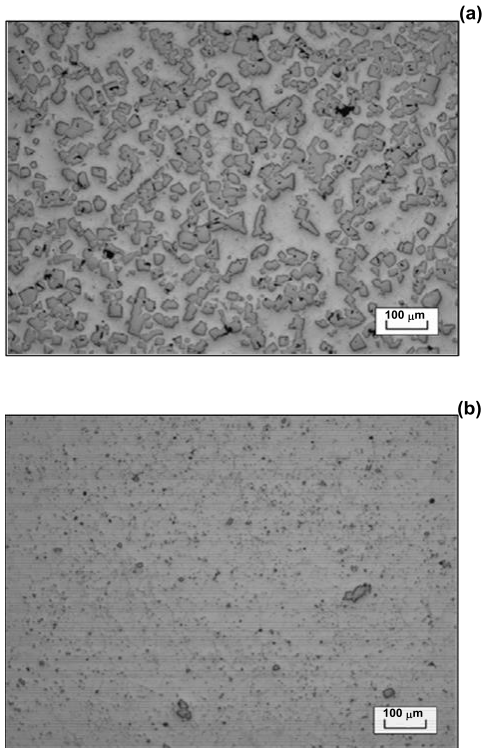


Figure 4. Microstructure; (a) in the carbide enriched layer, (b) in the inner zone.

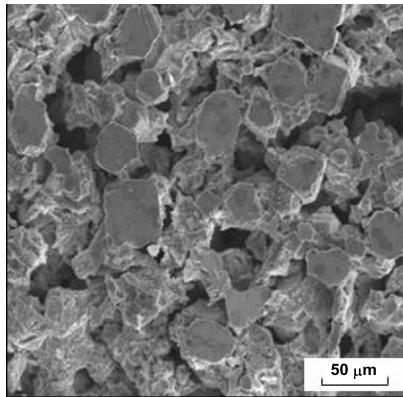


Figure 5. Deep etched sample in carbide enriched layer containing Nb-V-carbides (SEM).

The microstructure of the inner part contains only a small fraction of carbides, Figure 4(b). The carbide volume fraction in this area is typically lower than 5%. The profile of the fraction of carbides in the microstructure from the tip of the cutting edge to the inner diameter of the cutter ring is shown in Figure 6. The first 5 mm were rapidly solidified before the primary carbides were able to separate. This layer consists of the mean chemical composition of the cast melt. Next to this chilled layer, the carbide enriched layer shows a normal homogeneous structure, which is more than 20 mm thick. The thickness of the carbide enriched layer can be adjusted by the amount of niobium and carbon in the melt. Niobium contents of up to 15% in the melt are possible. To the inner side of the carbide enriched zone, a decrease of the carbide content follows to around 3% to 4% in the inner part of the ring.

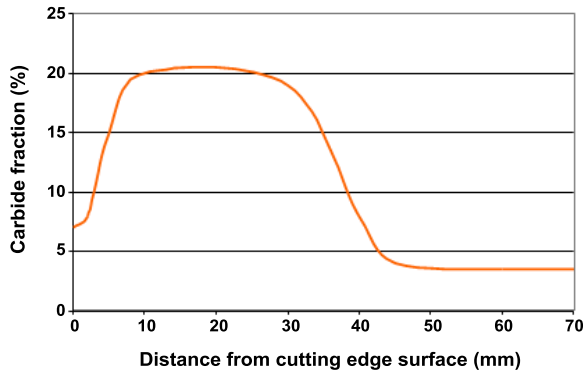


Figure 6. Fraction of carbides in the microstructure from the tip of the cutting edge to the inner diameter of the cutter ring.

Unexpectedly, the carbide enriched layer is not always homogeneous. As shown in Figure 7, it is possible that the layer includes a small ribbon containing less carbide. This behavior needs further investigations in order to be explained.



Figure 7. Carbide enriched layer with ribbon containing less carbide.

A specific heat treatment is essential to achieve the optimal properties of the whole ring. Depending on the chemical composition of the base melt, eg. hot-working tool steel, the toughness and hardness of the material can be optimized by the right heat treatment. A hardness of up to 70 HRC in the carbide enriched layer was achieved with a cold-working tool steel base material.

Machining of the carbide enriched zone with any kind of cutting material in the finally heat treated condition is nearly impossible. Only grinding is successful to shape the surface in the area of the cutting edge. Since the rings are mainly net shape cast, the outside surface does not have to be machined. Only the front faces and the inner diameter are machined in the annealed condition.

Performance

A few cutter rings have already been tested in a tunnel boring site. However, test statistics are currently insufficient to compare their performance to that of cutter rings made of forged hot working tool steel. Nevertheless, it can be said that the toughness of these cast rings can be high enough to fulfil the requirements of tunnel boring operations.

Since mechanical processing is so difficult, we expect a high performance of cutter rings, made of such material, at the working site. Several cutter rings are waiting for tests at different tunnel boring sites.

Conclusions

Cast cutter rings made out of high niobium containing material have been developed, which present a non-uniform carbide distribution that is repeatable in terms of carbide distribution, carbide content, microstructure and material properties. As these discs are produced mainly by net shape casting and present, therefore, unique properties, these cutter rings could be an economical alternative to the commonly used forged rings made out of tool steel. Performance testing is currently in progress under actual tunnel boring conditions. Also, other applications of this material are possible in mining industries or other technical fields, where high wear resistance and toughness are necessary.

Acknowledgements

Special acknowledgements and thanks to Kuhn Edelstahl GmbH, Germany, for their contributions and support.

References

1. Australian Tunneling Society, "Current & Emerging Rock Cutting Technology," www.ats.org.au, 5th February, 2015.
2. J. Roby et al., "The Current State of Disc Cutter Design and Development Directions," www.the Robbins Company.com, 5th February, 2015.
3. B. Feistritzer, "Erhöhung der Verschleißfestigkeit von Walzenwerkstoffen durch die Verwendung von Niob als Legierungselement" (Ph.D. thesis, Montanuniversität Leoben, 2000).

INFLUENCE OF NIOBIUM ON THE MICROSTRUCTURE AND PROPERTIES OF CrMo CAST STEEL FOR LINER PLATE

Xiangru Chen¹, Ming You², Aimin Guo³, Wei Zhang³, Hiacheng Li¹, Yang Xu¹ and Qijie Zhai¹

¹State Key Laboratory of Advanced Special Steel, Shanghai University, Shanghai, China

²CITIC Heavy Machinery Ltd, Luoyang, China

³CITIC Metal Co. Ltd, Capital Mansion 1903, Beijing, China

Keywords: CrMo Steel, Heat Treatment, Niobium, Impact Toughness, Ductility, Yield Strength

Abstract

In this paper the influence of heat-treatment and Nb on the microstructure and properties of a low alloy CrMo wear-resistant steel lining plate were investigated. Based on an appropriate chemical composition design, excellent combinations of hardness and impact toughness have been achieved for the lining plate application. It was found that with a double heat treatment of 920 °C (8 h) + 550 °C (20 h), adding Nb in the range 0.025 to 0.028 wt.% improved the strength and hardness of the low alloy CrMo wear-resistant steel by 13% and 16% respectively, while the impact toughness was slightly reduced. With a heat treatment of 880 °C (8 h) + 550 °C (20 h), adding 0.03 wt.%Nb increased the strength and hardness of the low alloy CrMo wear-resistant steel by 10% and 16% respectively, while the elongation and reduction of area were raised from 2 to 4% and 0.5 to 2% respectively, and the impact toughness was only slightly reduced. Analysis of the microstructure after heat treatment revealed the interlamellar spacing of the pearlitic matrix after the higher temperature processing is smaller than it is after the lower temperature processing.

Introduction

Nb is commonly used as a microalloying element, which can effectively improve the strength and toughness of steel [1]. In recent years, research about the toughening effect of Nb has focused on as-rolled low-C microalloyed steel. The main strengthening mechanisms of Nb are solid solution strengthening, precipitation strengthening by Nb carbonitrides and grain refinement strengthening. Solid solution strengthening and precipitation strengthening tend to reduce the steel toughness, however, grain refinement can simultaneously improve the strength and toughness. Additionally, the Nb carbonitrides can significantly increase the hardness and enhance the abrasion resistance [2]. Research about the effect of Nb in cast steel is not so common, especially in high-carbon wear-resistant steels. Under normal circumstances, wear-resistant steels are mainly treated through appropriate quenching and tempering, or normalizing and tempering processes, to acquire a good combination of strength, hardness and toughness. The maximum hardness of pearlitic wear-resistant low-alloy steels can be up to 400 HBW by a normalizing and tempering treatment. The service life of the pearlitic steel is longer than that of traditional high Mn steel, but lower than for martensitic wear-resistant CrMo steels after tempering at 260 °C, (hardness is in the range 555~601 HBW). Even though the pearlitic wear-resistant steel has the lower hardness, the service life is still higher than that of a

martensitic wear-resistant steel liner plate tempered at 480 °C, (hardness is in the range 477~514 HBW) [3].

Experimental Procedure

The influence of Nb on the CrMo steel equilibrium phase diagram has been analysed using Thermo-Calc software. The CrMo steel equilibrium phase diagram was determined at different Nb contents. The chemical compositions are shown in Table I.

Table I. Chemical Compositions used for Thermo-Calc Calculations (wt.%)

| | C | Mn | Si | P | S | Cr | Mo | Ni | Cu | Nb |
|-----------|----------|-----------|-----------|----------|----------|-----------|-----------|-----------|-----------|-----------|
| 1# | 0.85 | 0.60 | 0.60 | 0.03 | 0.03 | 2.50 | 0.40 | 0.05 | 0.20 | 0.00 |
| 2# | 0.85 | 0.60 | 0.60 | 0.03 | 0.03 | 2.50 | 0.40 | 0.05 | 0.20 | 0.04 |
| 3# | 0.85 | 0.60 | 0.60 | 0.03 | 0.03 | 2.50 | 0.40 | 0.05 | 0.20 | 0.05 |

The compositions of the materials used in the experimental work are shown in Table II. A2# was based on A1# with an addition of 0.028 wt.%Nb; B2# was based on B1# sample with an addition of 0.025 wt.%Nb. The steels were cast into a Y shaped mould. Test samples were then taken from the cast sections. The heat treatment process is shown in Figure 1 and is as follows: firstly, all samples were heated to 650 °C and held for 3 h: A1# and A2# were heated to 880 °C and held for 8 h whereas B1# and B2# were heated to 920 °C and held for 8 h: all samples were then spray cooled to 300 °C after which the specimens were air cooled to room temperature. The tempering process for the specimens was carried out at 550 °C, holding for 20 h, before air-cooling to room temperature.

Table II. Compositions of Experimental Steels (wt.%)

| | C | Mn | Si | S | P | Cr | Mo | Nb |
|------------|----------|-----------|-----------|----------|----------|-----------|-----------|-----------|
| A1# | 0.84 | 0.81 | 0.42 | 0.038 | 0.027 | 2.04 | 0.26 | 0.00 |
| A2# | 0.84 | 0.80 | 0.36 | 0.028 | 0.030 | 2.18 | 0.30 | 0.028 |
| B1# | 0.86 | 0.77 | 0.38 | 0.032 | 0.029 | 2.17 | 0.29 | 0.006 |
| B2# | 0.85 | 0.66 | 0.43 | 0.024 | 0.028 | 2.24 | 0.30 | 0.025 |

Tensile tests were carried out on a WE-100 Hydraulic Universal Testing Machine, according to the national Chinese standard GB/T 228-2002. Round bar specimens were used with a diameter of 10 mm, and a gauge length of 200 mm. Impact tests were performed on a NI500C Charpy impact test machine using standard specimens of dimensions 10 x 10 x 55 mm, which were tested at 20 °C. Metallographic and SEM samples were polished and etched with 4% nital solution. The microstructure was observed and evaluated with a Zeiss microscope and JSM-6700F SEM.

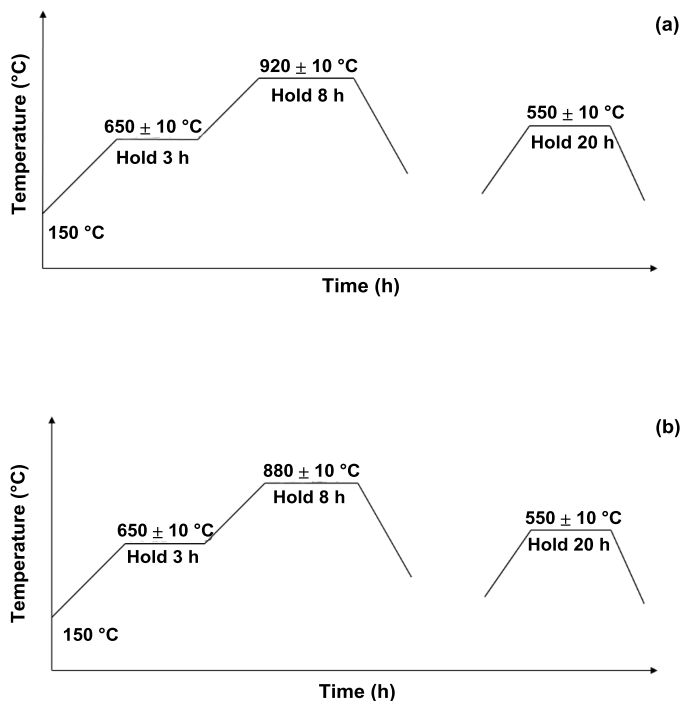


Figure 1. Sample heat treatments; (a) Heat Treatment process for samples B1# and B2#, (b) Heat Treatment process for samples A1# and A2#.

Experimental Results

The Effect of Nb on Mechanical Properties

Figures 2 and 3 show the mechanical properties following different heat treatments. Figure 2 shows data following normalizing and tempering at 880 °C (8 h) + 550 °C (20 h), and Figure 3 shows data following normalizing and tempering at 920 °C (8 h) + 550 °C (20 h). The addition of 0.028 wt.%Nb results in higher tensile strength, elongation and hardness compared to the 0 wt.%Nb steel, as shown in Figure 2. The tensile strength of A2# is 1089 MPa, and the tensile strength of A1# is 997 MPa, which has been given the same heat treatment as A2#. The tensile strength of B2# is 1117 MPa, and the tensile strength of B1# is 1112 MPa, which has been given the same heat treatment as B2#. After the heat treatment 880 °C (8 h) + 550 °C (20 h), the hardness of specimens without Nb or with Nb was 308 HB and 358 HB respectively. After the heat treatment of 920 °C (8 h) + 550 °C (20 h), the hardness of specimens without Nb or with Nb was 306 HB and 354 HB, respectively. However, the impact energy has declined a small amount

with the addition of Nb, after either of the two heat treatments. Normalizing and tempering at 880 °C (8 h) + 550 °C (20 h), resulted in impact energies for A1# and A2# of 50 J and 40.5 J, respectively. Normalizing and tempering at 920 °C (8 h) + 550 °C (20 h), produced impact energies for B1# and B2# of 52 J and 47.5 J, respectively. As shown in Figures 3 and 4, the tensile strength and elongation are better following the heat treatment of normalizing and tempering at 920 °C (8 h) + 550 °C (20 h) with similar hardness and impact energy values. The above analysis shows that the mechanical properties of the materials are better with an addition of Nb and normalizing and tempering at 920 °C (8 h) + 550 °C (20 h).

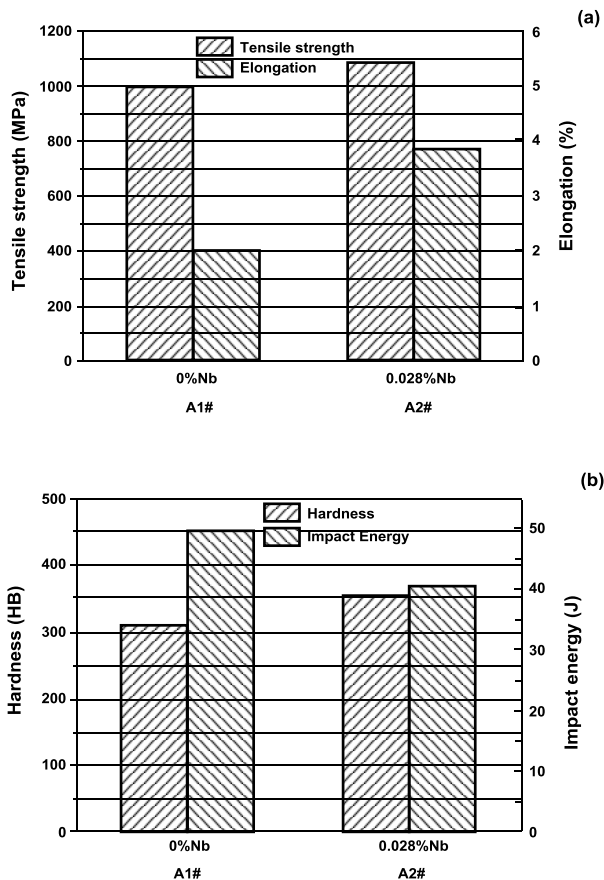


Figure 2. The mechanical properties of steels A1# and A2# after normalizing and tempering at 880 °C (8 h) + 550 °C (20 h).

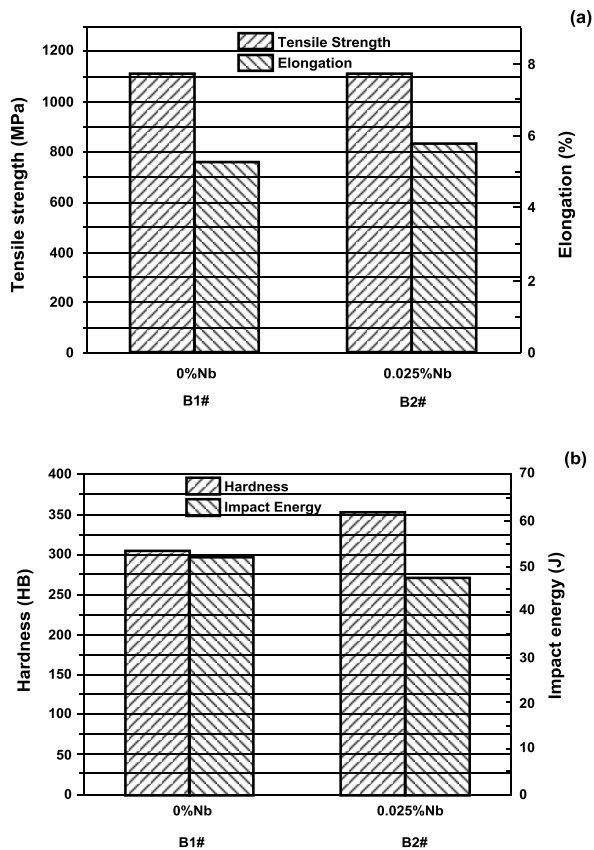


Figure 3. The mechanical properties of steels B1# and B2# after normalizing and tempering at 920 °C (8 h) + 550 °C (20 h).

The Effect of Nb on Grain Refinement

Figures 4(a) and (b) show micrographs revealing austenite grain boundaries in the 0 wt.%Nb and 0.028 wt.%Nb alloy, respectively, after normalizing and tempering at 880 °C (8 h) + 550 °C (20 h). It is evident that the austenite grain size of the sample with 0.028 wt.%Nb is much smaller than the sample with 0 wt.%Nb. Figure 5 shows the austenite grain boundaries in the steels with 0%Nb and 0.028 wt.%Nb after normalizing and tempering at 920 °C (8 h) + 550 °C (20 h). The austenite grains of the steel with 0.028 wt.%Nb are smaller than in the Nb-free sample. In addition, it can also be seen that for similar amounts of Nb, although the normalizing temperature has increased, the size of the austenite grains did not change significantly. This is

due to NbC particles pinning the austenite grain boundaries and inhibiting grain growth during austenitization [4].

The Effect of Nb on Microstructure

Figures 6 and 7 show the optical microstructure and SEM micrographs of the samples with and without Nb after normalizing and tempering at 880 °C (8 h) + 550 °C (20 h). The heat treatment process of normalizing is carried out in order to obtain a homogeneous pearlitic microstructure in the final product. Considering the heat treatment process, the microstructure of the samples should be pearlitic. Generally, the pearlite interlamellar spacing is too fine to be observed optically, although occasional colonies with smaller interlamellar spacing are resolved. Figure 6 shows grey and bright white areas which are colonies with smaller interlamellar spacing. The difference, however, is clear from SEM examination, Figure 7. Figures 8 and 9 show the equivalent observations after the 920 °C (8 h) + 550 °C (20 h) heat treatment.

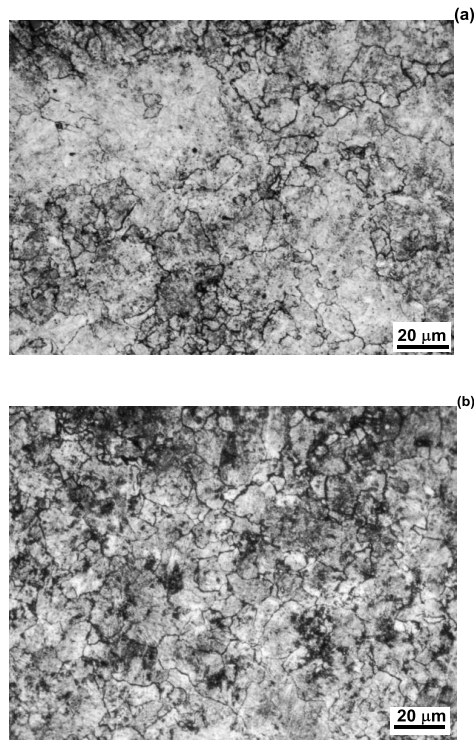


Figure 4. The austenite grain structure after normalizing and tempering at 880 °C (8 h) + 550 °C (20 h); (a) 0 wt.%Nb, (b) 0.028 wt.%Nb.

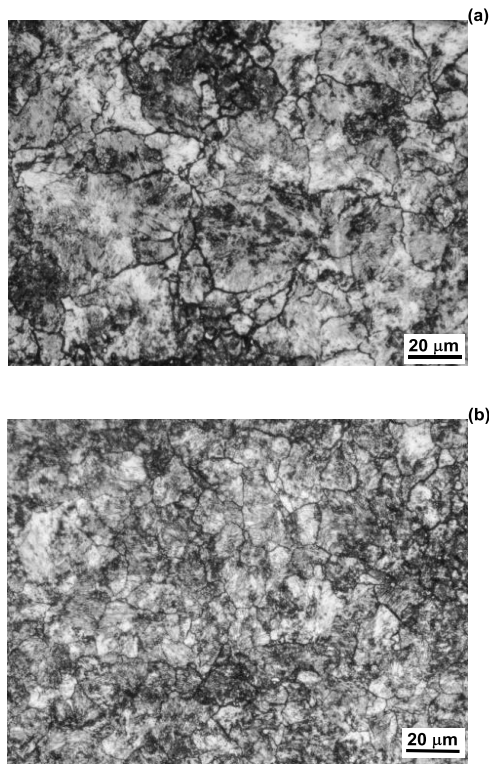


Figure 5. The austenite grain structure after normalizing and tempering at 920 °C (8 h) + 550 °C (20 h); (a) 0 wt.%Nb, (b) 0.025 wt.%Nb.

Comparing the SEM images in Figures 7 and 9, it is possible to observe that the samples with Nb contain pearlite with smaller interlamellar spacing than the sample without Nb. The smaller the interlamellar spacing of the pearlite, the higher the strength and hardness and the better the ductility [3]. However, the decrease of the interlamellar spacing will cause a deterioration in impact toughness [5]. This refinement of the interlamellar spacing is the main reason that tensile strength, hardness and elongation of the samples containing Nb are better than the Nb-free sample, and the impact energy is lower.

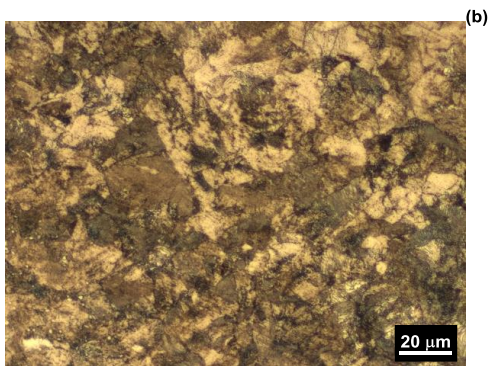
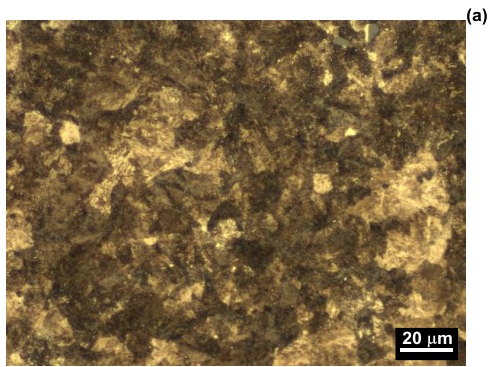


Figure 6. Microstructure after normalizing and tempering at 880 °C (8 h) + 550 °C (20 h);
(a) 0 wt.%Nb, (b) 0.028 wt.%Nb.

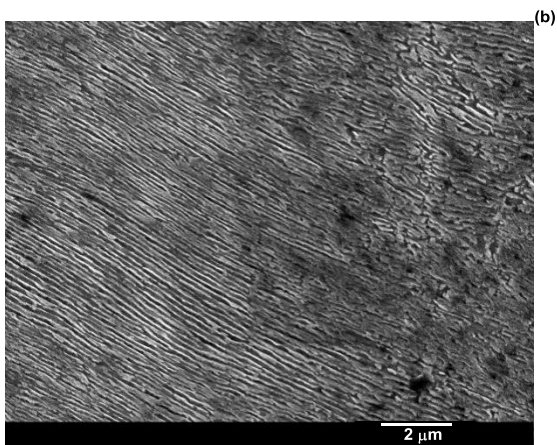
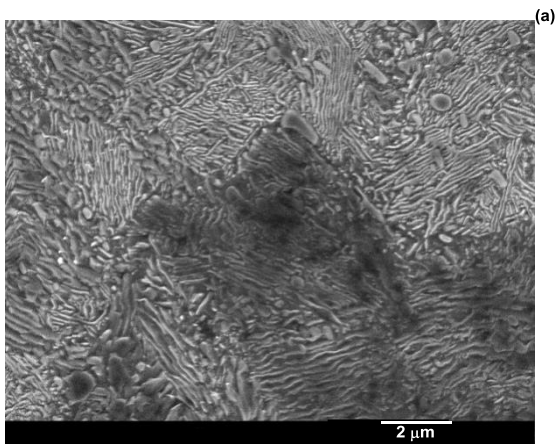


Figure 7. SEM micrographs after normalizing and tempering at 880 °C (8 h) + 550 °C (20 h);
(a) 0 wt.%Nb, (b) 0.028 wt.%Nb.

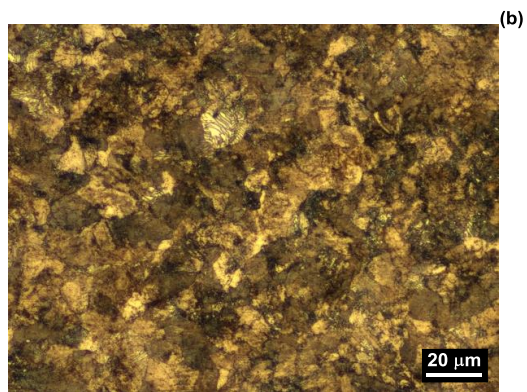
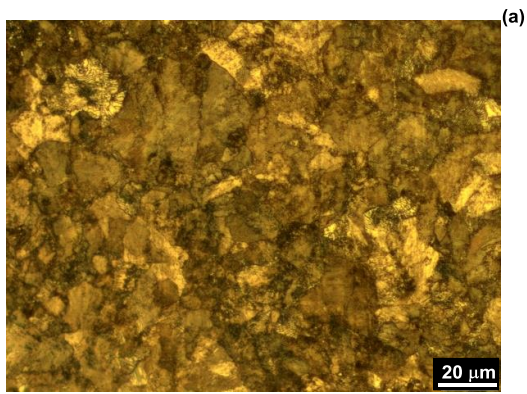


Figure 8. Microstructure after normalizing and tempering at 920 °C (8 h) + 550 °C (20 h);
(a) 0 wt.%Nb, (b) 0.025 wt.%Nb.

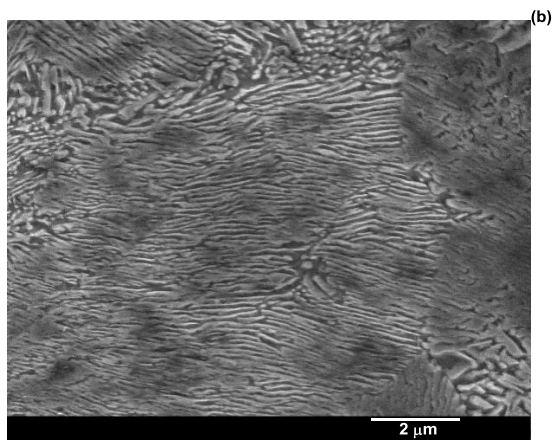
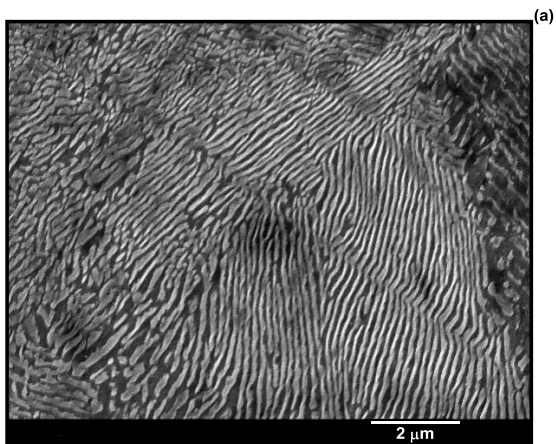


Figure 9. SEM micrographs of microstructure after normalizing and tempering at 920 °C (8 h) + 550 °C (20 h); (a) 0 wt.%Nb, (b) 0.025 wt.%Nb.

Discussion

In the production process of pearlitic wear-resistant steels, the grain size of the original austenite and the spacing and thickness of the pearlite lamellae determine the wear-resistance. Yang Chaofei et al. [6] found that the addition of small amounts of Nb in high-carbon steel refined the pearlite lamellar spacing significantly. The authors inferred that the addition of Nb, under continuous cooling conditions, lowers the transformation temperature of the pearlite, at the end of the incubation period, by interacting with carbon. This results in the Continuous Cooling Transformation (CCT) curve moving to the bottom right, ie lower temperature and longer time, which increases the transformation undercooling, ΔT , of pearlite. According to the Zener [7] semi-empirical formula: $S = \sigma V_m T_c / \Delta H \Delta T$ (S : the pearlite lamellar spacing, σ : specific Interfacial Energy, V_m : molar volume, T_c : the transition temperature of pearlite, ΔH : molar latent heat of phase transition, ΔT : undercooling degree), the pearlite lamellar spacing is inversely proportional to the level of undercooling and so the pearlite lamellar spacing becomes smaller with the addition of Nb.

Elwazri et al. [8] and Gladman [9] suggest that pearlite lamellar spacing is the most important factor in determining the strength of pearlite; the smaller the lamellar spacing, the higher the strength of the steel. Additionally, in the austenitizing process, the austenite grain size of the sample with Nb was smaller than observed in the Nb-free sample because of the niobium hindering austenite grain boundary migration. Finer austenite grains, leading to finer pearlite colonies and reduced lamellar spacing, are the main reasons that steel containing Nb is superior to the steel without Nb.

Under the two normalizing temperatures used, impact energies of the samples with Nb were lower than for the Nb-free samples. As described previously, the addition of Nb moves the eutectoid point to the left (lower carbon content), so for a given carbon content the amount of cementite at room temperature will increase, which can lead to an increase of hardness and the decreasing of the impact toughness. Because of the higher normalizing temperature, steel B2# should have more dissolved niobium during austenitization than steel A2#, meaning that the dissolution of Nb at higher temperatures is a bit more than that at low temperature. However, the solubility will still be rather low even at 920 °C [3]. Even so, it is evident that there is still sufficient niobium in solution to play a role in controlling austenite grain refinement and pearlite formation.

As reported previously, the austenite grain size has not increased with the increasing of the normalizing temperature. With the same grain size, sample B2# has a little added precipitation strengthening and has the better mechanical properties through the combined influence of grain refinement strengthening and precipitation strengthening.

Conclusions

Different heat treatments have been used to process a CrMo steel with and without Nb. Mechanical properties and microstructure of the wear-resistant steels after heat treatment were studied and the following conclusions are drawn from this work:

1. After both of the heat treatment cycles, A2# and B2#, which both contain Nb, have the better mechanical properties. B2#, containing 0.025 wt.%Nb, and austenitized at the higher temperature, has the best elongation and impact energy while having the same tensile strength and hardness as A2# which contains 0.028 wt.%Nb and was austenitized at the lower temperature.
2. The addition of Nb reduces the pearlite transformation temperature, resulting in the pearlite forming at a larger degree of undercooling, and consequently a finer interlamellar spacing is evident in the Nb containing steels.
3. Additionally, Nb precipitation was instrumental in hindering austenite grain growth during normalizing. The dissolution of Nb in the austenite at the higher (920 °C) normalizing temperature was a bit more than at that at the lower temperature (880 °C), which reduced the size of the precipitates, and the fine second phase precipitated during the cooling process.
4. The steel microalloyed with Nb and normalized at 920 °C (8 h) and tempered at 550 °C (20 h) has the better mechanical properties due to the combined action of grain refinement strengthening, pearlite refinement and precipitation strengthening.

References

1. M. Piette et al., "Effect of 0-0.1%Nb Additions on Mechanical Properties of Plates Processed by Thermomechanically Controlled Processing and Accelerated Cooling," *Ironmaking and Steelmaking*, (2001), 175-179.
2. A. DeArdo et al., "Fundamental Metallurgy of Niobium in Steel," *Metallurgical Society of AIME*, (1984), 685-759.
3. Y. Lou, *Casting Manual II* (Beijing: China Machine Press, 2011).
4. R. Coladas et al., "Austenite Grain Growth in Medium and High-carbon Steels Microalloyed with Niobium," *Journal Metal Science*, (1977), 509-516.
5. H. Ye, X. Zhang and H. Wu, *The Principle and Process of Metal Heat Treatment* (Beijing: Chemical Industry Press, 2011).
6. C. Yang, Q. Wu and Y. Chen, "Niobium on High Carbon Steel During Continuous Cooling Transformation and Pearlite Lamella Spacing," *International Journal of Materials for Mechanical Engineering*, 03 (2013),16-20.

7. J.D. Verhoeven, *Fundamentals of Physical Metallurgy* (New York, NY: John Wiley & Sons, 1975), 436-436.

8. A.M. Elwazri, P. Wanjara and S. Yue, "Metadynamic and Static Recrystallization of Hypereutectoid Steel," *The Iron and Steel Institute of Japan International*, 7 (43) (2003), 1080-1088.

9. T. Gladman, *The Physical Metallurgy of Microalloyed Steels* (London: Institute of Materials, 1997).

DEVELOPMENT OF FeNbC FOR WEAR RESISTANT APPLICATIONS

E.B. Cruz and D.P. Fridman

Companhia Brasileira de Metalurgia e Mineração (CBMM); Araxá, 38183-903, MG, Brazil

Keywords: Niobium Carbide, FeNbC, Wear, Castings

Abstract

Niobium carbide (NbC) exhibits outstanding properties such as high hardness and chemical stability that are very favorable for application in high performance wear resistant materials. FeNbC is a metal matrix composite that contains fine NbC particles homogeneously distributed in an iron matrix. This innovative material was developed as an alternative alloying source of NbC and it can be applied as an additive for castings or as a hard-facing material for manufacturing wear resistant parts such as liners, chutes, pump impellers, rolling mill rolls and ground engaging tools. This work presents the properties of FeNbC and the results of dissolution trials carried out in order to determine the best addition practices for FeNbC in cast irons and steels. The most efficient methods of addition were to melt the FeNbC with the metal charge and to add it on the bath surface. It was verified that the dissolution of the iron matrix in the liquid metal allows the transfer and dispersion of NbC particles into the melt. Since the density of NbC is similar to that of melted iron and steel, the hard NbC particles distribute uniformly. Therefore, the dissolution of FeNbC enables the development of different wear resistant cast irons or steels with high contents of hard primary NbC suitable for diverse applications in the mining and processing industries.

Introduction

Refractory carbides and nitrides are useful materials with numerous industrial applications. Although most of their applications are recent, they have been known for over one hundred years. Major industrial applications of refractory carbides and nitrides involve the production of hard metals or cemented carbides, which are sintered composite materials consisting of at least one hard and wear resistant phase, in the majority of cases this being tungsten carbide (WC), and a ductile and softer metallic phase, mainly cobalt and nickel. Hard metals constitute the backbone of the tool manufacturing industry, having diverse applications such as machining of metallic and non-metallic materials, forming (wire drawing, can tooling, forging, stamping, mill rolls, punches, dies and anvils) and mining (oil well drill bits and rock drill bits). They are the material of choice in all applications where the combination of wear resistance, toughness and strength is required, at both room and high temperatures [1,2].

As shown in Table I, when compared to WC, niobium carbide (NbC) possesses similar hardness but only half of its density. Moreover, it has a higher melting point and a higher oxidation resistance. These outstanding properties make it an attractive and innovative option for most of the traditional industrial applications. NbC also has a lower solubility in iron than WC and has a similar density to materials like cast iron and steel, opening the possibility of using NbC as a raw material for hard metals [3] and for the development of new wear resistant materials for castings

and hard-facing coatings with high levels of hard primary NbC homogeneously distributed in their microstructures.

Table I. Properties of Niobium Carbide (NbC) and Tungsten Carbide (WC) [1,4]

| Carbide | Density (g/cm³) | Vickers Hardness (GPa) | Melting Point (°C) | Oxidation Resistance in Air (°C) |
|----------------|---------------------------------------|-----------------------------------|-------------------------------|---|
| WC | 15.8 | 22 | 2870 | 500-600 |
| NbC | 7.85 | 19.65 | 3600 | 800 |

Traditionally niobium has been consumed as a microalloying element in high strength low alloy steels (HSLA). In such alloys, niobium is added as ferroniobium (FeNb) and it forms very fine NbC particles, controlling the grain size and thus improving the mechanical properties of the steel. More recently, niobium has also been applied as a very effective alloying element in cast iron, since it forms primary carbides with a homogeneous distribution. Niobium additions higher than 0.5 wt.% can lead to the precipitation of high hardness primary MC-type carbides, resulting in an improvement in the wear resistance of white cast iron, which is the main material employed when high wear performance is required in mining and earth moving equipment. Thus, NbC constitutes a promising alternative for improving erosion resistance because it forms hard and discontinuous MC carbides in cast irons. This can also be seen in indefinite chilled cast irons, materials that have been largely used in rolls for hot rolling, where the carbides improve abrasion resistance while the graphite decreases friction between the rolls and the rolled material. Additions of 1.5 wt.% niobium to indefinite chilled cast iron result in primary NbC particles that enhance hardness and wear resistance without changing the graphite morphology. As a result, improvements higher than 30% in the roll life have been reported [5].

Niobium contents of more than 5 wt.% have also been added in hard-facing materials, along with the stoichiometric amount of carbon in order to form primary NbC. The extremely hard niobium particles, finely dispersed in between the chromium carbides, have reduced spacing, ensuring the best protection from abrasive and erosive media of finer size [6].

In all these applications, niobium has been added regularly as FeNb through suitable alloying techniques, as it has to dissolve and react with carbon at its interface in order to form the hard NbC particles [5]. As an alternative to FeNb addition, CBMM has developed FeNbC, ie. niobium carbide iron matrix (NbC-Fe), a metal matrix composite (MMC) to be used mainly in applications where very high final contents of NbC are sought. This innovative material was developed as another source of NbC which can be applied as an additive for castings and hard-facing products for parts such as liners, chutes, pump impellers and ground engaging tools (GETs) for the mining and processing industry. This work presents the characteristics and properties of the FeNbC presently produced by CBMM, as well as the results of dissolution trials carried out in order to determine the best addition practices of FeNbC in cast iron and steels.

Characterization of FeNbC

FeNbC is a natural MMC that contains fine NbC particles homogeneously distributed in an iron based matrix, as shown in Figure 1.

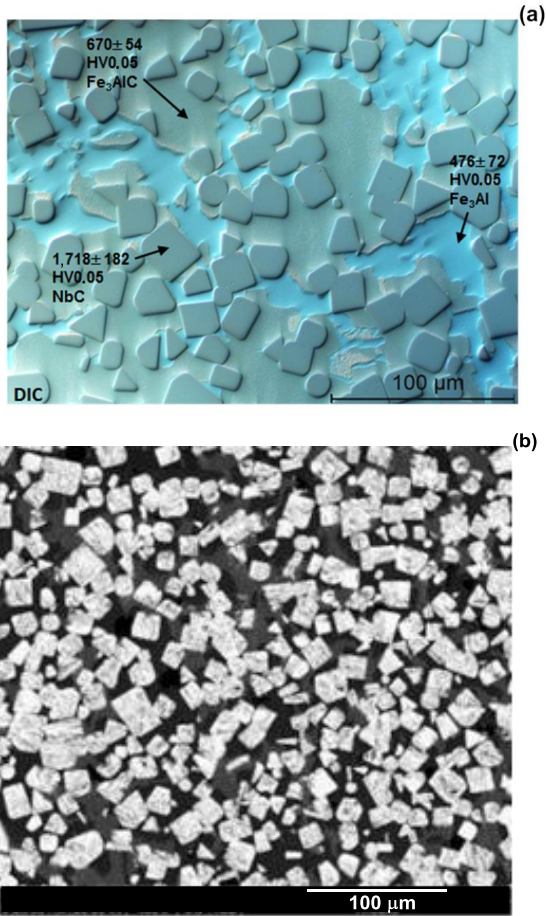


Figure 1. Typical microstructure of FeNbC shown by optical microscopy with differential interference contrast (a) and SEM/EDS (b) [7].

FeNbC is produced by an aluminio-carbothermic reduction process and can be produced in a wide range of NbC contents (typically between 40 and 80% of NbC) and grain sizes between 0 and 50 mm, Figure 2.

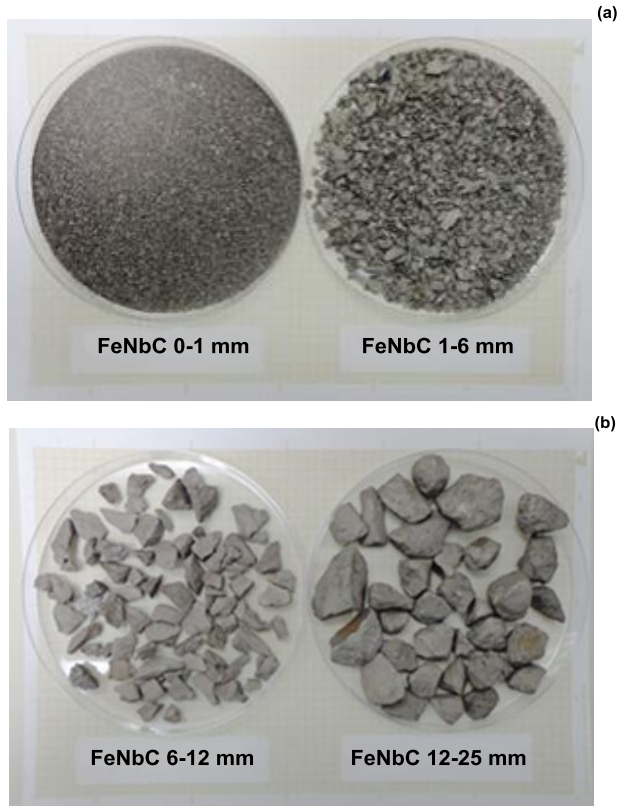


Figure 2. Appearance of different granules of FeNbC: <1 mm and 1-6 mm (a) and 6-12 mm and 12-25 mm (b).

The main phases found are NbC, Fe_3Al and Fe_3AlC , Figure 3. The microhardness of the intermetallic Fe_3Al ranges from 360 to 470 HV 0.05 and of Fe_3AlC from 630 to 670 HV 0.05 [8]. The high hardness of both NbC particles and the matrix indicate that FeNbC itself constitutes an interesting material for wear resistant applications such as hard-facing coatings for Ground Engaging Tools (GETs) [9].

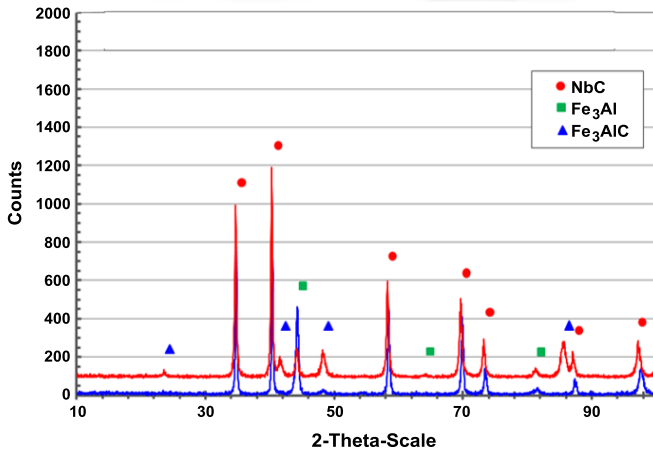


Figure 3. Main phases found in FeNbC [8].

The ranges of chemical composition and density of FeNbC are indicated in Table II. In addition to iron, niobium and carbon, other minor elements such as aluminum, manganese, silicon and titanium are found.

Table II. Range of Chemical Composition and Density of FeNbC

| Fe | Nb (wt.%) | C (wt.%) | Others | Density (g/cm ³) |
|------|--------------|-------------|----------------|---------------------------------|
| Base | 30-60 | 4-8 | Al, Ti, Mn, Si | 6-7 |

Dissolution of FeNbC in Iron-Based Alloys

In order to determine the best dissolution practices of FeNbC in iron-based alloys for castings, the following methods of addition were tested: (a) simple dumping on the bath surface, SD, (b) melting down together with the metallic charge, MC, and (c) addition to the metal stream during ladle tapping, MS, Figure 4.



Figure 4. Methods of addition of FeNbC in iron castings: simple dumping on the surface (a), melting down with the charge (b) and addition to the metal stream during tapping (c).

As shown in Table III, the first set of trials (1 to 15) were conducted by simple dumping of FeNbC on the metal bath surface and the second set (16 to 30) by melting it together with the metallic charge. In both cases, increasing quantities of FeNbC particles with increasing size ranges from 0 to 1 mm, 1 to 6 mm, 6 to 12 mm, 12 to 25 mm and 25 to 50 mm were added, to determine the effect of the mass and the particle size on the dissolution and dispersion rates of NbC in the metal bath.

Table III. Experimental Conditions of the FeNbC Addition Trials Carried Out by Simple Dumping on the Bath surface (SD) and by Melting with the Metallic Charge (MC)

| Trial (No) | Particle Size (mm) | Nb Target (wt.%) | NbC Target (wt.%) | Addition of FeNbC (Method) |
|-------------------|---------------------------|-------------------------|--------------------------|---------------------------------------|
| 1 | 0-1 | 2.5 | 2.8 | Simple Dumping on the Bath (SD) |
| 2 | 1-6 | | | |
| 3 | 6-12 | | | |
| 4 | 12-25 | | | |
| 5 | 25-50 | | | |
| 6 | 0-1 | 5 | 5.6 | |
| 7 | 1-6 | | | |
| 8 | 6-12 | | | |
| 9 | 12-25 | | | |
| 10 | 25-50 | | | |
| 11 | 0-1 | 10 | 11.3 | |
| 12 | 1-6 | | | |
| 13 | 6-12 | | | |
| 14 | 12-25 | | | |
| 15 | 25-50 | | | |
| 16 | 0-1 | 2.5 | 2.8 | Melting with the Metallic Charge (MC) |
| 17 | 1-6 | | | |
| 18 | 6-12 | | | |
| 19 | 12-25 | | | |
| 20 | 25-50 | | | |
| 21 | 0-1 | 5 | 5.6 | |
| 22 | 1-6 | | | |
| 23 | 6-12 | | | |
| 24 | 12-25 | | | |
| 25 | 25-50 | | | |
| 26 | 0-1 | 10 | 11.3 | |
| 27 | 1-6 | | | |
| 28 | 6-12 | | | |
| 29 | 12-25 | | | |
| 30 | 25-50 | | | |

The trials were carried out in a laboratory induction furnace containing, before the addition, 12 to 14 kg of liquid indefinite chilled cast iron with 3.5 wt.%C, 1.1 wt.%Si, 4.2 wt.%Ni and 2.2 wt.%Cr. The liquid metal at about 1530 °C was protected by argon shielding. The chemical composition of the FeNbC was approximately 46.2 wt.%Nb, 7.0 wt.%C, 3.8 wt.%Al, 0.5 wt.%Si and 0.04 wt.%Ti.

In the trials carried out by simple dumping on the metal bath, the total mass of FeNbC was added gradually in 3, 5 and 10 parts in order to obtain 2.8 wt.%, 5.6 wt.% and 11.3 wt.%NbC, respectively, while preventing the bath from cooling and freezing. After each addition, the liquid metal was manually stirred to promote the dissolution of the FeNbC particles and samples were taken by suction in quartz tubes to track the dissolution process by chemical analysis of the NbC content. Finally, the metal was tapped in a preheated ladle and cast in sand molds.

In the trials carried out by melting with the metallic charge, the whole mass of FeNbC particles with different size ranges was charged and melted down together with the solid charge. After adjusting the temperature to about 1530 °C, the metal bath was intermittently manually stirred to promote the dissolution process. Samples of the liquid metal were taken by suction in quartz tubes for chemical analysis, as before. Finally, the metal was tapped.

The experimental conditions of the third and fourth sets of trials are shown in Table IV. Trials 31 to 33 were carried out by simple dumping of FeNbC on the metal stream during pouring to the tapping ladle, and trials 34 to 39 were conducted by simple dumping of FeNbC on the metal surface. Increasing amounts of FeNbC with different particle size ranges (0 to 1 mm and 12 to 25 mm) to obtain 2.8 wt.%, 5.6 wt.% and 11.3 wt.%NbC in the metal bath were added, aiming at determining the effect of the mass and particle size on the FeNbC dissolution rate. The trials were carried out in an induction furnace containing from 40 to 47 kg of molten indefinite chilled cast iron with 3.5 wt.%C, 1.1 wt.%Si, 4.2 wt.%Ni and 2.2 wt.%Cr.

Table IV. Experimental Conditions of FeNbC Dissolution Trials carried out by Simple Dumping on the Metal Stream during Tapping (MS) and on the Metal Bath Surface in the Furnace (SD)

| Trial (No) | Particle Size (mm) | Nb Target (wt.%) | NbC Target (wt.%) | Addition of FeNbC (Method) |
|-------------------|---------------------------|-------------------------|--------------------------|-----------------------------------|
| 31 | 0-1 | 2.5 | 2.8 | Dumping on the Metal Stream (MS) |
| 32 | 0-1 | 5 | 5.6 | |
| 33 | 0-1 | 10 | 11.3 | |
| 34 | 0-1 | 2.5 | 2.8 | Simple Dumping on the Bath (SD) |
| 35 | 12-25 | | | |
| 36 | 0-1 | 5 | 5.6 | |
| 37 | 12-25 | | | |
| 38 | 0-1 | 10 | 11.3 | |
| 39 | 12-25 | | | |

In the simple dumping trials, the temperature of the metal bath was adjusted to 1530 °C before the addition of the particles. The total mass of FeNbC was added gradually in 3, 5 and 10 parts in order to obtain 2.8 wt.%, 5.6 wt.% and 11.3 wt.%NbC, respectively, while preventing the bath from cooling and freezing. To promote the dissolution of the FeNbC particles, the liquid metal was manually stirred after each addition. Samples of liquid metal were taken during the process and the bath was protected by argon shielding.

In the dissolution trials from the addition of FeNbC particles in the metal stream, only fine particles (<1 mm) were added during the pouring of the liquid metal to the tapping ladle. The bath temperature was adjusted in the induction furnace to 1600 °C in order to compensate for the heat losses in the preheated ladle. After the addition of FeNbC to the stream, the metal bath was manually stirred in the ladle to promote the dissolution of the fine FeNbC particles floating on the surface. Samples of liquid metal were taken by suction in quartz tubes to determine the increase in NbC content as a function of time and then the metal was tapped.

Results

In the dissolution trials using simple dumping, the finer particles (<6 mm) showed a tendency to keep floating, undissolved, on the bath surface even after manual stirring. On the other hand, the coarser particles (>6 mm) sank almost immediately into the bath, leading quickly to a clean surface bath appearance, indicative of a faster dissolution process, Figure 5. Similar behavior was observed in the dissolution trials carried out by melting with the metallic charge, where the finer particles floated to the bath surface after stirring while the coarser particles remained submerged in the molten metal.



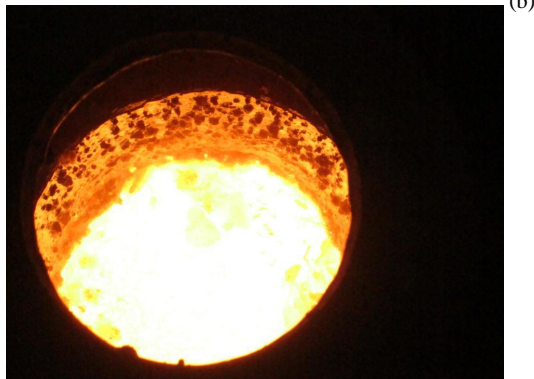
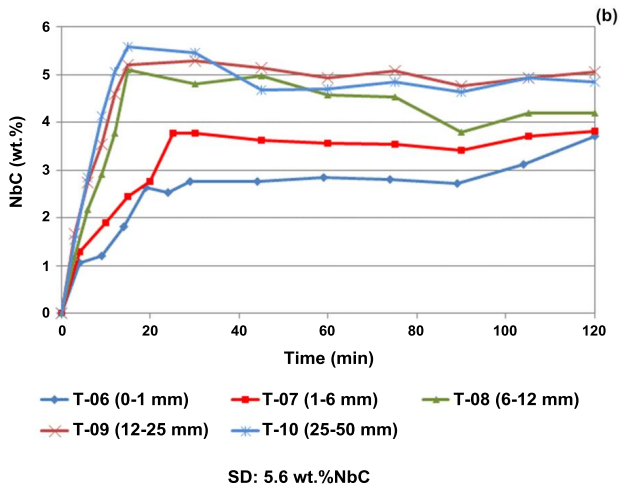
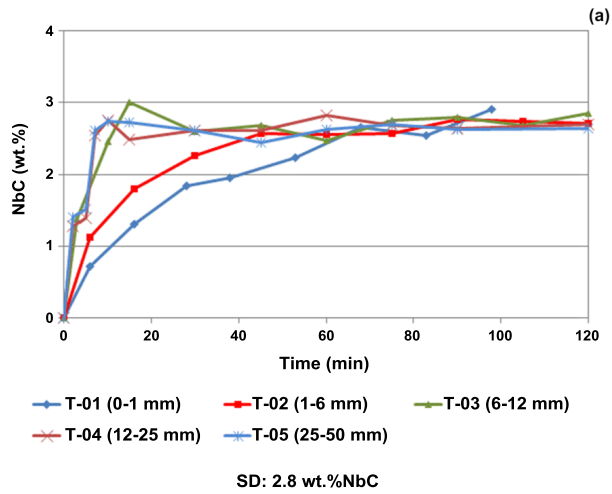


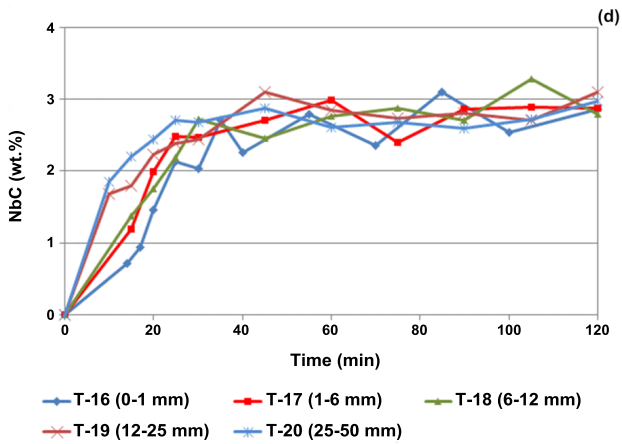
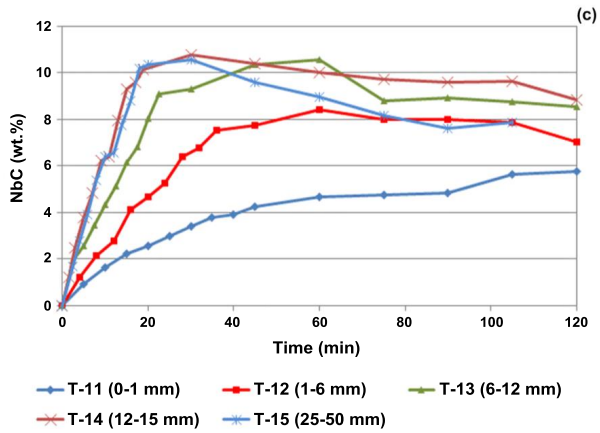
Figure 5. Appearance of the metal surface after the dissolution of FeNbC aiming to obtain 11.3 wt.%NbC. Fine particles (<1 mm) (a) and coarse particles (12-25 mm) (b).

Figure 6 displays the experimental results of the NbC content in the metal phase as a function of time from the dissolution trials of different particles sizes of FeNbC by simple dumping on the bath and by melting with the charge.

In the trials carried out by simple dumping, the total time (120 minutes) included the period for the addition of the FeNbC particles on the bath surface, in addition to the time spent for their dissolution at 1530 °C, Figures 6(a), (b) and (c). In the trials carried out by melting with the metallic charge, the total time (120 minutes) comprised the periods for heating, melting and holding the bath at 1530 °C for dissolution and sampling, Figures 6(d), (e) and (f).

In the dissolution trials carried out by simple dumping of FeNbC on the bath, coarser particles (>6 mm) dissolved faster and more effectively than the finer ones (<6 mm), reaching NbC contents equal, or very close to, the target values (2.8 wt.%, 5.6 wt.% and 11.3 wt.%) in less than 30 minutes, Figures 6(a), (b) and (c). The addition of the finer particles (<6 mm) led to NbC contents close to the target values only for the lowest NbC concentration (2.8 wt.%).





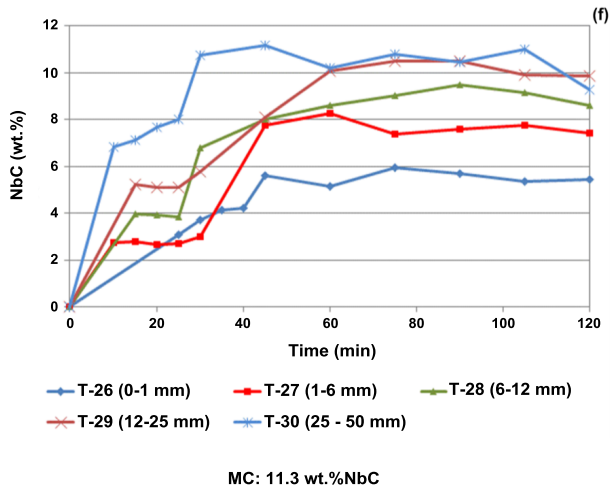
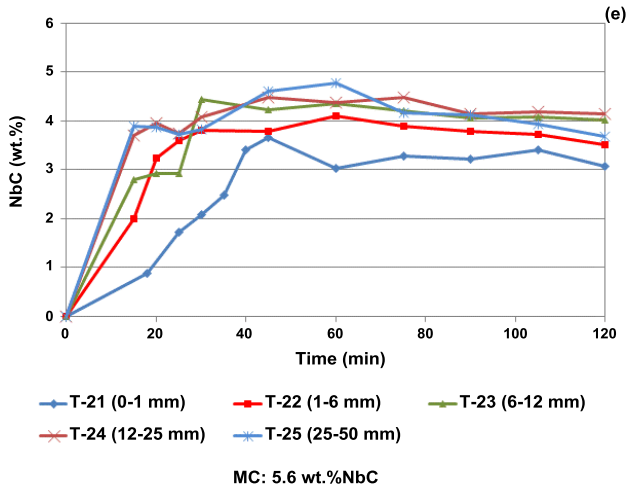


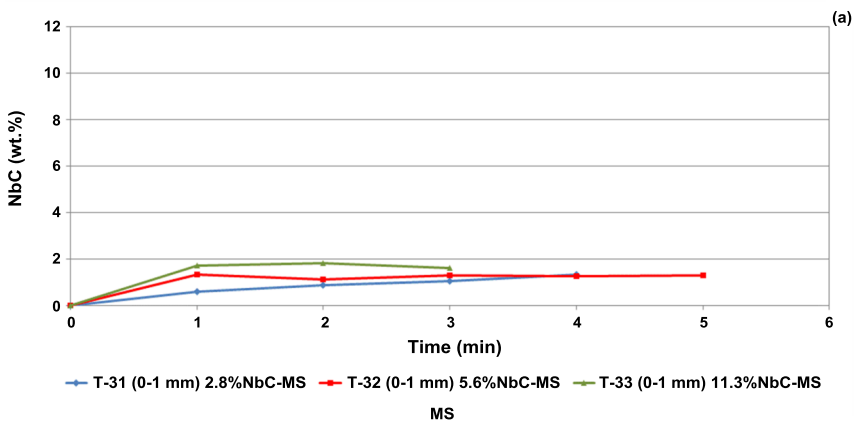
Figure 6. NbC content as a function of time. Addition of FeNbC with different particle sizes by simple dumping (SD) on the bath (a, b and c) and by melting with the charge (MC), (d, e and f).

The lower dissolution rate seen for the finer material is related to the fact that although having a larger surface area than the coarser material, the finer material agglomerated and remained undissolved floating on the bath surface, offering a smaller effective contact area for the dissolution reaction with the molten metal, Figure 5(a). Meanwhile, the coarser particles that remained totally submerged just after their addition to the metal bath presented an effectively larger contact area for the dissolution reaction in the liquid metal.

Figures 6 (d), (e) and (f) show that the results from the dissolution trials conducted by melting the FeNbC particles together with the metallic charge were very similar to those obtained in the dissolution trials carried out by simple dumping on the bath. However, in this MC process the dissolution of the finer particles (<6 mm) was improved during the melting process due to their closer and longer contact within the bath with all the particles remaining submerged in the liquid metal.

Both methods of adding FeNbC – simple dumping on the bath surface or melting down together with the metallic charge – were very effective for dissolving FeNbC particles in the bath with a slight advantage for finer particles when they were melted down together with the charge, as shown in Figure 6.

The results of the dissolution trials of FeNbC by simple dumping in the metal stream (MS) compared to simple dumping on the bath surface (SD) are shown in Figures 7(a) and (b) in terms of the NbC content of the metal phase as a function of time.



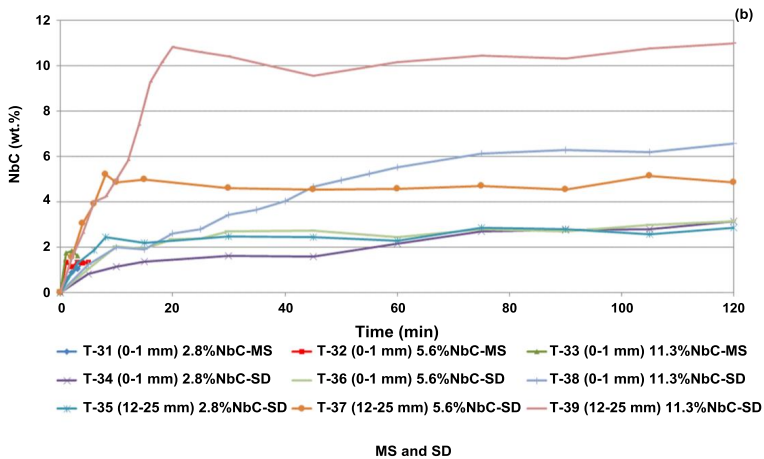
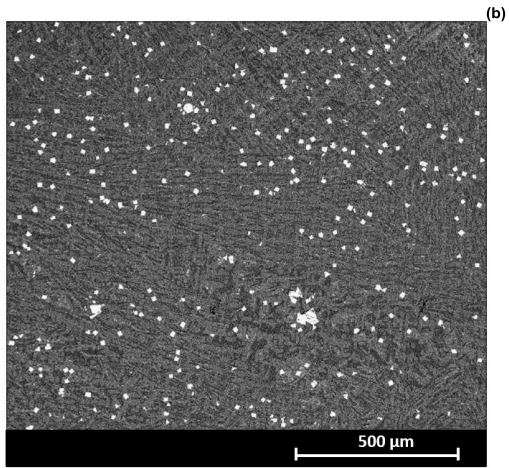
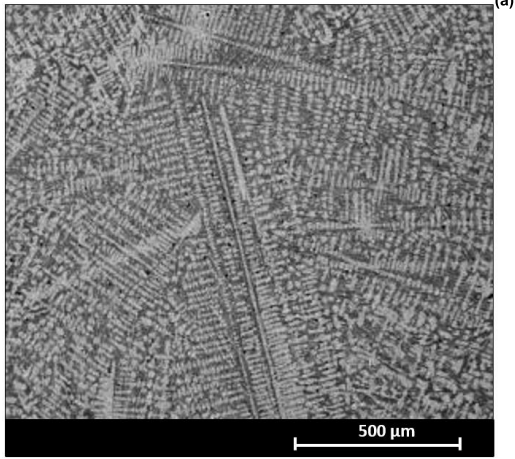


Figure 7. NbC content as a function of time. Addition of FeNbC by simple dumping on the metal stream (MS) during tapping (a) and compared to simple dumping on the metal bath (SD) in the furnace (b).

In the dissolution trials of FeNbC carried out by simple dumping in the metal stream, in spite of the good mixing between the particles and the falling stream, most of the fine material floated to the bath surface hindering its dissolution, mainly when high NbC contents were sought. As a result, Figure 7(a) shows that the addition of fine particles (<1 mm) added to the metal stream during pouring into the tapping ladle led to very low NbC contents in the metal phase for all the targeted NbC values. The poor dissolution was attributed to the short period available for dissolution during pouring, to the high drop in temperature of the liquid metal in the ladle and to the tendency of the fine material to float and agglomerate on the bath surface. On the other hand, it was observed that the addition of the same fine particles (<1 mm) by simple dumping on the metal surface led to higher NbC contents in the metal phase for all the targeted NbC contents, Figure 7(b). However, the addition of coarser particles (from 12 to 25 mm) by simple dumping on the metal surface resulted in NbC contents still higher than those achieved with the fine material (<1 mm). Those higher values were very close to the targeted contents (2.8 wt.%, 5.6 wt.% and 11.3 wt.%NbC) and confirmed the results achieved in the first set of trials carried out under similar experimental conditions, Figure 6(a) to (c).

Figure 8 shows the results of the microstructural analysis via SEM/EDS of indefinite chilled cast iron samples obtained after the dissolution trials of FeNbC aimed at producing a range of NbC contents (2.8 wt.%, 5.6 wt.% and 11.3 wt.%).



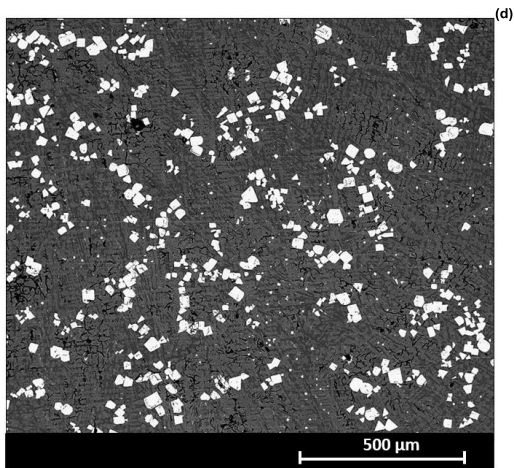
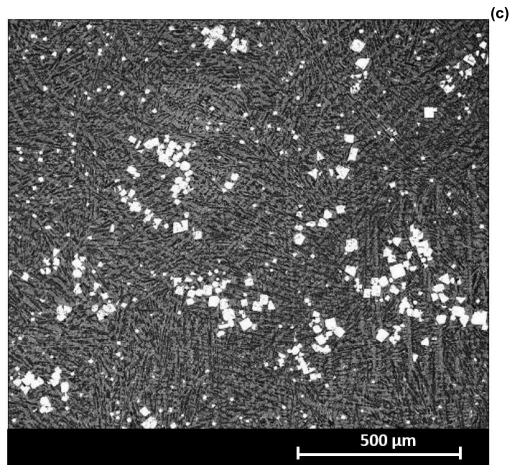


Figure 8. Microstructure (SEM/EDS) of an indefinite chilled cast iron before and after the dissolution of FeNbC from 12 to 25 mm.
(a) 0 wt.%NbC, (b) 2.8 wt%NbC, (c) 5.6 wt.%NbC, (d) 11.3 wt.%NbC.

The increase in the quantity of FeNbC added to the indefinite chilled cast iron resulted in microstructures with increasing volume fractions of hard primary NbC (white phases seen in the micrographs), Figures 8(b) to (d). Since the density of NbC is similar to the melted cast iron and likewise most of the iron alloys, the particles of NbC coming from the dissolution of the FeNbC matrix were spread out over the microstructure of the cast iron. It was observed that the higher the NbC content, the higher the tendency of the fine particles to coarsen and form bigger NbC particles. It seems also that the insertion of NbC, through the dissolution of the iron-aluminide matrix of FeNbC, led to finer as-cast microstructures than those obtained without the addition of niobium. In fact, as seen in Figure 8(a), the structure of the indefinite chilled cast iron without NbC is much coarser than the structures of the cast iron with increasing NbC contents, Figure 8(b) to (d).

Based on the experimental results, it is clear that the use of FeNbC enables the development of different wear resistant cast irons or steels containing high levels of hard primary NbC dispersed in the host metal matrix, which could be suitable for diverse applications in the mining and processing industry.

Conclusions

The properties and dissolution of FeNbC in iron-based alloys were investigated, aiming at developing wear resistant materials containing high contents of hard NbC. The dissolution trials were carried out by the addition of FeNbC in cast iron melted in laboratory induction furnaces. Three methods of addition were examined: dumping on the melt surface, melting down with the metal charge and adding to the metal stream during tapping.

The following conclusions were drawn:

1. FeNbC is a metal matrix composite that contains 40 to 80% of hard NbC homogeneously distributed in an iron-based matrix, with residual levels of aluminum, silicon and manganese.
2. Melting with the metallic charge was the most efficient method of dissolving FeNbC in the metal bath. The second most efficient method was by simple dumping on the metal surface.
3. The addition of FeNbC particles to the liquid metal stream during pouring showed the lowest dissolution rates.
4. Coarse FeNbC particles (>6 mm) dissolved faster and more effectively than the finer material since small particles tend to float and agglomerate, remaining undissolved on the bath surface.
5. Hard NbC particles from the dissolution of the FeNbC matrix were evenly dispersed within the iron alloy casts due to the similar densities of NbC and the liquid iron alloys. Thus, the dissolution of FeNbC enables the development of different wear resistant cast irons or steels with high contents of hard primary NbC suitable for diverse applications in the mining and processing industries.

References

1. H.O. Pierson, *Handbook of Refractory Carbides and Nitrides* (New Jersey, NJ: Noyes Publications, 1996), 1-117.
2. V.K. Sarin (Editor-in-Chief), L. Llanes and D. Mari (Vol. Eds.), *Comprehensive Hard Materials*, vol. 1, Hardmetals (Oxford, UK Elsevier Publishing Company, 2014), 3-139.
3. M. Woydt and H. Mohrbacher, "The Tribological and Mechanical Properties of Niobium Carbides (NbC) Bonded with Cobalt or Fe₃Al," *Wear*, 321 (2014) 1-7.
4. G. Berg et al., *Handbook of Ceramic Hard Materials*, vol. 2, Chapter 9, Data Collection of Properties of Hard Materials, (Wiley-VCH, 2000).
5. H. Mohrbacher, "Niobium in Cast Iron" (Practical Guide NiobelCon, Swaenebeecklaan 5, 2970 Schilde, Belgium, 2015) <http://www.niobelcon.com/NiobelCon/Publications>. (April 2015).
6. Catalogue of Wear Parts Products: CDP 4666- CastoDur Diamond Plates. Castolin Eutectic. <http://www.castolin.com/Wear-Parts> (April 2015).
7. M. Scheibe et al., "Comparing Different Preparation Techniques for the Characterization of Niobium Carbides" (Report BAM Federal Institute for Materials Research and Testing, DE-12200 Berlin, Germany, 2014).
8. M. Woydt, "Microstructure and Dry Sliding of Fe₃Al-NbC (MMC)" (Report BAM Federal Institute for Materials Research and Testing, DE-12200 Berlin, Germany, 2014).
9. E.T. Galvani et al., "Application of FeNbC as a Hardfacing Material using Laser Cladding" (Paper presented at the International Symposium on Wear Resistant Alloys for the Mining and Processing Industry, Campinas, São Paulo, Brazil, 4-7 May 2015).

THE TRIBOLOGICAL PROPERTY PROFILE OF HARD METALS AND METAL MATRIX COMPOSITES BASED ON NIOBIUM CARBIDE

M. Woydt¹ and H. Mohrbacher²

¹BAM Federal Institute for Materials Research and Testing, DE-12200 Berlin, Germany

²NobelCon bvba, BE-2970 Schilde, Belgium

Keywords: Niobium Carbide, Metal, Binder, Metal Matrix Composite, Friction, Wear, Hardness, Solubility, Toughness, Abrasion

Abstract

The term “tribology” relates to the friction and wear behavior of materials, as well as their lubrication, and is essentially a system property involving the material itself, the counterbody material, operating condition stresses and also environmental conditions. Hard metals have been used extensively under typical tribological conditions encountered in the mining and processing industry with the intention of increasing lifetime and performance of components. The typical and well-established hard metal is WC-Co and its modifications, which have been developed over the last several decades and are used in a vast range of applications. In contrast surprisingly little work has been done on niobium carbide (NbC) based hard metal, despite repeated indications that this material should have very favorable tribological properties. Therefore, an extensive research program has been initiated firstly to identify the intrinsic properties of NbC and their influencing factors and secondly to develop hard metal, as well as metal matrix composite (MMC) materials, based on NbC. This work is focused on the tribological profile of NbC-based materials, as well as their potential applications and environmental implications.

Microhardness and elastic properties depend on the C/Nb ratio. At room temperature hard metals of stoichiometric niobium carbide (NbC_{1.0}) have an elastic modulus of around 440 GPa. Those of under-stoichiometric niobium carbide (NbC_{0.88}) have an elastic modulus of around 405 GPa while melt grown NbC_{0.70} shows an elastic modulus of approximately 365 GPa. The microhardness, however, increases with decreasing C/Nb ratio. Stoichiometric and sub-stoichiometric NbC possess a pronounced intrinsic wear resistance, either as hard metal or as a hard phase in metal matrix composites.

Some of the recent activities have focused on the tribological behavior of Fe₃Al-NbC metal matrix composites prepared by pyro-metallurgical synthesis. It is compared to different Spark Plasma Sintered (SPS) NbC-based hard metals bonded by cobalt or Fe₃Al under dry sliding conditions. The wear resistance under dry sliding conditions of the present Fe₃Al-NbC, containing about 60 volume percent NbC, is shown to be close to that of NbC-based hard metals. No particle extraction or fragmentation of the NbC particles was seen in the wear tracks of the Fe₃Al-NbC composite, as a metallurgical interface was formed between the matrix and NbC grains. The physical properties of melt-grown NbC match those observed in sintered material originating from NbC powder converted from Nb₂O₅ by carbo-thermal reduction.

Introduction

Wear is defined as the irreversible, gradual and progressive loss of material due to the relative motion between the active body and a counterbody. Several basic principles can be involved in removing material from the surface: material can be disintegrated (fatigue) and detached mechanically (ploughing) or by tribo-chemical reactions occurring at the surface. Wear resistance of a material is a system property and not an inherent material property. It is controlled by a multitude of parameters consisting of material and counterbody properties, contact stresses and the environment.

The significant downtime and cost implications related to wear of components in earth moving and mining equipment, as well as in the materials processing industry, represents a continual challenge to material development. Components designed for sacrificial wear must possess, first of all, adequate abrasion resistance associated with impact loads and corrosive media. The requirement of good abrasion resistance, in combination with good toughness, is generally rather restrictive since, unfortunately, materials hard enough to resist wear are often found to be brittle. Therefore, a composite material, embedding the hard phase in a softer but ductile matrix, has the potential of offering a good property compromise. Such materials, depending on the combination of hard phase and matrix type, as well as their volume fractions, are known as hard metals, cermets or metal matrix composites (MMC).

Carbides of the transition metals, represented by groups IVB to VIB in the periodic table of elements, are typically used as hard phases in technical alloys. The hardness of these transition metal carbides is superior to that of most minerals, Figure 1. Metals with a high melting point, such as cobalt, nickel or molybdenum, can serve as ductile binders for hard metals and cermets. Casting alloys containing dispersed hard phase particles provide the platform for a wide variety of metal matrix composites.

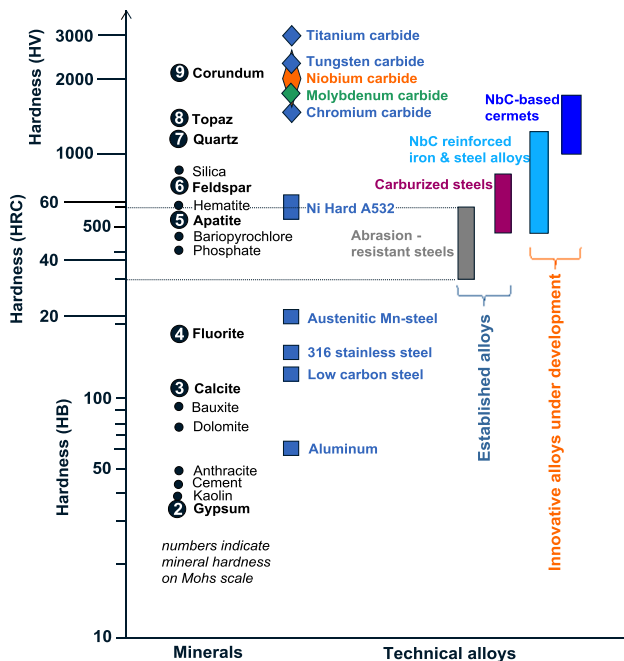


Figure 1. Hardness of mineral species compared to hardness of technical alloys.

In the arena of hard metals, tungsten carbide (WC) has been the dominating hard phase for decades. Other transition metal carbides, such as those of chromium, vanadium and titanium, are also well established. However, surprisingly, little attention has been paid to NbC. Nevertheless, NbC has been occasionally used as a minority phase in hard metals, castings and tool steels. In these applications it serves either as a grain refiner or as a hard phase helping to enhance wear resistance, limit grain growth and enhance hot hardness. While data on the fundamental properties of pure NbC have been reported [1], reliable information on its tribological performance was not readily available. Recently, it was shown however, that pure NbC and metal bonded NbC, have a pronounced wear resistance under dry sliding when compared to other monolithic ceramics and carbides [2].

Hard metals based on tungsten carbide are mainly produced by a powder metallurgy (PM) based sintering process due to the high solubility of the hard phase in alloys and in their melts, as well as the mismatch in density between the molten binder alloys and the hard phase. Cobalt and nickel primarily serve as the binder phase. The powder metallurgical route, however, limits the size of components, whereas a casting process would allow the fabrication of much bigger components. Alternatively, hard metals can be deposited as clad layers or thermally sprayed coatings onto a softer substrate material. Two well known properties of NbC are its similar

density to and its low solubility in iron. The density of NbC is very close to that of iron so that the mismatch in densities, depending on the carbide stoichiometry and iron alloy composition, is less than 10 percent. Its solubility in iron-based alloys, as well as in nickel and cobalt, is particularly small. Utilizing these two properties makes alternative production routes feasible for producing components as compared to PM-based processing routes.

Material health and safety issues with established hard metals have recently caused significant concerns. The European “Registration, Evaluation, Authorisation and Restriction of Chemical substances programme”, also known under the acronym REACH [3], currently classifies cobalt as very toxic for human health. Furthermore, the U.S. National Toxicology Program, (NTP) [4], states that tungsten carbide-cobalt hard metal dust was shown to be more toxic in combination than either pure cobalt or tungsten carbide alone. So far, nickel powders do not have the same hazardous classification as cobalt powders. Niobium, on the contrary, is known to be one of the most biocompatible metals. No particular hazards or critical notifications for its oxide (Nb₂O₅) and carbide (NbC) were filed in the framework of REACH.

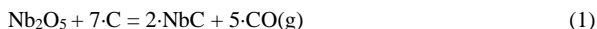
Based on the considerations outlined above, CBMM initiated an extensive research and development program with the aim of exploring the potential of NbC-based hard metals and alloys. The following specific activities have been defined within the program:

- Production and property characterization of pure NbC and its sub-stoichiometric variants (NbC_{1-x}), including consideration of the effect of particle size;
- Analysis of various binder materials and processing routes for NbC-based hard metals and characterization of their microstructure, mechanical properties and performance;
- Exploration of processing routes for NbC-based MMC materials, as well as NbC particle reinforced castings and their performance;
- Characterization and benchmarking of the tribological property profile of such NbC-based materials;
- Field trials with components made from such NbC-based materials in various applications.

In the present paper several results emanating from this ongoing program are presented with particular attention to the tribological property profile of NbC and NbC-based materials.

Methods of NbC Synthesis

NbC can be synthesized by various practical methods, of which three are considered here. One method is the carbo-thermal reduction of pure niobium oxide (Nb₂O₅) at elevated temperature (>800 °C) by the solid-state reaction:



Reaction (1) does not represent the actual steady state reaction, since the reduction process is controlled by a gas-solid phase reaction (2) involving the so-called Boudouard reaction (3) as an intermediate step:





Thermodynamic data indicate that reaction (2) is feasible at temperatures higher than 1000 °C. However, experiments indicated that for a complete conversion of Nb₂O₅ to oxide-free NbC, reaction temperatures of at least 1200 °C must be applied. Since NbC oxidizes rapidly at temperatures above 480 °C the reaction atmosphere must be oxygen-free. An inert and reducing atmosphere of 95%N₂ + 5%H₂ was found to be practicable.

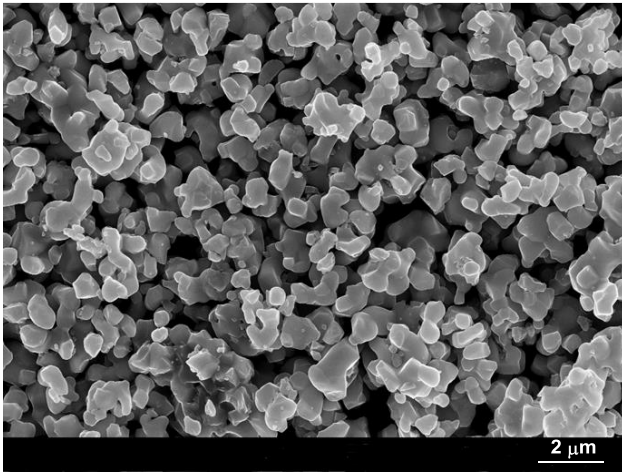


Figure 2. Morphology of NbC crystallites obtained by carbo-thermal reduction of CBMM's high purity Nb₂O₅ powder (de-agglomerated).

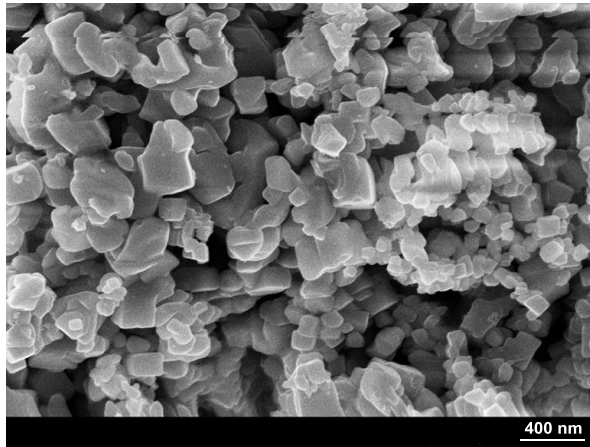


Figure 3. Agglomerated NbC crystallites after carbo-thermal reduction of CBMM's high purity Nb₂O₅ (used for NbC_{0.88}-12Co (H1)).

CBMM has a substantial production capacity for Nb₂O₅ powder that could be readily used in the above described process. Industrial trials utilizing converters that have been previously used for tungsten carbide synthesis demonstrated that stoichiometric NbC could be produced in a one-step carbo-thermal reduction, with high productivity. Thermal carbon black serves as the carbon supply in this process. Representative NbC powders have been synthesized from CBMM Nb₂O₅ powder, using the carbo-thermal reduction process described above, at two industrial powder manufacturers. The primary grain size of the NbC crystallites is in the sub-micron range (100 – 600 nm) reflecting the original oxide crystallite size, Figure 2. The NbC crystallites are agglomerated to larger particles, Figure 3, which can be broken down by an appropriate milling process after carbo-thermal reduction. XRD analysis indicated that these powders consisted of pure NbC, ie. without traces of residual oxides or free carbon.

A second method of producing NbC is by adding ferroniobium to an iron melt containing a substantial amount of carbon. Primary NbC is then precipitated as a solid phase in the liquid metal due to the very low solubility of NbC in iron. At the solidification temperature for eutectic iron (Fe-4.3%C), only around 0.1%Nb is soluble. At usual casting temperatures, the soluble amount of niobium increases to approximately 0.5%, suggesting that NbC particle reinforced iron alloys and MMCs can be produced directly by such in-situ carbide formation. A problem known to occur with this procedure is that in-situ formed carbide particles can grow to a large size with a branched morphology, thus having a detrimental effect on the toughness of the material [5]. On the other hand, large sized hard phases are beneficial in resisting severe abrasion.

As an alternative, CBMM developed an innovative ferroalloy containing a high amount of primary NbC, comprising a controlled size and compact morphology. The production route is based on the standard aluminothermic reduction process utilized for ferroniobium production.

Yet, by adding a carbon source directly to this process, primary precipitation of NbC occurs into an iron matrix instead of forming FeNb intermetallic phases, Figure 4. The carbide particles being formed in this process have sizes in the range of 10 to 50 μm and are of cubic morphology, Figure 5. At the current development stage, the volume fraction of NbC phase embedded in an iron matrix is around 60 percent. This ferroalloy can be directly added to an iron melt for producing iron-based alloys containing a lower volume fraction of dispersed carbide particles. On the other hand, the Fe-NbC ferroalloy, in particular after further increasing the carbide volume fraction, can serve as a source of pure carbide supply (melt grown NbC). In this process, the iron matrix is dissolved from the ferroalloy by a leaching process using either hydrochloric or sulfuric acid, Figure 5.

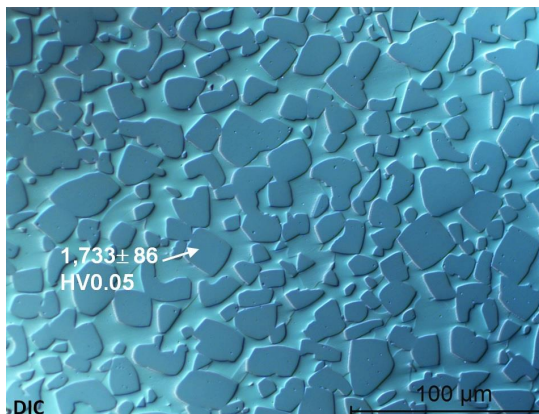


Figure 4. NbC particles formed by primary precipitation in a carbon-alloyed iron melt.

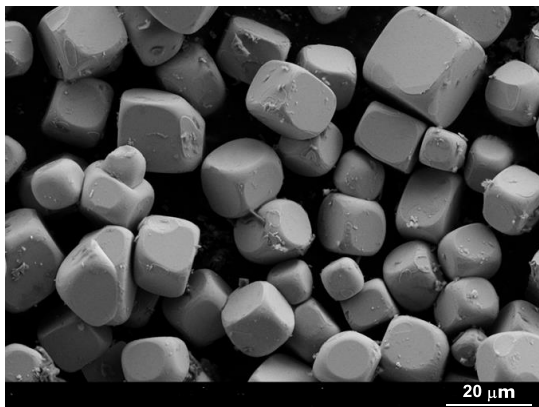


Figure 5. NbC particles precipitated in liquid iron after chemical leaching by sulfuric acid.

Basic Properties of NbC

The use of NbC as a hard material is much less established than that of tungsten carbide. Nevertheless, its physical and chemical properties indicate the outstanding potential of NbC for applications where currently tungsten carbide is being used as the standard material. Table I shows some of the key physical properties referring to room temperature measurements of stoichiometric NbC in comparison to those of tungsten carbide as published in the literature [1]. The melting temperature of NbC is particularly high, which is expected to limit thermal softening, as well as the tendency for adhesive wear. Data obtained by Kelly et al. [6] indicated that the yield strength of NbC at temperatures above 1000 °C is substantially higher than that of WC. The density of NbC is only about half that of WC. This means that for producing a given component only half the mass of carbide is needed, making the use of NbC potentially economically attractive. In dynamic applications where high accelerations and speeds are involved, the reduced mass results in lower inertia and kinetic energy. Since the density of NbC is very close to that of iron, gravity segregation should be rather low when dispersing solid NbC particles in melts of iron-based alloys. This, likewise, applies for spin casting processes where higher density particles segregate outwards and lighter density particles segregate inwards.

The Young's modulus of NbC is one of the highest amongst the refractory metal carbides, yet lower than that of WC. Hence, components made with NbC will show a somewhat higher elastic deflection under mechanical loading, compared to WC. On the other hand, contact stresses under a given load will be lower in NbC. Thermal stresses induced between NbC and metallic binder alloys can also be expected to be lower than for WC. This is because of the larger coefficient of thermal expansion which is closer to that of typical metallic binders, as well as to the lower Young's modulus of NbC.

Due to its metallic character, NbC has relatively good thermal and electrical conductivity. Its thermal conductivity increases at elevated temperatures. Frictional heat generated in tribological contacts can thus be efficiently conducted away. The reasonably good electrical conductivity allows processing of NbC by, for example, electrical discharge machining (EDM). It also helps avoid the build-up of substantial static electricity in tribo-contacts with electrical insulators, such as for instance, polymer-based composites.

Table I. Comparison of Basic Physical Properties of Niobium and Tungsten Carbide
Published in the Literature [1]

| | Melting point (°C) | Density (kg/m ³) | Young's modulus (GPa) | Shear modulus (GPa) | Vickers hardness (GPa) | CTE (ppm/K) | Thermal conductivity (W/m.K) | Specific heat (J/g.K) | Electrical resistivity (μΩ-cm) |
|------------|--------------------|------------------------------|-----------------------|---------------------|------------------------|-------------|------------------------------|-----------------------|--------------------------------|
| NbC | 3,520 | 7,780 | 380-480 | 214 | 17-22 | 6.6 | 14 | 0.351 | 35 |
| WC | 2,870 | 15,630 | 620-720 | 262 | 24-30 | 5.5 | 84 | 0.203 | 20 |

One of the most crucial properties with respect to wear resistant applications is the material hardness. From literature data and current experience, it is evident that the hardness of stoichiometric NbC is below that of tungsten carbide, Table I. However, its hardness is still far superior to most minerals and technical alloys, Figure 1, so that sufficient resistance against abrasive wear in such tribo-contacts should be available. On the other hand, finishing operations when manufacturing NbC tools, are expected to be easier than those for tungsten carbide tools.

The exact hardness value of these carbides is influenced by several parameters, such as the level of porosity, indentation load [7] and temperature [8,9]. An increase in each of these parameters results in a decrease of the measured hardness value. Considering the temperature dependence of hardness, a two-stage behavior can be observed. In the lower temperature range, hardness decreases moderately with increasing temperature. In the higher temperature range, this decrease becomes significantly steeper. The transition between the two regimes occurs in the temperature interval of 500-800 °C for WC [8]. NbC exhibits this transition at a higher temperature interval at around 900 °C [10]. This can result in a higher hot-hardness of NbC as compared to WC, which is of relevance for metal cutting operations. Recent hot-hardness measurements on NbC- and WC-based materials confirm this trend [11].

Contrary to WC, NbC can exist as sub-carbides, like Nb_6C_5 or Nb_4C_3 , over a wide range of carbon stoichiometry, according to the Nb-C binary phase diagram shown in Figure 6 [12]. Carbon deficiency in the range of NbC to $\text{NbC}_{0.8}$ has a significant influence on the physical properties of the material. With increasing carbon deficiency in that range, elastic moduli [13], lattice constant [14], density [14], heat capacity [15] and magnetic susceptibility [16] decrease. Yet, hardness strongly increases with increasing carbon deficiency in NbC, as shown in Figure 7, [17] exceeding the hardness level of WC. In summary, the properties of NbC can be tailored by adjusting the carbon deficiency in the compound.

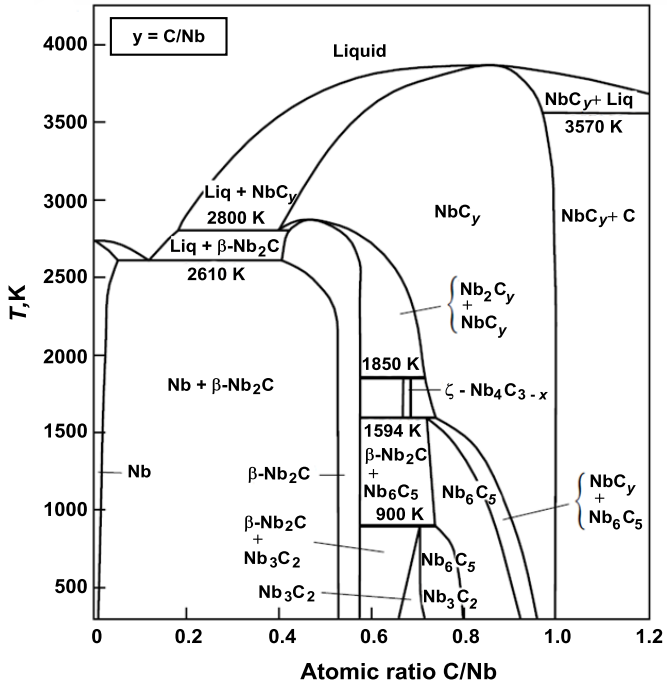


Figure 6. Binary Nb-C phase diagram indicating the existence of various sub-carbides [12].

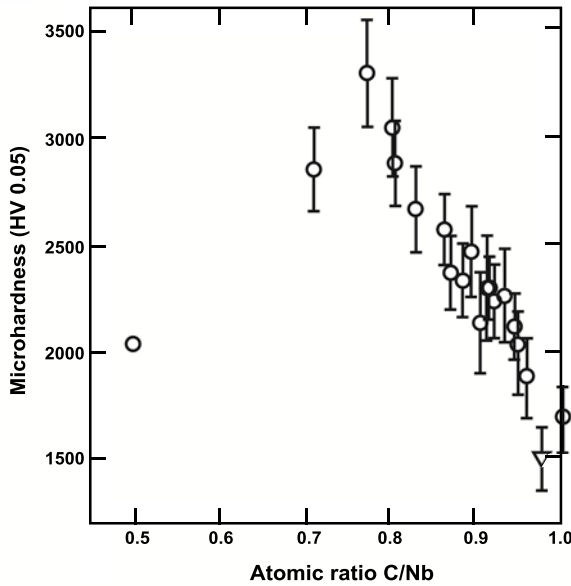


Figure 7. Microhardness of NbC as a function of C/Nb ratio in the compound [17].

The solubility of a carbide compound in a contacting metal at high temperature is a very important property with respect to the wear performance of the carbide in such hot tribo-contacts with that metal. The solubility of NbC in metals, such as iron, cobalt or nickel has been reported to be very low in contrast to the rather high solubility of tungsten carbides in these metals [18,19]. The solubility of NbC in austenite is shown in Figure 8, based on an established solubility product [20]. In this plot, equilibrium solubility isotherms of niobium and carbon are indicated for various temperatures. Only when the carbon content is extremely low, does niobium have a reasonably good solubility. In a hot tribo-contact scenario, NbC should dissociate into solute niobium and carbon according to the stoichiometric ratio. The intersection of the stoichiometry line with the solubility isotherm defines the maximum solubility of NbC in a tribo-contact situation at that specific temperature. Carbon, already present in an iron-based alloy, further limits the solubility of NbC to extremely low values. The solubility of tungsten carbide in austenite is several orders of magnitude larger than that of NbC [21]. Accordingly, WC-based components bear the risk of readily dissolving into iron-based alloys in hot tribo-contacts, whereas NbC-based tools will suffer very limited material loss by dissolution into the chips under the same conditions. Consequently, a protective coating, blocking the dissolution, is not necessary on NbC components.

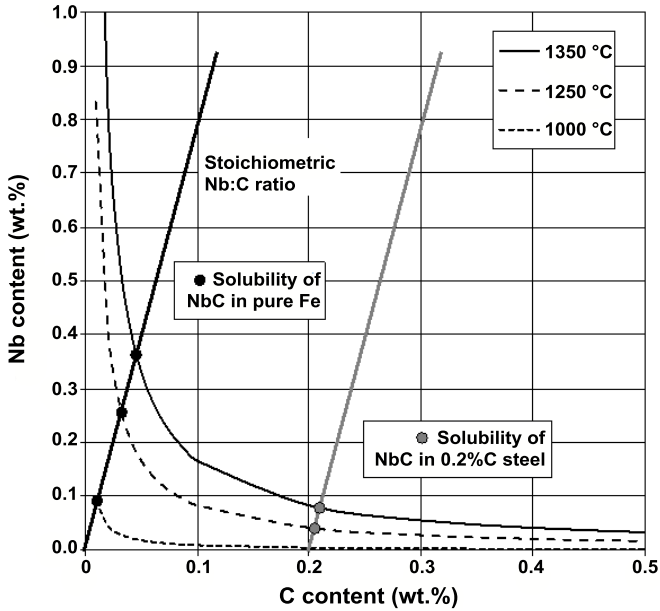


Figure 8. Solubility of NbC in austenite based on the solubility product $\log [\text{Nb}][\text{C}] = 3.4 - 7920/T$ where T is the absolute temperature; [Nb] and [C] are concentrations in wt.% [20].

Another chemical reaction that can lead to material loss in tribo-contacts is tribo-chemical or oxidative wear. The frictional work dissipated in the micro-asperities (hot spot temperatures) enhances this reaction with the surrounding atmosphere. Oxide layers form on the surfaces of the friction partners and are worn away as a result of relative movements between the bodies leaving oxide debris in, or close to, the wear track. NbC oxidizes when exposed to air at increased temperature, forming Nb_2O_5 and other block structure oxides ($\text{Nb}_{3n+1}\text{O}_{8n-2}$). The rate of oxidation increases significantly above 500 °C. However, the oxide does not form a passivating and protective layer. Nb_2O_5 and its polymorphs are also generated by tribo-oxidation on NbC and influence the friction and wear behavior, as well as having a microhardness in the range 500-650 HV 0.2. Tungsten carbide easily oxidizes, even in low energy tribo-contacts operated in an ambient environment [22], forming amorphous tungsten oxide debris, which tends to sublime at temperatures above 800 °C. In contrast, Nb_2O_5 , owing to its melting point of 1522 °C, forms a stable reaction layer on NbC.

Definition of NbC-based Materials for Tribological Performance Testing

Pure NbC

Although NbC is not likely to be used binderless for technical applications, it is still important to characterize the tribological performance of the pure material without having side effects from other constituents. Therefore, NbC was produced from a commercially available high purity niobium pentoxide (Nb_2O_5) powder (CBMM grade HP311) by the process described above [2]. The granulometry of the NbC powder was $d_{50} = 3.86 \mu\text{m}$ and $d_{90} = 18.12 \mu\text{m}$. This powder was then hot-pressed by Fraunhofer IKTS (Dresden, Germany) without the use of sintering additives at $2150 \text{ }^\circ\text{C}$ under 50 MPa (4 h, 10 K/min) reaching an average density of 7.68 g/cm^3 . The microhardness of the sintered NbC averaged $1681 \pm 92 \text{ HV } 0.2$.

NbC-Co and NbC-Fe₃Al Hard Metals

Since pure NbC is rather brittle, the addition of a metallic binder is necessary for use in technical applications. One of the most established binders in hard metals is cobalt. Consequently, it was chosen as a binder for NbC hard metals using 8 vol.% and 12 vol.%, respectively. The powders and the process conditions for the NbC bearing hard metals are given in references [2,24]. Some important details are as follows. The cobalt bonded NbC hard metals were spark plasma sintered (SPS) using a stoichiometric $\text{NbC}_{1.0}$ and commercially available NbC powder (Treibacher 100, Austria; Fisher Sub-Sieve Size (FSSS) = $1.18 \mu\text{m}$) and cobalt powder (Umicore grade Co-HMP, Belgium; FSSS = $0.55 \mu\text{m}$). The measured powder raw density was 7.60 g/cm^3 . NbC grades made from this $\text{NbC}_{1.0}$ powder (denoted as “T” in the following) had a granulometry of $d_{50} = 1.72 \mu\text{m}$ and $d_{90} = 3.78 \mu\text{m}$ using the Fraunhofer calculation model.

A second, sub-stoichiometric powder was used for producing $\text{NbC}_{0.88}\text{-}12\text{Co}$ (denoted in the diagrams as “H1” in the following). Combustion analysis revealed a C:Nb ratio of 0.88 for this NbC powder. The powder had a granulometry of $d_{50} = 1.47 \mu\text{m}$ and $d_{90} = 7.42 \mu\text{m}$ (using optical data of SiC and MIE-model). The measured powder raw density was 7.37 g/cm^3 with a carbon content of $9.95 \pm 0.28 \text{ wt.}\%$ or $\text{NbC}_{0.87}$, thus being lower than that of stoichiometric NbC.

The granulometric values of the currently used NbC powders do not reflect the sub-micron size of the primary NbC particles, as these tend to agglomerate, Figure 9. However, methods of degglomerating such NbC powders are under development.

The University of Leuven (KU Leuven, Belgium) densified the powder mixtures of cobalt or Fe_3Al bonded NbCs to discs of $\varnothing = 56 \text{ mm}$ by spark plasma sintering (SPS, type HP D 25/1, FCT Systeme, Germany). A pulsed electric current was applied with pulse/pause duration of 10/5 ms throughout all the experiments. The powder mixture was poured into a cylindrical graphite die with an outer diameter of 56 mm and sintered for four minutes at $1,280/1,300 \text{ }^\circ\text{C}$. The conditions of densification are detailed in references [2,23,24] and summarized in Table II. Graphite paper inserts were used to separate the graphite die/punch set-up and the powder mixture.

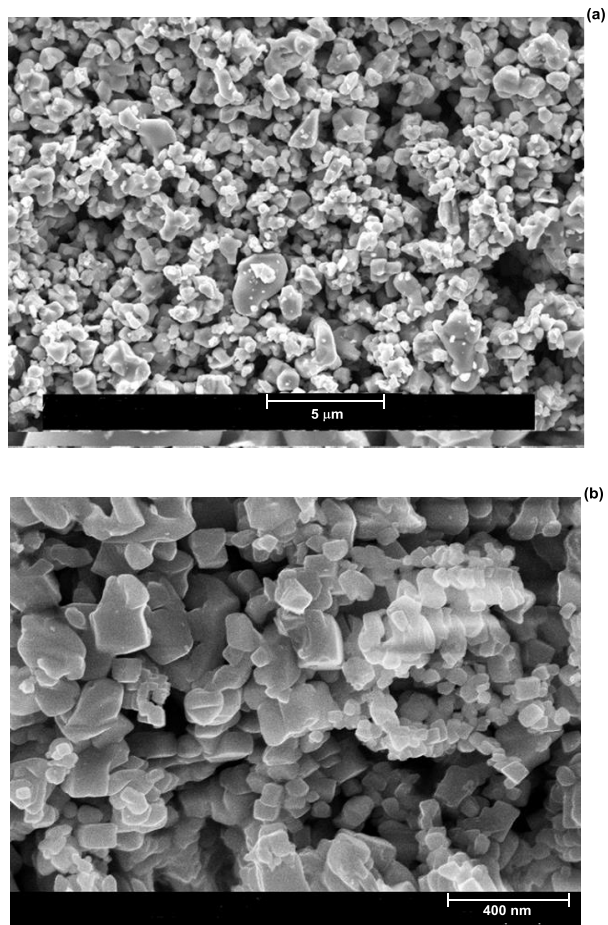


Figure 9. Morphology of NbC powders; (a) Treibacher NbC100, (b) NbC H1.

The intermetallic compound Fe_3Al represents an attractive alternative to cobalt, because it is composed of low cost elements and undergoes no phase transitions, except order-disorder transformations. N_2 -atomized Fe_3Al powder (-325 mesh obtained by AGH University of Science and Technology, Krakow, Poland) was used for producing the NbC-12 Fe_3Al samples via the same sintering process as was applied for the NbC-Co hard metal. Table II compiles the mechanical properties of all the NbC-based hard metals tested.

Table II. Properties of NbC-based Hard Metals

| Property | Temperature | Method | HP-NbC | NbC-8Co | NbC-12Co | NbC-12Fe ₃ Al | NbC _{0.88} -12Co |
|---|-------------|--------------|---------------------|----------------------------------|----------------------------------|--|---------------------------|
| Powder | - | - | NbC (AO7132) | NbC100 | NbC100 | NbC100 | NbC _{0.88} (H1) |
| Densification | - | - | HP | SPS | SPS | SPS | SPS |
| Densification temperature (°C), time and pressure | - | - | 2,150 (4 h; 50 MPa) | 1,280 (4 min; 30 MPa) | 1,280 (4 min; 30 MPa) | 1,300 (4 min; 30 MPa) | 1,285 (6 min; 30 MPa) |
| Phase composition | | XRD | NbC | NbC + fcc-Co + Nb ₂ C | NbC + fcc-Co + Nb ₂ C | NbC + Fe ₃ Al + (Al ₂ O ₃) | NbC + fcc-Co |
| | | EBSD | | NbC | NbC | NbC + Fe ₃ Al | NbC + Co |
| Binder (Vol.-%) | | - | 0 | 8 | 12 | 12 | 12 |
| Density (g/cm ³) | RT | | 7.67 | 7.78 | 7.76 | 7.50 | 7.62 |
| Elastic modulus (GPa) | RT | ASTM E1875 | 477 | 443 | 437 | 447 | 406 |
| | 1000 °C | | - | 382 | 368 | 379 | 341 |
| Bulk modulus (GPa) | RT | | - | 181 | 177.5 | 183.5 | 164 |
| Poisson ratio | RT | | - | 0.22 | 0.225 | 0.22 | 0.235 |
| 4-point bending strength (MPa) | RT | DIN EN 843-1 | 353 ± 42 | 742 ± 180 | 1,215 ± 197 | 822 ± 117 | 1,005 ± 158 |
| Microhardness | HV 0.2 | RT | 1,681 ± 92 | 1,451 ± 54 | 1,453 ± 41 | 1,632 ± 50 | 1,765 ± 130 |
| | HV 0.5 | 700 °C | 539 ± 20 | - | 734 ± 60 | 553 ± 30 | - |
| Wear rate k _v (0.1 → 10 m/s) (10 ⁻⁶ mm ³ /N·m) | RT | ISO 20808 | 0.2 → 0.5 | 1.8 → 0.6 | 3.9 → 0.4 → 1.0 | 3 → 0.4 → 3 | 2 → 0.7 |
| | 400 °C | | 0.7 → 0.5 | 2.5 → 1.0 | 8.0 → 1.0 | 10 → 1.0 | 2 → 0.5 → 2 |
| P.V value (0.1 → 10 m/s) (MPa·m/s) | RT | | 2 → 90 | 1 → 80 | 1 → >100 | 1 → 40 | 1 → 70 |
| | 400 °C | | 0.3 → 50 | 0.25 → 40 | 0.5 → 75 | 0.5 → 32 | 3 → 45 |

HP = Hot pressing; SPS = Spark plasma sintering

Metal Matrix Composites and Hard Metals by Casting

Metal matrix composites (MMCs), based on an iron-based alloy matrix reinforced by NbC or mixed NbCs, have the potential of greatly enhancing the wear resistance of parts subjected to dry sliding and abrasive wear occurring in closed and open tribo-systems [25-27]. The metallic binder in sintered hard metals ranges from >5 vol.% up to 25 vol.%. Castings can basically cover a much wider range of NbC hard phase contents from >5 vol.% up to 75 vol.%. The Fe-NbC ferroalloy, Figure 4, produced by CBMM as such is in fact an MMC. In the current investigation Fe₃Al-NbC MMC was considered, thus allowing a comparison with NbC-Fe₃Al hard metal. This MMC can be produced in the same metallurgical process used for Fe-NbC ferroalloy. Iron-aluminide formation is an exothermic reaction that may be integrated into the alumino-thermic reaction typically used for reducing oxides in the synthesis of Fe-NbC alloys. The formation of

Fe₃Al in the alumino-thermic reaction is achieved by adding a defined excess of aluminum. The resulting Fe₃Al-NbC ferroalloy can be remelted, eg. in an induction furnace, and further be purified using a slag prior to casting [28].

The values for microhardness and elastic modulus of metallurgically synthesized NbC, shown in Table III, are comparable to those of NbC generated by the powder metallurgical route. The elastic modulus of the intermetallic Fe₃Al matrix is similar to that of conventional iron alloys. Microprobe and EDX analysis of the NbC particles in the Fe₃Al-NbC MMC revealed a sub-stoichiometric composition of NbC_{0.70}, whereas combustion analysis (ELTRA CS-800) of leached hard phase indicated NbC_{0.94}. The mismatches underline the necessity to develop appropriate analytical procedures for NbC bearing materials. Based on the phase diagram [12], such a stoichiometry may be composed of Nb₄C₃, Nb₃C₂ as well as mixtures of these, or of ζ-Nb₄C_{3-x}, Figure 6.

Table III. Properties of a Fe₃Al-NbC Metal Matrix Composite

| Property | Intermetallic phase by XRD and EBSD (area-% by EBSD), balance NbC | Volume fraction hard phase (Vol.-% NbC) | Stoichiometry (by combustion analysis of leached grains) | Microhardness* (GPa) | | | E modulus (GPa) | | Microhardness (MPa) | | | |
|---------------------------------|---|---|--|-----------------------------|-------------------|-----------|-----------------|----------|---------------------|-------------------|-------------|-------------|
| | | | | NbC | Metallic matrices | | NbC | Matrix | NbC | Metallic matrices | | |
| Method | - | ASTM E562-11 | NbC _{0.94} [#] | Nano-indentor* XP (Egilent) | | | | | | Vickers HV 0.05 | | |
| Fe ₃ Al-NbC (AD5258) | 19% Fe ₃ Al, 19% Fe ₃ AlC | 54.0 (61.3 EBSD, 75% XRD) | | | 17.2 ± 0.8 | 6.3 ± 0.4 | 3.6 ± 0.2 | 362 ± 16 | 216 ± 14 | 17,330 ± 863 | 3,610 ± 254 | 6,340 ± 437 |

* Berkovich Indenter (CSM, 45 Hz, 2 nm), hardness for a penetration depth of 500 nm, values according to ISO 14577;

[#] 10.8 ± 0.4 wt.-% C or NbC_{0.94} by combustion analysis; whereas microprobe spot analysis of NbC grains revealed NbC_{0.70}.

Microstructural Characterization

The microstructure of pure NbC analyzed by FESEM (Field Emission SEM) is shown in Figure 10(a). The microstructure reveals dense sintering along the NbC grain boundaries. The microhardness averaged 1681 ± 92 HV 0.2. The HP-NbC did not, however, reach the theoretical density due to a reaction between the natural Nb₂O₅, present on the surfaces of the NbC grains, with NbC and significant grain growth which occurred as a consequence of the very high hot-pressing temperatures. The dark spots visible in Figure 10(a) are pores of 1–3 μm in size and are responsible for the reduced microhardness as compared to literature data. Vickers indentations made into the sintered carbide lead to the development of cracks particularly originating from the indent corners. The pronounced crack formation is indicative of a rather brittle material, Figure 10(b).

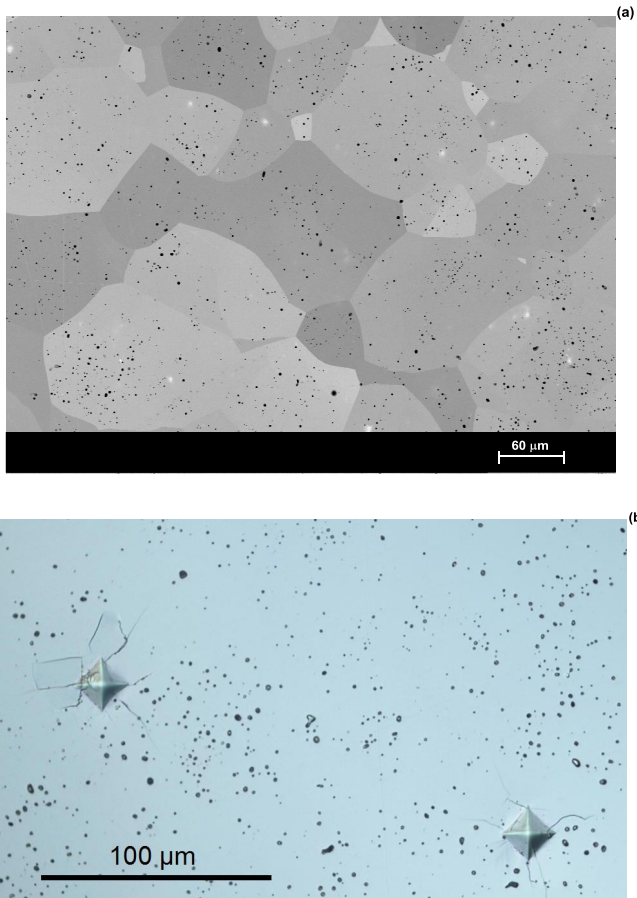


Figure 10. (a) Microstructure of pure NbC showing porosity inside the grains, (b) Vickers indents developing cracks at the corners (indentation load 5 kg).

The FESEM image taken with an SE detector and the SEM image of the metal-bonded NbC hard metals, Figure 11, revealed larger islands (situated deeper due to preparation) of the different metallic binders representing local inhomogeneity of the binder distribution. All metal-bonded NbC grades showed porosity-free NbC grains contrary to the pure NbC samples. Vickers indents made into the metal-bonded NbC samples led to less intense cracking as compared to pure NbC, as shown in Figure 12. This is indicative of an increased toughness and is likely to be due to the metal binder.

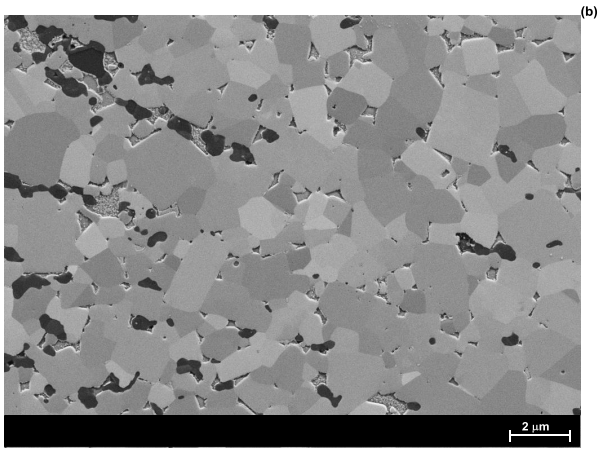
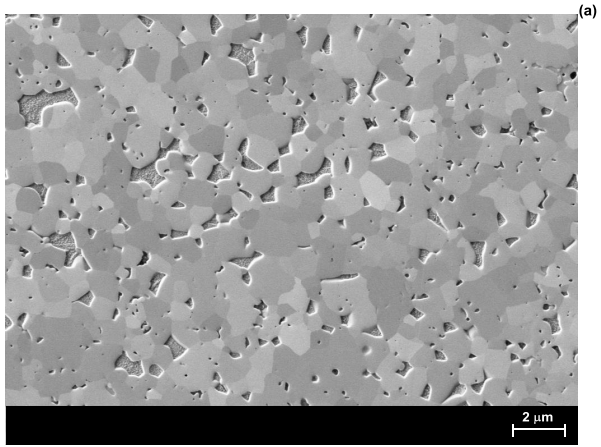


Figure 11. (a) Microstructure of NbC-8Co, (b) of NbC-12Fe₃Al.

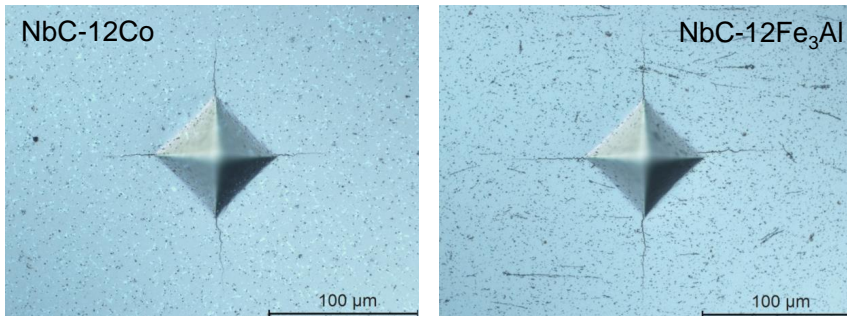


Figure 12. Microstructure of NbC (T) hard metal grades with 12% metal binder. Indents were made with a load of 5 kg.

The microhardness of pure and metal-bonded NbC is shown as a function of indentation load in Figure 13. Pure NbC, ie. without metal binder achieves, as expected, the highest hardness values of around 1900 HV 0.2 without showing a great influence of the process (hot-pressing versus SPS). The hardness steeply declines with increasing indentation load to a stable level of around 1400 HV. The strong load influence on the microhardness of NbC is well established in the literature and similarly applies for WC, W₂C, V₈C₇ and Mo₂C [13]. The effect is due to plastic deformation via dislocation movements at room temperature under indentation loading. In cubic carbides, the motion of dislocations occurs along the {111} planes in the direction <110>.

In the cobalt bonded NbC hard metals, the average microhardness is 1412 ± 51 HV 0.2 for NbC-8Co (T). Despite the increased amount of binder phase in NbC-12Co (T), the average microhardness is similar at 1410 ± 13 HV 0.2. Overall, the microhardnesses of the cobalt bonded NbC from the stoichiometric NbC “T” powder is less sensitive to load. The microhardness of NbC_{0.88}-12Co (H1) hard metal is 1712 ± 130 HV 0.2 which is clearly superior to that of the hard metals containing stoichiometric NbC. This is in agreement with the behavior shown in Figure 7 [17]. A second factor causing the higher hardness may be the finer particle size of the H1 powder. The hardness of the sub-stoichiometric NbC_{0.88}-12Co (H1) is also less sensitive to the indentation load, dropping to around 1500 HV 5. NbC_{0.88}-12Co (H1) at loads above 1 kg is the hardest NbC grade, Figure 13.

The microhardness of NbC-12Fe₃Al reaches values of 1632 ± 50 HV 0.2 and is considerably higher than that of cobalt bonded NbC, even using the same stoichiometric NbC “T” powder. Furthermore, NbC-12Fe₃Al hard metal had a significantly higher hardness than the other metal bonded NbC grades at indentation loads over 1 kg, as seen in Figure 13. The microhardness of NbC can be tailored through the stoichiometry and the type of binder.

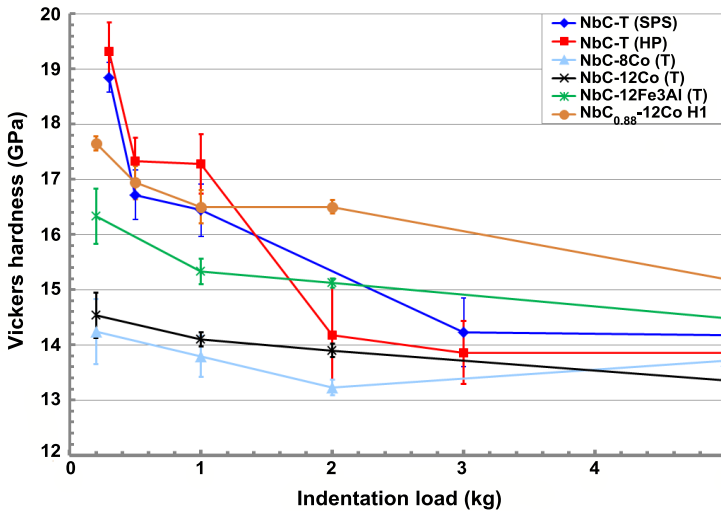


Figure 13. Microhardness as function of indentation load for pure and metal bonded NbC hard metal grades.

The phase composition of the $\text{Fe}_3\text{Al-NbC}$ MMC was determined by EBSD to be 19.5% Fe_3Al and 19.5% Fe_3AlC with the balance being 61%NbC hard phase. This agrees quite well with the hard phase content of 54% as determined by ASTM E562-11 and 75% measured by X-Ray Diffraction (XRD). The XRD measurement also confirmed the presence of the three crystalline phases. The procedure for preparing the microstructures is described in detail in reference [28]. The microstructure, Figure 14, shows a rim of $\text{Fe}_3\text{Al(C)}$ surrounding individual NbC particles. More detailed analysis indicated a carbon-enriched interphase zone. This carbon is replenished from NbC and dissolved into the surrounding Fe_3Al matrix. The microhardness of carbon-enriched Fe_3Al phase is significantly higher than that of the Fe_3Al phase. The presence of Fe_3AlC interphase also indicates a metallurgical bonding of NbC to the Fe_3Al matrix, which supports the transmission of tribological shear stresses between hard phase and matrix. Microprobe analysis revealed the C:Nb ratio in the NbC particles to be sub-stoichiometric at around 0.70, compared to the combustion analysis of 0.94 (see Table III).

Vickers indents (HV 0.05) were positioned within the NbC particles of the $\text{Fe}_3\text{Al-NbC}$ MMC, Figure 15. The typical crack pattern found in the nearly stoichiometric NbC particles of the hard metal samples showing cracks originating from the corners of the indent was not observed here. Some shallow cracks are oriented parallel or perpendicular to the sides of the indent. In some indents the material appears to show some plasticity. These features suggest that the sub-stoichiometric NbC grains should have a rather high toughness.

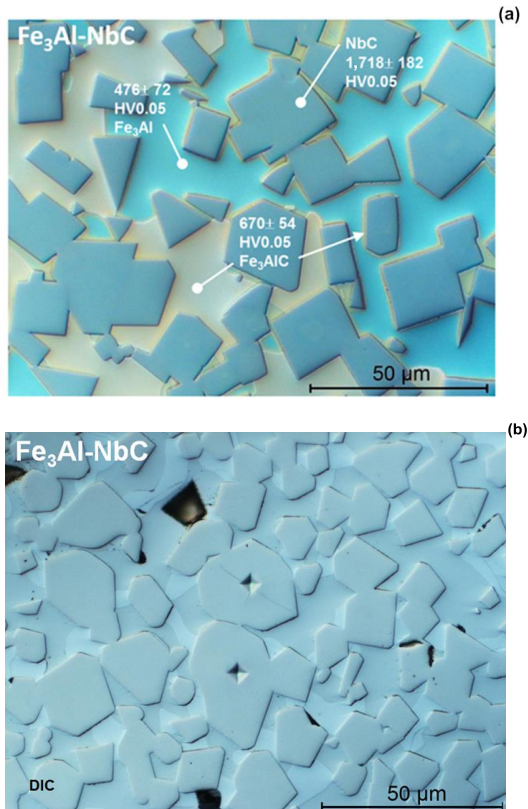


Figure 14. Microstructure and microhardness of the $\text{Fe}_3\text{Al-NbC}$ metal matrix composite; (a) light optical microscopy, (b) LOM of indented NbC grains.

Nano-indentation using a Berkovich indenter revealed an elastic modulus of 362 ± 16 GPa for the melt grown NbC particles. The microhardness for an indentation depth of 500 nm was measured to be 18.8 ± 1.1 GPa, whereas the Vickers microhardness of such NbC particles was determined to be 1718 ± 182 HV 0.05, Table III. The elastic modulus of the $\text{NbC}_{0.88-12}\text{Co}$ (H1) was also 10% lower than for the stoichiometric NbC grades, Table II. Thus, the elastic indentation modulus of sub-stoichiometric NbC is lower than that measured by the resonance method (ASTM E1875) or nano-indentation on stoichiometric NbC grades, Tables II and III, produced by carburization of niobium oxide. In comparison to stoichiometric NbC, having an elastic modulus of 477 GPa, the elastic modulus was reduced to 405 GPa for $\text{NbC}_{0.88}$ (measured by 4-point bending bars) and to ~ 365 GPa for the melt grown NbC (measured by nano-indentation), as can be seen from Table II and Table III.

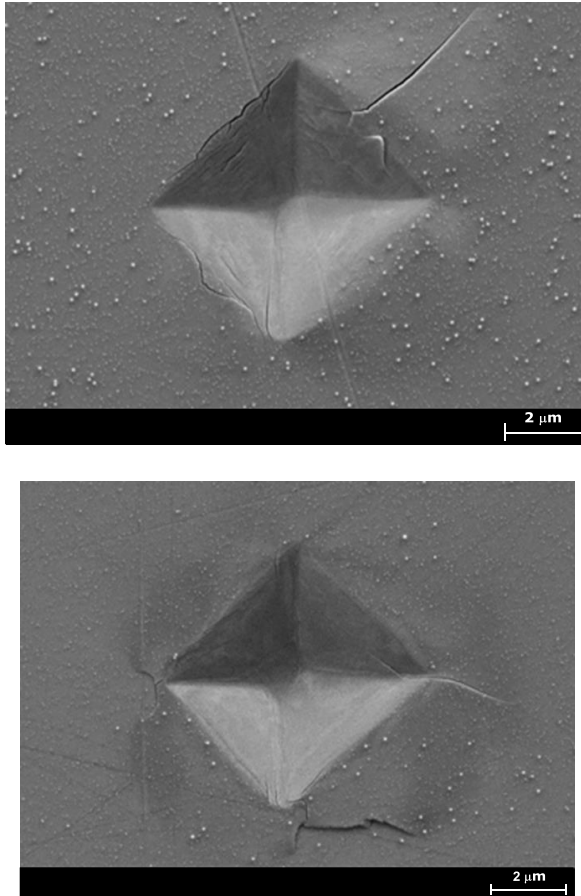


Figure 15. SEM analysis of Vickers indents in melt grown NbC particles of Fe₃Al-NbC MMC material.

Tribological Behavior of NbC-based Hard Materials

Friction and wear are complex system properties depending on many variables. Therefore, the tribological performance of carbides can only be reliably judged using specific tests simulating a defined tribo-contact condition. Such simulations have been performed for many hard materials, however, for NbC, no reliable tribological data could be found in the literature. Consequently, an extensive test program using a wide range of operating conditions has been set up to benchmark pure NbC, as well as NbC-based hard metals and MMCs against other established hard materials

The tribometers used for unidirectional sliding are proprietary developments of BAM and the details are disclosed elsewhere [29]. They comply with ASTM G99 (DIN 50324) and with DIN EN 1071-13:2010. The wear volumes of stationary and rotating specimens were calculated from stylus profilometry and the wear scar diameters were determined by using ASTM D7755-11 or DIN 51834-3. The wear rate k_V is defined as the ratio of volumetric wear to the product of normal load F_N and the sliding distance s . The coefficient of friction (CoF) and the total linear wear of both tribo-partners were recorded continuously. One test per combination of parameters was performed, because the testing philosophy at BAM is to screen over a wide range of operating conditions, rather than doing repeated tests. Repetitions can be done, however, for specific test conditions. The tribological data of WC-, Cr₃C₂- and (Ti,Mo)(C,N)-based materials evaluated under the same test conditions were available from references [30,32,33] for benchmarking.

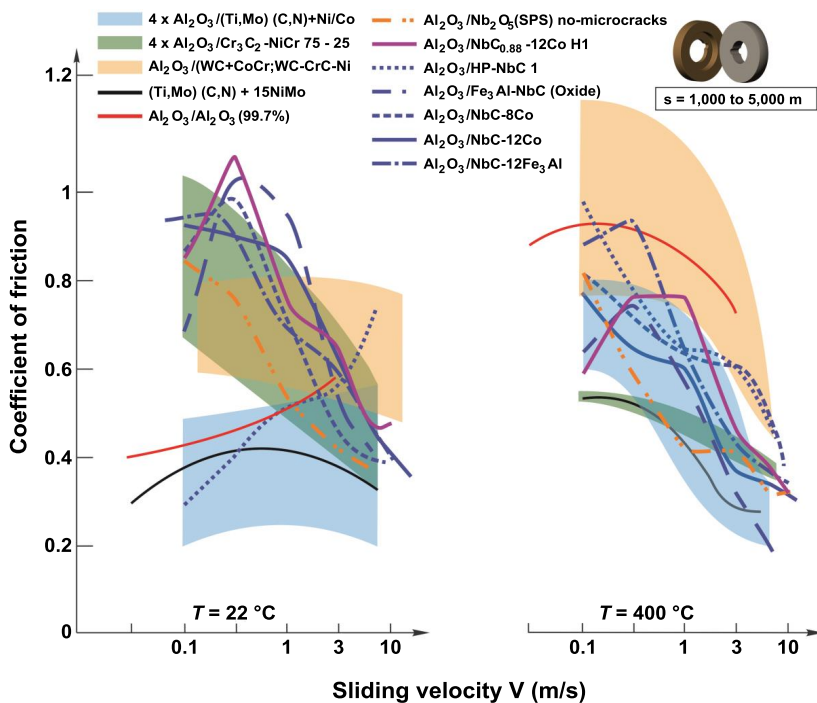


Figure 16. Coefficient of friction of NbC-based hard metals and Fe₃Al-NbC (MMC) compared for different ceramics and hard metals under dry friction at RT and 400 °C.

Unidirectional Sliding (Room Temperature and 400 °C)

Sintered alumina (99.7%) bodies were used as stationary disc shaped toroids (with $R_1 = 21$ mm and $R_2 = 21$ mm) using specimens with polished surfaces ($R_{pk} = 0.019$ mm), which were pressed against the planar surfaces of the rotating NbC-based materials. A normal force of 10 N was applied, resulting in an initial Hertzian contact pressure P_{0max} of approximately 660 MPa. The sliding distance was 5000 meters. Experiments were performed at 23 °C (RT) and 400 °C in air (relative humidity at RT approximately 35%) with sliding speeds of 0.1, 0.3, 1.0, 3.0, 7.5-8.0 and 10-12 m/s. The resolution limit of the wear rate for the rotating specimen corresponds to about 10^{-8} mm³/N·m.

The frictional level of different NbC grades and the Fe₃Al-NbC MMC displayed in Figure 16 compares well with different WC-based or Cr₂C₃-based hard metals or monolithic alumina [30]. At room temperature (RT), the friction of binderless HP-NbC₁ increased with increasing sliding speed having values of around 0.3 at low sliding speeds and reaching a level of 0.8 at high sliding speeds, similar to monolithic alumina, whereas all metal bonded NbCs presented an opposite trend. Friction decreased with increasing sliding speed. It thus qualifies NbC for traction and frictional applications such as clutches or brake rotors rather than for low friction bearings, Figure 16. Metal bonded NbC grades showed an opposite trend to pure HP-NbC as the coefficient of friction decreased with increasing sliding speed at RT, Figure 16 [34]. At low sliding speeds the value can reach unity, while at high sliding speeds it drops to a level of 0.4. This behavior is quite similar to that of Cr₂C₃-based hard metals. The friction behavior of the Fe₃Al-NbC MMC is very similar to that of the NbC-based hard metals.

At 400 °C, the coefficient of friction of all NbC and hard metal grades decreased with increasing sliding speeds above values of approximately 0.2, but values were on average lower as compared to WC grades. The friction of NbC grades at high sliding speeds was lower at 400 °C than at RT. Low friction at high sliding speeds is a favorable property for cutting tools, reducing cutting forces, thus achieving a given cutting performance at reduced machine power.

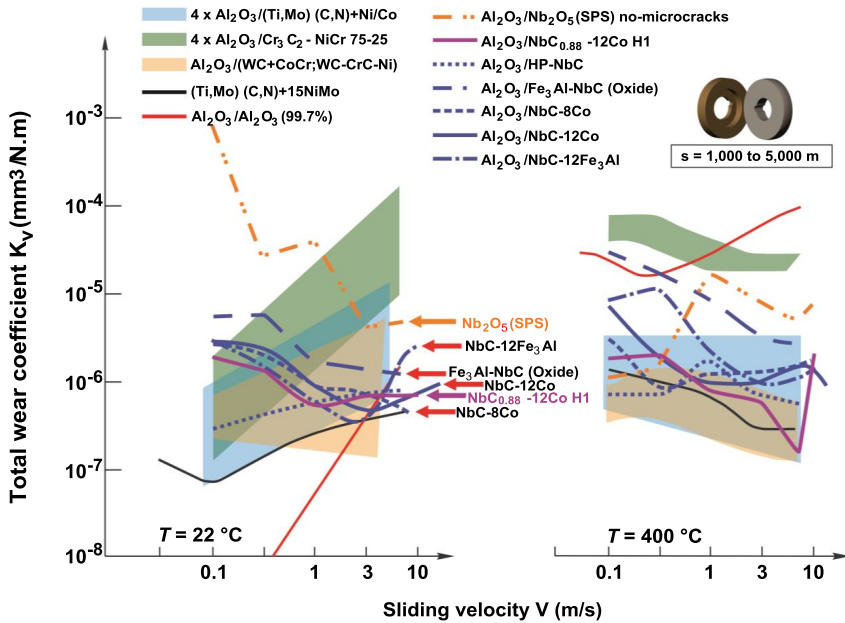


Figure 17. Total wear coefficients of NbC-based hard metals and Fe₃Al-NbC (MMC) compared to different ceramics and hard metals under dry friction at RT and 400 °C.

In comparison to other hard metals, binderless HP-NbC exhibited a particularly high wear resistance especially at RT, which is more or less independent of sliding velocity, Figure 17 [30]. The wear resistance of HP-NbC at RT is one of the highest and compares well with that of self-mating alumina (Al₂O₃): it compares also regarding its evolution with sliding speed. At RT the metal bonded NbC grades displayed a rather constant evolution of the wear rate with increasing sliding speed, Figure 17 [2]. The wear rates of the metal bonded NbC grades decreased with sliding speed by one order of magnitude to low wear rates at high sliding speeds. For a sliding speed of 8 m/s at RT, the wear rate range of $k_v = 4.4 - 7.8 \cdot 10^{-7} \text{ mm}^3/\text{N}\cdot\text{m}$ of the NbC-8Co rotating disc was outstandingly low in comparison to all other ceramics and hard metals. The wear rates of the rotating discs made from NbC-12Co reached values of $k_v = 9.6 \cdot 10^{-7} \text{ mm}^3/\text{N}\cdot\text{m}$ at RT at 12 m/s sliding speed.

At room temperature the wear rates of the Fe₃Al-NbC MMC are slightly higher than those of the NbC-bearing hard metals and decrease with increasing sliding speed, Figure 17. It is also apparent that metallurgically synthesized or sintered NbC bearing materials tribologically compete with WC and Cr₃C₂ bearing hard metals or cermets (Ti,Mo)(C,N), especially at high sliding speeds. It is beneficial for machining applications that coefficients of friction and wear rates decrease with increasing sliding speed.

At 400 °C, the dry sliding wear resistance of tribo-active materials ($Ti_{n-2}Cr_2O_{2n-1}$ -phases, $(Ti,Mo)(C,N)$), HP-NbC and thermally sprayed Cr_2O_3 or WC-based hard metals ranged between 10^{-6} $mm^3/N\cdot m$ and 10^{-7} $mm^3/N\cdot m$ on a level of mixed/boundary lubrication. The wear resistance of HP-NbC under dry sliding is better than that of Cr_3C_2 and better than, or similar to, that of WC-based systems. At 400 °C, the Co-bonded NbC hard metals showed lower wear rates than the Fe₃Al-bonded NbC hard metals and MMC. This can be attributed to the well-known effect of Co_3O_4 formed by tribo-oxidation thus lowering the wear rate [35].

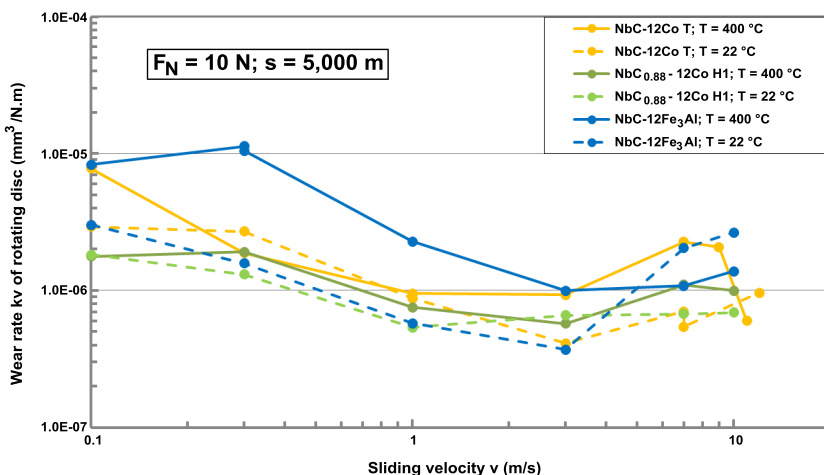


Figure 18. Wear rates of rotating discs of different NbC grades under dry sliding conditions.

Figure 18 indicates that the wear rates of the rotating discs (counterbody) made from different NbC grades decreased with increasing sliding speed and depend slightly on speed and temperature (RT and 400 °C). Consequently, the operating window of NbC in tribo-systems is wide. NbC thus represents an exceptional tribo-material offering such a large operating window in terms of sliding speed, ambient temperature and load carrying capacity under dry sliding conditions.

The morphology of the plateaus in the wear tracks is smooth for the discs slid at RT and 7.5 m/s. At 400 °C, the tribo-oxidation is beneficial to fully smoothen out the wear tracks [2,35]. For closed tribo-systems under dry sliding conditions, NbC is a favorable material because no wear particles visibly agglomerated on the wear tracks. The observation that no agglomerates were found on the wear tracks conforms to the low wear rates.

Table II summarizes the load carrying capacity, expressed as P·V values (contact pressure times sliding velocity), displayed in Figure 19, for all NbC grades. At room temperature the values increased from 1-2 MPa·m/s at 0.1 m/s up to 100 MPa·m/s at 8.0 m/s [1] because tribo-oxidation

was enhanced with increasing sliding speed (or generated frictional heat) and stable, non-volatile Nb_2O_5 was formed. In contrast the P-V values at 400 °C ranged more or less over the same level as measured at RT. The NbC grades exhibited a high wear resistance under dry sliding associated with exceptional load carrying capacity. Normally, P-V values [30,31] of dry sliding tribo-couples decrease with increasing sliding speed. The NbC-based materials are coming close to tribo-active materials [32,33] such as $\text{Ti}_{n-2}\text{Cr}_2\text{O}_{2n-1}$ phases, (Ti,Mo)(C,N) having slightly lower P-V values or maximum frictional heat flows.

The wear resistance of Co- and Fe_3Al -bonded NbC hard metals is highest at RT and high sliding velocities. Several factors are responsible for the wear resistance of NbC. Firstly, NbC has a very high melting point (3,522 °C). Secondly, Nb_2O_5 is relatively soft having a hardness of only 500-650 HV 0.2 and a melting temperature of 1,512 °C without sublimating. On the contrary, WO_3 formed by tribo-oxidation on WC starts sublimating above 750-800 °C and cannot serve for wear protection. Furthermore, it has to be taken into consideration that the modulus and hardness of NbC are less temperature dependent and its toughness increases with temperature.

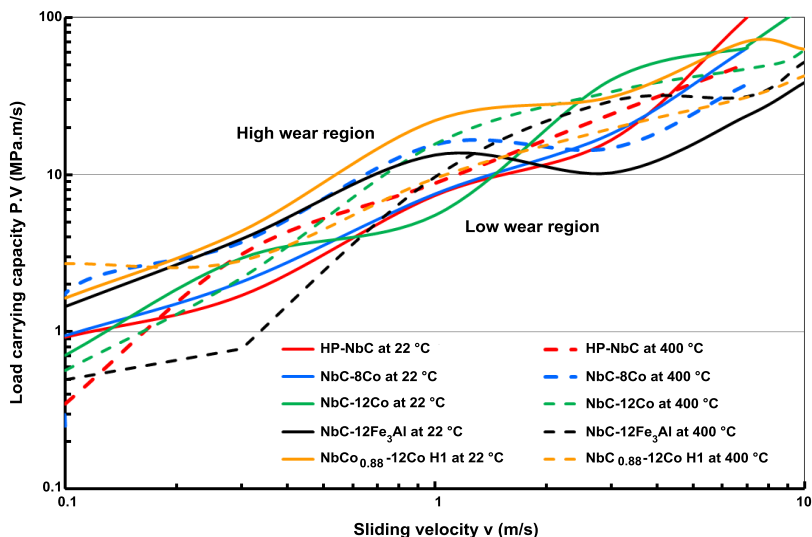
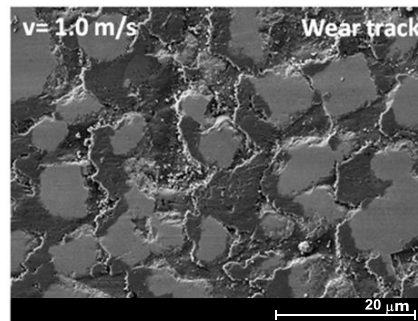
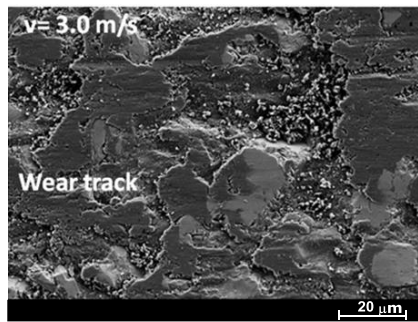
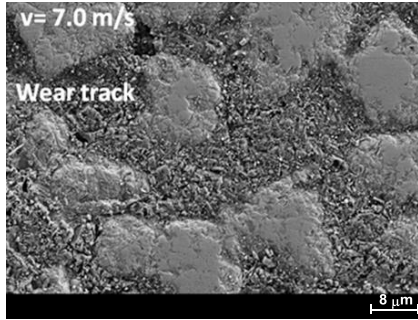


Figure 19. Load carrying capacity (maximum frictional power loss) of NbC-based materials as a function of sliding velocity under dry sliding conditions at room temperature and 400 °C.

Figure 20 shows wear tracks present on Fe_3Al -NbC MMC samples after sliding against alumina over 5000 m distance. The wear debris was removed from the wear tracks in order to better reveal the NbC grains. The micrographs clearly show NbC particles embedded in the matrix. There are no indications of NbC particle extraction because the carbon-enriched Fe_3AlC interface between particle and matrix withstands shear forces, Figure 14. Fragmentation of NbC

particles was not observed. One can thus conclude that the wear behavior of the composite is principally controlled by the wear behavior of the NbC hard phase.



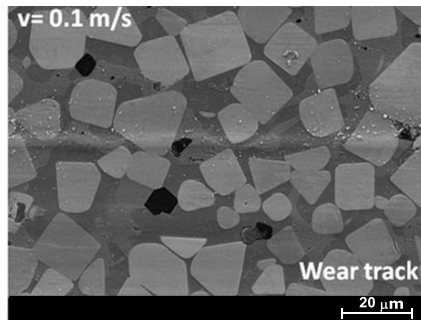


Figure 20. Morphology of RT wear tracks of Fe₃Al-NbC MMC after sliding against alumina over 5,000 m distance.

Oscillating Low-amplitude Sliding (Room Temperature – Different Relative Humidities)

The polished ball ($\varnothing = 10$ mm; alumina 99.7% or 100Cr6H equivalent SAE E52100) in the oscillating tribometer is fixed at the top of a lever with an integrated load cell for the measurement of the friction force. The ball (non-rotating) is positioned on a disc that is fixed on a table, oscillating at $\nu=20$ Hz with a stroke of $\Delta x=0.2$ mm. It is loaded by a dead weight acting as a normal force ($F_N = 10$ N) perpendicular to the sliding direction. The tests were run under three relative humidity levels of 2%, 50% and 98% up to one million cycles. The sensitivity of a couple against the impact of tribo-oxidation induced by humidity can be effectively quantified under dry oscillation.

The tribological profile (K_v versus CoF) is displayed in Figure 21 for alumina and, in Figure 22, for steel counterbodies. The arrows indicate an increasing relative humidity. The degree and trend of this sensitivity depends on the counterbody material being alumina or 100Cr6 steel. For alumina counterbodies all NbC-based materials behave in a similar manner. Against a polished alumina ball, Figure 21, the tribological profiles of steel and the ceramic samples, including WC-6Ni and pure HP-NbC, as well as cobalt and Fe₃Al bonded hard metals, are sensitive to relative humidity. The presence of cobalt (NbC-8Co, NbC-12Co) and Fe₃Al binders (NbC-12Fe₃Al) in NbC grades increases the sensitivity of their frictional behavior to relative humidity, when compared to binderless NbC. The coefficient of friction decreases under increasing relative humidity.

Ferrous alloys such as 100Cr6 steel, Figure 22, subjected to dry oscillation at RT exhibit tribo-oxidative [36] formation of Fe₂O₃ which may be hydrolyzed to α -, β - or γ -FeOOH and Fe(OH)₂. Particularly, in comparison to polished WC-6Ni, the wear resistance of NbC grades under dry oscillation is high having K_v values of 10^{-6} mm³/N·m. The wear rates of binderless NbC (HP-NbC1) and cobalt bonded NbC grades behave in a similar manner under dry oscillation.

A direct comparison between WC-6Ni and HP-NbC1 is difficult because the nickel binder in WC-6Ni (6.4 wt%Ni + 0.5 wt%Co) has a beneficial role in terms of tribo-oxidation (formation of double oxides). Furthermore, the WC grain size being around 2 μm is much smaller than that of HP-NbC and the surface roughness of WC-6Ni with $R_{pk} = 0.013 \mu\text{m}$ was also smoother than the one of HP-NbC with $R_{pk} = 0.143 \mu\text{m}$.

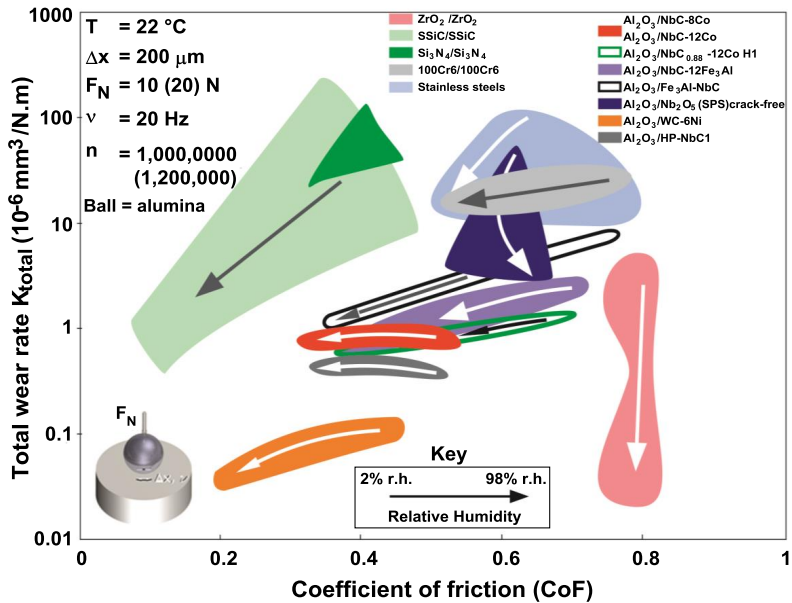


Figure 21. Total wear rate with the associated coefficient of friction of hard materials vs alumina counterbody under dry oscillation and different relative humidity levels.

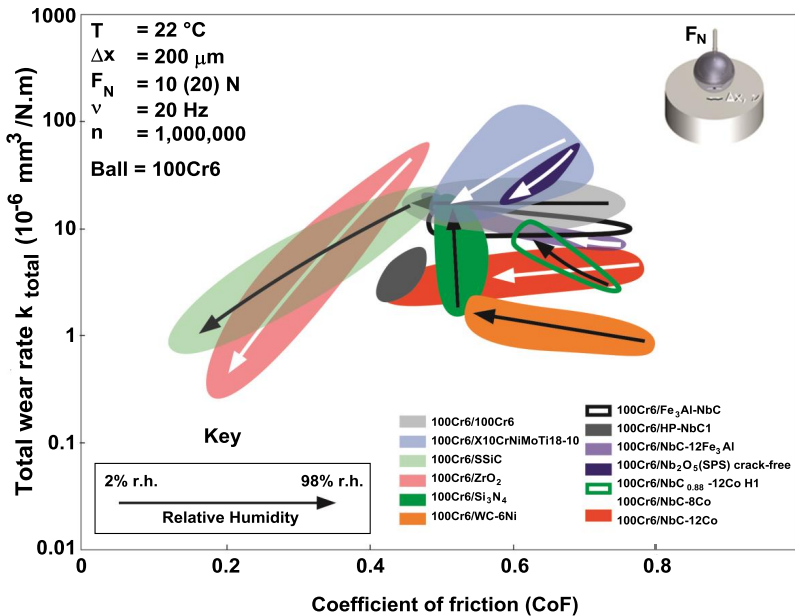


Figure 22. Total wear rate with the associated coefficient of friction of hard materials vs. 100Cr6 steel counterbody under dry oscillation and different relative humidity levels.

Conclusions

The potential of NbC as a hard material with respect to applications in mineral and metal processing has been investigated. NbC has a very high hardness which strongly depends on the stoichiometry (C:Nb ratio) in the material. By adjusting the stoichiometry, the hardness of NbC can be tailored to cover the entire range of other established transition metal carbides. Particular intrinsic advantages of NbC are its lower density that is very close to iron-based alloys, its low solubility in hot metals and its extremely high melting point. This allows the addition of NbC to liquid iron melts without significant gravity segregation effects. Moreover, NbC has a very low chemical wear rate under hot contact conditions with metals.

NbC can be processed via powder metallurgical processing using various metal binders, such as cobalt, nickel, molybdenum, iron aluminide, or stainless steel. It can also be produced in pyrometallurgical processes, either by in-situ primary precipitation in iron-based melts, or by addition of an NbC containing ferroalloy. These processing routes are able to cover a wide range of hard phase compositions, with NbC particles ranging from sub-micron to several tens of microns in size.

NbC itself, as well as hard metals or metal matrix composites containing NbC, were all shown to have a pronounced intrinsic wear resistance. Stoichiometric or sub-stoichiometric NbCs have, under dry sliding at RT and 400 °C, a pronounced intrinsic wear resistance associated with an exceptional high load carrying capacity, either as a hard metal or as a metal matrix composite. They can easily compete with ceramics, “tribo-active” materials and existing hard metals based on these properties. Thus, NbC qualifies for the group of tribological materials with enhanced wear resistance.

Tribological properties can be tailored through adjusting stoichiometry and/or binder content. The dry sliding wear resistance of the present Fe₃Al-NbC with ~60% NbC was close to that of known NbC-based hard metals and the wear resistance of the sub-stoichiometric NbC_{0.88}-12Co (H1) was at the lower end of values for the stoichiometric NbC grades. The NbC grains are metallurgically bonded into the Fe₃Al matrix by a metallurgical interphase. Thus, no grain pull-outs or fragmentations were seen in the wear tracks. Hence, NbC-based materials are expected to show excellent performance in mineral processing.

Remarkably, at increased sliding speeds the wear rate further decreases to outstandingly low values. Wear rates of NbC grades at 400 °C generally remained low, regardless of the applied sliding speed. The low wear rates of NbC were associated with high load carrying capacity (P-V value), which further increases at higher sliding speeds. Under dry oscillation, the wear resistance of pure NbC was insensitive to relative humidity, both for steel and alumina counterbodies, whereas the coefficient of friction of metal-bonded NbC grades was reduced with increasing relative humidity due to the effect of cobalt and Fe₃Al binders.

The low solubility of NbC in metals, its extremely high melting point, as well as the high P-V value are ideal prerequisites for cutting tool materials. Furthermore, the available levels of hardness, elastic modulus, strength and toughness are sufficient to support the loads prevailing at the cutting edge of a tool. From a tribological point of view, the cobalt binder in NbC hard metals can be substituted by intermetallic Fe₃Al.

Acknowledgements

Ms. Christine Neumann and Mr. Norbert Köhler are gratefully acknowledged for carefully performing the tribological tests and profilometric analysis, and Mr. Steffen Glaubitz is also gratefully acknowledged for the mechanical testing. The authors would like to express their special thanks to Ms. Sigrid Binkowski and Mr. Maximilian Scheibe for developing the metallographic procedures and performing the high quality imaging with light optical microscopy. The assistance of Ms. Sigrid Benemann is gratefully acknowledged in carefully performing SEM micrographs with EDX. The authors are grateful to Companhia Brasileira de Metalurgia e Mineração (CBMM), São Paulo, Brazil, for producing and supplying the NbC bearing MMCs and hard metals, as well as for supporting this test campaign.

References

1. H. O. Pierson, *Handbook of Refractory Carbides and Nitrides: Properties, Characteristics, Processing, and Applications* (Westwood, NJ: Noyes Publications, 1996), ISBN 0-8155-1392-5.
2. M. Woydt and H. Mohrbacher, "The Tribological and Mechanical Properties of Niobium Carbides (NbC) Bonded with Cobalt or Fe₃Al," *Wear*, 321 (2014), 1-7, (Open Access).
3. European Registration, Evaluation, Authorisation, and Restriction of Chemical Substances – REACH (n.d.), *What is REACH?*
(Available at: <http://ec.europa.eu/environment/chemicals/reach/reach_intro.htm>).
4. U.S. Department of Health and Human Services (n.d.), *National Toxicology Program*
(Available at: <<http://ntp-server.niehs.nih.gov/>>).
5. W. Theisen, S. Siebert and S. Huth, "Wear Resistant Steels and Casting Alloys Containing Niobium Carbide," *Steel Research International*, 78 (12) (2007), 921-928.
6. A. Kelly and D.J. Rowcliffe, "Deformation of Poly Crystalline Transition Metal Carbides," *Journal of the American Ceramic Society*, 50 (5) (1967), 253-256.
7. A. Nino et al., "Indentation Size Effect for the Hardness of Refractory Carbides," *Materials Transactions*, 51 (9) (2010), 1621-1626.
8. M-Y Lee, "High Temperature Hardness of Tungsten Carbide," *Metallurgical Transactions A*, 14 (8) (1983), 1625-1629.
9. G. Asai, D.L. Paulson and H.J. Kelly, "Properties of Cast Columbium Carbide-cast Alloys" (Report of Investigations RI 7479, Bureau of Mines, February 1971).
10. Y. Kumashiro and E. Sakuma, "The Vickers Micro-hardness of Non-stoichiometric Niobium Carbide and Vanadium Carbide Single Crystals up to 1500 °C," *Journal of Materials Science (Letters)*, 15 (5) (1980), 1321-1324.
11. J. Nunn, private communication, National Physical Laboratory, Teddington, UK, 2015.
12. H. Wiesenberger, W. Lengauer and P. Ettmayer, "Reactive Diffusion and Phase Equilibria in the V-C, Nb-C, Ta-C and Ta-N Systems," *Acta Materialia*, 46 (2) (1998), 651-666.
13. A.S. Kurlov and A.I. Gusev, "Effect of Nonstoichiometry of NbC_y and TaC_y Powders on Their High-energy Ball Milling," *International Journal of Refractory Metals and Hard Materials*, 46 (2014), 125-136.
14. C.P. Kempter, E.K. Storms and R.J. Fries, "Lattice Dimensions of NbC as a Function of Stoichiometry," *Journal of Chemical Physics*, 33 (6) (1960), 1873.

15. A.A. Rempel and A.I. Gusev, "Heat Capacity of Niobium Carbide in Different Structural States," *Physica Status Solidi (a)*, 113 (2) (1989), 353-358.
16. A.I. Gusev, A.A. Rempel and A.J. Magerl, *Disorder and Order of Strongly Nonstoichiometric Compounds* (New York, NY: Springer-Verlag Berlin Heidelberg, 2001), 43-112, ISBN 3-540-41817-2.
17. L. Ramqvist, "Variation of Hardness, Resistivity and Lattice Parameter with Carbon Content of Group 5b Metal Carbides," *Jernkontorets Annaler*, 152 (1968), 467-475.
18. R. Edwards and T. Raine, "The Solid Solubilities of some Stable Carbides in Cobalt, Nickel and Iron at 1,250° C," *Planseeber Pulvermetallurgie*, 1 (1952), 232-242.
19. J.P. Guha and D. Kolar, "Systems of Niobium Monocarbide with Transition Metals," *Journal of the Less-common Metals*, 29 (1) (1972), 33-40.
20. V.K. Lakshmanan and J.S. Kirkaldy, "Solubility Product for Niobium Carbide in Austenite," *Metallurgical Transactions A*, 15 (2) (1984), 541-544.
21. E.J. Pavlina, J.G. Speer and C.J. Van Tyne, "Equilibrium Solubility Products of Molybdenum Carbide and Tungsten Carbide in Iron," *Scripta Materialia*, 66 (5) (2012), 243-246.
22. H. Mohrbacher et al., "Raman Spectroscopy on Defective Wear Debris Generated by Contact Vibrations," *Journal of Materials Science Letters*, 14 (4) (1995), 279-281.
23. S. Huang et al., "Microstructure and Mechanical Properties of NbC-matrix Hardmetals with Secondary Carbide Addition and Different Metal Binder," *International Journal of Refractory Metals and Hard Materials*, 48 (2015), 418-426.
24. S.G. Huang et al., "Properties of NbC-Co Cermets Obtained by Spark Plasma Sintering," *Materials Letters*, 61 (2) (2007), 574-577.
25. H. Berns, "Comparison of Wear Resistant MMC and White Cast Iron," *Wear*, 254 (1-2) (2003), 47-54.
26. E. Franco et al., "Cermets Based on FeAl-NbC from Composite Powders: Design of Composition and Processing," *International Journal of Refractory Metals and Hard Materials*, 48 (2015), 324-332.
27. R.J. Chung et al., "Microstructure Refinement of Hypereutectic High Cr Cast Irons Using Hard Carbide Forming Elements for Improved Wear Resistance," *Wear*, 301 (1-2) (2013), 695-706.

28. M. Scheibe et al., "Comparison of Different Preparation Techniques for the Characterization of Niobium Carbides" (Report #19, Berlin, Germany, Struers, 2014). Available online as open access <http://www.struers.com/resources/elements/12/274090/Structure%20News%2019.pdf>
29. M. Woydt and K-H. Habig, "High Temperature Tribology of Ceramics," *Tribology International*, 22 (2) (1989), 75-88.
30. M. Woydt, "Tribologie des Céramiques (Tribology of Ceramics)," *Encyclopédie Techniques de l'Ingénieur*, Paris, March 2013, Ref. TRI4550.
31. M. Woydt, "Application des Données Tribologiques des Matériaux (The Use of Tribological Quantities of Materials)," *Encyclopédie Techniques de l'Ingénieur*, Paris, June 2012, Ref. BM7006v2.
32. L-M. Berger et al., "Dry Sliding up to 7.5 m/s and 800 °C of Thermally Sprayed Coatings of the TiO₂-Cr₂O₃ System and (Ti,Mo)(C,N)-Ni(Co)," *Wear*, 267 (5-8) (2009), 954-964.
33. L-M. Berger, S. Saaro and M. Woydt, "WC-(W,Cr),C-Ni – The 'Unknown' Hardmetal Coating," *Therm. Spray Bull.*, 1 (2008), 37-40.
34. M. Woydt and H. Mohrbacher, "Friction and Wear of Binder-less Niobium Carbide," *Wear*, 306 (1-2) (2013), 126-130.
35. M. Thoma, "High Wear Resistance at High Temperatures by Co+Cr₂O₃ Electrodeposited Composite Coating," *MTU-Berichte: Motoren- und Turbinen Union*, 41 (1985), or in *Wear*, 162-164 (1993), 1045-1047.
36. D. Klaffke, "On the Repeatability of Friction and Wear Results and on the Influence of Humidity in Oscillating Sliding Tests of Steel-steel Pairings," *Wear*, 189 (1-2) (1995), 117-121.

APPLICATION OF FeNbC AS A HARDFACING MATERIAL USING LASER CLADDING

E.T. Galvani¹, S. Simões², C.H.N. Banov², H.L. Rosa³ and E.B. Cruz³

¹Höganäs do Brasil; Mogi das Cruzes, 08810-020, SP, Brazil

²HRC Metalização; Piracicaba, 13413-087, SP, Brazil

³Companhia Brasileira de Metalurgia e Mineração (CBMM); Araxá, 38183-903, MG, Brazil

Keywords: Niobium Carbide, NbC, FeNbC, Hardfacing, Wear Protection, Abrasive Wear, Laser Cladding

Abstract

The sugar-cane and mining sectors experience substantial losses due to shut-downs and repair or replacement of worn out or obsolete components. Surface engineering studies have been widely developed aiming at optimizing the coating processes and, mainly, increasing the portfolio of higher wear resistant materials. HRC Metalização® (a joint venture between Höganäs and Oxipira), in partnership with CBMM, has been working on the development of niobium carbide (NbC) in iron matrix (FeNbC) hardfacing coatings, applied by laser cladding on wear components for mining. Field trials were conducted on the coated teeth of a Volvo wheel loader operating at CBMM's mine in Araxá, Brazil. The metallographic analysis of the coated teeth showed an excellent adhesion of the FeNbC coating layer, as well as a homogeneous dispersion of the hard NbCs. The loader's coated teeth achieved an increase of approximately 64% in service life above best performance, and 80% above the average service life of the regular uncoated, low alloy carbon steel teeth, demonstrating the significant potential of FeNbC as a hardfacing coating applied by laser cladding.

Introduction

Wear in industrial components and equipment for agriculture and mining activities is a key factor in capital depreciation and expenses related to maintenance, and to restoring and replacement of parts. It is often necessary to oversize components to avoid production stoppage due to the wear of those particular parts that directly influence production losses. Thus, the development of new wear resistant materials for coatings would be a way to increase productivity in the industry, particularly in Brazil's mining sector, which has expanded significantly in recent years. Therefore, the challenge is to develop new materials and processes that provide outstanding wear resistance and high toughness for use as a technological coating solution [1].

The laser cladding process is a deposition welding technique applied for the addition of a material or a mixture of materials on to the surface of a substrate, under controlled conditions. In this process, a stream of a coating powder is fed into a laser beam that is focused and scanned throughout the target area, leaving behind a fully fused layer of the desired material. Laser cladding can be used for many purposes, including the application of wear resistant or corrosion-resistant coatings, the restoring of worn out components and deposition welding of shaped parts.

Conventional deposition methods, such as plasma transferred arc welding, flame spray and high velocity oxy-fuel spraying are also used for situations where materials with high wear resistance are desired [2]. The intrinsic characteristics of the application method generally determine the coating quality, and these conventional methods usually result in low compliance, a high degree of porosity, high dilution and severe distortion of the material [3]. Materials clad by laser are attractive and advantageous since this method enables an extremely localized treatment area, overcoming problems described for conventional coating processes [3]. The low power input required by the laser coating technology results in less extensive heat-affected zones, low distortion and a minimum degree of substrate dilution. Additionally, high heating rates combined with fast cooling of localized areas promote the formation of fine-grained microstructures [3].

The mining and ore moving operations of pyrochlore at CBMM's open pit mine in Araxá, Brazil, are carried out by means of bulldozers, graders, excavators, wheel loaders and trucks. The weathered ore is soft enough that it does not require any blasting and there are no water inflows. One of the main causes for stoppages of the mining and ore moving equipment is downtime for replacing their ground engaging tools (GETs), such as bulldozer cutting edges, side cutters, grader blades, excavator and loader buckets, teeth or tip adaptors and bucket teeth or tips. Choosing the right GET material and design can result in reduced labor costs and reduced downtime required for change outs.

Regular laser cladding of materials comprises nickel- and cobalt-based alloys, carbide and hard metal blends for wear applications and carbide matrix materials for customized blends. The carbide based blends provide high toughness protection for components that are exposed to severe wear conditions. Tungsten carbide (WC) plus titanium composite coatings are normally used to protect drilling and mining components.

NbC possesses similar hardness to that of WC, but only half its density, and it has a higher melting point and higher oxidation resistance. Thus, it exhibits many outstanding properties that can make it an attractive option for most of the already consolidated industrial applications. NbC also presents lower solubility in iron than WC and has a similar density to materials like cast iron and steel, opening the possibility of using NbC as a raw material for hard metals, as well as of developing new wear resistant materials for castings and hard facing coatings with high levels of hard primary NbC homogeneously distributed in the microstructure [4].

Based on these scenarios, HRC Metalização® (a joint venture between Höganäs and Oxipira), in partnership with Companhia Brasileira de Metalurgia e Mineração (CBMM), conducted several field trials on the application of FeNbC as a new hardfacing material applied by laser cladding on wear parts for mining, earth moving and agricultural equipment. The present work reports the results of the characterization and performance in field trials of the FeNbC applied as a hardfacing coating by laser cladding on the bucket teeth of an ore wheel loader operating regularly at CBMM's mine in Araxá, Brazil.

Wear in Mining and Minerals Processing

In view of the extremely abrasive characteristics of the ore and overburden handled in mining, it is expected that abrasive wear represents an important percentage of the maintenance costs of mining operations. Therefore, increases in service life generally result in net cost reductions and as a consequence, economic earnings. The correct materials selection of abrasive resistant consumables may result in substantial increases in service life [5]. Wear resistant materials include metals like high alloyed steels and cast irons, ceramics, polymers and composites. Metallic components can be classified in four groups: castings, forgings, rolled plates and hardfacing or fusion-clad plates [5].

The wear behavior of materials used in mining and minerals processing depends on a number of factors that fall into three main groups: (1) the properties of the wear resistant material, (2) the characteristics of the abrasive material and (3) the nature and severity of the interaction between the abrasive and the wear resistant materials [6].

Depending on the nature of the interaction between the abrasive particle and the wear resistant material, abrasive wear can be classified in the following categories [5,6]:

- Low-stress abrasion: the abrasive particle remains intact as it moves freely across the wear surface, as occurs in chutes, excavation and general handling of loose granular minerals;
- High-stress abrasion: the abrasive particle is crushed during the wear interaction, occurring in crushing and grinding, as well as in hard rock excavation;
- Gouging abrasion: the removal of a large volume of material per event from the wear surface occurs as the result of deep individual wear grooves, as in primary crushers and impacts from very large rocks;
- Solid particle erosion: abrasive particles move in a fluid medium, as occurs in pumps, slurry pipelines and hydrocyclones;
- Impact abrasion: particles are coarse and the impact velocities of the particle are greater than 10 m/s, as in high-speed hammer mills and impact crushers.

In general, three conditions are required for abrasion to occur: an abrasive particle harder than the wear part, a contact force to press the abrasive particle into the wear part surface, and a sliding velocity sufficient to cut a groove in the surface of the wear part.

Function and design also influence the wear of earthmoving, mining and mineral processing components. In earthmoving operations, the abrasive wear from scraping operations is less severe than operations requiring earth penetration and removal, as in the wear of digger teeth on bucket excavators. Wear rates in crushing and grinding equipment are much higher than wear seen in chute linings, screens and classifiers. In fact, crushing and grinding operations account for about 95% of the material wear in general ore processing [6].

According to Gates [5] and the abrasive wear model of Rabinovicz [7] for single phase materials, hardness is a primary property for wear resistant parts. Abrasive particles will only penetrate the wear part surface if they are harder than the wear part material. If wear material can be found that is greater than 2/3 the hardness of the abrasive material, wear rates can be reduced substantially, staying in the mild wear regime. For instance, very hard quartzitic rocks can have hardness greater than 900 HV, so wear part materials with hardness higher than 600 HV would be necessary to reduce wear rates to acceptable values. Most commercial martensitic wear resistant steels exhibit hardness levels between 540 HV and 700 HV. Alternative materials reinforced by hard particles can be used, including NiHard and high-chromium white cast iron and hardfacing alloys with high contents of chromium carbide particles with an approximate hardness of 1400 HV. Although the bulk hardness of the composite may not be greater than 600 HV, the hard reinforcing particles can be very helpful in the prevention of abrasion from most minerals. Also, other hardfacing alloys, with tungsten and titanium carbides as reinforcing particles, are available for wear applications. Particle-reinforced materials or composites can be effective in increasing the service life of wear parts when working in low-stress abrasion conditions [5].

Castings are very appropriate for thick walled wear parts, but the volume fraction of reinforcing particles is limited to a maximum of approximately 35%. The mismatch in density between common hard phases and alloys, as well as their solubility in these alloys, limit cast metal matrix composites. Higher hard phase contents decrease toughness and can lead to breakage in service or during assembly. Higher percentages of hard particles are possible in hardfacing and clad coatings that are deposited on tough steel substrates for structural support [5]. For this reason, an area of recent and continuous development is the field of fusion-clad products applying modern weld-deposition and thermal spray technologies, including the laser cladding deposition process.

FeNbC Laser Cladding Process for the Wheel Loader Bucket Teeth

FeNbC was developed by CBMM for applications where very high NbC contents are sought. This material constitutes a source of hard primary NbCs and it can be applied as an alloying addition for castings and hardfacing products for surface protection of wear parts, such as crusher hammers and rolls, conveyor screws, chute liners and GETs. As shown in Figure 1, FeNbC is a natural composite that contains hard NbC, homogeneously distributed in an iron based matrix with residual elements, such as aluminum, silicon, titanium and manganese. The main phases are NbC, Fe₃Al and Fe₃AlC. The microhardness of the intermetallic Fe₃Al ranged from 360 to 470 HV 0.05 and of Fe₃AlC from 630 to 670 HV 0.05, which indicates that the metallic matrix itself is a very tough and wear resistant material [4]. These characteristics raised the possibility of applying FeNbC as a hardfacing material, even without using any other coating additives.

FeNbC is produced in a wide range of NbC contents (typically between 40 wt.% and 80 wt.%NbC) and granule sizes between 0 and 50 mm, Figure 2.

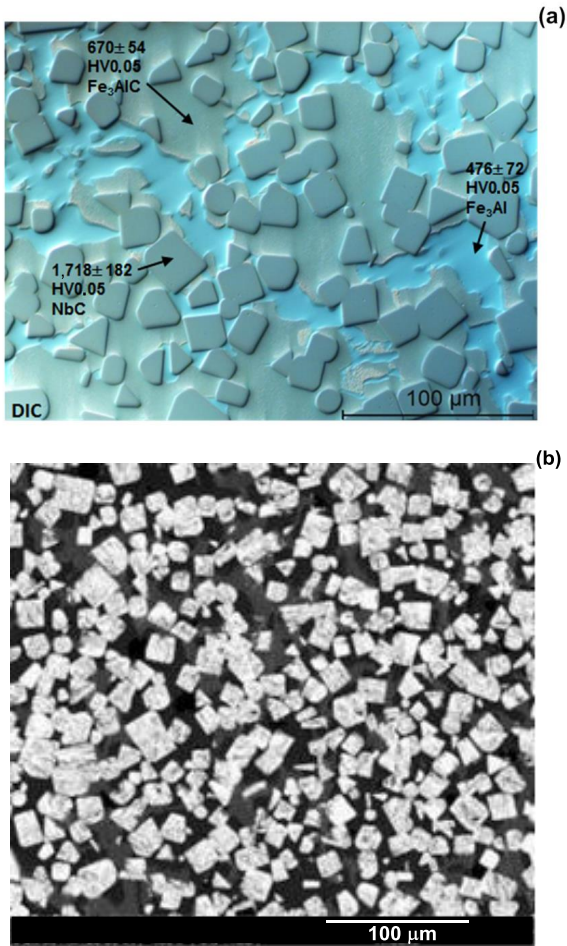


Figure 1. Typical microstructure of FeNbC observed using optical microscopy with differential interference contrast (DIC) (a) and mapping of niobium by SEM/EDS (b).

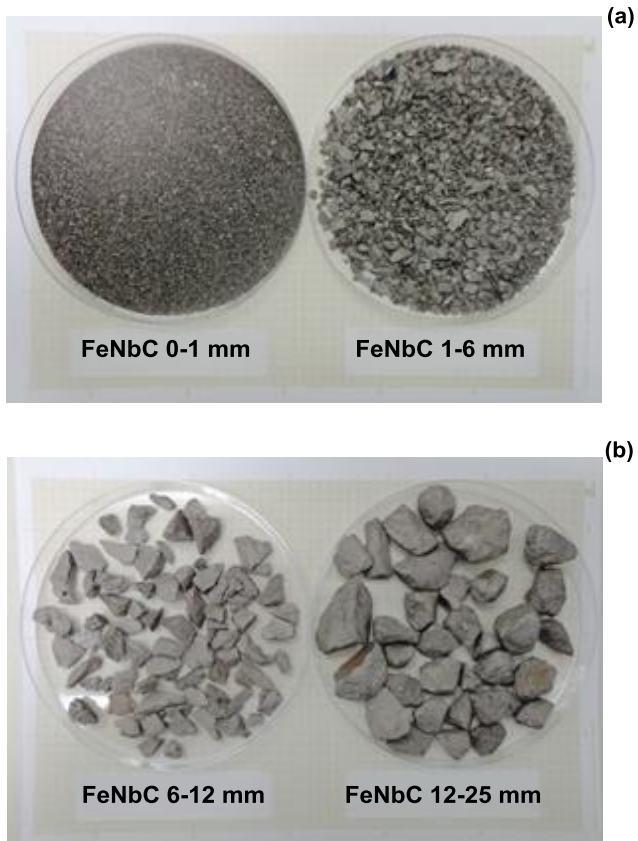


Figure 2. Appearance of different granules of FeNbC: <1 mm and 1-6 mm (a) and 6-12 mm and 12-25 mm (b).

The FeNbC powders used in the laser cladding trials of the loader bucket teeth were prepared from the <1 mm fraction. The chemical analysis of the FeNbC powder was approximately 35 wt.%Nb, 5 wt.%C, 7 wt.%Al and 2.5 wt.%Ti.

In order to evaluate the performance of the FeNbC powder as a hardfacing material for bucket teeth, a Volvo ore wheel loader was chosen for field trials, Figure 3.



Figure 3. Views of the Volvo wheel loader (a) and bucket teeth (b) at CBMM's mine.

The pyrochlore wheel loader bucket operates regularly with eight teeth or tips of low alloy carbon steel weighing approximately 11 kg each. The average service life of these conventional bucket teeth is 1,220 hours with best performance reaching approximately 1,340 hours.

In order to increase the lifetime and performance of the conventional low alloy carbon steel tips by using FeNbC as a hardfacing material, some teeth were coated at HRC Metalização® via High Power Direct Diode Laser technology in a Coherent High Light 8000D system, Figure 4.

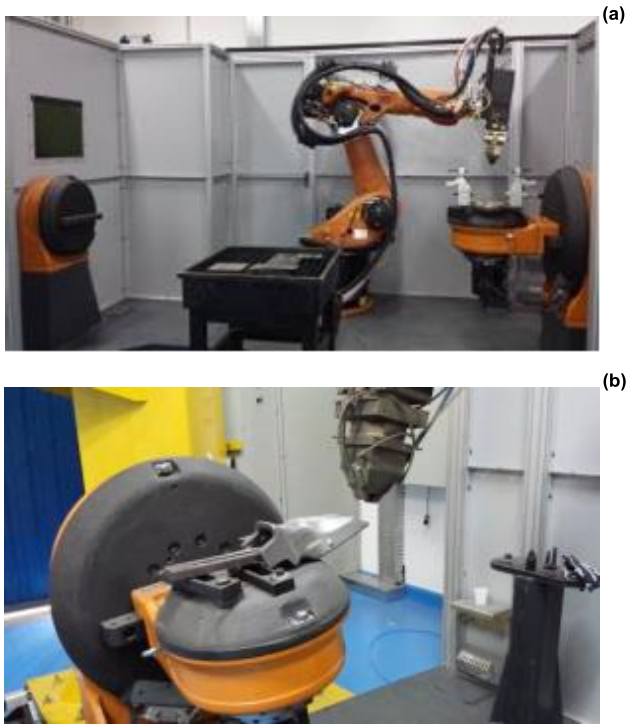


Figure 4. Coherent High Light 8000D laser system (a) and FeNbC laser cladding (b).

Figure 5 shows the low alloy carbon steel tips before and after coating with FeNbC by laser cladding. As can be observed, the tips used in the field trials were coated with FeNbC on the top, left and right faces but not the bottom. The total weight of the deposited FeNbC was about 200 grams per steel tip. The FeNbC was deposited in layers along the ore flow except on the front face where the deposit was transversal to the ore flow. Some of the tips showed small filling defects and cracks on the fused layers. As usual in similar hardfacing processes some of the tips showed small filling defects and cracks on the fused layers which, however, did not affect their good performance in service.

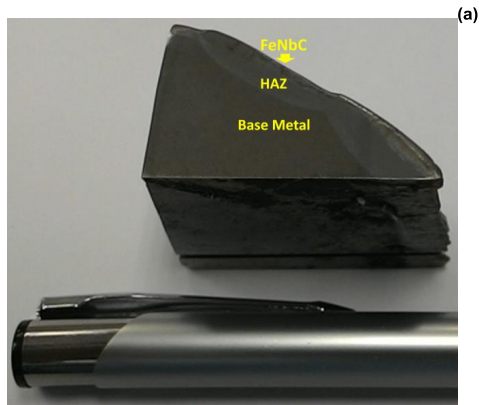


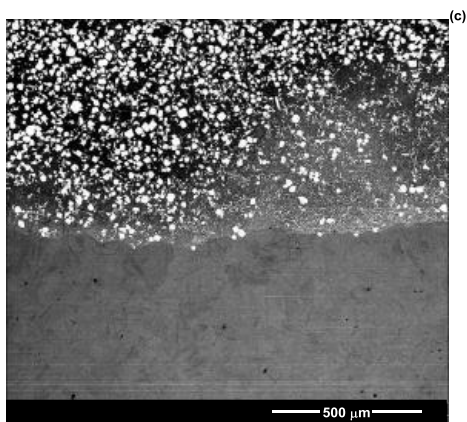
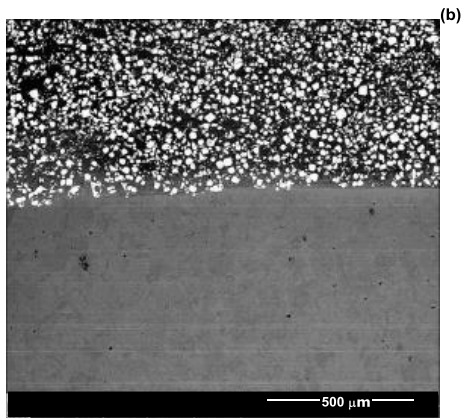


Figure 5. Volvo wheel loader steel teeth before (a) and after (b), (c) and (d) coating with FeNbC.

Figure 6 shows the macro and microstructural aspects of the interface between the carbon steel tip and the FeNbC coating deposited by laser cladding as revealed by SEM/EDS. There are three main regions: the base metal (low alloy carbon steel), the heat affected zone (HAZ) and the FeNbC hardfacing layer.

The FeNbC coating layer presented quite good adhesion to the base metal or substrate. It is possible to note that most of the deposited coating layer showed a similar appearance and presented the same phases found in the original particles of the FeNbC, Figure 1. Additionally, it can be seen that some NbC particles in the hardfacing layer suffered partial dissolution in the metal base areas closest to the interface, enhancing the bonding effect. Some small cracks and oxide inclusions were also observed in regions of the coating layer. As mentioned above, such features are usual in similar hardfacing processes and did not affect their good performance in service.





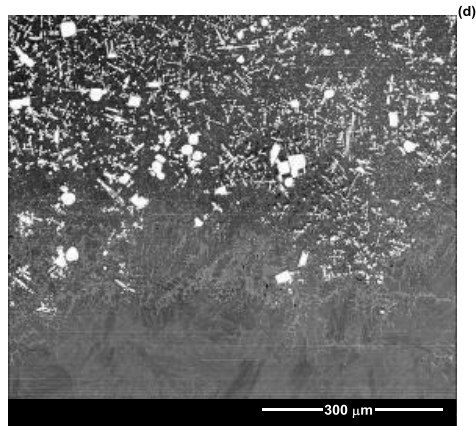


Figure 6. Macro (a) and microstructural (b), (c) and (d) images of the interface between the carbon steel tip and the FeNbC layer deposited by laser cladding.

Field Trials of the Loader Bucket Teeth

Aiming to evaluate the performance of the low alloy carbon steel teeth coated with FeNbC in relation to the same uncoated wear parts, both types of tips were assembled alternately on the same loader bucket, as shown in Figure 7. From the eight teeth coated with FeNbC, Figure 5(b), the tips numbered 5, 6, 7 and 8 were chosen for the first field trial and mounted initially in the positions i, iii, vi and viii (left to right as viewed in the figure), while the uncoated teeth occupied the positions ii, iv, v and vii.

The field trials were conducted from March to September, during the dry season of the year (2014). The Volvo wheel loader was used mainly for excavation and subsequent loading and filling of the ore transport trucks. It was also employed for building mine road berms, and cleaning and gross leveling of the pit benches. The equipment was operated approximately 21 hours per day during three shifts.



(a)



(b)

Figure 7. Assembling of the loader bucket teeth; (a) the four low alloy carbon steel tips coated with FeNbC are indicated with white arrows, (b) start of the field trials at CBMM's mine.

During the field trial of the coated and uncoated teeth, seven inspection stops were made to weigh and measure the tips. All worn coated and uncoated teeth and their respective adaptors were taken out and replaced after a total of 2,200 work hours. The criterion for replacing all the worn teeth, and consequently, for ending the trial was a minimum thickness of 3 mm of the heel of the bottom of the tip to ensure that it did not slip out of the locking mechanism. It is worth noting that in this trial none of the bottom surfaces of the tips were coated with FeNbC.

The total of 2,200 work hours before change outs represented an increase in the service life of the bucket teeth of approximately 64% above their best previous performance of 1,340 hours, and about 80% over the average service life, for uncoated tips, of 1,220 hours.

The field trial results related to the weight loss of the coated and uncoated tips registered during the inspections are shown in Figure 8.

The results of the final inspection after 2,200 working hours are presented in Table I. The uncoated tips in the middle positions iv and v were not disassembled for the inspections because they were welded to the tip adaptor.

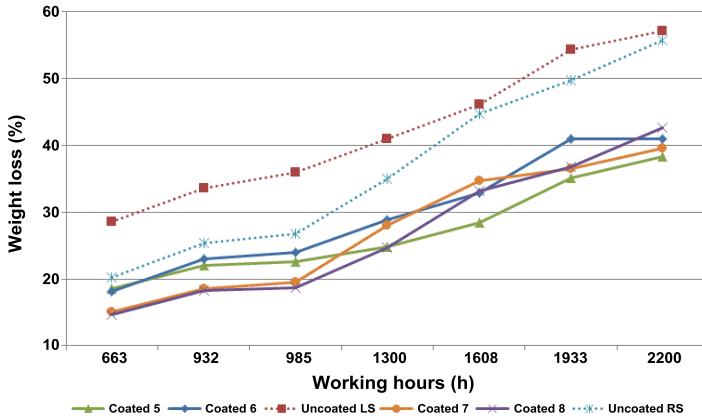


Figure 8. Weight loss of the coated and uncoated teeth during the field trial.

The weight loss of the uncoated tips was always higher than that of the coated parts at the seven inspections. After 2,200 working hours the weight loss of the uncoated teeth varied from approximately 56% to 57%, while the weight loss of the FeNbC coated teeth varied only from approximately 38% to 43%. The weight loss of the coated tips was 21% to 31% lower than the weight loss of the uncoated tips after 2,200 working hours.

Table I. Final Inspection Results of the Field Trial After 2,200 Working Hours.

| Tooth Number (Fig.5a) | Position | Original Weight (kg) | Type (FeNbC) | Coating (FeNbC) (kg) | Initial Service Weight (kg) | Final Weight (kg) | Weight Loss (kg) | Weight Loss (Absolute) (%) | Weight Loss (Relative*) (%) |
|-----------------------|----------|----------------------|--------------|----------------------|-----------------------------|-------------------|------------------|----------------------------|-----------------------------|
| 5 | i | 10.88 | Coated | 0.22 | 11.10 | 6.85 | 4.25 | 38.3 | -31.4 |
| - | ii | 10.85 | Uncoated | 0 | 10.85 | 4.65 | 6.20 | 57.1 | 0 |
| 6 | iii | 10.90 | Coated | 0.27 | 11.17 | 6.60 | 4.57 | 40.9 | -26.2 |
| - | iv | 10.85 | Uncoated | - | - | - | - | - | - |
| - | v | 10.85 | Uncoated | - | - | - | - | - | - |
| 7 | vi | 11.05 | Coated | 0.13 | 11.18 | 6.75 | 4.43 | 39.6 | -26.7 |
| - | vii | 10.85 | Uncoated | 0 | 10.85 | 4.80 | 6.05 | 55.8 | 0 |
| 8 | viii | 10.87 | Coated | 0.21 | 11.08 | 6.35 | 4.73 | 42.7 | -21.0 |

*Relative to the adjacent uncoated tooth, ii or vii

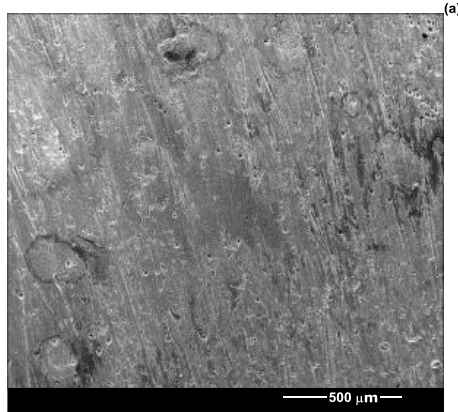
As illustrated in Figure 9, the weight loss of the coated teeth was higher on the bottom surface since none of them was coated with FeNbC. The uncoated teeth also suffered heavy wear in their upper and side regions. The reduction in the length of the coated teeth was from 16% to 18% lower than the length reduction of the uncoated tips after 2,200 working hours.

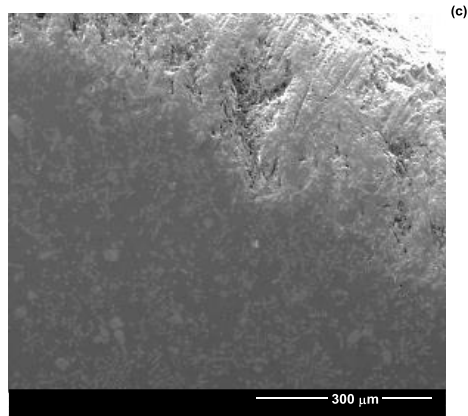
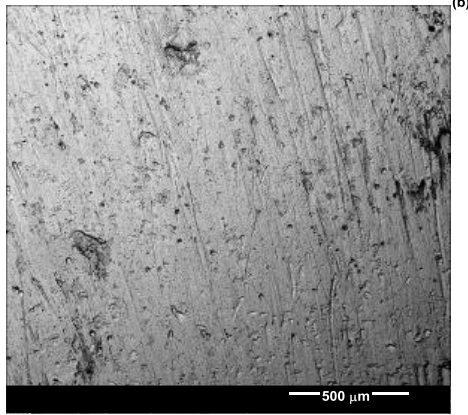


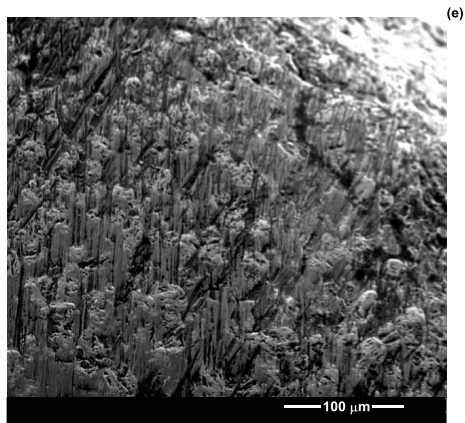
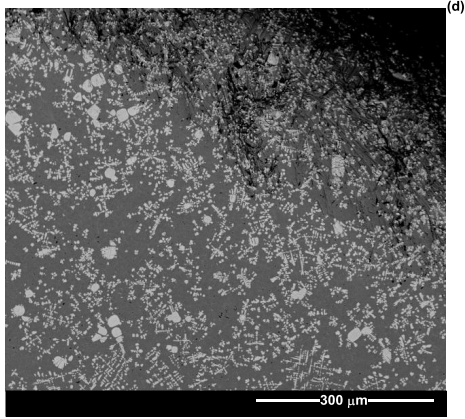


Figure 9. Wear patterns of the coated and uncoated teeth after the field trial. Top (a), (b), bottom (c), (d) and side (e), (f) views.

Figure 10 depicts microstructural aspects by SEM with secondary electron and backscattered electron images of the worn surfaces of both the uncoated (a) and (b) and coated teeth (c) to (f). The low alloy carbon uncoated steel teeth exhibited several scratches and micro-grooves throughout the worn surface (a) and (b) while the FeNbC coated tips showed similar scratches and micro-grooves only across the iron aluminide (Fe_3Al) matrix, with the remaining NbC particles well preserved (c) to (f). This wear morphology is analogous to that observed in Figure 11 after dry sliding tests of Fe_3Al -NbC carried out under controlled conditions (counter body: 99.7% alumina; $s = 5,000 \text{ m}$ (or 50,000 cycles), and initial maximum contact stress $P_{0\text{max}} = \sim 660 \text{ MPa}$). The wear tracks indicate that the interface NbC-matrix withstood shear and NbC remained almost unbroken while the iron aluminide experienced severe wear [8]. This is explained by the formation of a metallurgical interface between the Fe_3Al matrix and the NbC [9], because carbon is soluble in Fe_3Al forming the harder phase Fe_3AlC , Figure 1(a). Dissolution of some carbon from the NbC into Fe_3Al is unproblematic for the stability of NbC, as NbC can exhibit a range of carbon content of NbCx ($0.75 \leq x \leq 1.0$).







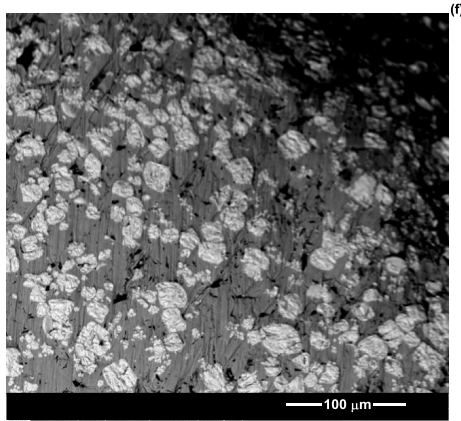
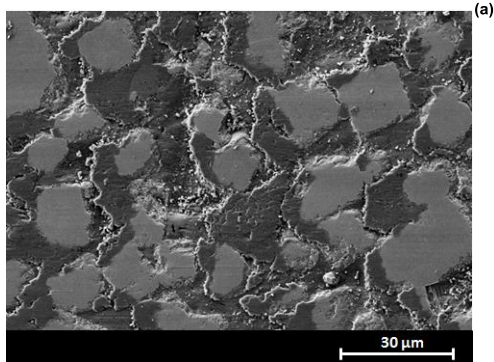


Figure 10. Morphologies of wear of the uncoated (a), (b) and coated (c) to (f) teeth after the field trial.

The worn surface in Figure 10 indicates that the wear of the FeNbC coated surface occurred mainly by the abrasion of the ductile iron aluminide matrix promoting later the fallout of free exposed reinforcing NbC particles. The metal loss was minimized in the FeNbC coated tips by the presence of a high volume of hard reinforcing NbC. Figure 10 also indicates no fragmentation of the NbC grains under rough mining operations. In consequence, it was shown under practical conditions, that NbC is well suited for wear protection.



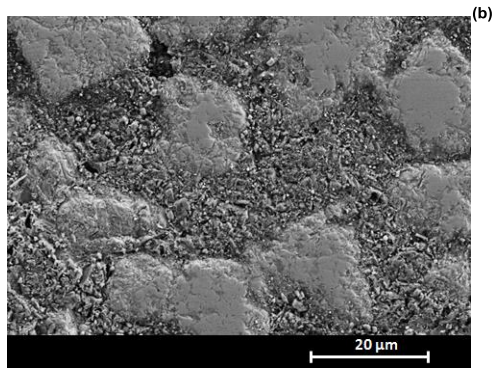


Figure 11. Morphology of the wear tracks at 22 °C after dry sliding tests of Fe₃Al-NbC (counter body: 99.7% alumina; s = 5,000 m (or 50,000 cycles), P_{0max} = ~660 MPa); (a) v = 1 m/s and (b) v = 7 m/s. [8]

In order to improve the performance of the FeNbC as a hardfacing material applied by laser cladding for coated loader teeth, additional trials are in progress under similar conditions, but with tips covered on all surfaces, including the bottom, as shown in Figure 12.





Figure 12. Volvo wheel loader steel tips coated with FeNbC; (a), (b) partial and (c), (d) total.

Conclusions

The application of FeNbC, a metal matrix composite, as a hardfacing material for ground engaging tools was investigated. The coating of conventional low alloy carbon steel bucket loader teeth with FeNbC deposited by laser cladding was characterized and their performance in field trials was evaluated. The following conclusions were drawn:

1. The FeNbC hardfacing layer deposited by laser cladding presented good adhesion to the low alloy carbon steel bucket teeth, and as a result it did not spall off under rough operation. The coating layer, on completion of the field test, showed the same morphology and phases found in the original deposited FeNbC particles.
2. The FeNbC coated bucket teeth worked for about 2,200 hours, representing an increase in the service life of 64% above best performance, and about 80% higher than the average service life of conventional carbon steel teeth.
3. The weight loss of the coated tips was between 21% to 31% lower than the weight loss of the uncoated tips after 2,200 work hours.
4. The reduction in the length of the coated teeth was between 16% to 18% lower than the length reduction of the uncoated tips after 2,200 work hours.
5. The wear of the loader bucket teeth occurred predominantly by abrasion, which caused metal loss due to surface micro-grooving. The metal loss was minimized by the presence of a high volume of hard reinforcing NbC. The wear of the coated surface occurred mainly by the erosion of the iron aluminide matrix, promoting the fallout of exposed reinforcing NbC particles. This indicates that FeNbC is well suited for wear protection as no fragmentations of the NbC particles were seen under severe mining operations.

References

1. H. Souto. “Laser Cladding: sua aplicação à deposição de revestimentos em lâminas de destroçadores de madeira” (Masters thesis, Faculdade de Engenharia, Universidade do Porto, Porto. 2013), 01-05.
2. C. Guo et al., “Effects of WC–Ni Content on Microstructure and Wear Resistance of Laser Cladding Ni-based Alloys Coating,” *Surface and Coatings Technology*, 206 (8) (2012), 2064-2071.
3. V. Weerasinghe and W. Steen, “Laser Cladding with Pneumatic Powder Delivery,” *Applied Laser Tooling*, ISBN: 978-94-010-8096-5, Springer, 1987, 183-211.
4. E.B. Cruz and D.P. Fridman, “Development of FeNbC for Wear Resistant Applications” (Paper presented at the International Symposium on Wear Resistant Alloys for the Mining and Processing Industry, Campinas, São Paulo, Brazil, 4-7 May 2015).
5. J. Gates, “Wear Plate and Materials Selection for Sliding Abrasion,” *Australian Journal of Mining*, July/August (2003), 26-32.
6. B. Bushan (Editor-in-Chief), J.A. Hawk and R.D. Wilson, (Chapter. Eds.), “Tribology of Earthmoving, Mining, and Minerals Processing,” vol. 2 *Modern Tribology Handbook* (Washington, DC: CRC Press LLC, 2001), 1331-1339.
7. E. Rabinovicz, “Abrasive Wear Resistance as a Material Test,” *Lubrication Engineering*, 33 (1977), 378 ff.
8. M. Woydt, “Microstructure and Dry Sliding of Fe₃Al-NbC (MMC)” (Report BAM Federal Institute for Materials Research and Testing, DE-12200 Berlin, Germany, 2014).
9. M. Woydt and H. Mohrbacher, “Hardmetals Based on Niobium Carbide (NbC) versus Casted NbC Bearing MMCs,” Proceedings of the 39th International Conference and Expo on Advanced Ceramics and Composites (ICACC), January 25th-30th, 2015, in Daytona Beach (FL, USA), Published in: Ceramic Engineering and Science Proceedings, 36 (2) (2015).

MECHANICAL CHARACTERIZATION OF HARD PHASES BY MEANS OF NANOINDENTATION

F. Pöhl, A. Weddeling and W. Theisen

Ruhr-Universität Bochum; Chair of Materials Technology;
Universitätsstr. 150; Bochum; 44801; Germany

Keywords: Carbide, NbC, VC, TiC, WC, Nanoindentation, Mechanical Properties, Matrix Influence, Finite Element Method

Abstract

Hard phases are important features of wear-resistant materials. Hard metals and most tool steels thus consist of a high amount of hard phases, such as carbides and nitrides embedded in a softer metallic matrix. The mechanical properties and wear resistance of the system are controlled by the mechanical properties of the hard phases and the matrix. Since hard phases are brittle and have sizes in the range of microns, mechanical characterization with standard test methods, such as the tensile test, is often impossible. Nanoindentation, however, can be used to determine important mechanical parameters, such as hardness or Young's modulus, of brittle phases on a small scale. This paper deals with the mechanical characterization of different hard phases (NbC, VC, TiC, and WC) using nanoindentation. The measurements reveal significant differences in the mechanical properties and deformation behavior of the investigated phases. The deformation behavior was investigated using atomic force microscopy (AFM) and scanning electron microscopy (SEM) with energy-dispersive X-ray spectroscopy (EDS) analysis for the determination of chemical composition. The influence of the matrix on the indentation result of small hard phases embedded in a softer metallic matrix was evaluated using finite element method (FEM) simulations. These simulations give an insight into the complex deformation behavior during indentation of an embedded hard phase.

Introduction

Wear-resistant metallic materials often consist of hard phases (carbides, borides, nitrides) embedded in a softer metallic matrix [1]. The softer matrix supports the hard phases and ensures that the compound system has an adequate toughness. Due to their particular mechanical properties, monocarbides, such as NbC, VC, TiC, and WC are frequently used as reinforcement particles in tool steels and hard metals [2]. The wear behavior of these multiphase materials is essentially controlled by the mechanical properties, morphology, distribution, and dimensions of the hard phases [3]. Mechanical characterization of single phases in multiphase materials is thus crucial to understand the mechanical behavior of the compound and its wear resistance.

Mechanical testing, including handling and preparation, is not a trivial task on account of the small dimensions, in the order of microns, and the high hardness combined with the relatively low fracture toughness. This means that standard test methods, such as the tensile test, cannot be applied. In this respect, there is a lack of knowledge about the mechanical properties of hard

phases and particularly of carbides in tool steels and hard metals. The compound properties of these materials are usually characterized, rather than the properties of the individual phases [1].

One possible method that allows local mechanical characterization of small and brittle phases with minimum sample preparation is nanoindentation [1,4,5]. The results of these tests provide numerous important mechanical parameters, eg. hardness, Young's modulus or indentation energy. Furthermore, pile-up and sink-in characteristics around residual indentation imprints or induced cracks give insight into the complex deformation behavior of hard phases [4,6]. However, nanoindentation of small hard phases and the analysis of data are not trivial. Attention must be paid to the matrix influence on the indentation results [7]. In contrast to the exploration of substrate influence on the indentation results of coatings [8–10], a systematic investigation of the influence of the matrix on hard phase indentation is still missing. Size effects that are well-known from the indentation of metals can also significantly affect indentation results of hard phases [11].

This paper deals with the mechanical characterization of monocarbides in tool steels and in one hard metal by nanoindentation. It is shown that nanoindentation is a suitable method for the mechanical characterization of small scale, hard and brittle phases. However, attention must be paid to size effects and matrix influence on the indentation results. The objective of this study is, firstly, the mechanical characterization and measurement of important parameters of NbC, VC, TiC, and WC monocarbides, and secondly, the exploration of deformation behavior using scanning electron microscopy (SEM) and atomic force microscopy (AFM). A detailed insight into the mechanical behavior of monocarbides during indentation loading is given. These aspects are complemented by numerical and experimental investigations of the influence of the matrix on the indentation results from small embedded carbides.

Materials and Methods

Materials and Sample Preparation

The examined materials and phases are the NbC, VC, TiC, and WC monocarbides. NbC, VC, and TiC were investigated as features in tool steel matrices, whereas WC was evaluated as part of a hard metal.

The sample preparation for nanoindentation and microstructure analysis included grinding with SiC paper, followed by successive polishing with diamond suspensions with average grain sizes of 6, 3, and 1 μm . Final polishing was performed using an oxide polishing suspension with an average grain size of 0.25 μm .

Nanoindentation

Nanoindentation tests were conducted with a CSM Instruments' Nano-Hardness Tester (CSM NHT) indenter equipped with a Berkovich diamond tip. The indentation parameters are given in Table I. The maximum indentation depth for NbC, VC, and TiC was 400 nm. In comparison, WC shows a distinctly smaller particle size so that the indentation depth was adjusted to a maximum of 100 nm. In order to induce cracks, individual tests were conducted with a

maximum indentation depth (h_{\max}) of 800 nm. The hardness and Young's modulus were calculated using the traditional Oliver and Pharr method [12,13]. In addition, the ratio between the elastic energy and the total indentation energy (W_{el}/W_{tot}) was determined. At least five load-displacement curves (P-h curves) were used to calculate the hardness, Young's modulus, and the W_{el}/W_{tot} ratio.

Table I. Nanoindentation Test Parameters

| Indentation depth | Loading/unloading rate | Dwell time at maximum depth |
|--------------------------|-------------------------------|------------------------------------|
| 100/400/800 nm | 50 mN/min | 10 s |

Atomic Force Microscopy

In order to characterize the deformation behavior, the topography of the indents was measured with an atomic force microscope in the contact mode (Bruker type nano). The scanning speed was varied between 10 and 40 $\mu\text{m/s}$. Image Plus 2.9 software was used for data evaluation and three-dimensional visualization.

Scanning Electron Microscopy

Scanning electron microscopy (SEM) with energy-dispersive X-ray spectroscopy (EDS) analysis was used to characterize the microstructure, carbide morphology, residual indents, and chemical composition. The indentation of small scale NbC was analyzed with an SEM in-situ indentation module from Nanomechanics.

Finite-element Modelling (FEM)

FE calculations were performed using the FE software ABAQUS (version 6.11). The axisymmetric 2D FE model is based on prior work [7,14]. The geometry, mesh (detailed view), and boundary conditions of the model are shown in Figure 1. The indenter is modeled as an axisymmetric conical, rigid tip with an included half-apex angle $\theta = 70.3^\circ$. A conical indenter with a half-apex angle of 70.3° leads to the same area-to-depth function as that of a Berkovich indenter. Numerous studies have shown that this approach sufficiently captures the response of a full-3D model [15–17]. Berkovich tips do not usually have ideal sharpness and show a tip rounding in the range of ~ 100 nm, which influences the P-h curve at shallow indentation depths [18]. The FE model took account of a typical tip rounding of 80 nm.

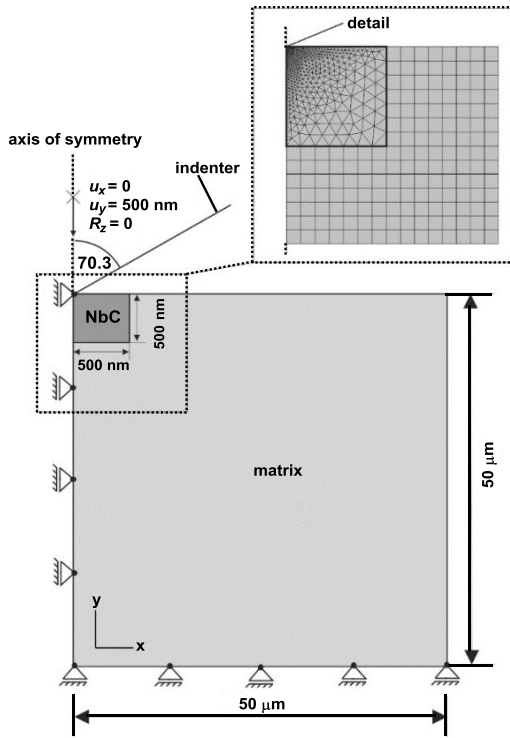


Figure 1. Schematic illustration of the geometry, mesh (detailed view), and boundary conditions of the FE model.

The domain has dimensions of $50 \times 50\ \mu\text{m}^2$. It consists of a hard phase (NbC) embedded in a softer steel matrix. Since most investigated Nb carbides in this study have a blocky morphology, it is assumed to be rectangular. The dimensions are given in Figure 1. Simulations were carried out under displacement-control in which the indenter is pushed perpendicularly into the material with a maximum displacement $u_y = 100\ \text{nm}$, Figure 1. All other degrees of freedom of the indenter are zero. The modeled sample is restricted by symmetry boundary conditions along the axis of symmetry and by floating supports along the lower edge. Contact between indenter and sample is assumed to be frictionless. Investigations have shown that the effect of friction can be neglected for the half-apex angle used in this study [19,20]. The area in close proximity to the point of contact is meshed finely with quad CAX3 elements with reduced integration and hourglass control. To minimize calculation effort, the fine mesh at the contact region is migrated to a coarse one consisting of quad CAX4R elements. The total number of elements is 25,424.

The elastic material behavior was modeled with Young's modulus E and Poisson's ratio ν . The J_2 von Mises flow theory was used to model plasticity [21]. The elasto-plastic material behavior of

the matrix is assumed to follow the Ludwik power law (Equation 1) with isotropic hardening and is described by three independent parameters: K , n , and E (Poisson's ratio ν is assumed to be equal to 0.3 for the matrix and to be 0.27 for NbC) [5]. The Young's modulus of the matrix was assumed to be 210 GPa with a typical strain hardening exponent n of 0.2 [22,23]. The Young's modulus of NbC was assumed to be 400 GPa with no strain hardening ($n = 0$) [24]. This leaves only parameter K to be used for the FEM simulations.

$$\begin{aligned} \sigma &= E\varepsilon_{el} & \sigma &\leq \sigma_y \\ \sigma &= K\varepsilon_{pl}^n & \sigma &> \sigma_y \end{aligned} \quad \text{and} \quad (1)$$

In order to determine the parameter K , the P-h curves of the matrix and a large NbC particle (no matrix influence) were determined. The P-h curves were then numerically calculated, and the material parameter K was adjusted until an agreement between experiment and simulation was achieved. The identified material parameters of the matrix and NbC are listed in Table II. The identified material parameters were used to establish the simulation of a compound consisting of a small NbC (edge length of 1 μm , see Figure 1) in a soft matrix. The numerical results were then compared to the experimental loading curve of a small embedded NbC.

Table II. Identified Material Parameters of the Steel Matrix and NbC for the FE Simulation

| Phase | K (MPa) | n | E (GPa) | ν |
|--------------|-----------|-----|-----------|-------|
| Steel matrix | 4,250 | 0.2 | 210 | 0.30 |
| NbC | 22,500 | 0 | 400 | 0.27 |

Results

Figure 2 shows SEM images of the investigated materials. The NbC, VC, and TiC, with different morphologies and sizes are features of tool steels. They are embedded in a softer metallic steel matrix. The relatively large NbC particles have a blocky and square/triangular shape, whereas the large VC particles are spherical and the smaller TiC particles are spherical and curve shaped. The smallest investigated hard phase is WC, which is part of the microstructure of a cobalt-based hard metal.

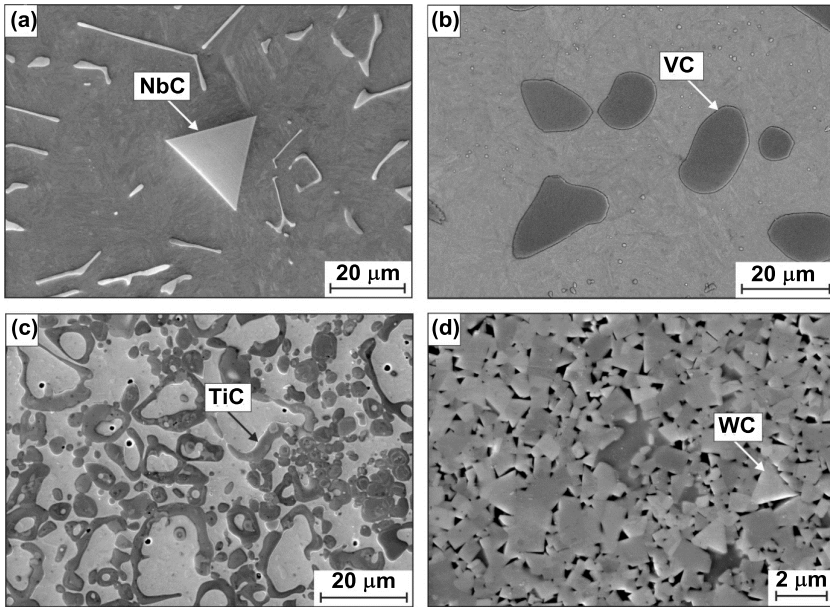


Figure 2. Metal-monocarbide microstructures; (a) Large blocky NbC in a tool steel matrix, (b) Large spherical VC in a tool steel, (c) Spherical and curve shaped TiC in a tool steel, (d) Small blocky WC in a hard metal with cobalt binder.

The chemical composition, measured by EDS, is listed in Tables III and IV. Although the measurement of carbon is not quantitative, the results illustrate that NbC and WC are relatively pure. In contrast, VC dissolves amounts of Fe and other alloying elements and TiC contains amounts of Fe, Mo, and Cr. Due to the presence of higher amounts of the elements Mo, Cr, W, Fe, and Nb, the VC corresponds more to a MC type, however, in this work it is declared as VC.

Table III. Chemical Composition in wt.% Measured by Energy-dispersive X-ray Spectroscopy Analysis. (Measurement of Carbon is not quantitative and is taken as the balance)

| Phase | Nb | V | Ti | W | C | Fe | Mo | Cr |
|-------|------|------|------|------|------|-----|------|-----|
| NbC | 84.4 | - | - | - | 13.3 | 1.1 | - | 1.2 |
| VC | 3.2 | 52.4 | 2.6 | 7.2 | 14.5 | 2.5 | 13.3 | 4.3 |
| TiC | - | - | 74.0 | - | 18.9 | 1.6 | 4.6 | 0.9 |
| WC | - | - | - | 92.6 | 7.4 | - | - | - |

Table IV. Chemical Composition in Atomic % Measured by Energy-dispersive X-ray Spectroscopy Analysis. (Measurement of Carbon is not quantitative and is taken as the balance)

| Phase | Nb | V | Ti | W | C | Fe | Mo | Cr |
|-------|------|------|------|------|------|-----|-----|-----|
| NbC | 44.3 | - | - | - | 53.6 | 1.0 | - | 1.2 |
| VC | 1.3 | 36.3 | 2.1 | 1.5 | 46 | 1.7 | 5.3 | 3.3 |
| TiC | - | - | 48.2 | - | 48.9 | 0.9 | 1.5 | 0.6 |
| WC | - | - | - | 45.2 | 54.8 | - | - | - |

Representative P-h curves of the hard phases are given in Figure 3. Due to the small size of the WC particles, the maximum indentation depth was set to 100 nm. The curves for all the hard phases are similar in shape and show a high amount of elastic recovery during unloading. It is known that fracture during indentation testing can cause pop-in events during loading (plateaus in the loading curve) [25]. However, the loading curves are smooth and do not show indications of brittle cracking.

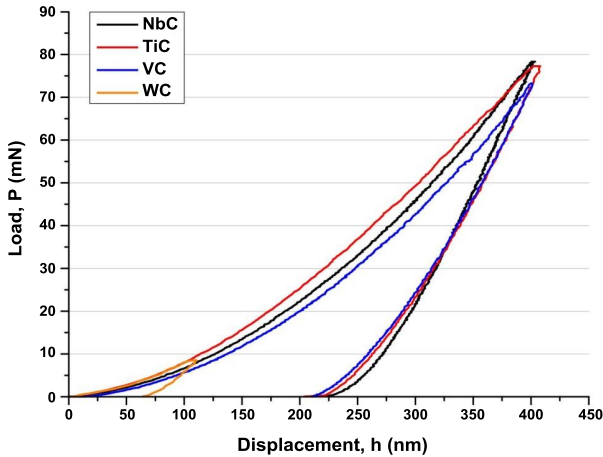


Figure 3. Mean P-h curves of the investigated hard phases.

The calculated mechanical parameters of the hard phases are summarized in Table V. The indentation hardness of all the carbides is within a similar range between 29.5 GPa and 32 GPa. The highest hardness was found for NbC, followed by VC, TiC, and WC. Another important mechanical parameter in indentation testing is the elastic energy to total indentation energy ratio (W_{el}/W_{tot}). The W_{el}/W_{tot} ratios for NbC, VC, and TiC are comparable with high values between 50 and 57%. In contrast, WC shows a distinctly lower ratio of 37%. A comparison of hardness and W_{el}/W_{tot} ratio is given in Figure 4.

Table V. Mechanical Parameters Measured by Nanoindentation. Indentation Hardness H_i was Converted to a Vickers Hardness Number (HV) According to DIN EN ISO 14577 ($HV = 92.62 \cdot H_i$ in GPa), Although the Indentation Depth h was $<6 \mu\text{m}$ [26]

| Phase | H_i (GPa) | HV | E (GPa) | W_{el}/W_{tot} |
|-------|----------------|----------------|--------------|------------------|
| NbC | 32.0 ± 3.8 | 2964 ± 352 | 431 ± 36 | 54 ± 4 |
| VC | 30.7 ± 2.0 | 2845 ± 182 | 423 ± 20 | 50 ± 3 |
| TiC | 29.7 ± 2.5 | 2763 ± 227 | 392 ± 26 | 57 ± 5 |
| WC | 29.5 ± 3.3 | 2672 ± 302 | 675 ± 44 | 37 ± 3 |

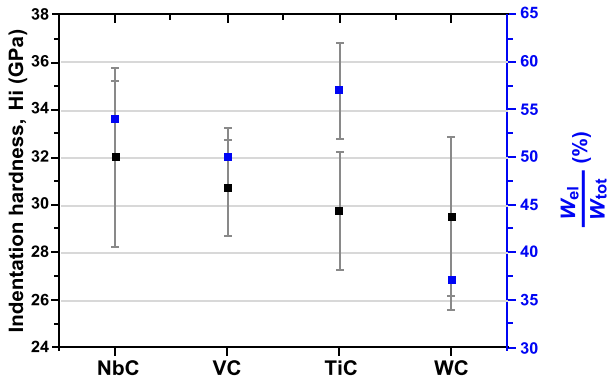


Figure 4. Comparison of hardness and W_{el}/W_{tot} ratio.

Size effects can significantly influence the indentation results of materials. In the case of self-similar indenters (eg. Berkovich), the indentation size effect (ISE) leads to an increase in measured strength with decreasing indentation depth. The ISE for self-similar indenters is characterized by measuring the hardness as a function of indentation depth [27]. Another way to detect an increase in strength with decreasing indentation depth is the analysis of the loading curvature C (related to Martens hardness). The loading curvature is dependent on the indenter geometry and the mechanical properties (strength) of the investigated material. For an ideal self-similar indenter and a homogeneous material without ISE, the loading curvature is constant and is given by Equation 2. In the case of ISE, the loading curvature is a function of indentation depth h and increases with decreasing h , which is caused by an increase in strength (Equation 3) [14].

$$P = Ch^2 \quad \text{with} \quad C = \text{const.} \quad (2)$$

$$P = Ch^2 \quad \text{with} \quad C = f(h) \quad (3)$$

The parameter C is plotted as a function of indentation depth in Figure 5. It increases with decreasing indentation depth h for all hard phases. The phases NbC, TiC, and WC show a similar and distinct increase in C . In contrast, the increase is considerably lower for VC.

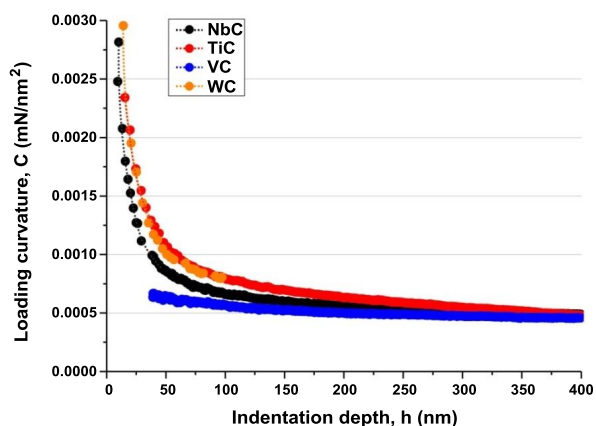


Figure 5. Increase of loading curvature C (related to strength) with decreasing indentation depth.

Figure 6 and Figure 7 illustrate the deformation behavior of NbC, VC, and TiC. The indentation imprints in WC are too shallow for an accurate analysis due to the low indentation depth and high elastic rebound during unloading. As can be seen in Figure 6(b) and 6(c), the indentation in VC and TiC causes fracture, with induced cracks at the edges and corners of the imprint. The deformation of TiC also shows the formation of discrete deformation bands. An example is given in Figure 6(d). In contrast, these observations were not found for NbC. From Figure 6(a) it is evident that there are no cracks or discrete deformation bands. The difference in deformation behavior (fracturing) between VC and NbC is also illustrated in Figure 7.

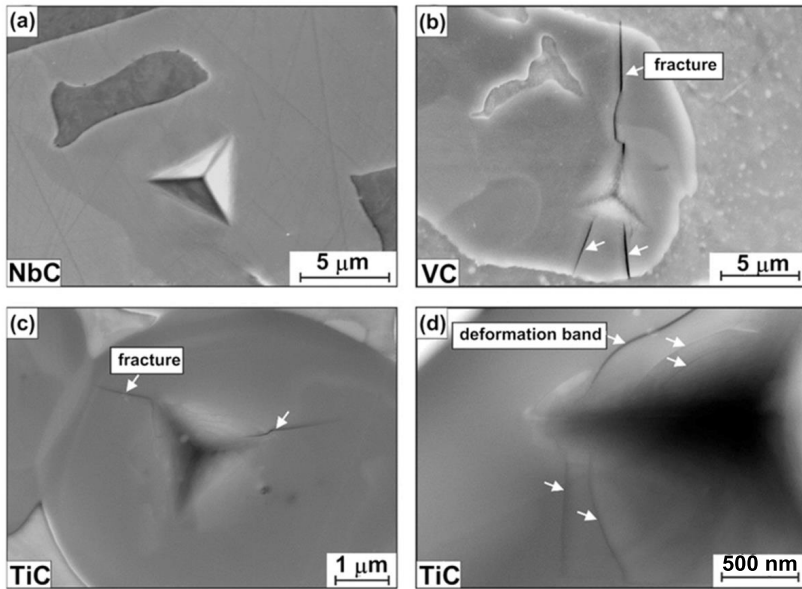


Figure 6. Deformation and fracture of: (a) NbC, (b) VC, (c) and (d) TiC.

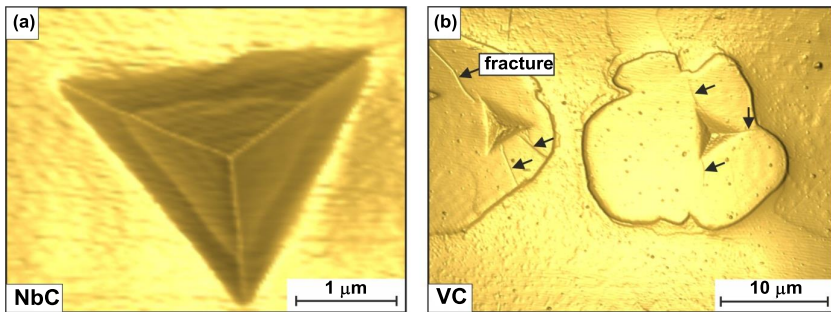


Figure 7. Topographic images of residual indentation imprints in: (a) NbC and (b) VC.

Topographic images of the imprints reveal that all investigated hard phases exhibit slight sink-in around the indentation, rather than pile-up. An example, including a height profile across an imprint, is given for NbC in Figure 8.

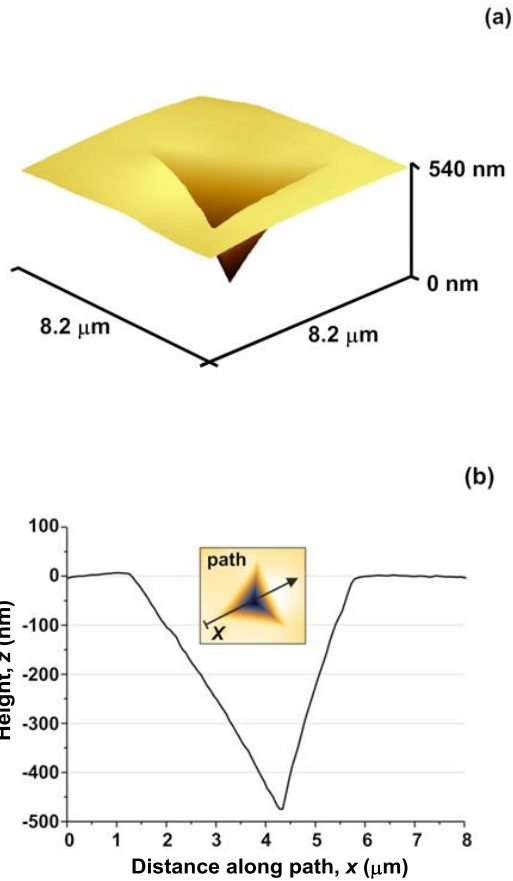


Figure 8. (a) 3D image of an imprint in NbC ($h_{\max} = 800$ nm) and (b) height profile along path x .

Another factor influencing the indentation results from an embedded hard phase is the surrounding matrix. As can easily be recognized in Figure 9, the indentation of small hard phases can lead to deformation of both the hard phase and the matrix. Thus, the P-h curve, as well as the calculated hardness, Young's modulus and W_{el}/W_{tot} ratio can be significantly affected by the matrix. However, indications of an influence of the matrix in a measured P-h curve cannot easily be detected.

In order to illustrate the matrix influence, the measured loading parts of the P-h curve for a large and a small NbC, as well as the pure matrix are plotted in Figure 10. At low indentation depths,

the loading curves of a small and a large NbC are in good agreement. At a depth of approximately 42 nm, the softer matrix begins to influence the P-h curve for the smaller NbC particle by shifting it to lower forces with increasing indentation depth. Lower forces are accompanied by a reduction in the measured strength (lower hardness and W_{el}/W_{tot} ratio). FEM simulations prove that the measured curve for the small NbC particle is significantly influenced by the softer matrix. The data points in Figure 10 are the results of FEM simulations that illustrate the force shift caused by the matrix influence. Due to the matrix influence, the loading curvature C of small NbC particles (rectangular 500 nm x 1000 nm) is reduced by $\sim 18\%$ at an indentation depth of 100 nm, Figure 11. This clearly shows the underestimation of strength as a result of matrix deformation. The von Mises stress distribution of the compound system (small NbC and matrix) at the maximum indentation depth (100 nm) clearly reveals matrix deformation that influences the P-h curve, Figure 12.

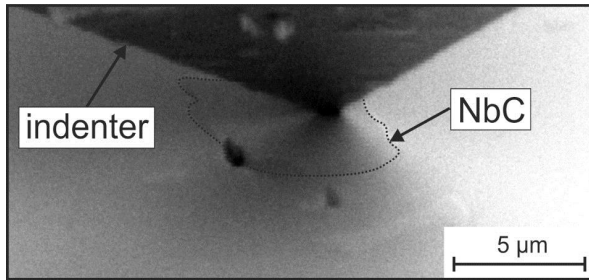


Figure 9. Indenter in contact with small NbC embedded in steel matrix.

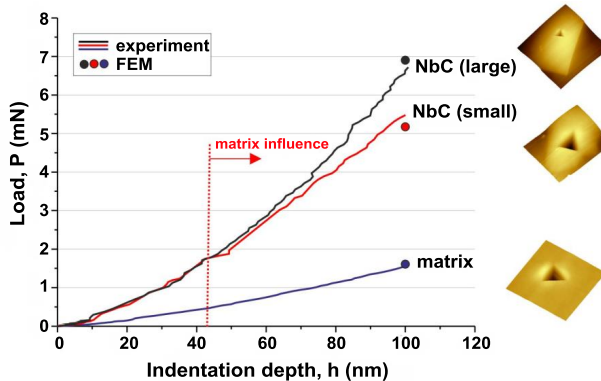


Figure 10. Experimental loading curves (solid lines) and results of FEM simulations (points) for a large NbC and a small embedded NbC, as well as the pure steel matrix. At indentation depths of approximately 42 nm and above, the matrix influences the indentation results from the small embedded NbC.

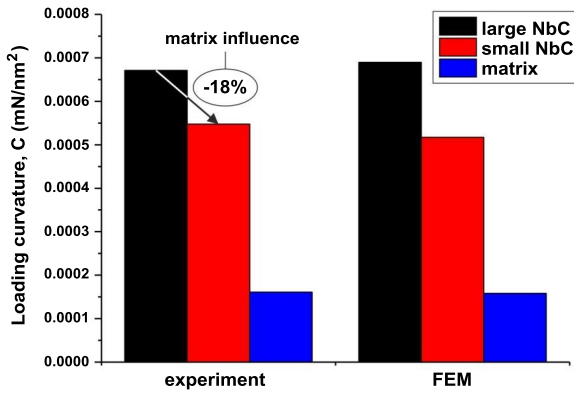


Figure 11. Comparison of loading curvature C of large NbC and small embedded NbC, as well as the pure matrix. The matrix influence leads to a reduction of 18% for the small NbC. The maximum indentation depth is 100 nm.

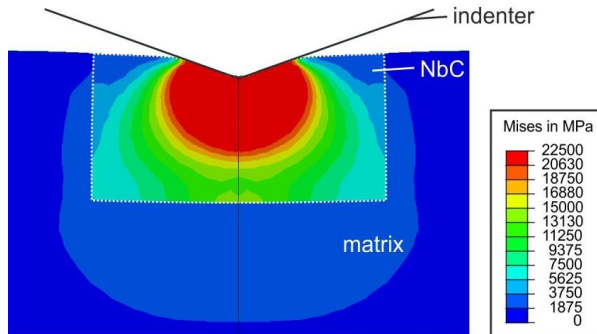


Figure 12. Numerically calculated von Mises stress distribution in small embedded NbC and the surrounding matrix. Deformation takes place in the NbC and in the matrix.

Discussion

The compound wear resistance of multiphase materials is dependent on the microstructure (including the single-phase mechanical properties) and the wear system [28]. In order to improve the abrasive wear resistance, microstructures often consist of high amounts of hard phases embedded in a softer metallic matrix.

It has often been shown that hard phases, as features in wear-resistant materials, need to be harder than the abrading particles in order to be effective [28]. One important property directly related to the abrasive wear resistance of the compound is thus the hardness of the hard phase. All investigated hard phases (NbC, TiC, VC, and WC) exhibit a high hardness in the range between 29.5 GPa and 32 GPa. Due to their hardness, which is higher than most abrading particles/minerals, these carbides are useful as reinforcement particles in wear-resistant materials. The highest measured hardness was found for NbC, followed by VC, TiC, and WC.

Variations of chemical composition of the monocarbides can lead to changes in stoichiometry and atomic bonding, which can significantly affect the mechanical properties. Hill et al. revealed a negative influence of Mo present in TiC [29]. In their investigations, the diffusion of Mo into the TiC led to a reduction of the hardness. The TiC and VC investigated in this study also contain Mo along with other alloying elements. In contrast, NbC and WC are relatively pure and do not dissolve high amounts of alloying elements. Negative influences caused by diffusion of alloying elements into NbC and WC can thus be excluded. Furthermore, Cr depletion of a corrosion-resistant matrix cannot occur with NbC and WC.

As is well-known from metallic materials, the indentation size effect (ISE) can significantly affect indentation results [27]. According to Nix and Gao, the ISE is usually related to the density of the geometrically necessary dislocations, which are dependent on material and indenter geometry. In the case of self-similar indenters, (eg. Berkovich), the ISE is a size-dependent increase in measured strength (hardness) with decreasing indentation depth [30]. Similar to metallic materials, an ISE was also observed for oxides and carbides [12]. Bull et al. related the ISE of ceramics to discrete deformation effects. They concluded that the deformation of hard phases takes place in discrete bands rather than being continuous [31,32]. A similar behavior can be seen in Figure 6(d).

Figure 5 reveals that all investigated monocarbides exhibit an ISE. It is related to discrete deformation effects with a size-dependent increase in measured strength. The ISE becomes apparent by an increase in C (loading curvature) with decreasing indentation depth h . The phases NbC, TiC, and WC show a similar ISE consisting of a distinct increase in C. In contrast, the ISE of VC is considerably lower. The hardness of WC was measured with a maximum indentation depth of 100 nm, but with a maximum indentation depth of 400 nm for all the other carbides. As Figure 5 clearly illustrates, the ISE in WC is still present at an indentation depth of 100 nm. Due to the small particle size of WC, it was not possible to increase the indentation depth without causing a significant matrix influence on the measurement, however, it can be expected that the hardness of WC measured with an indentation depth of 400 nm would be considerably lower than 29.5 GPa (equivalent to 2672 HV). Berns and Franco measured a Vickers hardness number for WC (1914 HV 0.05) at a higher indentation depth which is considerably lower [5]. It is thus concluded that the hardness of NbC, TiC, and VC is significantly higher than the hardness of WC. However, the investigations show that care must be taken when comparing the hardness of hard phases measured at different indentation depths.

Another important indentation parameter is the W_{el}/W_{tot} ratio. Niederhofer and Huth showed that the W_{el}/W_{tot} ratio is a potentially useful parameter which can be related to the wear behavior [33]. All monocarbides show a high amount of elastic recovery during unloading, which is typical for

hard phases. The W_{el}/W_{tot} ratio of NbC, TiC, and VC is considerably higher (50-57%) compared to WC (37%). Based on the investigations of Niederhofer and Huth, it is concluded that a high W_{el}/W_{tot} ratio might be beneficial for increasing the wear resistance, however, a systematic investigation has not yet been conducted.

Along with the hardness and the W_{el}/W_{tot} ratio, the fracture toughness has a crucial influence on the wear behavior. The deformation and cracking behavior of hard phases during indentation is related to the fracture toughness and to the mechanical behavior under wear attack. The indentation imprints in NbC feature a homogeneous deformation without fracture and cracking. Despite having a high W_{el}/W_{tot} ratio, the deformation is relatively ductile. At equal indentation depth (800 nm), TiC and VC show cracking. Furthermore, discrete deformation bands are observed for TiC, Figure 6. As a consequence, TiC and VC are likely to have lower fracture toughness than NbC. Due to the small phase sizes, the cracks (ending at the phase boundary) could not be analyzed in order to estimate the fracture toughness with empirical equations. Another aspect of the deformation behavior is the slight sink-in tendency around indentation imprints. Sink-in is usually observed for metallic materials with a high work-hardening potential, but is also related to the W_{el}/W_{tot} ratio [34]. It is concluded that the monocarbides do not exhibit significant work hardening and the slight sink-in is solely caused by the high elastic deformation component.

An important effect on the indentation results of embedded hard phases is exerted by the surrounding matrix. FEM simulations illustrate that the indentation of a hard phase can lead to the deformation of both the hard phase and the softer matrix, Figure 12. The deformation of a softer matrix affects the P-h curve by shifting the loading curve to lower forces. This leads to a lower measured hardness. The indentation of a small rectangular NbC particle (1000 nm x 500 nm) embedded in a steel matrix leads to a significant matrix influence at a depth of 42 nm and above, Figure 11. Measurements at shallow indentation depths may become inaccurate due to the ISE, indenter tip rounding, surface roughness, etc.

In summary, NbC, TiC, VC, and WC monocarbides have a high hardness and a high W_{el}/W_{tot} ratio. Both parameters are considered to be beneficial for improving the wear resistance. Taking into consideration the ISE, WC shows the smallest hardness and W_{el}/W_{tot} ratio. NbC is likely to have the highest toughness (no cracks and deformation bands), although it has the highest hardness. Furthermore, NbC is relatively pure and does not dissolve high amounts of alloying elements that could exert a negative influence on the mechanical properties or lead to Cr depletion of the corrosion-resistant steel matrix.

Conclusions

The main conclusions from this study are:

1. The NbC, TiC, VC, and WC monocarbides have a high hardness and a high W_{el}/W_{tot} ratio. Both are considered to be beneficial for improving wear resistance.
2. The TiC and VC investigated in this study contain Fe and other alloying elements. In contrast, NbC and WC are relatively pure and do not dissolve high amounts of alloying

elements. Negative influences caused by diffusion of alloying elements into NbC and WC can thus be excluded.

3. All investigated hard phases show a distinct ISE that is related to discrete deformation effects with a size-dependent increase in measured strength. The ISE leads to a higher measured hardness with decreasing indentation depth (Berkovich indenter). Due to the small indentation depth of 100 nm, the hardness of WC is higher than values reported in the literature [5]. It is concluded that the hardness of NbC, TiC, and VC is significantly higher than that of WC at a given indentation depth.
4. The indentation imprints in NbC feature homogeneous deformation without fracture and cracking. The W_{el}/W_{tot} ratio is high, whereas the deformation is relatively ductile. In contrast, TiC and VC exhibit cracking at equal indentation depth (800 nm). Furthermore, discrete deformation bands are observed for TiC. As a consequence, TiC and VC are likely to have a lower fracture toughness than NbC.
5. FEM simulations illustrate that the indentation of a small hard phase can lead to the deformation of both the hard phase and the softer matrix. Deformation of the softer matrix affects the P-h curve by shifting the loading curve to lower forces. This leads to a lower measured hardness and Young's modulus.

Acknowledgements

The authors gratefully acknowledge financial support by the Deutsche Forschungsgemeinschaft (project HU 1882/1-1).

References

1. H. Berns, "Microstructural Properties of Wear-resistant Alloys," *Wear*, 1995, no. 181-183:271-279.
2. S. Huang et al., "Microstructural Properties of Wear-resistant Alloys," *International Journal of Refractory Metals and Hard Materials*, 2015, no. 48:418-426.
3. N. Axén and K. Zum Gahr, "Wear of TaC and TiC Steel Composite Hardfacings by Soft and Hard Abrasives," *Materialwissenschaft und Werkstofftechnik*, 23 (10) (1992), 360-367.
4. D. Casellas et al., "Fracture Toughness of Carbides in Tool Steels Evaluated by Nanoindentation," *Acta Materialia*, 2007, no. 55:4277-4286.
5. H. Berns and S. Franco, "Properties of Hard Particles at Room Temperature and Elevated Temperature," *Proceedings of III Seminário Brasileiro* (1994).
6. J. Alcalá, A. Barone and M. Anglada, "The Influence of Plastic Hardening on Surface Deformation Modes Around Vickers and Spherical Indents," *Acta Materialia*, 2000, 48:3451-3464.

7. F. Pöhl, S. Huth and W. Theisen, "Finite Element Method-assisted Acquisition of the Matrix Influence on the Indentation Results of an Embedded Hard Phase," *Materials Science and Engineering: A*, 2013, 559:822-828.
8. N. Sakharova et al., "On the Determination of the Film Hardness in Hard Film/Substrate Composites Using Depth-sensing Indentation," *Ceramics International*, 2013, 39:6251-6263.
9. C. Gamonpilas and E. Busso, "On the Effect of Substrate Properties on the Indentation Behaviour of Coated Systems," *Materials Science and Engineering: A*, 2004, 380:52-61.
10. J. Antunes et al., "On the Determination of the Young's Modulus of Thin Films Using Indentation Tests," *International Journal of Solids and Structures*, 2007, 44:8313-8334.
11. Y. Milman, A. Golumbenko and S. Dub, "Indentation Size Effect in Nanohardness," *Acta Materialia*, 2011, 59:7480-7487.
12. W. Oliver and G. Pharr, "An Improved Technique for Determination Hardness and Elastic-modulus Using Load and Displacement Sensing Indentation Experiments," *Journal of Materials Research*, 1992, 7:1564-1583.
13. W. Oliver and G. Pharr, "Measurement of Hardness and Elastic Modulus by Instrumented Indentation: Advances in Understanding and Refinements to Methodology," *Journal of Materials Research*, 2004, 19:3-20.
14. F. Pöhl and W. Theisen, "Indentation of Self-similar Indenters: An FEM-assisted Energy-based Analysis," *Journal of the Mechanics and Physics of Solids*, 2014, 66:32-41.
15. K. Johnson, "The Correlation of Indentation Experiments," *Journal of the Mechanics and Physics of Solids*, 1970, 18:115-126.
16. P. Larsson, "Modelling of Sharp Indentation Experiments: Some Fundamental Issues," *Philosophical Magazine* 86 (33-35) (2006), 5155-5177.
17. N. Sakharova et al., "Comparison between Berkovich, Vickers and Conical Indentation Tests: A Three-dimensional Numerical Simulation Study," *International Journal of Solids and Structures*, 2009, 46:1095-1104.
18. A. Warren and Y. Guo, "Machined Surface Properties Determined by Nanoindentation: Experimental and FEA Studies on the Effects of Surface Integrity and Tip Geometry," *Surface & Coatings Technology*, 2006, 201:423-433.
19. M. Mata and J. Alcalá, "The Role of Friction on Sharp Indentation," *Journal of the Mechanics and Physics of Solids*, 2004, 52:145-165.
20. J. Bucaille et al., "Determination of Plastic Properties of Metals by Instrumented Indentation Using Different Sharp Indenters," *Acta Materialia*, 2003, 51:1663-1678.

21. ABAQUS (2009) User's Manual v. 6.9, ABAQUS Inc. Providence, USA.
22. M. Le, "Materials Characterisation by Dual Sharp Indenters," *International Journal of Solids and Structures*, 2009, 46:2988-2998.
23. X. Chen et al., "On the Uniqueness of Measuring Elasto-plastic Properties from Indentation: The Indistinguishable Mystical Materials," *Journal of the Mechanics and Physics of Solids*, 2007, 55:1618-1660.
24. X. Jiang and J. Zhao, "Correlation between Hardness and Elastic Moduli of the Covalent Crystals," *Computational Materials Science*, 2011, 50:2287-2290.
25. K. Fu et al., "Analysis on Cracking in Hard Thin Films on a Soft Substrate under Berkovich Indentation," *Vacuum*, 2015, 112:29-32.
26. DIN EN ISO 14577 (2012) Instrumentierte Eindringprüfung zur Bestimmung der Härte und anderer Werkstoffparameter.
27. G. Pharr, E. Herbert and Y. Gao, "The Indentation Size Effect: A Critical Examination of Experimental Observations and Mechanistic Interpretations," *Annual Review of Materials Research*, 2010, 40:271-292.
28. H. Berns, "Hard Alloys - Microstructure and Abrasion Resistance," *Proceedings of the III Brazilian Seminar on Wear Resistant Materials*, (1994), Fortaleza, Brasil.
29. H. Hill et al., "The Impact of Processing on Microstructure, Single-phase Properties and Wear Resistance of MMCs," *Wear*, 271 (9-10) (2011), 1895-1902.
30. W. Nix and H. Gao, "Indentation Size Effects in Crystalline Materials: A Law for Strain Gradient Plasticity," *Journal of the Mechanics and Physics of Solids*, 46 (3) (1998), 411-425.
31. S. Bull, "On the Origins and Mechanisms of the Indentation Size Effect," *Zeitschrift für Metallkunde*, 94 (7) (2003), 787-792.
32. S. Bull, T. Page and E. Yoffe, "An Explanation of the Indentation Size Effect in Ceramics," *Philosophical Magazine*, 59 (6) (1989), 281-288.
33. P. Niederhofer and S. Huth, "Cavitation Erosion Resistance of High Interstitial CrMnCN Austenitic Stainless Steels," *Wear*, 301 (1-2) (2013), 457-466.
34. G. Das, S. Gosh and R. Gosh, "Materials Characterization and Classification on the Basis of Materials Pile-up Surrounding the Indentation," *Materials Science and Engineering: A*, 2005, 408:158-164.

FORMATION OF NIOBIUM CARBIDE COATING ON AISI L2 STEEL USING THERMO-REACTIVE DIFFUSION (TRD) TECHNIQUE

M. Azizi and M. Soltanieh

Iran University of Science and Technology, Narmak, Tehran, 1684613114, Iran

Keywords: Niobium, Hard Coatings, TRD, Surface, Diffusion, Thermochemical Process, Niobium Carbide Coating

Abstract

In this study, a thin layer of niobium carbide was thermochemically formed on AISI L2 tool steel substrates using the thermo-reactive diffusion (TRD) method. Five different compositions of salt bath were selected and for each composition the treatment was performed at three different temperatures (900, 1000, 1100 °C) for three different times (two, four, eight hours). The morphology of the coating was characterized through optical and scanning electron microscopy (SEM), and the crystalline structure was studied through X-ray diffraction (XRD). The reaction layer of niobium carbide formed was uniform all over the surface and had a smooth interface with the substrate. The thickness of the coating varied from 3.6 to 33 μm depending on the chemical composition of the salt bath, process time and temperature. The chemical composition was evaluated via Energy-dispersive X-ray Spectroscopy (EDS) and the atomic distribution map of the coating and substrate was prepared. The hardness value of the coated samples was 2450 ± 50 HV 0.05 which was much higher than the hardness of the uncoated sample (280 HV). Corrosion properties of NbC coated samples in 3% NaCl solution were studied and the results showed that coated samples had better corrosion resistance in comparison to the uncoated steel.

Introduction

Since the 1960s, hard coatings have been applied as an effective solution to decrease wear and improve friction characteristics of tool steels, especially in cutting tools [1]. Niobium carbide (NbC) coatings have been attracting considerable attention owing to their excellent properties. In addition to the high melting point (3610 °C), excellent chemical stability, high toughness, excellent wear and friction properties [2,3], it possesses extremely high hardness [4].

Physical vapor deposition (PVD) and chemical vapor deposition (CVD) are the techniques which are used to produce NbC coatings on an industrial scale. These methods have advantages and disadvantages. For instance, both techniques require expensive and complicated equipment that must be operated under high-vacuum conditions [5]. The thermo-reactive diffusion technique (TRD), also known as TOYOTA Diffusion process (TD) [6] is another technique used to achieve NbC coatings. The main advantage of the TRD process appears to be its low cost, because the treatment is performed at atmospheric pressure and it does not require such expensive equipment as the high-vacuum techniques [7].

In the TRD process, one of the carbide or nitride forming elements such as Nb, Cr, V, Ti diffuses into the surface by a thermochemical process at elevated temperatures (800-1200 °C) and forms a carbide or nitride layer on the surface [8,9]. Most carbon-containing materials such as steels, cast irons, cobalt alloys, cemented carbides, carbide-metal cermets, carbide ceramics, and carbon may be used as the substrates for carbide coating [10]. The best applications for TRD coatings are tools that have demanding wear requirements and galling problems. This includes many types of forming and cutting tools, and die components. Examples of the applications of NbC coating include: draw-dies for sheet metal working, squeeze-rolls for pipe and tube manufacturing, die-casting cores and sleeves for aluminum and zinc casting, extrusion punches and dies for cold forging and warm forging, press-forging dies for hot forging, form dies for rubber and plastic forming, cutting tools and knives [11].

The aim of this study is the forming of thin reaction layers of NbC on AISI L2 tool steel using the TRD method and assessing its properties in addition to investigating the effect of some parameters including temperature, treatment time and chemical composition of the molten bath on the coating.

Experimental Method

Five different compositions of molten salt bath comprising borax ($\text{Na}_2\text{B}_4\text{O}_7$), boric oxide (B_2O_3 , added as boric acid) and ferroniobium (65 wt.% niobium) were selected according to Table I. Cylindrical samples of AISI L2 tool steel (ϕ 10 mm \times height 15 mm) were prepared for the TRD process. Forty-five specimens were coated by immersing in the molten bath. For each composition of the bath, treatment was performed at 900 °C, 1000 °C and 1100 °C for two, four and eight hours. Then samples were cooled in air and were cleaned of the remaining salt using boiling water.

Table I. Compositions* of Molten Salt Bath

| Composition Number | Ferroniobium Concentration (wt.%) | Borax Concentration (wt.%) | Boric Acid Concentration (wt.%) |
|--------------------|-----------------------------------|----------------------------|---------------------------------|
| Composition 1 | 5 | 90 | 5 |
| Composition 2 | 7 | 88 | 5 |
| Composition 3 | 10 | 85 | 5 |
| Composition 4 | 20 | 75 | 5 |
| Composition 5 | 30 | 65 | 5 |

*Compositions refer to the additions at room temperature

The microhardness of the coating was measured by means of the BUEHLER Micro Met instrument. The applied load of the microhardness test was 50 g for 15 seconds. Samples were sectioned, polished and etched with 2% nital. Microstructural details of the samples were studied using the Optical Microscope (OM), and the TESCAN VEGAII XMU Scanning Electron Microscope (SEM) equipped with Energy Dispersive X-ray Spectrometry (EDS). The atomic distribution profile in the coating and substrate was studied by X-ray Spectrometry. The thickness of the coating was measured by means of a micrometer attached to the optical

microscope. The values reported for thickness were the average of at least ten measurements. The coating phases were analyzed by JOEL-JDX-8030 X-Ray Diffraction (XRD) using Cu-K α radiation. The Tafel potentiodynamic polarization test was carried out to assess corrosion resistance of the coated samples in 3 wt.% NaCl solution.

Results and Discussion

Characterization of the Coating

Optical and SEM micrographs of the cross-section of the treated samples showed that a uniform layer of NbC was formed all over the surface with a dense and compact morphology. The coating had a smooth interface with the substrate for all of the treated samples. In Figure 1, the optical micrograph of the cross section of the sample treated for four hours at 1100 °C in bath composition 4, Table I, is shown. The NbC coating (light region) is clearly distinguished in this image, uniformly covering the substrate (dark region). The XRD analyses of the coated samples revealed that the composition of the coating was NbC for all the treatment temperatures and times, Figure 2. However, it has been reported that NbC coating treatment by the TRD method in a solid medium forms NbC/Nb₂C multiphase [12]. In Figure 3, the SEM image of the section from the treated sample in a molten bath containing 20 wt.% ferroniobium for two hours at 1100 °C is shown.

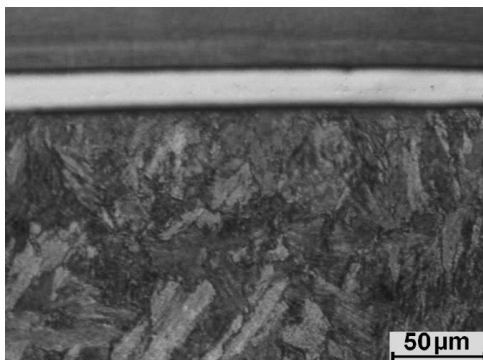
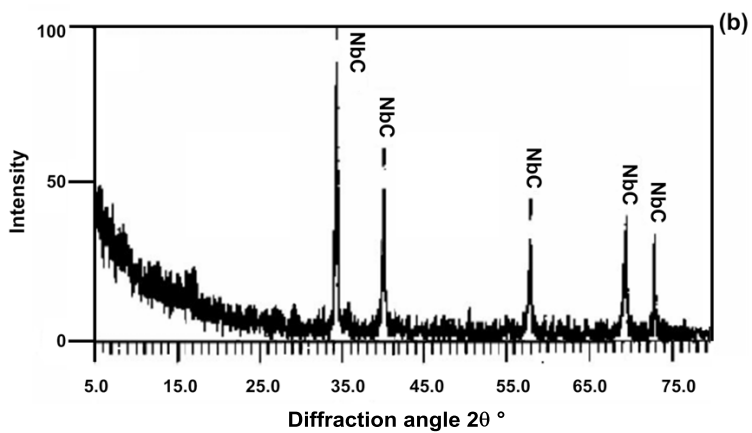
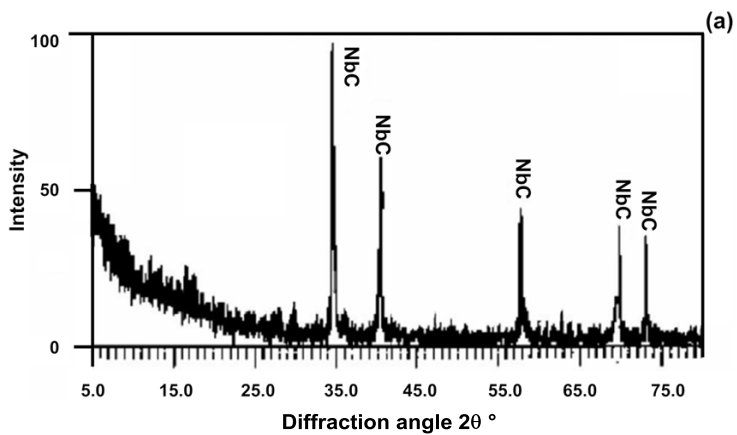


Figure 1. Optical micrograph of the section from the sample treated in a molten bath comprising 20 wt.% ferroniobium for two hours at 1100 °C.



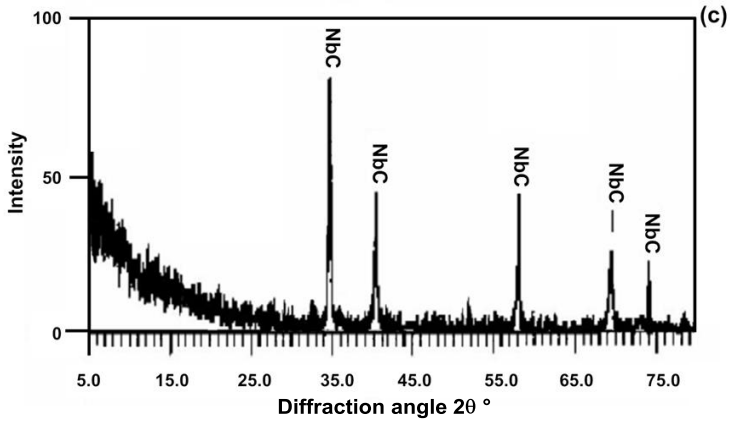


Figure 2. X-ray diffraction spectra of specimens; (a) treated in composition two for two hours at 1100 °C, (b) treated in composition four for eight hours at 1000 °C, (c) treated in composition three for four hours at 900 °C .

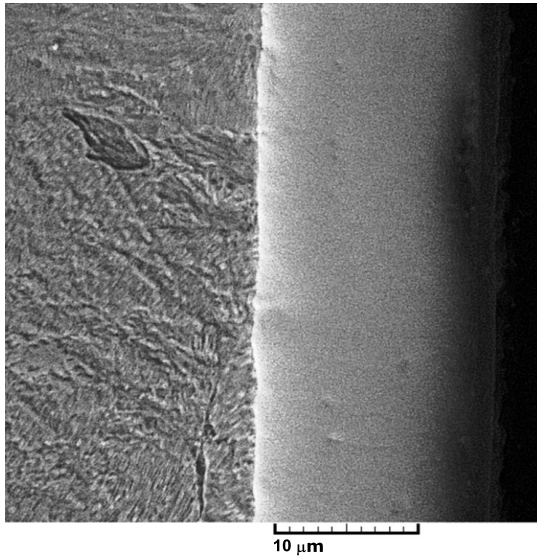


Figure 3. SEM micrograph of the cross section of the sample treated in a molten bath containing 20 wt.% ferroniobium for two hours at 1100 °C.

The result of point EDS analysis showed that the concentration of iron within the coating at different distances from the coating/substrate interface was insignificant (maximum 0.9 wt.%). In addition, the concentration of niobium within the substrate was a maximum of 0.1 wt.%. Carbon was detected in the coating and substrate, but because of apparatus error, the reported concentration of carbon was not accurate. However, the formation of NbC on the substrate confirms the outward diffusion of carbon to the coating. The linear distribution map of the elements Nb, C, Fe is shown in Figure 4. It is observed that diffusion of iron atoms from the substrate to the coating, and diffusion of niobium atoms from the coating to the substrate are limited. This intermixing generates an interface assuring a metallurgical bond. The distribution map of elements confirms the presumed mechanism that the dissolved niobium in the salt bath is adsorbed on the surface of the steel and carbon diffuses outward to the coating and combines with niobium and forms the NbC coating [13].

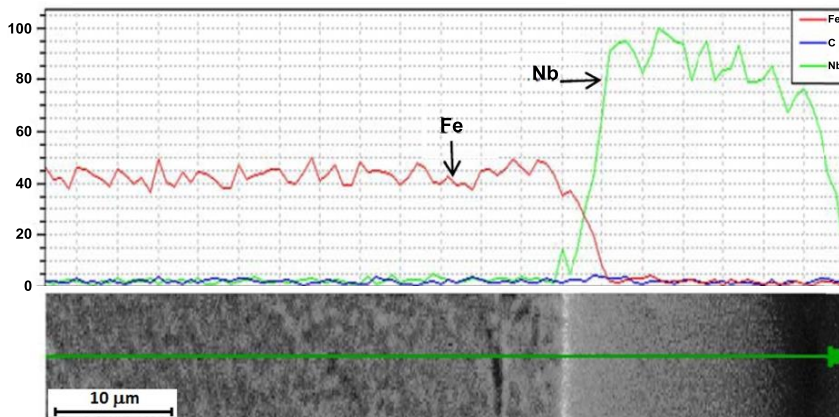
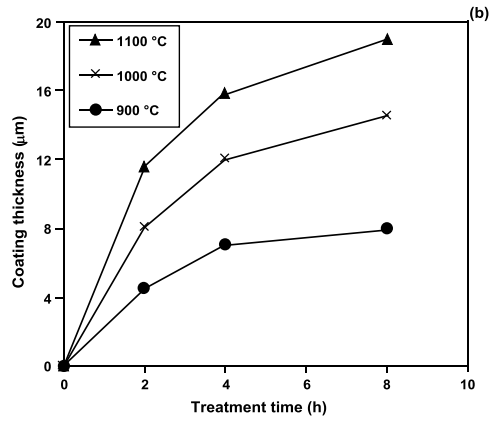
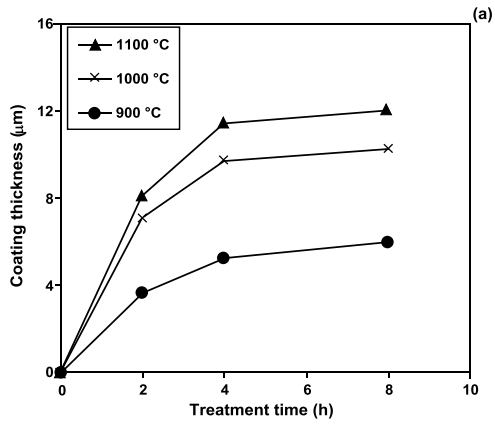
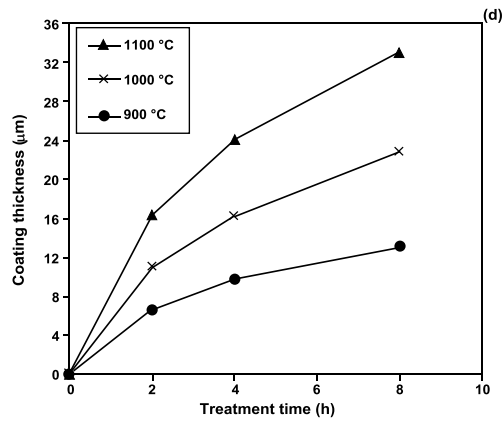
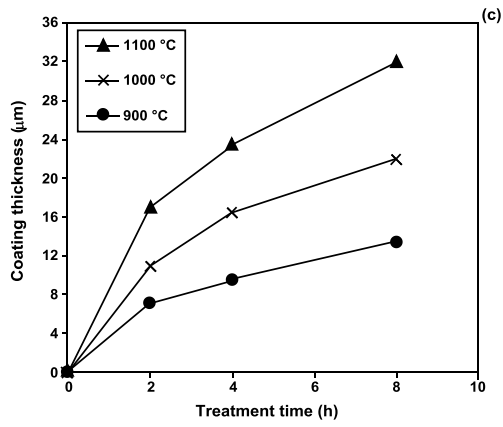


Figure 4. EDS line scan analysis of the section from the sample treated in a molten bath containing 30 wt.% ferroniobium for four hours at 1100 °C.

Effect of the Parameters on the Coating Growth

The thickness of the coating varied from 3.6 to 33 μm depending on process time, temperature and the chemical composition of the salt bath. The effect of treatment time on the thickness of the coating at different temperatures and different molten bath compositions is shown in Figure 5. Figures 5(a)-(e) exhibit the thickness of coating versus treatment time plots for the molten baths containing 5, 7, 10, 20, and 30 wt.% ferroniobium respectively. It is observed that for all of the molten bath compositions the thickness of the coating increases significantly with increasing time of treatment. In addition, the graphs show greater thicknesses at higher treatment temperatures. It shows the considerable effect of temperature on the rate of coating growth.





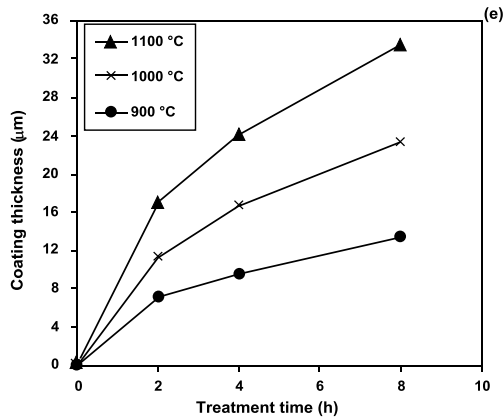
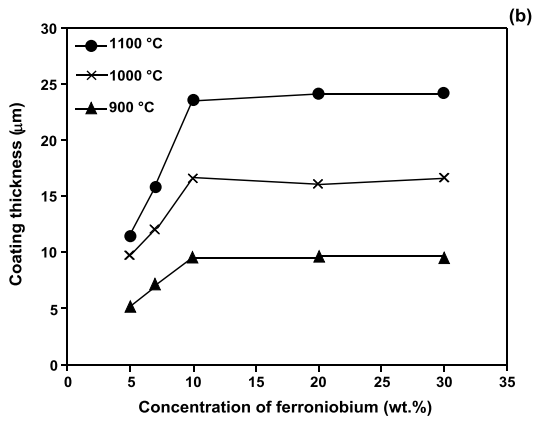
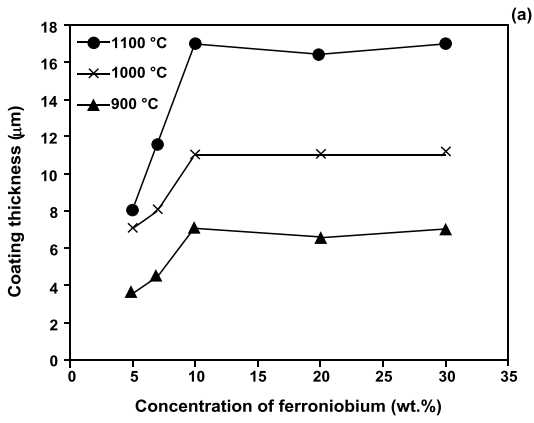


Figure 5. Coating thickness versus treatment time for different compositions of salt bath (Table I); (a) composition 1, (b) composition 2, (c) composition 3, (d) composition 4, (e) composition 5.

In Figure 6 the effect of chemical composition of the molten bath on the thickness of the coatings at different treatment temperatures is shown. It is observed that for the molten baths containing less than 10 wt.% ferroniobium, an increase in the concentration of niobium in the bath results in an increase in the thickness of the coating. However, for the molten baths containing more than 10 wt.% ferroniobium the concentration of niobium has an insignificant effect on the thickness of the coating. It is assumed that for the molten baths which contain a small amount of ferroniobium (less than 10 wt.%), the adsorption of niobium atoms on the surface of samples is the rate controlling step. However, for the molten baths comprising more than 10 wt.% ferroniobium, there are sufficient quantities of dissolved niobium and the growth kinetics of the coating are not under the control of the adsorption of niobium atoms on the surface.



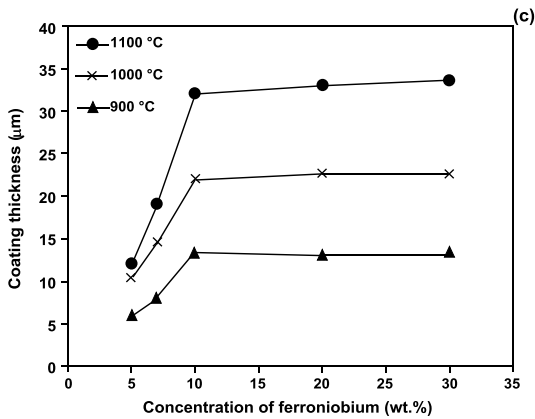


Figure 6. Coating thickness versus concentration of ferroniobium in the molten bath; (a) treated for two hours, (b) treated for four hours, (c) treated for eight hours.

Hardness

The results of the microhardness tests on the coated samples reveal a great increase in the hardness compared with the uncoated samples (280 HV). The microhardness of all the coated specimens was almost the same ranging from 2400 to 2500 HV. Figure 7 shows the microhardness test traverses and the hardness profile on the cross-section of the specimen treated in a molten bath comprising 10 wt.% ferroniobium at 1000 °C for four hours. In order to increase the number of readings, the hardness traverses were taken at an angle to the surface. The hardness profile shows that the hardness of the coating remains almost the same at all distances from the coating/substrate interface, but, it drops dramatically at the interface and within the substrate. Owing to the fact that the Vickers indentation imposed in the coating/substrate interface does not show the formation or propagation of cracks at the interface, it can be concluded that there is a strong metallurgical bond between coating and substrate.

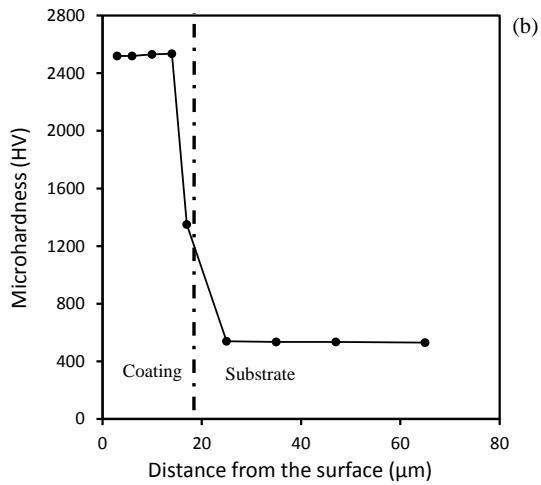
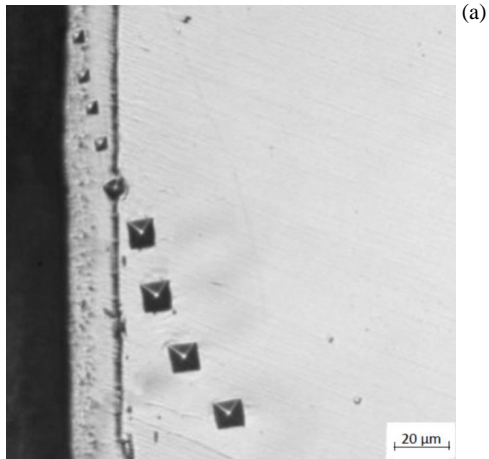


Figure 7. Microhardness versus distance from surface of the coated sample treated in a molten bath comprising 10 wt.% ferroniobium at 1000 °C for four hours; (a) image from microhardness test traverses, (b) microhardness profile.

The hardness of the NbC coating which is produced by the TRD technique is almost the same as the hardness of vanadium carbide TRD coatings (2430-2700 HV) [14] and higher than the hardness of other TRD coatings including chromium carbide (1350±30 HV) [15], chromium nitride (1780±58) [16], vanadium carbonitride (2220±40) [17], and boronized steel (1600-1900 HV) [10].

Corrosion Properties

Figure 8 shows polarization curves of the Tafel potentiodynamic polarization test in 3 wt.% NaCl solution of three coated specimens treated in a molten bath containing 10 wt.% ferroniobium for four hours at three different treatment temperatures (900, 1000, 1100 °C) and the uncoated specimen. A positive shift in corrosion potential has occurred due to the application of the coating. It is observed that the corrosion potential of the coated samples at different treatment temperatures is almost the same. Polarization curves of coated samples exhibit a passive behavior which can be affected by treatment temperature. In summary, coated specimens show better corrosion resistance in comparison with the uncoated specimen.

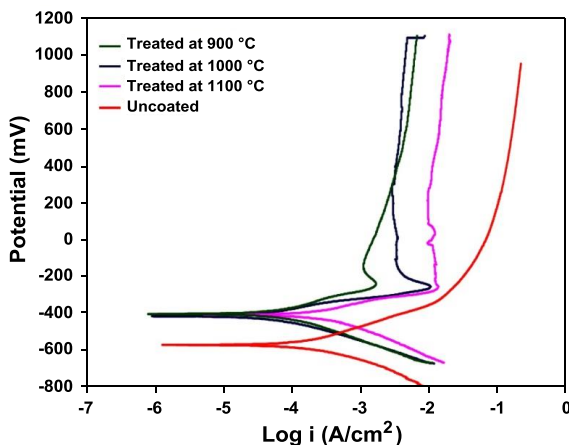


Figure 8. Potentiodynamic curves of three coated specimens treated in the molten bath containing 10 wt.% ferroniobium for four hours and the uncoated specimen.

Conclusions

The thermo-reactive diffusion technique has been employed to produce NbC coatings on AISI L2 tool steel, using different salt bath chemistries, temperatures and times.

1. NbC coating has a dense and compact morphology and good metallurgical bonding with the substrate.
2. The coating thickness increases with time (0-8 hours) and temperature (900, 1000, 1100 °C).
3. For the molten baths comprising less than 10 wt.% ferroniobium, an increase in the concentration of niobium in the bath results in an increase in the thickness of the coating for a given time and temperature. However, for the molten baths containing more than 10 wt.% ferroniobium the concentration of niobium has an insignificant effect on the thickness of the coating. It is assumed that for the molten baths which contain less than 10 wt.% niobium, the adsorption of niobium atoms on the surface of samples is the rate controlling step. However, for the molten baths containing more than 10 wt.% ferroniobium, there is a sufficient quantity of dissolved niobium and the growth kinetics of the coating are not under the control of the adsorption of niobium atoms on the surface.
4. The hardness value of the TRD coated samples is 2450 ± 50 HV 0.05 which is much higher than the hardness value of uncoated steel (280 HV). Comparing other TRD coatings, it is similar to vanadium carbide (2430-2700 HV) and higher than chromium carbide (1350 ± 30 HV), chromium nitride (1780 ± 58), and vanadium carbonitride (2220 ± 40).
5. NbC coating improves the corrosion resistance of steel in 3 wt.% NaCl solution.

References

1. W. Schintlmeister et al., "Cutting Tool Materials Coated by Chemical Vapor Deposition," *Wear*, 100 (1984), 153-169.
2. U. Sen, "Wear Properties of Niobium Carbide Coatings Performed by Pack Method on AISI 1040 Steel," *Thin Solid Films*, 483 (2005), 152-157.
3. C.K.N. Oliveira, R.M.M. Riofano and L.C. Casteletti, "Micro-Abrasive Wear Test of Niobium Carbide Layers Produced on AISI H13 and M2 Steels," *Surface and Coatings Technology*, 200 (2006), 5140-5144.
4. T. Amriou et al., "Investigations of Electronic Structure and Bonding Mechanism of NbC and NbN Compounds," *Physica B: Condensed Matter*, 325 (2003), 46-56.
5. D.H. Kuo and K.W. Huang, "Kinetics and Microstructure of TiN Coatings by CVD," *Surface and Coatings Technology*, 135 (2001), 150-157.

6. G. Seim, H. Glaser and S. Harper, "Case Studies in Practical Application of the TD Process" (Paper presented at the International Tribology Conference, Nagoya, Japan, 29 October – 1 November 1990), 1993-1997.
7. F.E. Castillejo et al., "Wear and Corrosion Resistance of Niobium-Chromium Carbide Coatings on AISI D2 Produced Through TRD," *Surface and Coatings Technology*, 254 (2014), 104-111.
8. N. Komatsu, T. Arai and M. Mizutani, "Process of Forming a Carbide Layer of Vanadium, Niobium, or Tantalum Upon a Steel Surface," (U.S. Patent 3719518), (1973).
9. T. Arai and S. Moriama, "Growth Behavior of Vanadium Carbide Coating on Steel Substrate by a Salt Bath Immersion Coating Process," *Thin Solid Films*, 249 (1994), 54-61.
10. Tohru Arai et al., *ASM Handbook*, Vol. 4 (Materials Park, OH, ASM International, 1991), 437 and 448.
11. J.R. Davis, *Surface Hardening of Steels*, (Materials Park, OH: ASM International, 2002), 232-236.
12. U. Sen, "Kinetics of Niobium Carbide Coating Produced on AISI 1040 Steel by Thermo-Reactive Deposition Technique," *Materials Chemistry and Physics*, 86 (2004), 189-194.
13. M. Azizi and M. Soltanieh, "Kinetic Study of Niobium Carbide Coating Formation on AISI L2 Steel Using Thermo-Reactive Deposition Technique" *International Journal of Engineering, Transactions B*, 23 (2010), 77-85.
14. M. Aghaie and N. Daemi, "Characterization of Vanadium Carbide Coating Deposited by Borax Salt Bath Process," *Advances in Materials Research*, 1 (2012), 233-243.
15. H.R. Karimi, M. Jalaly and M. Soltanieh, "Kinetics of Chromium Carbide Formation on AISI 1020 Steel by TRD Process," *Journal of Faculty of Engineering*, 36 (2008), 87-92.
16. O. Ozdemir, S. Sen and U. Sen, "Formation of Chromium Nitride Layers on AISI 1010 Steel by Nitro-Chromizing Treatment," *Vacuum*, 81 (2007), 567-570.
17. M. Aghaie and F. Fazlalipour, "Kinetics of V(N,C) Coating Produced by a Duplex Surface Treatment," *Surface and Coatings Technology*, 202 (2008), 4107-4113.

NbC-BASED CERMETS: INFLUENCE OF SECONDARY CARBIDE ADDITION AND METAL BINDER

S.G. Huang¹, J. Vleugels¹, H. Mohrbacher² and M. Woydt³

¹Department of Materials Engineering (MTM), KU Leuven, Kasteelpark Arenberg 44, B-3001
Heverlee, Belgium

²NiobelCon bvba, Schilde, Belgium

³BAM Federal Institute for Materials Research and Testing,
Division 6.3 Tribology & Wear Protection, Unter den Eichen 44-46, D-12203 Berlin, Germany

Keywords: Niobium Carbide, Hardmetal, Cemented Carbide, Sintering, Grain Growth,
Microstructure, Hardness, Fracture Toughness

Abstract

The influence of Al metal and WC, Cr₃C₂, VC, TiC and Mo₂C secondary carbide additions on the microstructure and mechanical properties of Fe, Co and Ni bonded NbC cermets was investigated. Powder mixtures were fully densified by pressureless liquid-phase sintering for one hour at 1420 °C in vacuum. Microstructural and compositional analysis, as well as the elemental distribution in the dense cermets, was performed by electron probe microanalysis (EPMA) to assess the effect of the additions on the NbC grain growth, NbC morphology and metal binder composition, allowing correlation of the microstructure with the fracture toughness and hardness of the cermets. The substitution of WC with 40 wt.%NbC in WC-12 wt.%Co cemented carbides resulted in a significant improvement of hardness when adding 0.9-3.6 wt.%VC or Cr₃C₂ as WC grain growth inhibitors. Compared to pure NbC-Ni, a limited NbC grain growth and homogeneous grain size distribution were obtained upon adding secondary phase carbides or Al metal. WC and Mo₂C significantly enhanced the hardness and toughness of NbC-Ni cermets. The Vickers hardness (HV 10) of 976 kg/mm² and indentation toughness of 9.2 MPa m^{1/2} of a NbC-15 vol.%Ni could be increased to 1357 kg/mm² and 10.1 MPa m^{1/2} respectively upon adding both 8.5 vol.%WC and 8.5 vol.%Mo₂C. The addition of 25-50 at.%Al in Fe binder also increased the hardness of NbC-Ni/Fe cermets, but with decreased toughness. The maximum hardness of the investigated cermets was obtained for a 40 wt.%NbC substituted WC-12 wt.%Co cemented carbide, exhibiting a Vickers hardness of 1697 kg/mm² and toughness of 7.8 MPa m^{1/2}, whereas the WC and Mo₂C added NbC-Ni cermets exhibited the optimum combination of hardness and fracture toughness.

Introduction

As a refractory carbide, niobium carbide (NbC) has a melting point of 3600 °C, density of 7.79 g/cm³, Vickers hardness of 19.6 GPa, Young's modulus of 338-580 GPa and electrical resistivity of 35 μΩ cm [1]. The density of NbC is much lower than that of the commonly used WC (15.68 g/cm³). Although WC-Co materials have been intensively investigated, NbC on the contrary has hardly been explored as the major carbide phase for cemented carbides and cermets. The solid solubility of NbC in Fe, Ni and Co at 1250 °C was reported to be only 1, 3 and 5 wt.% respectively, compared with 7 wt.% for WC in Fe [2]. Therefore, NbC matrix cutting tools and wear parts should be chemically more stable in contact with steel at elevated temperatures, than WC based materials. NbC-Co and NbC-Fe₃Al cemented carbides [3] were however very recently qualified as a competitive or even superior alternative in terms of wear resistance to WC- and Cr₃C₂-based cemented carbides and ceramics. Under dry oscillation, the wear resistance of binderless NbC was insensitive to relative humidity for both alumina and 100Cr6 bearing steel counterbodies, whereas the coefficient of friction of the cobalt- and Fe₃Al-bonded NbC grades was reduced with increasing relative humidity [4]. Although these tribological tests were conducted on KU Leuven based exploratory laboratory grades [4], they clearly illustrate the potential of these radically new NbC-based cermets for tribological applications. Earlier work revealed a remarkable NbC grain growth in NbC-Co based cermets when pressureless-sintered for one hour at 1360 °C [5]. NbC grain growth however can be largely suppressed when consolidating NbC-Co cermets in the solid state by hot pressing or spark plasma sintering (SPS) [5,6]. Huang et al. [7] investigated 0.45-60 wt.%NbC partially substituted WC-12 wt.%Co cemented carbides, processed by solid state SPS and conventional liquid-phase sintering (CS). A lower level of NbC addition (<0.9 wt.%) was found to limit WC grain growth during SPS and conventional sintering, whereas substantial (Nb,W)C grain growth was observed in the materials with higher NbC addition. To further improve the hardness of NbC-WC-Co cemented carbides, novel grade WC-Co cemented carbides containing a significant amount of NbC were developed by adding VC and Cr₃C₂ grain growth inhibitors [8]. Aluminides, a potential binder phase for NbC, are attractive for high-temperature structural material applications due to their good strength at intermediate temperatures and excellent corrosion resistance at elevated temperatures in oxidizing, carburizing and sulfurizing atmospheres [9,10].

In this study, the effect of Co, Ni, Fe, Ni-Al and Fe-Al metal binders on the microstructure and mechanical properties of pressureless liquid-phase sintered NbC-based cermets were investigated. An additional aim was to develop novel WC-Co cemented carbides containing 40 wt.% (54 vol.%) NbC. The influence of VC and Cr₃C₂ grain growth inhibitors on the microstructure and mechanical properties of WC-40 wt.% NbC-12 wt.%Co cemented carbides were investigated.

Experimental Procedure

Commercial carbide powders, NbC (Treibacher, FSSS: 1.18 μm , Austria), WC (Chongyi Zhangyuan Tungsten Co., 200 nm, China), Cr_3C_2 (Treibacher, FSSS: 1.95 μm , Austria), VC (Treibacher, FSSS: 1.15 μm , Austria) and Mo_2C (Chempur, 2 μm) and metal powders, Co (Umicore grade Co-HMP, FSSS: 0.55 μm , Belgium), Ni (Jingmen Gem Co. Ltd, FNiH-1b <1 μm , China) and Fe (Carbonyl, D₅₀: 3.4-4.5 μm , BASF, Germany) were used to prepare NbC-based cermets. The powders were mixed on a multi-directional mixer (Turbula, WAB, Switzerland) in ethanol for 24 hours using WC-6 wt.%Co milling balls (Cerazit grade H20C, \varnothing 10 mm). The suspension was dried in a rotating evaporator at 65 °C. The powder mixtures were then densified by conventional pressureless liquid-phase sintering of cold isostatically pressed (300 MPa) compacts (\varnothing 20 \times 10 mm) for one hour at 1420 °C in a dynamic vacuum (~7 Pa) at a heating/cooling rate of 20 °C/minute.

The bulk density of the sintered cermets was measured in ethanol. The microstructure of polished surfaces was examined by electron probe microanalysis (EPMA, JXA-8530F, JEOL Ltd.), equipped with five wavelength dispersive X-ray spectroscopy (WDS) and one Energy Dispersive X-ray spectroscopy (EDS) type detector. The reported grain size values are the actually measured average intercept lengths measured on scanning electron micrographs. The Vickers hardness (HV 10) was measured (Model FV-700, Future-Tech Corp., Tokyo) with an indentation load of 98.1 N. The fracture toughness, K_{IC} , was measured from the length of the radial cracks originating from the corners of these indentations and calculated according to the formula of Shetty [11]. The reported values are the mean and standard deviation of five indentations.

Results and Discussion

Influence of Metal Binder of NbC Cermets

Backscattered electron micrographs (BSE) of the liquid phase sintered NbC cermets with 12 vol.% metal binders, ie Co, Co+0.9 vol.% Cr_3C_2 , Fe, Fe-25 at.%Al, Ni and Ni-25 at.%Al, are compared in Figure 1. For the Co, Fe and Ni bonded cermets, two backscattered electron contrasting phases could be differentiated in the micrographs. The bright and dark phases correspond to the NbC carbide and metal binder respectively.

As shown in Figure 1(a), the NbC grains in the NbC-12vol.%Co cermet exhibited an irregular shape and formed a highly interconnected carbide network. Some NbC grains merged, apparently excluding the Co binder from their grain boundary. The addition of 0.9 vol.% Cr_3C_2 , Figure 1(b) resulted in a reduced NbC grain contact (contiguity) and more spherical shaped NbC grains. During liquid phase sintering, grain growth occurs with the dissolution of smaller grains and the reprecipitation of dissolved material on larger grains. According to the WDS elemental mapping of the Cr_3C_2 -doped NbC-12vol.%Co cermet in Figure 2, the additional dark contrast phase located at some of the NbC grain boundaries is a Cr-rich phase, whereas Cr was hardly detected in any NbC grains. This Cr-rich phase could be M_7C_3 or M_{23}C_6 carbide, precipitated during cooling. In the Co binder, a very strong Cr peak was identified, which is in agreement with the Cr solution in the Co binder phase of WC-Co cemented carbides [12]. With the Cr_3C_2

addition, the morphology of the NbC grains changed from irregular to spherical shape. Due to the dissolution of Cr and C into the Co binder, the surface energy of the Co binder phase is altered and the wetting of the NbC grains is improved, which influences the grain growth and morphology of NbC grains.

In the case of an Fe binder, Figure 1(c), the shape of the large NbC grains is well-faceted with a slight rounding of the edges, while the small grains are almost spherical, whereas all NbC grains are angular with a Ni binder, Figure 1(e). The NbC grain size is in the 5-20 μm range. The most profound effect of the Al addition to the Fe, Figures 1(c) and (d) and Ni, Figures 1(e) and (f), binders is the NbC grain size reduction ($<10 \mu\text{m}$). Besides the NbC and metal binder grains, dark Al_2O_3 grains were found in the Al-doped cermets. In comparison to the Fe and Ni bonded cermets, the addition of 25 at.%Al resulted in a considerable NbC grain growth inhibition, a decreased NbC grain contact and an angular NbC grain morphology. During liquid phase sintering, the small NbC grains dissolved in the Fe or Ni binder and re-precipitated on larger NbC grains, Figure 1(c) and (e). The reduction of surface energy of the solid particles is the major driving force for small grains to dissolve and large grains to grow. When Al is dissolved in the binder, the interface energy of the liquid binder and the NbC grains, as well as the NbC solubility in the binder, are reduced, lowering the driving force for NbC dissolution-precipitation. This mechanism is also observed in TiC/TiN based cermets doped with WC, Mo_2C and VC [13,14]. The Fe-Al and Ni-Al binders are evenly distributed and the NbC grains have a narrow grain size distribution in the 5-10 μm range.

The X-ray elemental maps of Nb, Ni, Al, C and O of the liquid phase sintered 12 vol.% (Ni-25 at.%Al) cermet is shown in Figure 3. A similar elemental distribution was found in the (Fe-25 at.%Al) bonded cermet. The mapping clearly indicates that the Nb is confined to the carbide phase and both Al and Ni, as well as C were present in the binder phase. Due to the dissolution of C in the Ni binder, it is clear that the Nb/C ratio in the NbC phase has shifted to a lower carbon content. The dark sub-micron sized Al_2O_3 grains can be either due to Al_2O_3 impurities in the Al starting powder or the Al reduction of residual Nb_2O_5 at the surface of the NbC starting powder.

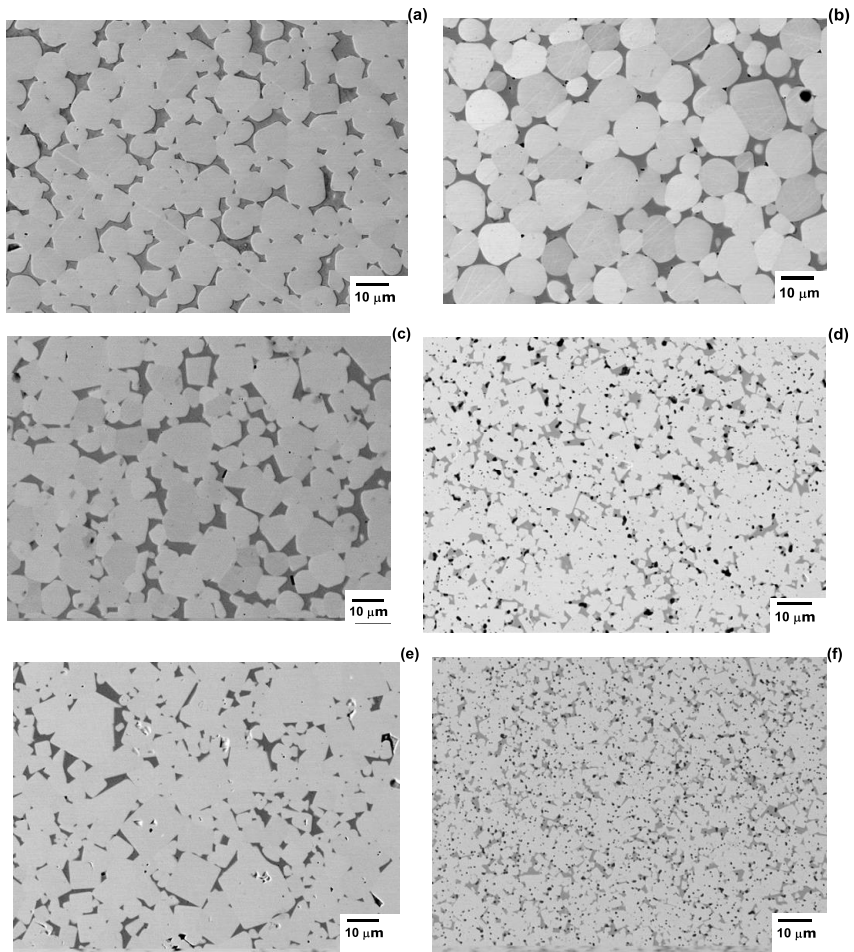


Figure 1. BSE micrographs of NbC cermets vacuum sintered at 1420 °C; NbC-12 vol.%Co (a), NbC-12 vol.%Co-0.9 vol.%Cr₃C₂ (b), NbC-12 vol.%Fe (c), NbC-12 vol.% (Fe-25 at.%Al) (d), NbC-12 vol.%Ni (e) and NbC-12 vol.% (Ni-25 at.%Al) (f).

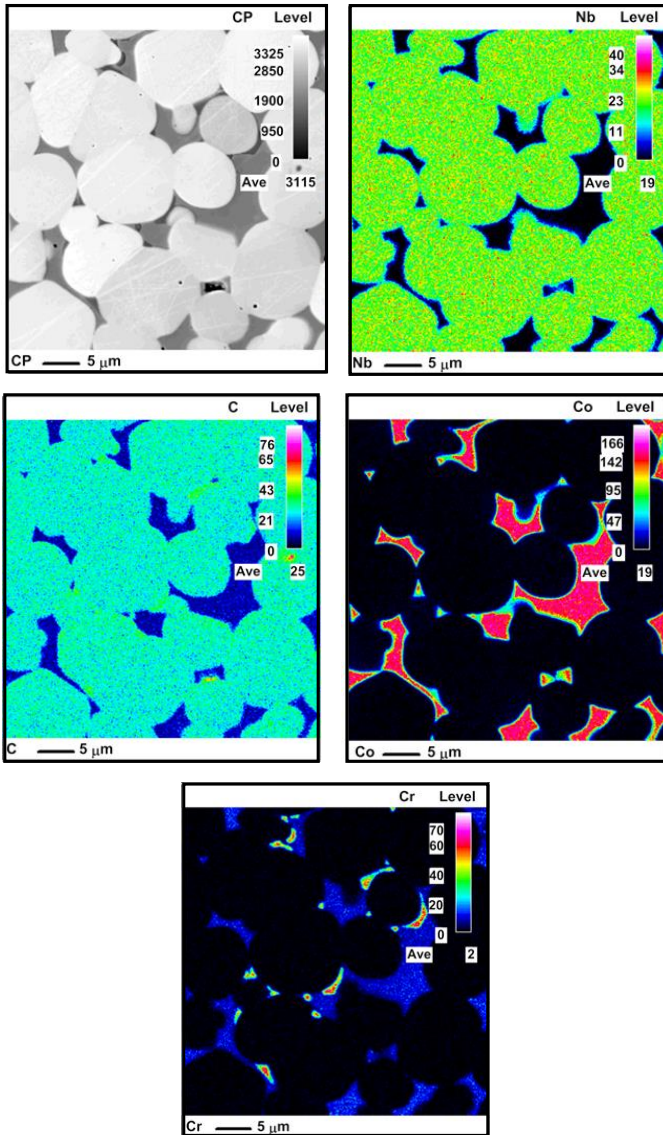
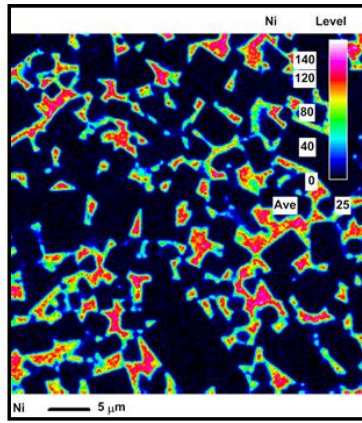
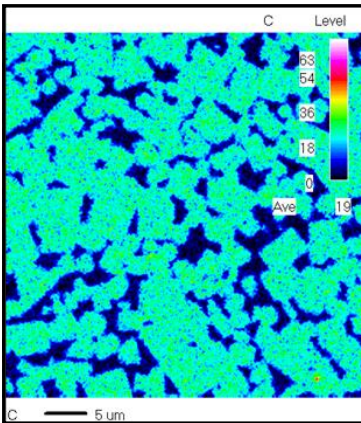
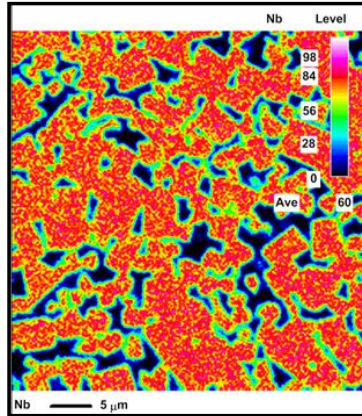
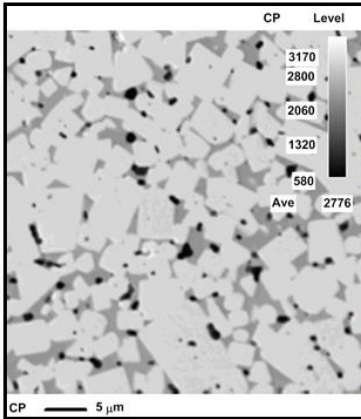


Figure 2. WDS elemental mapping of the NbC-12 wt.% Co-0.9 wt.% Cr₃C₂ cermet, liquid phase sintered for one hour at 1420 °C in vacuum.



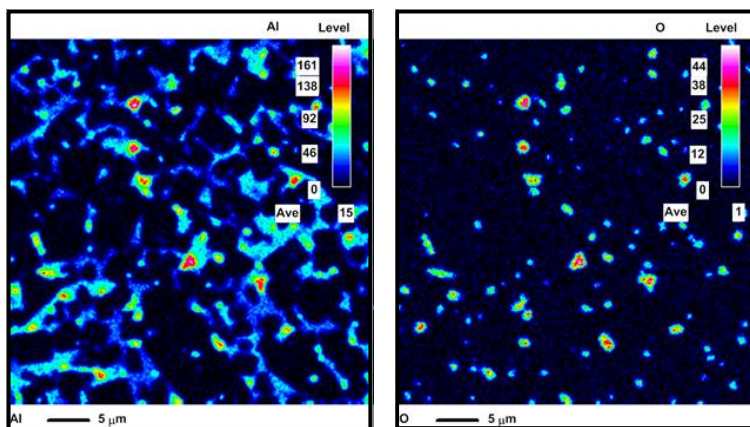


Figure 3. WDS elemental mapping of the NbC-12 vol.% Ni-25 at.%Al cermet, liquid phase sintered for one hour at 1420 °C in vacuum.

Influence of Secondary Carbide Additions

Cobalt Bonded WC-NbC Cemented Carbides. NbC substituted WC-Co cemented carbides with 40 wt.% (54 vol.%) NbC with and without VC or Cr₃C₂ addition were prepared by pressureless liquid-phase sintering for one hour at 1420 °C in vacuum.

BSE images of the WC-40 wt.% NbC-12 wt.%Co cemented carbides without and with 1.8 wt.% VC, 3.6 wt.% VC or 3.6 wt.% Cr₃C₂ are compared in Figure 4. Bright WC, grey NbC and dark Co binder phases could be differentiated based on their backscattered electron contrast. The grey NbC grains form a skeleton due to their 54 vol.% content and are actually (Nb,W)C solid solution grains. The Co binder is mainly present in-between the WC grains and not at the NbC grain boundaries, due to a different wetting between Co and WC/NbC [7]. In the 1.8 and 3.6 wt.% VC-doped grades, free VC grains could not be distinguished from NbC grains due to their similar atomic number. Compared to the NbC substituted WC-Co cemented carbide in Figure 4(a), it is apparent that the addition of 3.6 wt.% VC has a grain growth inhibiting effect on the WC grains. Similar to the VC-doped cemented carbide, the Cr₃C₂-doped grade, Figure 4(d) is composed of bright WC, grey (Nb,W,V/Cr)C and dark Co binder phases. The average WC grain size was only 0.16 and 0.21 μm when the cemented carbides were doped with 3.6 wt.% VC and Cr₃C₂, respectively.

The experimental results show that the NbC addition limits WC grain growth and a significant amount of WC grains dissolved into the NbC grains. The growth of the remaining WC grains was further inhibited with the VC or Cr₃C₂ addition. The WC grain growth inhibiting efficiency of VC in the WC-NbC-Co cemented carbide is higher than that of Cr₃C₂. When compared to plain WC-Co grades, a higher grain growth inhibitor content is needed in the NbC-substituted

WC-Co cemented carbide since the V and Cr not only dissolve in the Co binder and segregate at the WC interfaces, but also form (Nb,W,V/Cr) solid solution grains. However, the addition of VC and Cr₃C₂ has no clear influence on the (Nb,W)C grain size.

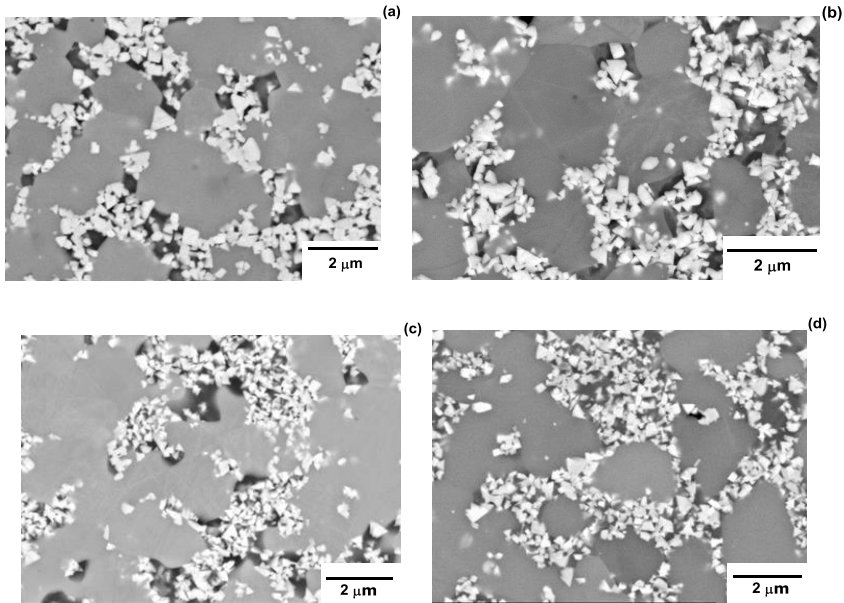


Figure 4. BSE micrographs of vacuum sintered (one hour at 1420 °C) WC-40 wt.% NbC-12 wt.%Co; without additives (a) and with 1.8 wt.% VC (b), 3.6 wt.% VC (c) and 3.6 wt.% Cr₃C₂ (d).

Nickel Bonded NbC-MeC Cermets. The microstructures of the NbC-15 vol.%Ni without and with 5 vol.%Mo₂C, 8.5 vol.%WC + 8.5 vol.%Mo₂C or 8.5 vol.%WC + 8.5 vol.%Mo₂C + 8.5 vol.%TiC addition, prepared via vacuum liquid-phase sintering for one hour at 1420 °C, are compared in Figure 5. Although some of these cermets have a high secondary carbide content phase addition, they all exhibited only a bright-grey NbC phase and a dark-grey Ni based metal binder. The NbC-15 vol.%Ni cermet, Figure 5(a) has relatively large (<15 μm) facet shape NbC grains with a slight rounding of the edges and mostly separated by the Ni binder. The addition of 5 vol.%Mo₂C significantly decreased the NbC grain size (<3 μm), as shown in Figure 5(b).

The NbC grain size is further reduced to 1-2 μm upon extra addition of WC and WC + TiC, as shown in Figures 5(c) and (d). These carbides are known to have a very high solubility (WC > Mo₂C > TiC) in Ni at the sintering temperature [15]. The surface energy of the liquid Ni binder was changed during sintering and dissolution of the secondary phase carbides, thereby influencing the NbC grain growth. The combined addition of WC + Mo₂C + TiC is a more efficient NbC grain growth inhibitor than the combination of WC + Mo₂C.

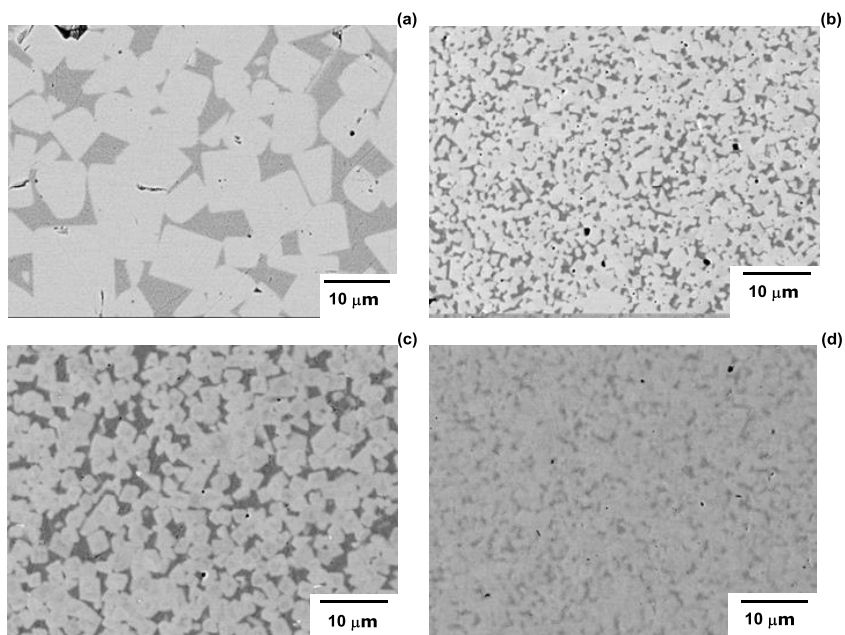


Figure 5. BSE micrographs of NbC-15 vol.%Ni cermets, vacuum sintered for one hour at 1420 °C; without additives (a) and with 5 vol.%Mo₂C (b), 8.5 vol.%WC + 8.5 vol.%Mo₂C (c) and 8.5 vol.%WC + 8.5 vol.%Mo₂C + 8.5 vol.%TiC (d).

Mechanical Properties

The Vickers hardness (HV 10) and fracture toughness (K_{IC}) of all investigated NbC cermets, prepared under exactly the same sintering conditions, are compared in Figure 6 and summarized in Table I. The theoretical density was calculated based on the mixture rule. Generally, the hardness of the cermets can be divided into four categories. The Co bonded WC-NbC-VC/Cr₃C₂ cemented carbides have the highest hardness, followed by the Ni bonded NbC-MeC cermets and the NbC-Ni and -Fe cermets which have a lower hardness. The CS prepared NbC-Co cermets exhibited the lowest hardness level. Since all grades have a comparable binder content, the difference in hardness of the NbC matrix cermets can be directly attributed to the nature of the binder and the constituent components, ie the binder composition and the NbC grain size. Based on the microstructural analysis, the refinement of the NbC grain size in the Al-doped Fe/Ni binder NbC cermets improved the hardness. The hardness of the Fe-Al, Ni-Al, Co and Ni binders are difficult to compare since they exhibit a different grain size. Considering the pure metal binder, the Fe bonded NbC cermets had the highest hardness of 1293 kg/mm², followed by the Ni and Co bonded cermets.

For the Co bonded WC-NbC-VC/Cr₃C₂ cemented carbides, the hardness increases with increasing grain growth inhibitor content. The highest hardness was obtained when adding 3.6 wt.% VC, followed by 3.6 wt.% Cr₃C₂ and 1.8 wt.% VC. For straight WC-Co cemented carbides, the hardness is mainly dependent on the WC grain size (Hall-Petch relationship) and the Co content. The finer the WC grain size, the higher the hardness for a given Co volume fraction.

In the NbC substituted cemented carbides, the fine WC grains are evenly dispersed in the (Nb,W,V/Cr)C-Co matrix. The critical factors affecting the mechanical properties of these cemented carbides are the properties of the (Nb,W,V/Cr)C and WC phases. Since the WC grain size refinement is accompanied by a reduction of the residual WC volume fraction, the increased hardness of the VC and Cr₃C₂-doped grades might also be partially due to solid solution hardening of the NbC phase. The higher hardness of the (Nb,W,V/Cr)C phase, however, remains to be proven.

Regarding the fracture toughness, there is a negative correlation between the hardness and fracture toughness of NbC matrix materials, ie the hardness increases and fracture toughness decreases with decreasing NbC grain size for a given binder type and binder content. The binder plays a crucial role in shielding the stress field in front of a crack tip to improve the toughness [16]. Ductile failure of the Co, Ni and Fe binder is usually found on fractured NbC-Co/Ni/Fe surfaces. Since the Fe-Al and Ni-Al have an intrinsically low room temperature ductility, the Al-doped cermets have a lower fracture toughness. For a given low hardness value of around 1250 kg/mm², the Ni bonded NbC cermet had the highest toughness of 12 MPa m^{1/2}, whereas the Fe and Co bonded cermet exhibited a toughness of only 6-7 MPa m^{1/2}. With increased hardness to 1500 kg/mm², the MeC-added NbC-Ni cermet still had the highest toughness of 8.5 MPa m^{1/2}, whereas the corresponding NbC-12 vol.% (Fe-25 at.%Al) cermet had a toughness of 5.9 MPa m^{1/2}. Analysis of the microstructures and mechanical properties in Figures 2-6 reveals that the addition of Al and secondary carbides have a great impact on the final NbC grain size and microstructure as well as the concomitant increased hardness and reduced toughness.

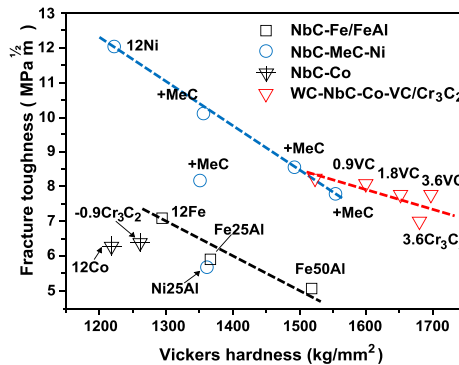


Figure 6. Vickers hardness and fracture toughness of all investigated NbC cermet and WC-NbC-Co cemented carbides.

Table I. Hardness and Fracture Toughness of the Investigated Cermets and Cemented Carbides

| Materials | Density (g/cm ³) | R.D. (%) | HV 10 (kg/mm ²) | K _{IC} (MPa m ^{1/2}) |
|---|---------------------------------|-------------|--------------------------------|--|
| Cobalt bonded NbC cermets | | | | |
| NbC-12 vol.%Co | 7.83 | 98.8 | 1218 ± 32 | 6.30 ± 0.41 |
| NbC-12 vol.% Co-0.9 vol.%Cr ₃ C ₂ | 7.78 | 98.5 | 1260 ± 13 | 6.40 ± 0.20 |
| Iron bonded NbC cermets | | | | |
| NbC-12 vol.%Fe | 7.75 | 99.3 | 1293 ± 27 | 7.09 ± 0.50 |
| NbC-12 vol.% (Fe-25 at.%Al) | 7.68 | 100 | 1366 ± 8 | 5.90 ± 0.26 |
| NbC-12 vol.% (Fe-50 at.%Al) | 7.42 | 98.2 | 1518 ± 17 | 5.05 ± 0.10 |
| Nickel bonded NbC-MeC cermets | | | | |
| NbC-12 vol.%Ni | 7.90 | 99.4 | 1222 ± 15 | 12.04 ± 0.75 |
| NbC-12 vol.% (Ni-25 at.%Al) | 7.94 | 98.4 | 1360 ± 14 | 5.68 ± 0.20 |
| NbC-15 Ni-5 Mo ₂ C (vol.%) | 7.93 | 100 | 1351 ± 13 | 8.16 ± 0.57 |
| NbC-15 Ni-8.5 Mo ₂ C-8.5 WC (vol.%) | 8.74 | 100 | 1357 ± 29 | 10.11 ± 0.82 |
| NbC-15 Ni-8.5 Mo ₂ C-8.5 WC-8.5 TiC (vol.%) | 8.51 | 100 | 1553 ± 26 | 7.78 ± 0.19 |
| NbC-15 Ni-8.5 Mo ₂ C-8.5 WC-17.0 TiC (vol.%) | 8.10 | 98.5 | 1492 ± 6 | 8.55 ± 0.48 |
| Cobalt bonded WC-NbC cemented carbides | | | | |
| WC-12Co-40NbC (wt.%) | 10.50 | 99.9 | 1523 ± 21 | 8.26 ± 0.39 |
| WC-12 Co-40 NbC-0.9 VC (wt.%) | 10.38 | 100 | 1599 ± 14 | 8.11 ± 0.15 |
| WC-12 Co-40 NbC-1.8 VC (wt.%) | 10.06 | 98.0 | 1651 ± 14 | 7.80 ± 0.21 |
| WC-12 Co-40 NbC-3.6 VC (wt.%) | 10.06 | 100 | 1697 ± 6 | 7.78 ± 0.10 |
| WC-12 Co-40 NbC-3.6 Cr ₃ C ₂ (wt.%) | 10.17 | 100 | 1680 ± 15 | 7.03 ± 0.20 |

Conclusions

Full densification of Fe, Co and Ni bonded NbC based cermets was achieved by pressureless liquid phase sintering in vacuum for one hour at 1420 °C. The hardness and toughness of the NbC matrix cermets can be mainly tailored by the binder composition and secondary carbide additions. The addition of Al in an Fe or Ni binder based NbC cermets, or the addition of multiple carbides (WC, Mo₂C or TiC) in NbC-Ni cermets, not only influenced the morphology of the NbC grains, but also the NbC grain growth. For a given binder phase, the investigated materials show a similar trend in hardness and toughness, ie the higher the hardness, the lower the fracture toughness. Ni binder based NbC cermets allow the combination of high hardness and improved toughness. The addition of small amounts of VC/Cr₃C₂ in a NbC partially substituted WC-Co cemented carbide increased significantly the hardness in combination with a moderate fracture toughness.

Acknowledgements

We gratefully acknowledge the financial support of the Companhia Brasileira de Metalurgia e Mineração (CBMM), São Paulo, Brazil. The authors thank the Hercules Foundation (project ZW09-09).

References

1. H.O. Pierson, Handbook of Refractory Carbides and Nitrides (New Jersey, US: Noyes, 1996).
2. J.P. Guha and D. Kolar, "Systems of Niobium Monocarbide with Transition Metals," *Journal of the Less-Common Metals*, 29 (1) (1972), 33-40.
3. M. Woydt and H. Mohrbacher, "The Tribological and Mechanical Properties of Niobium Carbides (NbC) Bonded with Cobalt or Fe₃Al," *Wear*, 321 (2014), 1-7.
4. S.G. Huang et al., "Microstructure and Mechanical Properties of NbC-matrix Hardmetals with Secondary Carbide Addition and Different Metal Binder," *International Journal of Refractory Metals and Hard Materials*, 48 (2015), 418-426.
5. S.G. Huang et al., "Influence of WC Addition on the Microstructure and Mechanical Properties of NbC-Co Cermets," *Journal of Alloys and Compounds*, 430 (1-2) (2007), 158-164.
6. S.G. Huang et al., "Properties of NbC-Co Cermets Obtained by Spark Plasma Sintering," *Materials Letters*, 61 (2) (2007), 574-577.
7. S.G. Huang et al., "NbC as Grain Growth Inhibitor and Carbide in WC-Co Hardmetals," *International Journal of Refractory Metals and Hard Materials*, 26 (5) (2008), 389-395.
8. S.G. Huang et al., "VC- and Cr₃C₂-doped WC-NbC-Co Hardmetals," *Journal of Alloys and Compounds*, 464 (1-2) (2008), 205-211.
9. P.R. Munroe, "High Temperature Ordered Intermetallic Compounds," *Materials Forum*, 21 (1997), 79-99.
10. R. Subramanian and J.H. Schneibel, "FeAl-TiC and FeAl-WC Composites-melt Infiltration Processing, Microstructure and Mechanical Properties," *Materials Science and Engineering: A*, 244 (1) (1998), 103-112.
11. D.K. Shetty et al, "Indentation Fracture of WC-Co Cermets," *Journal of Materials Research*, 20 (1985), 1873-82.
12. V. Chabretou et al., "Distribution of Cr or V in the Phases of Cemented Carbides WC-Co," *Proceedings of the 1998 Powder Metallurgy World Congress & Exhibition*, Granada, Spain, (October 18-22, 1998), Volume 4, 146-50.
13. S. Zhang, "Titanium Carbonitride-based Cermets: Process and Properties," *Materials Science and Engineering: A*, 163 (1993), 141-148.
14. S.Y. Ahn and S. Kang, "Formation of Core/Rim Structures in Ti(C,N)-WC-Ni Cermets via a Dissolution and Precipitation Process," *Journal of the American Ceramic Society*. 83 (6) (2000), 1489-1494.

15. H.E. Exner, "Physical and Chemical Nature of Cemented Carbides," *International Materials Reviews*, 24 (1) 1979, 149-173.

16. M. Kotoul, "On the Shielding Effect of a Multiligament Zone of a Crack in WC-Co," *Acta Materialia*, 45 (8) (1997), 3363-3376.

COMPARISON OF THE LIFE-SPAN OF NbC-Co AND WC-Co INSERTS DURING DIFFERENT MACHINING OPERATIONS ON 100Cr6 (SAE 52100) BEARING STEEL

G. Le Quilliec¹, R. Leroy¹, C. Richard¹, M. Woydt² and A. Morandea³

¹Laboratory of Mechanics and Rheology (LMR) EA2640 – Research Center for Cutting Tools
(LMR-CEROC) – University of Tours, France

²Federal Institute for Materials Research and Testing (BAM), Berlin, Germany

³Sandvik Coromant SAS, France

Keywords: Niobium Carbide, Cobalt, Fe₃Al, Inserts, Cutting Tools, Wear, Turning

Abstract

Carbide products have in recent years become indispensable for the machining of steels and indeed carbide tools generally show longer tool life and produce higher dimensional accuracy. In the majority of cases, carbide tools will leave a better finish on the part and allow faster machining. Carbide tools can also withstand higher temperatures than high speed steel tools. Nevertheless carbide tools are more expensive per unit than other typical tool materials and tend to be brittle, making them more susceptible to chipping and breaking.

The aim of the study presented in this paper is to highlight the potential of niobium carbide cutting tool inserts for machining and to compare their performance to commercially available tungsten carbide inserts. In this work, a comparison between a conventional WC-Co insert (with 6%Co) and NbC-Co inserts (with 8% and 12%Co) was carried out under hard machining conditions on specimens made of 100Cr6 bearing steel grade (SAE 52100). The objective was to determine if NbC-Co type inserts were a good candidate as an alternative material to WC-Co. The results showed the significantly higher wear resistance of the NbC-Co inserts but a lack of toughness compared to the WC-Co insert.

Further comparisons were made between a WC-Co insert and an NbC-Fe₃Al (with 12%Fe₃Al) insert in semi-finishing operations. Here again, the higher wear resistance of the NbC-12Fe₃Al insert was evident with no collapse after about one hour of machining. The crater wear was three times larger for the WC-Co inserts compared with the NbC inserts while the flank wear was the same for each type of insert.

All these results are promising regarding the high abrasive resistance of the NbC inserts but improvements are still needed to increase the toughness for hard machining operations and work is currently in progress to attain this toughness enhancement.

Introduction

Niobium carbide (NbC) is already used in some industrial coatings in order to decrease the friction coefficient [1]. Recently, niobium carbide has been densified into monolithic materials [2] from which cutting tool inserts can be produced, as an alternative to those made of tungsten carbide.

The present work utilizes niobium carbide grades as described by Woydt et al. [3] for tribological applications. The aim of this paper is to highlight the potential of niobium carbide cutting tool inserts for machining and to compare their performance to commercially available tungsten carbide inserts. The experimental evaluation consisted of turning tests on specimens made of 100Cr6 bearing steel grade (SAE E52100), which is often used to test cutting tool inserts and assess their performance.

Methodology

Rough Turning Inserts

Under hard turning conditions, three inserts were tested: one commercially available tungsten carbide (WC) insert (*Sandvik Ref. SNMA 12 04 16-KR grade 3215*) and two custom-made niobium carbide (NbC) inserts with two different cobalt (Co) contents. The WC insert contained 6%Co and its flanks were coated with (Ti,Al)N, while the NbC inserts contained 8% and 12%Co and were uncoated. The NbC inserts were cut by wire electrical discharge machining. The nose radius of the NbC inserts was set to 1.5 mm, very close to the WC nose radius of 1.6 mm. All the inserts had an equivalent edge radius between 30 and 40 μm and a clearance angle of 0° . As shown in Figure 1, the edge of all the inserts was modified in order to get a cutting edge of 0.2 mm and a cutting angle of 12° .

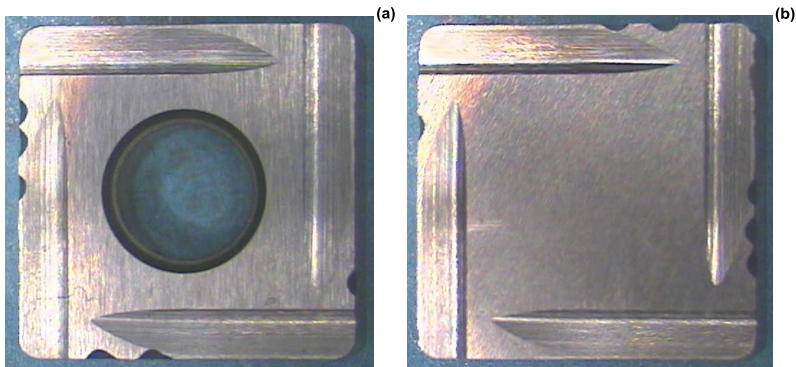


Figure 1. Geometry of the WC (a) and NbC (b) cutting tool inserts.

Semi-finishing Inserts

In semi-finishing turning, two inserts were tested: one commercially available WC insert (*Sandvik Ref. SNMA 12 04 08-KR grade 3215*) with the same grade as previously used for the rough turning and one custom-made NbC insert containing 12%Fe₃Al. The NbC insert was cut by wire electrical discharge machining. The nose radius of the NbC insert was set to 0.8 mm to achieve the same geometry as the WC insert. All the inserts had an equivalent edge radius between 30 and 40 μm and a clearance angle of 0°. The edge of all the inserts was modified in order to get a cutting edge of 0.2 mm and a cutting angle of 12°.

Milled Material and Machining

For all experimental tests (hard and semi-finishing turning), the milled material was a 100Cr6 bearing steel grade (composition given in Table I). This steel is commonly used for such tests when comparing the performance of different tools. The tool holder was *Sandvik CSBNL 2525M12* with a lead angle of 75°. The machining was carried out in lubricated mode with a 10 bar fluid pressure. The turning center was a *Victor Taichung Vturn-A26* with the cutting conditions given in Table II. The cutting parameters are explained in Figure 2.

Table I. Composition of the Milled Material 100Cr6 Bearing Steel (SAE E52100)

| 100Cr6 (205 HB) (wt.%) | | | | | | | | | | | |
|-------------------------------|-----------|-----------|----------|----------|-----------|-----------|-----------|-----------|-----------|-----------|----------|
| C | Si | Mn | P | S | Cr | Ni | Mo | Cu | Al | Ti | O |
| 0.96 | 0.31 | 0.67 | 0.012 | 0.007 | 1.66 | 0.16 | 0.23 | 0.20 | 0.039 | 12 ppm | 5.4 ppm |

Table II. Cutting Conditions for the Rough Machining Tests and for the Semi-finishing Tests

| Parameter | Symbol | Hard turning | Semi-finishing |
|-------------------|---------------|---------------------|-----------------------|
| Cutting speed | V_c | 100 m/min | 100 m/min |
| Feed rate | f | 0.415 mm/rev | 0.207 mm/rev |
| Chip thickness | h_{ex} | 0.40 mm | 0.20 mm |
| Depth of cut | a_p | 3 mm | 1.5 mm |
| Lead angle | Kr | 75° | 75° |
| Emulsion pressure | P | 10 bar | 10 bar |

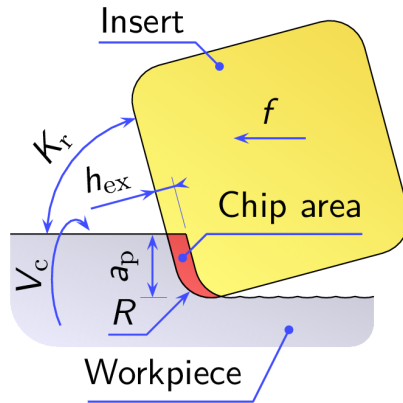


Figure 2. Definition of the cutting parameters.

Results

Hard Turning Tests

For the WC insert, the cratering is substantial while the flank wear (WC inserts have a (Ti,Al)N coating) remains acceptable as shown in Figure 3.

For the uncoated NbC insert, the flank wear and cratering remained acceptable as shown in Figure 4. The initial machining striae from the edge preparation are still visible indicating low crater wear. On the other hand, after about five minutes of machining, a crack appeared. These cracks were responsible for the collapse of the 8% and 12%Co inserts. The toughness of the present NbC grades needs to be improved.

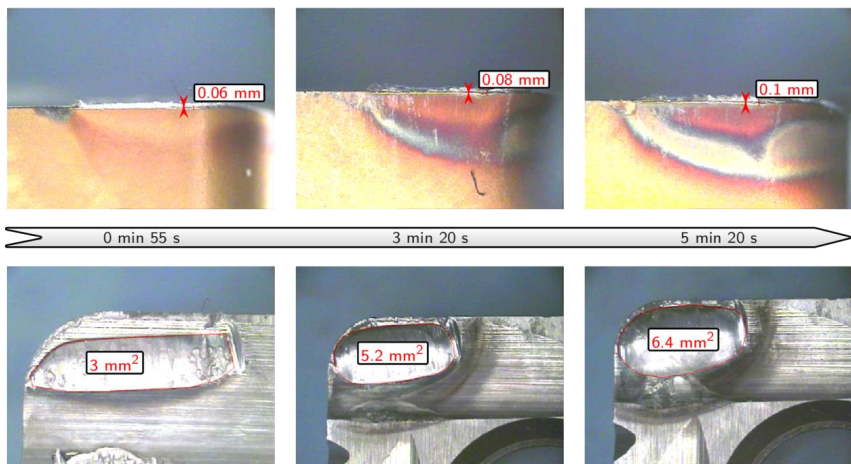


Figure 3. Flank (top row) and crater wear (bottom row) for rough turning tests with the WC-6%Co insert.

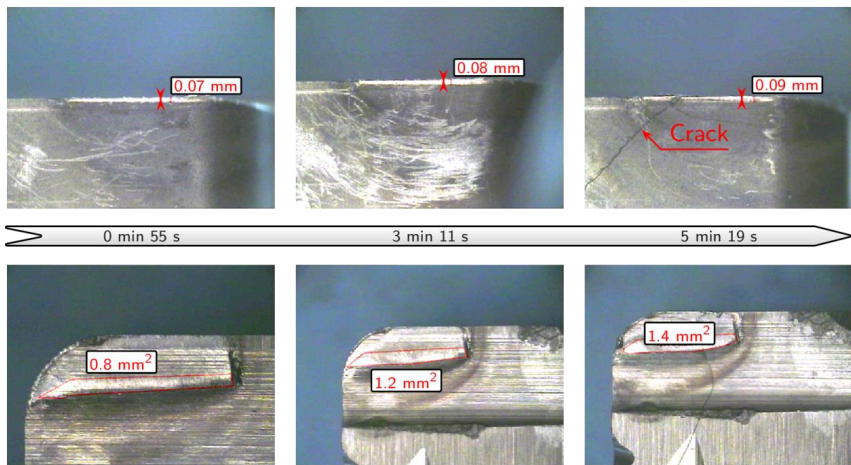


Figure 4. Flank (top row) and crater wear (bottom row) for rough turning tests with the NbC-8%Co insert.

Semi-finishing Turning Tests

For the WC-6%Co insert, the cratering is again significant as shown in Figure 5. A large pitting area was observed in the crater of the WC-6%Co insert after 30 minutes machining.

For the NbC-12%Fe₃Al inserts, the cratering is reduced as shown in Figure 6. On the contrary, the wear due to the hardened layer shows a more significant notch than on the WC inserts. No cracks appeared during all the semi-finishing tests, contrary to the hard turning tests.

Comparative SEM photographs of the inserts after 5 and 58 minutes are shown in Figure 7. The machining striae on the NbC-12%Fe₃Al insert are still visible, as is a reduced tendency for iron to stick on the edge. The presence of iron is more significant on the WC insert than on the NbC insert. This is obviously due to bonding of steel particles.

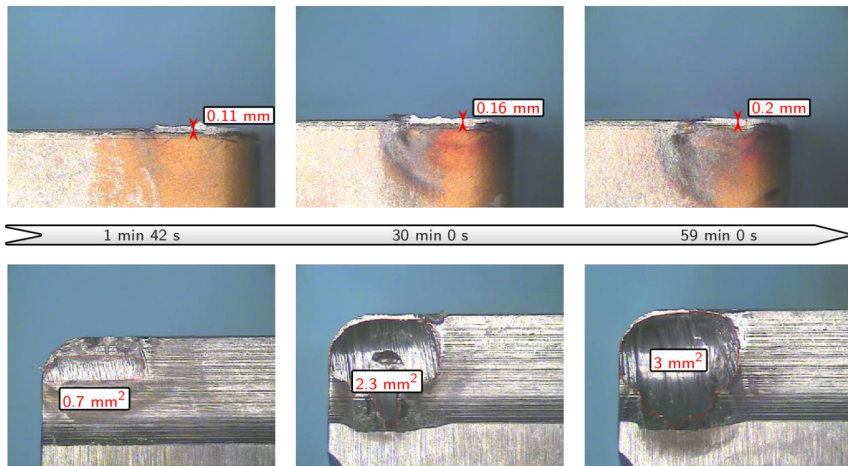


Figure 5. Flank (top row) and crater wear (bottom row) for the semi-finishing tests with the WC insert.

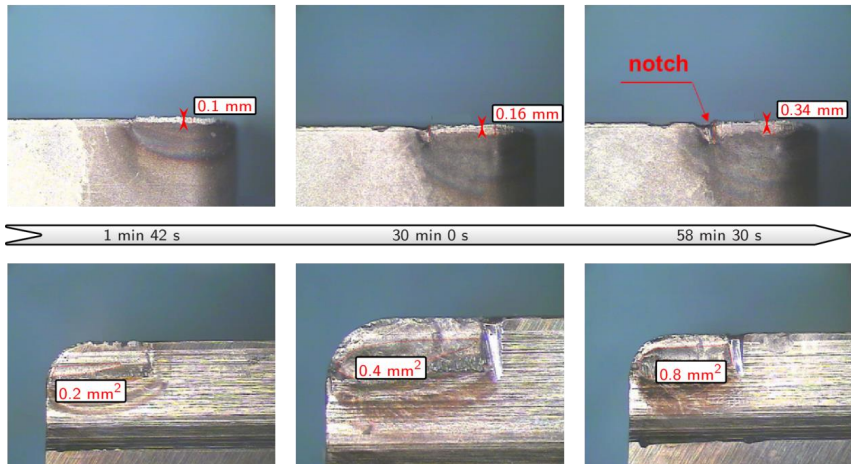
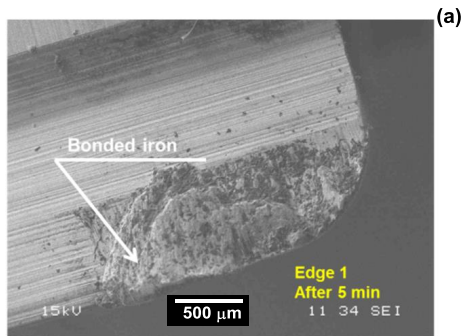


Figure 6. Flank (top row) and crater wear (bottom row) for the semi-finishing tests with the NbC-12%Fe₃Al insert.



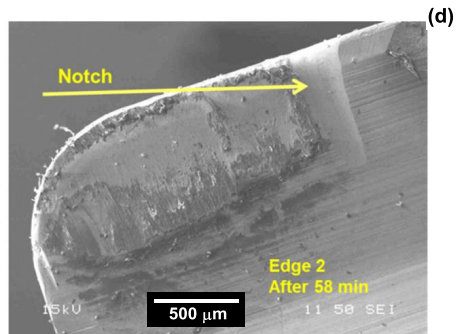
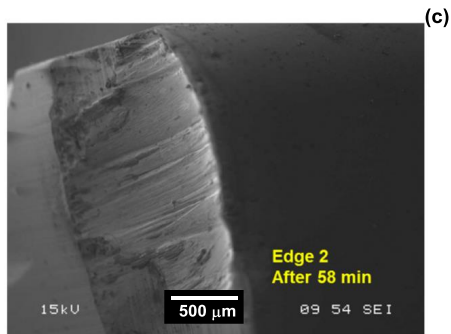
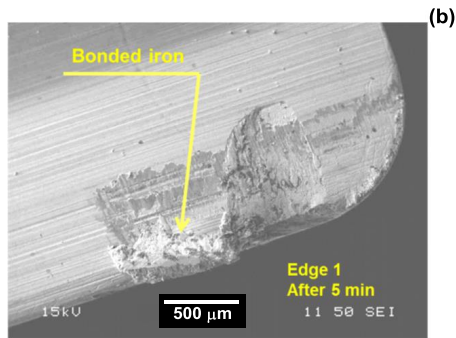


Figure 7. SEM photographs of the wear after 5 minutes (a and b) and 58 minutes (c and d) between WC-6%Co insert (a and c) and NbC-12%Fe₃Al (b and d) for the semi-finishing tests.

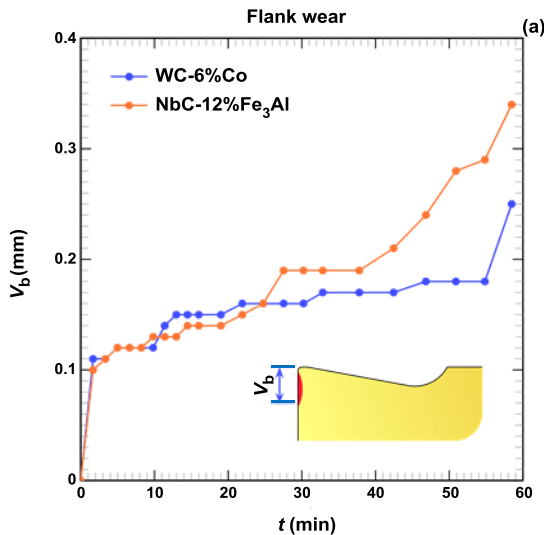
Discussion

Hard Turning Case

Cobalt usually improves the toughness of inserts, however in the hard turning tests and regardless of the cobalt content, the current NbC inserts lacked toughness. The edges spalled after about five minutes of hard turning, either with 8% or 12%Co.

Semi-finishing Turning Case

In semi-finishing, the NbC inserts have very good strength. The NbC insert is less sensitive to sticking of machined material. The comparison of the flank wear and the crater wear are shown in Figures 8(a) and (b) respectively for WC-6%Co and NbC-12%Fe₃Al. The advantages in flank wear of the WC-6%Co insert can be explained by its (Ti,Al)N coating. This coating was not removed from the flank surface during the preparation of the WC insert (rectification of the cutting edge and cutting angle), however the coating on the rake face of the WC insert was removed during the preparation. In this case, it is obvious that the crater wear is more significant for the WC-6%Co inserts than for the uncoated NbC-12%Fe₃Al inserts, as shown in Figure 8(b). The crater wear was three times greater for the WC-6%Co than for the NbC-12%Fe₃Al after only one minute of machining. These results show that uncoated NbC inserts exhibit a higher resistance to abrasive wear than uncoated WC inserts.



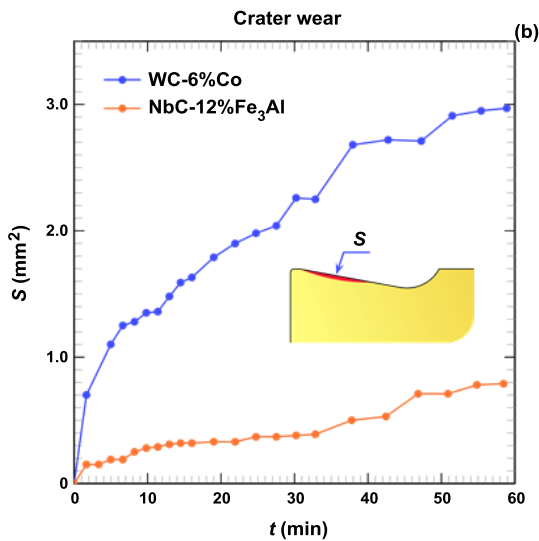


Figure 8. Comparison of the flank wear (a) and the crater wear (b) between the WC-6%Co insert and the NbC-12%Fe₃Al insert for the semi-finishing tests.

The amount of bonded steel on the inserts seems to be proportional to the crater wear. It is assumed that the repeated deposition of steel on the insert during machining is mainly responsible for the crater wear. Thus, WC insert sensitivity to bonding of steel particles (chips) can explain the greater crater wear in comparison to NbC-12%Fe₃Al inserts.

Conclusions

Niobium carbide inserts have been shown to be very efficient for semi-finishing operations and it is expected that future improvements in toughness will ensure their suitability for hard turning.

Cobalt usually improves the toughness of inserts, however, in the hard turning tests and regardless of the cobalt content, the current NbC inserts lacked toughness. The edges spalled after about five minutes of hard turning, either with 8% or 12%Co.

The test results for a semi-finishing operation are promising regarding the use of niobium carbide inserts instead of the more conventional tungsten carbide inserts. Fe₃Al bonded NbC was shown to be suitable as a substitute for cobalt bonded NbC.

On the flank face of the tungsten carbide inserts, where the coating has been preserved, the abrasive wear is lower than for the fully uncoated niobium carbide inserts. However, when they are uncoated, tungsten carbide inserts exhibit a significantly lower resistance to abrasive wear

than niobium carbide inserts. The crater wear was three times larger for the WC-Co inserts compared with the NbC inserts, while the flank wear was the same for each type of insert.

The results also tend to show that bonded particles (chips) of machined material can be responsible for the lower wear resistance of tungsten carbide inserts.

References

1. U. Sen, "Wear Properties of Niobium Carbide Coatings Performed by Pack Method on AISI 1040 Steel," *Thin Solid Films*, 483 (2005), 152-157.
2. Y. Chen et al., "Facile Synthesis, Characterization and Photocatalytic Activity of Niobium Carbide," *Advanced Powder Technology*, 24 (2013), 207-211.
3. M. Woydt and H. Mohrbacher, "The Tribological and Mechanical Properties of Niobium Carbides (NbC) Bonded with Cobalt or Fe₃Al," *Wear*, 321 (2014), 1-7.

WEAR AND MECHANICAL PROPERTIES OF SPARK PLASMA AND LIQUID PHASE SINTERED WC AND NbC BASED CEMENTED CARBIDE INSERTS

R.M. Genga^{1,2}, L.A. Cornish^{2,3}, M. Woydt⁴, K. Sobiyi^{2,3} and C. Polese^{1,2}

¹School of Mechanical, Industrial and Aeronautical Engineering,
University of the Witwatersrand, South Africa

²DST-NRF Centre of Excellence in Strong Materials, University of the Witwatersrand,
South Africa

³School of Chemical and Metallurgical Engineering, University of the Witwatersrand,
South Africa

⁴BAM Federal Institute for Materials Research and Testing, Germany

Keywords: WC, NbC, SPS, Co, Fe₃Al, Hard-turning, Interrupted Milling, Flank Wear, Coolant-free, Crater Wear, Machinability

Abstract

The effects on the mechanical properties, thermal behaviour, response to cutting forces and wear mechanisms have been investigated for different manufacturing processes and materials for cemented carbide inserts. Spark plasma sintering (SPS) has been compared with liquid phase sintering (LPS), including NbC substitution for WC inserts, Ni and Fe₃Al substitution for the Co binder, and with Cr₃C₂, Mo₂C and TiC additions. The comparisons were conducted for coolant-free hard-turning and interrupted milling. Turning was carried out on 440B martensitic stainless steel (X90CrMoV18, 408 HV or 71.3 HRA) and interrupted milling was conducted on a structural steel (SABS 1431: 300WA, 184 HV or 55.1 HRA). The turning speed was varied from 80-120 m/min with a depth of cut between 0.5-1 mm, while the milling speed was varied from 100-250 m/min with a depth of cut of 1 mm. The cutting edge temperature (>1000 °C) was measured using a thermal camera (30 thermal readings per second) and force measurements were made by a Kistler dynamometer attached to the workpiece clamp. During turning, both SPS and LPS WC inserts had lower flank wear rate (FWR) values than the NbC inserts at all speeds. The LPS inserts had lower FWR values than the SPS inserts at low speeds, but the opposite occurred at high speeds. However, during milling, the NbC-12Co (ie NbC with 12 wt.%Co binder alloy) insert had a lower FWR than the SPS WC-10Co insert at 100 m/min and performed better than both the SPS and LPS WC-10Co at 250 m/min. Additions of TiC and Mo₂C to the WC inserts lowered FWR and improved the crater wear resistance in both turning and milling. No crater wear was observed in the NbC inserts due to its low solubility in the alloys. During hard turning, the NbC-12Co inserts performed better than the NbC-12Fe₃Al inserts. Wear was investigated by optical microscopy and high angle annular dark field scanning transmission electron microscopy (HAADF-STEM), and the results are explained by the composition and mechanical properties of the inserts.

Introduction

Tungsten carbide (WC) cemented carbides consist of a high volume fraction of hard ceramic (WC) within a tough metal binder matrix (Co, Ni or Fe) [1,2]. WC-based cemented carbides are commercially one of the oldest and most successful powder metallurgy products due to their good combination of hardness, toughness, strength, chemical stability and wear resistance [1-3]. Their unique combination of good physical, mechanical and chemical properties, as well as their proven service record in diverse applications over the past decades, have led to WC-based cemented carbides being the most well-used tool material today [4]. Approximately 70% of metal cutting tools (inserts) are made from WC cemented carbides; the remaining 30% comprises high speed steel (HSS), ceramics and TiC-based cemented carbides [4].

During metal cutting, the temperature at the insert/workpiece interface and chemical interaction at the insert/chip interface are the two main phenomena which affect the tool life [4,5]. Cutting temperatures around 1000 °C and above have been recorded during machining [4,6], reducing the hardness and strength of WC-based inserts, despite their good room temperature properties [1,4]. Interaction between the insert cutting edge and the workpiece, due to high contact pressure and cutting temperatures, leads to chemical adhesion and eventually tool wear by crater wear [1,4]. Crater wear results from the diffusion of atoms from the insert into the flowing nascent surfaces of chips from the workpiece, which are carried away from the insert/chip interface [5,7]. This material transport results in the formation of a “crater” on the rake face at a short distance from the cutting edge and, with continued machining, the crater increases in size and weakens the cutting edge, leading to failure [7]. Crater wear in WC-based inserts is mostly observed during machining of steel alloys, because of Fe’s higher affinity for C than W [1,8,9].

To improve the tool life of WC-Co-based inserts during machining of steels, better high temperature properties and chemical stability are required. Hot hardness and abrasion wear resistance can be increased by additions of VC, Cr₃C₂, TiC, TaC and Mo₂C [1,6,7,10]. Spark plasma sintering (SPS) significantly increases the hardness and abrasion wear resistance of WC cemented carbides compared to conventional liquid phase sintering (LPS) [6,11]. The technique employs high heating rates and high compressive pressure to consolidate powder compacts to a high density in a short time [12]. Its main advantage is the high degree of densification obtainable at low temperatures within a short period of time, compared to LPS [13]. The short sintering time does not allow for continuous Ostwald ripening, resulting in fine carbide grains and hence higher hardness [14]. Hot hardness, resistance to thermal cracking, abrasion wear resistance and corrosion resistance can also be increased by substitution of the Co binder with Ni [15]. Due to its more ductile austenitic structure, Ni reduces loss of WC grains by extruding outwards to replace the eroded binder between the WC grains, improving the wear resistance [16]. The chemical stability of WC-based inserts can be increased by additions of TiC and NbC [1]. Also, Ni has higher solubility and better wetting of TiC than Co [17], improving the resistance to diffusion wear, particularly for machining of steel [11]. Crater wear can also be prevented through complete substitution of WC by NbC, which has significantly lower solubility in steel [8,9]. NbC has good mechanical and physical properties, such as high hardness (19.6 GPa), very high melting point (3600 °C) (good for high temperature applications) and low density (7.89 g/cc) [1,9,14,18]. Intermetallic aluminides, such as iron aluminide, have also been studied as potential Co binder substitutes [19], because of their good strength at intermediate

temperatures and corrosion resistance at elevated temperatures [19]. Fe₃Al has no phase transitions over temperature and is composed of cheap elements. Use of iron aluminide (Fe₃Al) as a WC binder significantly improves the hardness, wear resistance, elastic modulus and corrosion resistance compared to Co [19]. However, Fe₃Al as a binder reduces the fracture toughness (K_{ic}) and transverse rupture strength (TRS) of the WC cemented carbide compared to Co [19].

The effect of SPS, WC substitution with NbC, Co substitution with Ni and Fe₃Al, variation of binder content and TiC, Mo₂C, Cr₃C₂ additions on the mechanical properties and tool life of inserts under coolant-free, hard-turning and interrupted milling conditions, were investigated and compared to plain WC-10Co (wt.%) (ie WC with 10 wt.%Co binder alloy) inserts produced by SPS and LPS. The interest in NbC is because of its ready availability and its recently recognised intrinsic wear resistance [8].

Experimental Procedure

Materials

The starting powders and their characteristics are given in Table I. The powder compositions, Table II, were wet milled in 99% pure ethanol for 15 hours in a steel container with WC milling balls. They were then dried using a Rota evaporator at 64 °C at 80 rpm for 1 hour. The NbC grades were received from the University of Leuven (Katholieke Universiteit Leuven, Belgium).

Table I. Specifications of Starting Powders

| Compound | D50 Particle size (µm) | Crystal Structure | Purity (wt.%) | Source |
|--------------------------------|------------------------|-------------------|---------------|---|
| WC | 0.8 | hexagonal | >99.00 | H.C. Starck, Germany |
| Co | 0.9 | hexagonal | >99.80 | OMG Americas, USA |
| Ni | 0.2 | cubic | >99.80 | Dong Yang (HK) International Group, China |
| Cr ₃ C ₂ | 0.8 | orthorhombic | >99.00 | H.C. Starck, Germany |
| TiC | 1.5 | cubic | >99.00 | Treibacher, Austria |
| NbC | 1.2 | cubic | >99.00 | Treibacher, Austria |
| Mo ₂ C | 1.7 | orthorhombic | >99.00 | Treibacher, Austria |

Table II. Nominal Compositions of the Cemented Carbides (wt.%)

| Abbreviation | Binder Phase | | | Alloying Additives | | | | Hard Phase | |
|--------------|--------------|----|--------------------|--------------------|-------------------|--------------------------------|--------------------------------|------------|---------|
| | Co | Ni | Fe ₃ Al | TiC | Mo ₂ C | Cr ₃ C ₂ | Al ₂ O ₃ | WC | NbC |
| WC-10Co | 10 | - | - | - | - | ✓ | - | Balance | - |
| WC-11Ni | - | 11 | - | ✓ | ✓ | ✓ | - | Balance | - |
| WC-7Ni | - | 7 | - | ✓ | ✓ | ✓ | - | Balance | - |
| NbC-12Co | 12 | - | - | - | - | - | - | - | Balance |
| NbC-12FA | - | - | 12 | - | - | - | ✓ | - | Balance |

Sintering

The milled composite powders were consolidated in a spark plasma sintering furnace (HP D5, FCT Systeme, Germany). The powders were poured into cylindrical graphite dies with inner and outer diameters of 20.9 mm and 40 mm, respectively and 48 mm height. The composite powder assemblies were heated in a vacuum (2 Pa) in two steps, for example WC-10Co powders were first heated to 1000 °C at a rate of 200 °C/min and subsequently to 1220 °C at a heating rate of 100 °C/min, and the temperature was held at 1220 °C for five minutes during sintering. A cooling rate of 200 °C/min was applied to all samples. The applied pressure was adjusted from 16 MPa to 30 MPa at 1000 °C, and from 30 MPa to 50 MPa at 1220 °C within 30 seconds. The pressure was then held constant at 50 MPa throughout the rapid sintering cycle. Horizontal and vertical graphite papers were used to separate the powders from the die and punch setup. Hexagonal boron nitride was placed on the graphite paper to prevent C diffusion from the graphite paper to the powders during sintering. The graphite die was wrapped in a C cloth to minimize the heat loss from the die surface. The temperature was controlled by an optical pyrometer focused on a central borehole on the upper punch, 1 mm above the top surface of the sample, to give an accurate estimation of the sample temperature [14]. Consolidation of the composite powder assemblies in the axial direction was monitored by following the position of the plunger. Different sintering profiles, depending on the powder compositions, were used to achieve good densification, Table III.

Table III. Sintering Conditions

| Composition (wt.%) | Abbreviation | Temperature and Dwell Time | Pressure (MPa) |
|---|--------------|----------------------------|----------------|
| WC-Cr ₃ C ₂ -10Co | 10Co-S | 1220 °C for 5 min | 50 |
| WC-Cr ₃ C ₂ -10Co | 10Co-L | 1430 °C for 75 min | 4.4 |
| WC-Cr ₃ C ₂ -Mo ₂ C-TiC-11Ni | 11Ni-S | 1320 °C for 5 min | 70 |
| WC-Cr ₃ C ₂ -Mo ₂ C-TiC-11Ni | 11Ni-L | 1430 °C for 75 min | 4.4 |
| WC-Cr ₃ C ₂ -Mo ₂ C-TiC-7Ni | 7Ni-S | 1380 °C for 5 min | 70 |
| WC-Cr ₃ C ₂ -Mo ₂ C-TiC-7Ni | 7Ni-L | 1430 °C for 75 min | 4.4 |
| NbC-12Co | NbC-12Co | 1280 °C for 4 min | 30 |
| NbC-12Fe ₃ Al | NbC-12FA | 1300 °C for 4 min | 30 |

S = spark plasma sintered, L = liquid phase sintered

Liquid phase sintering (HIP, Ultra Temp, USA) was done by heating the compositions in a vacuum (0.04 MPa) at an initial heating rate of 2.4 °C/min up to 1200 °C. At 1200 °C, Co loss protection (CLP) was carried out by the addition of argon gas at a pressure of 0.37 MPa, and a heating rate 3.5 °C/min up to 1430 °C. The temperature was held constant for 75 minutes, and for the last 20 minutes, hot isostatic pressing (HIP) was done at 4.4 MPa to eliminate all the surface porosity [1]. The furnace was then water cooled at a rate of 3.5 °C/min.

Characterization and Mechanical Testing

Archimedes' principle was used to determine the density of the sintered samples (ED224S, Sartorius, Germany). Vickers hardness (HV 30) was measured on polished specimens after standard metallographic preparation, using a load of 30 N (VHT 003 MTA, Vickers Limited, United Kingdom), calculating an average from five indentations at different regions on each sample. The criteria for the accurate derivation of fracture toughness (K_{Ic}) using Shetty's equation were satisfied [20]: $1.25 \leq c/a \leq 2.25$ and $0.25 \leq l/a \leq 2.5$, where c is the Palmqvist crack length from the centre of indentation to the crack tip, a is half the diagonal length of indentation and l is the difference between c and a .

Turning trials were carried out on 440B martensitic stainless steel (440B-SS, X90CrMoV18), the chemical composition of this workpiece is shown in Table IV [21]. The 440B-SS has a Rockwell-A hardness of 71.31 ± 0.43 HRA. An EFAMATIC RS-20.2 CNC turning machine using an Oi-TD Fanuc series controller was used for the trials. The cutting tool inserts were secured on a CSBNL 3225P12 tool holder which matched the shape of the inserts. The inserts were square-shaped (12.7 x 12.7 x 4.3 mm), with a nose radius of 1.6 mm. All the inserts had a 0.2 mm land (chamfer) to reduce the stress concentration along the sharp cutting edges. The turning conditions are shown in Table V. The diameter of the workpiece was 50 mm and the length was 200 mm. The average tool wear was measured after each pass and the ISO 3685-1993 flank wear failure criterion was used [22,23]. According to this standard, a maximum flank wear of 300 μm is acceptable, beyond which the insert can no longer achieve an acceptable surface finish [22].

During the coolant-free milling trials, the inserts were secured on to a Pilot F75SN12080 cutting tool holder attached to a Bridgeport GX1000 CNC milling machine with an Oi-MC Fanuc series controller. The milling trials were carried out on SABS 1431:300WA structural steel, of composition shown in Table IV [24]. The 300WA-SS had a hardness of 55.11 ± 0.65 HRA. The milling inserts had the same shape as the turning inserts. The milling conditions are shown in Table VI. The workpiece width was 60 mm and the radial depth of cut was 80 mm, ensuring that the inserts would disengage from the workpiece for rapid cooling every revolution. The flank wear was also measured after every pass and the ISO 3685-1993 flank wear failure criterion was used [23]. Maximum temperatures and thermal variation per second were measured using a thermal imaging camera (D5000, NIKON Japan), with Flir tool software; an example of a thermal image during turning is shown in Figure 1. The thermal camera took 30 thermal readings per second, facilitating measurement of the temperature change of the inserts. Force measurements were carried out using Kistler force gauges (9265, 3 axis dynamometer Kistler, Switzerland, for turning and 9366CC0, Kistler multicomponent force link, Switzerland, for milling). The Kistler force gauges were attached to the workpiece clamp.

The flank wear and crater wear were evaluated using an optical microscope (DM6000M, LEICA, Germany) with a digital camera (DFC490, LEICA, Germany) and high angle annular dark field scanning transmission electron microscopy (HAADF-STEM) (JEOL 2100, with a LaB₆ filament, JEOL, Japan).

Table IV. Chemical Compositions of the Workpiece Materials [21,24]

| Workpiece Alloy | Constituent Elements (wt.%) | | | | | | | | | |
|-----------------|-----------------------------|------|------|-----|------|-------|------|------|------|---------|
| | C | Si | Mn | V | Mo | Cr | P | S | Al | Fe |
| 440B-SS | 0.9 | 0.45 | 0.40 | 1.0 | 1.10 | 17.50 | - | - | - | Balance |
| 300WA-SS | 0.18 | 0.34 | 1.35 | - | - | - | 0.02 | 0.03 | 0.04 | Balance |

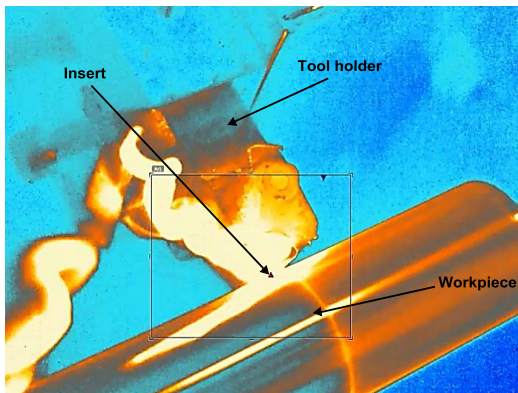


Figure 1. Thermal image during coolant-free turning.

Table V. Turning Conditions for the WC Cemented Carbide Inserts, a Feed Rate (V_f) of 0.1 mm/rev was used for all Cutting Tests

| Cutting Speed, v_c (m/min) | Depth of Cut, a_p (mm) |
|------------------------------|--------------------------|
| 80 | 1.0 |
| 100 | 1.0 |
| 120 | 0.5 |

Table VI. Milling Conditions for the WC Cemented Carbide Inserts, a Feed of 0.1 mm/tooth was Used for all Cutting Tests

| Milling Test Variables | | CNC Parameters | |
|------------------------------|--------------------------------|---------------------|--------------------|
| Cutting speed, v_c (m/min) | Axial depth of cut, a_p (mm) | Spindle speed (rpm) | Feed rate (mm/min) |
| 100 | 1.0 | 398.00 | 39.80 |
| 250 | 1.0 | 995.00 | 99.50 |
| 255 | 0.5 | 995.00 | 99.50 |

Results and Discussion

Densification

The NbC-based cemented carbides were produced by SPS, while the WC-based cemented carbides were produced by both SPS and LPS, Table III. All the sintered compositions achieved densifications above 99% and had negligible open porosity, Table VII, affirming the ability of SPS to produce dense compacts at much lower temperatures and shorter dwell times than LPS [12]. The WC-Ni samples required higher sintering temperatures (1320-1380 °C) and pressure than the WC-Co samples (1280 °C) to achieve good densification, yet they were all produced by SPS, Table VII. Sintering temperatures depend on several factors, such as diffusion rates, wetting of WC by the binder, solubility of WC in the binder, additives and binder proportion [1,11]. Therefore, the higher sintering temperatures can be attributed to the lower solubility of WC in Ni [10], the poorer wetting of WC by Ni [1,11] and the fact that the solubility of Mo₂C in Ni increases with increased sintering temperature [25]. The 7Ni-S sample was spark plasma sintered at a higher temperature (1380 °C) than the 11Ni-S sample (1320 °C), and this was attributed to the reduction in volume fraction of the lower melting point Ni binder [1,26].

The WC-10Co (wt.%) (10Co) sample required a lower SPS temperature than the NbC-12Co sample, Tables III and VII, to achieve good densification, because Co has much higher solubility and better wetting of WC than NbC [14]. The Fe₃Al binder, NbC-based sample (NbC-12FA) required a higher sintering temperature (T = 1300 °C, 30 MPa) than the NbC-12Co sample to achieve good densification (T = 1280 °C, 30 MPa), because of the better solubility between NbC and Co at temperatures above 1200 °C than in Fe₃Al [27].

Table VII. Density and Open Porosity of Sintered Samples

| Abbreviation | Densification (%) | Volume open porosity (%) |
|--------------|-------------------|--------------------------|
| 10Co-S | 99.75 ± 0.09 | 0.01 ± 0.00 |
| 10Co-L | 99.85 ± 0.14 | 0.07 ± 0.01 |
| 11Ni-S | 99.61 ± 0.24 | 0.02 ± 0.01 |
| 11Ni-L | 99.75 ± 0.16 | 0.03 ± 0.02 |
| 7Ni-S | 99.02 ± 0.20 | 0.04 ± 0.01 |
| 7Ni-L | 99.76 ± 0.12 | 0.00 ± 0.00 |
| NbC-12Co | 99.20 ± 0.12 | 0.02 ± 0.01 |
| NbC-12FA | 99.27 ± 0.02 | 0.03 ± 0.01 |

S = spark plasma sintered, L = liquid phase sintered

Mechanical Properties

All the WC-based samples produced by SPS had higher Vickers hardnesses than the similar samples produced by LPS, Table VIII and Figure 2. This trend was confirmed by the Rockwell hardness tests, Table VIII. This was attributed to the lower sintering temperatures and shorter sintering dwell times which resulted in finer WC microstructures due to reduced Ostwald ripening [11,26]. Additions of TiC and Mo₂C to the WC-Ni cemented carbides produced by both LPS and SPS increased the hardness compared to WC-10Co, with the 7Ni-S grade having the highest hardness of >20 GPa, Table VIII. This increased hardness was due to TiC having higher hardness than WC by ~5 GPa [28]. Also, Ti is a good inhibitor for the growth or dissolution of WC by forming an atomic layer of TiC at the WC/Ni interface, altering the interfacial energy [6]. Mo₂C additions improved the hardness by improving the wetting of WC by Ni [1], leading to better binder distribution and higher hardness [1,14]. Furthermore, Mo₂C also acts as a WC grain growth inhibitor, refining the WC grain size by delaying the aggregation of fine WC and the transformation of the aggregates to single large grains (coalescence) during sintering [26,29]. Both the NbC-based samples had lower hardnesses than the WC-based samples, because NbC has a lower hardness (~19.4 GPa) than WC (~22.5 GPa) [30]. The lower hardnesses could also result from the lower solubility and poorer wetting of NbC by Co and Fe₃Al [14,27]. The NbC-12FA sample had a slightly higher hardness than the NbC-12Co sample, most likely due to the intermetallic Fe₃Al having a higher hardness than Co [19]. However, for cutting tool applications, inserts with similar hardnesses are normally compared.

The WC-10Co samples produced by SPS and LPS had the highest fracture toughnesses (K_{Ic}) compared to the WC-Ni-based samples, because of the good wetting of WC by Co compared to Ni, improving the Co binder distribution [6,11,26]. Liquid phase sintered WC-10Co had a higher K_{Ic} than the similar sample produced by SPS, and this trend was also observed in the WC-Ni-based samples. The higher K_{Ic} was due to better binder pool distribution from the formation of the Co-liquid phase during sintering [11,26] which enhanced WC solubility [1], as well as the capillarity action of the liquid phase between the pores during the secondary rearrangement stage of sintering [1]. However, during SPS, the liquid binder phase only exists momentarily, followed by rapid solidification [11,12], preventing enhanced WC solubility and secondary rearrangement due to capillary action of the liquid phase, resulting in poorer binder distribution. The 11Ni-L sample had a higher K_{Ic} than the 7Ni-L sample, due to the higher volume fraction of the tougher

binder phase [1]. The tougher metallic binder phase shields the stress field at the front of the crack tip during crack propagation and bridges the crack ligaments behind the crack tip [31]. The NbC-12Co sample had a much lower K_{Ic} value than all the 10Co-S samples, although with a higher Co binder amount. This was attributed to the poorer solubility and wetting of Co with NbC than with WC [14], leading to formation of brittle interconnected NbC networks, due to poorer distribution of Co [31]. The NbC-12FA sample had a lower K_{Ic} than NbC-12Co, due to the even poorer solubility and wetting of the Fe_3Al with NbC than Co [27], as well as the lower ductility of Fe_3Al than Co [19].

Table VIII. Mechanical Properties of the Samples

| Abbreviation | Vickers Hardness, HV 30 (GPa) | Rockwell-A Hardness, HRA (60 kgf) | Fracture Toughness, K_{Ic} (MPa.m ^{1/2}) |
|--------------|-------------------------------|-----------------------------------|--|
| 10Co-S | 17.34 ± 0.10 | 93.02 ± 0.13 | 11.84 ± 0.16 |
| 10Co-L | 15.03 ± 0.13 | 90.20 ± 0.18 | 12.71 ± 0.23 |
| NbC-12Co | 12.86 ± 0.14 | 89.86 ± 0.11 | 7.87 ± 0.18 |
| NbC-12FA | 13.21 ± 0.11 | 89.86 ± 0.28 | 6.65 ± 0.19 |
| 7Ni-S | 20.36 ± 0.11 | 94.60 ± 0.35 | 10.18 ± 0.15 |
| 7Ni-L | 18.00 ± 0.27 | 93.48 ± 0.12 | 10.69 ± 0.23 |
| 11Ni-S | 18.85 ± 0.19 | 93.58 ± 0.24 | 10.38 ± 0.43 |
| 11Ni-L | 15.96 ± 0.15 | 92.02 ± 0.27 | 11.22 ± 0.16 |

S = spark plasma sintered, L = liquid phase sintered

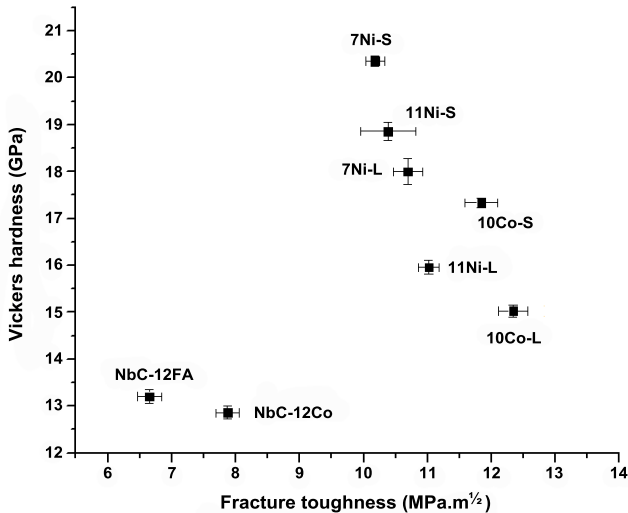


Figure 2. Relationship between Vickers hardness and Palmqvist fracture toughness.

Flank and Crater Wear During Hard-turning

The flank wear rate (FWR), average resultant force (F_R) and temperature measurements during turning at a cutting speed (v_c) of 80 m/min and a depth of cut (a_p) of 1 mm are shown in Table IX. The 7Ni-L insert had the lowest FWR followed by the 10Co-S insert, while the NbC-12Co insert had the highest FWR, Figure 3, although all the inserts experienced similar average temperatures and maximum recorded temperatures of above 1380 °C, Table IX. The high maximum temperature recorded gives an indication of the aggressive cutting conditions the inserts were exposed to during hard turning of 440B martensitic steel.

Generally, insert failure during machining can be attributed to two main causes: chemical wear (diffusion) and mechanical wear (abrasion, attrition and fracture) [5,21]. Compared to WC, NbC is chemically more stable, forms Nb_2O_5 (a non-volatile reaction layer) and has better higher temperature properties than WC, especially during machining of steels [8,9]. However, the NbC insert had the highest FWR compared to all the WC-based inserts, which was attributed to mechanical wear [5]. Flank wear is mainly caused by rubbing at the insert cutting edge/nascent workpiece interface, resulting in abrasive and/or adhesive wear at high temperatures [5]. Abrasion is the main flank wear mechanism and is characterised by formation of grooves, Figure 3, in the direction which the insert slides against the workpiece surface [5]. The flank wear was mainly due to mechanical wear attributed to the high hardness of the 440B-SS workpiece (71.31 ± 0.43 HRA) which acted as an abrasive body. Additionally, the debris from the workpiece that normally gets trapped at the cutting edge/workpiece interface during turning would undergo plastic deformation and strain hardening, forming hard abrasive bodies [32], increasing the flank wear [5]. The higher flank wear in the NbC-12Co sample than the WC-based inserts could also be due to mechanical wear from vibration of the workpiece at the low turning speed of 80 m/min [33], which led to high cutting forces, Table IX. The average cutting forces at 80 m/min were much higher than at 100 m/min, although the same depth of cut (1 mm) was used, Figure 4, and that was attributed to reduced vibration at the higher cutting speed [33]. The NbC-12Co insert had a lower K_{Ic} , Table VIII, and lower TRS than the LPS inserts [6,34,35], lowering the resistance to the cyclic impact force introduced by the vibrations at 80 m/min, leading to higher flank wear, but did not show any flaking like the 10Co-S sample, Figure 3. The NbC-12FA insert shattered at a $v_c = 80$ m/min and $a_p = 1$ mm during turning because of its even lower K_{Ic} and TRS than all the other inserts, leading to some fracture of NbC grains along the cutting edge, Figure 5. It has to be noted that the 7Ni-S also shattered under these conditions, Table IX.

All the inserts produced by LPS had better FWR than similar compositions produced by SPS during turning at 80 m/min, which could be due to their higher K_{Ic} and TRS values. The lower TRS in the SPS samples was also due to higher residual stresses from the rapid cooling rates compared to LPS [6,34], explaining why only SPS inserts shattered during turning. Generally, the average F_R increased with increased FWR, due to flank wear leading to blunting of the cutting edge, which increased the cutting force because of increased shear area [36]. Cutting force increases with increased shear force, and the shear force increases with increased shear area [36]. Crater wear was observed on the rake of the 10Co-S insert, but not on any of the Ni-bonded WC inserts, Figure 3. The main mechanism during crater wear was diffusion of WC from the insert cutting edge into the workpiece, leading to dissolution of the insert surface by the chips

flowing over it, which was activated by high cutting temperature [1,5]. Crater wear occurred on 10Co-S due to the diffusion of W and C (mainly C) into the steel due to good chemical affinity, particularly above 1200 °C [1,8]. Additions of TiC and Mo₂C to WC-based cemented carbides improve the resistance to crater wear by forming the (W,Ti,Mo)C solid solution which has very good chemical stability at high temperatures [1], explaining the resistance to crater wear in the 7Ni and 11Ni inserts. No crater wear was observed in any of the NbC inserts, Figure 3, because NbC is chemically stable at high temperatures and is nearly insoluble in Fe above 1200 °C [8,9].

Table IX. Comparison of Insert Behaviour During Coolant-free Turning at a $v_c = 80$ m/min and $a_p = 1$ mm

| Insert | Flank Wear Rate, FWR ($\mu\text{m}/\text{min}$) | Average Resultant Force, F_R (N) | Average Cutting Temperature ($^{\circ}\text{C}$) | Maximum Recorded Temperature ($^{\circ}\text{C}$) |
|----------|---|------------------------------------|--|---|
| 10Co-S | 15.65 | 1054.42 \pm 19.76 | 1117 \pm 201 | 1435 |
| NbC-12Co | 40.16 | 1079.81 \pm 20.67 | 1067 \pm 137 | 1380 |
| NbC-12FA | Shattered | - | - | - |
| 7Ni-S | 20.26 | 1031.65 \pm 30.43 | 1044 \pm 185 | 1418 |
| 7Ni-L | 13.38 | 960.19 \pm 16.82 | 1110 \pm 214 | 1489 |
| 11Ni-S | Shattered | - | - | - |
| 11Ni-L | 18.87 | 963.89 \pm 23.46 | 1018 \pm 216 | 1457 |

S = spark plasma sintered, L = liquid phase sintered

The FWR and average F_R of the inserts due to turning at $v_c = 100$ m/min and $a_p = 1$ mm are shown in Table X. There were lower cutting forces at 100 m/min than at 80 m/min, which was attributed to the reduced vibration on the workpiece at the higher cutting speed [33]. The LPS inserts had lower FWR than the SPS inserts, with 11Ni-L having the lowest FWR and NbC-12FA having the highest FWR. The aggressive nature of hard-turning meant that mechanical wear could be the major cause of flank wear at 100 m/min, hence the lower TRS and K_{Ic} of the SPS inserts than the LPS inserts explains the higher FWR of the SPS inserts [6], as well as the shattering of the 7Ni-S insert. The NbC-12Co insert had a slightly lower FWR than the 10Co-S insert, Table X and Figure 6, which could be due to the lower average F_R (reduced workpiece vibration, eliminating the effect of cyclic impact at the cutting edge), and the better high temperature properties of NbC than WC [8,9]. The NbC-12FA insert had the highest FWR and highest average F_R , and the latter was because of blunting of the cutting edge, which increased with increased flank wear [6,36].

Lower average resultant forces were observed while turning at $v_c = 120$ m/min and $a_p = 0.5$ mm than at the lower cutting speeds, Table X, due to the reduced a_p [6]. Similar to the previous trends, the WC-Ni-based inserts had lower FWR than the 10Co-S and NbC-12Co inserts, with 7Ni-S having the lowest FWR, Table X. Abrasion and adhesion are key mechanical wear mechanisms at high cutting speeds [5], and are dependent on the hardness and bonding strength of the material (inserts) [1,5,6], and usually materials with similar hardnesses are compared. Additions of TiC and Mo₂C improve the high temperature hardness [1], increasing the resistance to abrasion, while Mo₂C improves the bonding between WC and Ni [11], thus increasing

resistance to adhesion [5]. Consequently the 10Co-S insert had a lower abrasion wear resistance than the WC-Ni inserts [6] and lower resistance to deformation at high temperature due to the absence of TiC and Mo₂C, increasing its FWR at 120 m/min [6].

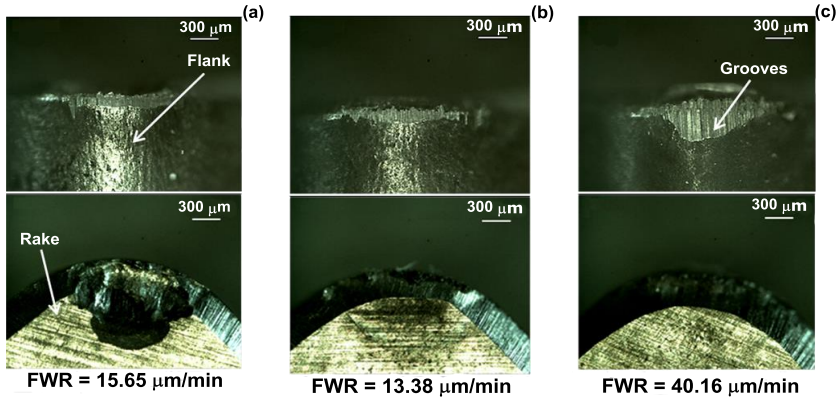


Figure 3. Wear on the flank and rake of; (a) 10Co-S, (b) 7Ni-L, (c) NbC-12Co cutting tool inserts from coolant-free turning at a $v_c = 80$ m/min and $a_p = 1$ mm.

NbC has a low solubility in Fe, Ni, or Co at 1250 °C [27] and can, therefore, form a brittle NbC interconnected network with poor binder distribution [31]. The present NbC grades have regions without binder material and thus regions without any toughness provided by the binder.

Table X. Comparison of Insert Behaviour during Coolant-free Turning $v_c = 100$ and 120 m/min

| Insert | $v_c = 100$ m/min, $a_p = 1$ mm | | $v_c = 120$ m/min, $a_p = 0.5$ mm | |
|----------|----------------------------------|------------------------------|-----------------------------------|------------------------------|
| | FWR ($\mu\text{m}/\text{min}$) | Average Resultant, F_R (N) | FWR ($\mu\text{m}/\text{min}$) | Average Resultant, F_R (N) |
| 10Co-S | 30.44 | 726.69 \pm 15.67 | 132.09 | 497.91 \pm 16.67 |
| NbC-12Co | 26.12 | 639.52 \pm 19.44 | 288.73 | 512.45 \pm 26.44 |
| NbC-12FA | 40.32 | 780.80 \pm 11.93 | - | - |
| 7Ni-S | Shattered | - | 101.32 | 536.90 \pm 37.13 |
| 7Ni-L | 20.99 | 748.89 \pm 10.64 | 62.93 | 517.41 \pm 20.64 |
| 11Ni-S | 22.77 | 734.89 \pm 16.37 | 66.06 | 501.21 \pm 15.83 |
| 11Ni-L | 18.33 | 650.11 \pm 23.38 | 72.14 | 531.21 \pm 26.61 |

S = spark plasma sintered, L = liquid phase sintered

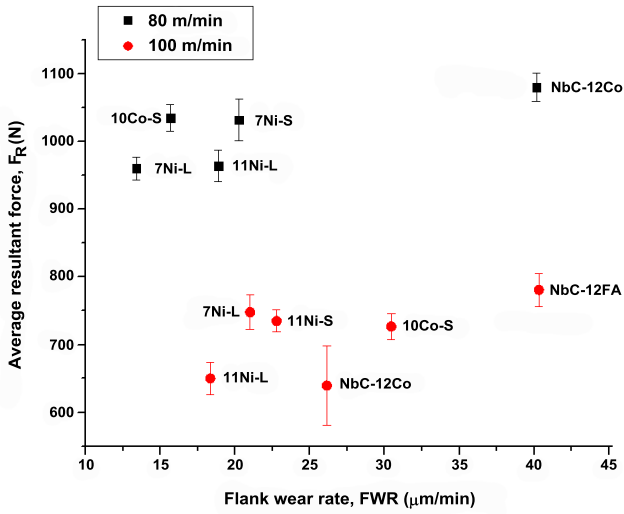


Figure 4. Comparison between average resultant force and FWR at $v_c = 80$ and 100 m/min and $a_p = 1$ mm during coolant-free turning.

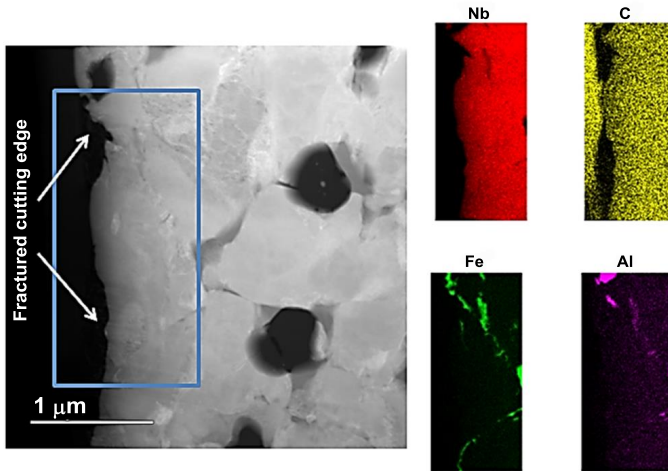


Figure 5. HAADF-STEM mapping images of the fracture cutting edge of the NbC-12Fe₃Al (wt.%) from coolant-free turning, showing Nb (red), C (yellow), Fe (green) and Al (purple).

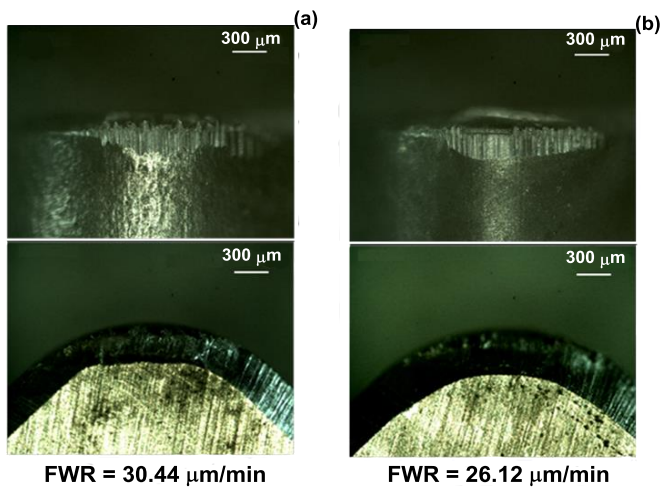


Figure 6. Flank wear on: (a) 10Co-S, (b) NbC-12Co cutting tool inserts from coolant-free turning at $v_c = 100$ m/min and $a_p = 1$ mm.

The cyclic impact and rapid changes in temperature per revolution led to both mechanical wear from the cyclic impact and thermal shock [6], as well as chemical wear from the chemical affinity between the inserts and the 330WA-SS workpiece [1,5,6]. The inserts produced by LPS had lower FWR values because of the better thermal shock and impact resistances than inserts produced by SPS [6]. The good thermal shock and impact resistance were associated with higher TRS and K_{Ic} of the LPS inserts than the SPS inserts [6,35]. The 10Co-L insert had a higher FWR than the other liquid phase sintered inserts, and similarly, the 10Co-S had a higher FWR than the other spark plasma sintered inserts, Table XI.

Table XI. Comparison of Insert Behaviour during Coolant-free Milling at $v_c = 100$ m/min and $a_p = 1$ mm

| Insert | Flank Wear Rate, FWR ($\mu\text{m}/\text{min}$) | Average Resultant Force, F_R (N) | Average Temperature Variation per Second, $\Delta T/s$ ($^\circ\text{C}/\text{second}$) |
|----------|---|------------------------------------|---|
| 10Co-S | 79.92 | 390.73 ± 47.41 | 440.70 ± 31.85 |
| 10Co-L | 35.86 | 285.77 ± 32.28 | 384.75 ± 25.70 |
| NbC-12Co | 39.14 | 312.74 ± 34.63 | 393.34 ± 15.15 |
| 7Ni-S | 70.44 | 352.25 ± 37.79 | 405.54 ± 24.24 |
| 7Ni-L | 37.23 | 258.64 ± 30.17 | 388.71 ± 24.61 |
| 11Ni-S | 44.91 | 376.68 ± 36.83 | 369.79 ± 10.96 |
| 11Ni-L | 10.36 | 246.17 ± 27.58 | 370.71 ± 20.74 |

S = spark plasma sintered, L = liquid phase sintered

The higher FWR in the 10Co-S insert than the other SPS inserts was attributed to chemical wear and was confirmed by crater wear on the rake face of 10Co-S, Figure 7 [1]. The additions of TiC and Mo₂C improved the resistance to chemical wear in the 7Ni and 11Ni inserts. No crater wear and little flank wear were observed in the Nb-12Co insert, Figure 7, because of the good chemical stability of NbC [8,9]. The average F_R increased with increased FWR, Figure 8, which was attributed to blunting of the cutting edge [36]. The average temperature variation per second ($\Delta T/s$) also increased with increased FWR, due to blunting of the cutting edge which increased the friction at the cutting edge/workpiece interface [6]. Increasing v_c from 100 m/min to 250 m/min, while maintaining the same a_p (1 mm) resulted in both increased FWR and average F_R , Table XII. The increase in FWR was due to increased impact (increased number of collisions with workpiece per second), increasing the average F_R , as a result of increased blunting of the cutting edge [6]. Mostly, the $\Delta T/s$ reduced with increased v_c , because of the reduced cooling time per revolution (time between the insert disengagement with the workpiece and re-engagement with the workpiece in one revolution) due to increased spindle speed. This leads to increased minimum temperatures per revolution and hence reduced difference between the maximum and minimum temperature per second. The inserts produced by SPS had higher FWR than the similar ones produced by LPS, with 10Co-S having the highest FWR. The NbC-12Co insert had a significantly lower FWR than both 10Co-S and 10Co-L, Table XII and Figure 9, because of its better high temperature properties and higher resistance to chemical wear [8,9].

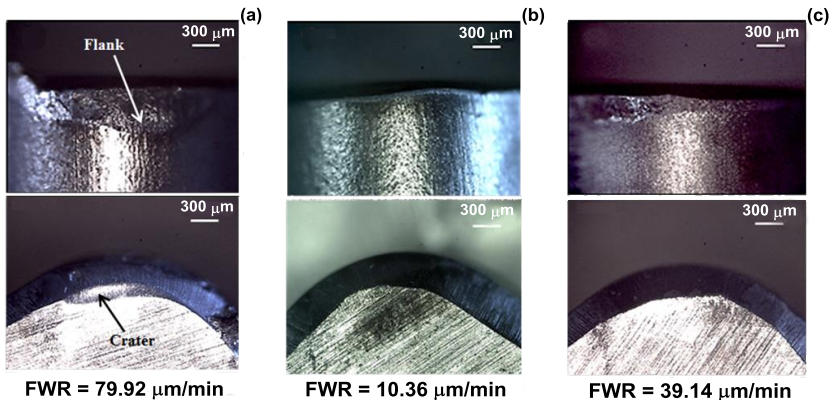


Figure 7. Wear on the flank and rake of; (a) 10Co-S, (b) 11Ni-L, (c) NbC-12Co cutting tool inserts from coolant-free milling at $v_c = 100$ m/min and $a_p = 1$ mm.

Crater wear was observed on the rake face of 10Co-L and was confirmed by HAADF-STEM mapping images of the rake face, Figure 10 which revealed a curved interface with smoothly worn WC grains, indicating diffusion between the insert and the workpiece [37]. However, HAADF-STEM mapping images of the rake face of the NbC-12Co insert revealed a straight interface, Figure 11, demonstrating the good chemical stability of NbC during machining of the steels [8,9]. Notching was observed on the flank of NbC-12Co, Figure 9, which was due to increased mechanical impact with increased v_c [6] and the lower K_{Ic} of the NbC cermets than the other inserts, Table VIII.

Table XII. Comparison of Insert Behaviour during Coolant-free Milling at $v_c = 250$ m/min and $a_p = 1$ mm

| Insert | Flank Wear Rate, FWR ($\mu\text{m}/\text{min}$) | Average Resultant Force, F_R (N) | Average Temperature Variation per Second, $\Delta T/s$ ($^\circ\text{C}/\text{second}$) |
|----------|---|------------------------------------|---|
| 10Co-S | 300.57 | 541.22 ± 46.41 | 365.48 ± 38.95 |
| 10Co-L | 237.15 | 330.91 ± 39.05 | 369.60 ± 18.42 |
| NbC-12Co | 75.83 | 324.00 ± 24.61 | 331.51 ± 19.57 |
| 7Ni-S | 74.65 | 383.49 ± 26.83 | 318.26 ± 38.94 |
| 7Ni-L | 49.63 | 274.56 ± 35.49 | 271.21 ± 36.42 |
| 11Ni-S | 142.01 | 408.05 ± 42.18 | 386.24 ± 21.11 |
| 11Ni-L | 38.60 | 259.22 ± 22.05 | 296.87 ± 26.17 |

S = spark plasma sintered, L = liquid phase sintered

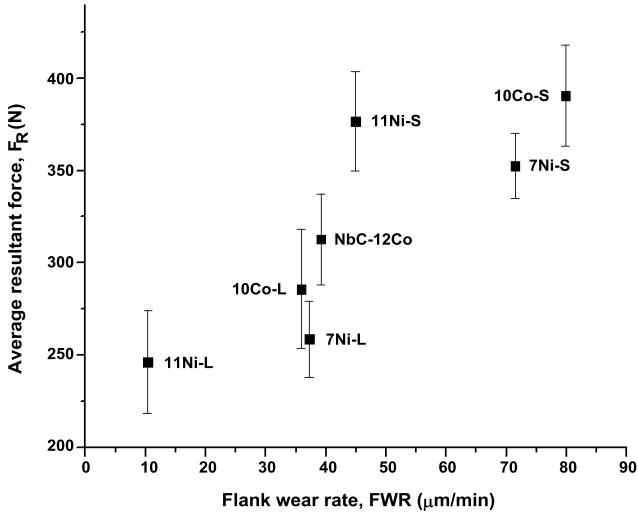


Figure 8. Comparison between average resultant force and FWR at $v_c = 100$ m/min and $a_p = 1$ mm during coolant-free milling.

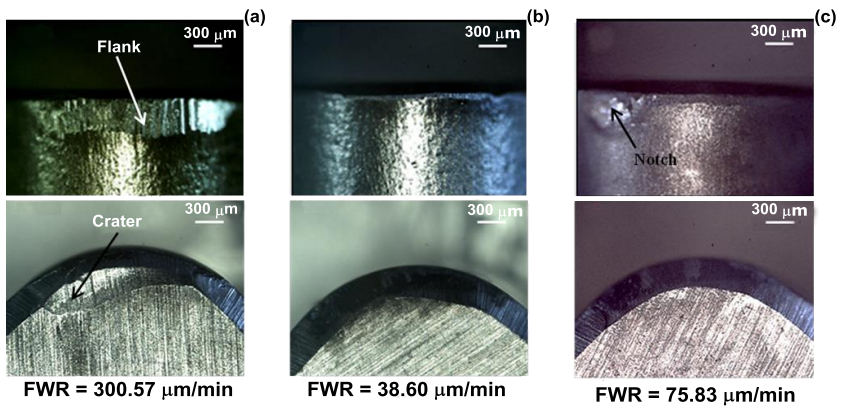


Figure 9. Wear on the flank and rake of; (a) 10Co-L, (b) 11Ni-L, (c) NbC-12Co cutting tool inserts from coolant-free milling at $v_c = 250$ m/min and $a_p = 1$ mm.

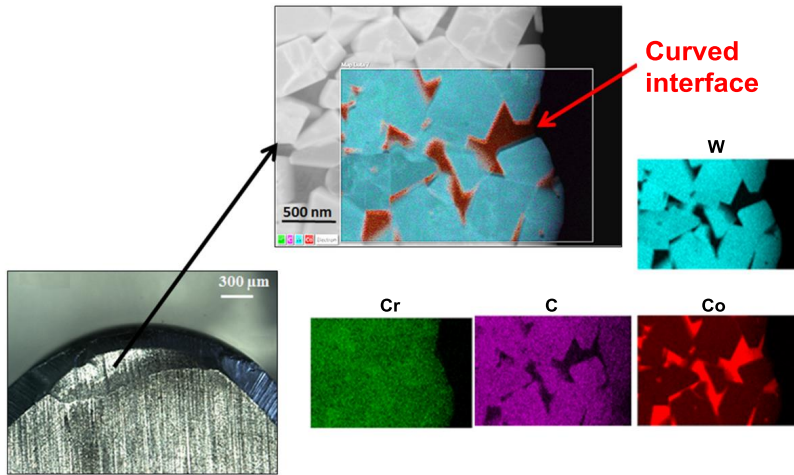


Figure 10. HAADF-STEM mapping images of the crater on the rake face under coolant-free milling of WC-10Co (wt.%), showing W (blue), Cr (green), C (purple) and Co (red).

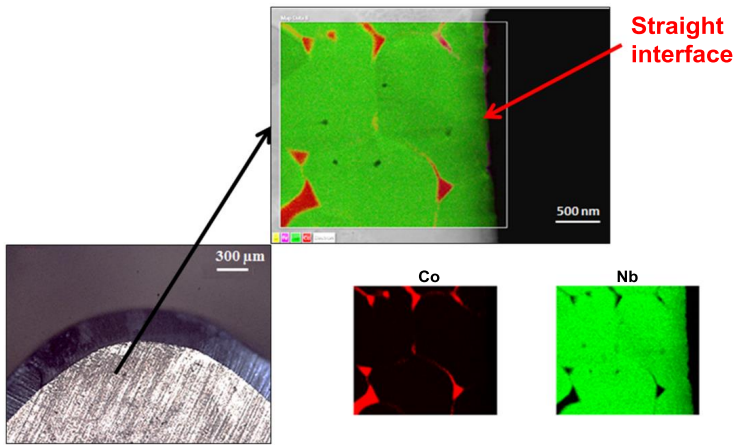


Figure 11. HAADF-STEM mapping images of the rake face under coolant-free milling of NbC-12Co, showing Co (red) and Nb (green).

Conclusions

1. Spark plasma sintering and liquid phase sintering were used to consolidate the WC- and NbC-based cemented carbides, producing inserts with good densification (above 99%) and negligible open porosity. The inserts produced by SPS had significantly higher hardness and lower K_{Ic} than similar LPS samples.
2. During hard-turning at 80 and 100 m/min, the inserts produced by LPS had lower FWR values than similar inserts produced by SPS, which were attributed to their better resistance to mechanical wear due to higher K_{Ic} and TRS.
3. Higher cutting forces were observed at 80 m/min than at 100 m/min, although the same a_p (1 mm) was used, which was attributed to vibration of the workpiece. The 7Ni-S insert had the lowest FWR at 120 m/min and a_p of 0.5 mm, due to its high hardness which improved its abrasion wear resistance.
4. The NbC-12Co inserts had a lower FWR than the 10Co-S at 100 m/min because of the reduced mechanical wear (reduced vibration effect) and better resistance to chemical wear, although during machining tests, inserts with similar hardnesses are normally compared.
5. Crater wear was observed in the 10Co-S insert, but not in the WC-Ni-based inserts, because of TiC and Mo₂C additions. No crater wear was observed in either NbC-12Co or NbC-12FA inserts, because of the good chemical stability of NbC and its low solubility in the machined steels.

6. During interrupted milling, inserts produced by LPS performed better than those produced by SPS for all cutting speeds, due to lower thermal shock resistance and lower impact resistance of the SPS.
7. Crater wear was also observed in the 10Co-S and 10Co-L inserts. No crater wear was observed on the WC-Ni grades and NbC-12Co inserts during milling. The NbC-12Co insert performed better than the standard WC-10Co grades at all milling speeds, showing potential as a possible replacement for WC-Co-based inserts for milling of steels. The 7Ni-L and 11Ni-L performed the best in all hard-turning and interrupted milling tests.

Acknowledgments

This work was financially supported by Department of Science and Technology and the National Research Foundation, South Africa. The authors are grateful to Pilot Tools (Pty) Ltd for assisting in the production of the cutting tools, Department of Mechanical Engineering Science at the University of Johannesburg for use of their turning machine, Professor Rolf Laubscher and Mr. Gerrard Peters for discussions and advice. The authors are grateful to Companhia Brasileira de Metalurgia e Mineração (CBMM), São Paulo, Brazil, for supplying the NbC grades.

References

1. G.S. Upahyaya, *Cemented Tungsten Carbide Production, Properties and Testing* (New Jersey, USA: Westwood, 1998), 55-301.
2. Z. Yao, J.J. Stiglich and T.S. Sudarshan, *Nano-Grained Tungsten Carbide-Cobalt (WC/Co)* (Virginia, USA: Material Modification, Inc, 1999).
3. K. Bonny et al., "Dry Reciprocating Sliding Friction and Wear Response of WC-Ni Cemented Carbides," *Tribology Letters*, 31 (2008), 199-109.
4. V.K. Sarin et al., *Comprehensive Hard Materials* (Oxford, UK: Elsevier, 2014).
5. S.A. Kumar, A.R. Durai and T. Sornakumar, "The Effect of Tool Wear on Tool Life of Alumina-based Ceramic Cutting Tools while Machining Hardened Martensitic Stainless Steel," *Journal of Materials Processing Technology*, 173 (2006), 151-156.
6. R.M. Genga et al., "Abrasion Wear, Thermal Shock and Impact Resistance of WC-Cemented Carbides Produced by PECS and LPS," *International Journal of Refractory Metals and Hard Materials*, 49 (2015), 133-142.
7. J. Hua and R. Shivpuri, "A Cobalt Diffusion Based Model for Predicting Crater Wear of Carbide Tools in Machining Titanium Alloys," *ASME*, 127 (2005), 136-144.
8. M. Woydt and H. Mohrbacher, "The Tribological and Mechanical Properties of Niobium Carbide (NbC) Bonded With Cobalt or Fe₃Al," *Wear*, 321 (2014), 1-7.

9. S.G. Huang et al., "VC and Cr₃C₂ Doped WC-NbC-Co Hardmetals," *Journal of Alloys and Compounds*, 488 (2008), 205-211.
10. N. Lin et al., "Effect of Mo and Co Additions on the Microstructure and Properties of WC-TiC-Ni Cemented Carbides," *International Journal of Refractory Metals and Hard Materials*, 30 (2012), 107-113.
11. R.M. Genga, L.A. Cornish and G. Akdogan, "Effect of Mo₂C Addition on the Properties of SPS Manufactured WC-TiC-Ni Cemented Carbide," *International Journal of Refractory Metals and Hard Materials*, 41 (2013), 12-21.
12. M. Tokita, *Mechanism of Spark Plasma Sintering*, (Kawasaki-shi Kanagawa, Japan: Sumitomo Coal Mining Company Ltd., 1999), 3-7.
13. X. Song, X. Liu and J. Zhang, "Neck Formation and Self Adjusting Mechanism of Neck Growth of Conducting in Spark Plasma Sintering," *Journal of the American Ceramic Society*, 89 (2006), 494-500.
14. S.G. Huang et al., "NbC as Grain Growth Inhibitor and Carbide in WC-Co Hardmetals," *International Journal of Refractory Metals and Hard Materials*, 26 (2008), 389-95.
15. A.M. Human and H.E. Exner, "Electrochemical Behaviour of Tungsten-Carbide Hardmetals," *Materials Science and Engineering*, 209 (1996), 180-191.
16. B. Wittmann, W.D. Schubert and B. Lux, "WC Grain Growth and Grain Growth Inhibition in Nickel and Iron Binder Hardmetals," *International Journal of Refractory Metals and Hard Materials*, 20 (2002), 51-60.
17. S.K. Bhaumik, S.G. Upadhyaya and M.L. Viadya, "Design of WC-Co Hard Metals with Modifications in Carbide and Binder Phases," *International Journal of Refractory Metals and Hard Materials*, 11 (1992), 9-22.
18. S.G. Huang, O. Van der Biest and J. Vleugles, "VC Doped WC-NbC-Co Hardmetals," *Materials Science and Engineering*, 488 (2008), 420-427.
19. S.G. Huang, O. Van der Biest and J. Vleugles, "Pulse Electric Current Sintered Fe₃Al Bonded WC Composites," *International Journal of Refractory Metals and Hard. Materials*, 27 (2009), 1019-1023.
20. D.K. Shetty et al., "Indentation Fracture of WC-Co Cermets," *Journal of Materials Science*, 20 (1985), 1873-1882.
21. K. Sodiya et al., "Performance of Mixed Ceramics and CBN During Hard Turning of Martensitic Stainless Steel," *International Journal of Advanced Manufacturing Technology*, 77 (2015), 861-871.

22. ISO 3685:1993, Tool-Life Testing with Single-Point Turning Tools (International Organization for Standardization, Geneva, 1993).
- 23 W.A. Knight and G. Boothroyd, *Fundamentals of Machining and Machine Tools, 3rd Edition* (Florida, USA: Taylor and Francis Group, LLC, 2006).
24. SABS 1431:1987 South Africa Bureau of Standards for Structural Steels.
25. P.M. Kemp and R.M. German, "Grain Growth in Liquid Phase Sintered W-Mo-Ni-Fe Alloys," *Journal of the Less Common Metals*, 175 (1991), 353-68.
26. R.M. Genga, L.A. Cornish and G. Akdogan, "Optimization of WC Particle Size, Ni Binder Content and Mo₂C Addition for Improved SPS WC-TiC-Ni Cemented Carbide" (Paper presented at the 18th Plansee Seminar, Reutte, Austria, 4 June 2013), 26.
27. R. Edwards and T. Raine, "The Solid Solubility of Some Stable Carbides in Cobalt Nickel and Iron at 1250 °C," *Powder Metallurgy, Springer-Verlag*, (1952), 232-242.
28. H.C. Kim, D.K. Kim and I.J. Shon, "Sintering Behaviour and Mechanical Properties of Binderless WC-TiC Produced by Pulse Current Activated Sintering," *Journal of Ceramic Processing Research*, 8 (2007), 91-97.
29. X. Wang, Z.Z. Fang and H.Y. Sohn, "Grain Growth during the Early Stage Sintering of Nanosized WC-Co Powders," *International Journal of Refractory Metals and Hard Materials*, 26 (2008), 232-42.
30. R.M. Genga et al., "Microstructure and Material Properties of PECS Manufactured WC-NbC-Co and WC-TiC-Ni Cemented Carbides," *International Journal of Refractory Metals and Hard Materials*, 49 (2015), 240-248.
31. S.G. Huang et al., "Properties of NbC-Co Cermets Obtained by Spark Plasma Sintering," *Materials Letters*, 61 (2007), 574-577.
32. B. Basu and M. Kalin, *Tribology of Ceramics and Composites: A Material Science Perspective* (New Jersey, USA: John Wiley & Sons, Inc., 2011), 51-54.
33. V.B. Gaba, J. Nookala and S.G. Babu, "The Impact of Cutting Conditions on Cutting Force and Chatter Length for Steel and Aluminium," *International Journal of Engineering and Advanced Technology*, 2 (2013), 919-924.
34. F. Zhang et al., "Spark Plasma Sintering of Macroporous Calcium Phosphate Scaffolds from Nanocrystalline Powders," *Journal of the European Ceramic Society*, 28 (2008), 539-545.
35. J. Gurland and P. Bradzil, "Relation of Strength, Composition and Grain Size of Sintered WC-Co," *Transactions of the Metallurgical Society of AIME*, 203 (1955), 311-315.

36. F.E. Gorczyca, *Application of Metal Cutting Theory* (New York, NY, USA: Industrial Press, 1987), 144-153.

37. E.M. Trent, *Metal Cutting, 4th Edition* (London, UK: Butterworth-Heinemann, 1991) 188-195.

Common Acronyms and Abbreviations

| | |
|--------------------------|--|
| α | Ferrite or Coefficient of Expansion |
| γ | Austenite |
| ΔH | Molar Latent Heat of Phase Transition |
| ΔT | Temperature Difference or Transformation Undercooling |
| $\Delta T/s$ | Average Temperature Change per Second |
| Δx | Stroke (Oscillating Wear Test) |
| ϵ_{el} | Strain - Elastic |
| ϵ_{pl} | Strain - Plastic |
| ν | Poisson's Ratio |
| ρc | Radius of Curvature |
| σ | Stress or Specific Interfacial Energy |
| σ_0 | Material Constant – Starting Stress for Dislocation Movement |
| σ_{bd} | Dynamic Tensile Strength |
| σ_F, σ_P | Brittle Fracture Stress or Cleavage Fracture Stress |
| σ_{FE} | Allowable Bending Stress |
| σ_{Flim} | Nominal Bending Stress |
| σ_{FO} | Nominal Tooth Root Bending Stress |
| $\sigma_{FO50\%}$ | Nominal Tooth Root Bending Stress at Endurance Life for 50% Probability of Failure @ 10^7 cycles |
| σ_{Hlim} | Allowable Contact Stress |
| σ_{HO} | Nominal Contact Stress at Pitch Point |
| σ_T | Peak Tensile Stress |
| σ_y | Yield Strength |
| σ_{yd} | Dynamic Yield Strength |
| $\Sigma_{(50\%@N=10^7)}$ | Rotating Fatigue Strength Limit for 50% Probability of Failure @ 10^7 Cycles |
| Φ | Diameter |
| ν | Frequency |

| | |
|----------------------------------|--|
| a | Distance from Centre or Half the Diagonal Length of Vickers Indentation |
| a_p | Depth of Cut |
| ACC | Accelerated Cooling |
| A_{FB} | Local Material Exposure – Ratio of Locally Occurring Equivalent Stresses to Locally Available Strength of the Gear Flank |
| AFM | Atomic Force Microscopy |
| A_{gt} | Elastic plus Plastic Uniform Elongation at Maximum Force |
| AHSS | Advanced High Strength Steel |
| AISI | American Iron and Steel Institute |
| A_{kv} | Charpy Impact Energy |
| ASTM | American Society for Testing and Materials |
| A_v | Impact Energy (Charpy) |
| A%, A₅₀ | Elongation (Tensile Test) |
| b | Face Width (Gear) |
| b_H | Local Semi-Hertzian Contact Width |
| BEI | Back Scattered Electron Image |
| BMAT | Ball Mill Abrasion Test |
| BMECT | Ball Mill Edge Chipping Test |
| BMIFT | Ball Mill Impact Fatigue Test |
| BSE | Back Scattered Electron |
| c | Average Length of Cracks Measured from Centre of Vickers Indentations |
| C | Loading Curvature Parameter or Palmqvist Crack Length |
| CAD | Computer Aided Design |
| CAE | Computer Aided Engineering |
| CCO | Chromium Carbide Overlay |
| CCT | Continuous Cooling Transformation |
| CE/CET/CEV/C_{eq} | Carbon Equivalent |
| CHD | Case Hardened Depth |
| CHD_{opt} | Optimum Case Hardened Depth |

| | |
|-------------------------|---|
| CLP | Cobalt Loss Protection |
| CoF | Coefficient of Friction |
| CR | Controlled Rolling |
| CrE | Chromium Equivalent |
| CS | Conventional Sintering |
| CSR | Controlled Soft Reduction |
| CTE | Coefficient of Thermal Expansion |
| CTS | Controlled Thermal Severity (Weldability Test) |
| CVD | Chemical Vapor Deposition |
| CVF | Carbide Volume Fraction |
| CVN | Charpy V-notch |
| d | (Average) Grain Size |
| d_{case} | Case Carburizing Depth |
| d_{eff} | Effective Grain Size |
| d_{lath} | Mean Lath Size |
| d_{ND} | Average Grain Size – Normal to Rolling Direction |
| d_{RD} | Average Grain Size - Parallel to Rolling Direction |
| d_{TD} | Average Grain Size – Transverse to Rolling Direction |
| d₅₀ | 50% of Particles below Value |
| d₉₀ | 90% of Particles below Value |
| d_{90%} | Effective Grain Size from Cumulative Size Distribution (90 th percentile) |
| DBT | Dropped Ball Test |
| DBTT | Ductile Brittle Transition Temperature |
| DI | Critical Diameter for Hardenability |
| DIC | Critical Diameter of Iron-carbon Base Composition or Differential Interference Contrast |
| D_{max} | Maximum Scatter Range of Distortion |
| D_{mean} | Mean Scatter Range of Distortion |
| D_{min} | Minimum Scatter Range of Distortion |

| | |
|-----------------------|---|
| Do | Hydrogen Diffusivity |
| DP | Dual Phase |
| DQ | Direct Quench |
| DQT, DQ+T | Direct Quenched and Tempered |
| DRX | Dynamic Recrystallization |
| DSC | Differential Scanning Calorimetry |
| D₅₀ | 50% of Particles Greater than Value Given |
| E | Young's Modulus |
| EBS | Electron Back Scattered Diffraction |
| ECD | Equivalent Circle Diameter |
| ECS | Standard Calomel Electrode |
| EDM | Electrical Discharge Machining |
| EDS/EDX | Energy Dispersive (X-ray) Spectroscopy |
| EHSS | Extra High Strength Steel |
| Eht | Case Hardened Depth |
| EME | Energy, Mining and Environment |
| EMF | Experimental Wear Resistant Material |
| EN | Euronorm |
| EPMA | Electron Probe Microanalysis |
| ESR | Electro Slag Remelting |
| E(US) | Upper Shelf Energy (Charpy) |
| EW | Electrowinning (Process) |
| f | Feed Rate |
| f_m | Profile Deviation |
| F | Contact Normal Force |
| FE | Finite Element |
| FEM | Finite Element Modelling |
| FESEM | Field Emission Scanning Electron Microscopy |
| FLC | Field Laboratory Correlation |

| | |
|-------------------------------------|---|
| F_{max} | Maximum Load |
| F_N, F_n | Normal Force |
| FP | Ferrite/Pearlite (Annealed) |
| F_r | Average Resultant Force |
| FRT | Finish Rolling Temperature |
| FSSS | Fisher Sub-sieve Size |
| F_t | Nominal Tangential Load |
| FWR | Flank Wear Rate |
| F_{yd} | Yield Load |
| F80 | Ore Feed 80% Passing Size |
| GB | Granular Bainite |
| GET | Ground Engaging Tool |
| GMAW | Gas Metal Arc Weld |
| h | Indentation Depth or Displacement (Nanoindentation) |
| h_{ex} | Chip Thickness |
| h_{max} | Maximum Indentation Depth/Displacement (Nanoindentation) |
| H | Hardness of Material Being Worn |
| HAADF-STEM | High Angle Annular Dark Field Scanning Transmission Electron Microscopy |
| HAZ | Heat Affected Zone |
| HB, HBW | Hardness Brinell |
| HDPE | High Density Polyethylene |
| HEM | High Efficiency Mining |
| H_i | Indentation Hardness (Nanoindentation) |
| HIP | Hot Isostatic Pressing |
| HNSA | High Normal Stress Abrasion |
| H_p | Hardness Relationship between Interacting Wear Components |
| HP | Holloman Parameter or Hot Pressing |
| HR | Hot Rolling |
| HRA | Rockwell A Hardness |

| | |
|---|--|
| HRC | Rockwell C Hardness |
| HSA | High Stress Abrasion |
| HSCA | High Stress Comminution Abrasion |
| HSGA | High Stress Grinding Abrasion |
| HTT | High Temperature Tempering |
| HV | Vickers Hardness |
| HV_{ret} | Relative Hardness (Vickers) |
| IC-SBAT | Inner Circumference Sliding Bed Abrasion Test |
| IC-WPET | Inner Circumference Wet Particle Erosion Test |
| IF | Interstitial Free |
| IPF | Inverse Pole Figure |
| ISE | Indentation Size Effect (Nanoindentation) |
| ISO | International Organization for Standardization |
| k, k_v | Wear Rate |
| K | Wear Coefficient in Abrasive Wear Equation |
| K_B | Hall-Petch Coefficient in Ductile Brittle Transition Temperature Predictive Equation |
| K_r | Hall-Petch Coefficient for Cleavage |
| K_{1c} | Fracture Toughness Parameter |
| K_r | Lead Angle |
| KS | Kurdjumov-Sachs (Crystallographic Relationship) |
| K_v, k_{total} | Total Wear Rate |
| K_y | Hall-Petch Coefficient for Strength |
| K₁ | Constant Indicating the Sharpness of Abrasive Particles |
| K₂ | Ratio of Volume of Material Removed to Volume of Groove |
| LB | Lower Bainite |
| LF + RH | Ladle Furnace + Degassing |
| LNG | Liquid Natural Gas |
| L_o | Gauge Length |
| LOM | Light Optical Microscopy |

| | |
|------------------------------|---|
| LPG | Liquid Petroleum Gas |
| LPS | Liquid Phase Sintering |
| LSA | Low Stress Abrasion |
| LSCM | Laser Scanning Confocal Microscopy |
| LSSA | Low Stress Sliding Abrasion |
| LTT | Low Temperature Tempering |
| m_n, M_n | Gear Module |
| M | Martensite |
| MA | Martensite Austenite (Constituent) |
| MBT | Marked Ball Test |
| MBWT | Marked Ball Wear Test |
| MC | Carbide Type or Melting down with the Metallic Charge |
| ME | Gear Quality Requirements which can be met by Experienced Manufacturers |
| MF | Multiplying Factor |
| ML | Minimum Quality Requirement for Gears |
| MMC | Metal Matrix Composite |
| MQ | Quality Requirements for Gears Suitable for Higher Allowable Stresses |
| MRO | Maintenance, Repair and Operations |
| M_s | Martensite Start Temperature |
| MS | Addition to the Metal Stream During Ladle Tapping |
| n | Number of Cycles (Fatigue) or Strain Hardening Exponent |
| N | Normalized |
| ND | Normal Direction (Through Thickness) |
| NRC | National Research Council (Canada) |
| NTP | National Toxicology Program |
| OEM | Original Equipment Manufacturer |
| OHS | Operational Health and Safety |
| OIM | Orientation Imaging Microscopy |

| | |
|-------------------------|--|
| OM | Optical Microscopy |
| p_H | Local Hertzian Contact Stress |
| pH | Acidity/Alkalinity Index |
| ppm | Parts per Million |
| P | Load or Emulsion Pressure |
| PAGS | Prior Austenite Grain Size |
| PAT | Pin Abrasion Test |
| PM | Powder Metallurgy |
| PN | Plasma Nitriding |
| P_{0max} | Maximum Contact Stress |
| PREN | Pitting Resistance Equivalent Number |
| PSC | Primary Separation Cell |
| PTAW | Plasma Transferred Arc Welding |
| PVD | Physical Vapor Deposition |
| P.V | Load Carrying Capacity (Contact Pressure x Sliding Velocity) |
| P80 | 80% Passing Size of the Mill Product |
| Q | Activation Energy or Quenched |
| QD | Quantitative Data |
| QT, Q&T | Quenched and Tempered |
| r | Aspect Ratio (of Grains) |
| rpm | Revolutions per Minute |
| R | Gas Constant or Radius |
| Ra | Surface Roughness Measurement |
| RA | Retained Austenite or Residual Austenite |
| RCR | Recrystallization Controlled Rolling |
| Rd | Bar Diameter |
| RD | Relative Density or Rolling Direction |
| REACH | Registration Evaluation Authorization and Restriction of Chemical Substances |
| RLT | Recrystallization Limit Temperature |

| | |
|-------------------------------------|---|
| R_m, R_m | Tensile Strength |
| R_{pk} | Surface Roughness Measurement |
| R_{p0.2} | 0.2% Proof Strength |
| RQ | Reheat Quenched |
| RQT, RQ-T | Reheat Quenched and Tempered |
| RST | Recrystallization Stop Temperature |
| RT | Room Temperature |
| RTE | Reverse Temper Embrittlement |
| R_{tot} | Total Reduction below Recrystallization Temperature |
| RWAT | Rubber Wheel Abrasion Test |
| R0 | Reduction of Area of Uncharged Specimen (Hydrogen Charging) |
| R1 | Reduction of Area of Charged Specimen (Hydrogen Charging) |
| S, s | Sliding Distance or Crater Wear Depth or Pearlite Interlamellar Spacing |
| SAE | Society of Automotive Engineers |
| SAG | Semi-autogenous Grinding |
| SD | Simple Dumping on the Bath Surface |
| SE | Secondary Electron (Detector) |
| SEI | Secondary Electron Image |
| SEM | Scanning Electron Microscope/Microscopy |
| SIMS | Secondary Ion Mass Spectroscopy |
| SMAW | Submerged Metal Arc Weld |
| S_o | Cross Sectional Area |
| SPS | Spark Plasma Sintering |
| SRX | Static Recrystallization |
| SSC | Sulfide Stress Cracking |
| S_v | Surface Area per Unit Volume |
| SWAT | Steel Wheel Abrasion Test |
| S-N | Stress v Number of Cycles (Fatigue Endurance) |
| t | Tool Life |

| | |
|---------------------------------------|---|
| T | Temperature |
| T_a | Fracture Time in Air |
| T_{AUS} | Austenitization Temperature |
| T_B | Ductile Brittle Transition Temperature (Charpy) |
| TBM | Tunnel Boring Machines or Thyssen Blowing Metallurgy |
| T_c | Pearlite Transition Temperature |
| TD | Toyota Diffusion (Process) or Transverse to Rolling Direction |
| TEM | Transmission Electron Microscope or Microscopy |
| TIFF | Tooth Interior Fatigue Fracture |
| TMCP | Thermomechanical Controlled Processing |
| T_{nr}, T_{NR} | Non-recrystallization Temperature |
| T_o | Temperature at which Yield Strength Equals Cleavage Stress |
| TRD | Thermo-reactive Diffusion |
| TRS | Transverse Rupture Strength |
| T_s | Fracture Time in Solution |
| TS | Tensile Strength |
| TSRU | Tailings Solvent Recovery Units |
| T(US) | Upper Shelf Temperature (Charpy) |
| T(34J/cm²) | 34J Transition Temperature (Charpy) |
| u_y | Maximum Displacement (Nanoindentation) |
| UTS | Ultimate Tensile Strength |
| v | Tangential Sliding Velocity or Fatigue Testing Frequency |
| v_b | Flank Wear |
| V, v | Cutting Speed or Sliding Velocity |
| VAR | Vacuum Arc Remelting |
| V_b | Flank Wear Depth |
| V_c | Cutting Speed |
| V_f | Feed Rate |
| VIF | Vickers Indentation Fracture |

| | |
|--------------------------|---|
| V_m | Molar Volume |
| VSI | Vertical Shaft Impact (Crusher) |
| V_{10min} | Critical Cutting Speed for 10 Minute Tool Life |
| V_{30min} | Critical Cutting Speed for 30 Minute Tool Life |
| V_{45min} | Critical Cutting Speed for 45 Minute Tool Life |
| W | Wear Rate Expressed as Volume Removed or Volume of Debris Created per Unit Time |
| WCI | White Cast Iron |
| WDS | Wavelength Dispersive X-ray Spectroscopy |
| W_{el} | Elastic Energy (Nanoindentation) |
| W_{tot} | Total Indentation Energy (Nanoindentation) |
| XRD | X-ray Diffraction |
| y | Material Depth |
| YS | Yield Strength |
| Y_x | Size Factor for Tooth Root Bending Strength |
| z | Number of Teeth (Gear) |

AUTHOR INDEX

International Symposium on Wear Resistant Alloys for the Mining and Processing Industry

A

| | |
|-------------------|-----|
| Albertin, E. | 253 |
| Araki, K. | 187 |
| Azizi, M. | 505 |

B

| | |
|--------------------|-----|
| Banov, C.H.N. | 463 |
| Barreto, J.L. | 75 |
| Bennet, P.J. | 289 |
| Bonnevie, M. | 19 |

C

| | |
|-----------------------------|---------|
| Canpolat, A. | 159 |
| Cardoso, M.K. Ferreira | 75 |
| Cayla, J.L. | 173 |
| Chen, Xiangru | 393 |
| Cornish, L.A. | 547 |
| Cruz, E.B. | 407,463 |

D

| | |
|-------------------|-----|
| Dietrich, A. | 159 |
|-------------------|-----|

F

| | |
|----------------------|-----|
| Feistritzer, B. | 385 |
| França, É. | 75 |
| François, H. | 19 |
| Fridman, D.P. | 407 |

G

| | |
|--------------------|--------------|
| Galvani, E.T. | 463 |
| Gates, J.D. | 289 |
| Genga, R.M. | 547 |
| Gu, Linhao | 47 |
| Guo, Aimin | 47, 235, 393 |

H

| | |
|----------------------|----------|
| Hansson, P. | 223 |
| Hippenstiel, F. | 277, 351 |
| Huang, S.G. | 521 |
| Hui, S. | 67 |
| Huth, S. | 197 |

J

| | |
|--------------------|-----|
| Jianhua, Ding | 235 |
| Just, C. | 173 |

K

| | |
|-----------------|-----|
| Kern, A. | 159 |
| Krauss, G. | 93 |

L

| | |
|----------------------|-----|
| Le Quilliec, G. | 535 |
| Leroy, R. | 535 |
| Li, Hiacheng | 393 |
| Liandeng, Yao. | 235 |

M

| | |
|---------------------|-------------------|
| Ma, Changwen | 47 |
| McInnes, L.J. | 289 |
| Mohrbacher, H. | 93, 351, 427, 521 |
| Morandau, A. | 535 |
| Morris, J.W. | 93 |
| Murota, Y. | 187 |

N

| | |
|----------------------------|----|
| Nogueira, M.A. Stuart | 75 |
|----------------------------|----|

O

| | |
|-----------------|-----|
| Ohmori, A. | 187 |
|-----------------|-----|

P

| | |
|-----------------|-----|
| Pérez, V. | 1 |
| Pöhl, F. | 487 |
| Polese, C. | 547 |

R

| | |
|------------------|---------|
| Richard, C. | 535 |
| Rosa, H.L. | 75, 463 |

S

| | |
|----------------------|-----|
| Schneider, A.S. | 173 |
| Schwinn, V. | 173 |
| Seifert, M. | 197 |
| Siebert, S. | 197 |
| Silvestre, L.M. | 75 |
| Simões, S. | 463 |
| Sinatora, A. | 253 |
| Sixin, Zhao | 235 |
| Sobiyi, K. | 547 |
| Soltanieh, M. | 505 |

T

| | |
|-----------------------|----------|
| Takayama, N. | 187 |
| Theisen, W. | 197, 487 |
| Tobie, Th. | 351 |
| Tschersich, H-J. | 159 |
| Tunstall, B.R. | 289 |

V

| | |
|--------------------|-----|
| Villaseca, D. | 1 |
| Vleugels, J. | 521 |

W

| | |
|----------------------|--------------------|
| Wang, Zhenqiang | 47 |
| Weddeling, A. | 487 |
| Woydt, M. | 427, 521, 535, 547 |

X

| | |
|---------------|-----|
| Xu, Yang | 393 |
|---------------|-----|

Y

| | |
|----------------------|-----|
| Yongqing, Zhang | 235 |
| You, Ming | 393 |

Z

| | |
|----------------------|-----|
| Zhai, Qijie | 393 |
| Zhang, Wei | 393 |
| Zhang, Yongqing | 47 |
| Zhou, Deguang | 47 |

SUBJECT INDEX

International Symposium on Wear Resistant Alloys for the Mining and Processing Industry

A

| | |
|------------------------------------|--------------|
| Abrasion | 67, 253, 427 |
| Abrasion Resistance | 187 |
| Abrasion Resistant Materials | 253 |
| Abrasive Wear | 19, 463 |
| AHSS | 47 |
| Alloy Modifications | 351 |

B

| | |
|-------------------------------|-----|
| Ball Mill Abrasion Test | 289 |
| Bearing Steels | 197 |
| Binder | 427 |
| Buckets | 75 |

C

| | |
|-------------------------------|-----|
| Carbide | 487 |
| Carbide Distribution | 385 |
| Carbide Separation | 385 |
| Case Carburizing | 93 |
| Case Carburizing Steels | 351 |
| Castings | 407 |
| Cement and Aggregates | 19 |
| Cemented Carbide | 521 |
| Centrifugal Casting | 385 |
| Charpy Toughness | 173 |
| Chromium Iron | 19 |
| Co | 547 |
| Cobalt | 535 |
| Collaboration | 67 |
| Consortium | 67 |
| Coolant-free | 547 |
| Copper Mining | 1 |
| Cost Reduction | 67 |
| Cost Saving | 1 |
| Crater Wear | 547 |
| CrMo Steel | 393 |
| Cutter Rings | 385 |
| Cutting Tools | 535 |

D

| | |
|--------------------------------------|--------------|
| Delayed Fracture | 235 |
| Diffusion | 505 |
| Diffusion Alloying | 197 |
| Direct Quenching | 93, 173, 235 |
| Direct Quenching and Tempering | 235 |
| Disc Cutters..... | 385 |
| Ductility | 393 |

E

| | |
|----------------------------|-----|
| EBSD | 173 |
| Effective Grain Size | 93 |
| Embrittlement | 93 |
| Erosion-corrosion | 67 |

F

| | |
|------------------------------------|----------|
| Fe ₃ Al | 535, 547 |
| FeNbC | 407, 463 |
| Ferrous Alloys | 1 |
| Field-laboratory Correlation | 289 |
| Finish Rolling Temperature | 173 |
| Finite Element Method | 487 |
| Flank Wear | 547 |
| Forging Tools | 277 |
| Fracture Modes | 93 |
| Fracture Toughness | 521 |
| Friction | 427 |

G

| | |
|----------------------------|----------|
| Gear Failures | 351 |
| Gear Performance | 351 |
| Gear Strength Values | 351 |
| Gear Testing | 351 |
| Gears | 351 |
| Grain Growth | 521 |
| Grain Refinement | 187, 351 |
| Grain Size | 173 |
| Grinding Balls | 1 |

H

| | |
|-----------------------------------|--------------------|
| Hard Coatings | 505 |
| Hard Rock Mining | 67 |
| Hardenability | 351 |
| Hardfacing | 463 |
| Hardmetal | 521 |
| Hardness | 173, 277, 427, 521 |
| Hard-turning | 547 |
| Heat Treatment | 393 |
| Heavy Plate | 235 |
| Heavy-duty Mining Dump Truck..... | 47 |
| High Normal Stress Abrasion | 289 |
| Hot Work Steel | 277 |
| Hydrogen Embrittlement | 187 |

I

| | |
|------------------------|-----|
| Impact Toughness | 393 |
| Impact Wear | 19 |

| | |
|---------------------------|-----|
| Inserts | 535 |
| Interrupted Milling | 547 |

L

| | |
|-----------------------------------|-----|
| Laser Cladding | 463 |
| Lightweight | 47 |
| Liners | 1 |
| Low Stress Sliding Abrasion | 289 |
| Low Temperature Toughness | 187 |

M

| | |
|------------------------------------|-----------------|
| Machinability | 547 |
| Manufacturing | 197 |
| Manufacturing Time | 223 |
| Martensite | 93 |
| Martensitic Stainless Steels | 197 |
| Martensitic Steels | 289 |
| Matrix Influence..... | 487 |
| Mechanical Properties | 235, 487 |
| Metal..... | 427 |
| Metal Matrix Composite | 19, 427 |
| Microalloying..... | 187, 277 |
| Microstructure | 173, 521 |
| Milling | 223 |
| Mining | 19, 253 |
| Molybdenum | 1, 93, 159, 351 |
| Mould | 223 |

N

| | |
|-------------------------------|------------------------------|
| Nanoindentation | 487 |
| NbC | 463, 487, 547 |
| Nickel | 351 |
| Niobium | 47, 75, 93, 159, 173 |
| | 187, 235, 253, 351, 393, 505 |
| Niobium Carbide | 197, 385, 407 |
| | 427, 463, 521, 535 |
| Niobium Carbide Coating | 505 |
| Nitriding | 223 |

O

| | |
|-----------------|----|
| Oil-sands | 67 |
|-----------------|----|

P

| | |
|--------------------|-----|
| Plate | 173 |
| PM Steels | 197 |
| Precipitates | 93 |

R

| | |
|-------------------------|-----|
| Recrystallization | 173 |
| Reheat Quenching | 93 |

S

| | |
|-----------------------------------|-----|
| SAG Mills | 1 |
| Sintering | 521 |
| Sliding-bed Abrasion Test | 289 |
| Slurry Erosion | 67 |
| Solubility | 427 |
| SPS | 547 |
| Steel | 75 |
| Steels For Polymer Industry | 197 |
| Strength | 173 |
| Surface | 505 |
| Surface Engineering | 223 |

T

| | |
|------------------------------|------------------------|
| Tempering | 93 |
| Tempering Resistance | 351 |
| Thermochemical Process | 505 |
| Thermodynamic Equilibrium | |
| Calculations | 197 |
| TiC | 487 |
| Tool Steel | 223 |
| Toughness | 47, 235, 277, 351, 427 |
| TRD | 505 |
| Tunnel Boring | 385 |
| Turning | 535 |

U

| | |
|---------------------------|-----|
| Ultra High Strength | 235 |
|---------------------------|-----|

V

| | |
|----------|-----|
| VC | 487 |
|----------|-----|

W

| | |
|--------------------------------|-------------------|
| WC | 487, 547 |
| Wear | 75, 407, 427, 535 |
| Wear Evaluations | 67 |
| Wear Protection | 463 |
| Wear Rates | 1 |
| Wear Resistance | 47, 187, 277 |
| Wear Resistant | 159 |
| Wear Resistant Materials | 67 |
| Wear Resistant Steel | 173 |
| Wear-simulation | 159 |
| Weldability | 47, 187, 235 |
| Wheel Loaders | 75 |
| White Cast Irons | 289 |

Y

| | |
|----------------------|-----|
| Yield Strength | 393 |
|----------------------|-----|